

NATIONAL AERONAUTICS AND SPACE ADMINISTRATION

Space Programs Summary No. 37-40, Volume IV

for the period June 1, 1966 to July 31, 1966

Supporting Research and Advanced Development

FACILITY FORM 602	N67 12101	N67 12149
	(ACCESSION NUMBER)	(THRU)
	242 242	1
	(PAGES)	(CODE)
	CR-79917	34
	(NASA CR OR TMX OR AD NUMBER)	(CATEGORY)



JET PROPULSION LABORATORY
CALIFORNIA INSTITUTE OF TECHNOLOGY
PASADENA, CALIFORNIA

GPO PRICE \$ _____

August 31, 1966

CESTI \$ _____

HC) 3.75

MF) 1.25

NATIONAL AERONAUTICS AND SPACE ADMINISTRATION

Space Programs Summary No. 37-40, Volume IV

for the period June 1, 1966 to July 31, 1966

Supporting Research and Advanced Development

JET PROPULSION LABORATORY
CALIFORNIA INSTITUTE OF TECHNOLOGY
PASADENA, CALIFORNIA

August 31, 1966

Preface

The *Space Programs Summary* is a six-volume, bimonthly publication that documents the current project activities and supporting research and advanced development efforts conducted or managed by JPL for the NASA space exploration programs. The titles of all volumes of the *Space Programs Summary* are:

- Vol. I. The Lunar Program (Confidential)
- Vol. II. The Planetary-Interplanetary Program (Confidential)
- Vol. III. The Deep Space Network (Unclassified)
- Vol. IV. Supporting Research and Advanced Development (Unclassified)
- Vol. V. Supporting Research and Advanced Development (Confidential)
- Vol. VI. Space Exploration Programs and Space Sciences (Unclassified)

The *Space Programs Summary*, Vol. VI consists of an unclassified digest of appropriate material from Vols. I, II, and III; an original presentation of technical supporting activities, including engineering development of environmental-test facilities, and quality assurance and reliability; and a reprint of the space science instrumentation studies of Vols. I and II.



W. H. Pickering, Director
Jet Propulsion Laboratory

Space Programs Summary No. 37-40, Volume IV

Copyright © 1966, Jet Propulsion Laboratory, California Institute of Technology

Prepared under Contract No. NAS 7-100, National Aeronautics & Space Administration

Contents

GUIDANCE AND CONTROL DIVISION

I. Spacecraft Power	1
A. Thermionic Converter and Generator Development,	
Task No. 323-30201-2-3420 (123-33-02-01), P. Rouklove	1 ✓
References	14
II. Spacecraft Control	15
A. Strapdown Electrically Suspended Gyro Development,	
Task No. 325-70501-2-3440 (125-17-01-02), T. J. Donlin	15 ✓
B. Spacecraft Antenna Pointing,	
Task No. 325-90401-2-3440 (125-19-03-02), G. E. Fleischer	16 ✓
III. Guidance and Control Research	20
A. Titanium Oxide Thin Films,	
Task No. 329-21801-1-3450 (129-02-05-09), J. Maserjian	20 ✓
B. The Feasibility of Achieving Optical Densities in Magnetic Information Storage,	
Task No. 329-21401-1-3450 (129-02-05-06), D. I. Tchernev	22 ✓
References	23

ENGINEERING MECHANICS DIVISION

IV. Materials	25
A. Ceramic Research,	
Task No. 329-31101-1-3510 (129-03-04-01), E. C. de Wys and M. H. Leipold	25 ✓
References	26
V. Applied Mechanics	27
A. The effect of Uncertainties in Transport Properties on Prediction of Stagnation Point Heat Transfer,	
Task No. 324-71401-2-3530 (124-07-01-01), D. W. Zeh and T. E. Horton	27 ✓
B. Comparison of Entry-Body Shapes for Total Equilibrium Radiation Under Mars Entry Conditions,	
Task No. 324-71401-2-3530 (124-07-01-01), H. J. Stumpf	28 ✓
C. Flow Field Computations for Blunt Bodies in Planetary Atmospheres,	
Task No. 324-71401-2-3530 (124 07-01-01), H. J. Stumpf	31 ✓
D. Environmental and Physical Effects on the Response of Balsa Wood as an Energy Dissipator,	
Task No. 384-60101-2-3530 (186-68-01-01), A. C. Knoell	33 ✓
E. Continuing Development of Phenolic Honeycomb as an Energy Dissipator,	
Task No. 384-60101-2-3530 (186-68-01-01), A. C. Knoell	34 ✓
References	35

Contents (Cont'd)

VI. Electronic Parts Engineering	36
A. Accelerated Life Testing of Transistors,	
Task No. 384-00501-2-3540 (186-70-01-05), E. Klippenstein	36 ✓
VII. Electromechanical Engineering Support	37
A. Development of Wirecon Utility Test Module,	
Task No. 384-85301-2-3570 (186-58-13-03), E. R. Bunker, Jr.	37 ✓
ENVIRONMENTAL SIMULATION DIVISION	
VIII. Aerodynamic Facilities	41
A. Wind Tunnels,	
Task No. 324-70400-2-3733 (127-07-04-02), J. T. Welton;	
Task No. 324-70100-7-3732 (124-07-04-01), B. Walker and W. R. Kerr;	
Task No. 324-70100-7-3734 (123-07-04-01), W. Marko;	
Task No. 324-70100-7-3735 (124-07-04-01), E. R. Bate, Jr.	41 ✓
PROPULSION DIVISION	
IX. Liquid Propulsion Systems	47
A. Advanced Liquid Propulsion Systems,	
Task No. 331-10201-2-3840 (731-12-03-03), L. R. Toth, H. B. Stanford,	
and W. F. MacGlashan	47 ✓
X. Research and Advanced Concepts	50
A. Lithium-Boiling Potassium Rankine Cycle Heat-Transfer Data,	
Task No. 320-70201-2-3830 (120-27-06-02), G. M. Kikin	50 ✓
B. Liquid MHD Power Conversion,	
Task No. 320-70301-2-3830 (129-27-06-03), D. G. Elliot, D. J. Cerini, and L. G. Hays	63 ✓
References	72
XI. Solid Propellant Engineering	73
A. Applications Technology Satellite (ATS) Motor Development,	
Task No. 724-00081-7-3810 (630-01-00-00), R. G. Anderson and R. A. Grippi	73 ✓
B. The Interior Ballistics of the Fluid Controlled Solid Rocket Motor,	
Task No. 328-21101-2-3810 (128-32-06-01), O. K. Heiney	75 ✓
Reference	79
XII. Polymer Research	80
A. Degree of Crosslinking of Styrene Butadiene Rubber Glass Bead Composites,	
Task No. 328-20301-1-3820 (128-32-05-02), R. F. Fedors and R. F. Landel	80 ✓
B. A Theory of Particle-Particle Interaction Describing the Mechanical Properties of Dental Amalgam,	
Task No. 328-20301-1-3820 (128-32-05-02), B. G. Moser and R. F. Landel	84 ✓

Contents (Cont'd)

C. Nuclear Magnetic Resonance Spectroscopy of Derivatives of Trifluoromethylsulfenyl Chloride,	93 ✓
Task No. 328-20401-1-3820 (128-32-05-03), D. D. Lawson and J. D. Ingham	
D. The Reaction of Carboxyl and Amino Terminated Prepolymers With Polyepoxides,	95 ✓
Task No. 329-30501-1-3820 (129-03-11-04), S. H. Kalfayan and B. A. Campbell	
E. Studies on Sterilizable Elastomers,	98 ✓
Task No. 384-62701-1-3820 (186-68-13-03), E. F. Cuddihy and J. Moacanin	
F. An Automatic Ethylene Oxide Decontamination System,	103 ✓
Task No. 384-83802-2-3820 (186-58-13-02), R. H. Silver and S. H. Kalfayan	
References	106

SPACE SCIENCES DIVISION

XIII. Space Instruments	109
A. Pulse Height Analyzer Memory,	109 ✓
Task No. 383-32601-2-3230 (185-37-20-04), W. J. Schneider	
XIV. Bioscience	119
A. Gas Chromatography Column Development for Analysis of the Martian Atmosphere,	119 ✓
Task No. 386-51201-2-3260 (189-55-02-08), W. F. Wilhite	
B. Soil Studies—Desert Microflora. XIII. Identification of Some Algae From Antarctica,	123 ✓
Task No. 386-50301-1-3260 (189-55-04-01), R. E. Cameron	
References	133
XV. Physics	134
A. On Rostoker's Test Particle Theorem,	134 ✓
Task No. 329-20901-1-3280 (129-02-07-02), C.-S. Wu	
B. Reaction of O(¹ D) With Hydrogen, Part II: The Unscavenged Case,	137 ✓
Task No. 329-21001-1-3280 (129-02-03-02), W. B. DeMore	
References	140

TELECOMMUNICATIONS DIVISION

XVI. Spacecraft Telemetry and Command	143
A. A System Reorganization of the Spacecraft Encoder,	143 ✓
Task No. 325-31601-2-3340 (125-23-02-15), J. R. Kinkel	
B. A Definition of System Reliability,	154 ✓
Task No. 325-31601-2-3340 (125-23-02-15), J. F. Meyer	
C. On the Spectrum of Single-Sideband Phase Modulation by Normal Noise,	163 ✓
Task No. 384-61301-2-3340 (186-68-04-04), J. C. Springett	

Contents (Cont'd)

D. Tape Recorder With Incremental Playback Capabilities,	170	✓
Task No. 384-60901-2-3340 (186-68-03-01), E. Bahm		
References	175	
XVII. DSIF Engineering	176	
A. Antenna Structures: Evaluation Techniques of Reflector Distortions,	176	✓
Task No. 451-30600-2-3320 (150-22-13-06), M. S. Katow and L. W. Schmele		
References	184	
XVIII. Communications Elements Research	185	
A. RF Techniques: 90-Gc Millimeter Wave Work,	185	✓
Task No. 325-10901-1-3330 (125-21-03-04), C. T. Stelzried and W. V. T. Rusch		
B. RF Techniques: Mismatch Errors on Noise Temperature Measurements,	190	✓
Task No. 350-10700-1-3330 (150-22-11-07), T. Y. Otoshi		
References	197	
XIX. Spacecraft Radio	198	
A. Low Data Rate Telemetry RF System Development,	198	✓
Task No. 350-70600-2-3360 (150-22-17-06), R. B. Postal and C. M. Potts		
B. High Impact Antenna Study: Coaxial Cavity Radiator,	201	✓
Task No. 384-61501-2-3360 (186-68-04-06), K. Woo		
Reference	206	
XX. Communications Systems Research	207	
A. Combinatorial Communications: Search for Cyclic Hadamard Matrices,	207	✓
Task No. 325-10701-1-3310 (125-21-01-01), R. Thoene and S. W. Golomb		
B. Combinatorial Communications: Enumeration of a Special Class of Permutations,	208	✓
Task No. 325-10701-1-3310 (125-21-01-01), R. Stanley		
C. Coding Theory: Moments of Weight Distributions,	214	✓
Task No. 350-10900-1-3310 (150-22-11-09), R. Stanley		
D. Coding Theory: Efficient Solutions of Equations for Decoding,	216	✓
Task No. 350-10900-1-3310 (150-22-11-09), R. McEliece		
E. Coding Theory: The Index of Comma Freedom in Iterative Codes,	218	✓
Task No. 325-10601-1-3310 (125-21-02-03), J. Stiffler		
F. Digital Communications and Tracking: Calculation of Range-Clock Jitter,	219	✓
Task No. 451-20300-1-3310 (150-22-12-03), R. Tausworthe		
G. Data Compression: A Lower Bound for Epsilon Entropy,	225	✓
Task No. 350-70800-1-3310 (150-22-17-08), E. Posner and H. Rumsey, Jr.		

Contents (Cont'd)

H. Information Processing: A Bivariate Goodness-of-Fit Test, <i>Task No. 350-10900-1-3310 (150-22-11-09), T. Pitcher</i>	228 ✓
I. Communications Systems Development: Probability Distributions and Error Rates in Spacecraft Receivers, <i>Task No. 350-10800-1-3310 (150-22-11-08), W. Lindsey</i>	230 ✓
References	234

GUIDANCE AND CONTROL DIVISION

N67 12102

I. Spacecraft Power

A. Thermionic Converter and Generator Development

P. Rouklove

1. Introduction

The effort presented in this *Summary* covers a phase of the development of the Solar Energy Thermionic (SET) program. It describes the evaluation made at JPL of a four-converter thermionic generator designated JG-3. This generator was assembled by Thermo-Electron Engineering Company (TEEC) of Waltham, Massachusetts under Contract 950671. Also presented are the results of an effort directed to demonstrate automatic cesium reservoir temperature control. This effort was performed by Electro-Optical Systems (EOS), Pasadena, California, under Contract 951228.

2. JG-3 Thermionic Generator

a. Description. Tests of a five-converter generator were performed in a laboratory with electron bombardment

heating and also at the Table Mountain, California, test site using solar energy heating (Refs. 1 and 2). These tests indicated that: (1) the solar energy distribution in the generator cavity did not have a symmetric "ball of fire" configuration, and that (2) it was difficult to heat uniformly the emitters of converters located on five sides of a cubical cavity. Depending on the rim angle of the concentrator and its geometrical accuracy, the converter located in the side of the cavity opposite to the aperture could not be isothermally heated as compared with the four converters located on the sides of the generator block.

For these reasons it was decided to design and assemble a four-converter generator, locating the converters only on the four sides of the cubical cavity. The rear portion of the cavity was used as a radiator of excessive heat and as a reflector to obtain a better heat distribution in the cavity. A sectional view of the generator is presented in Fig. 1, and a view of the generator mounted on a test support is shown in Fig. 2.

Calculations performed during the design phase indicated the thermal distribution presented in Fig. 3. As a

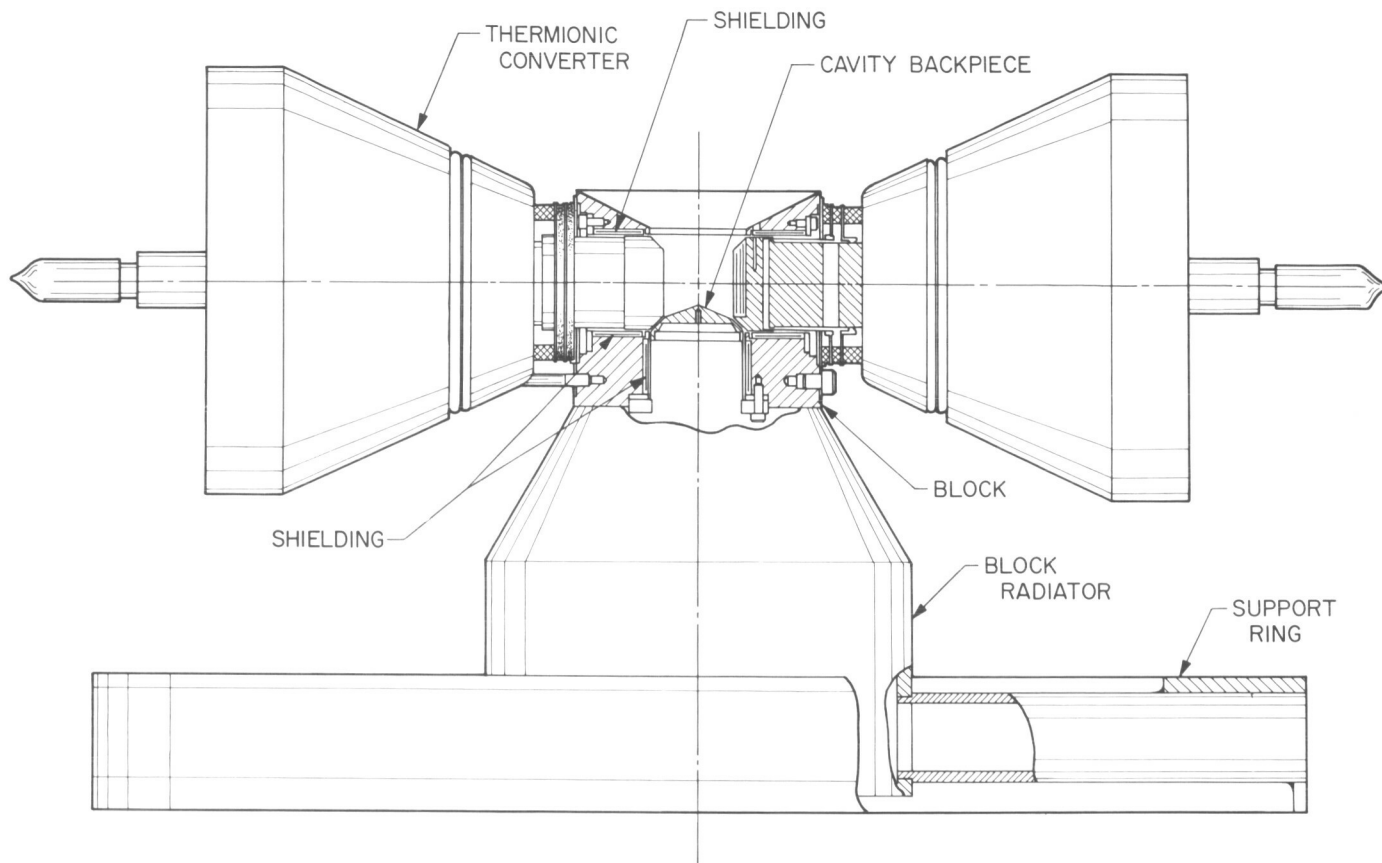


Fig. 1. Configuration IV, four-converter generator

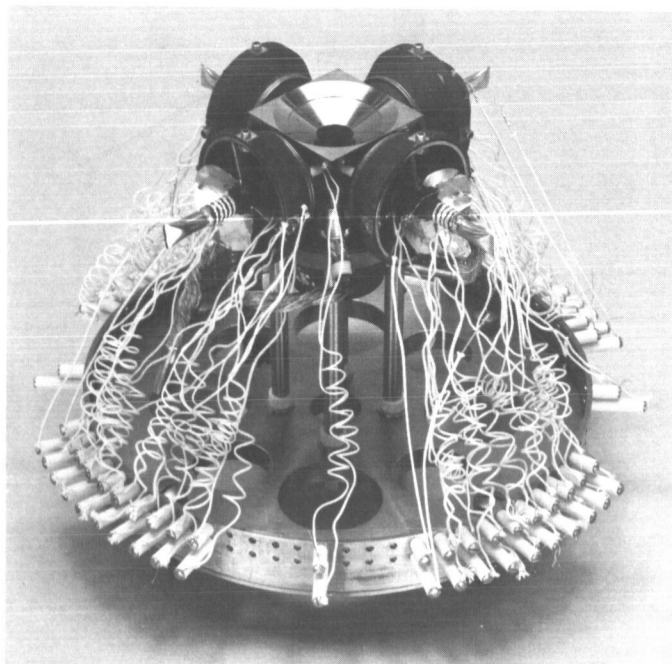


Fig. 2. Generator JG-3 mounted on test support

result of the geometrical inaccuracy of the concentrator (SPS 37-26, pp. 34-38; SPS 37-30, pp. 35-39), the cavity aperture was enlarged from the 0.5-in. diameter used in the previous generators to 0.7-in. diameter; and the front cone, made of polished tungsten, was insulated by heat shields from the generator block. Heat shields were also added between the converter body and the generator block to reduce thermal losses.

Prior to assembly, a mockup of the generator was subjected to environmental and thermal distribution tests. This mockup included dummy converters representing the weight, mass distribution, and attachment method of real thermionic converters. The mockup successfully completed vibration tests in three orthogonal axes of 0 to 20 *g* at frequencies up to 2000 cps and shock tests of 100 *g* for 0.5 msec without apparent damage.

b. Converters. The converters used in the generator JG-3 are of the recently developed Series VIII (SPS 37-31, pp. 53-58). A cutaway section of converter VIII-P-3 is presented in Fig. 4. Fig. 5 presents the *I-V* characteristics

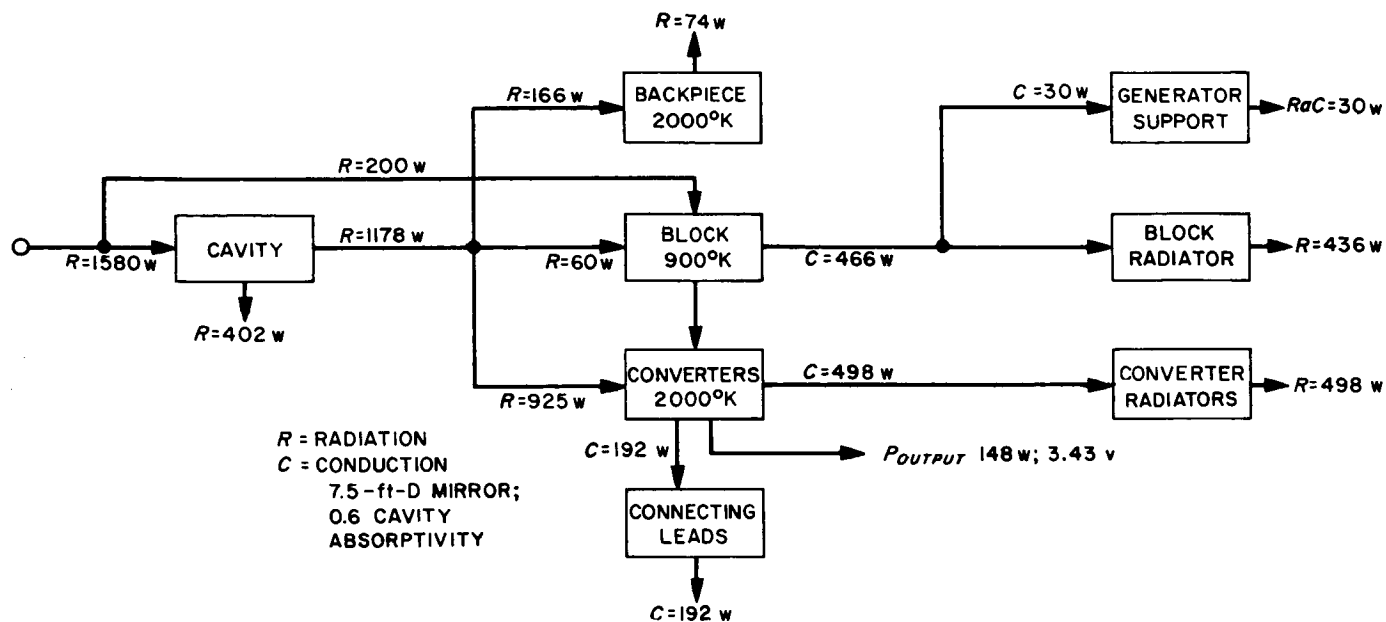


Fig. 3. Four-converter generator thermal analysis

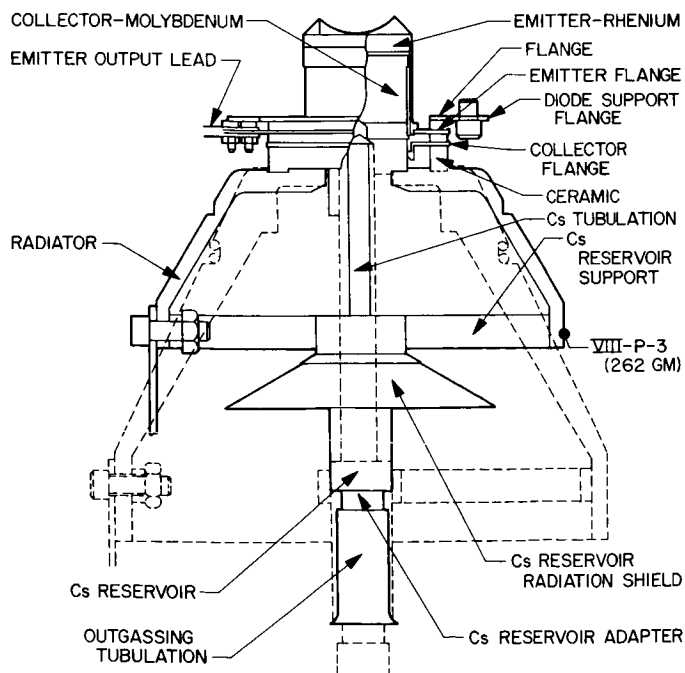


Fig. 4. Series VIII converter cutaway view

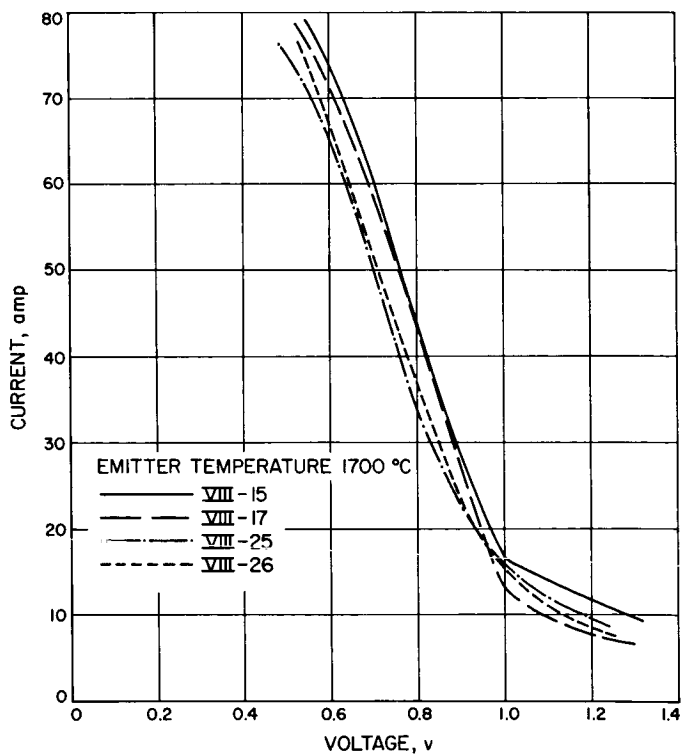


Fig. 5. Series VIII converter characteristics

of the four converters of this series used in the generator JG-3; further characteristics are presented in Table 1. The emitter slug of the converters of Series VIII is a composite with a 20-mil thick rhenium disk, as an emitting surface, attached by isostatic pressure bonding to a

100-mil thick tantalum slug. This technique was used to avoid the excessive cost of machining massive electrodes of costly rhenium. Also, the technique for welding rhenium parts was not perfected at the time of converter procurement.

Table 1. Converter characteristics

Parameter	VIII-15				VIII-17				VIII-25				VIII-26			
	1700		1800		1700		1800		1700		1800		1700		1800	
E_b	0.8	0.6	0.8	0.6	0.8	0.6	0.8	0.6	0.8	0.6	0.8	0.6	0.8	0.6	0.8	0.6
I_b	42.5	75.3	63.5	85.5	42.5	70.0	54.5	84.0	35.1	66.3	59.0	81.5	33.3	64.5	60.0	82.5
W	34	45	51	51	34	42	48	50	28	40	47	49	27	39	48	50
E_{oc}	2.1	1.7	1.8	1.6	1.9	1.9	1.9	1.7	2.1	1.8	1.8	1.7	2.0	1.7	1.2	1.6
W_{in}	344	445	469	532	330	409	434	518	311	399	447	518	302	396	462	526
η_o	9.9	10.2	10.8	9.7	10.3	10.3	11.0	9.7	9.0	10.0	10.6	9.4	8.8	9.8	10.4	9.4
$T_{csr}^{\circ}C$	321	353	344	352	330	346	348	353	316	344	345	354	311	332	341	360
$T_{sealr}^{\circ}C$	586	657	658	705	602	667	672	730	597	674	678	719	593	669	679	728
$T_{colr}^{\circ}C$	624	764	724	850	577	683	668	720	610	737	745	819	617	762	765	873
$T_{radr}^{\circ}C$	540	625	622	680	533	605	612	657	530	615	617	666	524	615	617	675

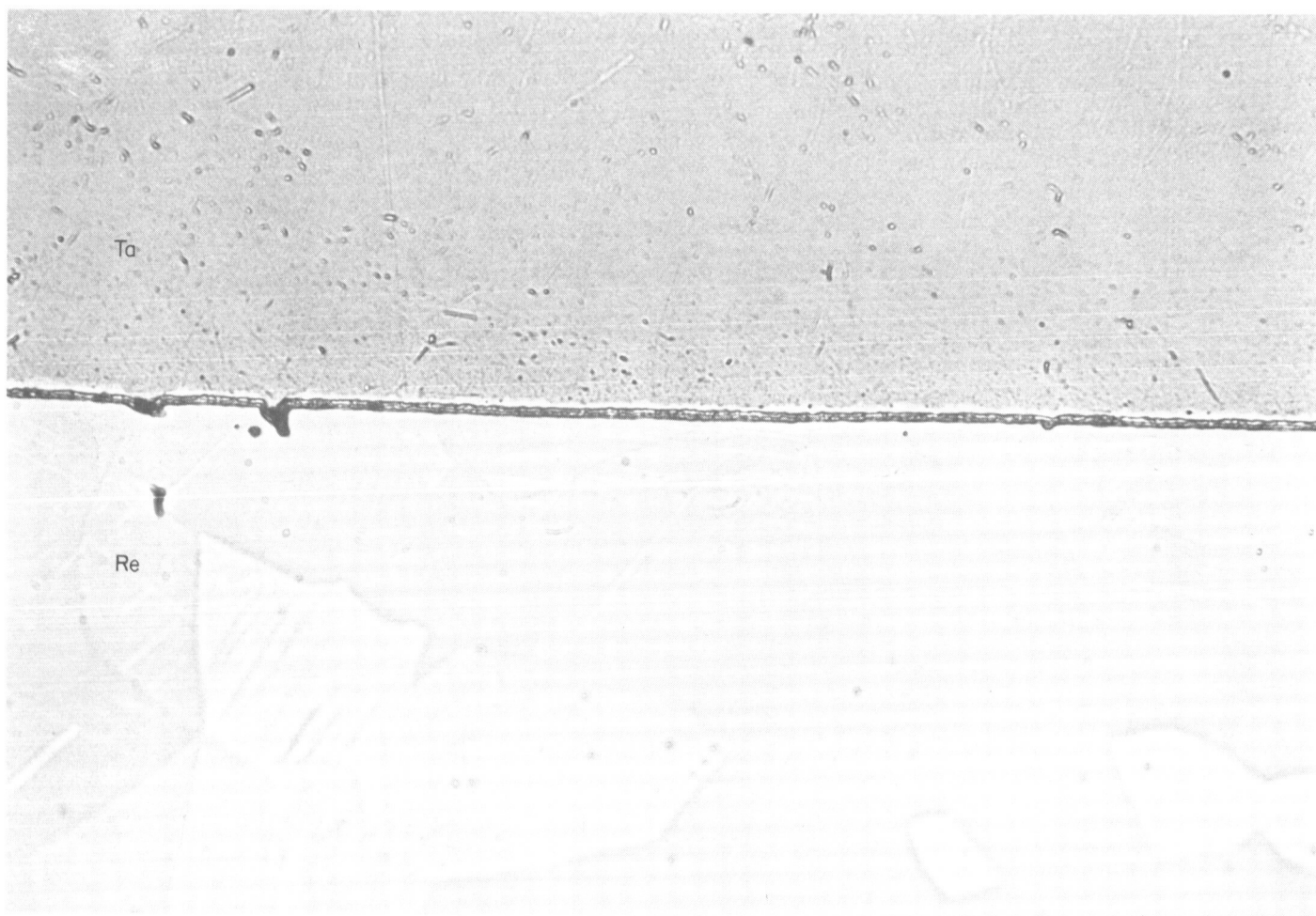


Fig. 6. Tantalum-rhenium interface in new converter

At the beginning of the Series VIII development, scant experience existed on the behavior of the rhenium-molybdenum configuration, and no extensive life tests had been performed. Since that time, several converters of such construction have been life-tested at JPL. All failed after 2000 to 5000 hr. The common mode of failure was the interdiffusion of the tantalum into the rhenium with creation of brittle intermetallics and modification of the heat transfer characteristics of the emitter. The ultimate effect was the separation of the rhenium emitter sheet from the tantalum substrate. The rhenium-tantalum boundary of an emitter slug in "as received" condition is presented in Fig. 6 ($\times 1000$). The intermetallic layer is approximately $20\text{ }\mu\text{m}$ thick. Fig. 7 ($\times 1000$) presents a section through an emitter which operated several thousand hours. The Kirkendall holes resulting from the diffusion of the tantalum into the rhenium and the crack through the hard and brittle rhenium-tantalum inter-

metallic greatly affected the thermal transfer pattern through the emitter slug, and finally resulted in separation of the emitter sheet.

c. Test equipment. The equipment used to test the generator is presented in Fig. 8. It is composed of, from left to right: (1) an electron-bombardment heating power control cabinet, (2) a vacuum system containing the generator under test and exhausted to the 10^{-8} torr range with a 600 liter/sec ion pump, (3) a generator operating control and visual monitoring cabinet, and (4) a 100-channel automatic data recording and printing system. In previous tests of such generators (SPS 37-20, pp. 7-11; SPS 37-34, pp. 38-42), the cavity formed by the outer faces of the emitters was bombarded during laboratory tests from a single, helical-wound filament. Extremely careful centering and special precautions were required to avoid the uneven heating of all the emitters. During

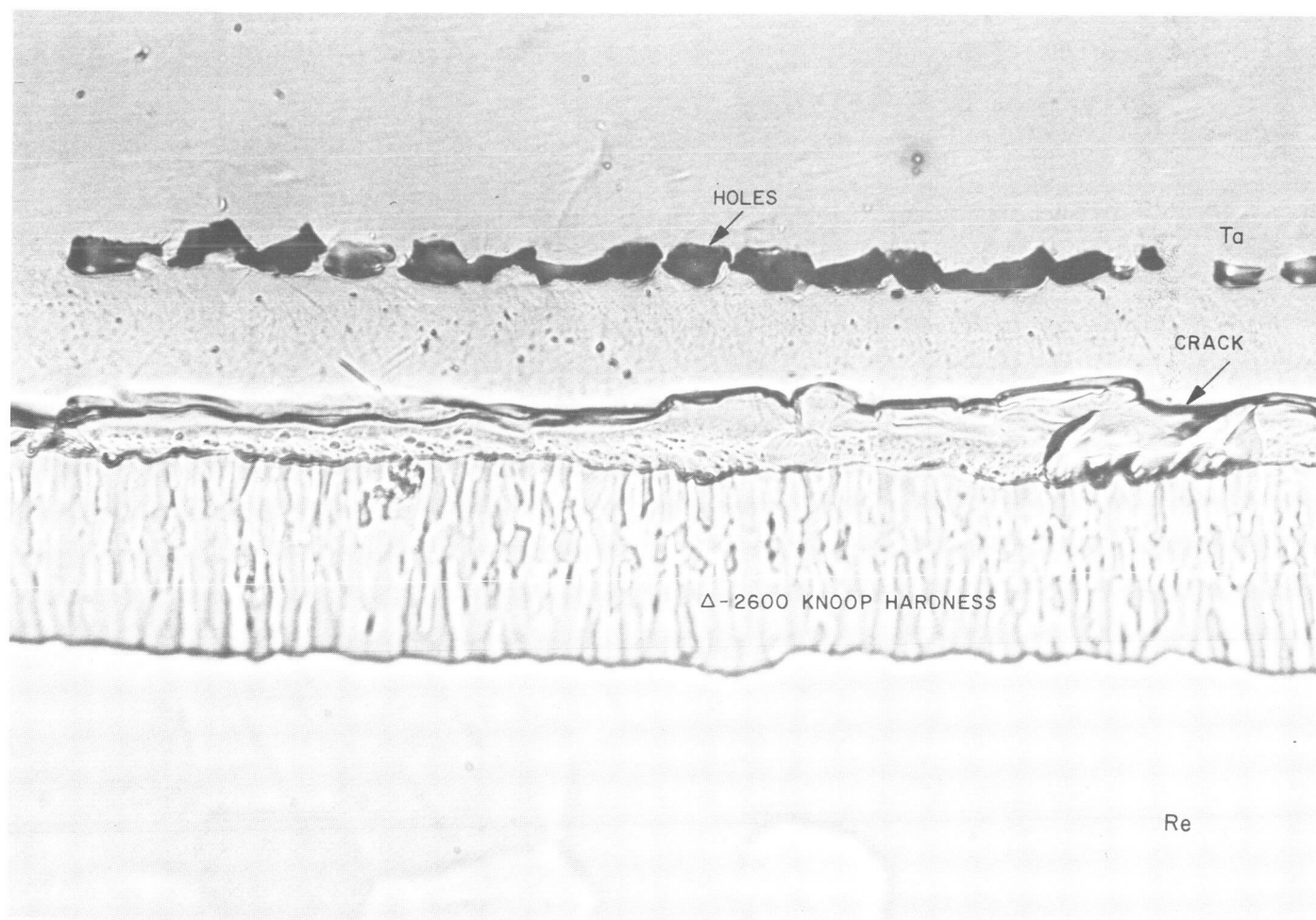


Fig. 7. Tantalum-rhenium interface after several thousand hours



Fig. 8. Generator test equipment

individual converter optimization, the differences in electron-cooling resulted in an unbalance of the thermal distribution in the cavity. Also, thermal feedback resulted in electronic runaway of the electron-bombardment equipment. The thermal runaway, which occurred during tests of the generator at the contractor's facilities, resulted in severe damage to the generator and the destruction of four converters, necessitating rebuilding the generator.

During the tests at JPL, each converter was bombarded from an individual filament regulated to produce equal electron bombardment current for each converter. As additional precautions, each of the individual electron bombardment currents and the total current were carefully monitored with meters provided with sensitive overload relays to avoid possible transient current surges. The primaries of the four independent filament transformers were fed through an electronic control loop and a saturable core reactor. This arrangement assured a very constant, easily adjustable and self-regulating electron bombardment power input. A schematic representation of the system including the generator controls is presented in Fig. 9. Fig. 10, representing the generator in operation, clearly shows the electron gun arrangement.

The load circuit was composed of carbon-pile variable resistors connected in series and/or parallel to cover a wide range of values. A 750 VA transformer with a 10-v low-impedance output was connected in series with the loading circuit and was used to obtain additional I - V

characteristics by a dynamic sweep of the generator output with 60 cps.

d. Generator tests. The generator tests were performed at four different values of heat input: 900, 1000, 1100 and 1200 watts. These values constituted the total heat input into the generator cavity. No allowance was made for conduction or radiation losses (estimated to be approximately 450 w). Also, the generator was tested at four values of emitter temperature (1600, 1650, and 1700°C and also 2000°K) and at four discrete values of voltage output (4.0, 3.2, 2.8 and 2.4 v). During the tests at constant-power input and constant emitter temperature, the outputs of the individual converters were optimized for each thermal input condition; during constant-voltage output tests, the outputs of individual converters were optimized for the specific value of voltage and current, and the heat input was adjusted to maintain the output condition. During all the tests, the converters were connected in series. The temperature of the emitter of one converter was monitored by an optical pyrometer sighted through a prism into the hohlraum of the converter. Prior to the

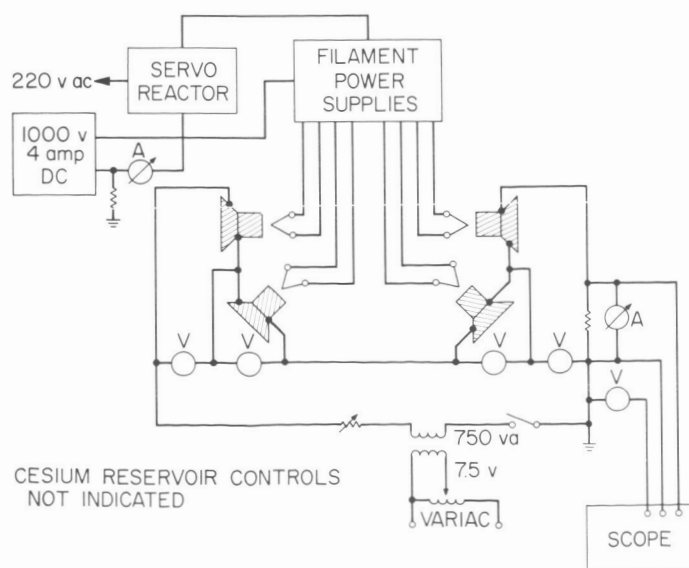


Fig. 9. Generator test schematic

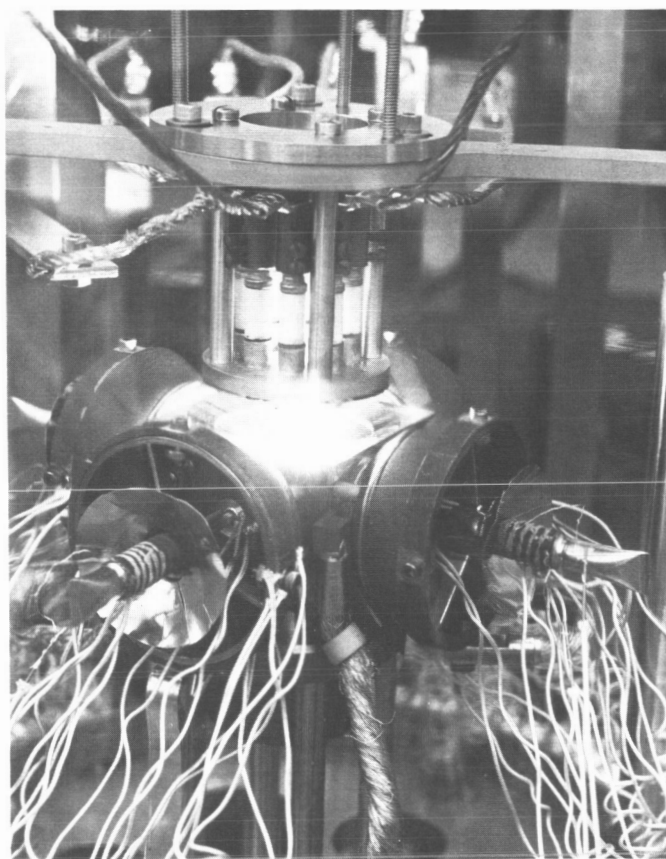


Fig. 10. Generator JG-3 during tests

initiation of the tests, the system was checked against a brightness standard lamp calibrated by the National Bureau of Standards.

e. Generator test results. The JG-3 thermionic generator was tested in the laboratory for a total of 166 hr of operation and underwent 22 complete thermal cycles. The

Table 2. Generator performance, constant power input

Power input, watts	Voltage output, volts	Current output, amp	Power output, watts	Efficiency, %
900, avg	1.6	28.8	46.0	5.0
	2.4	21.3	51.1	5.6
	3.2	16.0	51.0	5.7
	4.0	12.9	51.4	5.6
	4.8	10.7	51.2	5.6
1000, avg	1.6	37.4	60.2	5.9
	2.4	29.3	70.4	7.0
	3.0	23.8	71.4	7.1
	3.2	21.8	69.8	7.0
	3.4	21.4	61.4	7.1
	4.1	16.2	66.8	6.7
	4.8	13.6	65.1	6.5
1100, avg	1.6	44.3	71.4	6.4
	2.4	36.3	87.1	7.8
	3.0	29.6	88.9	7.9
	3.2	28.2	90.3	8.2
	4.0	22.1	88.2	8.0
	4.8	16.8	80.6	7.4
1200, avg	1.7	49.7	87.9	7.0
	2.4	41.9	100.3	8.3
	3.2	32.8	105.0	8.8
	4.0	24.9	100.5	8.5
	4.8	20.0	95.9	8.1

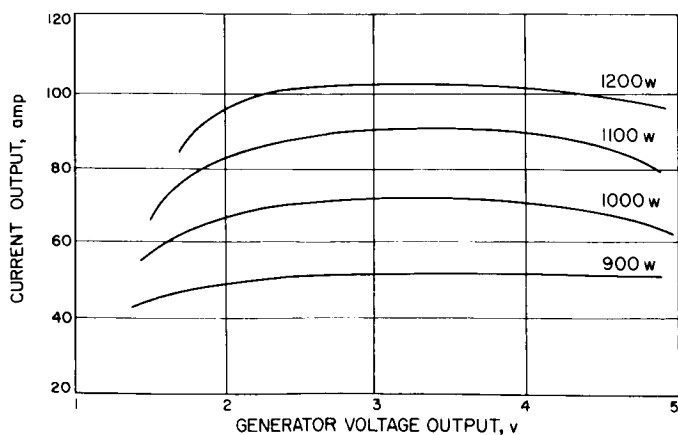


Fig. 11. Generator JG-3 performance at constant power input

performance data of the generator are presented in Tables 2 and 3 and are graphically displayed in Figs. 11 and 12. The maximum power output of 154 w was observed at 2.8 v output for a total power input of 1620 w. The observed efficiency was 9.5%. Observation of the dynamic *I-V* characteristics on an oscilloscope failed to reveal irregularity in the *I-V* characteristics of the generator as a result of successive ignition of individual converters. Three of these characteristics obtained at different values of power input are presented in Fig. 13.

Table 3. Generator performance, constant emitter temperature

Temp, °C	Power input, watts	Voltage output, volts	Current output, amp	Power output, watts	Efficiency, %
2000°K avg	1774	2.0	67.3	135.3	7.6
	1400	2.9	44.8	128.6	9.2
	1117	3.4	28.9	99.1	8.5
	986	3.9	16.8	66.0	6.7
	940	4.8	14.5	60.2	6.3
1700°C, avg	1583	2.0	62.0	123.9	7.8
	1434	2.4	52.6	126.7	8.8
	1186	3.2	31.9	102.6	8.7
	970	4.0	15.2	61.2	6.3
	880	4.8	9.7	46.6	5.3
1600°C, avg	1505	1.6	59.3	95.3	6.3
	1204	2.0	46.4	93.0	7.7
	1048	2.4	31.6	75.9	7.2
	752	3.2	9.1	29.2	3.9
	719	4.0	7.2	28.9	4.0
	698	4.7	5.2	24.8	3.6

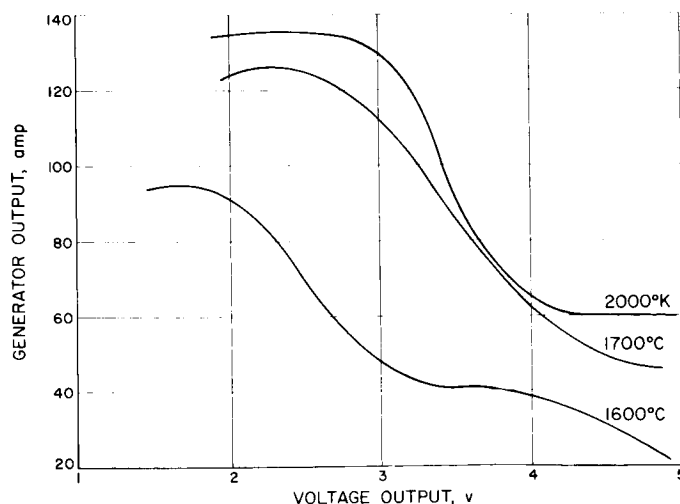


Fig. 12. Generator JG-3 performance at constant emitter temperature

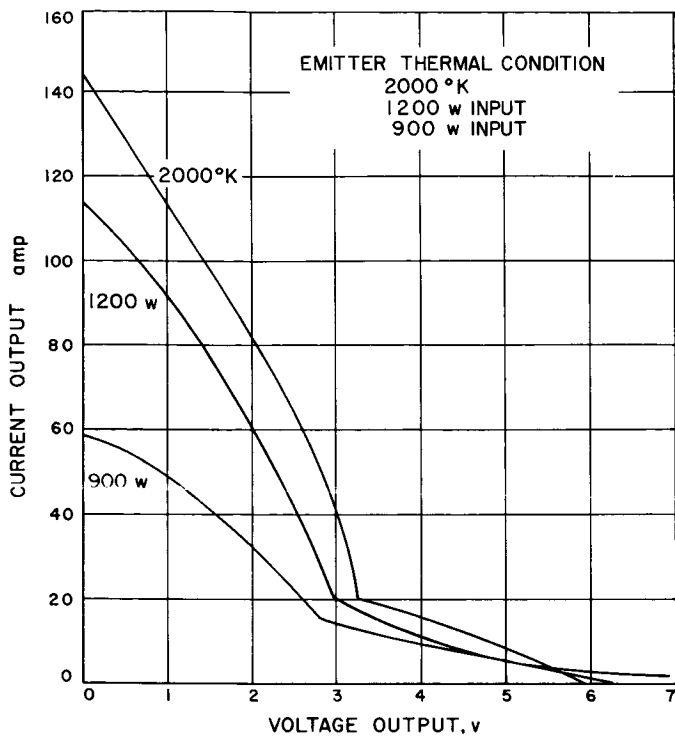


Fig. 13. Dynamic I - V characteristics at different values of power input

Additional tests were performed while keeping the individual converter output voltage as close as possible to a predetermined value and optimizing the generator output to obtain specific values of current output. This optimization is performed by both the individual optimization of the cesium pressure of each converter and by the adjustment of the power input to obtain the maximum generator performance. The voltage values selected for the converter output optimization were 1.0, 0.8, 0.7 and 0.6 v, resulting in a generator voltage output of 4.0, 3.2,

2.8 and 2.4 v. The results of these tests are summarized in Table 4 and are graphically presented in Fig. 14. A very close matching was obtained in the voltage output of the individual converters (recorded on a four-digit digital voltmeter).

Tentative attempts were made to correlate the emitter temperature and the converter voltage output, the output current being used as a variable. This effort was initiated to compare the performance of the converter operating in the generator with the test data from individual converters. Table 5 presents some of the data, and Fig. 15 displays I - V characteristics. The initial results presented a discrepancy which at present time cannot be satisfactorily explained. Tests are now underway to resolve the apparent difference in behavior.

3. Cesium Reservoir Control

The individual optimization of the performance of thermionic converters by adjustment of the cesium pressure presents problems during space operation. In multi-converter generators, the simultaneous adjustment of the temperatures of several cesium reservoirs, by ground control, to suit the changes in thermal energy input and load variations creates complex control problems. It was the intent of the effort under contract 951228 with EOS to design and fabricate automatic cesium reservoir control units. The approach was twofold: (1) an active control consisting of a thermal sensor, an electronic network and a reservoir heater; and (2) a passive control composed of vane-type radiation shields mechanically actuated to control the thermal energy radiated from the reservoir surface. The control was to be operated by a bimetallic sensing element. Both devices had to be designed to

Table 4. Converter optimization data

Parameter	Emitter temperature, °K							
	2013	2002	1973	1998	2003	2003	2003	2003
E_b	1.2	1.0	0.8	0.6	1.2	1.0	0.8	0.6
I_b	12.1	16.5	25.3	51.9	11.7	16.3	50.0	72.5
$T_c, ^\circ K$	818	835	860	953	765	785	902	987
T_{cs}	589	590	612	624	581	586	608	625
T_c/T_{cs}	1.38	1.42	1.41	1.53	1.32	1.34	1.48	1.58
Φ_c, ev	1.66	1.63	1.63	1.55	1.71	1.69	1.58	1.52
T_c/T_{cs}	3.42	3.40	3.22	3.20	3.44	3.41	3.29	3.20
Φ_E, ev	3.13	3.11	2.86	2.83	3.16	3.12	2.96	2.83

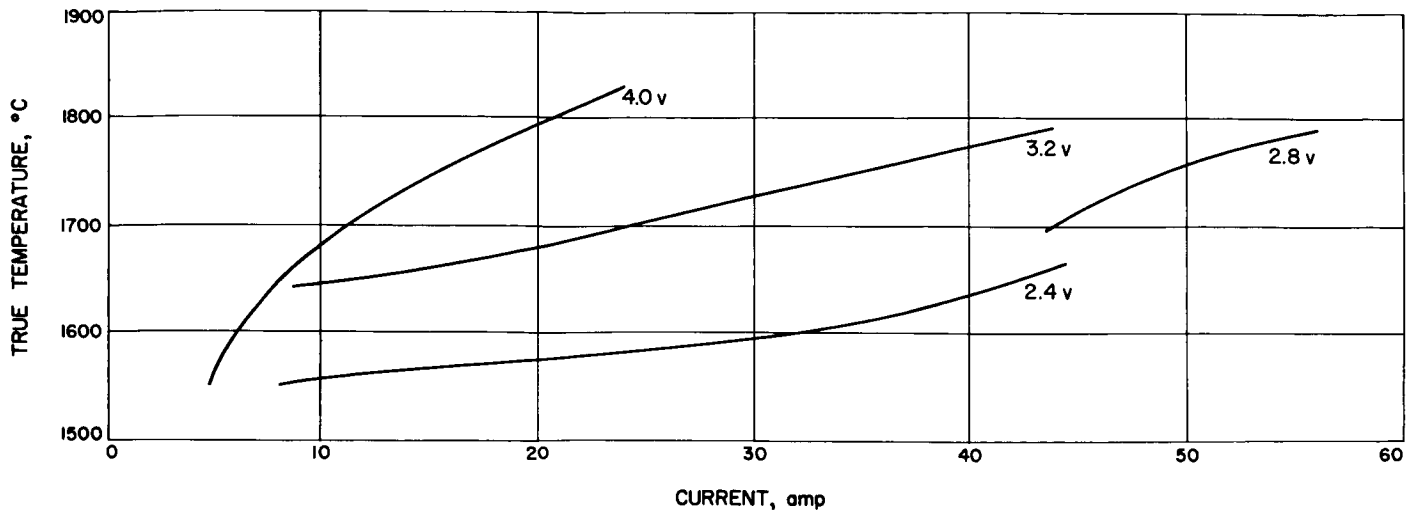


Fig. 14. Generator JG-3 current versus temperature

Table 5. Generator performance data

Individual converter voltage, (nominal)	Converter parameter	Generator current, amps								
		5	10	15	20	30	40	47	50	55
1.0 v	1	1.000	1.000	1.000	1.000					
	2	1.010	1.000	1.000	1.000					
	3	0.990	0.990	0.990	1.000					
	4	1.000	1.000	0.990	1.010					
	V	4.00	3.99	3.98	4.01					
	W	20.12	40.02	59.81	80.50					
	%	3.1	4.9	6.1	7.5					
0.8 v	1	—	0.800	0.800	0.800	0.800	0.800			
	2	—	0.810	0.800	0.800	0.802	0.800			
	3	—	0.802	0.800	0.798	0.810	0.800			
	4	—	0.800	0.800	0.800	0.800	0.802			
	V	—	3.21	3.20	3.20	3.21	3.00			
	W	—	32.63	64.26	64.25	96.58	120.3			
	%	—	4.2	6.6	6.6	8.4	9.1			
0.7 v	1	—	—	—	—	—	—	0.700	0.700	0.700
	2	—	—	—	—	—	—	0.700	0.700	0.697
	3	—	—	—	—	—	—	0.700	0.700	0.705
	4	—	—	—	—	—	—	0.703	0.700	0.700
	V	—	—	—	—	—	—	2.803	2.800	2.802
	W	—	—	—	—	—	—	130.4	140.0	154.0
	%	—	—	—	—	—	—	9.3	9.3	9.5
0.6 v	1	—	0.600	0.600	0.600	0.600				
	2	—	0.602	0.603	0.600	0.600				
	3	—	0.602	0.600	0.605	0.599				
	4	—	0.605	0.600	0.600	0.602				
	V	—	2.41	2.40	2.41	2.40				
	W	—	24.23	47.92	72.24	96.09				
	%	—	3.3	5.5	7.1	8.3				

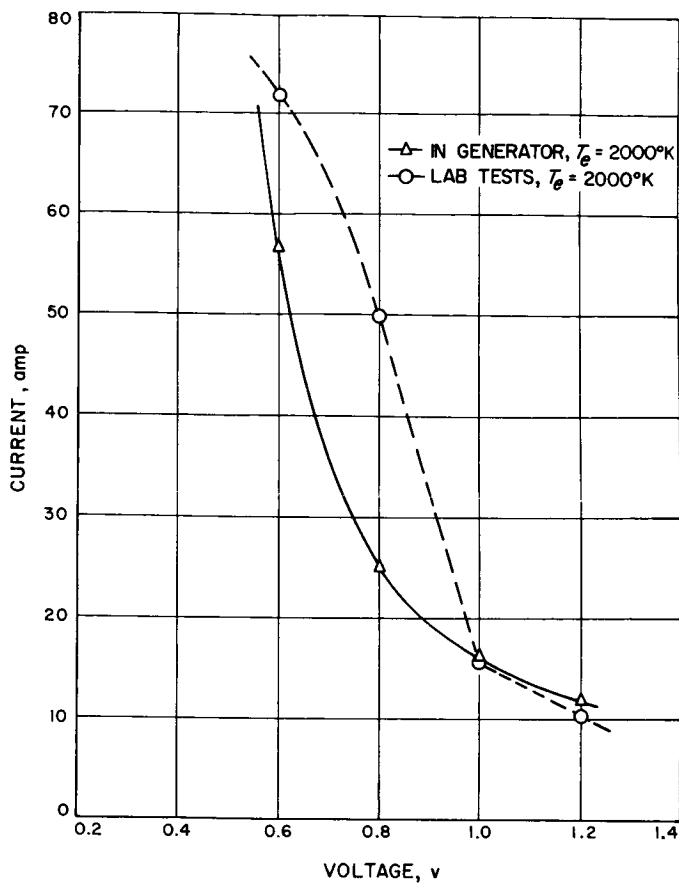


Fig. 15. Converter VIII-17 characteristics

maintain the cesium reservoir temperature at a given level within 5°C when the temperature of the reservoir without control varied from 325°C to 375°C . The controls were to weigh less than 3 oz.

Fig. 16 presents a concept of the passive control. Fig. 17 indicates the range of thermal radiation expected from two concepts of thermionic converters as a function of the cesium reservoir temperature; the emissivity was assumed to be 0.65.

The active control system, using a platinum thermal sensor and the electronic circuit presented in Fig. 18, operated successfully. The thermal response ranged between 7 and 10 min for the two different converter configurations, and a typical response is illustrated in Fig. 19. The total weight of a breadboard model was 8 oz. The effect of load changes on the cesium reservoir temperatures is illustrated in Fig. 20. The results of the passive control device were rather disappointing; the operation was erratic, very large variations of temperature were required before any motion was observed, and the prototype as constructed probably lacked strength to pass normal

environmental requirements. Any further activities in this area should be directed toward reducing the weight of the active system.

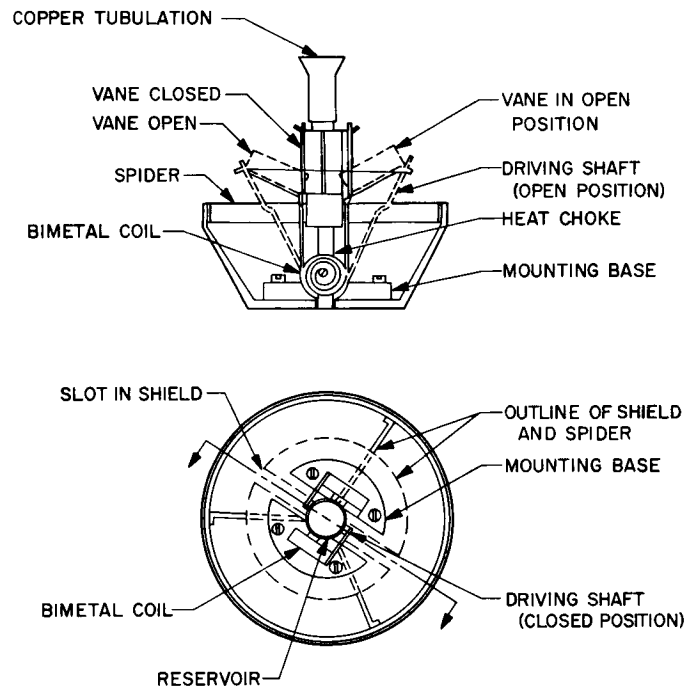


Fig. 16. Passive reservoir control

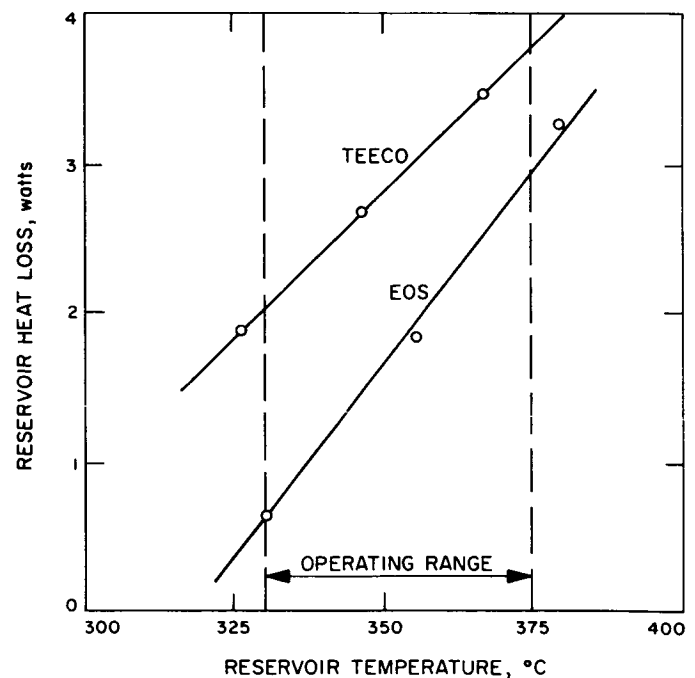


Fig. 17. Reservoir control range

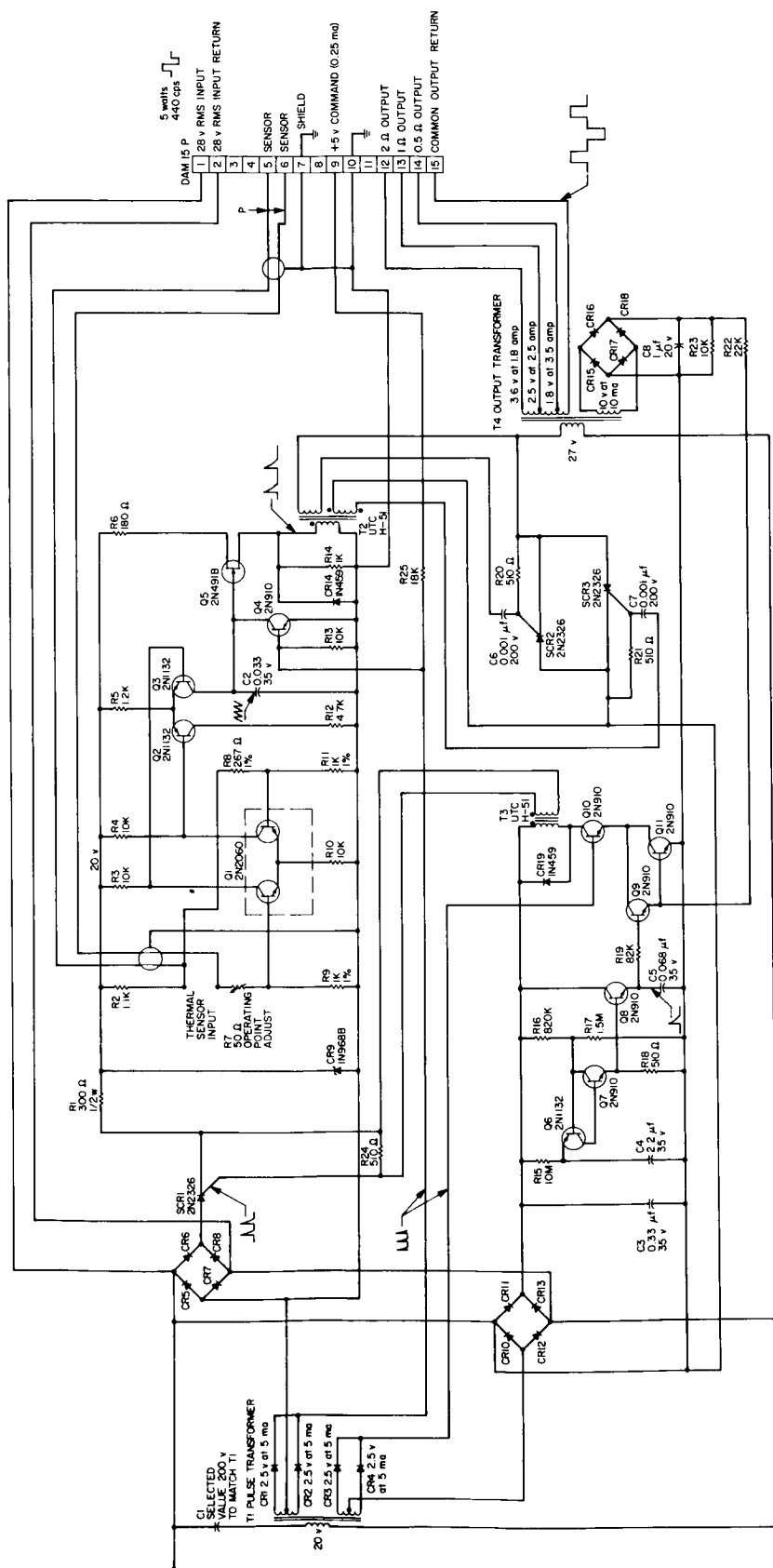


Fig. 18. Cesium reservoir heater control schematic

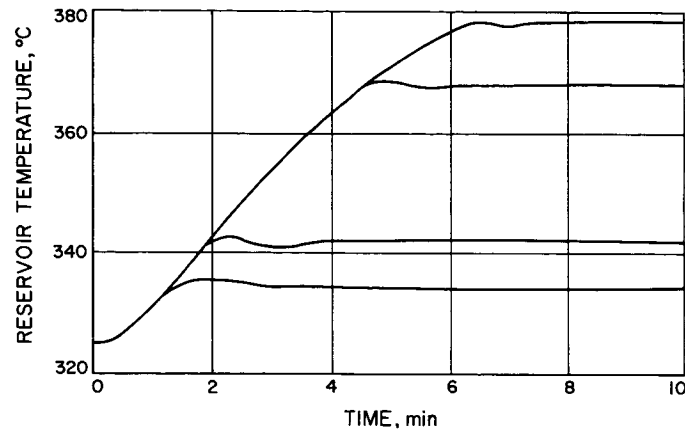


Fig. 19. Thermal response of active control system

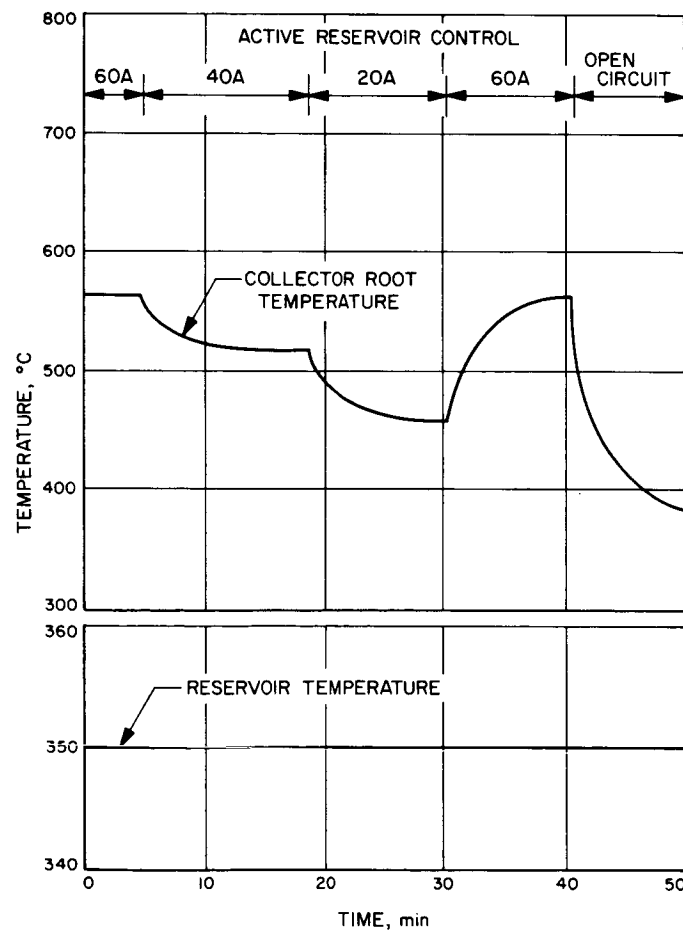


Fig. 20. Effect of load on converter temperature with active control

References

1. Blake, F. A., and Rouklove, P., "Performance Testing of a Solar Electrical Thermionic Generator System," *Solar Energy Society*, Phoenix, March 1965.
2. Rouklove, P., "Thermionic Generator Performance," *Proceedings of the International Thermionic Energy Conference*, London, October 1965.

N67 12103

II. Spacecraft Control

A. Strapdown Electrically Suspended Gyro Development

T. J. Donlin

The development of the Electrically Suspended Gyro (ESG) has progressed by contract with Honeywell, Inc., Minneapolis, through the study, design, component development and construction phases. These efforts have been reported in SPS 37-38, Vol. IV, pp. 19-23. As part of the present contract, compatibility tests were successfully conducted between the ESG rotor-housing assembly, the suspension electronics, the readout electronics, and the control console. While conducting the readout alignment procedure on the first ESG, the suspension of the free-spinning rotor in the electric field was lost, allowing the rotor to strike the electrode in the housing. This rotor drop caused the housing to lose its vacuum seal. At first, electrical connections were suspected until an instability was detected in the current feedback loop of the suspension electronics. A high-speed recorder was necessary to detect

this instability as rotor suspension loss occurred almost simultaneously with the instability. The suspension of the rotor and the stability of the loop was restored immediately after rotor drop. Conducting the same checks upon the second gyro resulted in the same condition.

In examining the conditions that existed and the data obtained, it was concluded that a net electrical charge was developing on the rotor; i.e., the algebraic sum of the instantaneous rotor charges no longer equaled zero. The suspension electronics could not accommodate the net charge that resulted. The rotor drop allowed the net charge to be removed from the rotor, and stability returned until the next rotor charge buildup.

The rotor suspension error system uses the same frequency as the forcing voltage. The parameter measured by the error detecting system is the rotor-to-electrode capacitance. Control of the rotor position is effected by the forcing voltage applied to the electrodes surrounding the rotor. If the capacitance error sensing is to have broader capability for control, it must be decoupled from the forcing voltage.

The means developed to do this uses three different frequencies, one on each axis, to detect rotor-to-electrode capacitance. These three frequencies are also different from the forcing voltage frequency. The use of the three different frequencies is intended to eliminate any interaction between axes and any interaction with the forcing voltage frequency. This means of detecting rotor position allows greater stability of the rotor position with regard to dimensional changes, temperature changes, and rotor electrical charge changes. With the addition of the three frequencies, the rotor suspension system is more complex, but the additional margin of suspension capability makes it attractive.

an examination of the two degree of freedom pointing system with respect to (1) its geometry, (2) errors caused by attitude drift, and (3) methods of correcting antenna position for attitude drift using sensor error signals.

2. Two-Degree of Freedom Pointing

The two-axis pointing geometry may be represented by a hinge axis, H , and a swivel axis, S , which are mutually perpendicular. Fig. 1 illustrates the location of axes H and S with respect to the familiar spacecraft body-fixed axes, X , Y , and Z . The unit hinge axis vector is given by:

$$\mathbf{h} = \cos \phi \cos \theta \mathbf{i} + \cos \phi \sin \theta \mathbf{j} + \sin \phi \mathbf{k}$$

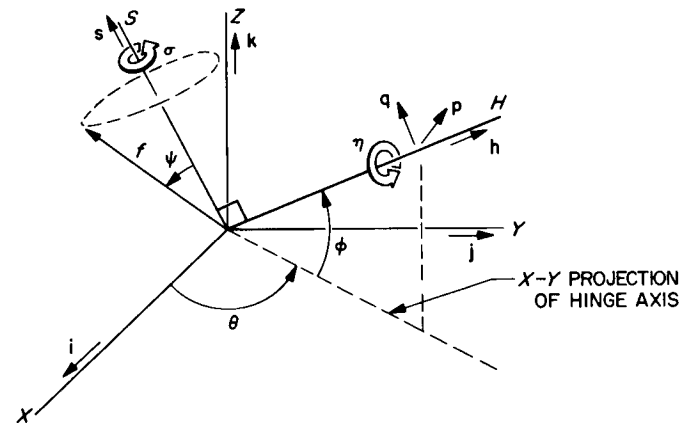


Fig. 1. Location of H -axis and S -axis relative to body-fixed axes

B. Spacecraft Antenna Pointing

G. E. Fleischer

1. Introduction

In examining the characteristic inaccuracies of a pre-programmed high-gain antenna pointing system, the effects of spacecraft attitude errors, as embodied in pitch, yaw and roll limit cycle activity, are of major concern. If the pointing accuracy requirements for a particular mission allow the use of a single degree of freedom pointing system, it is doubtful whether a method of correcting antenna position for spacecraft attitude errors would be worthwhile. This is because the pointing error due to fitting a plane curve to a three-dimensional trajectory would probably be at least as large as the additional pointing errors due to attitude drift within the deadbands. Further, trying to correct pointing for pitch, yaw, and roll drifts by adjusting a single hinge angle is relatively ineffective.

However, a mission may require antenna pointing accuracies that (1) can only be met by two degree of freedom positioning or that (2) at least, are quite marginal for a single axis system to achieve. A two-axis pointing system is certainly capable of correcting completely, within the limits of its resolution, for errors caused by attitude perturbations provided such perturbations can be measured. Sun sensor and star sensor output signals are measures of spacecraft attitude misalignments and, as such, might be used to generate position correcting information to the antenna servo drives. The following is

and if unit vectors \mathbf{p} and \mathbf{q} are defined as:

$$\mathbf{p} = \frac{\mathbf{k} \times \mathbf{h}}{|\mathbf{k} \times \mathbf{h}|}, \quad \mathbf{q} = \frac{\mathbf{h} \times \mathbf{p}}{|\mathbf{h} \times \mathbf{p}|}$$

then the unit swivel axis vector is given by:

$$\mathbf{s} = \cos \eta \mathbf{p} + \sin \eta \mathbf{q},$$

where η is the hinge angle.

Let us also define a unit vector, \mathbf{r} , as:

$$\mathbf{r} = \frac{\mathbf{s} \times \mathbf{h}}{|\mathbf{s} \times \mathbf{h}|}.$$

If the unit antenna feed vector, \mathbf{f} , is assumed to rotate perpendicularly about S , i.e., $\psi = \text{constant} = 90$ deg,

N67 12104

then \mathbf{f} is given by:

$$\mathbf{f} = \cos \sigma \mathbf{h} + \sin \sigma \mathbf{r}.$$

where σ is the swivel angle

$$\mathbf{p} = \frac{\begin{vmatrix} \mathbf{i} & \mathbf{j} & \mathbf{k} \\ 0 & 0 & 1 \\ (\cos \phi \cos \theta) & (\cos \phi \sin \theta) & \sin \phi \end{vmatrix}}{|\mathbf{k} \times \mathbf{h}|}$$

$$= \frac{\cos \phi \cos \theta \mathbf{j} - \cos \phi \sin \theta \mathbf{i}}{\cos \phi}$$

$$\mathbf{p} = -\sin \theta \mathbf{i} + \cos \theta \mathbf{j}$$

where $\mathbf{i}, \mathbf{j}, \mathbf{k}$ are unit vectors

$$\mathbf{q} = \frac{\begin{vmatrix} \mathbf{i} & \mathbf{j} & \mathbf{k} \\ (\cos \phi \cos \theta) & (\cos \phi \sin \theta) & \sin \phi \\ -\sin \theta & \cos \theta & 0 \end{vmatrix}}{|\mathbf{h} \times \mathbf{p}|} = \frac{-\sin \theta \sin \phi \mathbf{j} + \cos^2 \theta \cos \phi \mathbf{k} + \sin^2 \theta \cos \phi \mathbf{k} - \sin \phi \cos \theta \mathbf{i}}{1}$$

$$\mathbf{q} = -\sin \phi \cos \theta \mathbf{i} - \sin \theta \sin \phi \mathbf{j} + \cos \phi \mathbf{k}$$

$$\therefore \mathbf{s} = -(\sin \theta \cos \eta - \sin \phi \cos \theta \sin \eta) \mathbf{i} + (\cos \theta \cos \eta - \sin \phi \sin \theta \sin \eta) \mathbf{j} + (\cos \theta \sin \eta) \mathbf{k}$$

$$\therefore \mathbf{r} = (\sin \phi \cos \theta \cos \eta - \sin \theta \sin \eta) \mathbf{i} + (\sin \phi \sin \theta \cos \eta + \cos \theta \sin \eta) \mathbf{j} - (\cos \phi \cos \eta) \mathbf{k}$$

$$\therefore \mathbf{f} = \cos \phi \cos \theta \cos \sigma \mathbf{i} + \cos \phi \sin \theta \cos \sigma \mathbf{j} + \sin \phi \cos \sigma \mathbf{k} + \sin \sigma \mathbf{r}$$

$$= (\sin \phi \cos \theta \cos \eta \sin \sigma - \sin \theta \sin \eta \sin \sigma + \cos \phi \cos \theta \cos \sigma) \mathbf{i} + (\sin \phi \sin \theta \cos \eta \sin \sigma + \cos \theta \sin \eta \sin \sigma + \cos \phi \sin \theta \cos \sigma) \mathbf{j} + (\sin \phi \cos \sigma - \cos \phi \cos \eta \sin \sigma) \mathbf{k}$$

Assuming that the hinge axis is located in the X-Y plane, i.e., $\phi = 0$, \mathbf{f} is simplified as follows:

$$\mathbf{f} = (-\sin \theta \sin \eta \sin \sigma + \cos \theta \cos \sigma) \mathbf{i} + (\cos \theta \sin \eta \sin \sigma + \sin \theta \cos \sigma) \mathbf{j} + (-\cos \eta \sin \sigma) \mathbf{k}$$

$$\mathbf{f} = \alpha_F \mathbf{i} + \beta_F \mathbf{j} + \gamma_F \mathbf{k}$$

H is fixed to the body reference axes X, Y , and Z , and if these are assumed to be perfectly aligned to the inertial axes, L, M, N , the feed vector's body components may be equated to the desired Earth-pointing vector's inertial components:

$$\mathbf{e} = \alpha_E \mathbf{i} + \beta_E \mathbf{j} + \gamma_E \mathbf{k} = \alpha_F \mathbf{i} + \beta_F \mathbf{j} + \gamma_F \mathbf{k}$$

$$\alpha_F = \alpha_E = -\sin \theta \sin \eta \sin \sigma + \cos \theta \cos \sigma \quad (1)$$

$$\beta_F = \beta_E = \cos \theta \sin \eta \sin \sigma + \sin \theta \cos \sigma \quad (2)$$

$$\gamma_F = \gamma_E = -\cos \eta \sin \sigma \quad (3)$$

$$\therefore \cos \sigma = \alpha_F \cos \theta + \beta_F \sin \theta \quad (4)$$

$$\cos \eta = \frac{-\gamma_F}{\sin \sigma} \quad (5)$$

where $\sin \sigma = + (1 - \cos^2 \sigma)^{1/2}$, and the sign of $(\sin \eta)$ must satisfy Eqs. (1) and (2). Another unique set of σ and η values is given by choosing $\sin \sigma = - (1 - \cos^2 \sigma)^{1/2}$.

3. Hinge and Swivel Angle Error Correction

In general, body-fixed axes X, Y , and Z are not coincident with L, M, N but drift about them under the torques applied to the spacecraft by solar winds, leaky gas jets, dust particle collisions, instrument outgassing, and articulating members. However, to begin with, the body and inertial axes may be assumed coincident so that the nominal set of σ and η values may be computed from Eqs. (4) and (5). The nominal values thus computed will be denoted by primes as follows:

$$\cos \sigma' = \alpha_F' \cos \theta + \beta_F' \sin \theta \quad (6)$$

$$\cos \eta' = \frac{-\gamma_F'}{\sin \sigma'} \quad (7)$$

where $\alpha_F', \beta_F', \gamma_F'$ are the nominal feed vector components in body coordinates which, in turn, are equivalent to the exact Earth-vector components in inertial coordinates.

Let the spacecraft now be rotated slightly to some other arbitrary attitude. The body-fixed feed vector's components in the *inertial frame* can now be obtained from an orthogonal coordinate transformation matrix A :

$$\begin{Bmatrix} \alpha_F' \\ \beta_F' \\ \gamma_F' \end{Bmatrix} = [A]^{-1} \begin{Bmatrix} \alpha_F \\ \beta_F \\ \gamma_F \end{Bmatrix}$$

where items within (\cdot) denote inertial frame components

$$\text{and where } A = \begin{bmatrix} 1 & \theta_R & -\theta_Y \\ -\theta_R & 1 & \theta_P \\ \theta_Y & -\theta_P & 1 \end{bmatrix}, \text{ for small angles,}$$

and θ_P , θ_Y , and θ_R are pitch, yaw, and roll attitude errors, respectively.

$$\therefore (\alpha_F) = \alpha'_F - \beta'_F \theta_R + \gamma'_F \theta_Y$$

$$(\beta_F) = \beta'_F + \alpha'_F \theta_R - \gamma'_F \theta_P$$

$$(\gamma_F) = \gamma'_F - \alpha'_F \theta_Y + \beta'_F \theta_P$$

Now, since the antenna feed vector is not pointed at Earth, correction terms $\delta\eta$ and $\delta\sigma$ must be added to η' and σ' to rotate the feed vector with respect to the body axes so that it is again aligned with

$$\mathbf{e} = \alpha_E \mathbf{l} + \beta_E \mathbf{m} + \gamma_E \mathbf{n}.$$

The new feed vector components in body coordinates will then be given by:

$$\begin{pmatrix} \alpha_F \\ \beta_F \\ \gamma_F \end{pmatrix} = [A] \begin{pmatrix} \alpha'_F \\ \beta'_F \\ \gamma'_F \end{pmatrix}$$

Therefore,

$$\alpha_F = \alpha'_F + \beta'_F \theta_R - \gamma'_F \theta_Y$$

$$\beta_F = \beta'_F - \alpha'_F \theta_R + \gamma'_F \theta_P$$

$$\gamma_F = \gamma'_F + \alpha'_F \theta_Y - \beta'_F \theta_P$$

and $\eta = \eta' + \delta\eta$, $\sigma = \sigma' + \delta\sigma$,

$$\cos \eta = \cos (\eta' + \delta\eta) \simeq \cos \eta' - \delta\eta \sin \eta'$$

$$\cos \sigma = \cos (\sigma' + \delta\sigma) \simeq \cos \sigma' - \delta\sigma \sin \sigma'$$

$$\sin \sigma = \sin (\sigma' + \delta\sigma) \simeq \sin \sigma' + \delta\sigma \cos \sigma'$$

Substituting these expressions into (4) and (5):

$$\begin{aligned} \cos \sigma' - \delta\sigma \sin \sigma' &= \alpha'_F \cos \theta + (\beta'_F \theta_R - \gamma'_F \theta_Y) \cos \theta \\ &\quad + \beta'_F \sin \theta + (\gamma'_F \theta_P - \alpha'_F \theta_R) \sin \theta \\ &= (\sin \sigma' + \delta\sigma \cos \sigma') (\cos \eta' - \delta\eta \sin \eta') \\ &= -\gamma'_F - \alpha'_F \theta_Y + \beta'_F \theta_P. \end{aligned}$$

Since relations (6) and (7) also hold,

$$\delta\sigma = -\frac{1}{\sin \sigma'} [(\beta'_F \theta_R - \gamma'_F \theta_Y) \cos \theta + (\gamma'_F \theta_P - \alpha'_F \theta_R) \sin \theta] \quad (8)$$

$$\delta\eta = \frac{1}{\sin \sigma' \sin \eta'} [\alpha'_F \theta_Y - \beta'_F \theta_P - \delta\sigma \cos \sigma' \cos \eta']. \quad (9)$$

Also, α'_F , β'_F , and γ'_F can be eliminated by using equations (1), (2), and (3) so that the final result is:

$$\delta\sigma = -\theta_R \sin \eta' + (\theta_P \sin \theta - \theta_Y \cos \theta) \cos \eta' \quad (10)$$

$$\begin{aligned} \delta\eta &= -\frac{\cos \eta'}{\tan \sigma'} \theta_R - (\theta_Y \sin \theta + \theta_P \cos \theta) \\ &\quad + \frac{\sin \eta'}{\tan \sigma'} (\theta_Y \cos \theta - \theta_P \sin \theta) \end{aligned} \quad (11)$$

By aligning the antenna hinge axis along either the spacecraft X or Y axis, Eqs. (10) and (11) can be simplified. Except for the second and higher order terms lost in the small angle approximations, relations (10) and (11) are "exact" expressions for the desired hinge and swivel angle corrections. The mechanization of corrections $\delta\sigma$ and $\delta\eta$ might be realized in a system such as that shown schematically in Fig. 2. The arithmetic unit must do trigonometric resolution as well as the multiply and sum operations.

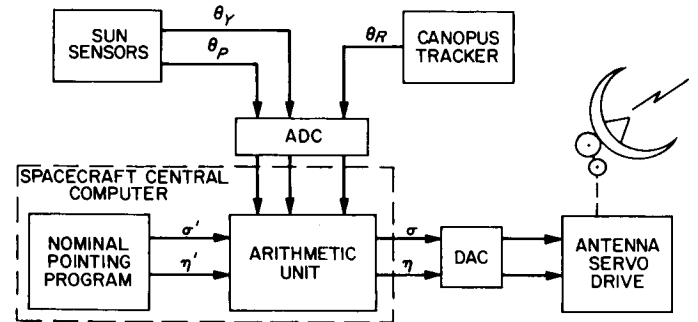


Fig. 2. Mechanization of corrections $\delta\sigma$ and $\delta\eta$

However, under certain circumstances, a full-blown arithmetic unit may be replaced by a simple accumulating register without need for stored subroutines and the associated memory capacity. These circumstances are illustrated by the example of a 512-day Jupiter flyby mission. A plot of Earth position in cone-clock coordinates is given in Fig. 3. The Earth pointing vector is confined to relatively small cone angles as the mission progresses. The effect on the nominal hinge and swivel angles is shown in Fig. 4. If the assumption is made that:

$$\sigma'(t) \simeq \text{constant} \cong 90 \text{ deg}$$

$$\therefore \sin \sigma' = 1, \quad \cos \sigma' = 0, \quad \tan \sigma' = \infty$$

and

$$\theta = 0$$

$$\eta'(t) \simeq \text{constant} \cong 180 \text{ deg}$$

$$\therefore \sin \eta' = 0, \quad \cos \eta' = -1$$

then

$$\delta\sigma = \theta_Y \text{ and } \delta\eta = -\theta_P.$$

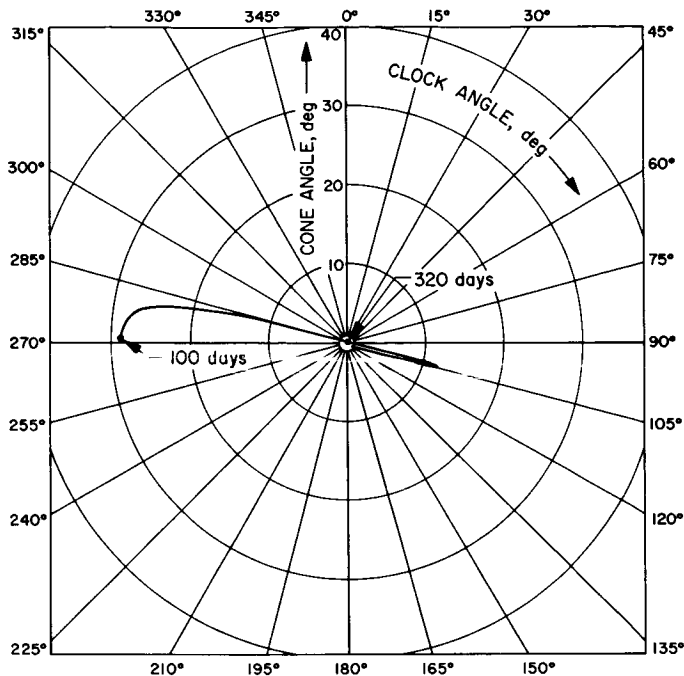


Fig. 3. Earth coordinates for 512-day Jupiter flyby

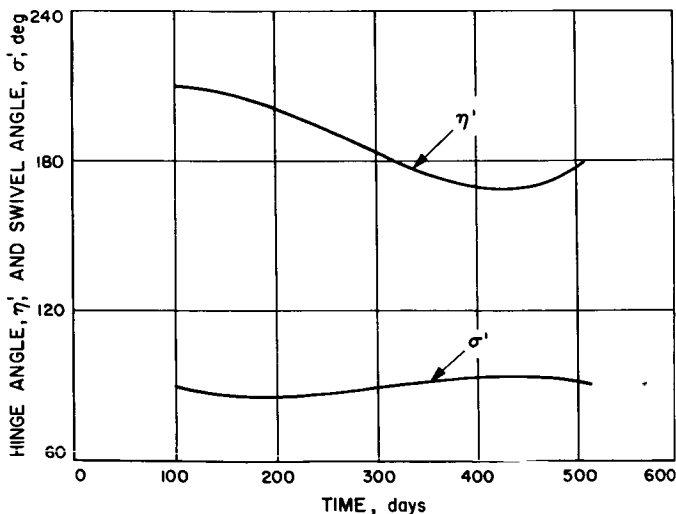


Fig. 4. Nominal antenna hinge and swivel angles for Jupiter flyby

The antenna pointing angles may then be corrected by simple additions of pitch and yaw error signals while roll errors may be ignored. Fig. 5 illustrates the resultant maximum pointing errors due to attitude drift only. At all points on the curves, the spacecraft is assumed to be in a worst possible attitude, i.e.,

$$\theta_P = 1 \text{ deg}, \theta_Y = -1 \text{ deg}, \theta_R = 1 \text{ deg}$$

where the pitch, yaw, and roll deadbands are symmetrical and 2 deg wide.

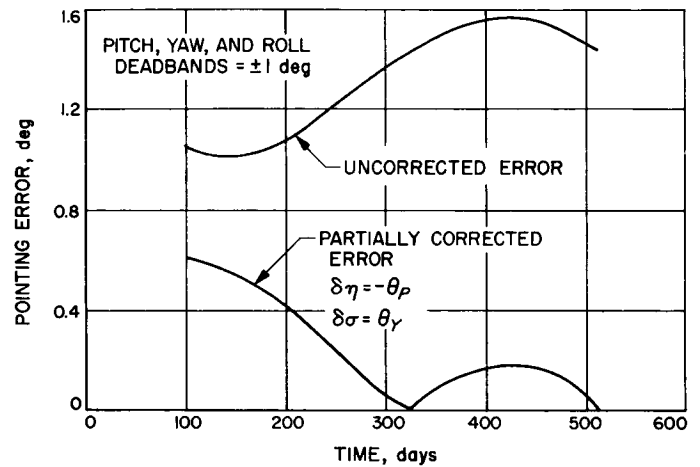


Fig. 5. Maximum pointing errors due to spacecraft attitude misalignments

4. Future Work

The question of spacecraft and antenna dynamic behavior remains as a major consideration. Particularly as antenna size becomes more and more comparable to that of the spacecraft, the movement of the antenna will interact appreciably with the spacecraft and serious stability problems may arise. Presently a single-axis representation of a spacecraft-antenna combination, coupled through a dissipative elastic joint, is being simulated to determine parameter effects on attitude control and pointing stability. This simulation can then be extended to a full three-axis representation capable of including all attitude control and antenna components, i.e., sensors, actuators, and pointing program. The stability problems inherent in mechanizing the pointing correction scheme described above are of particular interest.

N67 12105

III. Guidance and Control Research

A. Titanium Oxide Thin Films

J. Maserjian

1. Introduction

In our investigation of thin titanium-oxide films, the experimental results have been interpreted in earlier reports in terms of a physical model which includes the effect of a large ionic space charge in the films (SPS 37-31, Vol. IV, p. 98; SPS 37-37, Vol. IV, p. 61). The theory has since been extended and shown to give good agreement with a wide range of experimental results, including measurements of both current and capacitance as a function of voltage, temperature, and frequency. A detailed description of both the theory and the experimental results has been recently completed (Ref. 1).

With the physical understanding of the phenomena in these films on fairly solid ground, we are in a position to consider in more detail some promising device possibilities. One such possibility which is presently under study is a new thin-film thermal detector, tentatively designated a "thermactor" (Ref. 2).

The thermactor is essentially a thin film capacitor which exhibits a large temperature dependence. Changes in capacitance caused by a temperature rise due to incident radiation enables this device to be used as a detector of infrared radiation. This temperature dependence has been observed in our Al-TiO₂-Al thin film structures, and is correctly predicted by the theory, where it is shown to arise as a consequence of an effective barrier width in the oxide film which varies as a function of temperature (see Ref. 1).

2. General Considerations on the Thermactor

The temperature dependence of the capacitance C may be expressed for small changes ΔC , corresponding to a small temperature change ΔT at some absolute temperature T , by the approximate relation

$$\frac{\Delta C}{C} \simeq \alpha \frac{C}{A} \frac{\Delta T}{T}$$

where A is the active area of the device, and α is a characteristic parameter of the oxide with a typical value of

about 2×10^5 cm²/f. The capacitance temperature coefficient equal to $\alpha C/AT$ has values of approximately 0.002 to 0.004 deg⁻¹ between 300°K and 78°K, and is comparable with the resistive temperature coefficient of metal film bolometers. However, an important advantage is gained in this case because the response to the thermal change is observed in a pure reactance, while noise is generated in only the dissipative part of the device. For this reason the device noise is reduced by the quality factor Q which may be expressed by $2\pi f_0 RC$, where R and C represent the equivalent parallel resistance and capacitance at the frequency f_0 of the applied ac voltage. We have measured Q to be approximately 50 over the frequency range from 1 to 100 kc for the samples thus far studied.

The performance of a thermal detector is often characterized by its noise equivalent power NEP, defined by the amount of absorbed power required to make the signal-to-noise ratio of the detector equal to unity. The detectivity D^* is also used as a figure of merit, since it factors out area A and frequency bandwidth Δf , and is given by

$$D^* = (A\Delta f)^{1/2}/\text{NEP}.$$

The best D^* (or smallest NEP) obtainable in any thermal detector occurs when the noise is determined only by temperature fluctuations due to the random exchange of photons between the detector and its environment. The mean square temperature fluctuation in a frequency bandwidth Δf is (see Ref. 3),

$$\overline{\Delta T^2} = \frac{4kT^2 Z\Delta f}{1 + (2\pi f\tau)^2}$$

where Z is the thermal impedance between the detector and its environment, and τ is the thermal response time. We wish to compare the magnitude of this noise with that due to the Nyquist noise generated in the dissipative part of the device.

If we assume an ideal bridge circuit for measuring ΔC , we obtain a mean-square noise voltage given by

$$\overline{V_N^2} = \frac{4kTR\Delta f}{1 + Q^2}.$$

On the other hand, the equivalent mean-square noise voltage due to temperature fluctuations becomes

$$\overline{V_T^2} = \frac{Q^2}{1 + Q^2} \left(\frac{V_0}{2} \right)^2 \left(\frac{\alpha C}{TA} \right)^2 \overline{\Delta T^2}$$

where V_0 is the amplitude of the applied ac voltage across the device. An upper limit on this voltage is determined by the point where the thermal effect ceases and is given approximately by

$$V_0/2 \simeq \beta T^2$$

where β is a constant of the device, typically about 10^{-3} V/deg². We then obtain the ratio

$$\overline{V_T^2}/\overline{V_N^2} = \left(Q\alpha\beta \frac{C}{A} \right)^2 \frac{Z}{R} T^3/[1 + (2\pi f\tau)^2].$$

The maximum thermal impedance of the device is limited to the impedance of a purely radiative heat transfer such as might be achieved if the device were suspended on a thin-film membrane in vacuum. We then obtain

$$Z_{max} = 1/8\sigma A T^3$$

where σ is the Stefan-Boltzmann constant. The ratio for this case becomes

$$\overline{V_T^2}/\overline{V_N^2} = (Q\alpha\beta C/A)^2/8\sigma RA [1 + (2\pi f\tau)^2]$$

which is nearly temperature independent. (The temperature dependence of C is nearly offset by the dependence of α and β which was neglected above.) Considering the ratio below frequency cutoff (i.e., $2\pi f\tau < 1$), and inserting typical values, including $C/A \simeq 3 \times 10^{-4}$ f/cm² and $RA \simeq 50$ ohm-cm², we obtain

$$[\overline{V_T^2}/\overline{V_N^2}]_{max} \simeq 4.$$

Thus, it should be possible to achieve the theoretical limit for the best possible performance of a thermal detector without any significant improvement in the parameters. This limit for D^* is given generally by

$$D^* = [16\sigma kT^3]^{-1/2} = 2 \times 10^{16} T^{-5/2}$$

and is independent of all device parameters.

The above assumption that the radiative thermal impedance can be achieved is not unreasonable for the thin-film structure involved. Furthermore, the thermal time constant τ is not increased for this case; that is, $\tau = ZC_T$ where C_T is the thermal capacity, and C_T becomes correspondingly smaller as Z is increased to its maximum. The thermactor also offers other practical advantages such as ac operation, ideal performance under ambient temperature, and easy adaptation to imaging arrays.

B. The Feasibility of Achieving Optical Densities in Magnetic Information Storage

D. I. Tchernev

The highest magnetic information storage density achieved to date is in magnetic recording where the present state of the art is about 1 square mil per bit of information, or about 10^5 bits/cm². This density is limited by the transducers used in this method, namely the record and playback heads. There is considerable interest in magneto-optic methods of information storage and retrieval which would be limited by the wavelength of light to about 10^8 bits/cm². The end objective of the current Magnetism Research task is to demonstrate the feasibility of a magnetic memory having a storage density on the order of 10^8 bits/cm².

The Faraday effect in many magnetic materials is sufficiently strong to permit optical readout with sufficient signal-to-noise ratio. This effect is exhibited when a beam of polarized light is transmitted through a magnetized material parallel to the direction of the magnetization. The polarization is rotated clockwise or counterclockwise, depending on the relative orientation of the magnetization with respect to the direction of propagation of the light beam. The largest Faraday effect in thin films is exhibited when the magnetization is perpendicular to the plane of the film; however, this orientation creates large demagnetizing fields. This orientation also requires materials having a large anisotropy with the easy-axis perpendicular to the plane of the film in order to insure the proper geometry. Such a material is, for example, the compound MnBi, which is ferromagnetic at room temperature and has been shown (Refs. 4, 5) to exhibit a Faraday rotation of ± 8 deg in the visible light region. However, the large anisotropy presents problems during the write process, which will be discussed in a future SPS article.

Another method for overcoming the demagnetizing field in a film magnetized perpendicular to the plane of the film, is to make the film discontinuous. In this case the magnetic film consists, on a microscopic scale, of small ellipsoidal or needle-shaped particles with the long axis of each particle perpendicular to the plane of the film. The magnetization of the particles would be along the axis of the needles because of shape anisotropy. Either acicular particles, in a suitable binder, or evaporated ellipsoids on a substrate can be used for this purpose.

The idea of evaporating elongated magnetic particles with the long axis perpendicular to the plane of the film is a new one and, therefore, will be discussed in more detail. If one evaporates a very thin film (50 Å) of gold or silver on a substrate at elevated temperature, the film is not continuous but consists of small islands (Ref. 6). Using such films as a starting point, one could, by oblique evaporation, make magnetic material (e.g., Permalloy) grow only on the islands and form elongated ellipsoids with the long axis almost perpendicular to the plane of the film. Alternatively, one could electrodeposit the magnetic material in such a way that deposition would take place only on the gold islands (by passivating the rest of the surface). Again, because of the concentration of the electric field lines, the result will be elongated ellipsoids perpendicular to the plane of the film. The main problem in the case of discontinuous films is the scattering of light from the magnetic particles, and, in order to minimize this scattering, one has to make the dimensions of the particles much smaller than the wavelength of light which may present some technological problems.

The most promising method for high-density magnetic writing appears to be thermal writing, also called Curie point writing. In this method one heats a small area of the magnetic material to the vicinity of the Curie point and thus reduces its coercive force so that a weak applied magnetic field can change the direction of magnetization within this area without affecting the areas which are not heated. The heating can be achieved by use of an electron beam or a light beam of sufficient intensity focussed on the area to be heated. Curie point writing on MnBi films with an electron beam has been demonstrated by Mayer (Ref. 7). This method has the disadvantage of being possible only in high vacuum and being limited by the focusing and deflection systems for the electron beam. While focusing of light beams is easier when using collimated laser sources, the deflection of such beams still presents some problems. Electromechanical deflection systems are commercially available; however, the deflection in this case is sequential, which would lower the access time of a totally random access memory. Electro-optical deflection systems, capable of fast random access, are still in the process of development, and it is hoped that they will be commercially available by the time they are needed.

At the beginning of this feasibility study there was some concern about the speed of thermal writing, because of the long time constants usually involved with thermal processes. A more accurate estimate of the heating

process, however, shows no reason for concern. The specific heat of Bi is about 0.03 cal/g, and for Mn about 0.17 cal/g. Assuming that the MnBi compound has a specific heat of 0.2 cal/g, which is a conservative estimate, and taking 10 g/cm³ (again conservative) for the specific gravity of MnBi, the specific heat per unit area of the film will be 0.2×10^{-12} cal/micron². Focusing a 1-watt CW laser, which is already commercially available, on a 1-micron spot will give an energy density of 1 watt/micron². In this case the heating speed of the film would be about 10⁻¹² sec/°C, or about 1 nanosecond for 1000°C.

Assuming that half of the heat is lost due to thermal conduction to the substrate and the neighboring area of the film, it is still possible to heat a 1-micron spot to above the Curie point in less than 1 nanosecond. For a real-time computer, writing speeds of the order of 100 nanoseconds are considered satisfactory, so that the thermal writing will not be a limiting factor in our case.

The main difficulty in obtaining magnetic information storage at optical densities is the interaction between separate bits of information at such short distances. In the case of continuous magnetic films, this interaction consists of the demagnetizing field of the surrounding film at the site of a given spot. This field can be considerable at short distances, and will require a prohibitively large external applied field in order to switch a given spot. This problem is now under study and will be reported later in an SPS contribution. In the case of discontinuous films, the interaction is expressed by the magnetic coupling energy between two acicular particles. This interaction in iron-oxide particles is being measured experimentally.

It is hoped that the results of this research project will determine the closest distance between two magnetic bits of information which will permit them to remain independent. In conclusion, we believe that it is feasible to store magnetic information at densities of 10⁸ bits/cm.

References

1. Maserjian, J., *Conduction Through Thin Titanium Dioxide Films*, Technical Report 32-976, Jet Propulsion Laboratory, Pasadena, Calif., October 1, 1966.
2. Maserjian, J., *A New Thermal Detector*, a paper to be presented at the Langley Research Center/Research Triangle Institute Conference on Thin Films and Sensors, September 1966.
3. Davis, L., *The Threshold Sensitivity Limits of Thermal Infrared Detectors*, Technical Report 6-90-61-78, Lockheed, October 1961.
4. Williams, H. J., Sherwood, R. C., Foster, F. G., and Kelley, E. M., *Journal of Applied Physics*, 28: 1181, 1957.
5. Chen, D., and Gondo, Y., *Journal of Applied Physics*, 35: 1024, 1964.
6. Doremus, R. H., *Journal of Applied Physics*, 37: 2775, 1966.
7. Mayer, L., *Journal of Applied Physics*, 29: 1454, 1958.

ENGINEERING MECHANICS DIVISION

N67 12107

IV. Materials

A. Ceramic Research

*E. C. de Wys and M. H. Leipold***1. Introduction**

The research program to determine the role of grain boundaries and their associated impurities on the mechanical behavior of polycrystalline ceramics continues. Present research is being conducted on magnesium oxide (MgO). Studies, so far, have revealed the following: (1) Impurities in MgO are segregated to the grain boundaries when the total quantity of impurity present is far below the equilibrium solubility limit; (2) impurities may form multiple phases at the grain boundary; (3) lack of visible second phase at the grain boundary is not enough evidence to neglect impurity segregation; (4) many impurities are introduced in the form of agglomerates, but the presence of such agglomerates is not related to the ultimate existence of segregated impurities; (5) anion impurities are significant, although grain boundary segregation has not been determined.

The development of a theoretical model for a pure grain boundary in MgO has been started. Random network theory, which has had success in the description of the structure of glasses, has yielded a model for any interface in an ionic material. The model is based on variations in the coordination number near the interface between a crystal lattice and another phase. SPS 37-37, Vol. IV, pp. 84 and 85, reported analytical techniques for the detection of impurities, the finding of hydroxyl ions, and a thermodynamic study on the decomposition reaction occurring in the preparation of MgO. Hot isostatic pressing — a new method for the fabrication of mechanical testing specimen blanks — was reported in SPS 37-39, Vol. IV, pp. 62-65.

2. Recent Development on Preferred Orientation

The development of preferred orientation during grain growth in hot-pressed MgO was detected by means of the standard proportional-counter transmission technique (Ref. 1). The material source, fabrication procedures and reheating conditions are available in the literature (Ref. 2).

Thin sheets of MgO were prepared from sections cut parallel and at 90 deg to the longitudinal axis of an as-pressed rod (average grain diameter = 5μ) and one in which grain growth had occurred (average grain diameter = 160μ). The grain growth conditions were 2160°C for 1 hr under a gradient of $20^\circ\text{C}/\text{cm}$ parallel to the longitudinal axis. No indication of preferred orientation was found in the as-pressed materials. Pole Figs. 1 and 2

from the parallel and 90-deg orientation sections revealed that an orientation mechanism accompanied the grain growth. Optical examination of the grain structure did not reveal an elongated shape.

The data indicate that the majority of the $[100]$ poles are confined to a 30-deg arc from the thermal gradient direction.

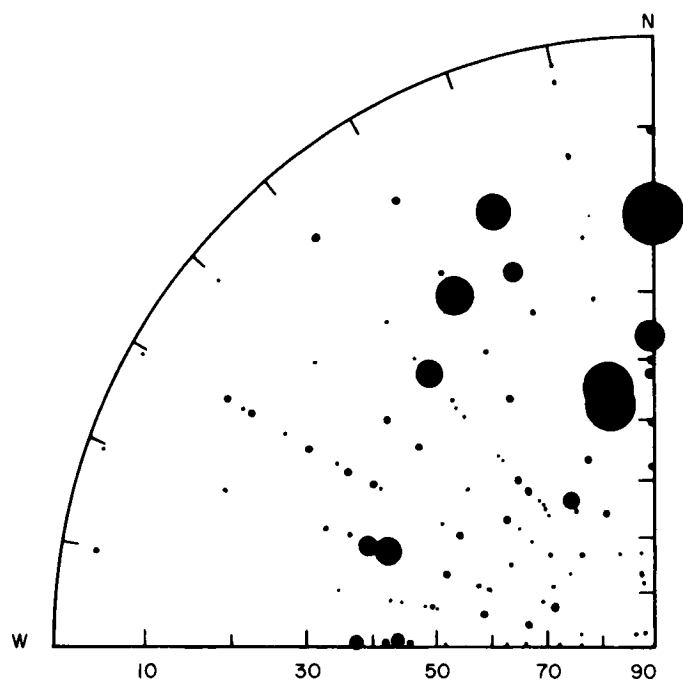


Fig. 1. $[100]$ Pole figure parallel to the axis of hot pressed MgO rod

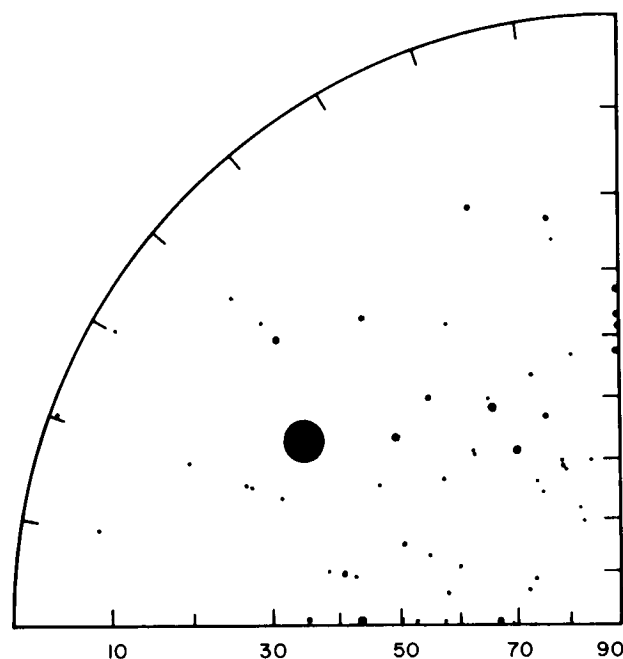


Fig. 2. $[100]$ Pole figure at 90 deg to the axis of pressed MgO rod

References

1. Decker, B. F., Asp, E. T., Harker, D., "Preferred Orientation Determination Using a Geiger Counter X-ray Diffraction Goniometer," *Journal of Applied Physics*, Vol. 19, p. 388, 1948.
2. Nielsen, T. H., and Leipold, M. H., "Thermal Expansion of Ceramic Oxides to 2200°C ," *Journal of the American Ceramic Society*, Vol. 46, p. 8, 1963.

N67 12108

V. Applied Mechanics

A. The Effect of Uncertainties in Transport Properties on Prediction of Stagnation Point Heat Transfer

D. W. Zeh and T. E. Horton

In a previous analysis (Ref. 1) it was shown that significant differences existed in the transport properties generated by various workers. Further, it was shown that in a simplified Couette flow case the predicted heat transfer varied markedly when the different sets of transport properties were used. The purpose of the present study was to confirm similar trends in predicted flow and convective heating in the more complicated, but more important, case of the stagnation region of an axisymmetric blunt body.

The flow was assumed to be laminar, in chemical equilibrium, and described by the usual compressible form of the boundary layer equations, with real gas effects accounted for by use of the total property concept. Viscous dissipation and work of compression were ignored.

Then, the transformation coordinate

$$\eta \propto \int_0^y \frac{dy}{\mu};$$

where

y = coordinate normal to surface

μ = viscosity

and stream function f , of Ref. 2 were used to reduce the momentum and energy equations to the following form:

$$\left(\frac{f'}{\phi_\rho \phi_\mu} \right)'' + 2f \left(\frac{f'}{\phi_\rho \phi_\mu} \right)' - \frac{(f')^2}{\phi_\rho \phi_\mu} + \phi_\mu = 0$$

$$\left(\frac{h'}{P_r} \right)' + 2f h' = 0$$

with the boundary conditions

$$\begin{array}{ll} \eta = 0 : f = 0 & \eta \rightarrow \infty : f' = 1 \\ & f' = 0 \\ & h = h_w \end{array} \quad \begin{array}{l} h = h_e \end{array}$$

N67 12109

B. Comparison of Entry-Body Shapes for Total Equilibrium Radiation Under Mars Entry Conditions

H. J. Stumpf

where

$$\phi_p = \rho/\rho_e,$$

$$\rho = \text{density}$$

$$\phi_\mu = \mu/\mu_e,$$

$$h = \text{static enthalpy.}$$

The subscript *e* denotes conditions at the edge of the boundary layer, *w* denotes conditions at the wall, and primes denote differentiation with respect to η .

The above equations were solved by an iterative numerical technique for a wall temperature of 1000°K and a stagnation pressure of 1 atm, using three different sets of transport properties for air (Refs. 3, 4, 5). The predicted heat-transfer results are shown in Fig. 1. The thermodynamic properties, solution technique, and transport properties near the wall temperature were the same in each case, so that the results obtained were influenced only by differences in the high-temperature transport properties.

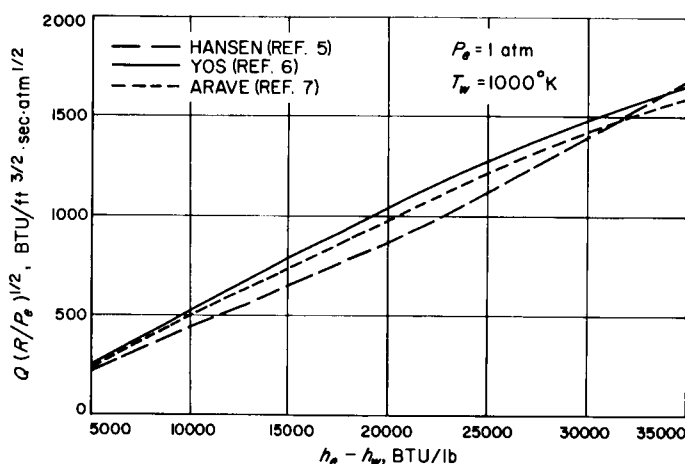


Fig. 1. The effect of transport properties on the stagnation point convective heat transfer in air

The results presented in Fig. 1 are in general agreement with the findings of Ref. 1, and the maximum difference in predicted heat transfer is seen to be about 20%. Since discrepancies may be even more pronounced at higher temperatures and in different mixtures, due caution must be exercised in utilizing heat-transfer estimates based upon transport properties generated from various theoretical formulations, until experimental validation is available.

The Avco Advanced Research and Development Division, Wilmington, Massachusetts, is conducting an experimental program for measuring and comparing the total (over the whole body) equilibrium shock-layer radiative heat transfer for three entry body shapes (Figs. 2 and 3) in a simulated Mars atmosphere. The work is being performed under JPL Contract 951331.

The flight conditions to be simulated correspond to:

$$\text{Velocity} = 19,600 \text{ ft/sec}$$

$$\text{Ambient density} = 9.9 \times 10^{-7} \text{ slug/ft}^3$$

$$\text{Atmospheric composition} = 30\% \text{ CO}_2, 70\% \text{ N}_2 \\ \text{(by volume)}$$

$$\text{Ambient temperature} = 180^\circ \text{R}$$

These flight parameters are similar to those encountered in typical hyperbolic Mars entry trajectories where maximum stagnation point convective or radiative heat transfer occur.

The experimental total radiation results are to be obtained by a combination of measurements in a ballistic range, a shock tube, and a shock tunnel. A model of each entry body will be fired in the ballistic range at zero angle of attack. These data provide information on the shock shape and stand-off distance to adjust the zero angle of attack results in the shock tube. The shock tube work will include tests on each of the three bodies at 0-, 45-, and 90-deg angles of attack using a cone-frustum aft-body. In addition a model of the 60-deg blunt cone, instrumented with fiber optics (quartz light pipes), will be tested at these three angles of attack in order to get some estimate of the radiation distribution about the body and to provide comparative data for the indirect radiation measurements. Finally, a passive model of the blunt cone will be tested at zero angle of attack at free stream pressure levels of 10, 1, 0.5, and 0.25 mmHg in order to assess the effect of the shock layer density on the radiation. The incident shock speed will be adjusted to maintain the same stagnation point gas temperature as in the other shock tube tests. The shock tunnel tests will be run with

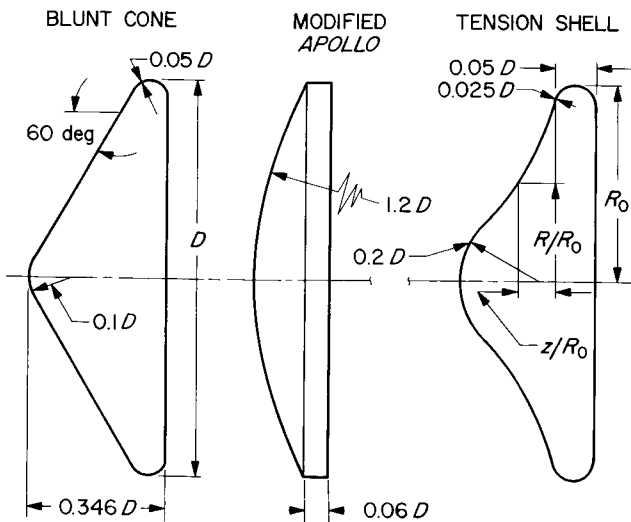
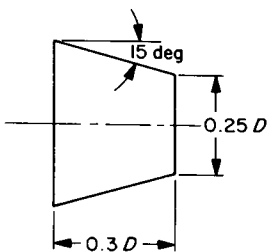


Fig. 2. Entry-body shapes

CONE-FRUSTUM AFT BODY

COORDINATES FOR TENSION SHELL



R/R_0	z/R_0
0.00	0.6301
0.05	0.5835
0.10	0.5372
0.15	0.4913
0.20	0.4463
0.25	0.4022
0.30	0.3594
0.35	0.3180
0.40	0.2784
0.45	0.2406
0.50	0.2050
0.55	0.1716
0.60	0.1407
0.65	0.1129
0.70	0.0869
0.75	0.0643
0.80	0.0448
0.85	0.0285
0.90	0.0155
0.95	0.0059
1.00	0.0000

BALLISTIC RANGE MODEL AFT BODY

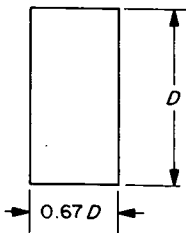


Fig. 3. After-body shapes

CF_4 gas to simulate the low value of ratio of specific heats γ , as in the free flight case and will provide shock shape and stand-off distance information at angle of attack to adjust the shock tube data.

Only the equilibrium shock layer radiation will be measured, since simulating nonequilibrium radiation over

a wide range of angle of attack is impractical. In order to insure that primarily equilibrium radiation will be measured, the nonequilibrium radiation must be suppressed. This is accomplished in the ballistic range by increasing the ambient pressure to 150 mmHg as compared to the expected pressures in the upper Mars atmosphere of approximately 1 mmHg. This introduces complexities, since the increased pressure changes the equilibrium composition of the gas in the shock layer from that expected for the flight condition. In $\text{N}_2\text{-CO}_2$ mixtures for the flight conditions and spectral range stipulated the CN molecule is the most important source of radiation, and a simple correction for the mol fraction of CN from the test conditions to the flight conditions may be sufficient. Another problem introduced by increasing the pressure level is that self-absorption may be significant in the ballistic range and shock tube tests.

A simple analysis¹ of the ballistic range tests can be made by use of Ref. 6 to estimate the importance of self-absorption. If the shock layer at the stagnation point is approximated by a plane parallel slab whose thickness is equal to the shock stand-off distance ℓ , the amount of self-absorption will be small if $\mu^* \ell \ll 1$, where μ^* is a non-gray absorption coefficient defined in Ref. 6. For the ballistic range tests ($V = 15,800$ ft/sec and $P_{\text{stag}} = 50$ atm), $\ell \approx 0.05$ cm and μ^* (CN violet) ≈ 2 cm⁻¹, hence $\mu^* \ell \approx 0.1$. This implies that self-absorption in the range tests is small. The shock tube and flight vehicle shock layers will be affected to a lesser degree so that self-absorption should not be significant in scaling the model test results to flight conditions. No sufficiently accurate experimental data exist to verify these results, so the problem cannot be fully resolved at the present time.

The ballistic range, at present, offers the best means of simulating the actual Mars flight conditions of velocity and density ratio across the bow shock wave. The disadvantages are that the models are small (several orders of magnitude smaller than flight models), and the measurements are limited to zero angle of attack. Although the correct shock shape and stand-off distance can be simulated in the ballistic range, the model size makes it difficult to measure the shock layer thickness accurately.

The Avco Ballistic Range Facility is shown schematically in Fig. 4. A caliber 0.60 three-stage hydrogen gun is used to accelerate the sabot 0.4-in. aluminum model to a velocity of 15,800 ft/sec. The model is spin-stabilized by means of a rifled launch tube and a spin rate of approximately 1600 rps is attained at peak velocity. A flash

¹Dyner, H. B., staff scientist, AVCO-Rad, private communication.

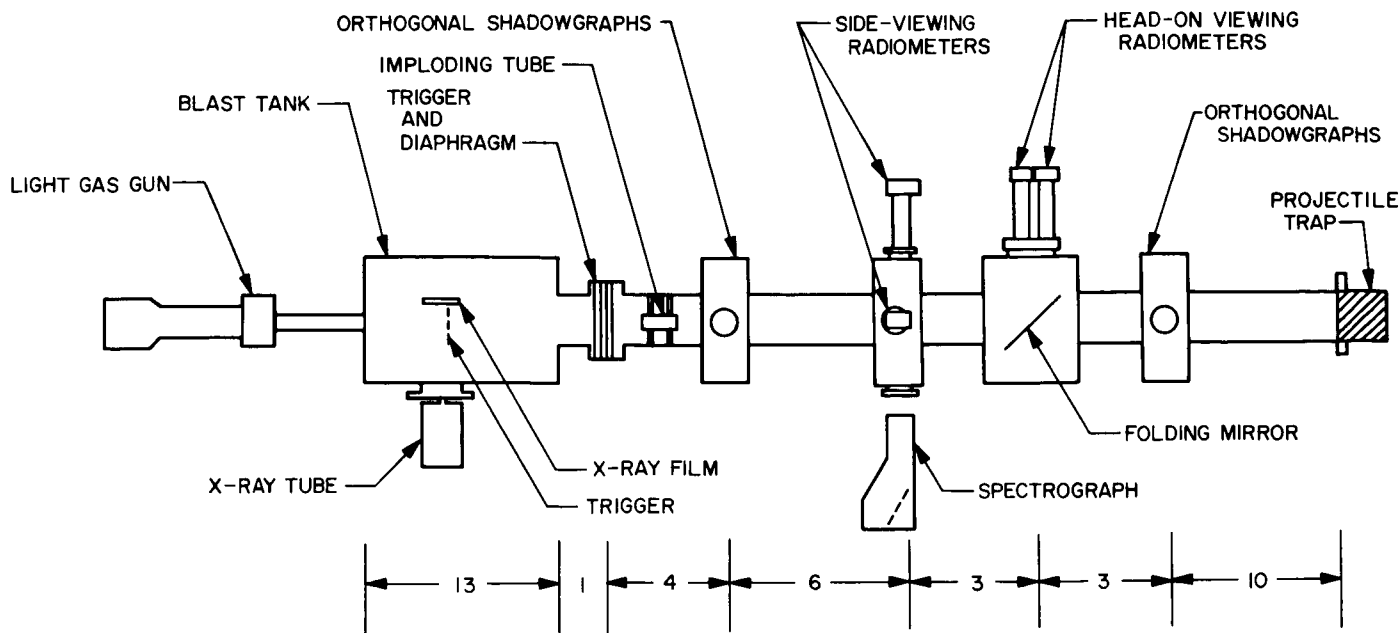


Fig. 4. AVCO ballistic range test facility

X-ray of the model is taken 3 ft from the muzzle to monitor structural failures which may have occurred during the acceleration. The test section is filled with a 30% CO_2 -70% N_2 mixture at a pressure of 150 mmHg. A 1½-in.-D thin-walled aluminum tube wrapped with primer cord is explosively closed 20 to 40 μsec after the model has passed, stopping spurious particles and gases from entering the test section.

Two sets of orthogonal shadowgraph stations are used to obtain angle of attack before and after the radiometer stations, so that an extrapolated angle of attack history between the two stations can be obtained. A 10-Mc chronograph is used to measure the traversal time between the two stations to determine the speed of the model.

The first radiometer station is used to monitor the occurrence of ablation and views the model as it passes collimated slits in front of the two photomultipliers. One photomultiplier is filtered to monitor an aluminum line (3944Å), and the other is filtered to monitor background or continuum radiation off the aluminum line. A grating spectrograph has been installed at this station to monitor a broad band of radiation (3700 to 6200Å).

The last radiometer station views the noscap radiation head-on by means of a 45-deg folding mirror made of a piece of aluminized mylar. Two photomultipliers are used

to monitor broad bands of radiation in the blue and red regions of the spectrum.

The shock tube and shock tunnel can be adapted to making angle-of-attack measurements of the total radiation. The shock tube can match the stagnation point enthalpy of the flight model, but it cannot simulate the high-density ratio across the shock wave; thus, the shock stand-off distance as measured in the shock tube is too large. The test section of the shock tube is filled with a 30% CO_2 -70% N_2 mixture at a pressure of 5 mmHg. The combustion driver produces an incident shock velocity of 3.65 mm/ μsec , resulting in a stagnation point gas temperature and a stagnation point pressure-model diameter product equal to that obtained in the ballistic range. External radiation measurements will be made in two wavelength regions, 3400 to 6000Å and 6000 to 12,000Å. The noscap radiation from the model will be split by a beam splitter mirror and two double convex lenses will image the radiation onto the photocathodes of the photomultiplier tubes.

Shock tunnel measurements on shock shape and stand-off distance will be made to support the shock tube tests, since a flow Mach number of 2 to 3 is the best that can be attained in the shock tube. These experiments are performed in the Avco RAD 20-in.-D shock tunnel. The high-pressure, high-temperature working gas is provided by a 1½-in.-D shock tube. To study the effect of Mach number on the shock shape and stand-off distance, it is desirable

that the γ achieved in the tunnel match that of the shock tube. Since the shock tunnel operates at a rather low stagnation enthalpy, it is not possible to generate the required value of γ by equilibrium decomposition of the Mars model atmosphere. It is achieved by using a gas such as CF_4 , which has a low predictable γ at the low stagnation temperature ($<2000^\circ\text{K}$) expected in the shock tunnel runs. A flow Mach number of approximately 8 is achieved in the shock tunnel. A double-pass coincidence schlieren system will be used to obtain photographs of the flow over each model at three angles of attack.

On July 10 the ballistic range and shock tunnel tests were completed. The work remaining to be done in the shock tube is the instrumented model tests and the blunt cone tests at various free stream pressures. Preliminary indications from the ballistic range tests are that the modified *Apollo* shape is subject to much higher equilibrium shock layer radiation than either the blunt cone or tension shell. A final report describing the test program and results is scheduled for early September 1966.

N67 12110

C. Flow Field Computations for Blunt Bodies in Planetary Atmospheres

H. J. Stumpf

A contract is presently being negotiated for flow field calculations about blunt bodies in a simulated inner planet atmosphere. The purpose of these computer studies is to determine by numerical techniques, the state and motion variables and heat-transfer distributions (both convective and radiative) about spherically blunted and spherically edged "very blunt" conical bodies, traveling at hypersonic velocities. The free-stream conditions and blunt-body velocities will be similar to those encountered in typical hyperbolic Mars entry trajectories where maximum stagnation point convective or radiative heat transfer occur. The results will also be approximately applicable to Venus entry from orbit, when high-altitude deceleration is considered.

These calculations are very useful for planetary entry studies, and, in addition, will be helpful in interpreting the results of two JPL contracts with the AVCO Advanced Research and Development Division. The first of these contracts (JPL Contract 951070) is for the develop-

ment of a set of computer programs for preliminary entry vehicle design studies. The other contract (JPL Contract 951331) is an experimental program for measuring and comparing the total (over the whole body) equilibrium shock-layer radiative heat transfer for several shapes of entry bodies in a simulated inner planet atmosphere (see Sect. B).

Several of the computer programs of the entry-vehicle design study are utilized to predict the convective and radiative heat-transfer distributions about blunt bodies, and because the study treats all aspects of the vehicle design problem, the analysis is simplified to a large extent. The body pressure distribution is treated by Newtonian theory; little flow detail is given in the shock layer; the radiative and convective heat-transfer distributions are computed using simple models; no coupling effects among the flow field and the convective and radiative heat-transfer modes are considered; and nonequilibrium radiation is treated in a very approximate way. There is a strong incentive to use the programs developed by the AVCO RAD Division for a large amount of preliminary work, since they require relatively little machine time. It is very important, however, to assess the accuracy of the results. The proposed flow field computations would serve as an excellent check on the radiative and convective heat-transfer distributions, and the equilibrium and nonequilibrium radiation from the shock layer as determined by these computer programs.

One of the objectives of the experimental total radiation program described in Sect. B is to predict from the test results the total radiative heat transfer to a full-size vehicle for given flight conditions. Scaling to a full-size vehicle gives rise to a number of problems:

- (1) Body size must be scaled up by several orders of magnitude, since the ballistic range models are 0.4-in. in diameter, and the shock tube and shock tunnel use 2-in.-D models.
- (2) The accuracy of the corrections to shock shape and stand-off distance made in the shock-tube tests must be determined.
- (3) The importance of self-absorption in the shock layer on the total radiation measurements made in the ballistic range tests must be determined.
- (4) The relative importance of equilibrium and non-equilibrium radiation must be evaluated. This is particularly important in the shoulder region, since relatively small changes in heat-shield thickness in this area may result in substantial increases in the total heat-shield weight.

- (5) The accuracy of scaling rules must be determined.

The flow field computer study is intended to obtain calculations utilizing well-developed numerical techniques that will serve as a theoretical check on these uncertainties. The following series of calculations will be made.

1. Ballistic Range Conditions (Equilibrium)

To check the total radiation measurements made by Avco in the ballistic range a calculation will be made for each of the two bodies shown in Fig. 2. The model diameter and flight conditions listed below match those of the range tests.

$$\text{Velocity} = 15,800 \text{ ft/sec}$$

$$\text{Ambient density} = 5 \times 10^{-4} \text{ slug/ft}^3$$

$$\text{Atmospheric composition} = 30\% \text{ CO}_2, 70\% \text{ N}_2 \\ \text{(by volume)}$$

$$\text{Ambient temperature} = 540^\circ \text{R}$$

$$\text{Model diameter} = 0.4 \text{ in.}$$

$$\text{Angle of attack} = 0 \text{ deg}$$

2. Flight Conditions (Equilibrium)

To assess the accuracy of the scaling procedure used by Avco and to check the results of the Entry Vehicle Design Computer Program a calculation will be made on each of the two bodies (blunt cone and modified *Apollo*) of Fig. 2 in Sect. B. The body diameter will be similar to a full-size vehicle, and the flight conditions listed below will be typical of those encountered in a hyperbolic Mars entry trajectory where maximum stagnation point convective or radiative heat transfer occur.

$$\text{Velocity} = 19,600 \text{ ft/sec}$$

$$\text{Ambient density} = 1 \times 10^{-6} \text{ slug/ft}^3$$

$$\text{Atmospheric composition} = 30\% \text{ CO}_2, 70\% \text{ N}_2 \\ \text{(by volume)}$$

$$\text{Ambient temperature} = 180^\circ \text{R}$$

$$\text{Model diameter} = 12.0 \text{ ft}$$

$$\text{Angle of attack} = 0 \text{ deg}$$

The flow model will be that of a radiating and conducting gas in chemical and thermal equilibrium. The shock layer is assumed to consist of an outer inviscid layer and a boundary layer. The effects of viscous-inviscid coupling, self-absorption, coupling between the heat-transfer modes, and the effect of radiation cooling on the flow field will be determined. The numerical techniques utilized in determining the inviscid flow field will be the direct method of Gravalos (Ref. 7) for the transonic region, a relaxation method for the subsonic region, and the method of characteristics for the supersonic regime. The viscous flow field is determined by a finite difference, nonsimilar boundary layer solution based upon work by Flügge-Lotz and Blottner (Ref. 8).

3. Flight Conditions (Nonequilibrium)

To estimate the importance of nonequilibrium radiation for hyperbolic Mars entry conditions the calculation in (2) will be repeated for a gas in chemical nonequilibrium. Preliminary estimates for this flight condition indicate that nonequilibrium chemistry effects may be significant.

Except for the nonequilibrium chemistry, the flow model will be the same as that for calculations (1) and (2). The numerical techniques used will be the one-strip method of integral relations (Ref. 9) for the subsonic region, and the method of characteristics in the supersonic region. The velocity gradient at the stagnation point will be computed by the method of Lighthill (Ref. 10) since the one-strip integral relations method is not sufficiently accurate in the region of the stagnation point.

4. Flight Conditions (Numerical Technique Check)

To determine the effect of the different numerical techniques on the flow field solution, the calculation in Sect. 2 will be repeated for the blunt cone, using the one-strip integral relations method.

The calculations will provide information that can be utilized in assessing the accuracy of the simplified computational techniques for blunt bodies now available as computer programs, the experimental measurements of total radiation now in progress, and methods of predicting radiative heat transfer to flight vehicles from model testing. In addition, the calculations will indicate the importance of nonequilibrium radiation for typical Mars hyperbolic entry conditions and will compare the results from two computational schemes, the Gravalos method and the integral relations method.

N67 12111

D. Environmental and Physical Effects on the Response of Balsa Wood as an Energy Dissipator

A. C. Knoell

1. Introduction

Balsa wood, an RF transparent material, is known to be a structurally and materially efficient energy dissipator in an Earth environment. Initial investigations (Ref. 11), which established the response of balsa wood at discrete levels of moisture content and temperature, have demonstrated that balsa wood develops high specific energy dissipation capacities at relatively low crushing stresses. These investigations have led to the design, fabrication, and prototype testing of spherical impact limiters using balsa wood as the energy-dissipating material.

The design capability associated with balsa wood impact limiters could be further enhanced, however, by a better understanding of physical and environmental effects on the response of balsa wood as an energy dissipator. To forward this understanding, an in-house development program (previously described in SPS 37-34, Vol. IV, pp. 91-92) was undertaken to provide engineering data in the form of design relations establishing the effects of temperature, pressure, moisture content, and density on the energy-dissipating capabilities of balsa wood. This report summarizes the results of that program.

2. Scope of Effort

In establishing the above-mentioned relations, a range of program parameters was selected to cover potential environmental and physical conditions of the balsa wood impact limiter at lunar or planetary impact. The ranges of parameters considered were:

$$-125 < \text{mean temperature } (^{\circ}\text{F}) < 300$$

$$10^{-5} < \text{pressure (mmHg)} < 760$$

$$0 \leq \text{moisture content (\%)} < 20$$

$$5 < \text{nominal balsa wood density (lb/ft}^3\text{)} < 15$$

Engineering data were obtained within the ranges of these parameters by performing static penetration tests parallel to the grain of balsa wood specimens. Penetration

testing, rather than platen testing, was selected to simulate more closely the crushing of a doubly curved impact limiter, since a certain amount of lateral confinement of the loaded element is afforded by the adjacent balsa wood. The program was predicated on providing data points which represent an average of at least three tests.

3. Results

The results of this program, including a detailed description of the test specimens, equipment, instrumentation, and procedure, are presented in Ref. 12. A summary, however, of the effects of temperature, pressure, and moisture content on the energy-dissipating capacity of balsa wood is presented in Fig. 5.

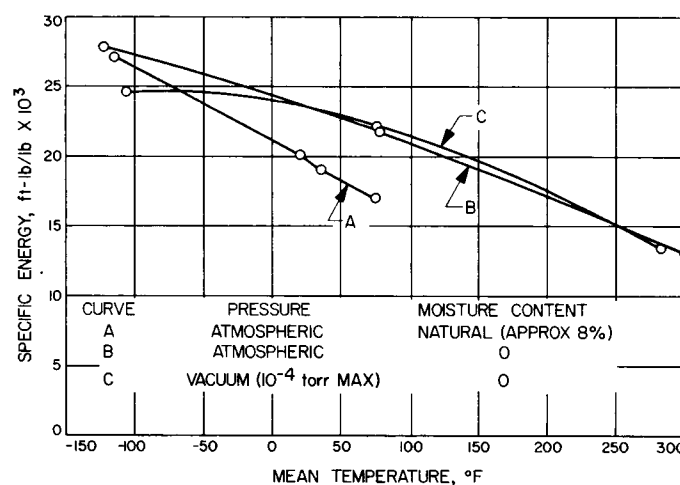


Fig. 5. Specific energy versus mean temperature for nominal 6 lb/ft³ confined balsa wood

Here one sees that the energy-dissipating capacity of nominal 6 lb/ft³ balsa wood increases with decreasing temperature. This response is characteristically true, regardless of the pressure environment or the moisture content of the wood. Of course, the exact design relationship (as indicated by curves A, B, and C) depends on the environment and physical condition of the balsa.

By comparing the ordinates of curves B and C at a given temperature it is evident that pressure has little effect on the response of balsa wood as an energy dissipator. However, a slight decrease in the specific energy dissipation of vacuum-tested balsa wood occurred in the low-temperature range, as compared to the response of balsa tested at atmospheric pressure.

The effect of moisture content on the energy-dissipating capacity of balsa wood is indicated by comparing the

ordinates of curves A and B at a given temperature. At ambient temperature (approximately 75°F) a significant increase in specific energy dissipation resulted when the balsa was tested in the dry (0% moisture content) condition. At approximately -125°F there was virtually no difference in the energy-dissipating capacity of dry and natural moisture content (approximately 8%) balsa wood. This shows that a temperature dependence exists to a specific energy-moisture content relationship developed for balsa wood.

4. Conclusions

Conclusions derived from data obtained in this program are:

- (1) Specific energy dissipation and crushing stress of the balsa wood increased with decreasing moisture content, decreasing temperature, and increasing density.
- (2) Environmental pressure has little effect on response.
- (3) Thickness efficiency is insensitive to physical and environmental variables.
- (4) Specimen response is unaffected by a small amount of lateral confinement.
- (5) Crushing stress varies in magnitude during static crushing of the balsa wood.
- (6) Frequency of balsa wood splitting increases with increasing density.
- (7) Specimen response varied as much as $\pm 15\%$ of the average response of specimens tested under the same physical and environmental conditions.

N67 12112

E. Continuing Development of Phenolic Honeycomb as an Energy Dissipator

A. C. Knoell

A development program designed to improve the energy-dissipating characteristics of phenolic honeycomb

is being conducted by the General Electric Company, Valley Forge, Pennsylvania, under contract to JPL. The main objectives of this program are to: (1) improve the response of this material under high velocity (500 ft/sec) impact, (2) determine its response after sterilization (3 cycles at 300°F for 36 hr in dry N₂), (3) establish feasibility of improving double curvature capability through the use of nonhexagonal cell configurations.

Results obtained to date indicate that use of a thin dip technique for resin buildup on the honeycomb glass-cloth core appears sufficient to preclude previously experienced (JPL Contract No. 950564) failures of the honeycomb at the node bond lines during crushing. This development is significant, as it applies directly to the performance of phenolic honeycomb specimens under high velocity impact. Tests conducted statically and at an impact velocity of 50 ft/sec have shown that the improved specimens crush uniformly, with no evidence of separation at the node bond lines. Specific energies of approximately 19,000 ft-lb/lb (including thickness efficiency) with corresponding crushing stresses of 2000 psi have been achieved for those specimens having a bulk density of approximately 11 lb/ft³.

It has also been shown that:

- (1) The use of new "high temperature" resins in the fabrication of honeycomb specimens does not increase the energy-dissipating capability of the honeycomb over that of specimens fabricated with the standard phenolic resin system.
- (2) Substitution of paper in place of glass cloth as the honeycomb skeletal core causes a reduction of approximately 40% in the energy-dissipating capacity of the honeycomb.
- (3) Resin cure temperature has a definite effect on the crushing strength of phenolic honeycomb in that the lower cure temperatures result in lower values of specific energy dissipation.
- (4) A prefabricated depth of approximately 0.3 in. is required to insure that the initial peak force will not exceed the quasi-steady-state crushing force of phenolic honeycomb.

References

1. Horton, T. E., "Effect of Transport Properties on Couette Flow," SPS 37-31, Vol. IV, Jet Propulsion Laboratory, pp. 115-117, February 28, 1965.
2. Hoshizaki, M., "Heat Transfer in Planetary Atmospheres at Super Satellite Speeds," *ARS Journal*, Vol. 32, p. 1544, 1962.
3. Hansen, C. F., "Approximations for the Thermodynamic and Transport Properties of High Temperature Air," NASA TR 50, National Aeronautics and Space Administration, Washington, D.C., 1959.
4. Yos, J. M., "Transport Properties of Nitrogen, Hydrogen, Oxygen and Air to 30,000°K," RAD-TM-63-7, Avco Corporation, Wilmington, Massachusetts, March, 1963.
5. Arave, R. J., "Approximate Thermodynamic, Transport and Electrical Properties of High Temperature Air," D2-11781, Boeing Company, Seattle, Washington, January, 1963.
6. Meyer, H. G., Ohrenberger, J. T., and Thompson, T. R., "Emission and Absorption of Radiant Energy in a Model Planetary Atmosphere," *AIAA Journal*, Vol. 3, No. 12, December 1965.
7. Gravalos, F. G., Edelfelt, I. H., Emmons, H. W., "The Supersonic Flow About a Blunt Body of Revolution for Gases at Chemical Equilibrium," Proceedings of the 9th Annual Congress of the International Astronautical Federation, Amsterdam, 1958.
8. Flügge-Lotz, I., and Blottner, F. G., "Computation of the Compressible Laminar Boundary Layer Flow Including Displacement Thickness Interaction Using Finite Difference Methods," Stanford University, Division of Engineering Mechanics TR 131, January, 1962.
9. Belotserkovskii, O. M., "Supersonic Symmetrical Flow of Perfect and Real Gases Around Blunt Bodies," *Journal of Computing Mathematics and Mathematical Physics*, Vol. II, No. 6, 1962.
10. Lighthill, J. J., *Journal of Fluid Mechanics*, Vol. 2, p. 1, 1957.
11. "Impact Technology Document," Publication No. U-3031 (JPL Contract No. 950996), Aeronutronic Division of Ford, Newport Beach, California, February, 1965.
12. Knoell, A. C., "Environmental and Physical Effects on the Response of Balsa Wood as an Energy Dissipator," Technical Report No. 32-944, Jet Propulsion Laboratory, Pasadena, California, June 15, 1966.

N67 12113

VI. Electronic Parts Engineering

A. Accelerated Life Testing of Transistors

E. Klippenstein

A basic problem with normal life testing of transistors is the long time required to obtain significant and meaningful results. A solution to this problem is the acceleration of life tests. However, a major difficulty exists in validly relating the performance characteristics resulting from accelerated tests to the performance characteristics that would be obtained at stress conditions of normal use.

A program has been initiated to study the techniques of accelerated testing and to determine the acceleration obtained by both incremental increases in stress and high constant stresses. The test device for this study is a Motorola 2N2222 transistor, and the applied stress is the temperature at the collector-base junction. The test design is such that relationships can be derived between effects observed at various stress levels and effects observed at normal rated life tests. A large group of transistors will be tested at rated levels for a long period of time and will be the basis for comparison.

Since junction temperature was the selected stress, it was necessary to have a means for accurately determining the junction temperature. Therefore, preliminary to the actual testing phase of the accelerated test program, a study program was completed for determining the opti-

mum method for measurement of thermal resistance. Thermal resistance is the temperature rise at a specified junction per unit of applied power. Thermal resistance can be measured indirectly by taking advantage of the temperature-sensitive characteristics of the base-emitter voltage (VBE). Two techniques for determining thermal resistance using the VBE method were investigated in detail, using different instrumental setups. Thermal resistance measurements were performed at various power levels and during various modes of operation. Accuracy of the techniques was independently compared with results obtained by direct methods: (1) thermocouple bonded to the junction, (2) temperature-sensitive paint, and (3) infrared microscope. The VBE method proved to be the most repeatable and most accurate. The accuracy was independently verified within experimental error by the direct methods. It appears from this study that junction temperature can be determined to within $\pm 2\%$ and is repeatable to within $\pm 1.5\%$. It is anticipated that junction temperature cannot be controlled to better than $\pm 5^\circ\text{C}$ at a target temperature of 300°C because of tolerances in ambients, applied power, and components. Therefore, it was concluded that the thermal resistance measurements by the VBE method would be sufficiently accurate.

Because the purposes of this program are to investigate several testing schemes and to develop valid relationships between accelerated and rated tests, it is expected that most difficulties still lie ahead. Some time will be required before this accelerated test program is completed, and valid acceleration factors are demonstrated.

N67 12114

VII. Electromechanical Engineering Support

A. Development of Wirecon Utility Test Module

E. R. Bunker, Jr.

1. Introduction

A small electronic module, which would employ regular spacecraft packaging techniques and high-reliability components, was needed for various programs such as the *Voyager* electronic components embedment investigation, a sterilizable equipment investigation, the low-temperature embedment pressure transducer development, and an evaluation of heat sinks and thermal flow. The final module, utilizing cordwood packaging on the Wirecon (wire-connected) header packaging approach being developed at JPL, can be used as a standard test configuration for tests of operation at temperature extremes, evaluation of the embedment pressures generated by various encapsulation systems on electronic components, and the effects of sterilization. Specific design objectives of this module were as follows:

- (1) To employ a circuit similar to those used in spacecraft systems.
- (2) To provide a capability to determine the effects of pressure, temperature, etc., on individual components.
- (3) To make available internal provisions for measuring the compressive forces of the encapsulant.

- (4) To employ JPL high-reliability components throughout.
- (5) To provide sources of internal heat so that thermal profiles may be established in the module to determine the effectiveness of various heat sinks.
- (6) To choose a circuit which could be used in large numbers in a specific test without requiring an excessive amount of peripheral equipment to monitor their operation.
- (7) To employ the latest module packaging and welding techniques.
- (8) To use high-reliability techniques throughout.

2. Description

Fig. 1 is a sketch showing the size and locations of major parts. The two holes are for a measurement of the embedment pressures generated, using the mercury thermometer technique described in SPS 37-34, Vol. IV, pp. 93-96. Since pressure measurements by thermometers have limited practicality in module tests, the region immediately adjacent to each hole is reserved for the embedment pressure transducers being developed.

The schematic diagram is shown in Fig. 2. With the jumpers connected as shown in the dotted lines, the circuit is a six-transistor flip-flop of conventional configuration. Transistors Q1 and Q4 provide a high impedance

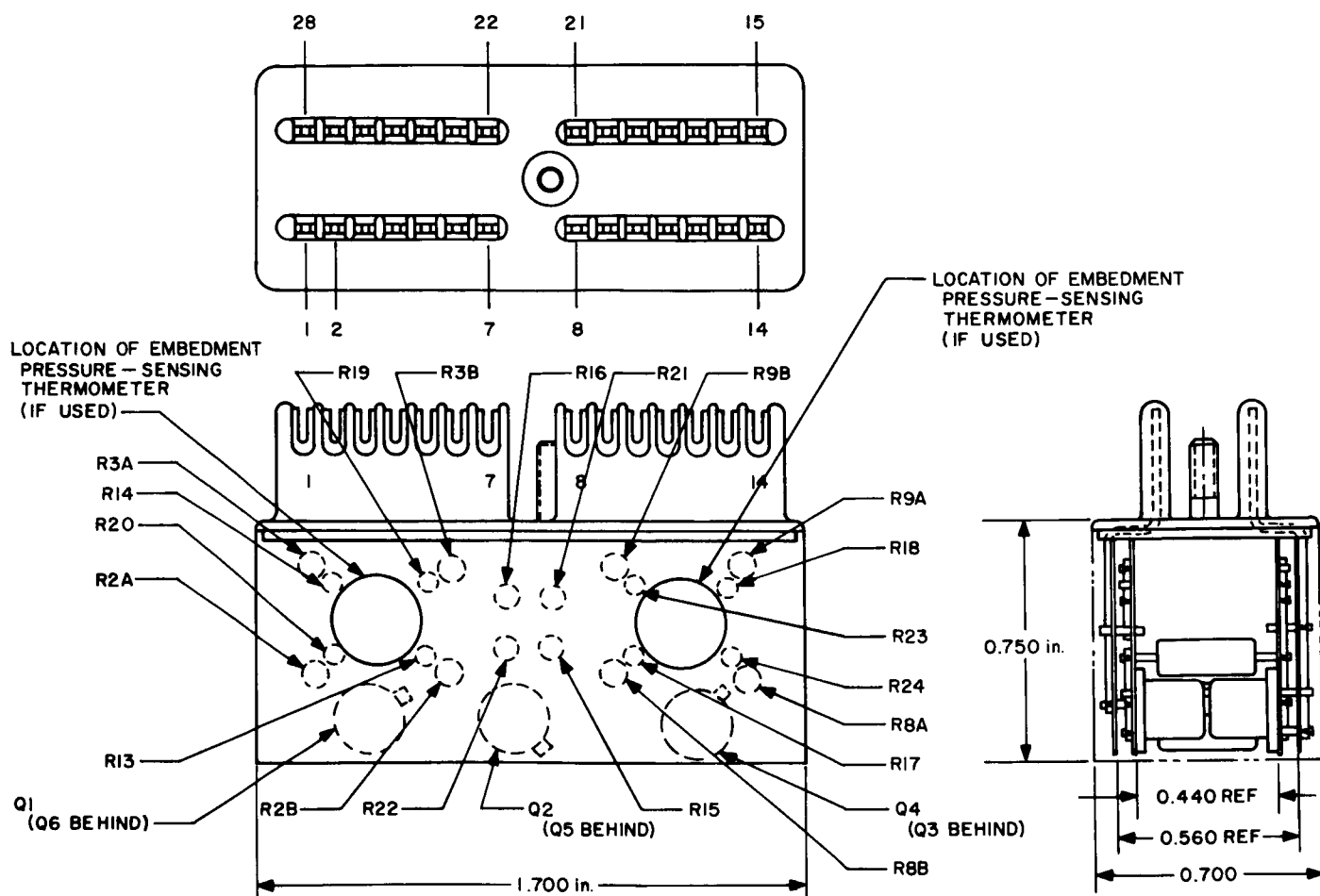


Fig. 1. Wirecon utility module configuration

input and steering of the trigger pulse. Transistors Q2 and Q5 comprise the flip-flop proper and transistors Q3 and Q6 provide a low impedance output and isolation of the flip-flop stage. Arbitrarily defining the conduction of Q2 as the *zero* state, and conduction of Q5 as the *one* state, a negative pulse applied to pin 28 provides the *set* function causing Q5 to conduct setting the flip-flop in the *one* condition. Pin 15 is the *reset* input which will restore the flip-flop to the *zero* condition. Pin 19 is the complementary input which switches the flip-flop into the opposite condition for every negative pulse applied. The output square wave from either output pin 2 or 12 is a scale of 2 countdown of the pulse rate applied to the *complementary* input.

The 28 available pin connections from the Wirecon header allow a connection to every node in the circuit which enables almost every component to be monitored separately and independently when the jumpers are removed. For example, the characteristics of transistor Q1

can be measured by an external transistor checker connected to Pin 5 for the emitter, Pin 3 for the base, and Pin 14 for the collector. Each of the 10 diodes can be measured for forward and back resistance.

Resistors R13 through R24 comprise the three pressure-sensing bridges which may be used to measure the embedment stresses generated by the encapsulant. As was mentioned before, two of these are located adjacent to the space reserved for the two pressure-sensing thermometers.

Resistors R2, R3, R8, R9, are located so that a temperature profile may be generated through the module. Actually, each resistor consists of two in series (designated A and B on Fig. 1), so that a greater volume may be heated during thermal tests. Application of voltage to the proper terminals will simulate the generation of heat by other circuits employing the 28-pin Wirecon module.

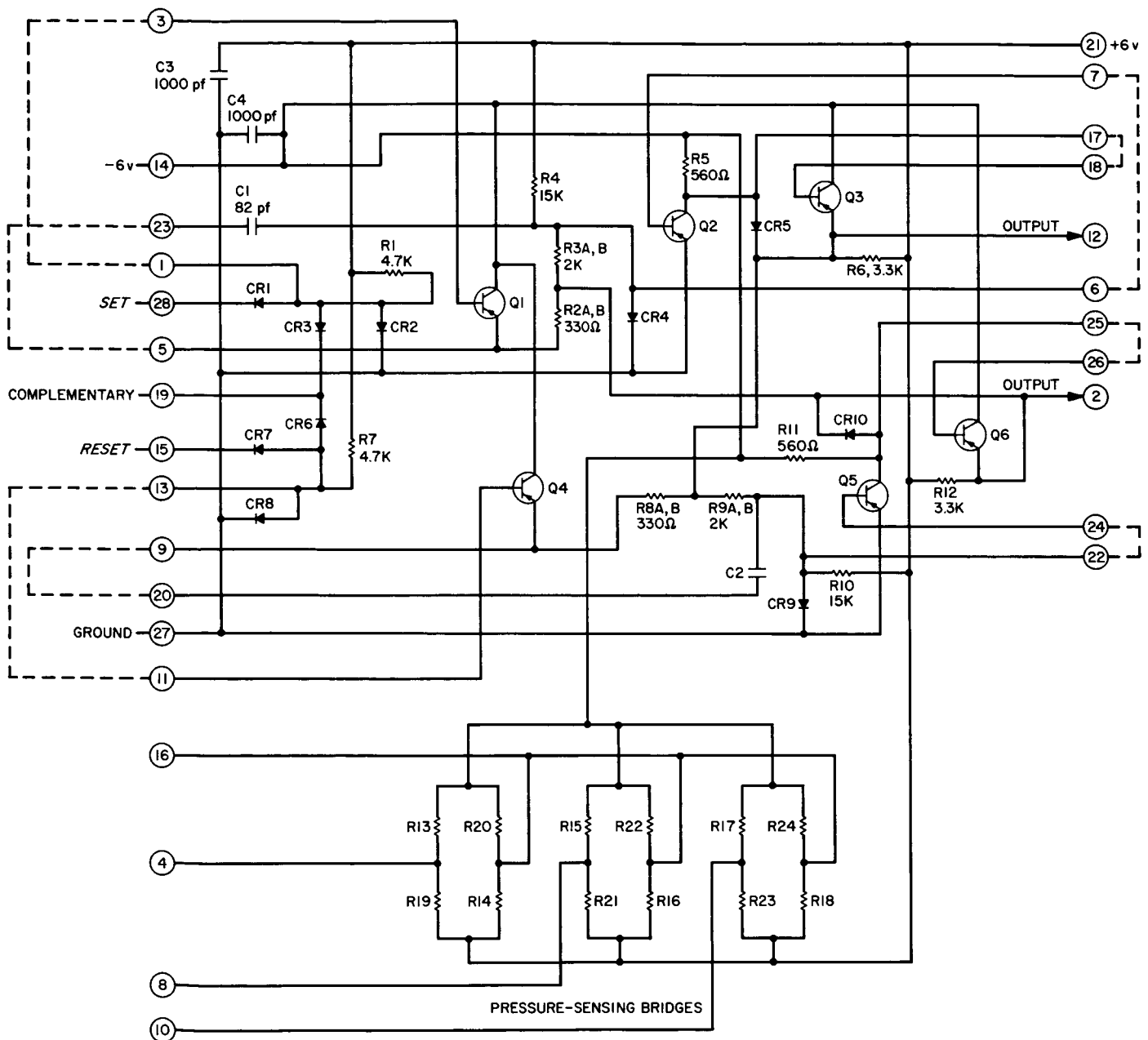


Fig. 2. Wirecon utility test module showing jumpers for flip-flop operation

The circuit is not critical as to the types of components employed, and it can be used for evaluation of other components. Substitution of transistors by others with greatly differing gains and other characteristics would require some readjustment of the component values. Capacitors C1 and C2 are used to improve the transient response of the flip-flop circuit and consequently depend somewhat on the transistor characteristics. However, Capacitors C3 and C4 were originally intended for the purpose of filtering the 6-v and -6-v power inputs. However, these values

are not critical, and any capacitor of any value and type which will fit in the space allocated can be included for the purposes of evaluating or testing that particular type.

Interconnection of a large number of modules can be achieved, as shown in Fig. 3. An RC differentiator or peaker circuit is required between the output of one module and the input of the next. Digital equipment can be used to monitor the countdown operation of the cascaded circuits while the modules are undergoing environmental

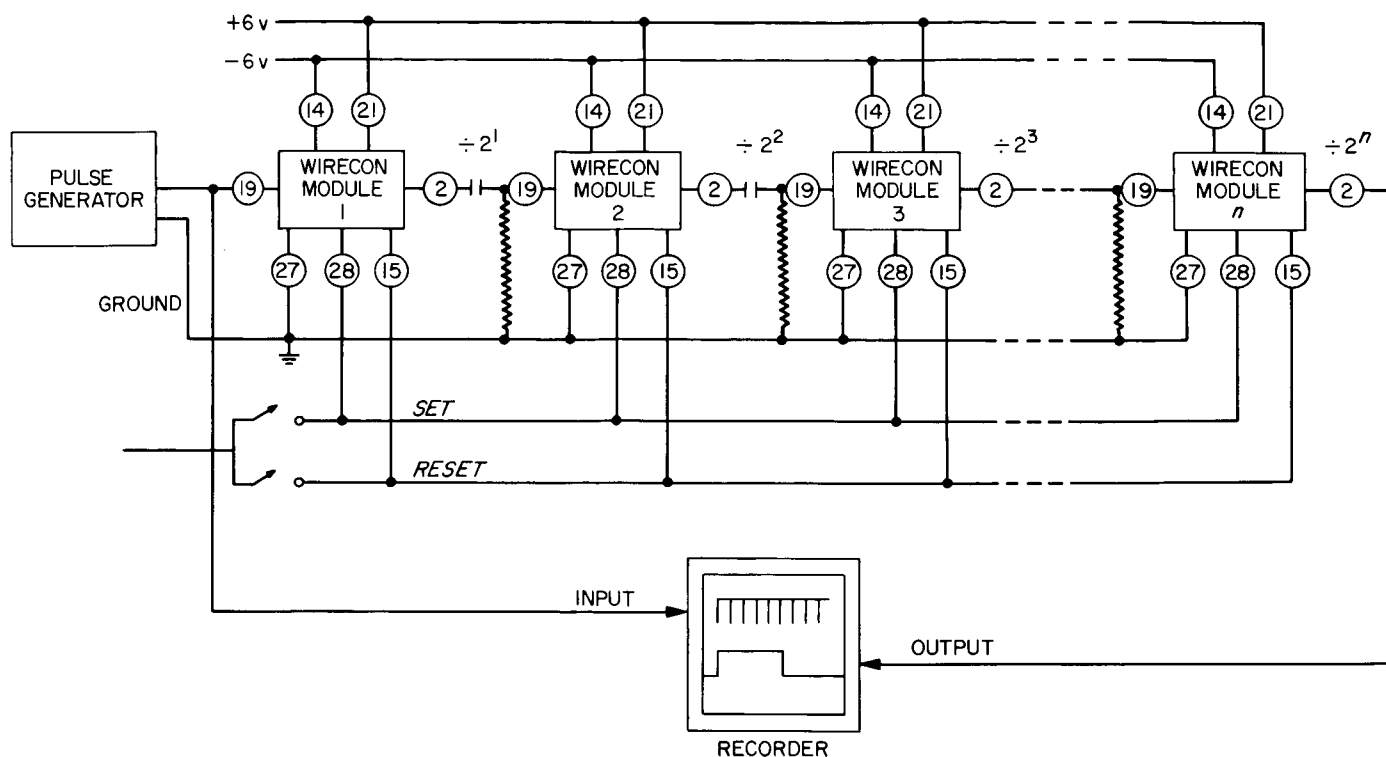


Fig. 3. Interconnection of Wirecon modules

tests in order that a skip or miss of a count can be detected. On the other hand, with suitable external indicators connected to each module, the *set* and *reset* functions can be applied by means of push buttons connected to all of the circuits in parallel so that the operation of the flip-flops can be observed.

3. Test Results

During the development of this module three configurations were constructed and tested. These were a breadboard, a twice scale model module and a normal scale module. During the test it was found that all three modules performed nearly identically, except at the higher pulse rates, where the effect of lead length in the breadboard module became serious at the 100-kHz repetition frequency. The trigger voltage amplitude for reliable triggering of the flip-flop circuit should be greater than 1.6 v peak negative at frequencies from 0 to 10 kHz. At a 100-

kHz triggering rate the threshold voltage rises to 4.1 v peak. Over all frequencies and temperatures the output voltage was a square wave of approximately 4.1 v amplitude. All three configurations were exposed to the sterilization cycle of 250°F for 72 hr. Before returning to ambient temperature, power was applied to the breadboard module and a test run was made of triggering voltage amplitude versus reliable triggering. It was found that there were regions of input voltage amplitude which would not result in triggering of the module, while on either side of these regions reliable triggering would be obtained. The cause of this phenomenon has not been determined. The breadboard and the twice scale module were exposed to temperatures as low as -100°F and tested as before. At this low temperature it was found that reliable triggering would occur up to 6 v amplitude input. This was more pronounced in the breadboard than in the twice scale module, showing that lead length probably was a factor.

ENVIRONMENTAL SIMULATION DIVISION

N67 12115

VIII. Aerodynamic Facilities

A. Wind Tunnels

*J. T. Welton, B. Walker, W. R. Kerr,**W. J. Marko, and E. R. Bate, Jr.***1. Hypersonic Wind Tunnel Stagnation Conditions,** *J. T. Welton*

Test 21-186 is a continuing effort to document the maximum and minimum stagnation conditions in the Hypersonic Wind Tunnel. Data have been obtained at Mach numbers, 5.0, 5.5, 6.0, 6.5, 7.3, 8.0, 8.5, 9.0, 9.5, 10.1, and 11.0. The one remaining Mach number, 4.0, will be documented as time permits. This test is one of several operations-oriented tests designed to better define the operating capabilities of the JPL wind tunnels. Data to determine Mach number variation as a function of supply pressure will be obtained in the near future.

2. Wedge Wake Study, *B. Walker and W. R. Kerr*

The purpose of Tests 20-626 and 20-626A was to make detailed flow measurements in the near wake of a slender two-dimensional wedge with injection of gaseous nitrogen from the base. These tests were performed in

cooperation with TRW Systems of Redondo Beach, California. The tests were conducted in the 20-Inch Supersonic Wind Tunnel at a Mach number of 4.0 and a Reynolds number per inch of about 0.25×10^5 .

The model (Figs. 1 and 2) was a 6-deg half-angle wedge with a porous base 1 in. high through which gaseous nitrogen could be injected into the flow. In addition, the model had cooling passages through which liquid nitrogen could be circulated, thus allowing tests to be run in either adiabatic or cold wall condition. The measurements in the wake were obtained by use of static and pitot pressure probes and by the use of a hot-wire anemometer, all of which were mounted on a vertical traversing rig. In addition to the wake measurements, surface pressure and temperature measurements were made.

The data show that small rates of injection of gaseous nitrogen from the base of the model can cause significant changes to the wake structure. These changes are illustrated in Figs. 3, 4, and 5. Fig. 3 shows a comparison of wake-centerline static pressure with and without base injection. The relatively low injection rate, which was about 4% of the mass flow intercepted by the projected frontal area of the wedge, creates an unusually uniform

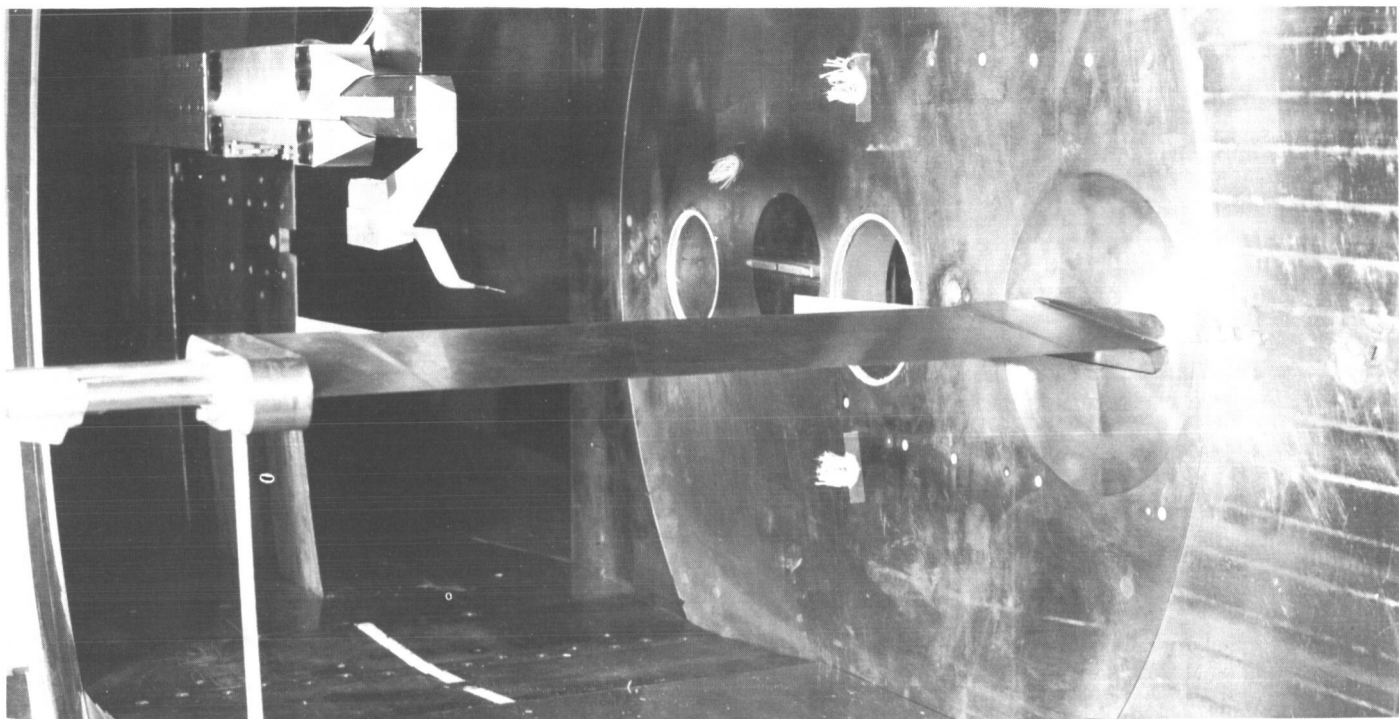


Fig. 1. Installation of wedge and static probe

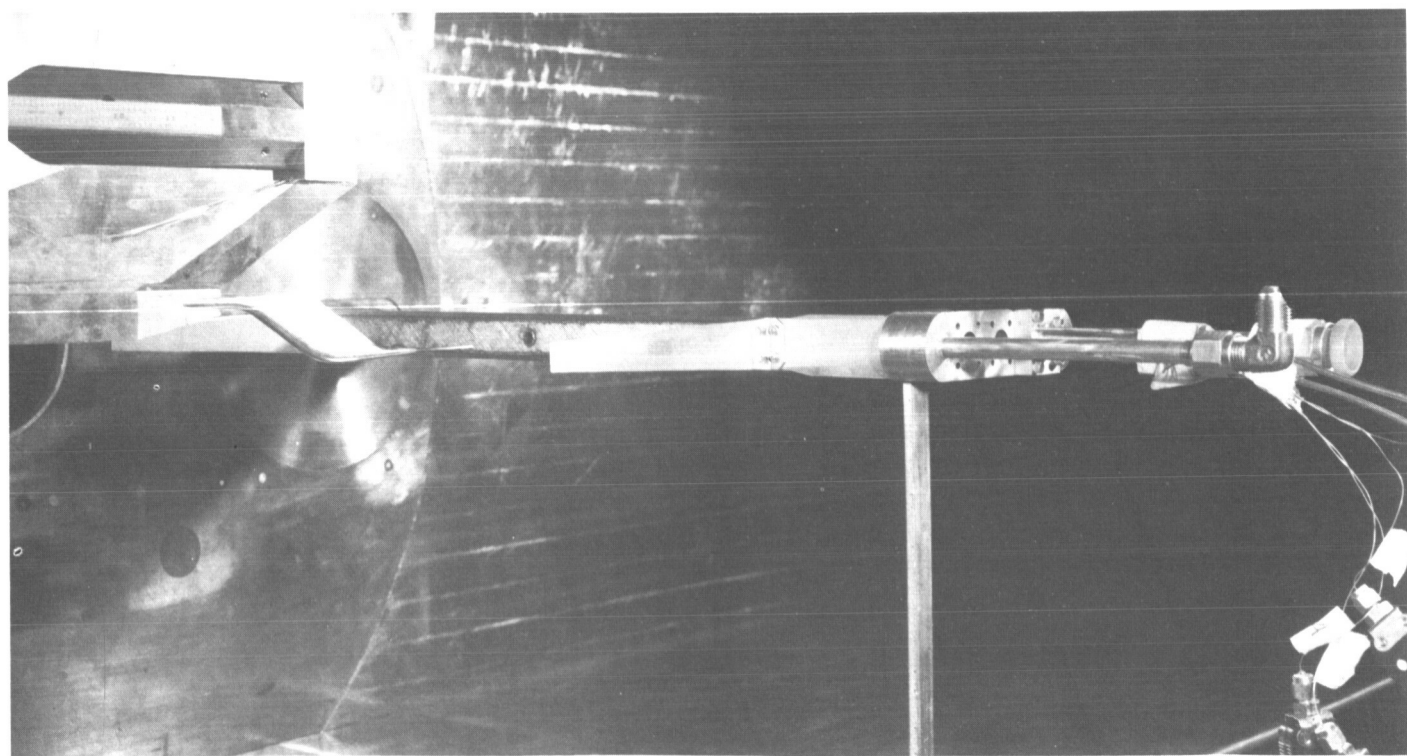


Fig. 2. Installation of wedge and pitot probe

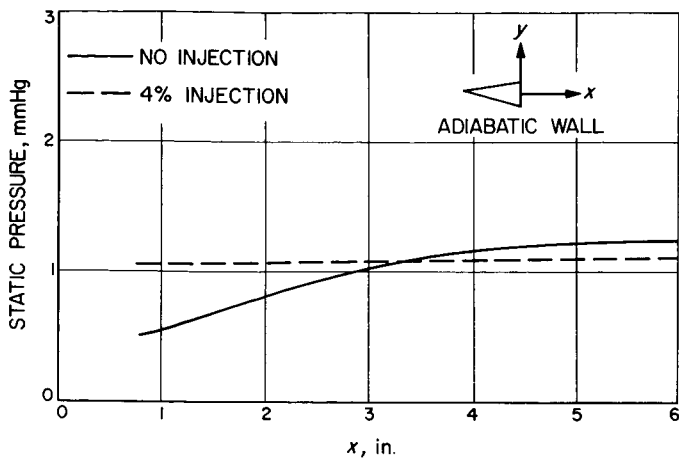


Fig. 3. Static pressure with and without base injection

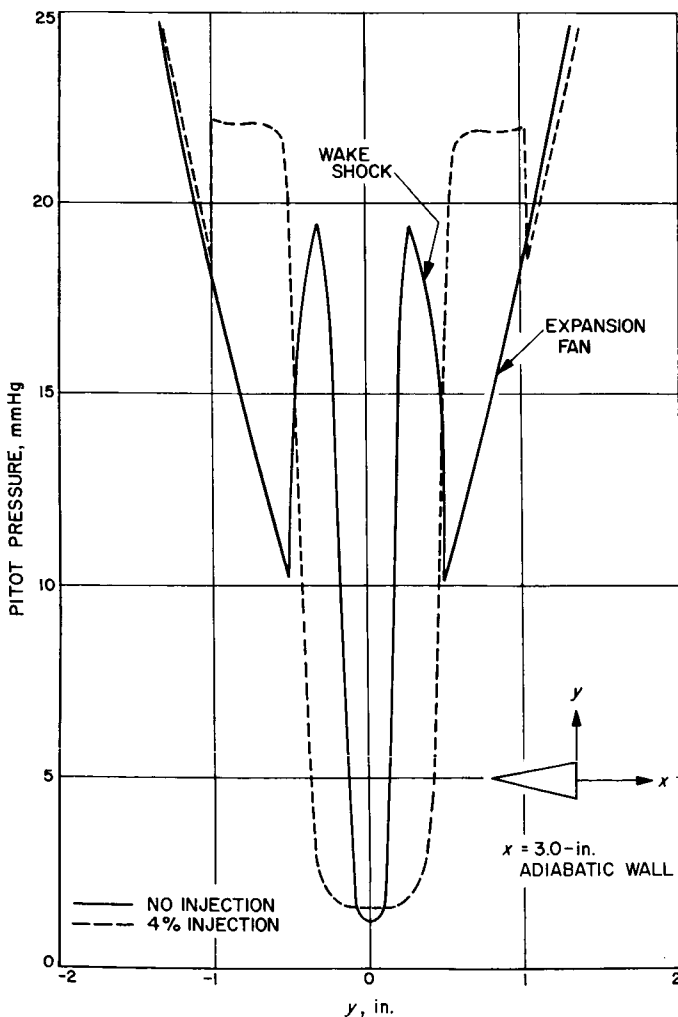


Fig. 4. Pitot pressure with and without base injection at 3 in. aft of the base

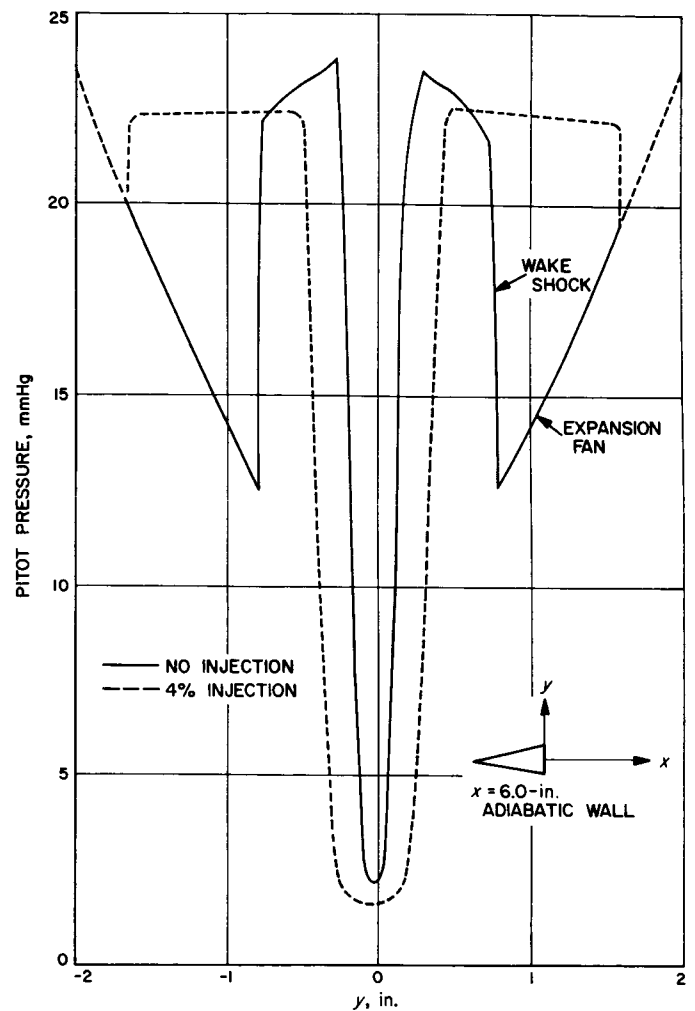


Fig. 5. Pitot pressure with and without base injection 6 in. aft of the base

pressure distribution along the wake axis. It appears that the effects of the injectant persist quite far downstream of the base. This is indicated in Figs. 4 and 5, which show a comparison of the pitot pressure variation with and without base injection at stations 3 and 6 in. aft of the base. These figures show the changes in the flow that occur with injection. The wake shock is shifted and greatly weakened, and the viscous wake "bucket" is widened.

3. Transonic Entry Capsule Configuration Study, W. Marko

As part of a study of the static aerodynamic characteristics of possible entry shapes, a test has been carried out in the 2- × 2-ft Transonic Wind Tunnel at the Ames Research Center (ARC Test 189) of a series of configurations based on a 60-deg (half-angle) blunted cone. These

tests were performed at the request of JPL in cooperation with ARC. Earlier tests of these configurations in the JPL Supersonic and Hypersonic Wind Tunnels were reported in SPS 37-38, Vol. IV, pp. 65-78.

ARC Test 189 was conducted over a Mach number range from 0.6 to 1.3 at Reynolds numbers of $1 \times 10^6/\text{in.}$ and $0.3 \times 10^6/\text{in.}$ Static force and moment data were obtained over an angle-of-attack range from -1 to 29 deg on a six-component internal strain gage balance. The data were reduced to coefficient form in both body axis and stability axis systems.

The models tested and a new standardized system of configuration notation are described in Fig. 6 and Table 1. Three cone half angles (56, 60, and 65 deg) and three edge-radius-to-maximum-diameter ratios (r_e/d) (0.0, 0.5, and 0.10) were tested. Since the earlier supersonic tests indicated that small changes in the nose radius r_n were less important than changes in edge radius, a constant nose radius of 0.10 diameters was used here. Balance

Table 1. Entry capsule model configurations

Configuration	θ , deg	r_n/d	r_e/d
$M_{56}N_{10}E_{05}$	56	0.10	0.05
$M_{60}N_{10}E_{05}$	60	0.10	0.05
$M_{65}N_{10}E_{05}$	65	0.10	0.05
$M_{60}N_{10}E_0$	60	0.10	0.00
$M_{60}N_{10}E_{10}$	60	0.10	0.10

shields of 0.75 and 1.25 in. were run, and the effect of sting diameter over this range was shown to be very small.

A small amount of additional testing in the 2×2 -ft Wind Tunnel is planned for the immediate future in order to complete the static tests of these entry configurations.

4. Experimental Internal Pressure Distribution of a Conical Nozzle With a Variable Position Pintle, E. R. Bate, Jr.

An experimental investigation has recently been concluded using the Hypersonic Wind Tunnel's auxiliary flow channel (AFC). The test involved the measurement of the internal pressure distribution of a 15-deg conical pintle nozzle with an exit Mach number of 4.5.

The pintle was positioned by means of a long tapered sting, supported in the nozzle entrance cone and projecting downstream into the nozzle throat. The pintle was placed so that its maximum diameter was located at the nozzle throat. The pintle could be moved off-axis in the nozzle throat by rotating the tapered sting in the yaw plane at its upstream support point. Fig. 7 shows the pintle, sting, and support ring assembly, and Fig. 8 shows this assembly installed in the entrance cone of the nozzle. The purpose of the test was to determine if thrust vector control could be achieved by moving the pintle to various off-axis positions.

An electromechanical multiple pressure measuring system (MPMS) was used to instantaneously measure the individual static pressures inside the nozzle. In all, 98 separate pressures were thus measured. In addition, the tunnel supply pressure and temperature were recorded. Fig. 9 shows the tubes from the static pressure taps on the nozzle surface connected into the MPMS. All of the

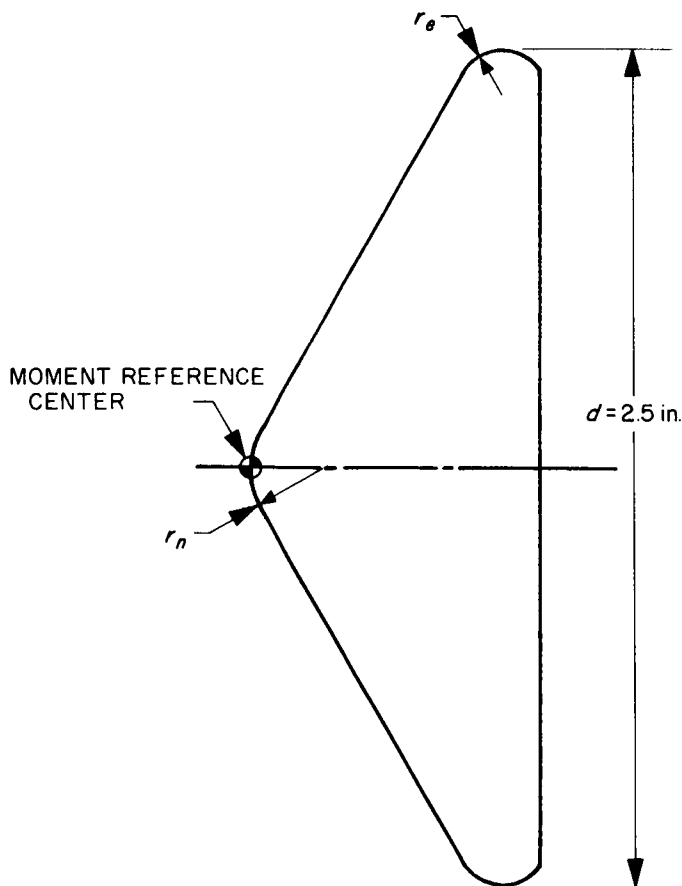


Fig. 6. Model of entry capsule

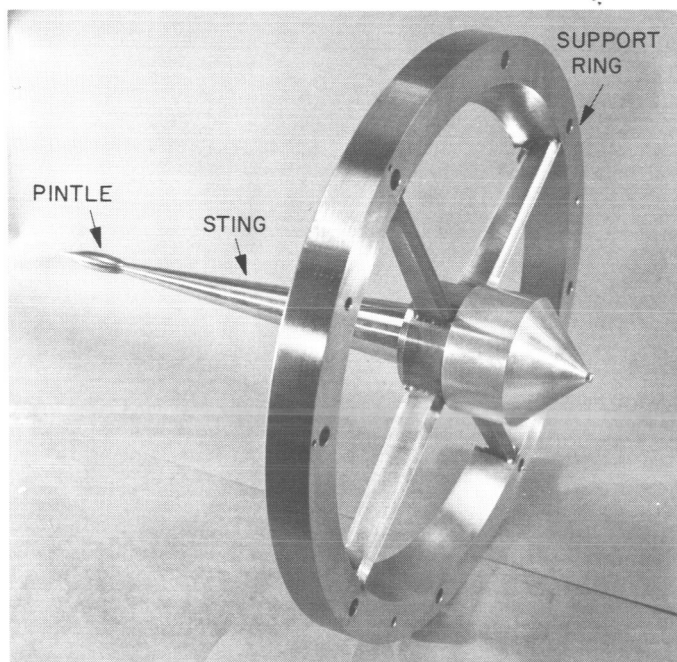


Fig. 7. Pintle and tapered sting shown assembled in the upstream support ring

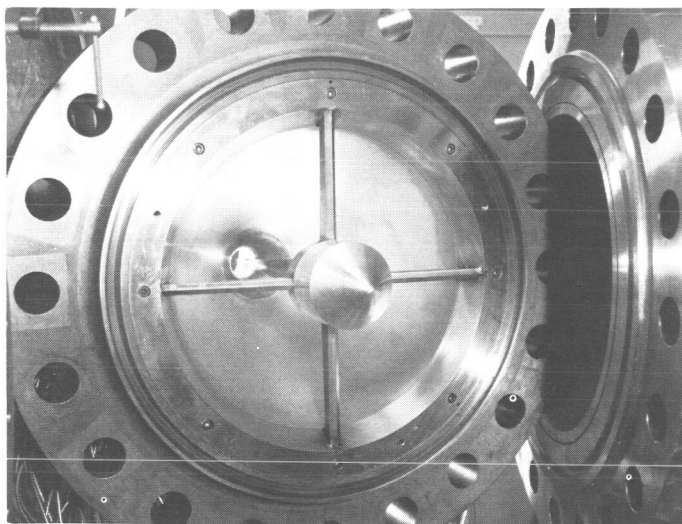


Fig. 8. Pintle and support ring assembly shown in position in the nozzle entrance cone, pintle projecting downstream into the nozzle throat

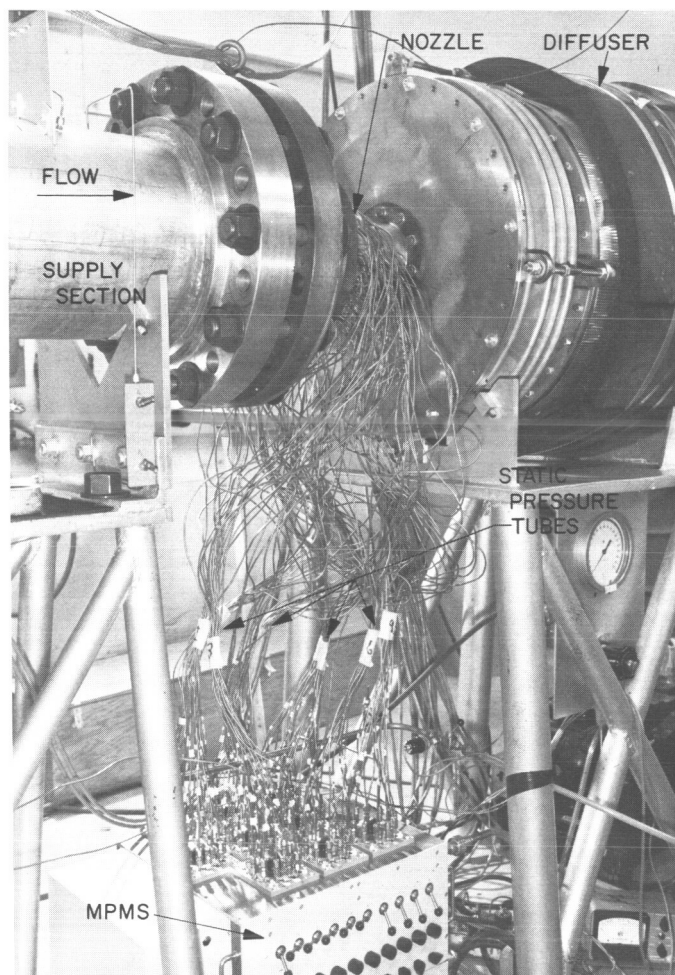


Fig. 9. Nozzle bolted in position between supply section and diffuser of the auxiliary flow channel

pressure and temperature data were automatically recorded by means of the wind tunnel data acquisition system.

The variation of experimental conditions included five different pintle positions at three different supply pressures (100, 400, and 600 psia). The supply temperature was held constant for all the runs at a value (220°F) which would prevent liquefaction at the highest supply pressure. Analysis of the data has not yet been completed.

PROPULSION DIVISION

N67 12116

IX. Liquid Propulsion Systems

A. Advanced Liquid Propulsion Systems

L. R. Toth, H. B. Stanford, and W. F. MacGlashan

1. Introduction, L. R. Toth

The Advanced Liquid Propulsion Systems program is investigating selected problems generated by spacecraft operational requirements for propulsion systems capable of high inherent reliability, long-term storage in the space environment, multiple start in free fall (zero gravity), and engine throttling. The solutions proposed to satisfy these requirements are coordinated for practical application in a system.

Periodic reports (starting with SPS 37-38, Vol. IV) describe the progress of work on the various parts of a specific system. Recent accomplishments are outlined below. These include:

- (1) Laminating aluminum foil to Teflon film for composite bladder construction.
- (2) Some results using a laser beam process to simulate pinholes in metal foil.

2. Bladder Development, H. B. Stanford

The permeability of Teflon bladder film materials to the oxidizer nitrogen tetroxide (N_2O_4) has long been a subject of concern to which a considerable effort has been directed by the advanced development program for liquid expulsion devices at JPL. More recently the problem of propellant saturation by pressurant gases such as helium and nitrogen permeating through Teflon bladders has been evidenced in such programs as *Surveyor*, *Lunar Orbiter*, *Apollo*, etc. Efforts to reduce the permeation of either the propellants or pressurants through Teflon by means of metal plating Teflon or the addition of fillers such as aluminum flake, metal powder, mica, etc., to the Teflon dispersions have shown little practical success. The results of many permeation tests on candidate bladder materials have indicated that only those which include a metal foil in their structure are capable of preventing permeation by the subject propellants and pressurant gases. Several metal foils have been tried, including gold, tantalum and aluminum. Of these the most practical one from considerations of availability, cost, and application is aluminum foil and FEP Teflon-aluminum. Laminates with good resistance to delamination in contact with the subject propellants have been available for some time. This material was fabricated in flat sheets up to 30 in. wide

but with a minimum foil thickness limitation of approximately 0.002 in., necessitated by the chemical etching required for a good mechanical bond. Fabrication of spherical or hemispherical bladders from the flat laminate has never been satisfactorily accomplished because of the problems of forming the material and generating the necessary seams.

After the propellant gas saturation problem encountered in the *Surveyor* Project, the necessity for reducing permeation through a Teflon bladder became more urgent. In this instance, it was considered more important to retain the flexibility and light weight of the *Surveyor* bladders, which have a wall thickness of 0.006 in., rather than to attempt to achieve 100% impermeability. A high percentage of reduction in permeating area would probably extend the saturation time of the propellant by the helium pressurizing gas to something greater than the storage time specified by *Surveyor* requirements. It was therefore decided to laminate some *Surveyor* sprayed and sintered Teflon bladders with aluminum foil 0.0005 in. thick. For, even though aluminum foil of this thickness was subject to pinholes and fractures, it still reduced the permeating area by more than 98%. Normal etching for adequate bond strength would have seriously deteriorated the 0.0005-in. aluminum foil; therefore, the foil for these first assemblies was not etched. Samples cut from one of the first sprayed and sintered aluminum-clad bladders received for the *Surveyor* Project and tested under the bladder development program delaminated in both of the propellants N_2O_4 and N_2H_4 in less than 24 hr. After notification of this failure the vendor, Dilectrix Corporation of Farmingdale, New York, devised a surface treatment for the aluminum foil that has appeared satisfactory in recent tests at JPL. This treatment of the aluminum surfaces involves the following steps:

- (1) Clean the aluminum foil with acetone.
- (2) Dip-coat the aluminum foil with DuPont Teflon primer for aluminum, Product Code 850-202.
- (3) Dry the above coating at temperatures between 120 and 160° F.
- (4) Fuse the coating at a temperature of 720° F.

The aluminum surfaces thus treated are receptive to subsequent coatings of Teflon/FEP, DuPont Product Code 120, in thicknesses from 1 to 4 mils for the initial or top coat layer.

Swatches of this Teflon aluminum laminate were supplied by the Dilectrix Corporation to JPL for test. These

samples were composed of a ½-mil layer of aluminum foil between a 3-mil layer of FEP on one side and a 3-mil layer of TFE/FEP on the other side, essentially duplicating the *Surveyor* bladder wall structure, but with the aluminum foil built into it.

In one half of the swatches the aluminum surfaces had been treated by the above-described process; in the other half the aluminum was not treated. All subsequent processing of the test swatches was identical.

Test samples $\frac{3}{8} \times 2$ in. cut from the swatches were placed in vials of the propellants N_2O_4 and N_2H_4 . After 24 hr all of the untreated aluminum foil samples had delaminated either partially or completely in both N_2O_4 and N_2H_4 , and one of the treated samples had separated in N_2H_4 . Periodic examinations indicated no further delaminations. After 30 days it was noted that the N_2O_4 was turning black in some of the vials and that the aluminum was etched from between the Teflon at the edges of the samples in these vials. Tests indicated that the N_2O_4 was absorbing moisture, forming nitric acid and attacking the exposed aluminum foil. Identical laminate samples were then placed with N_2O_4 in sealed glass containers. Subsequent visual checks indicated no delamination, no color change in the N_2O_4 and no etching away of the aluminum foil. After 90 days the sealed vials were opened for inspection, and no indication of delamination was observed. The original samples in N_2H_4 showed no further delamination after 120 days.

3. Pinhole Study for Bladder Development,

W. F. MacGlashan

This is a continuation of the study of the migration rate of a gas through typical holes in foil sheets (SPS 37-37, Vol. IV). The purpose of this study is to point the way toward the reduction of gas permeation through laminated foil-elastomer type expulsion bladders.

In an attempt to produce a controlled hole size in the range of 0.0001- to 0.005-in. D in foil for gas migration study, a series of laser beam holes were pierced through Invar Shim stock foil. Variable laser intensities were used to provide a range of hole sizes. Fig. 1 shows the light-projected photo of six laser-perforated foils grouped together. The photo was obtained by the method described in SPS 37-34, Vol. IV. The method consists of playing a strong light in a grid pattern over the foil, which is separated from a sheet of photographic paper by a piece of window glass. The black spots on the developed paper indicate the holes in the foil. The clouded overlay in

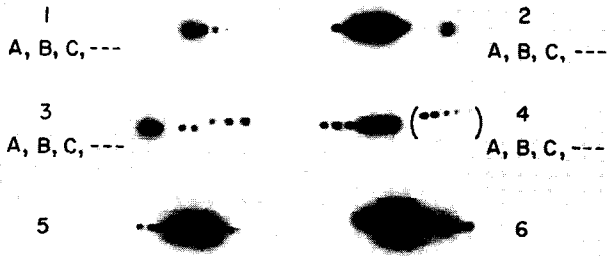


Fig. 1 is caused by stray light from the larger holes. Table 1 lists the size and shape of the holes in the Fig. 1 specimens as determined by a 40-power microscopic examination of the back-lighted foils.

A few of the laser holes were round and clean. Other holes were irregular with solidified metal above the surface at the hole edge. The half-round holes were caused by molten metal that fell back into the hole.

More practice and experience in operating the laser equipment is needed in this range so that uniform holes of predetermined size can be produced in foils of the same or of a different thickness.

Fig. 1. Light projected through perforated foil samples

Table 1. Size of holes in foil samples

Foil No.	Foil thickness, in.	Hole No.	Hole shape	Hole size, in.
1	0.003	A	Round	0.001
		B	Round	0.001
		C	Irregular	0.009
		D	Oval	0.005
		E	Round	0.002
		F	Square	0.0015
		G	Round	0.001
2	0.001	A	Round	0.0025
		B	Round	0.003
		C	Rectangular	0.008 × 0.011
		D	Rectangular	0.0095 × 0.012
		E	Irregular	0.016 × 0.021
		F	Round	0.003
		G	Round	0.0035
		H	Round	0.006
3	0.003	A	Half round	0.0075 × 0.0115
		B	Round	0.005
		C	Round	0.0025
		D	Half round	0.002 × 0.003
		E	Round	0.001
		F	irregular	0.002
		G	Round	0.003
4	0.001	A	Oval	0.002 × 0.003
		B	Round	0.002
		C	Oval	0.001 × 0.0015
		D	Round	0.001
		E	Round	0.001
5	0.0005			Not measured
6	0.0005			Not measured

N67 12117

X. Research and Advanced Concepts

A. Lithium-Boiling Potassium Rankine Cycle Heat-Transfer Data

G. M. Kikin

1. Introduction and Objectives

In order to properly evaluate and integrate nuclear reactor and power conversion systems into nuclear-electric spacecraft concepts, it is necessary to determine the characteristics of these systems including materials compatibility, fabrication techniques, and operational performance. The long-range development cycle for nuclear power systems of the type contemplated for electric propulsion application requires investigation of these areas many years prior to their actual anticipated use.

The two-loop lithium-boiling potassium facility at JPL represents an attempt to simulate the major elements and working fluids of two-loop nuclear turboplant concept of interest for spacecraft propulsion.

The primary objectives are:

- (1) To investigate transient and steady-state characteristics of a two-loop Rankine cycle alkali metal

system and attempt to correlate observed dynamic behavior to analog simulated studies.

- (2) To determine local and overall boiler heat-transfer coefficients and two-phase boiler pressure drops as a function of mass flow rate, potassium vapor quality, and saturation temperature in axial-flow and cross-flow liquid metal boilers.
- (3) To undertake studies of boiling stability as a function of pertinent thermal and hydraulic parameters.
- (4) To study specific component performance.

2. Summary of Preceding Loop Operations

A schematic and an isometric diagram of the lithium-boiling potassium loop are shown in Figs. 1 and 2. The uninsulated test loop is shown in Fig. 3, and the loop control room and graphic display/control panel are shown in Fig. 4.

The lithium-boiling potassium test loop operations were begun January 11, 1966. Initial outgassing operations were accomplished by heating the loop and insulation with trace heaters to between 400 and 500°F while maintaining a vacuum in the loop enclosure tank.

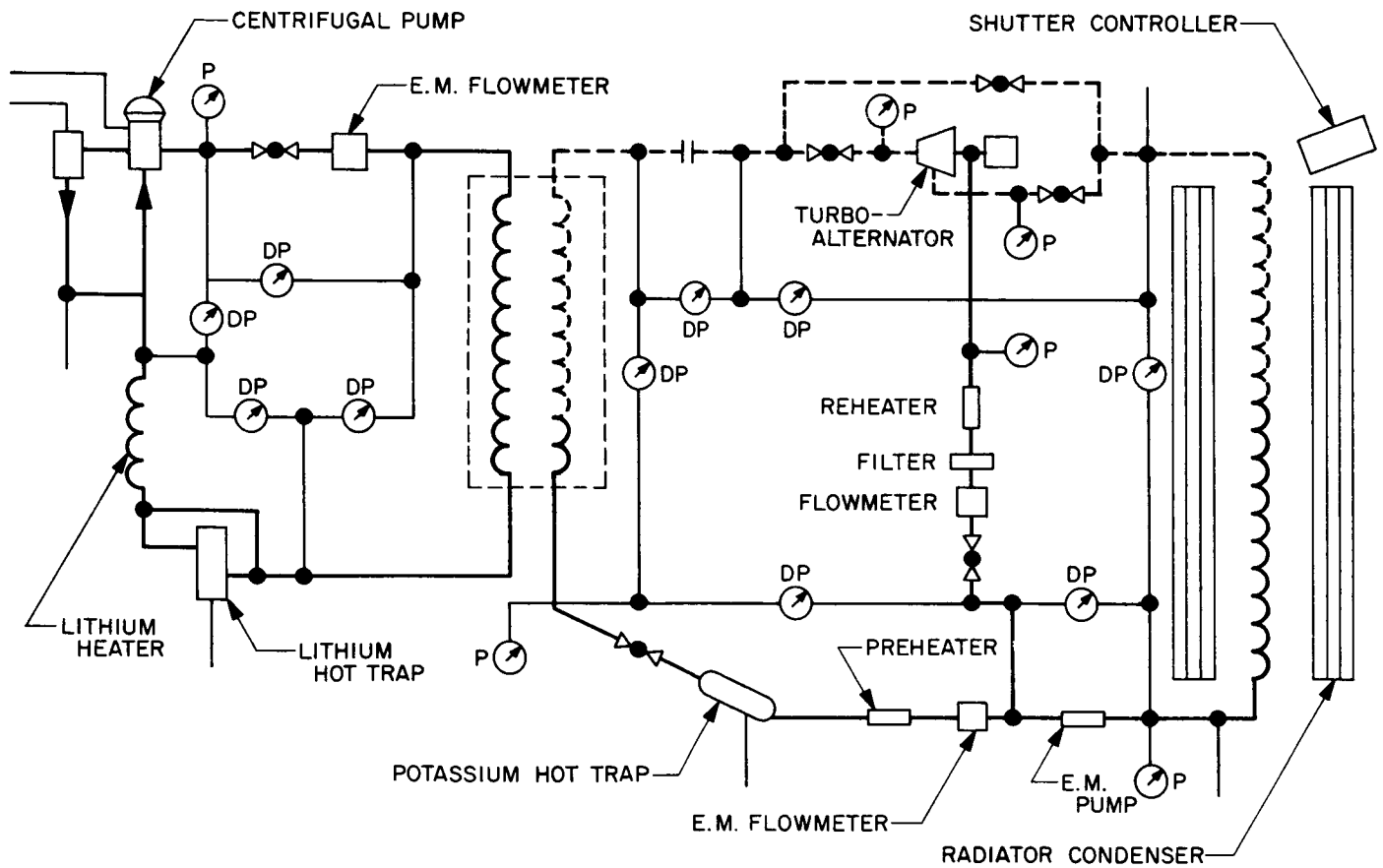


Fig. 1. Lithium-boiling potassium loop flow diagram

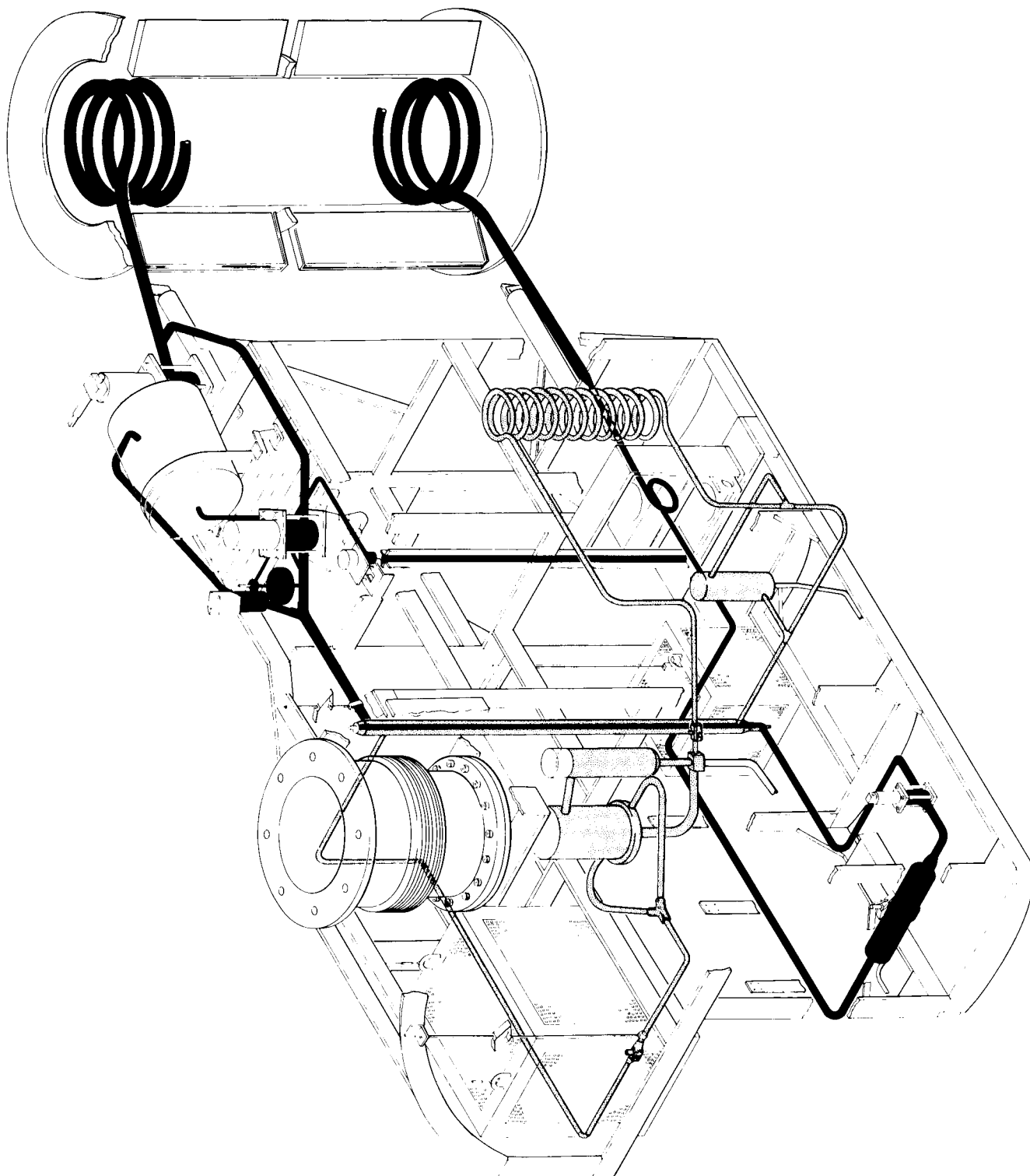


Fig. 2. Lithium-boiling potassium test loop, isometric view

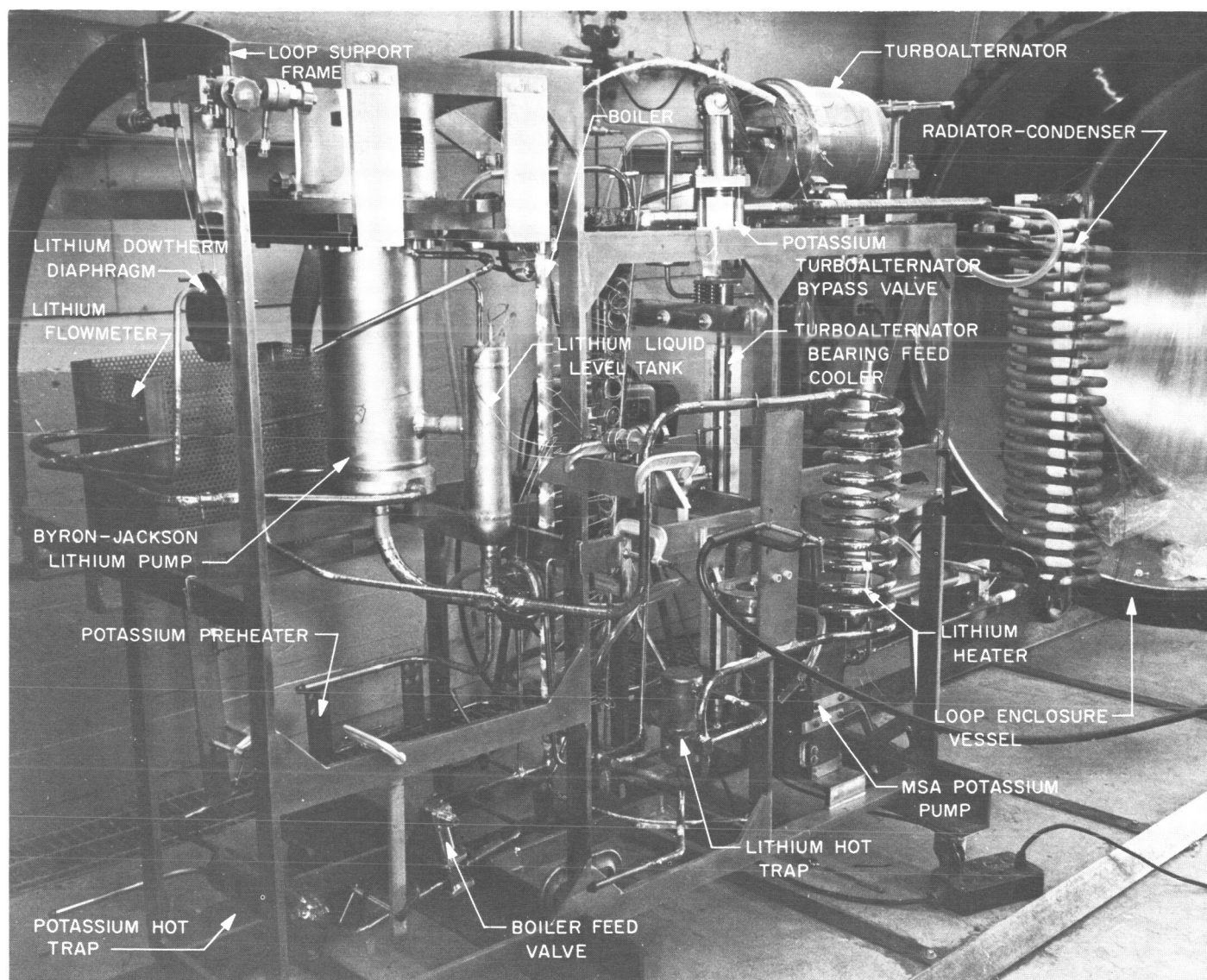


Fig. 3. Lithium-boiling potassium test loop

Following the outgassing procedures, the potassium loop was first loaded completely full with potassium (hard fill). Then the lithium loop was loaded with its nominal operating amount of lithium. Both loops were circulating in the 1000°F temperature range, all-liquid nonboiling mode, for several hours, when the lithium centrifugal pump impeller suddenly seized and sheared the shaft coupling it to the motor.

The loop was shut down, and the pump dome and pump motor were removed. Examination showed that the pump shaft had sheared at a point where a deep keyway had been machined in the niobium shaft. The break was

readily accessible, and a new coupling was bolted to the sheared lithium pump impeller shaft.

The test loop was again reheated, and the lithium pump was restarted. Potassium flow was then reestablished. After about 170 hr of operation, the lithium pump seized again at 1200°F. It was determined that this seizure was a result of the greater differential growth of the impeller shaft with respect to the pump casing as the pump was heated to higher temperatures. The problem was alleviated by shimming the motor and impeller shaft approximately 0.020 in. Operation of both loops in the liquid-liquid mode was then continued, and calibra-

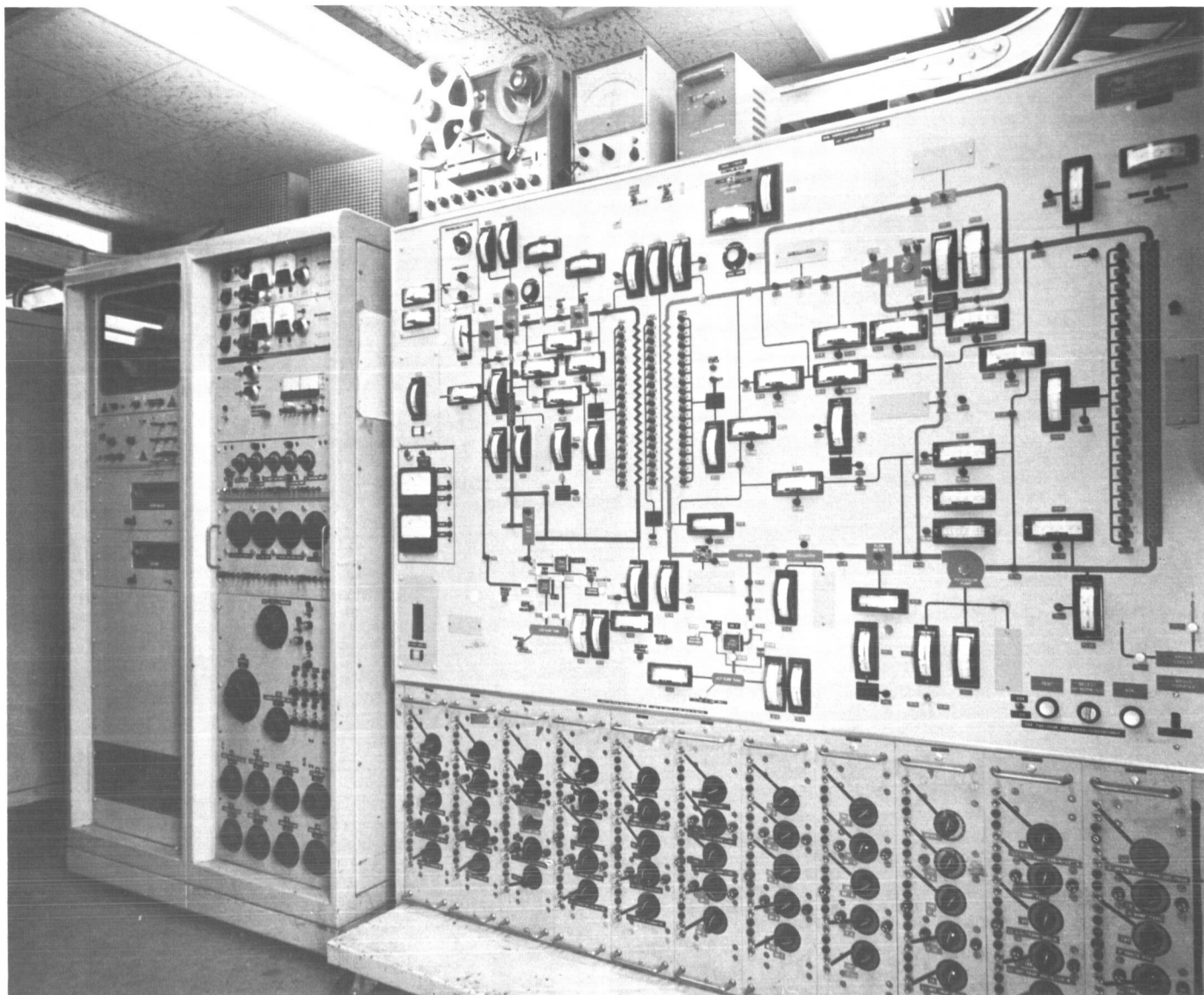


Fig. 4. Lithium-boiling potassium loop graphic display/control panel

tions of the lithium and potassium flowmeters were performed calorimetrically, using the lithium heater and potassium preheater, respectively.

Following initial liquid-liquid data accumulation, the potassium level was slowly drained to its operating level, with attendant commencement of boiling. The initial boiling operations were stable; pressures, temperatures and potassium vapor quality were within expectations. At potassium boiler temperatures of 1350 to 1400°F, some boiling instabilities were first encountered. These instabilities showed up mainly as periodic nondivergent oscillations in the potassium flow rate. A Sanborn strip chart recording of important loop parameters is shown

in Fig. 5. The mean of the oscillatory potassium flow was greater than the previously observed flow rate under stable operating conditions. During this period of instabilities the potassium pump head was generally lower, indicating that the boiler pressure drop was lower, due to the lower potassium vapor exit quality. These potassium hydraulic instabilities were readily controlled and removed by adjusting the potassium flow rate and/or lithium temperature by relatively small increments. Following this short period of unstable operation (~1 hr), stable boiling at ~1500°F (1700°F lithium temperature) proceeded for ~20 hr. The lithium pump seized again but was successfully restarted after reshimming an additional 0.020 in.

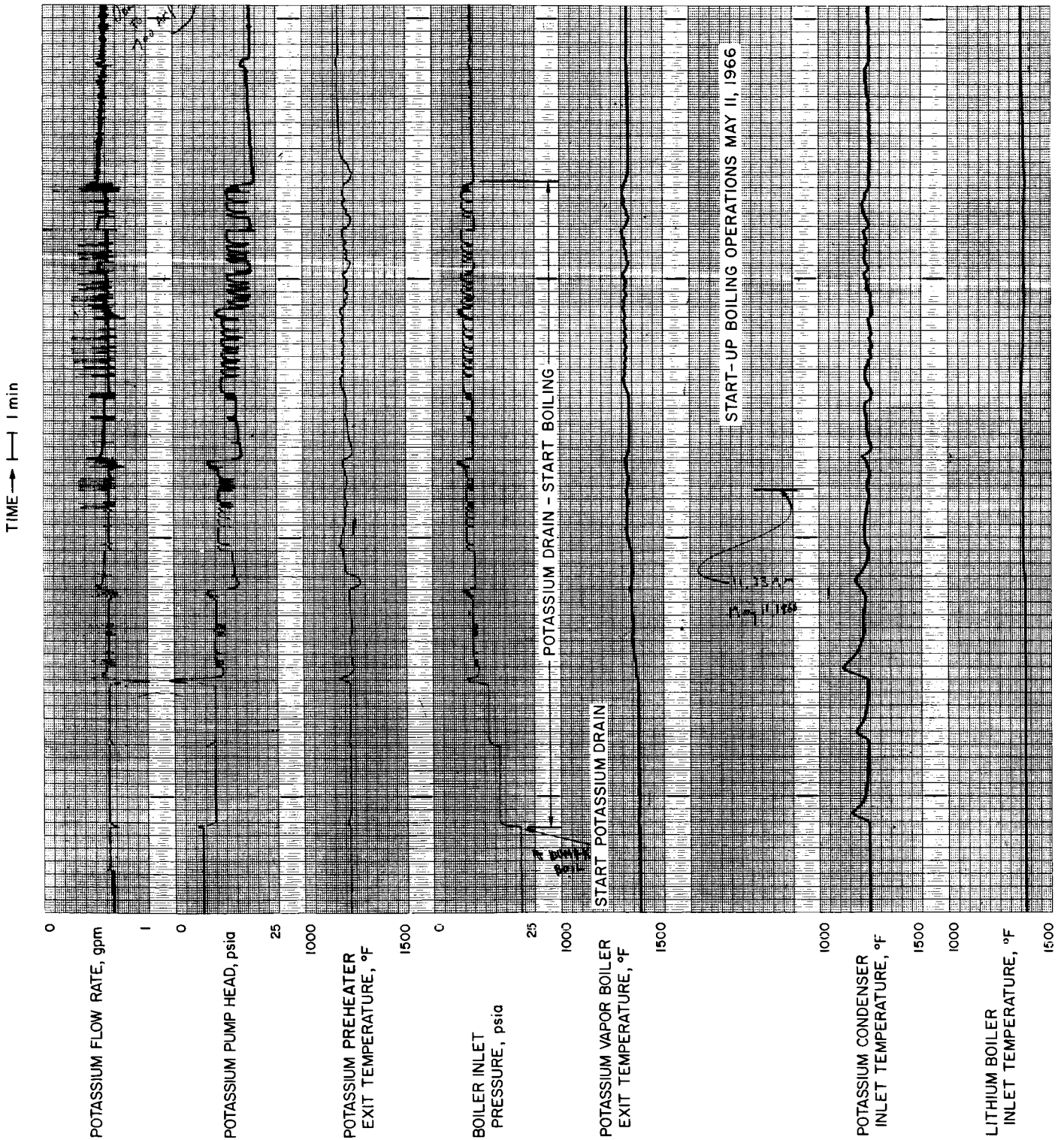


Fig. 5. Sanborn strip chart recording of start-up and boiling instabilities

At a power input of ~ 20 kw and at a boiler inlet lithium temperature of 1700°F , an overall power failure occurred, resulting in a rapid loop cool-down to under 800°F .

After power was restored, temperatures were being returned to their previous level when another power failure occurred. Loop cooldown to $\sim 800^\circ\text{F}$ again occurred before power was restored. Approximately 20 hr thereafter, with lithium temperatures back to $\sim 1600^\circ\text{F}$, a large reduction in the lithium flow signal initiated an automatic heater scram. Tests indicated that the lithium pump was operating satisfactorily, but apparently a plug had formed somewhere in the loop, resulting in almost complete blockage of flow. The system was cooled down to ambient, and radiographs were taken of the loop to determine if the plug could be detected and to see if any significant mass transfer could be observed. Of particular concern was the possibility that the yttrium oxygen scavenger in the lithium hot trap had mass-transferred and precipitated in the boiler. However, no such evidence could be seen in the radiographs.

3. Current Tests

A logical sequence of tests was performed on the lithium loop to determine the location of the plug. The conclusion was that the plug was located in the lithium annulus at the bottom of the boiler¹. It was considered possible that the plug could be broken by pressurizing one side of the plug or by dumping the lithium from the loop, refilling with fresh clean lithium, and reheating. Pressurization did not break the plug; therefore, the old charge of lithium was dumped, and a fresh charge loaded into the loop. Heating of the lithium loop and the boiler was accomplished using trace heaters and attendant circulation of hot potassium through the boiler, the potassium loop having been previously hard-filled. Heating of the potassium was accomplished with the use of the preheater. Raising the loop and boiler temperatures to approximately 1200°F caused breakage and/or dissolution of the plug.

With full lithium flow reestablished, the hard-filled potassium loop, which was maintained at 1600°F , was slowly drained to its nominal, boiling-mode, potassium

level of approximately two thirds the height of the radiator-condenser. A plot of temperature versus radiator condenser coil location before and after the draining and boiling operation reveals the height of potassium in the radiator condenser (Fig. 4). This level was chosen to ensure against the possibility of pump cavitation.

As the level was lowered in the potassium loop, boiling started and potassium flow fluctuations occurred for about a total of 30 min [Fig. 7(a)].

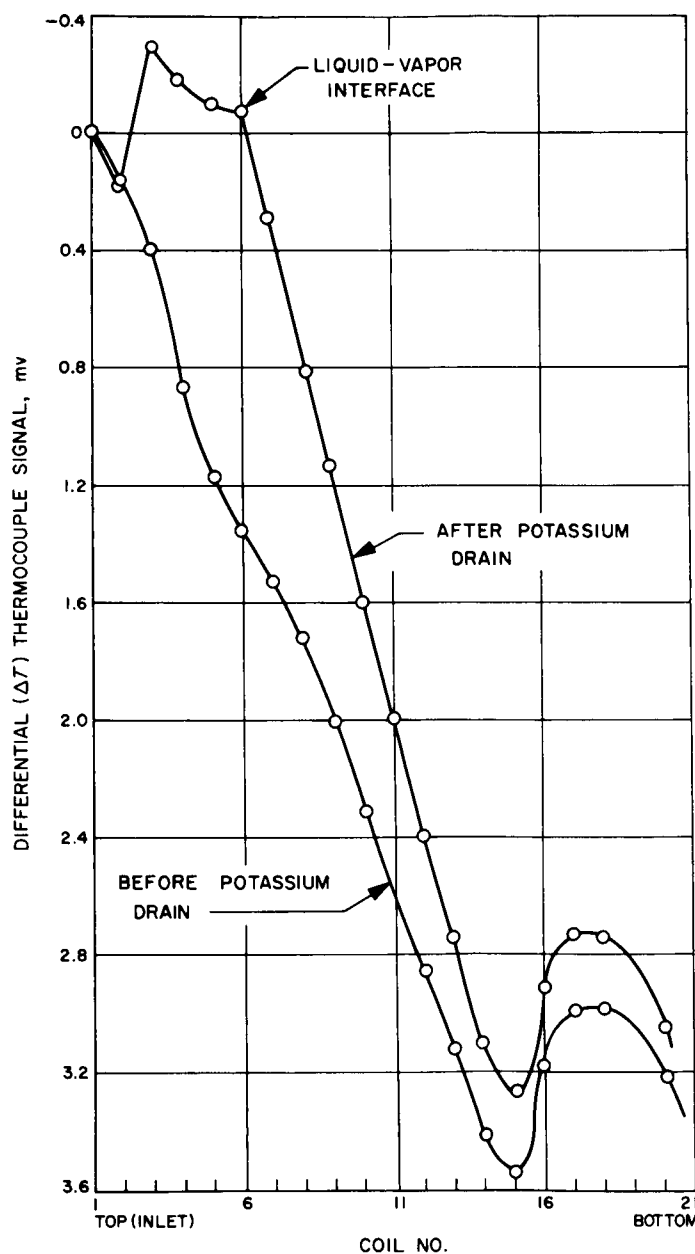
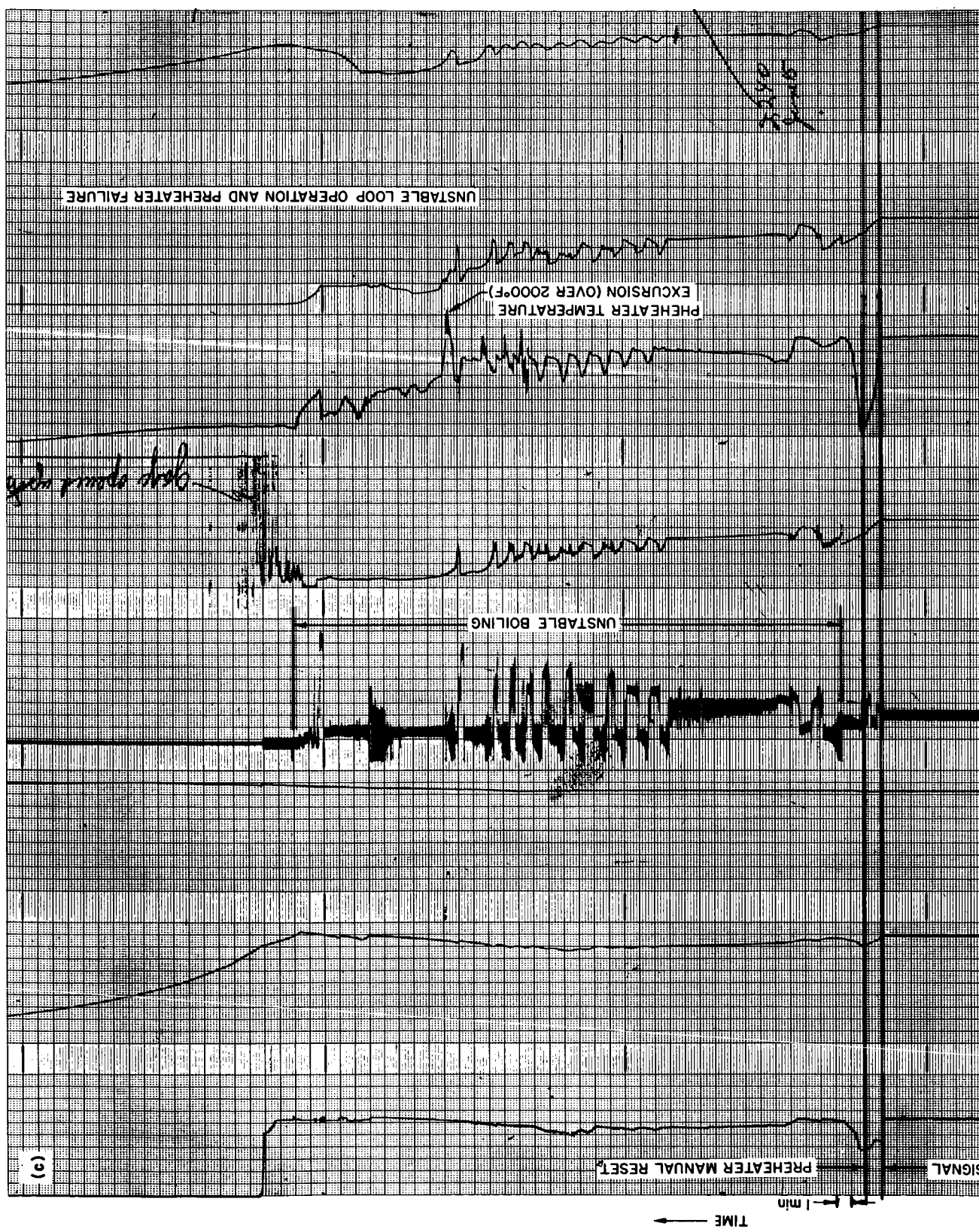
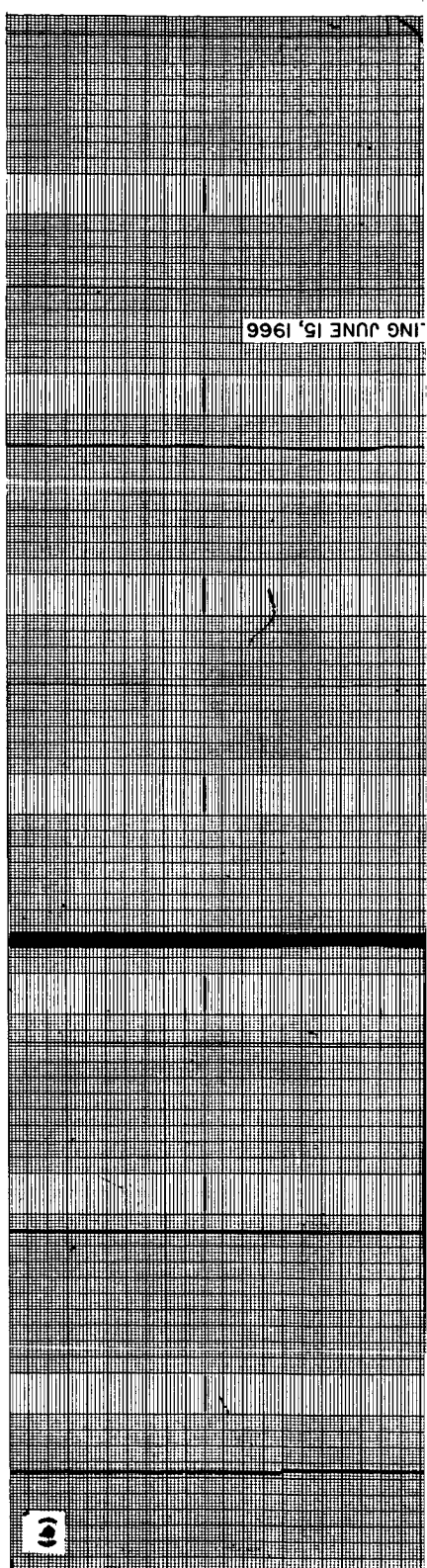
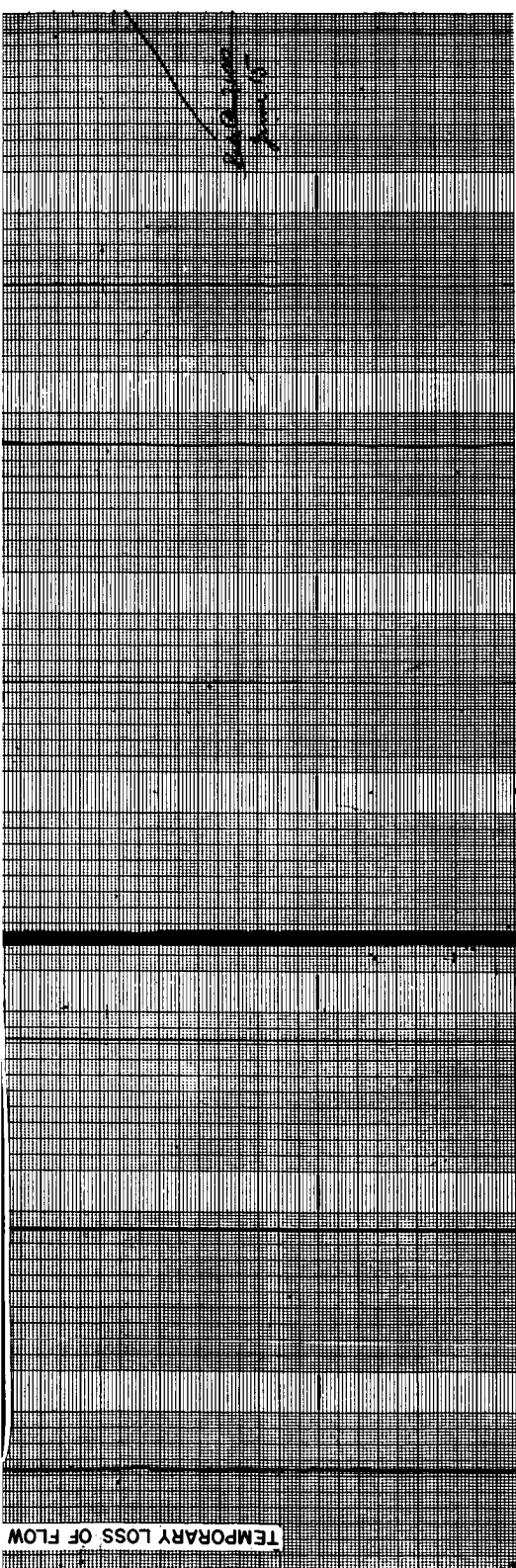


Fig. 6. Radiator-condenser temperature versus coil position before and after draining potassium

¹This location of the plug explains why it is not visible on the radiographs. The lithium flow passage is an annular ring, 0.875 in. OD \times 0.062 in. wide. If the density of the plug material in this relatively thin annular passage (boiler OD, 1.000 in.) is not greatly different than the surrounding fluid or not as dense as the niobium boiler structure, then it would not be visible on a radiograph.



57-1



ING JUNE 15, 1966

3

57-2

1 min 1 sec

573

1998

שמו

[illegible]

100

姓名: 王明 性别: 男 年龄: 25 职业: 程序员
 地址: 北京市朝阳区 邮编: 100000 电话: 13901234567
 电子邮箱: wangming@example.com 身份证号: 110101199801010001

2007	1.0
2008	1.0
2009	1.0
2010	1.0
2011	1.0
2012	1.0
2013	1.0
2014	1.0
2015	1.0
2016	1.0
2017	1.0
2018	1.0
2019	1.0
2020	1.0
2021	1.0
2022	1.0
2023	1.0
2024	1.0
2025	1.0
2026	1.0
2027	1.0
2028	1.0
2029	1.0
2030	1.0
2031	1.0
2032	1.0
2033	1.0
2034	1.0
2035	1.0
2036	1.0
2037	1.0
2038	1.0
2039	1.0
2040	1.0
2041	1.0
2042	1.0
2043	1.0
2044	1.0
2045	1.0
2046	1.0
2047	1.0
2048	1.0
2049	1.0
2050	1.0
2051	1.0
2052	1.0
2053	1.0
2054	1.0
2055	1.0
2056	1.0
2057	1.0
2058	1.0
2059	1.0
2060	1.0
2061	1.0
2062	1.0
2063	1.0
2064	1.0
2065	1.0
2066	1.0
2067	1.0
2068	1.0
2069	1.0
2070	1.0
2071	1.0
2072	1.0
2073	1.0
2074	1.0
2075	1.0
2076	1.0
2077	1.0
2078	1.0
2079	1.0
2080	1.0
2081	1.0
2082	1.0
2083	1.0
2084	1.0
2085	1.0
2086	1.0
2087	1.0
2088	1.0
2089	1.0
2090	1.0
2091	1.0
2092	1.0
2093	1.0
2094	1.0
2095	1.0
2096	1.0
2097	1.0
2098	1.0
2099	1.0
2100	1.0

THE UNIVERSITY OF CHICAGO

THE

[illegible][illegible]

15

70

◆ 2007年1月

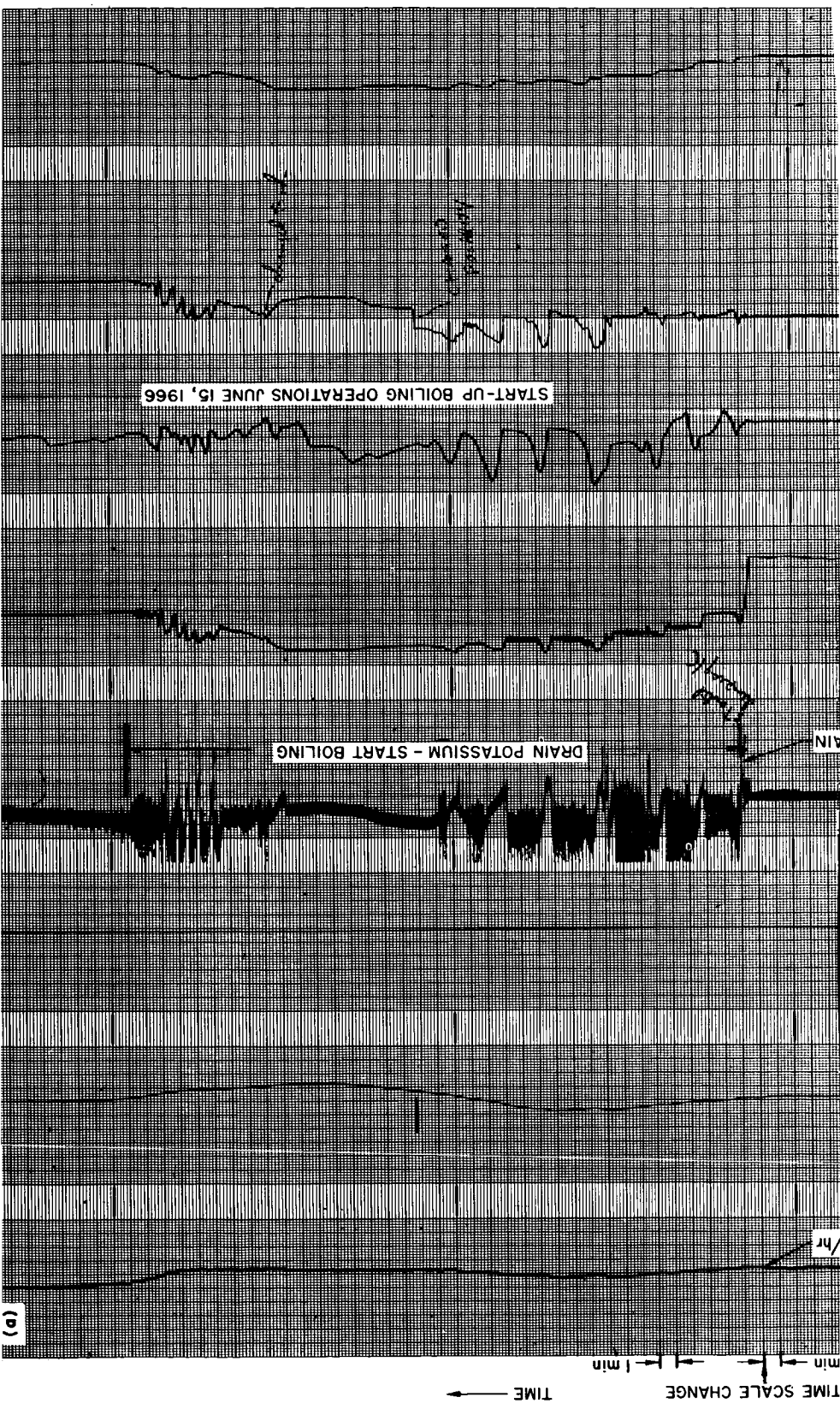
33

9

1. $\frac{1}{2}$ cup sugar
 2. 1 cup milk
 3. 1 cup flour

STEADY-STATE BOIL

58 ①



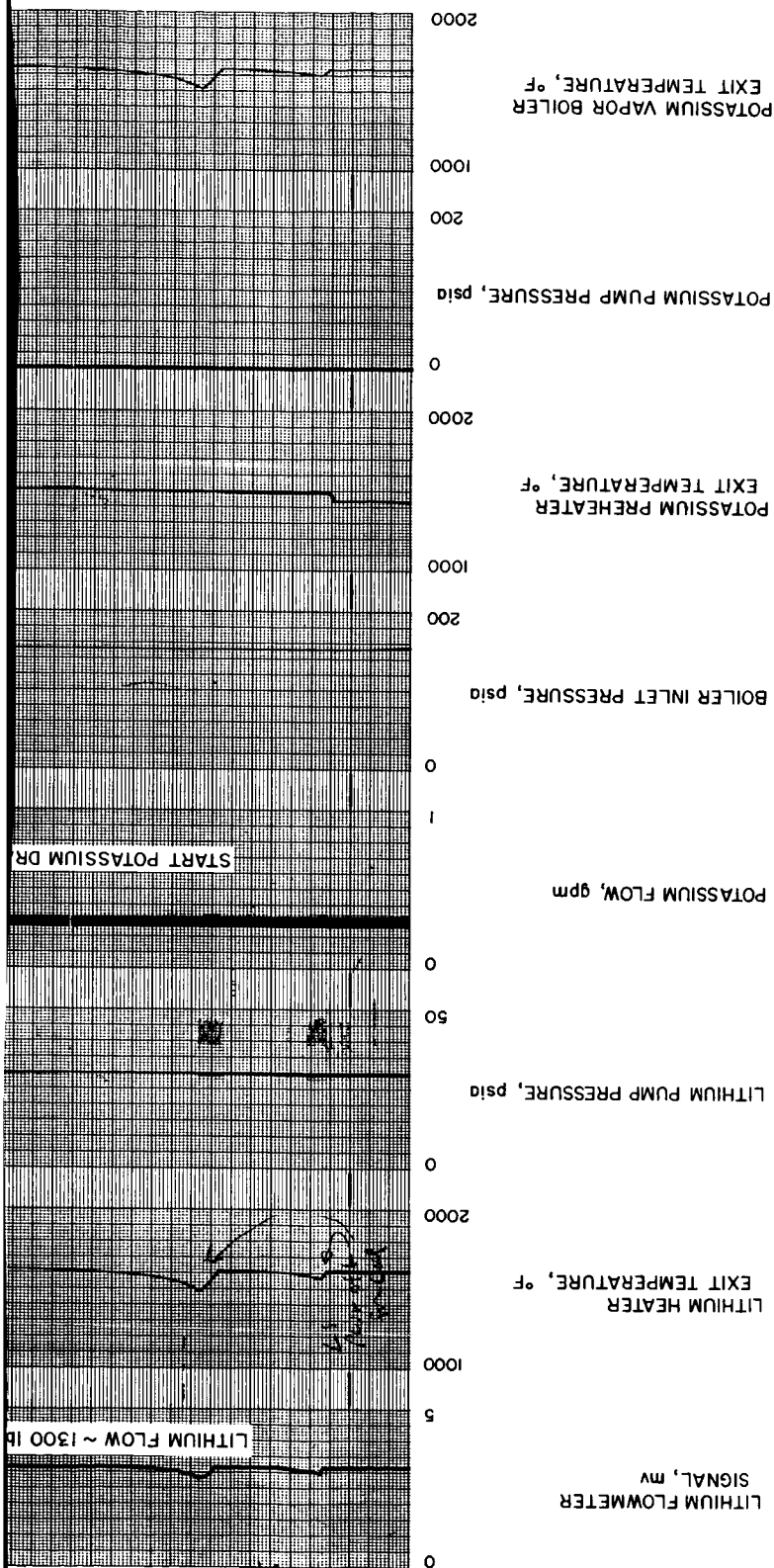


Fig. 7. Sanborn strip chart recording during (a) potassium drain, (b) stable boiling, and (c) unstable system behavior of boiling potassium loop followed by melt-down of potassium preheater

Stable boiling was attained by increasing potassium pump power and operating at higher temperatures. Stable boiling of the potassium at about 1850°F continued for 8 hr [Fig. 7(b)] with the lithium at 1900°F and at full power operation of 30 kw.

This phase of operations ended abruptly when uncontrollable flow oscillations resulted in burnout and meltdown of the potassium preheater. These oscillations started when a sudden reduction in lithium pump flow² initiated an automatic shutdown of the lithium heater

and potassium preheater power supplies. This resulted in a very rapid drop of potassium boiler feed temperature, which probably flooded the boiler. When the power supplies were manually reset, the temperatures then rose very rapidly back to their nominal values. Flooding of the boiler and the cessation of the boiling process caused a large decrease in the net pressure drop through the loop, with an attendant rise in the potassium flow rate. After the power supplies were turned on again, the potassium in the boiler absorbed heat until it flashed and started boiling again in a very explosive manner. This sudden explosive boiling evidently caused not only a reduction in flow (due to the much greater loop pressure drop during the vaporization mode) but also flow reversals. This "chugging" effect on the potassium flow

²This sudden reduction in lithium flow was apparently due to either a momentary pump seizure or a momentary formation and freeing of a plug in a lithium flow passage.

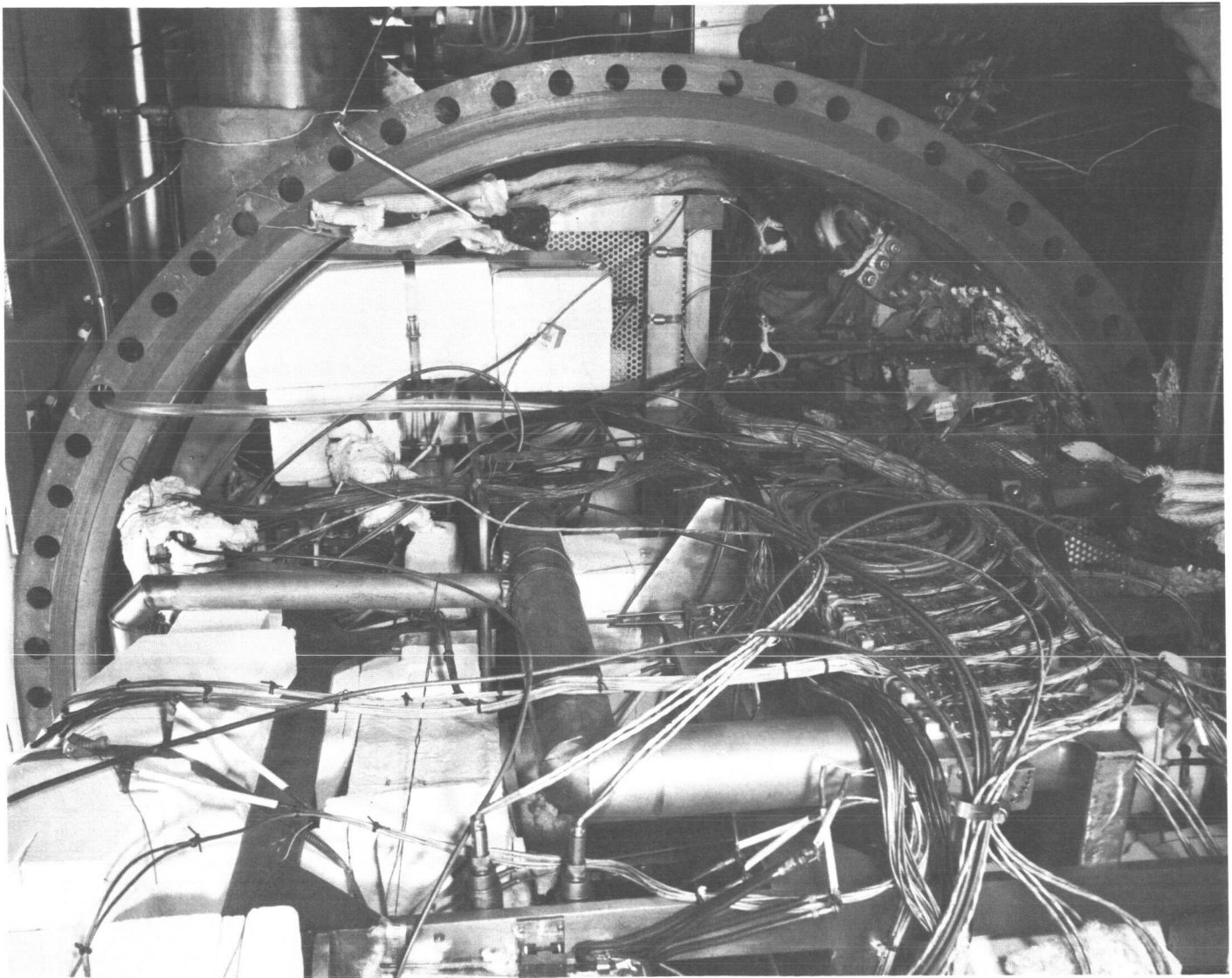


Fig. 8. Test loop in opened tank enclosure showing failed preheater

is seen on the Sanborn strip chart recording [Fig. 7(c)]. With zero flow or a flow reversal, there is effectively no heat being removed by the potassium in the preheater and within a short period of time ($< \frac{1}{2}$ min) it is possible to have a meltdown of the niobium tubing in the preheater when a large amount of power is being fed into the preheater (in this case ~ 6 kw before failure). Fig. 8 shows the opened loop enclosure with the failed preheater in the lower right-hand corner. The hot potassium leaking out of the preheater reacted with the Glassrock foamed silica insulation; as seen in Fig. 9. The preheater melted at two points between the center power feed bus-bar and the outer ground straps.

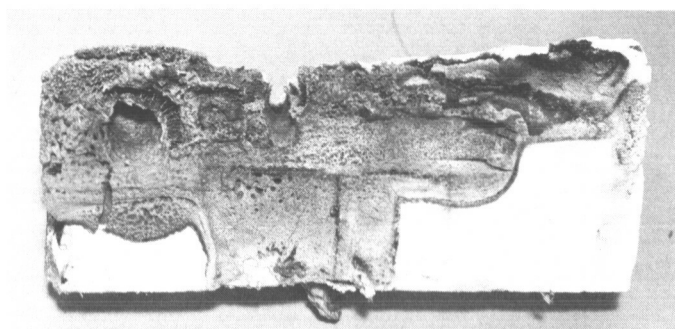


Fig. 9. Insulation after reaction with hot potassium during heater failure

The loop is now down for repairs and a new preheater (Fig. 10) will be installed in the loop and welded in place with the field welder described below. A boiler feed valve (Fig. 11) was included in the system at the boiler inlet for the specific purpose of varying inlet pressure drop to

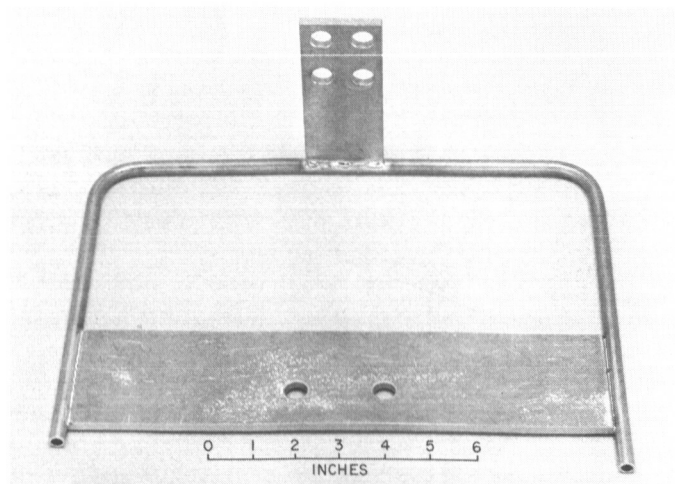


Fig. 10. Replacement potassium preheater

quantitatively study the effect of this important parameter on boiling stability. The valve has tungsten insert disks on both faces of the swinging gate. One of these disks was not properly captured. It dislodged, prohibiting the valve from closing. Total liquid pressure drop from pump discharge to boiler inlet was then less than 1 psi, and a substantial stabilizing influence was unavailable for subsequent loop operations. However, even under these unfavorable conditions, stable boiling was achieved most of the time during the boiling runs. It can be seen that this valve, after being cleaned of liquid metals, has a clean, bright appearance indicating very little, if any, oxygen contamination of the niobium during the total operating time of the potassium loop.

Stability in the boiling potassium loop will probably be greatly enhanced by providing a high pressure drop through the boiler feed valve.

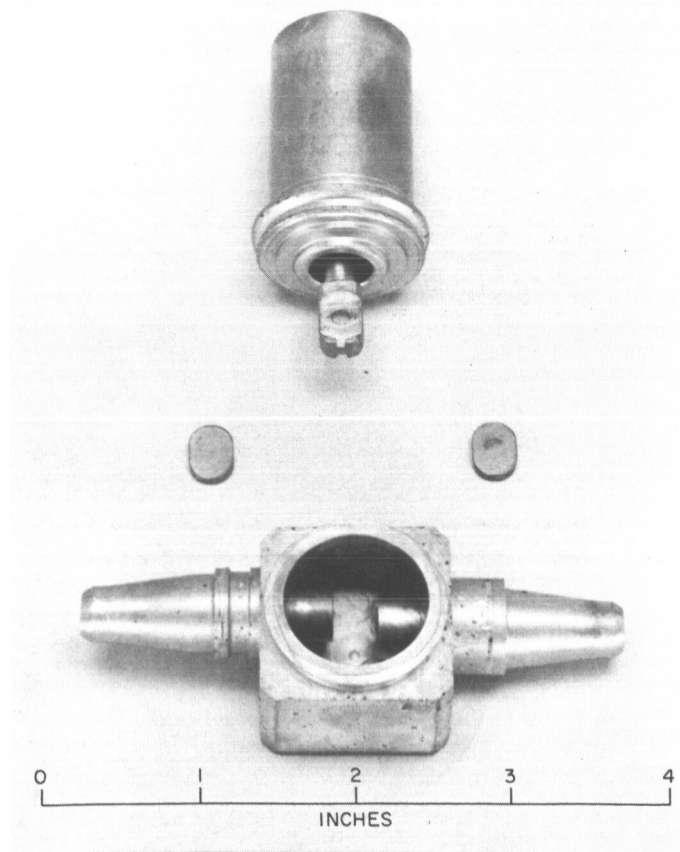


Fig. 11. Disassembled boiler feed valve

4. Fabrication Techniques — TIG Field Welder

Changes are being made in the design of the lithium-boiling potassium heat-transfer loop currently in test. Any change of columbium components necessitates inert atmosphere TIG welding in a confined area. Techniques have been developed at ORNL (Ref. 1) to facilitate this type of welding operation. The methods developed by them utilize equipment which is still too large to be used in the available space in the JPL test loop.

A refinement of the ORNL method was evolved at JPL to meet space restrictions. Components of the weld jig are shown in Fig. 12(a). The standard ceramic tip was removed from a TIG weld torch. The torch was then bolted through a hole in a length of pyrex tubing using an O-ring for a seal. The pyrex tubing-torch assembly rotates around split water-cooled copper blocks which are bolted to the columbium tube ends. Sealing between

the pyrex and the copper chill blocks is accomplished by double O-ring seals. A combination vent and atmosphere sampling line was placed in one of the copper chill blocks. Argon was purged through the columbium tubing and through the TIG torch argon line. The assembled jig is shown in Fig. 12(b).

A photomicrograph of the fusion weld pass is shown in Fig. 13(a). A filler ring was made from Cb-1Zr wire. This was then fused into place. A photomicrograph of this cross-section is shown in Fig. 13(b). Analyses of the weldments are shown in Table 1.

Table 1. Analyses of welded samples

Sample	Component, ppm		
	H	O	N
Tubing	9	330	50
Fusion pass	5	450	40
Filler pass	6	500	260

5. Summary of Pertinent Loop Component and Behavioral Experiences

a. Outgassing. Outgassing of the loop and attainment of satisfactory moisture and hydrogen levels was successfully achieved, following application of the argon purifier for on-stream purification.

b. Lithium pump. Prevention of further Byron-Jackson lithium pump impeller seizures was successfully accomplished by shimming the impeller up a total of 0.040 in. This corrected for the differences in impeller and pump casing growth during heating.

c. E.M. Potassium pump. The MSA potassium E.M. pump operation was quite satisfactory. Potassium wetting of the niobium pump coils resulted in increasing the pump performance to a level which was ~5% greater than its nominal design head-flow characteristic.

d. Valves. Experience gained shows that considerable attention must be given to liquid metal valve design and manufacture, including operating mechanisms. A malfunction of the boiler feed valve is being corrected, and subsequent reliable valve operation will assist in the suppression of unstable boiling by creating a large pressure drop prior to entrance of the potassium into the boiler.

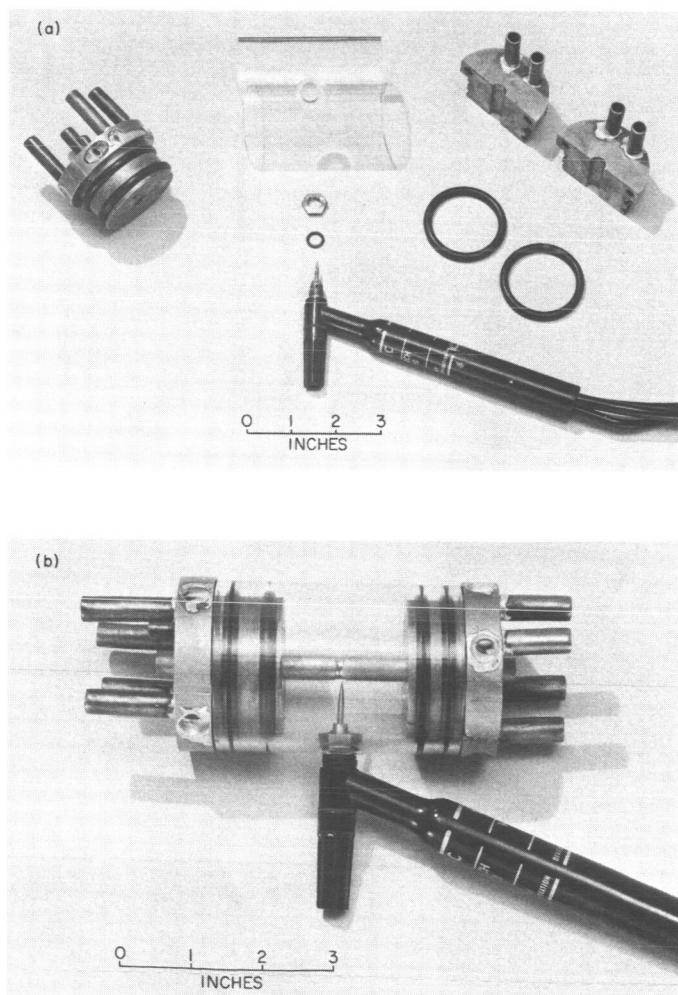


Fig. 12. TIG field welder (a) unassembled (b) assembled

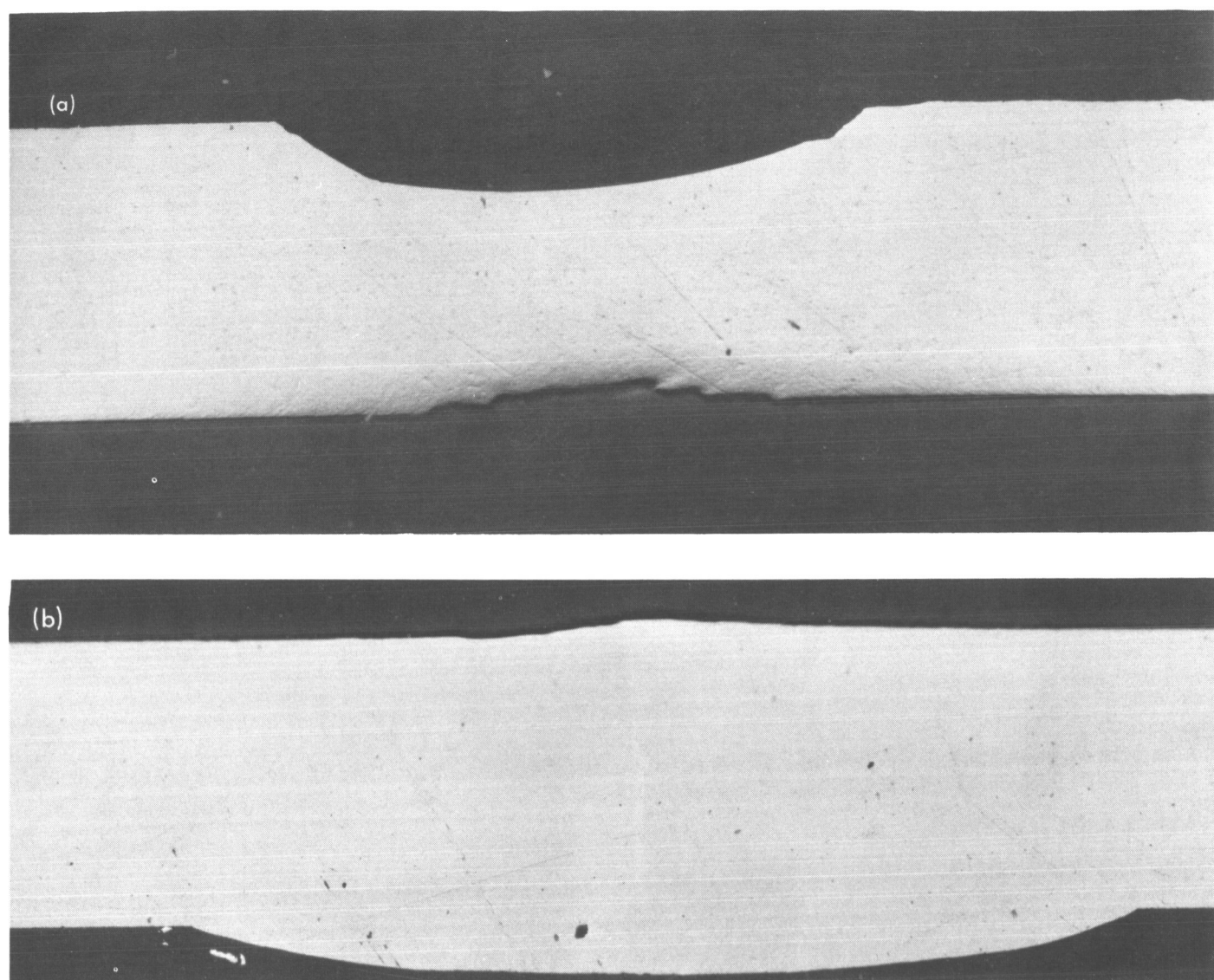


Fig. 13. Macrographs of TIG field welds (a) fusion pass (b) filler wire

e. Radiator-condenser. Radiator-condenser heat rejection was greater than expected. This is being compensated for by installation of additional radiator-condenser heaters and blanking off the argon coolant flow to the portion of the loop enclosure housing the radiator-condenser.

f. Potassium preheater. The original installation of the potassium preheater was upstream of the boiler feed valve and the potassium hot trap and at some distance from the boiler inlet. The heat losses through this portion of the system resulted in a large drop in temperature (as much as $\sim 150^{\circ}\text{F}$) between the preheater exit and the boiler inlet. Thus the potassium coolant entered the boiler with a large amount of subcooling, because the operation

of the preheater at temperatures close to or actually greater than the saturation temperatures in the boiler would result in unwanted boiling in the preheater. Due to the previously described boiler throttle valve malfunction, operation of the preheater at a high power input (to reduce the much greater than expected potassium subcooling) resulted in boiling in the preheater. This apparently initiated the potassium loop instabilities which resulted in failure of the preheater. A new preheater which is longer than the original unit (to operate at lower heat fluxes) will be installed immediately upstream of the boiler inlet between the boiler feed valve and the potassium hot trap.

g. Tantalum foil. Examination of the inner protective wraps of tantalum foil indicate that they are still ductile

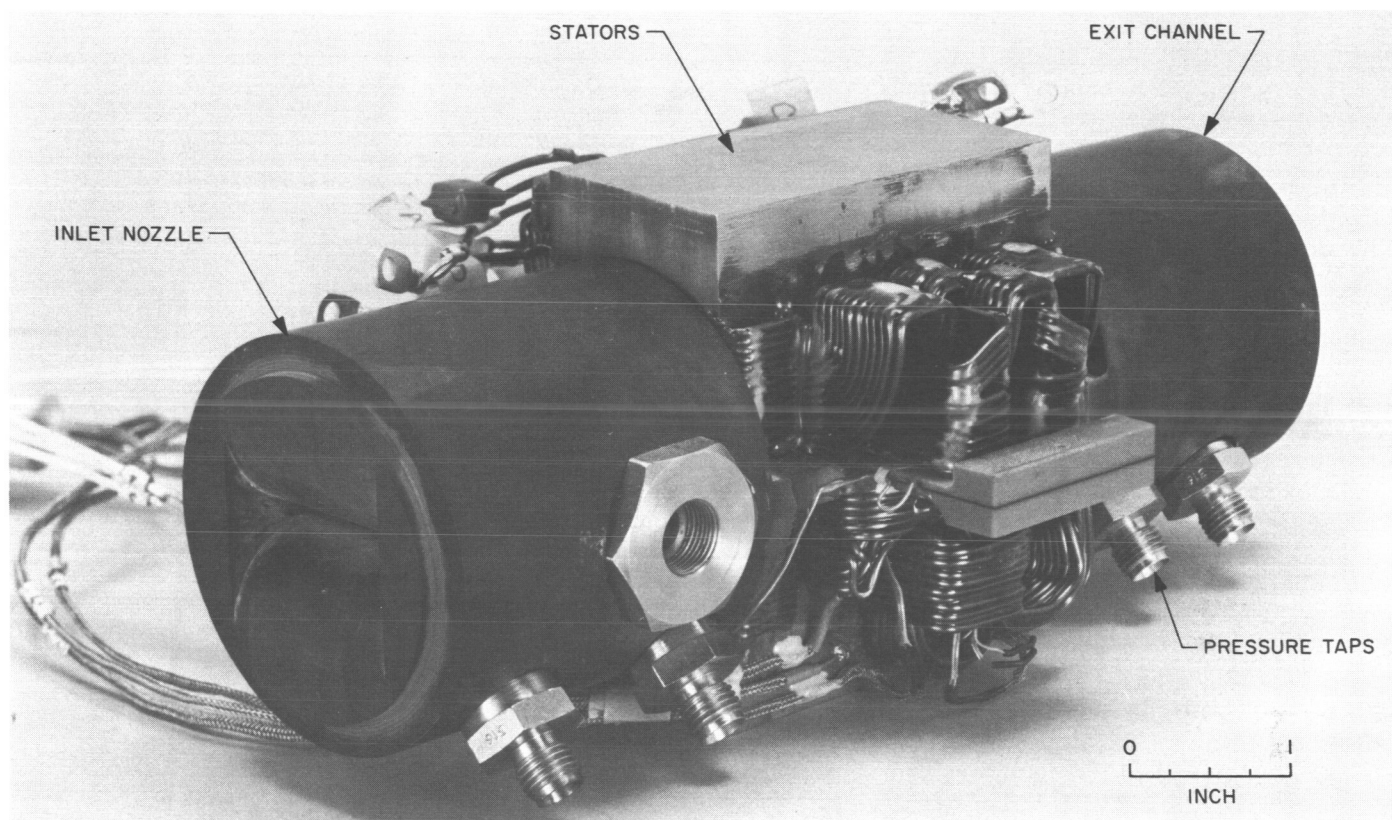


Fig. 15. Experimental AC MHD generator

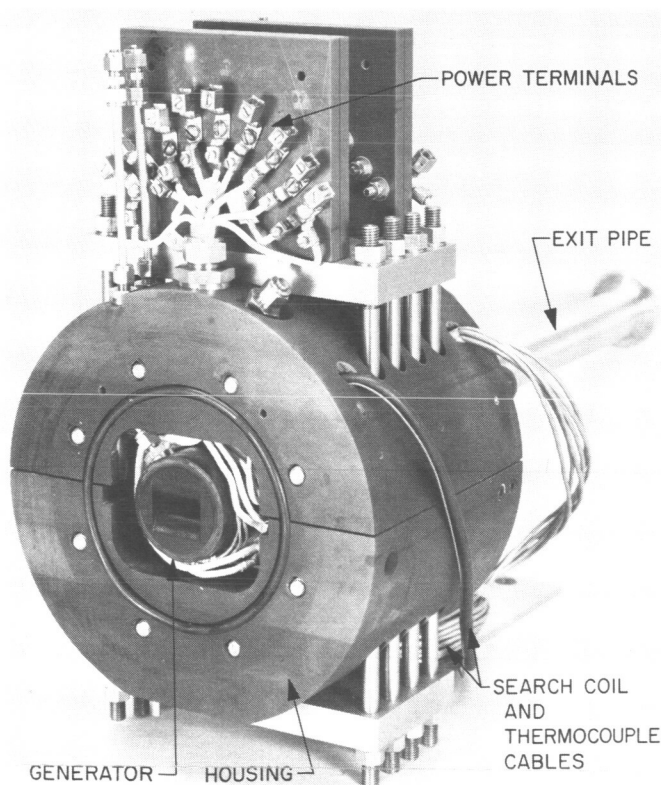


Fig. 16. AC MHD generator in housing

to each of the three MHD generator phases. The capacitor bank provided the reactive power required by the MHD generator windings and thus reduced the current demand on the motor-generator set to that corresponding to the real power being dissipated in the windings. Two multi-tapped dual-primary transformers were used to mix two of the three generator phases to produce a fourth and fifth phase shifted in phase and reduced in magnitude to excite compensating coils at the inlet and exit of the generator. The coolant tank contained mineral oil which was pumped through the housing to cool the windings. The coolant was later changed to nitrogen gas when this was found to provide adequate cooling.

The tests were conducted in two stages: empty channel tests and flow tests. The empty channel tests were conducted with the inlet flange removed to permit gauss-meter traversing of the flow channel between the stator blocks. The phase currents were adjusted in magnitude to produce a uniform mean field amplitude in the traveling wave region as shown in Fig. 18. The local amplitude variations are due to the teeth and slots. The currents were shifted in phase by alternator shaft adjustments and capacitor adjustments to ensure that the magnetic field was traveling down the channel at a uniform speed.

and, therefore, oxygen contamination to date is not a problem. A total of about 750 hr of loop operation in excess of 500°F has been accumulated in the argon cover gas environment of the test chamber.

h. Instrumentation. Postoperative recalibration of loop and boiler thermocouples is being performed as required for reduction and correlation of operational data which will be used in boiler heat-transfer calculations.

During loop operation, pressure transducers required frequent calibration. Increased confidence and ease of calibration of the pressure transducers will be attained by installation of stainless steel Bourdon-type pressure gauges at the boiler inlet and at the potassium pump outlet.

6. Conclusions

A great amount of valuable experience has been gained in liquid metal loading; start-up, shut-down, steady- and unsteady-state operations of a two-loop lithium-boiling potassium system.

Boiling of potassium, in stable and unstable modes, has been carried on for a total accumulated time of approximately 40 hr at power levels of 20-30 kw and at temperatures of 1600 to 1900°F. Further loop operations will be concerned with accumulation of boiler heat-transfer data, operation of the turbo-alternator and further experimental investigations of stable, unstable, and transient system performance.

The results of these experiments will be used to guide the modifications necessary for refinement of the formulated analytical models describing the dynamic behavior of the system.

N67 12118

B. Liquid MHD Power Conversion

D. G. Elliott, D. J. Cerini, and L. G. Hays

The long lifetimes required of electric-propulsion powerplants make cycles without rotating components attractive. Such a cycle under investigation at JPL is the liquid-metal magnetohydrodynamic system shown schematically in Fig. 14. In this cycle a fluid, such as cesium, circulates in the vapor loop and causes a liquid metal,

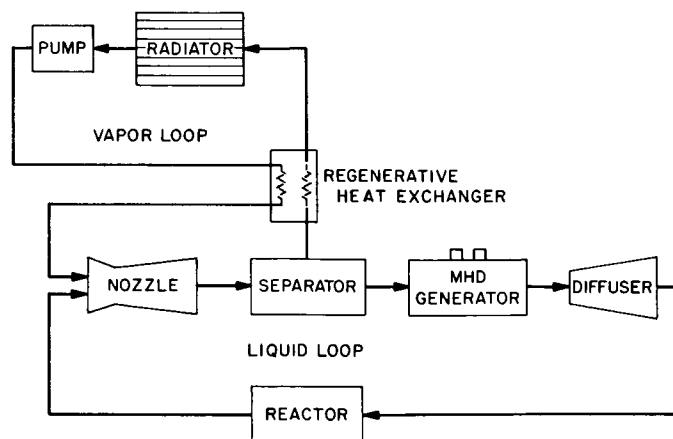


Fig. 14. Liquid MHD power conversion system

such as lithium, to circulate through an MHD generator in the liquid loop. The cesium leaves the radiator (or radiator-loop condenser) as condensate, flows through an EM pump and regenerative heat exchanger to the nozzle, separates from the lithium in the separator, and returns to the radiator through the regenerative heat exchanger. The lithium leaves the separator at high velocity (typically 500 ft/sec), decelerates through the production of electric power on the MHD generator, and leaves the generator with sufficient velocity (typically 300 ft/sec) to return through a diffuser to the reactor (or reactor-loop heat exchanger) where the lithium is reheated.

1. AC Generator

Tests were conducted on a compensated AC MHD generator with successful conversion of NaK pressure-drop energy to net AC electric power output on a self-excited basis. The stator and inlet-exit channel assembly is shown in Fig. 15 and is as described in detail in SPS 37-36, Vol. IV, except that the coils were changed from 8 turns of 0.062×0.125 rectangular magnet wire to 16 turns of 0.062-D round wire to reduce the AC to DC resistance ratio of the windings. The inlet-exit blocks shown in Fig. 15 were fabricated from epoxy. This assembly was installed in a Micarta housing (Fig. 16), which served as the structural support and coolant jacket for the windings.

The generator is shown installed in the NaK test facility in Fig. 17. The motor-generator (MG) set provided excitation of the MHD generator by means of three single-phase aircraft alternators on a common shaft which were driven by a 25-HP motor and variable speed coupling. The load bank dissipated the generator output power by transformer coupling of light bulb combinations

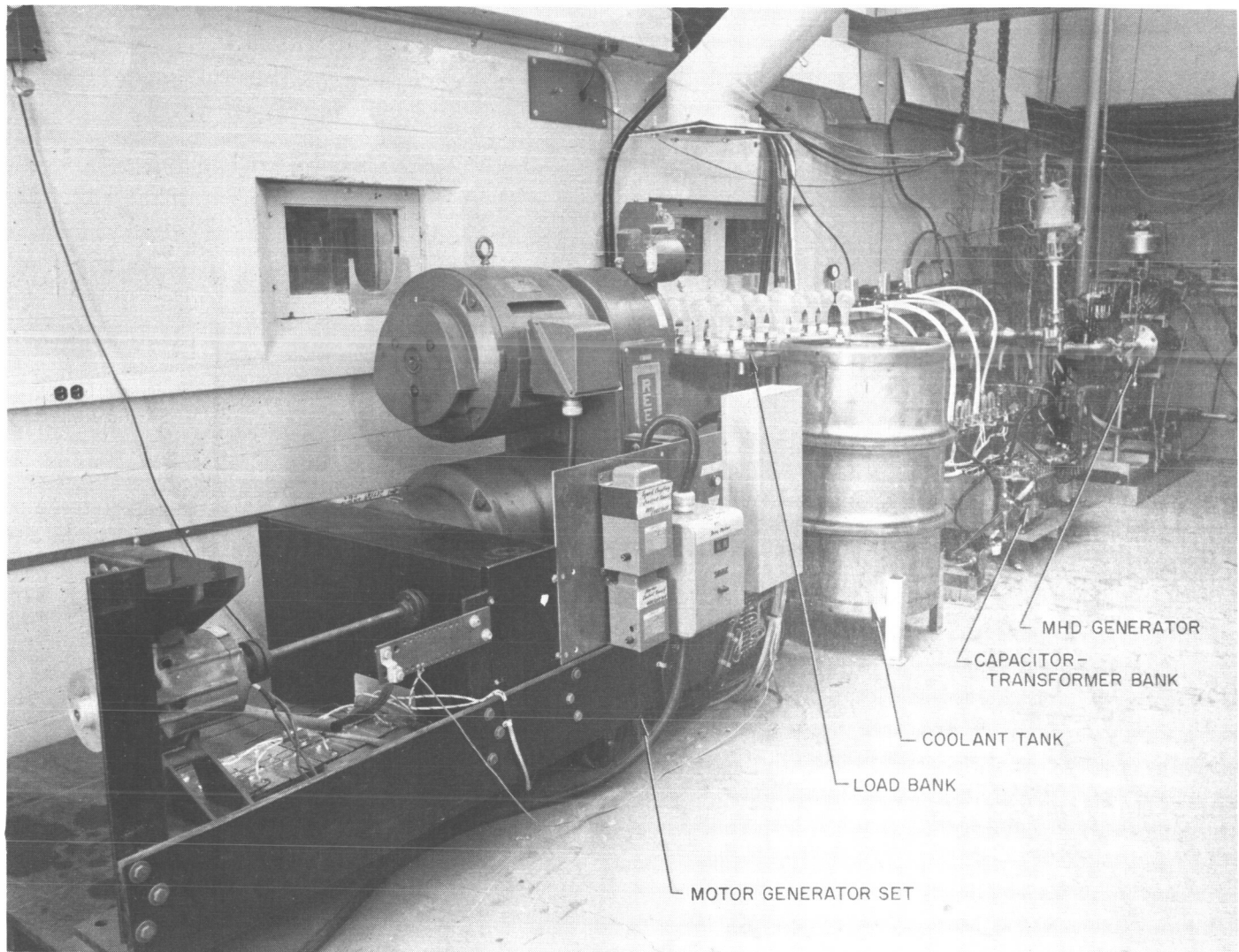


Fig. 17. AC MHD generator test installation

This was verified by observing that there were equal phase angles between the three equally spaced traveling wave search coils, placed as shown in Fig. 18. The magnitude and phase of the compensating coil currents were set by adjusting turns ratios on the two compensating coil transformers to make the voltages of the compensating pole search coils half that of the traveling-wave search coils. The desired balanced five-phase system produced the flux wave shown in Fig. 19. Nineteen successive wave positions are shown, representing the travel of the field over one fourth the length of the generator. At $\omega t = 0$, the time at which the B-phase current is maximum, the compensating pole flux is maximum and equal to half the flux in one pole of the traveling-wave region, as required for minimizing AC end effects by compensation as described in SPS 37-33, Vol. IV.

The initial flow tests were at low flow rate to maximize the slip of the fluid velocity U , relative to the magnetic field wave velocity U_s , where slip is defined as

$$s = |U - U_s|/U_s.$$

The uniform magnetic field of the empty channel tests was repeated by setting the same search coil voltages. This required different current settings, since the field was now the resultant of the coil currents and the fluid currents. In most of the low flow tests the NaK flow rate was 5 lbm/sec, the velocity was 90 ft/sec, the excitation frequency was 1200 cps, and the slip was 0.5. The slip in this case produced an accelerating force on the fluid, which appeared as a decrease in pressure drop when the generator was excited. This required pumping power input from the MG set to maintain the same flow.

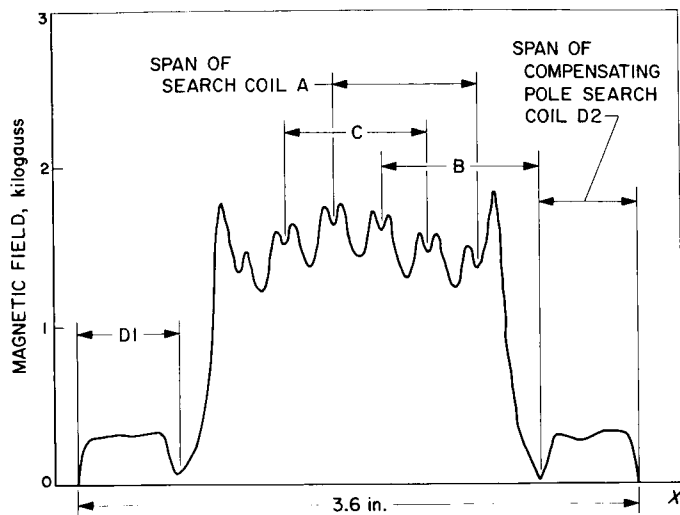


Fig. 18. Measured RMS magnetic field amplitude in AC generator for 10-amp RMS current per phase

The measured efficiencies are compared with the ideal values in Fig. 20. The net pump efficiency η_{ep} , is defined as the ratio of the decrease in fluid input power (decrease in $\dot{v}\Delta p$) to the total power supplied to the MHD generator. The gross pump efficiency η_{op} is defined similarly, except that the denominator is reduced by the I^2R power dissipated in the windings, as determined in the empty channel tests. In one run the fluid input power reduction was 196 w, when 671 w were supplied to the MHD generator and 192 w was dissipated in the windings, making the efficiencies $\eta_{ep} = 196/671 = 0.29$ and $\eta_{op} = 196/(671 - 192) = 0.41$, as compared to the ideal value $\eta_{op} = 1 - s = 0.50$ shown by the curve in Fig. 20. The large data scatter resulted from operating at only 20% of the nominal generator current which reduced the pressure drop change with excitation to 4% of nominal.

The flow velocities were then raised to higher values in the generator regime, where it was observed that with

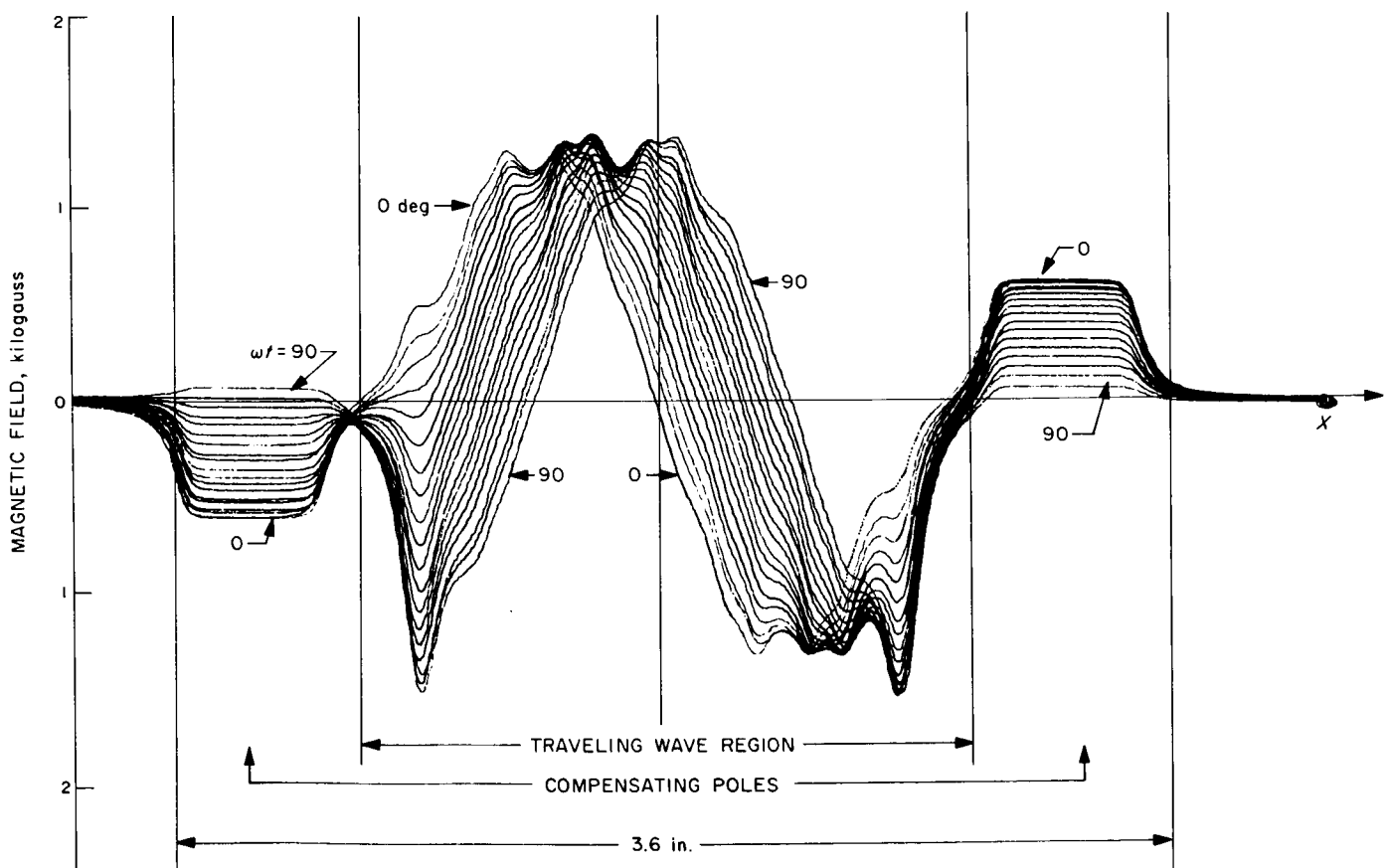


Fig. 19. Measured magnetic field profiles in AC generator at 5-deg intervals for DC currents equivalent to 10-amp peak phase current

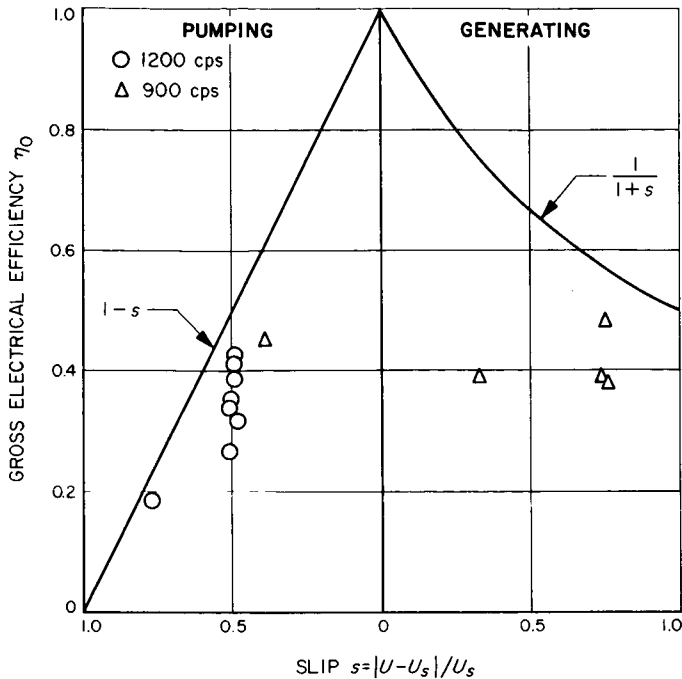


Fig. 20. Comparison of theoretical and experimental gross electrical efficiency of AC generator

increasing velocity, first one phase, then a second, and finally, at a velocity of 242 ft/sec and slip of 0.75, all three phases of the generator were delivering power. In one run a total power of 185 w was delivered to the MG set while the fluid input power increase due to power generation was 737 w ($\pm 20\%$) with 172 w being dissipated in the windings. The generator efficiencies, which are the reciprocal of the pump efficiencies defined previously, were $\eta_{eg} = 185/737 = 0.25$ and $\eta_{og} = (185 + 172)/737 = 0.48$ as compared to the ideal value $\eta_{og} = 1/(1 + s) = 0.57$.

The overall efficiency, the ratio of net output power to total input power including friction, which is the significant quantity in applications, was less than 1.0% at the low current employed. The overall efficiency at full power (5 kw) with this generator is expected to be about 15% and with a larger generator of optimum design would be 50% or more, as shown in SPS 37-39, Vol. IV.

In the next test two 300-w bulbs were added to the B and C phases, which were disconnected from the MG set. Operation was then obtained by applying excitation to the A phase only, which transferred excitation power to the B and C phases, resulting in net power output on all three phases. The next step was to disconnect the A phase from the MG set and demonstrate self-excited stable operation. This was successfully done

on the next test, except that the stable operating point was at 100-v output, whereas the MG set had been maintaining the phase voltages at 60 v. The increased operating voltage produced an insulation breakdown between the A and C phases before a data scan could be taken. The tests with this generator were thus concluded with the successful demonstration that a one-wavelength generator can: (1) operate on a self-excited basis, and (2) achieve a gross electrical efficiency of at least 70% of the ideal $1/(1 + s)$ value.

It was observed during the tests that excitation of the compensating poles had no effect on efficiency within the $\pm 20\%$ uncertainty of the low-current tests. The fins under the compensating poles were evidently sufficient by themselves to block end currents so that compensation would be required only with fewer fins.

Additional tests were performed by exciting only the compensating pole coils to determine the effectiveness of the fins in blocking compensating-field-induced currents. It was found that there was no observable pressure-drop effect of the applied compensating field, further verifying that the fluid currents were highly blocked and that the number of fins can be reduced from the seven used, an unexpectedly favorable result. Another generator is under fabrication which has coils that have been tested to 1000 v and which employs only three fins at each end.

2. High-Temperature Tests

A 2000°F lithium erosion test of 100-hr duration was completed during which the performance of high-temperature loop components was determined. During the period of operation at 2000°F the maximum lithium velocity in the flow nozzles was varied from 180 to 270 ft/sec. Preliminary evaluation of the materials exposed to the high-velocity lithium has been completed. Detailed examination of the test specimens by electron microprobe and chemical analysis is continuing.

The power input for heating the lithium and the feed pressure for producing the high-velocity flow were provided by a helical induction EM pump which operated at 2000°F. The test materials were Cb-1%Zr, W-2%ThO₂, TaC, TiC and ZrC fabricated in the form of wedges. The test wedges were mounted downstream of a pair of flow nozzles which produced impingement of lithium at velocities ranging from about 110 to 150 ft/sec. The test section, flow loop, and pump duct were all fabricated of Cb-1%Zr alloy and were operated in a vacuum chamber.

The experimental facility used for this test was described in detail in SPS 37-35, Vol. IV and SPS 37-38, Vol. IV.

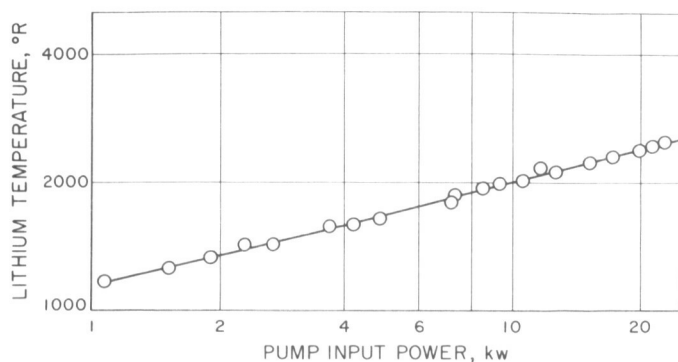


Fig. 21. Lithium temperature vs pump input power

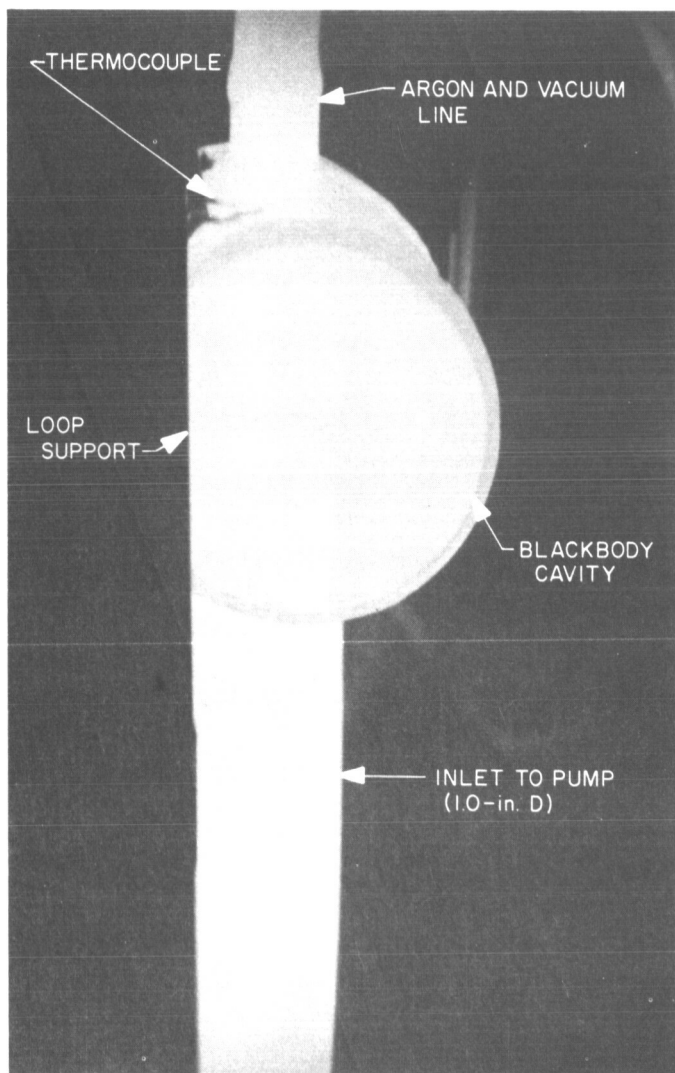


Fig. 22. Lithium test section at 1700°F

Testing was initiated after the Cb-1%Zr test loop, which had been oxidized during a previous test (SPS 37-38, Vol. IV), was cleaned and reinstalled. Approximately 60 hr operating time was required to reach 2000°F. During this time the lithium temperature was gradually increased by increasing the power to the pump. Fig. 21 gives the dependence of lithium temperature on pump input power. To maintain the lithium at 2000°F, about 23 kw of electrical power were required. The heat input was rejected by radiation from the Cb-1%Zr loop to the walls of the vacuum chamber, which were maintained at about 500°F by cooling air. Fig. 22 shows the test section at 1700°F as it appeared through a view port.

The measured performance of the GE helical induction pump was very satisfactory and agreed quite well with the predicted performance. Fig. 23 provides a comparison of the measured and predicted performance. A maximum

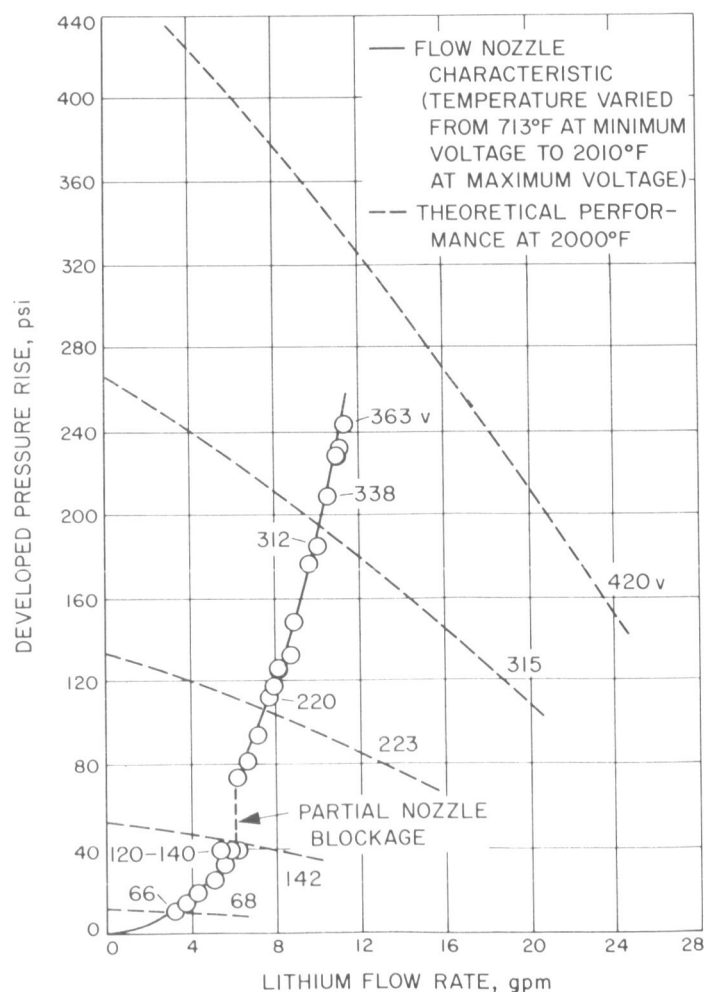


Fig. 23. Performance of lithium pump

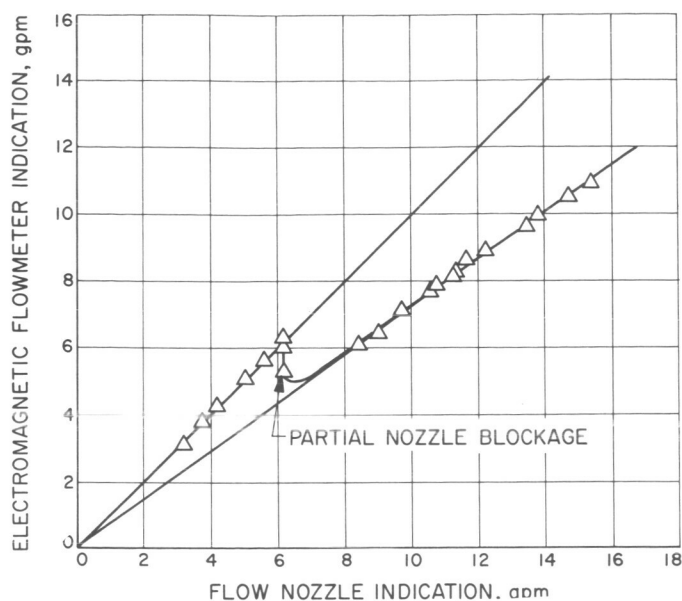


Fig. 24. Comparison of flow rates indicated by EM flowmeter and by flow nozzle

pressure rise of 243 psi was obtained at a flow rate of 11.4 gal/min. The measured performance is based on pressure readings taken upstream and downstream of the flow nozzles and on the electromagnetic flowmeter reading. Both the pressure transducers and flowmeter were calibrated during the test and gave close agreement with pretest or theoretical values. For example, Fig. 24 shows a comparison of the flow indicated by the flowmeter, with the flow indicated by the flow nozzle pressures, using the previously determined discharge coefficient of 0.93. The discontinuity in the curve was caused by partial blockage of one of the nozzles by a piece of one of the test specimens. This was manifested during the test as an abrupt drop in EM flowmeter indication.

The erosion specimens are shown in Fig. 25 after exposure to the 2000°F lithium. The Cb-1%Zr wedge suffered the least material loss and was relatively unaffected by the flowing lithium. Fig. 26 shows the Cb-1%Zr specimen tip before and after exposure to the 2000°F

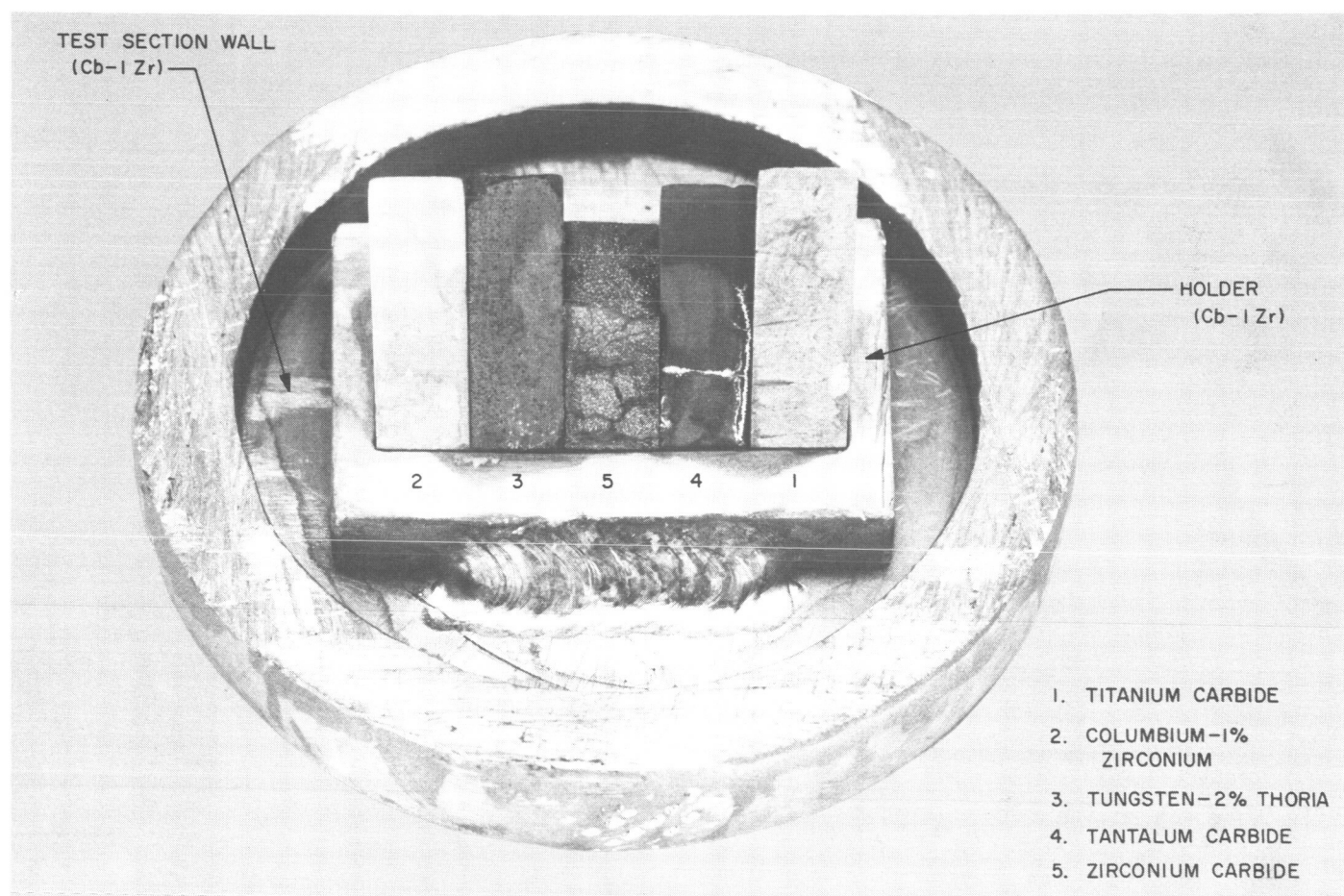


Fig. 25. Erosion test specimens after exposure to high-velocity lithium for 100 hr at 2000°F

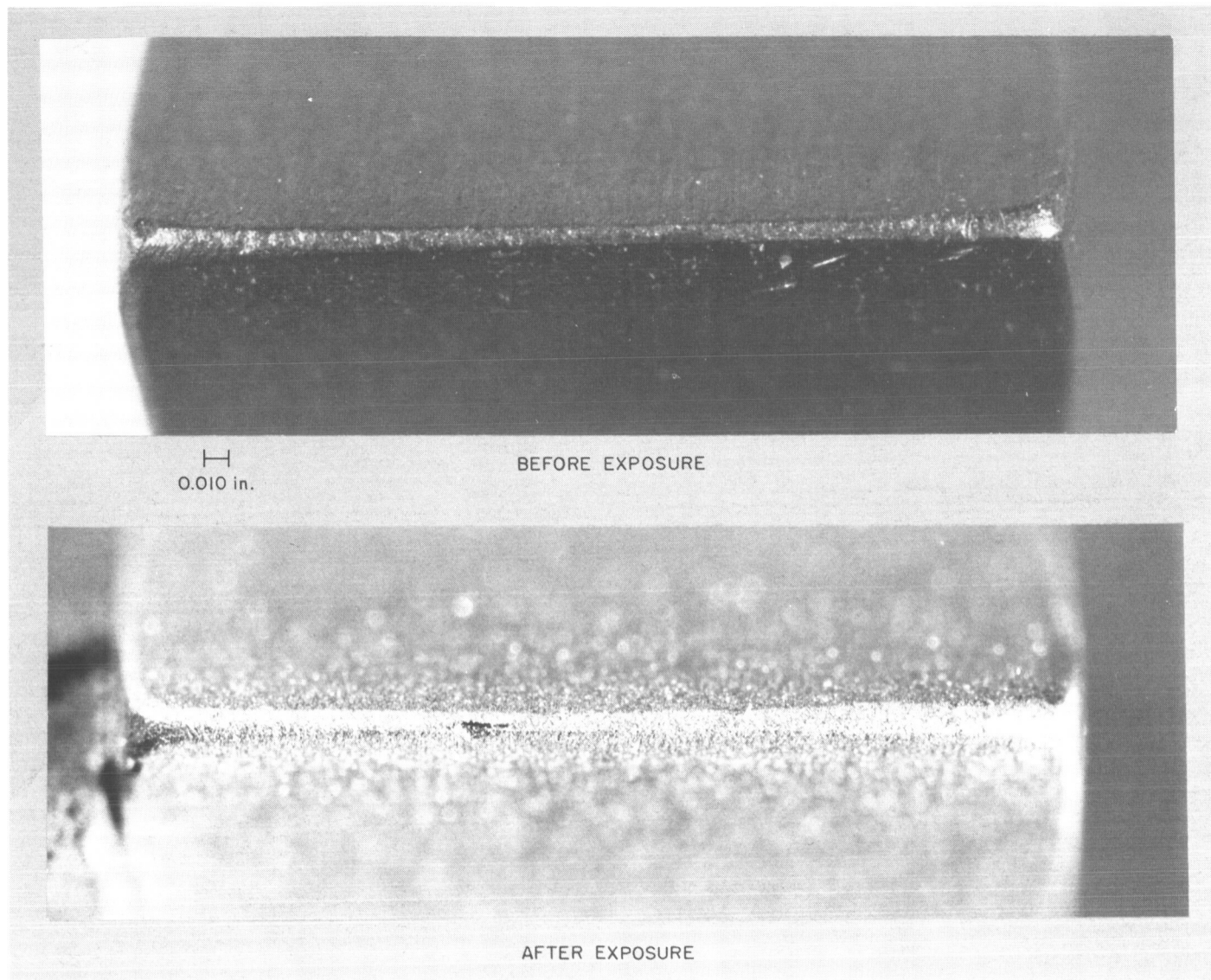


Fig. 26. Columbium-1% zirconium wedge tip before and after exposure to high-velocity lithium for 100 hr at 2000°F

lithium. The only measurable material loss was two small chips, which may have been lost due to previous flaws in the material. The tool marks and tip appear visually to have been slightly worn by the flow, but this could not be measured.

Heavy cracking was observed in all three carbides tested. The zirconium carbide, Specimen 5, suffered the heaviest damage. The entire tip had fractured and circulated through the loop to plug one flow nozzle. Specimen 4, tantalum carbide, apparently underwent a chemical reaction with the flowing lithium. The normal gold color was changed to black, and gold-colored sur-

face layers were observed on the tungsten and on the titanium carbide specimens. The reaction is evident in Fig. 27, which shows the tip of the TaC wedge before and after exposure to the flowing lithium. The titanium carbide (Specimen 1) was also heavily cracked with material loss from the tip.

The cracking of the carbides was probably due to the reaction of lithium with impurities or free carbon segregated at the grain boundaries. All the carbides have good thermal shock resistance and have previously been tested in static lithium with little deterioration (SPS 37-35, Vol. IV). The high velocities of this test probably

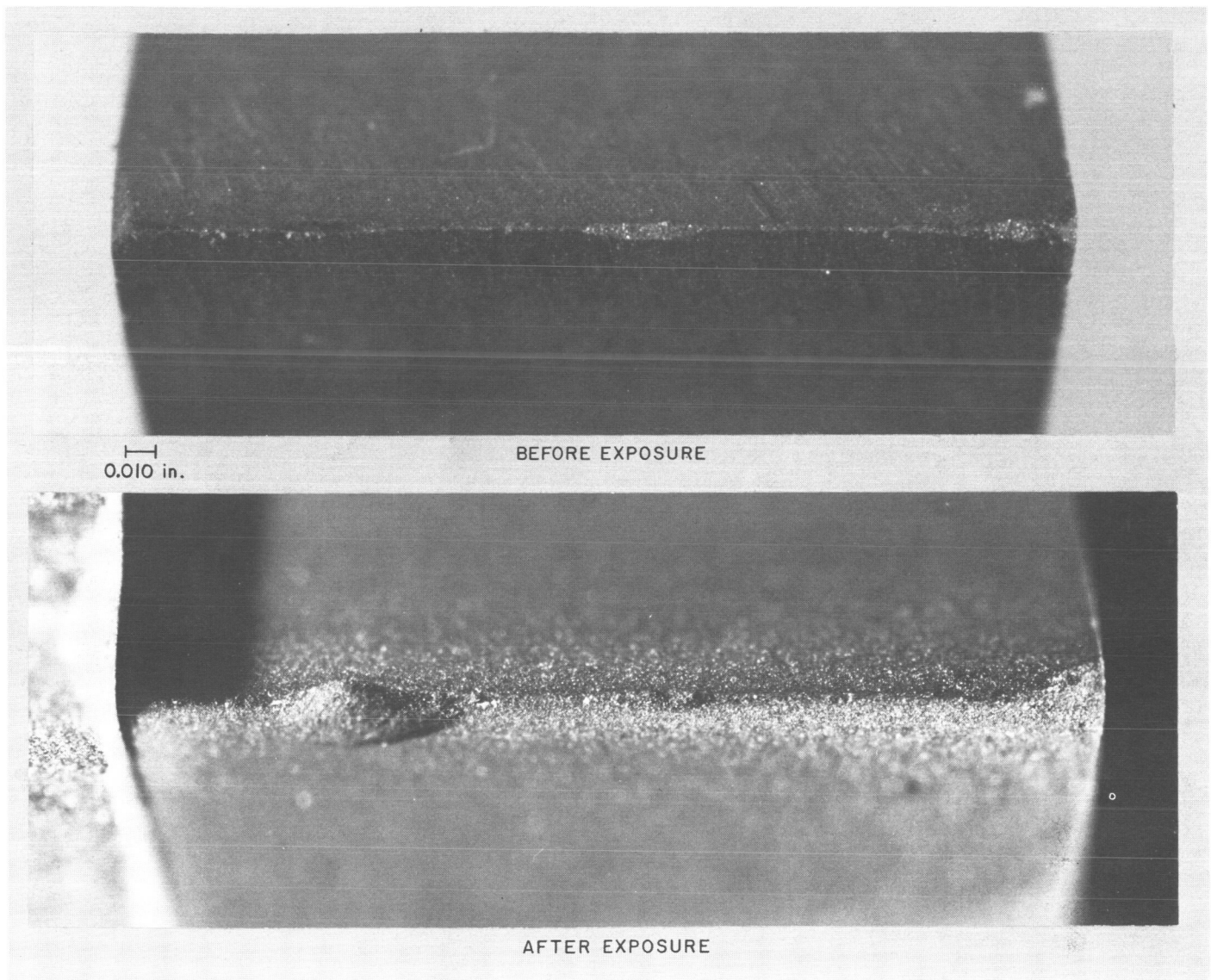


Fig. 27. Tantalum carbide wedge tip before and after exposure to high-velocity lithium for 100 hr at 2000°F

contributed to the rapid attack by removing the reaction products from the active zone. Since these specimens were fabricated from high purity material by carefully controlled vacuum hot-pressing techniques, the results would seem to eliminate these carbides from further consideration as separator materials.

The thoriated-tungsten wedge also suffered extensive damage as shown in Fig. 28. Initial damage was sustained on the edges of the test specimen prior to installation; however, a measure of the material loss can be obtained by considering the central portion of the tip. A total material depth of approximately 60 mils was lost during the 100-hr test.

In summary, the erosion test conducted did not negate the use of Cb-1%Zr as a containment or separator material for high-velocity lithium in the liquid MHD system.

Further tests are planned to use this facility to determine if the use of Cb-1%Zr can be affirmed and to evaluate the influence of high velocities on corrosion rate. The test did eliminate TaC, TiC, ZrC, and W-2%ThO₂ as possible separator materials, at least for the best purity presently attainable at reasonable cost. The helical induction pump, electromagnetic flowmeter and pressure measurement technique gave very satisfactory results at 2000°F and will be used without change for the cesium-lithium loop under construction.

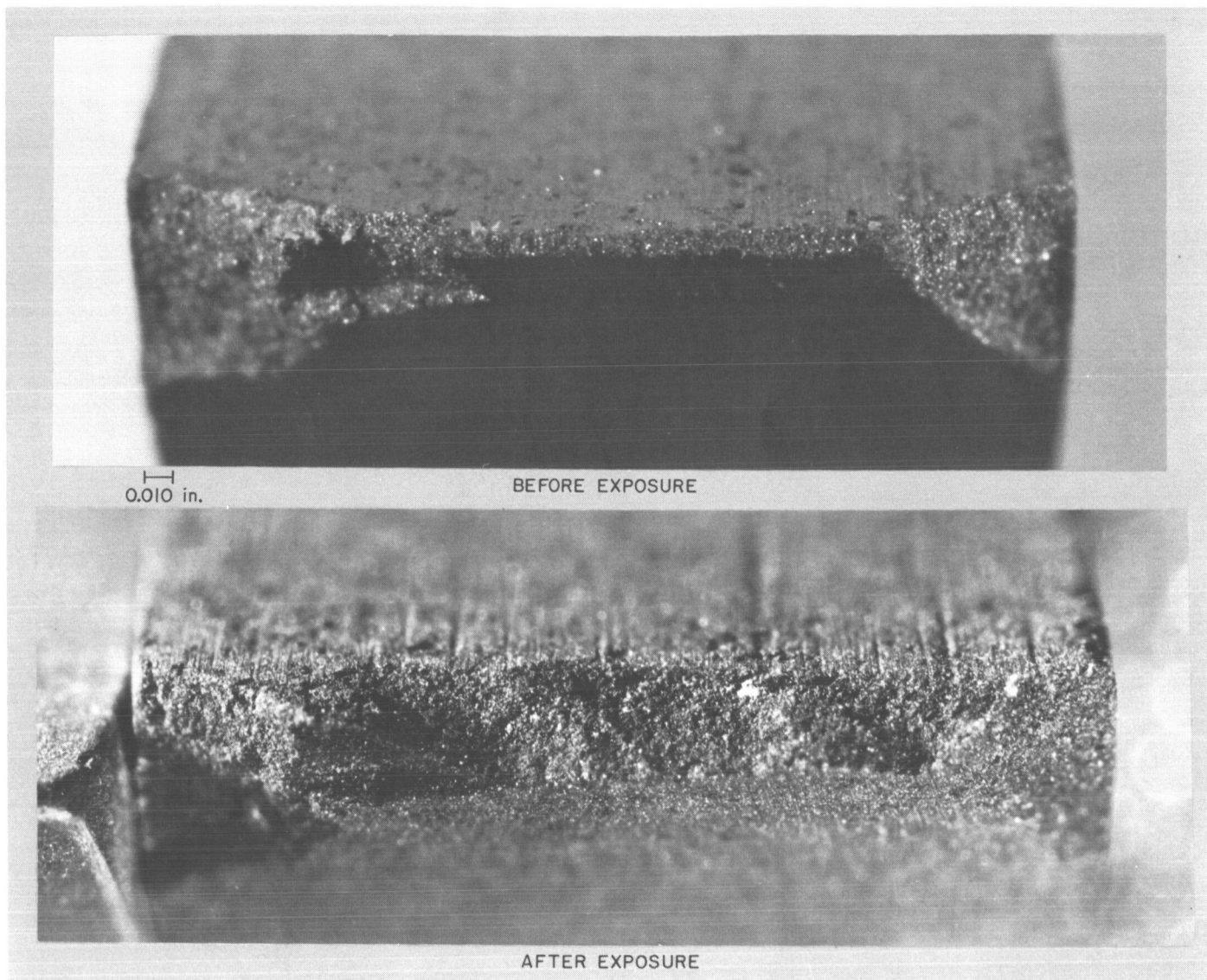


Fig. 28. Tungsten-2% thoria wedge tip before and after exposure to high-velocity lithium for 100 hr at 2000°F

Reference

1. Thurber, W. C., "Metals and Ceramics Division Annual Report for Period Ending June 30, 1964," Sect. 14, ORNL 3670 TID 4500, 34th Ed., p. 83.

N67 12119
~ ~ ~ ~

XI. Solid Propellant Engineering

A. Applications Technology Satellite (ATS) Motor Development

R. G. Anderson and R. A. Grippi

1. Introduction

In January 1963 JPL initiated a development program to provide a solid propellant apogee motor for a second generation SYNCOM satellite. This program, under the management of the Goddard Space Flight Center, was designated Advanced SYNCOM. It was to result in a spin-stabilized, active repeater communications satellite weighing about 750 lbs., operating at a synchronous altitude (22,300 mi) which would handle voice communications, teletype, and monochrome and color television signals.

In January 1964 the Advanced SYNCOM communication program was redirected to include a number of experimental instruments in addition to the original communication instruments. This expanded program is the Applications Technology Satellite (ATS) program and will result in a general purpose satellite capable of operation at a synchronous altitude with experimental instruments in the areas of meteorology, communications, radiation,

navigation, gravity gradient stabilization and various engineering experiments. For those satellites to be placed in synchronous orbit JPL will provide a solid propellant rocket motor to supply the final required velocity increment at the apogee of the elliptical transfer orbit. This rocket motor is designated the JPL SR-28-1 (steel chamber) or JPL SR-28-3 (titanium chamber) rocket motor. At present only the JPL SR-28-3 unit is intended for flight use.

Reports of progress on the development of this motor have been published in SPS 37-20 to 37-33, Vol. V, and SPS 37-34 to 37-39, Vol. IV.

2. Program Status Summary

The motor development program calls for static firing of four heavywall motors and 25 flightweight motors including two with flight design titanium chambers prior to conducting a nine motor qualification program. To date, the four heavywall motors plus 22 flightweight motors have been static fired, four of which were under simulated high altitude conditions at Arnold Engineering Development Center (AEDC) Tullahoma, Tennessee. All of the flightweight motors tested to date have been with type 410 chromium steel chambers with the exception of DEV G-8T, G-9T and E-3T, which used titanium chambers.

a. ATS storage units. The three storage rounds, cast during September, 1965, are presently in storage. These units were removed in April 1966 after approximately six months of storage and were given critical visual and physical inspections. No detrimental effects due to storage were observed.

One unit will be stored for one year before static testing. The remaining two units will be stored for two years before testing. Periodic visual and physical inspections will be made at designated times.

b. ATS qualification motors. On March 3, 1966, the last qualification motor for tests at AEDC in July-August of this year was cast. Of the nine motors cast for this purpose, eight of them will be fired while spinning at 100 rpm. The eight motors will be divided into two groups, with the first group being tested following a 40°F temperature conditioning period and the second group following a 110°F temperature conditioning period. The ninth motor will remain in reserve to be tested only if during any of the first tests, the objectives are not completed.

The qualification units have been subjected to various environmental tests, dimensional checks, and have been shipped to AEDC for testing. Testing commenced July 11th and should be completed during August.

c. Static test of Dev E-3T. On June 2, 1966, Dev E-3T was statically fired at AEDC in test cell J-5. This firing was the first combination apogee motor-spacecraft test. The apogee motor-spacecraft assembly was mounted on a soft test stand to evaluate the vibrational inputs to the spacecraft. Of primary importance was the evaluation of thermal inputs to the spacecraft as a result of the apogee motor firing. Approximately 80 thermocouples were attached to the apogee motor and spacecraft to monitor temperatures during and after apogee motor burn. The complete safe and arm ignition system was also evaluated during this test.

Test results show that the apogee unit functioned nominally in all respects. Fig. 1 shows the positions of the thermocouples attached to the apogee unit. Table 1 summarizes the temperature data obtained from these externally mounted thermocouples.

Four strain gages were affixed to the external surface of the motor chamber in order to monitor motor chamber pressure. Two circumferential (SC-1 and SC-4) and two axial (SC-2 and SC-3) strain gages were employed (Fig. 1). A plot of the data obtained from SC-1 is shown in Fig. 2. A

Table 1. Applications technology satellite apogee motor temperature data—test DEV E-3T

Thermocouple (TC) No. ^b	Temperatures, °F		
	Initial	Run end (43 sec)	Peak @ time, sec
5	73	138	723 @ 510
11	77	133	695 @ 550
7	72	73	878 @ 256
12	77	77	695 @ 300
8	72	158	718 @ 480
9	72	308	723 @ 136
10	73	63	Footnote ^a
6	73	73	459 @ 780

^aTSC-10 gave erratic readings starting at 36 sec after motor ignition.
^bAll thermocouples mounted on external motor surfaces (Fig. 1).

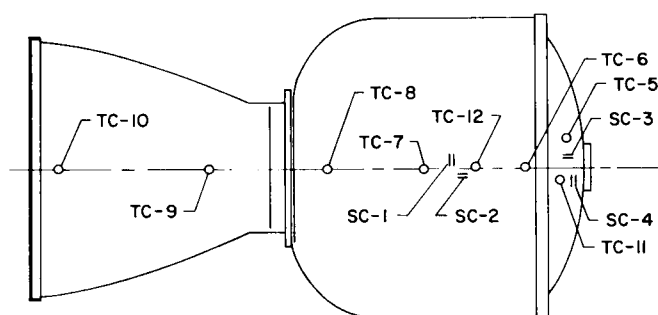


Fig. 1. Thermocouple locations—test DEV E-3T

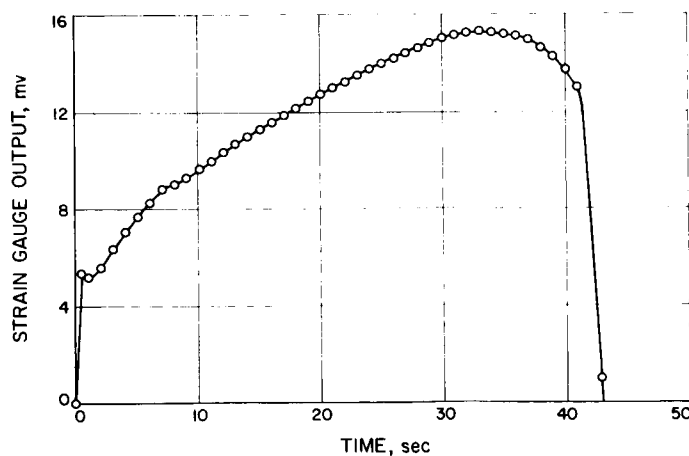


Fig. 2. Motor test DEV E-3T, plot of SC-1

comparison of the strain gage data with previously recorded pressure-time data shows excellent agreement of both times and strain gage pressure levels.

d. Static test of Dev I-1. On May 3, 1966 the test of Dev I-1 was conducted. The test was primarily used to evaluate the mechanical compatibility of the closure portion of the safe and arm (S/A) device built by the Harry Diamond Laboratory (HDL) with the apogee motor and the ability of the device to withstand the heat loads encountered during a full duration motor firing. Thermocouples were installed on the safe and arm hardware to assist in evaluating the temperature loads seen by the hardware during and immediately following the test. The safe and arm hardware provided two special pressure taps which allowed the igniter basket pressure and the motor chamber pressure to be measured throughout the test.

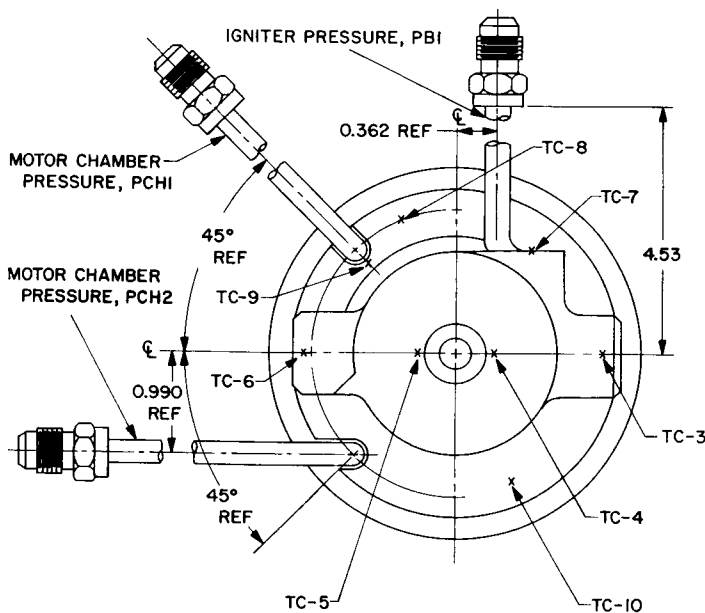


Fig. 3. S/A device thermocouple locations

Table 2. Applications technology satellite apogee motor temperature data—test DEV I-1 HDL S/A device

Thermocouple (TC) No. ^a	Maximum temperature/time, °F/sec
3	334 @ 6
6	245 @ 11
4	204 @ 30
5	209 @ 30
8	170 @ 43
10	168 @ 43
7	216 @ 5
9	264 @ 6

^aSee Fig. 3 for location of thermocouples.

Test results show that the mechanical portion of the S/A device can withstand the pressures and temperatures of a full duration apogee motor firing. Eight thermocouples attached to the upper housing of the S/A device (Fig. 3) recorded temperatures during and after the motor run. Table 2 lists the maximum temperature and time for each thermocouple during the motor run of 43 sec. A post-fire inspection of the S/A device revealed no deleterious effects due to motor burn.

N67 12120

B. The Interior Ballistics of the Fluid Controlled Solid Rocket Motor

O. K. Heiney

1. Introduction

Of the methods proposed to obtain a throttlable solid rocket motor with start-stop capability, the fluid control concept is among the more promising. The basic concept is that a fully oxidized solid propellant grain is configured with an oversized nozzle throat area such that the propellant burning by itself is insufficient to pressurize the chamber; thus, for pressurization to occur a fluid must be injected into the combustion chamber. Variation of the mass flow rate of the fluid will provide operation in the pressure range of 50 to possibly 1500 psia. Start-stop capability is provided by having the grain and fluid hypergolic.

2. Analysis

The ballistics of the fluid control motor may be simply derived from the conservation of mass and the equation of state. The procedure parallels that in Ref. 1 for a conventional solid motor.

The mass balance equation will give:

$$\dot{m}_l + r S_b \rho_p = \frac{d}{dt} (\rho_c v_c) + \frac{P_c A_t}{c^*} \quad (1)$$

with the equation of state,

$$P_c = \rho_c R T$$

and the following identities

$$\dot{m}_s = r S_b \rho_p$$

$$c^{*2} = RT/\Gamma^2$$

$$K_N = S_b/A_t$$

$$\Gamma^2 = \gamma \left(\frac{2}{\gamma + 1} \right)^{\frac{\gamma+1}{\gamma-1}}$$

Eq. (1) becomes

$$r S_b \rho_p \left(1 + \frac{\dot{m}_l}{\dot{m}_s} \right) = v_c \frac{d\rho_c}{dt} + \rho_c \frac{dv_c}{dt} + \frac{P_c A_t}{c^*} \quad (2)$$

Neglecting the second term on the right as second order there is

$$\frac{dP_c}{dt} = \frac{RT}{v_c} \left[r \frac{S_b \rho_p}{g} \left(1 + \frac{\dot{m}_l}{\dot{m}_s} \right) - \frac{P_c A_t}{c^*} \right]$$

and finally with corrected units

$$\frac{dP_c}{dt} = \frac{12 \Gamma^2 A_t c^*}{v_c} \left[r \frac{K_N \rho_p}{g} c^* \left(1 + \frac{\dot{m}_l}{\dot{m}_s} \right) - P_c \right] \quad (3)$$

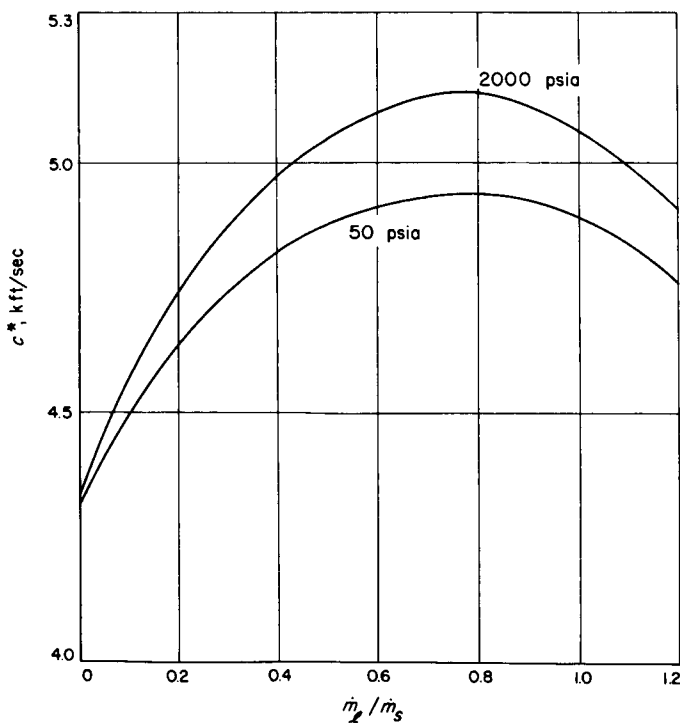


Fig. 4. Theoretical c^* LPC 615A CTF injection

For steady state operation the term in the brackets must be zero or

$$P_c = r \frac{K_N \rho_p}{g} c^* \left(1 + \frac{\dot{m}_l}{\dot{m}_s} \right) \quad (4)$$

To completely determine the performance of the propellant and injectant selected, the burning rate of the

$K_N = 70$ PROPELLANT IS LPC 615A			
P_c	$c^* \left(1 + \dot{m}_l/\dot{m}_s \right)$	c^*	\dot{m}_l/\dot{m}_s
50	6038.25	4766.70	0.266
100	6361.73	4824.74	0.318
150	6597.35	4856.62	0.358
200	6785.84	4881.92	0.389
250	6958.14	4903.30	0.419
300	7077.95	4917.51	0.439
350	7249.41	4937.69	0.468
400	7383.56	4953.39	0.490
450	7491.38	4962.84	0.509
500	7579.93	4967.74	0.525
550	7695.28	4974.13	0.547
600	7794.13	4982.19	0.564
650	7879.77	4989.60	0.579
700	7954.70	4996.08	0.592
750	8047.97	5003.74	0.608
800	8131.39	5010.24	0.622
850	8206.46	5016.10	0.635
900	8274.35	5021.39	0.647
950	8343.76	5026.81	0.659
1000	8407.24	5031.76	0.670
1050	8465.51	5036.30	0.680
1100	8519.18	5040.49	0.689
1150	8602.52	5044.47	0.705
1200	8680.37	5042.87	0.721
1250	8753.24	5041.37	0.736
1300	8821.60	5039.96	0.750
1350	8885.85	5038.64	0.763
1400	8946.36	5037.40	0.776
1450	9029.01	5035.69	0.793
1500	9107.54	5032.26	0.809

Fig. 5. Steady state motor performance

propellant as a function of pressure, and the c^* value as a function of liquid injection must be determined. The burning rate vs pressure function may be determined by means of a Crawford Bomb, and the c^* function determined by means of a series of computer thermochemical calculations. For a given propellant, say Lockheed Propulsion Company LPC 615A, with liquid chlorine trifluoride (CTF) injection, the theoretical c^* plot is shown in Fig. 4, for the range of pressures between 50 and 2000 psia.

For this work 100% c^* efficiency has been assumed. Realization of this level of performance will necessitate a sophisticated injector design such that proper atomization and introduction of the liquid takes place. Inadequate atomization would result in varying amounts of unreacted fluid escaping and a corresponding drastic decrease in combustion efficiency and performance.

An assumption implicit in this approach is that the burning rate and injectant concentration are coupled only

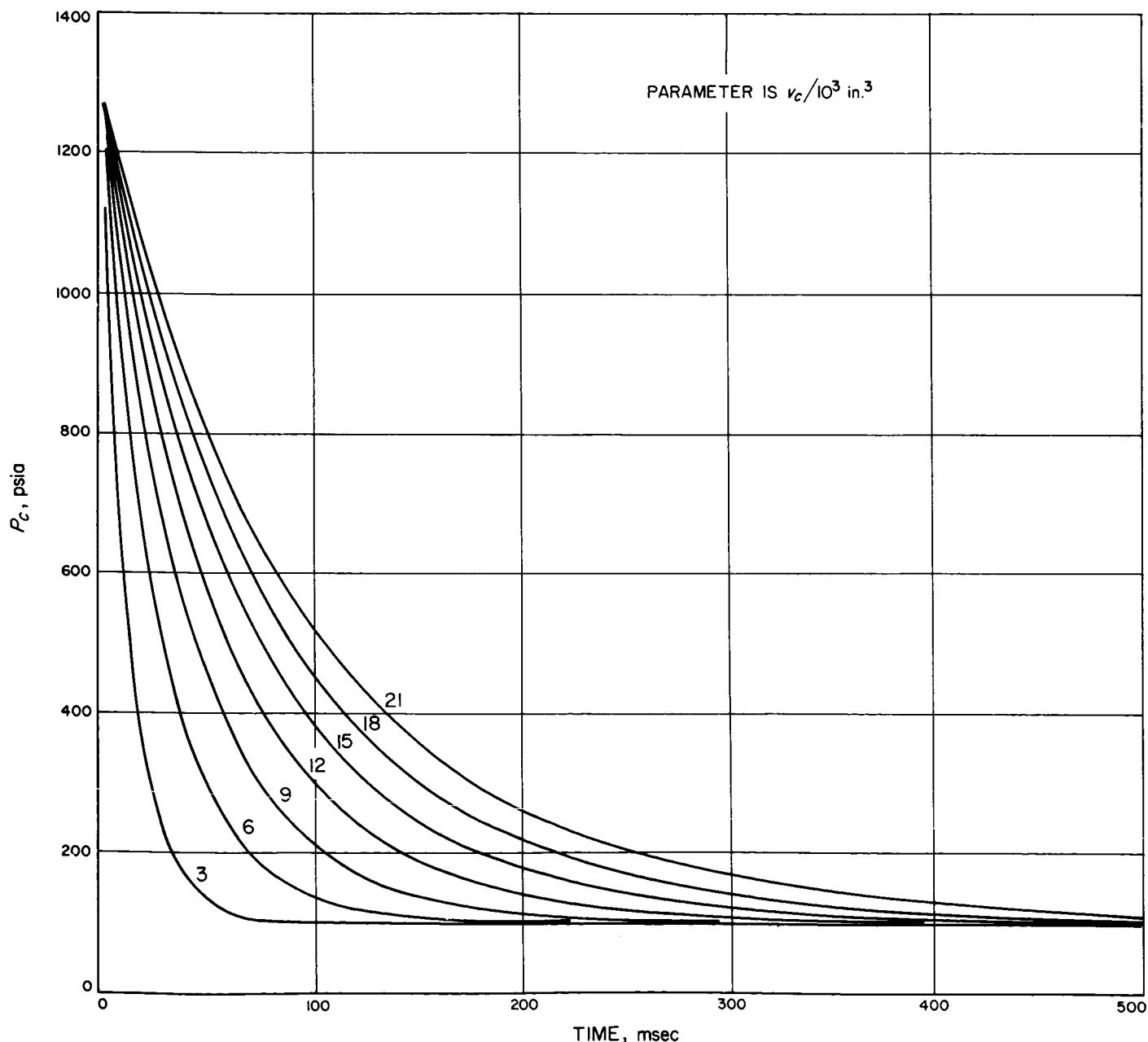


Fig. 6. Dynamic response of fluid controlled motor step change to lower injection rate

through pressure. From the form of Eq. (4) it is seen that for an optimized system the regression rate exponent should be close to 1 to keep the utilization rates of liquid and solid at a constant ratio. If the exponent n in the simplified equation

$$r = bP^n$$

were 1, the ratio of liquid and solid utilization will be constant. As n differs from 1 the excursion rate will have to vary over a commensurately wide range.

Fig. 5 shows the output of a 1620 computer program for the solution of Eq. (4).

The given propellant is marginal for the fluid control mode of operation. Its burning exponent n ranges from 0.80 to 0.95. This causes the wide mixture ratio variance, from 0.27 to 0.81. Also, the range of K_N values which the motor may assume is extremely narrow. For this propellant, if the K_N is raised to 75 the fuel will burn by itself with no injection; if it is lowered to 65 the liquid

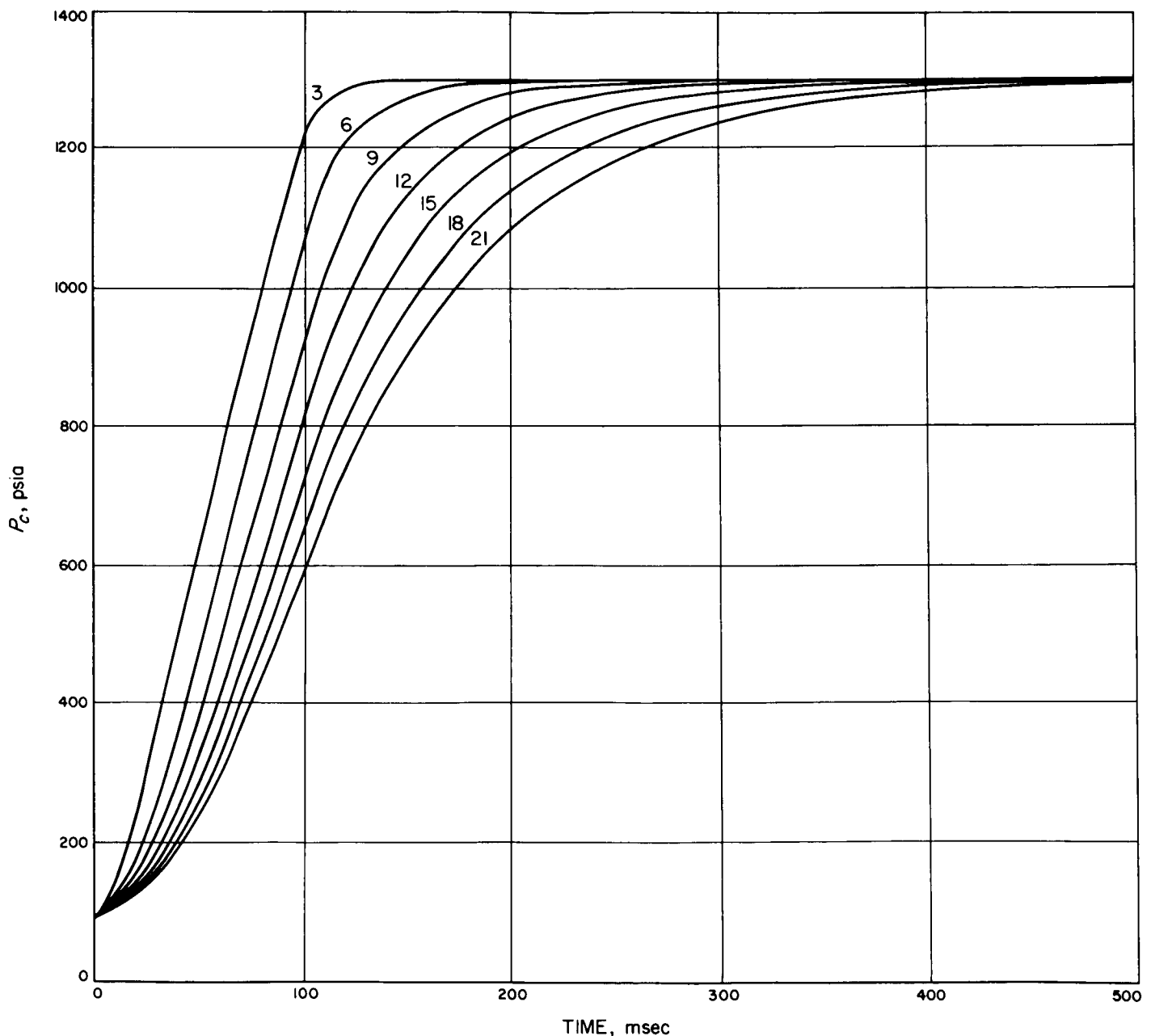


Fig. 7. Dynamic response of fluid controlled motor ramp change to higher injection level

injection ratio required at the higher pressures would be so large as to severely decrease combustion efficiency. Another drawback is the high burning rate of the propellant, 0.85 in./sec at 1000 psia. The high burning rate necessitates the low value of K_N , as may be seen from Eq. (4). Suitable neutral grain geometry at such a low K_N would be difficult to attain.

It is then seen that precise propellant tailoring is far more critical for a fluid control solid motor than for typical solid motors. A study was conducted to examine the dynamic response of this type motor utilizing Eq. (3) as the analytical model. For this study parameters were set as follows: $K_N = 70$, $A_t = 20$ in², LPC 615A propellant, and CTF injectant. The chamber volume was allowed to vary from 3,000 to 21,000 in³. The results are described below.

Fig. 6 is the response to a step change in the injection rate from equilibrium at 1300 psia, to the fluid injection level required for equilibrium at 100 psia at several chamber volumes. When little of the initial charge has been burned the response is quite prompt, requiring about 100 msec for the thrust level change; however, as a greater percent of the grain is burned the response

becomes more sluggish, so that near burnout the thrust change requires about 400 msec.

Fig. 7 is the motor response to an increase in the injection rate from equilibrium at 100 psia to an eventual level of 1300 psia. The increase in injection level may not be done in a step manner, as in the case above, as this would entail an instantaneous \dot{m}_l/\dot{m}_s value much greater than the motor is designed to handle. The increase is put in as a ramp function lasting 100 msec. Again, as would be expected, the more nearly empty motor chamber has a slower response.

3. Conclusion

The fluid control concept is an attractive and feasible method for obtaining a controllable solid rocket motor. The problems of propellant tailoring and suitable injector design require a refined engineering approach, but are amenable to eventual solution. Lockheed Propulsion Co., Redlands, California, has a contract (NAS 7-444) to obtain an adequate propellant and further define the problems and potentiality of the system. The goal of the current program is to lay the groundwork for future motor development effort.

Nomenclature

A_t	motor throat area	K_N	burning surface to throat area ratio
c^*	characteristic exhaust velocity	r	regression rate of propellant
\dot{m}_l	liquid mass injection rate	v_c	chamber volume
\dot{m}_s	solid mass injection rate	ρ_c	density of propellant gases in chamber
P_c	chamber pressure	ρ_p	density of solid propellant
S_b	burning surface of solid grain	Γ	flow parameter

Reference

1. Hugget, C., Bartley, C. E., and Mills, M. M., *Solid Propellant Rockets*, Princeton Aeronautical Paperbacks, Princeton, New Jersey, 1960.

N67 12121

XII. Polymer Research

A. Degree of Crosslinking of Styrene Butadiene Rubber Glass Bead Composites

R. F. Fedors and R. F. Landel

In SPS 37-32, -35, Vol. IV, pp. 120-126, 93-98, respectively, a series of crosslinked styrene butadiene rubber (SBR) composites containing varying amounts of a glass bead filler were characterized. The results obtained from equilibrium swelling measurements in benzene indicated that the concentration of effective network chains ν_e , increased with an increase in volume fraction of filler ϕ . Subsequent studies of the mechanical behavior of these composites provided data which indicated that ν_e was essentially independent of ϕ . Since ν_e is an important parameter in any description of mechanical behavior (Ref. 1), an independent estimate of ν_e was obtained by means of compression measurements on disks swollen to equilibrium in benzene. The results obtained by this procedure show that ν_e is essentially independent of ϕ , in agreement with the results from the ultimate property studies. In this article the origin of the error in the value of ν_e , calculated from swelling measurements, will be analyzed.

For unfilled elastomers, ν_e can be conveniently calculated from equilibrium swelling measurements by means of the modified Flory-Rehner equation (Ref. 2).

$$\nu_e = -\frac{g}{V_o} \left[\frac{\ln(1 - v_r) + v_r + \mu v_r^2}{g^{2/3} v_r^{1/3} - \frac{v_r}{2}} \right] \quad (1)$$

where g is the gel fraction; v_o is the molar volume of solvent; v_r is the volume fraction of rubber in the swollen gel at equilibrium; and μ is the solvent-polymer interaction parameter. For SBR vulcanizates in benzene, μ is taken equal to 0.34.

For systems containing fillers, the situation is more complicated because Eq. (1) is strictly applicable to gum vulcanizates only, and furthermore, the calculation of appropriate v_r values from the measured equilibrium swelling behavior of the composite should exclude possible contributions from the presence of filler itself.

If swelling produces a complete separation of the filler from the binder, the swelling of the binder will be normal except that each particle will be surrounded by a cavity filled with swelling liquid. On the assumption that each particle of filler behaves independently of all others, Bills and Salcedo (Ref. 3) pointed out that a value

of v_r independent of ϕ can be calculated from the measured swelling behavior of the composite by means of:

$$v_r = \frac{w_c/\rho_c}{w_c/\rho_c + w_1/\rho_1} \quad (2)$$

where w_c and w_1 are the weights of composite and swelling liquid respectively in the swollen composite at equilibrium, and ρ_c and ρ_1 are the corresponding densities.

Alternatively, there may be cases where the filler induces a restricted swelling in the binder, either because the forces between the filler particle and the binder are not disrupted in the swelling process, or because a nonuniform distribution of crosslinks is produced in the neighborhood of the filler surface. To deal with this situation, Kraus (Ref. 4) has derived the following expression:

$$\frac{v_r}{v_{ra}} = 1 - [3c(1 - v_r^{1/3}) + v_r - 1] \frac{\phi}{1 - \phi} \quad (3)$$

where v_r is the true volume fraction of the binder in the swollen gel (i.e., the value which would be obtained for a corresponding gum vulcanizate in the absence of filler); v_{ra} is the apparent volume fraction of rubber in the swollen composite calculated from:

$$v_{ra} = \frac{(w_c/\rho_c)(1 - \phi)}{(w_c/\rho_c)(1 - \phi) + w_1/\rho_1} \quad (4)$$

and c is a parameter, independent of ϕ and v_r , which is a measure of the ability of the filler to restrict swelling of the binder. If $c = 0$ then the filler does not restrict swelling and Eq. (3) reduces to Eq. (2). Eq. (3) is most convenient to use in those instances where the degree of crosslinking in the binder is independent of ϕ ; for, in this case, a plot of $1/v_{ra}$ vs $\phi/(1 - \phi)$ will yield a linear relationship with intercept $1/v_r$ and slope $[1 - v_r - 3c(1 - v_r^{1/3})]/v_r$.

Table 1 shows values of both v_r and v_{ra} , as calculated from the swelling data according to Eqs. (2) and (3), respectively. As can be seen, v_r increases and v_{ra} decreases with increasing ϕ . There are several effects which might be invoked in order to explain an increase in v_r with ϕ , viz.,

- (1) The appropriate value of c for the present composites may differ appreciably from zero.
- (2) The degree of crosslinking in the binder phase may increase with ϕ .

Table 1. Physical properties of SBR-glass bead composites

Sample designation	ϕ	v_r	v_{ra}	$v_e \times 10^{6a}$ moles/cm ³	$v_e \times 10^{6b}$ moles/cm ³
CA	0	0.130	—	88	91.5
3A	0.0922	0.146	0.135	111	101
4A	0.132	0.145	0.129	108	102
5A	0.169	0.148	0.126	115	104
6A	0.204	0.155	0.128	124	105
7A	0.234	0.151	0.120	121	96.2
8A	0.270	0.157	0.120	131	102
9A	0.289	0.160	0.120	133	97.8
10A	0.337	0.163	0.114	142	100

^aFrom swelling using Eq. (1) with $\mu = 0.34$.
^bFrom compression using Eq. (5).

- (3) The models used in deriving Eqs. (2) and (3) may not be valid over the entire range of ϕ . These various possible explanations for v_r increasing with ϕ will be considered in more detail.

a. Variation of c with ϕ . Based on the direct microscopic observation of swollen polyurethane composites containing glass beads reported by Bills and Salcedo (Ref. 3), it may be concluded that the beads did not interact strongly with the polyurethane binder for ϕ values from 0 to 0.61. They were able to observe directly that the dioxane solvent used caused complete separation of the binder from the filler surface, resulting in the formation of a cavity filled with excess swelling liquid. Their results would, therefore, imply that $c = 0$ over the whole range of ϕ which they investigated. On this basis, it is reasonable to suppose that $c = 0$ for the present glass bead composites also, especially since the SBR binder, unlike the polyurethane, is essentially nonpolar in nature. Furthermore, Eq. (3) predicts that for a constant value of c (regardless of its actual value, be it zero or a small positive constant) a plot of the data in the form $1/v_{ra}$ vs $\phi/(1 - \phi)$ will be nonlinear if v_r varies with ϕ .

The data from Table 1, in addition to data from another set of swelling experiments, are treated in this manner in Fig. 1. Although the scatter is relatively great, the data seem to be best represented by a nonlinear relationship, since, if a linear fit to the data is attempted, a value of $c = 0.33$ is required. This value is believed to be much too large for a system such as glass-SBR.

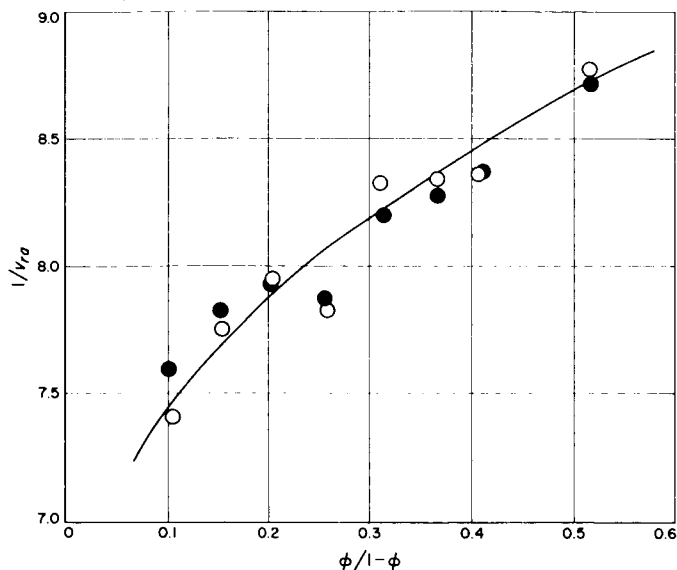


Fig. 1. Dependence of the reciprocal apparent volume fraction of rubber in swollen composites $1/v_{ra}$ on a function of the filler loading for data obtained from two independent swelling experiments. O, data from Table 1; ●, data obtained about six months later from similar experiments

Hence, it was concluded that v_r indeed increases with ϕ and on this premise the values of v_e shown in Table 1 were calculated using Eq. (1) with $\mu = 0.34$. These results would indicate that v_e increases slowly with ϕ ; although the increases are small, they nevertheless appear to be real.

b. Variation of v_e with ϕ . In an attempt to obtain an independent measure of v_e compression-deflection measurements (Ref. 5) were carried out on disks of the composites swollen to equilibrium in benzene. In compression of swollen gels, measurements can be carried out at relatively small deformation. Furthermore, if $c \approx 0$, then the filler becomes detached from the binder and immersed in the liquid in the cavity and should not contribute appreciably to the observed stress-strain response. This will be more nearly true when v_r is small and becomes progressively poorer an approximation as $v_r \rightarrow 1$.

For the compressive stress-strain measurements (Ref. 5), disks about 0.75 in. in diameter and about 0.080 in. thick were allowed to swell to equilibrium in benzene. The swollen specimens were then subjected to uniaxial compression, in the presence of excess swelling agent, using a special jig attached to the testing machine. The crosshead speed was 0.02 in./min and the test was

terminated after the specimens had undergone strains of about 15%. Under these conditions the test is considered to be rapid enough to prevent any change in v_r with strain (Ref. 6). The relationship between the relevant variables for small strains was taken to be:

$$v_e = \frac{gh_oS}{3RTA_o\phi} \quad (5)$$

where g is the gel fraction, h_o and A_o are the height and area of the dry specimen, respectively, before swelling, and S is the slope of the linear load-deflection curve for the swollen gel. The results for v_e obtained by this technique are given in Table 1. It may be seen that this experimental technique indicates that, except possibly for the gum vulcanizate, the degree of crosslinking is essentially the same for all composites.

c. Examination of the model. The apparent discrepancy in the values obtained for v_e using the two independent test methods may be explained on the basis of a breakdown in the models employed in the derivation of both Eqs. (2) and (3). The applicability of these equations depends in part on the assumptions that:

- (1) The presence of one particle does not influence the swelling behavior of the binder in the vicinity of neighboring particles.
- (2) No particle agglomeration or clustering exists. To the extent that these conditions are invalid, values of v_r calculated from either Eq. (2) or (3) would tend to be high and hence lead to high estimates for v_e .

For the present composites, only the second assumption concerning the absence of agglomeration will be important, and hence, this effect will be considered in more detail. In order to do this, it will be convenient first to consider the state of affairs existing in the composite when no particle agglomeration is assumed present.

For this case, the situation existing in the swollen composite can be approximated schematically, as shown in Fig. 2(a). The particle radius is r , and the volume fraction of rubber in the swollen gel for a corresponding identical binder in the absence of filler is v_r . When swelling is isotropic, all dimensions will increase by the factor $1/v_r^{1/3}$ to a first approximation. Thus, the volume of excess solvent in the cavity surrounding the particle is $4/3 \pi r^3(1/v_r - 1)$. If there are n_i particles of radius

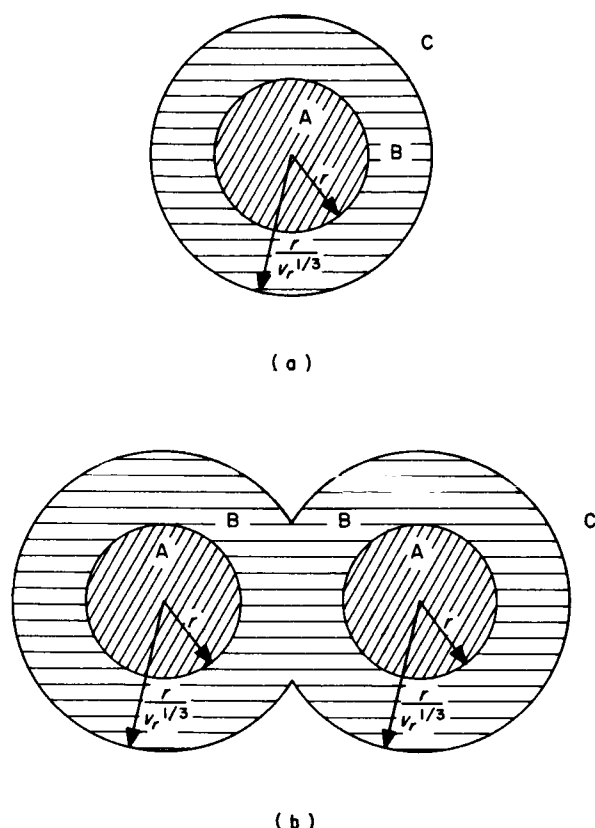


Fig. 2. Schematic representation of the swelling behavior of a binder containing particles: (a) swelling of a composite containing one particle; (b) swelling behavior for two particles which were in contact in the unswollen composite, (A) particle, (B) excess solvent, (C) swollen binder

r_i and n_{i+1} particles of radius $r_{i+1} \dots$, the total volume of excess solvent in cavities is

$$v_s = (1/v_r - 1) \sum_{i=1}^N \frac{4}{3} \pi n_i r_i^3 = V_p (1/v_r - 1) \quad (6)$$

where V_p is the volume occupied by the particles, and N is the total number of particles present in the system. It is interesting to note that Eq. (6) is independent of both particle size and particle size distribution. The equation leads directly to Eq. (2) since,

$$\begin{aligned} v_r &= \frac{(1 - \phi)}{(1 - \phi) + v_1/v_c - \phi(1/v_r - 1)} = \frac{v_c}{v_c + v_1} \\ &= \frac{w_c/\rho_c}{w_c/\rho_c + w_1/\rho_1} \end{aligned} \quad (7)$$

where v_1 is the total volume of solvent present in the swollen composite, and v_c is the volume of composite before swelling.

When agglomeration occurs, however, Eq. (6) will overestimate the value of v_s , as will now be demonstrated for a simplified model. In Fig. 2(b) the situation prevailing at equilibrium swelling is depicted for two particles of equal radius which were in contact (agglomerated) in the dry composite. For isotropic swelling, all linear dimensions will increase, as before, by the factor $1/v_r^{1/3}$. In this case, however, the volume of excess solvent is equal to the volume of a truncated sphere which can be taken as equal to the difference between the volume of the spherical shell less the volume of a spherical segment whose altitude is $r(1/v_r^{1/3} - 1)$. If h represents the fraction of particles which were in contact and f the number of contacts per particle in the unswollen composite, then the volume of excess solvent can be written as:

$$\begin{aligned} v_s &= \sum_i^{N_i} f \frac{4}{3} \pi r_i^3 \left(\frac{1}{2v_r} + \frac{3}{4v_r^{2/3}} - 5/4 \right) \\ &+ \left(\frac{1}{v_r} - 1 \right) \sum_i^N \frac{4}{3} \pi r_i^3 \end{aligned} \quad (8)$$

or, if the particles are monodisperse,

$$v_s = V_p \left[\frac{fh}{4} \left(\frac{2}{v_r} + \frac{3}{v_r^{2/3}} - 5 \right) + (1 - h) \left(\frac{1}{v_r} - 1 \right) \right] \quad (9)$$

It is expected that f , the number of contacts per particle, will be relatively insensitive to ϕ . The fraction of particles in contact h , however, is expected to be strongly dependent on ϕ , inasmuch as $h = 0$ when $\phi = 0$ and $h \rightarrow 1$ when $\phi \rightarrow \phi_m$. Since v_s as given by Eq. (6) will always be larger than that given by Eq. (9), it is evident that use of Eq. (6) will always yield larger values of v_r . Thus, it is apparent that Eq. (2) can provide values of v_r which increase with ϕ even though v_e is maintained constant.

Hence, it may be concluded that for the present SBR-glass bead composites, and perhaps for other composites with $c \approx 0$ as well, the observed increase in v_r , as calculated from Eq. (2), with increase in ϕ is the result of particle agglomeration or clustering.

N67 12122

B. A Theory of Particle-Particle Interaction Describing the Mechanical Properties of Dental Amalgam

B. G. Moser and R. F. Landel

1. Introduction

We have previously shown how the modulus or the viscosity of filled systems, such as cured and uncured propellant, can be explained in terms of the actual and the limiting volumetric loading (SPS 37-30, Vol. IV, pp. 97-100). Next, the theory of the limiting volumetric loading was derived (SPS 37-34, Vol. IV, pp. 133-137). Essentially this theory described how particles will pack randomly into beds. Since this is a general theory, it applies to particle beds other than just those found in solid propellants, and so in this article we show one "spin-off" of significant practical importance — an application to dental amalgams.

Since the inception and first use of silver-tin amalgam in dental restorations, the parameters that dictate the mechanical properties have been poorly understood. "Rule of thumb" and "make-do" have been the key notes. Demaree and Taylor (Ref. 7) give a brief and excellent review of the various conclusions and outlooks presently in vogue. The parameters which they mention as being important can be summarized as: particle size, particle shape, specific surface area, and residual mercury.

Particle size and shape have long been recognized by most workers as important. It has been noted especially that the expansion, upon hardening of an alloy, is reduced as the particle size is reduced, though others have thought that the specific surface, rather than the particle size, per se, was controlling the volume change. It has also been reported that the expansion was a linear function of the surface area. As far as mechanical strength is concerned, compressive strength and tensile strength have been studied as a function of particle size. To paraphrase Demaree and Taylor, many authors have talked about the importance of particle size, but none have done anything about it.

The influence of residual mercury in the set amalgam also has been long recognized as an important parameter, but there has been some difficulty in separating its effect from that of particle size. Another difficulty in assessing

this parameter has arisen from the different mixing and condensing techniques. The Eames technique was introduced to standardize this variable so as to arrive at a single base line of mercury content.

The present study was undertaken as one facet of a larger study of the mechanical properties of filled systems. While it confirms the importance of the particle size and mercury content on the mechanical properties of dental amalgam, a slightly different approach is employed, which leads to a satisfactory rationale not only for shrinkage and strength but also for the variation in these with mixing technique. Following the pattern of our earlier work, we consider the amalgam mix as a slurry of solid particles whose interstices are filled with a liquid. In this case, of course, the solid is the silver alloy and the liquid is the mercury. The prior studies of slurries have shown that their mechanical properties are functions of the particle size and surface energy. Moreover, there is a fundamental parameter which expresses both of these attributes — the sedimentation volume or the maximum volume fraction of loading, designated as ϕ_m . Furthermore, it was shown that a particle-particle interaction controls the properties of filled systems by controlling ϕ_m .

Before applying these concepts to dental amalgams, it will be helpful to review the technical background and to present some of the conclusions published elsewhere. Interestingly enough, all of this background is from work done on the properties of powders as applied to composite solid propellant.

2. Technical Background

In this brief review we must weave a fabric of logic from the compressive strength of dental amalgam and filled systems, in general, to the apparent Newtonian viscosity of slurries and from this to the sedimentation volume and its dependence on the particle size and surface energy. For the first step we can reference Hollenback (Ref. 8), who showed a mathematical relationship between tensile and compressive strengths of dental amalgam. Landel and Smith (Ref. 9) have shown a relationship among the Young's modulus of a cured solid propellant (a filled system, like dental amalgam), the viscosity of the mix before it was cured (analogous to condensing), and the amount of filler:

$$\eta/\eta_0 = E/E_0 = \left(1 + \frac{k\phi}{1 - \phi/\phi_m}\right)^2 \quad (1)$$

This relationship was based on the empirical viscosity work of Eilers and van Dyke (Ref. 10) and the fact that the filler dependence of E/E_0 should theoretically be the same as that for η/η_0 (Ref. 11)

where

η is the viscosity of the slurry

η_0 is the viscosity of the liquid medium

E is the modulus of the cured system

E_0 is the modulus of the cured, unfilled binder

ϕ is the volumetric concentration of filler particles

From Eq. (1) it can be noted that the controlling parameter is the term ϕ_m , or sedimentation volume.

In subsequent, more detailed work (Ref. 12), a parallel plate viscometer was used to measure the apparent viscosity of slurries of many different particle systems in various media. For example, glass beads, ammonium perchlorate, powdered aluminum, copper powder, calcium carbonate, sodium chloride, and silicon carbide powder were slurried in a straight chain hydrocarbon mixture [United States Pharmacopoeia (USP) mineral oil] and in a polar liquid, polyoxypropylene glycol. In addition, the surface characteristics of the above powders (i.e., surface energy) were changed by reducing the surface of one of the metals, copper, and coating the surface of all of the different types with an effective surfactant or wetting agent. In the case of the above experiments, asolectin, a mixture of natural phospholipids, was used as a wetting agent at a characteristic optimum concentration, determined in a separate set of experiments. As a result of many experiments, an equation describing the relative viscosity η/η_0 of slurries as a function of the relative volumetric loading ϕ/ϕ_m was published by Landel, Moser and Bauman as the LMB equation (Ref. 12). This equation can be written as

$$\eta/\eta_0 = (1 - \phi/\phi_m)^{-2.5} \quad (2)$$

The parameter ϕ_m is the maximum volume fraction of filler that can be loaded into a given system. It can be determined independently in a sedimentation experiment, and so is also called the sedimentation volume. (Ref. 6 gives a detailed description of the centrifugation technique of sedimentation.)

As shown in Fig. 3, the LMB equation was found to be valid for slurry concentrations from 0.01 up to 0.80 volume fraction of solids ϕ (corresponding to a range of ϕ/ϕ_m of 0.025 up to 0.93), independent of factors such as

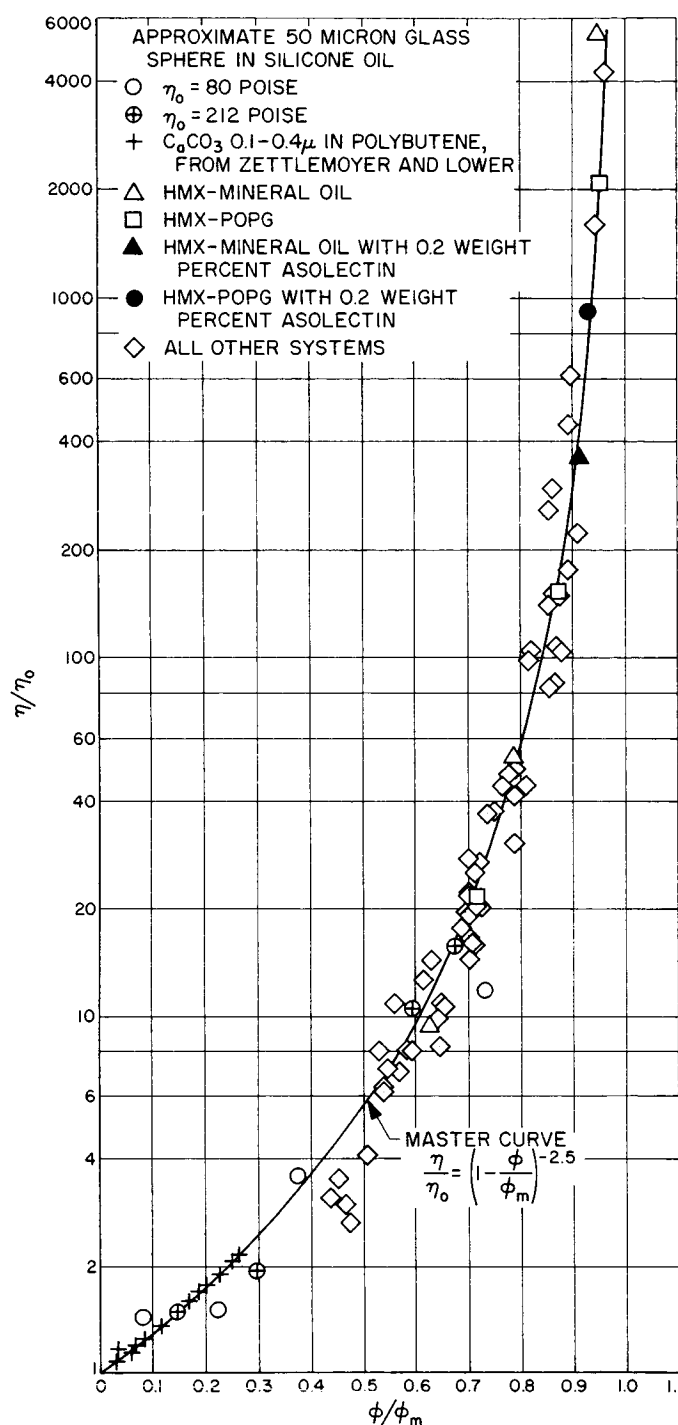


Fig. 3. The dependence of relative viscosity η/η_0 on relative concentration ϕ/ϕ_m . Points, experimental, line LMB equation

polarity of medium, type of particles, surface condition, particle size and surface area. Quite obviously the fit is excellent over a very wide range and the single characterization ϕ_m is the controlling parameter.

The obvious importance of ϕ_m (sedimentation volume) as the essential parameter for many of the mechanical properties of filled systems led us to examine ϕ_m itself. From this examination (Ref. 9) it appears that it is particle-particle interactions which play the dominant role in establishing ϕ_m . This interaction is completely independent of the suspending medium (including no medium at all!) for the particle sizes and systems studied thus far. The complete theoretical treatment is given by Moser, Weich and Landel elsewhere (Ref. 13), so we merely note that the theory predicts the value of ϕ_m from the statistics of a randomly packed bed of monodisperse spheres of diameter d , which can attract each other to any arbitrary extent. Incidentally, the statistics turn out to be Fermi-Dirac. The attractive force is considered to originate in the London-van der Waals attractive forces and is expressed in terms of a parameter β , which is a measure of the surface energy of the particle. The final equation is found to be

$$\phi_m = 0.37 [1 + (1 + 0.424 \exp \beta/d)^{-1}] \quad (3)$$

The solid line in Fig. 4 is a generalized plot of Eq. (3), with $\beta = 1$. It is seen that with decreasing particle size, ϕ_m decreases from 0.63 to a minimum of 0.37. The region of 0.63 and above is termed the "cannonball" region because the ratio of surface forces to body forces is very small. The predicted maximum value is in excellent agreement with the earlier experimental value of 0.629, found by Scott for the random packing of small ball bearings (Ref. 14). In the transition region the ratio of surface to body forces is intermediate, and it is here that most of the work on slurries has been done. In the region of 0.37 and below (termed the sticky region) the ratio is large, and surface forces dominate the behavior.

A number of particle systems were studied in this earlier work to test the master curve (Ref. 13). These included two types of spherical aluminum powder, glass beads, silicon carbide grinding powder, and calcium carbonate. For future work we plan a study of tungsten and more detailed work on silver dental amalgam alloy, both spherical and filings. The fit of all the data, except the dental alloy, which is reserved for a later section of this article, can be seen in Fig. 5. This composite plot was obtained by first superposing the points for the individual systems and then transposing the theoretical curve to obtain the best fit. As can be seen, the latter describes the results very well, considering the differences between the real and model powders, as defined by the theory. As a matter of fact, it is appropriate at this point to note that the general nature of the packing

and the transition from the sticky to the "cannonball" range is apparently not too sensitive to minor variations in particle shape or to moderate polydispersity, i.e. as long as the distribution of particle sizes is not broad enough to contain an appreciable quantity of fines which are small enough to fit into the interstices of the larger particles.

In any event, in separate experiments reserved for the dental section of this article it appears that polydispersity will result simply in a vertical shift of the curve. It would, therefore, seem that Eq. (3) can be taken as an adequate first approximation to the packing behavior of real particles, providing the axial ratios do not deviate radically from unity. And it would further appear that for each discrete material, e.g. glass, aluminum, silver, copper, etc. there exists a curve relating ϕ_m to particle size. The horizontal shift of this curve (when plotted as a function of $\log d$) is proportional to the surface energy of the particles, and β is the proportionality constant.

If the parameter β could be assessed independently, it would be possible to determine the particle size at which the transition occurs, i.e. where agglomeration sets in. One method of doing this, recalling that β represents a surface energy term, is to turn to gaseous adsorption measurements. According to the BET theory (Ref. 15) the volume of gas (V) adsorbed at pressure (P) when the saturation vapor pressure is (P_0) is:

$$\frac{P}{V(P_0 - P)} = \frac{1}{V_m C} + \frac{C - 1}{V_m C} \frac{P}{P_0} \quad (4)$$

where V_m is the volume of adsorbate adsorbed into a full monolayer and C is a constant whose value (to a first approximation) is given as:

$$C = C' \exp (q_A - q_L)/RT \quad (5)$$

where

C' is a pre-exponential factor related to entropy of adsorption

q_A is the heat of adsorption of the first monolayer

q_L is the latent heat of liquefaction of the adsorbate

R is the gas constant and

T is the absolute temperature

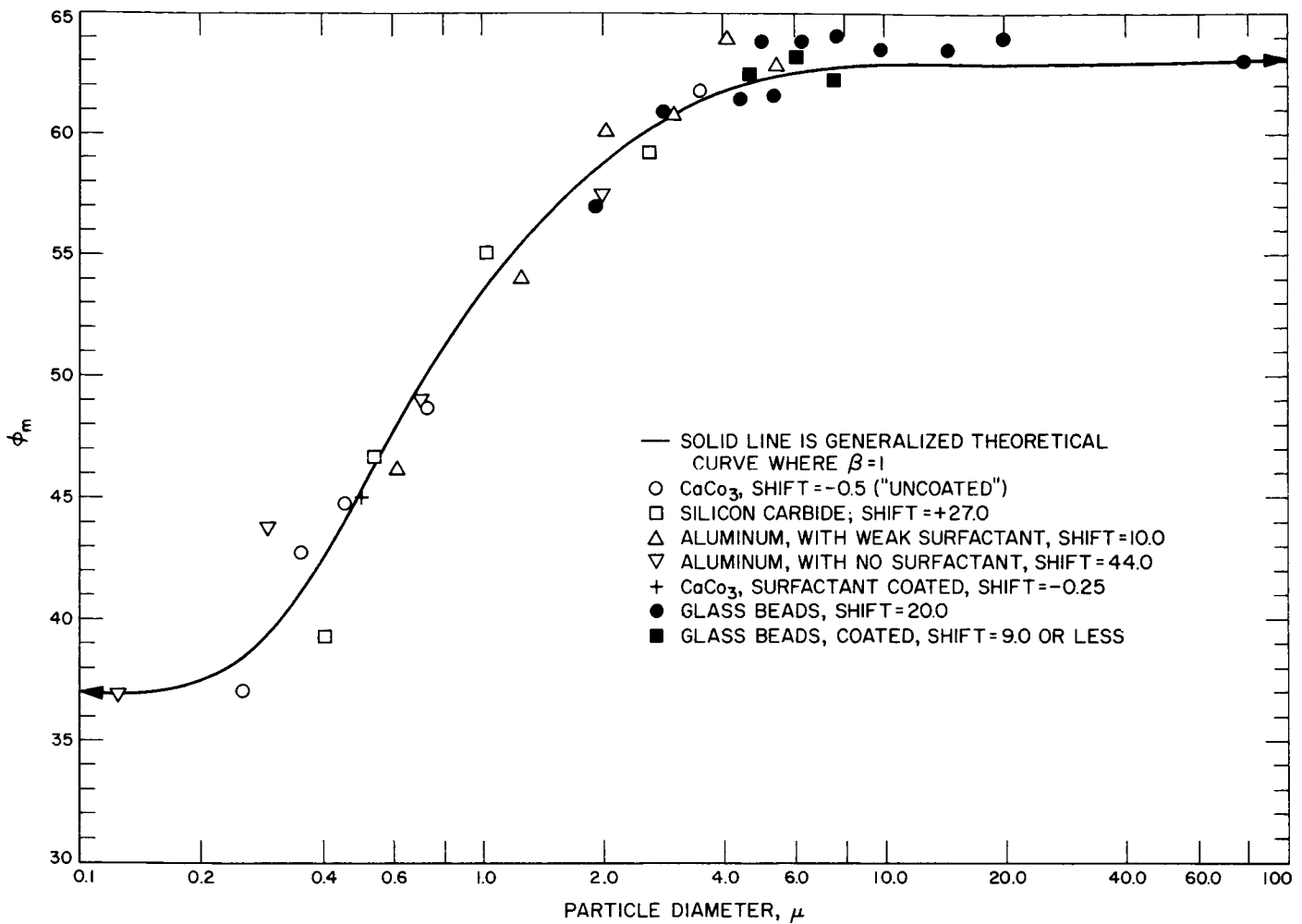


Fig. 4. Sedimentation volume vs particle size for several materials compared with generalized master curve with $\beta=1$. The point for Al at $\phi_m=0.37$ actually at $d=0.02\mu$; there are several points for glass at 0.63 for $d > 100\mu$

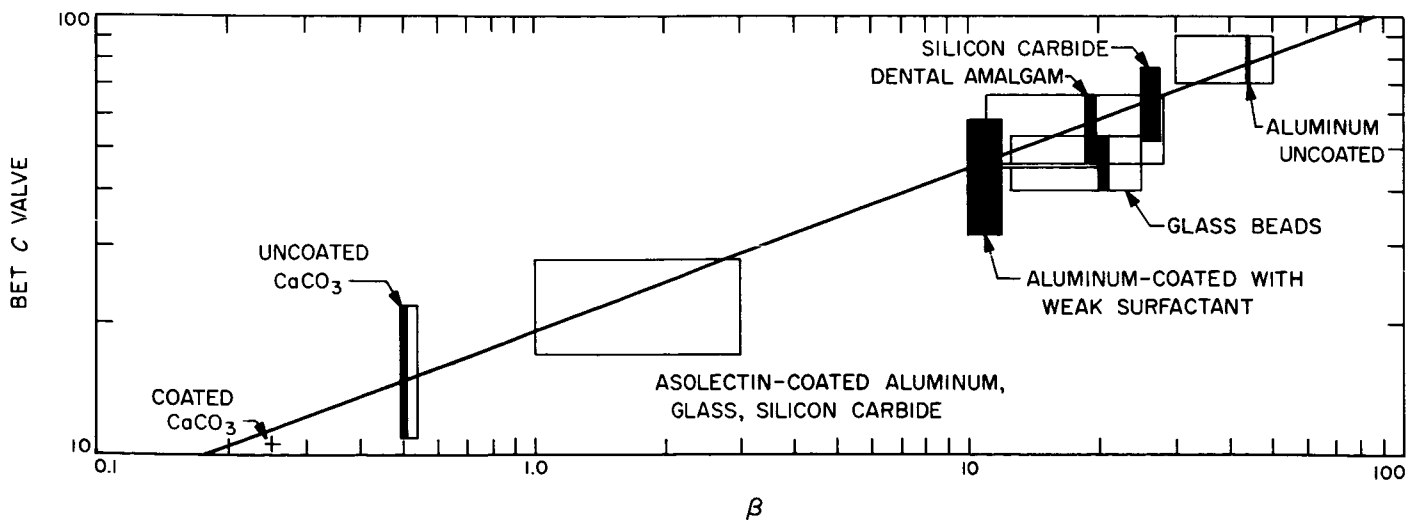


Fig. 5. BET surface energy term C as a function of β

Hence, C is seen to be an energy related term and is easily evaluated independently for comparison with β^1 .

BET measurements² of C values have been carried out by Dr. William Cannon, using krypton as the adsorbent, primarily as a method of determining the surface area of the particles. The technique has been described elsewhere (Ref. 10) and will not be repeated here. Because very large variations in C result from surface pretreatment and sample history, it is difficult to establish a single value, and a range will be reported instead. In spite of this uncertainty and in spite of an inadequate range of particle sizes in our system, resulting in some horizontal uncertainty in fitting to our master curve, a well defined empirical relationship between C and β is obtained (Fig. 5). This can be expressed as:

$$\log C = 1.28 + 0.37 \log \beta \quad (6)$$

At this point it is instructive to examine the magnitude of the change in surface energy associated with changes in C . Let us examine the difference between the heat of adsorption of krypton on glass powder and on aluminum powder at 77°K (the temperature of measurement). It is assumed that the entropy of adsorption is constant, then

$$\ln C_{al} - \ln C_{gl} = [q_{al} - q_{gl}]/RT$$

$$\Delta q = (2) (77)/\ln (23) = 0.49 \text{ kcal/mole}$$

It is astonishing that such a very small difference in surface energy is enough to change ϕ_m of 20 μ beads from 0.42 to 0.63. This represents a very large change in the viscous flow behavior of the two slurries, i.e. for slurries of $\phi = 0.21$, ϕ/ϕ_m will decrease from $\frac{1}{2}$ to $\frac{1}{3}$ and the viscosity will drop by a factor of roughly two, while at $\phi = 0.35$ it will drop by a factor of ten. In the case of dental amalgam, as we shall see in the next section, such a radical change in surface energy would result in one of the alloys lying far outside the acceptable range and it would fail to meet specifications. It is this rapid change in properties with surface energy which accounts for the critical importance of the so-called "annealing" step in the manufacture of

dental amalgam alloy for the annealing results in a lowering of the surface energy of the particles.

3. Application of the Theory to Dental Amalgam

We have presented a coherent explanation of the behavior of particle system in general and are now ready to see if this explanation will fit a specific and quite different case such as the mechanical properties of dental amalgam.

Table 2. Particle-size distribution of experimental dental alloy

Size No.	Method of separation	Size range diameter, μ	Amount of each size range, Gm	Total amount, ^a %
1	Elutriation	1-4	114.0	9.3
2	Elutriation	4-8	138.0	11.2
3	Elutriation	8-14	146.5	11.9
4	Elutriation	14-30	326.0	26.6
5	Elutriation	30-50	221.0	18.0
6	Elutriation and sieving	50-74	98.0	8.0
7	Sieving	74-105	62.5	5.1
8	Sieving	105-149	66.5	5.4

^a 4.5% lost in the cleaning and separating process.

Materials. We have drawn heavily on the data of Demaree and Taylor, from their now classical paper on the properties of dental amalgams made from spherical alloy particles (Ref. 7). Table 2 is repeated from their paper and shows the particle size distribution of their experimental dental alloy. In addition to these data, we have made some measurements on several commercially available dental alloys including one experimental spherical one. We will refer to these simply as alloys A, B, C, D, and S. These alloys, with the exception of S, the spherical one, have been manufactured by standard techniques. Fig. 6 is the plot of the micromerigraph determinations of particle sizes for A, B, C, D, and S. The particle size at which these curves cross the 50 cumulative weight percent mark of the ordinate is designated the mean weight diameter. As can be seen from the figure, the commercial alloys that we have chosen range in particle size from 24.5 μ to over 100 μ . (The size of the largest particles, shown as D, is an estimate made with the microscope. The particles are so large that they are completely out of the range of the micromerigraph.) Close examination of the curve for the experimental spherical alloy indicates a broader distribution, but not a bimodal blend of particle sizes, though the latter is indicated from a microscopic

¹We should point out that the significance of C as a surface energy term, in an absolute sense, has been frequently questioned. This point is beyond the scope of this article, and so we merely note that we use C only in a comparative relationship. Since the C value as a quantitative energy term is not directly germane to the argument, there should be no question about the validity of our approach.

²Measurements made at Douglas Aircraft Company, Astropower Division, under JPL subcontract and open purchase order.

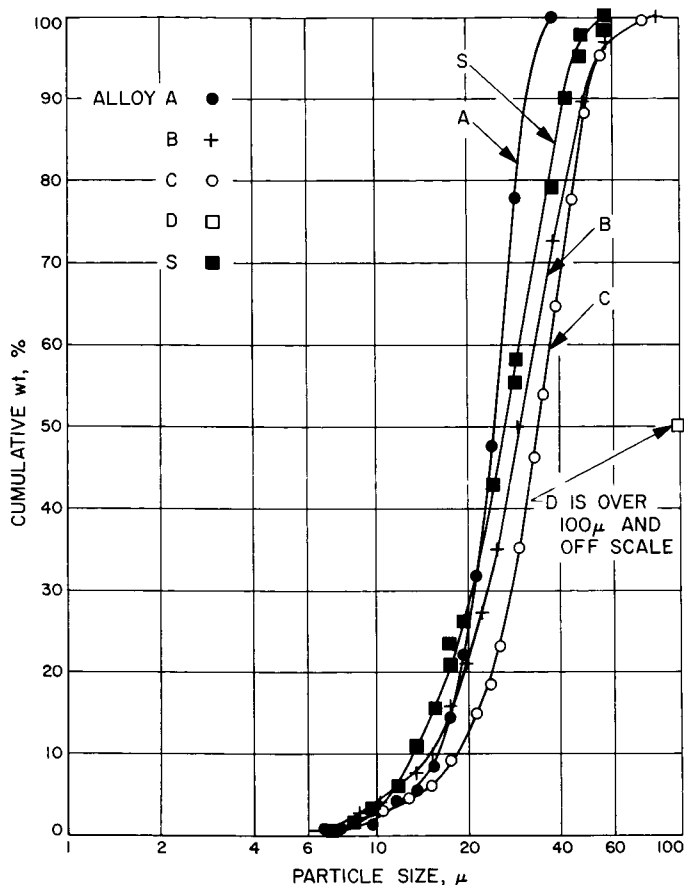


Fig. 6. Composite plot of particle size distribution of commercial asymmetrical and experimental spherical alloy

examination (Fig. 7). This results in greater packing density of particles by fitting fine particles into the interstitial space between the larger ones. Much more work is planned on these commercial alloys in order to fill in gaps that exist in our data.

Specimen Preparation and Experimental Methods. In order to try to maintain some continuity with the data of Demaree and Taylor we followed their technique as closely as possible in the preparation of samples. That is, an 8:5 mercury-to-alloy ratio was used. Amalgamation was done on a wiggle bug with a plastic pestle and the start of trituration of the mix was taken to be the zero time for the age of each specimen. Time of trituration varied from alloy to alloy, but was subjectively judged to be right for condensation when a smooth, plastic mix was attained. After trituration each mix was squeezed in a squeeze cloth to express some of the excess mercury. Since part of the experiments were designed to study the effect of residual mercury on the physical properties, it was in this step of



Fig. 7. Photomicrograph of experimental spherical alloy

expressing that we allowed more or less of the excess mercury to remain. Specimens were condensed by hand with 1 and 2 mm instruments maintaining approximately 2,000 psi packing pressure.

Flow and setting change specimens were made to meet requirements of the American Dental Association, Specification Number 1 for dental amalgam, and were approximately the same size and configuration as those used by Demaree and Taylor. A notable difference was the setting change specimen. We did not taper it to a blunt point, but rather the ends were flat and parallel as a result of having been condensed into a carefully machined and polished steel die. The change in length was monitored continuously from the time the specimen was placed into the jig. This was done with a linear variable differential transformer and a strip recorder. Readings were to the nearest $0.5 \mu/\text{cm}$. Flow was measured with the same instrument setup and a slightly different jig and is reported to the nearest 0.1%.

Residual Mercury. Residual mercury was one of the most critical determinations that we had to make on our specimens. The weights were taken with an analytical balance to the nearest 0.1 mg. The technique used on the hardened amalgam was the same as that employed by Demaree and Taylor and will not be discussed in detail here. Suffice it to say that the method uses the weight loss of the sample upon retorting rather than weight of mercury boiled out, to calculate the residual mercury content.

Sedimentation Volume or ϕ_m . Maximum volumetric loadings (ϕ_m) were determined by centrifuging slurries of the various alloys prepared with medium USP mineral oil and also by tapping the dry powder in a cylinder until the tightest packing resulted. The same results were obtained within experimental error in both cases. In the case of the mineral oil-alloy slurry, the slurries were mixed in polyethylene bags and aliquots were weighed into the centrifuge tubes. Then ϕ_m was calculated as the ratio of the volume of particles V_p in the sediment to the total volume of the sediment V_T . Since the slurry was not mixed in the centrifuge tubes, V_p was calculated from the weight of the aliquot M and the known initial volume fraction of particles ϕ as

$$V_p = M\phi [\phi_{\rho_p} + (1 - \phi)\rho_m]^{-1} \quad (7)$$

where ρ_p is the density of the particles and ρ_m is the density of the medium. Substantially the same results can be obtained by mixing the slurries and letting the particles settle to the bottom with time. The centrifugation merely accelerates the process.

In the case of the above experiment a typical value of 9.7 gm/cc was taken as the density of the silver alloy. It should be pointed out that this is not strictly true as the density will vary with the composition and the various commercial alloys do enjoy different compositions. However, the composition of any alloy that meets specifications and is certified is close enough to the average to result in a density approximately the same as above and certainly within experimental error of our other measurements.

4. Results

We have but few data to report except that from the literature. We are proceeding as rapidly as possible to perform experiments to substantiate conclusions drawn from evaluating the data in the literature, especially that of Demaree and Taylor.

Because it was not possible to measure sedimentation volume ϕ_m on the same particles that Demaree and Taylor

did their work (the original supply was exhausted) ϕ_m was calculated according to Eq. (3). The particle diameter is known and β was evaluated by measuring the BET krypton adsorption C value on many samples of the commercial alloys that we were working with. These values are given in Table 3. As can be seen, the spread is generally between 45 and 60. If one takes this value to the master curve in Fig. 5 it can be seen that this corresponds to a β of between 11 and 28. If we assume that the chemically similar alloy of Demaree and Taylor lay somewhere within these boundaries, we are then ready to draw a theoretical plot of the various size fractions as a function of ϕ_m . This is shown in Fig. 8 where the solid line represents the theory found on an average value of β of 19. Quite clearly, for dental amalgam, there is very little

Table 3. Surface areas and BET "C" values for same commercial alloys

Alloy	Surface area cm ² /gm	BET C
A	1570	60
B	1200	55
C	1000	55
D	—	—
S	475	45

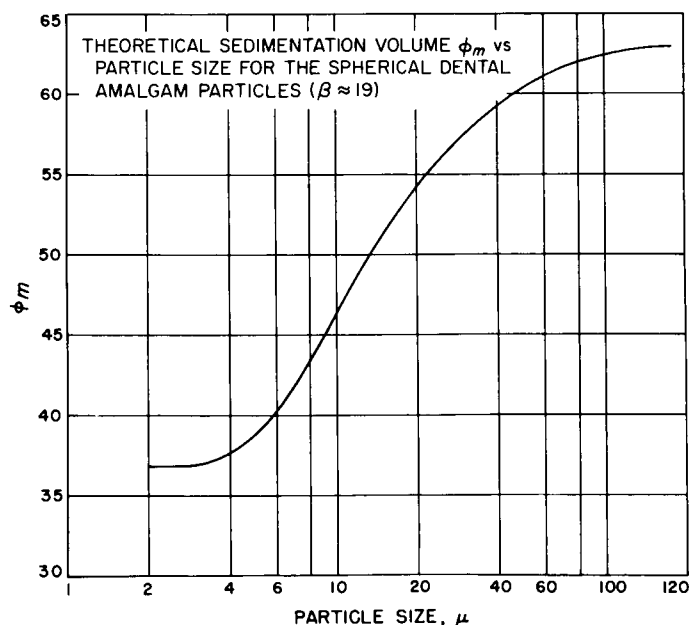


Fig. 8. Theoretical sedimentation volume, ϕ_m as a function of particle size for monomodal spheres of dental amalgam where $\beta \approx 19$

decrease in ϕ_m below the maximum possible value of 0.63 for monomodal spheres until the particle size falls below 40μ , and it enters the transition region rapidly below about 35μ , the range covered by samples 1-5 of Demaree and Taylor.

The volumetric loadings used by Demaree and Taylor are presented in Table 4. These were calculated from their data by considering the silver alloy to be the solid phase and the residual mercury as the liquid, using Eq. (7).

Table 4. Volumetric loadings of the amalgams investigated

Size	Volumetric loading ϕ	Maximum volumetric loading possible for distribution when wetted with Hg
1	50.50	0.63
2	53.50	0.63
3	55.50	0.63
4	58.57	0.63
5	64.00	0.63
6	65.60	0.63
7	66.50	0.63
8	66.75	0.63
A	—	—
B	—	—
C	—	0.64
D	—	—
S	—	~ 0.70

^a 1 through 8 calculated reference text.

To show the relationship between mechanical properties and volumetric loadings, the change in length (in μ/cm) upon setting of the amalgam is plotted in Fig. 9, as a function of ϕ . Significantly the expansion goes toward infinity (the point for size fraction 8 is at over $200 \mu/\text{cm}$, entirely off the scale of the plot) as the volumetric loading goes through the 0.63 region, the maximum possible value with monomodal spheres. As a matter of fact, the shape of this curve correlates nicely with the master curve of the LMB equation, shown in Fig. 3, in the sense that the curves approach infinity as ϕ/ϕ_m approaches 1. However, these results would indicate that all samples had the same value of ϕ_m , 0.63, and not a series of values as implied by Fig. 8 and Table 2.

In Fig. 10 we have shown a plot of ϕ/ϕ_m versus the change in length on setting. In this case ϕ_m is taken to be

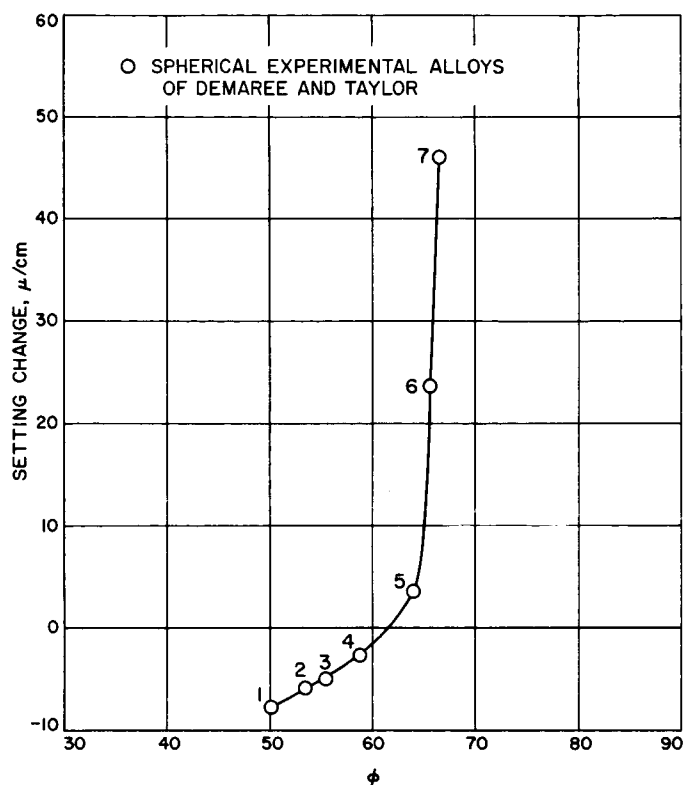


Fig. 9. Setting change as a function of ϕ

0.63, the value that monomodal spheres must assume when they are randomly packed. As above, ϕ is taken to be the residual mercury. As can be seen when the ratio is greater than 1 the alloy is expanding, when it is less than 1 the alloy is contracting. This would say that the volume of mercury present in an alloy of a given distribution should exactly equal the interstitial void space at the theoretical minimum. That is, to predict the optimum properties, ϕ_m should be taken as the maximum attainable (in the cannonball region) for the given particle size distribution and not that measured on the original powders. The reason for this is probably that the surface amalgamation takes all systems, even those having diameters less than 40μ , to the "cannonball" region. This is analogous to the effect of a good surface active agent, as discussed in detail in Ref. 12.

Fig. 9 is a plot of ϕ/ϕ_m versus the compressive strength at 24 hr. We can see that the same type of relationship is also true for this parameter, in the sense that the desired properties fall off rapidly above $\phi/\phi_m = 1$.

To confirm these results, setting change and compressive strength experiments are planned on A, B, C, D, and S. These experiments will be run at various residual mercury

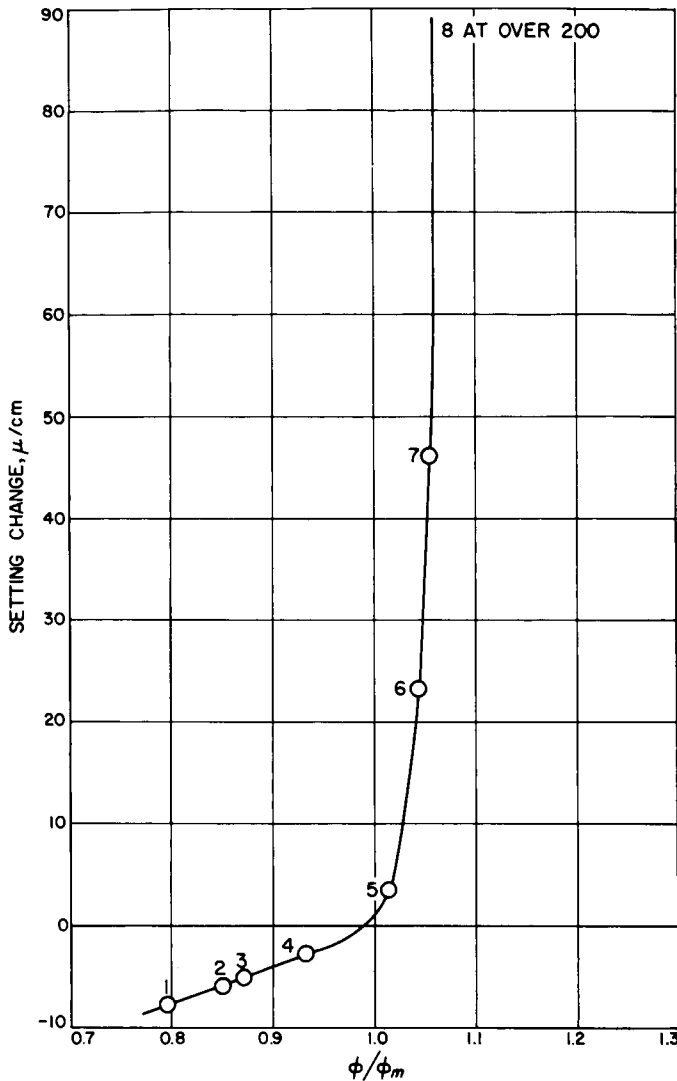


Fig. 10. Setting change as a function of ϕ/ϕ_m

contents for each alloy in order to vary ϕ/ϕ_m from approximately 0.75 to 1.1. However, our data are too preliminary to report on at this time.

Even a brief look at Fig. 10 clearly indicates that, for an alloy to meet specifications (at least in the case of Demaree and Taylors' data calling for from 0 to 20μ setting expansion), ϕ/ϕ_m must lie between 1.01 and 1.035. The importance of the mixing and packing technique, the responsibility of the dentist, is now quite obvious. It is now apparent why excess mercury must be expressed from the mix and removed upon condensation. If this is not done, ϕ/ϕ_m will be less than 1 and no matter how much the alloy has been found to expand by the manufacturer, it will shrink and the restoration may eventually give trouble.

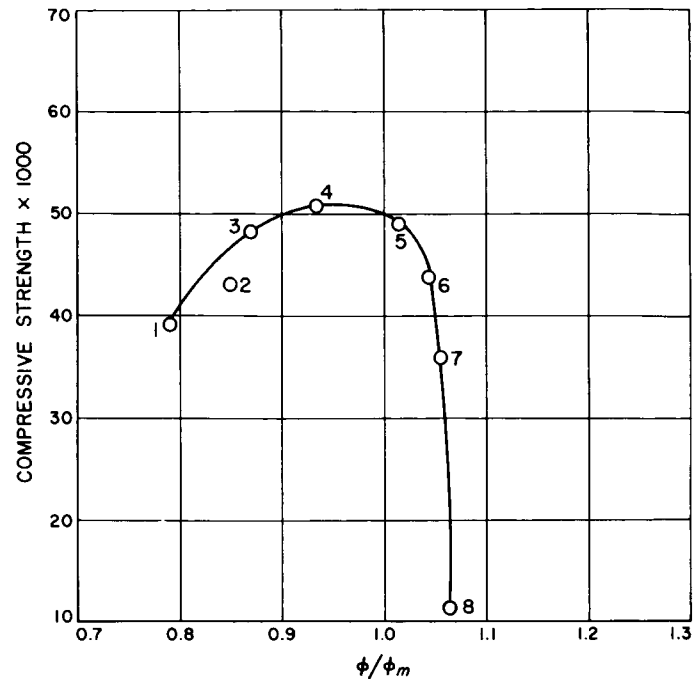


Fig. 11. Compressive strength as a function of ϕ/ϕ_m

On the other hand, it is possible, although difficult, to take the amalgam out of specifications on the high expansion side by expressing too much mercury. In clinical application, however, this is not too likely because of the difficulty of working with a mix so dry.

5. Conclusions

- (1) The mechanical properties of dental amalgam are governed by the same parameters which govern the rheological behavior of other filled systems.
- (2) The particle size, size distribution, surface area and surface energy of the alloy affect the amalgam's properties but are all reflected by a single parameter, ϕ_m .
- (3) The properties vary with residual mercury, which is $(1 - \phi)$, where ϕ is the volumetric concentration of alloy particles. However all properties can be normalized to a single master curve by considering a reduced concentration scale ϕ/ϕ_m .
- (4) Careful expressing and condensing of excess mercury from amalgams is still the best method of insuring a good restoration that lies within the specifications.

N67 12123

C. Nuclear Magnetic Resonance Spectroscopy of Derivatives of Trifluoromethylsulfenyl Chloride

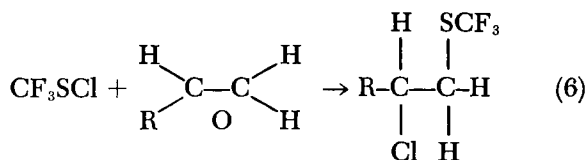
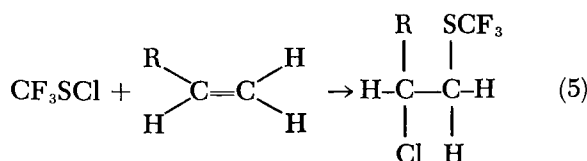
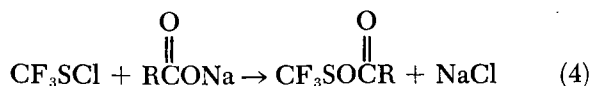
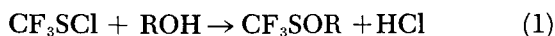
D. D. Lawson and J. D. Ingham

1. Introduction

Earlier nuclear magnetic resonance (NMR) studies (SPS 37-37, 37-33, 37-31, 37-26 and 37-24, Vol. IV, pp. 145, 224, 143, 108 and 94, respectively, and Ref. 17) have shown that F^{19} resonances from the trifluoroacetate esters of the hydroxyl groups of poly(alkylene oxides) are applicable to determinations of terminal group structural environments. These configurational or positional structures affect the relative reactivity of the hydroxyls and, therefore, are of great importance in understanding prepolymer reactions and degradative processes and in assessing the utility of specific prepolymers for propellants and spacecraft component applications. Although studies thus far have been concerned primarily with terminal hydroxyls of poly(urethane) precursors [poly(alkylene oxides)] reagents other than trifluoroacetic anhydride are being investigated to:

- (1) Increase the chemical shifts resulting from specific structural perturbations.
- (2) Determine structures in the vicinity of groups or segments along the polymer chains in addition to terminal OH groups.

The first of these reagents is trifluoromethylsulfenyl chloride (I) which reacts with a variety of active groups:



Although preliminary work has been carried out on reaction 5, only products of reactions 1 and 2 will be discussed. [Reaction 5 is expected to be of particular value for studies of diene-isobutylene copolymers and poly(butadienes)].

2. Sulfenate Esters

Reaction 1, which yields an alkyl trifluoromethylsulfenate ester, will proceed only if pyridine or some other tertiary amine is present to react with the hydrogen chloride. Although the sulfenate esters are also referred to as thioperoxides and some can initiate photolytic vinyl polymerization, the corresponding trichloro primary and secondary esters are stable up to about 180°C, and apparently S-O bond homolysis does not occur readily (Ref. 18). Some preliminary F^{19} spectra of sulfenates are indicated in Fig. 12. Although most of the spectra showed some contamination of the esters by undetermined side products, and the shifts from the reference $BrCF_2CF_2Br$ are relatively inexact, the striking feature of these results is that products of primary and tertiary hydroxyls show strong NMR signals that are nominally separated by 1400 to 100 Hz, respectively, from the secondary in a field of 14,000 gauss at an oscillator frequency of 56.4 MHz [Fig. 12(a), (b), (c), (d), (f) and (g)]. These separations are approximately one hundred times those observed previously (Ref. 17) for the corresponding trifluoroacetates.

Perhaps the large difference in chemical shifts is caused by partial intramolecular association of the fluorines and the nearest methyl or methylene protons. Although such association is geometrically feasible for trifluoroacetates it is less likely because of the interference of the carbonyl oxygen and greater electronic delocalization.

In studies of the ditrifluoroacetates of poly(propylene oxides), the F^{19} resonance of the secondary ester was observed as a doublet with about 2.1 Hz splitting, with the higher intensity member at the higher magnetic field. It was clearly established that the doublet was caused by two types of secondary hydroxyl that differed only in the stereoconfiguration of the respective terminal diads. The trifluoromethylsulfenates also show corresponding

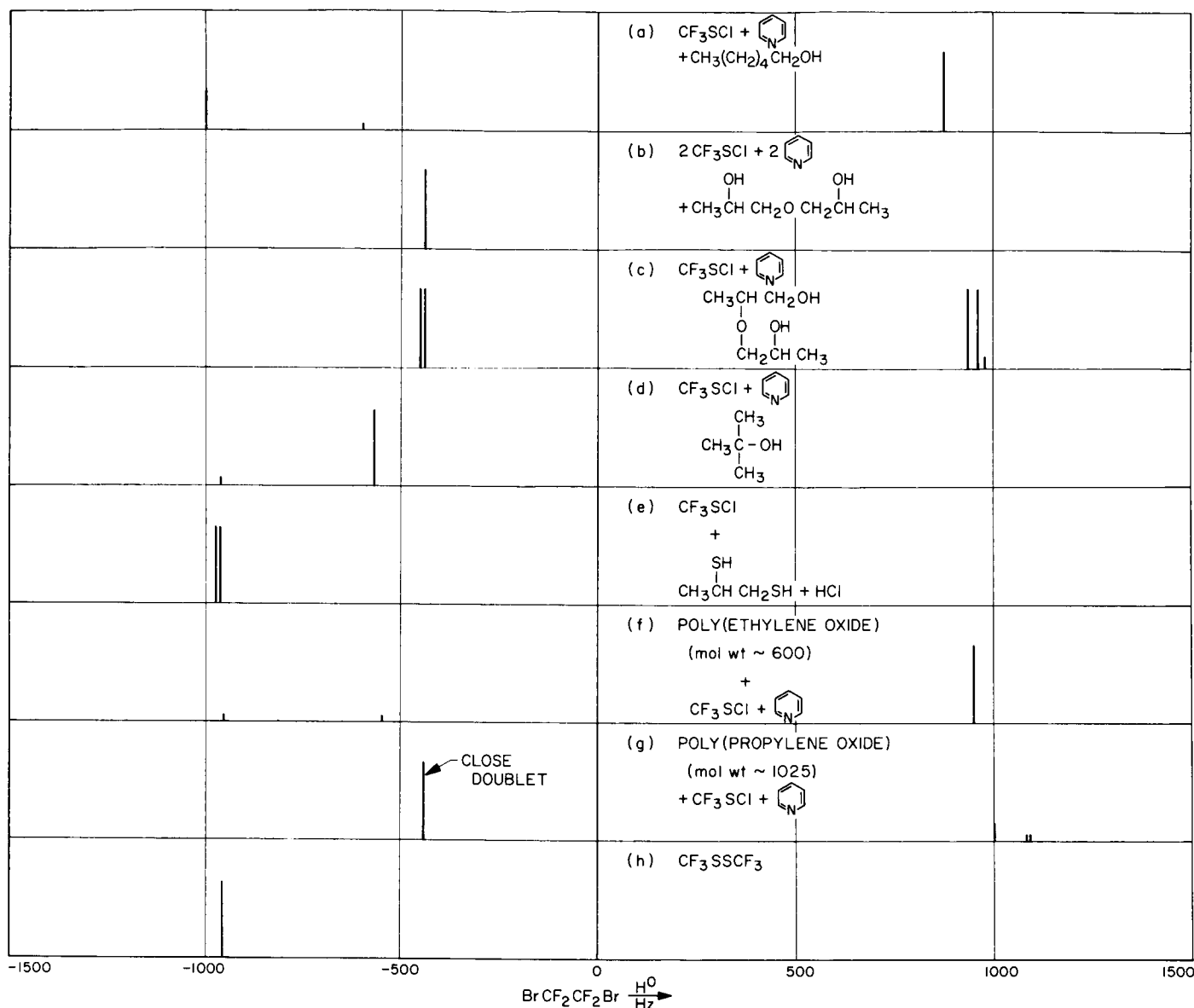


Fig. 12. F^{19} chemical shifts of trifluoromethylsulfonyl chloride reaction products at 56.4 MHz in carbon tetrachloride solvent with $\text{BrCF}_2\text{CF}_2\text{Br}$ reference

doublets, again with the slightly higher signal at high field; however, the splitting is still of the order of 2-3 Hz.

Apparently the shift difference caused by this relatively remote perturbation depends primarily on the distance from the F^{19} , which is nearly the same for either the sulfonate or the trifluoroacetate. The shift may be smaller than expected also because of effects on electron density near the fluorine, if intramolecular association exists.

Although positive assignments have not yet been established, the doublets indicated for the mixed primary-secondary esters [Fig. 12(c)] probably arise from formation of both primary and secondary monodiester, and the doublet (15 Hz splitting) from the thiol product [Fig. 12(e)] may represent primary and secondary products.

Although further work would be required to optimize reaction conditions to obtain maximum yields of the

sulfonate esters and to determine the unassigned resonances, it has been shown that sulfenyl chloride can be advantageously employed to obtain products with large F^{19} chemical shift differences for primary, secondary and tertiary hydroxyl compounds and compounds or polymers containing several different types of reactive groups. Because the chemistry of this particular sulfenyl chloride has not yet been thoroughly investigated, the reaction conditions for maximum desired products from reactions 1 through 6 must be determined in nearly every case; however, because of the specificity of conditions, it appears that certain functional groups can be studied simultaneously or successively in the presence of each other. For example, reaction with hydroxyl is negligible in the absence of a base (to shift the equilibrium) and reaction of unsaturation can be controlled by suitably adjusting the temperature.

N67 12124

D. The Reaction of Carboxyl and Amino Terminated Prepolymers with Polyepoxides

S. H. Kalfayan and B. A. Campbell

Studies on the reactions of carboxyl and amino-ending prepolymers with polyaziridines were reported previously (SPS 37-35, -39, Vol. IV, pp. 123 and 103, respectively). Results of the reactions of these prepolymers with epoxides are given presently.

Experiments on the catalysis of the carboxyl-epoxide reaction were carried out using one of the prepolymers, namely, Telagen CT, a carboxyl-terminated poly(butadiene), with two epoxides, Epon 828 and Shell X 801, and various acidic and basic catalysts.

The homopolymerization of the epoxides, with and without catalysts, was attempted. These results, as well as those obtained after the thermal sterilization of some of the products of this study, are also reported.

1. Experimental

a. Materials. The prepolymers used were: the carboxyl terminated poly(butadienes) HC-434, Telagen CT and Butarez CTL; the carboxyl-terminated poly(propylene

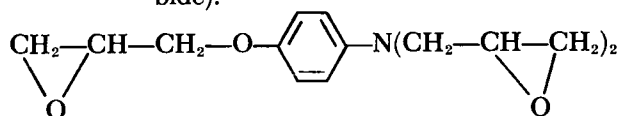
oxide) PPO-COOH, and the amine terminated poly(propylene oxide) L-3. These prepolymers were described in SPS 37-39, Vol. IV, pp. 103-106).

The epoxides (or oxiranes) used were:

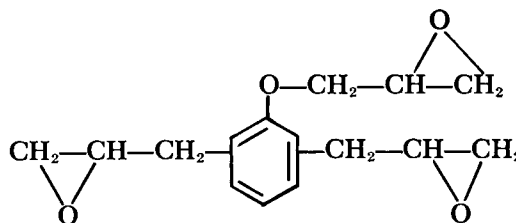
DEN 438 — An epoxy novolac; epoxide equivalent 180 (Dow Chemical Company).

Epon 828 — A glycidyl ether of bisphenol A; epoxide equivalent 195 (Shell Chemical Company).

ERL 0510 — N,N-Diglycidyl-p-aminophenyl glycidyl ether; epoxide equivalent 92 (Union Carbide).



Shell X 801 — 2,6-(2,3-Epoxypropyl) phenyl glycidyl ether; epoxide equivalent 87 (Shell Chemical Company).



b. Determination of gel time. Gelation experiments were carried out by mixing stoichiometric amounts of reactants in glass test tubes and placing them in constant temperature baths. Gel time was measured from the instant the tube was placed in the bath, until the time when the inverted test tube showed no flowing of the reaction mixture.

Hardness measurements were taken on samples cured in aluminum dishes, in constant temperature air ovens.

2. Results and Discussion

a. The carboxyl-epoxide reaction. Gel times and Shore A hardnesses are given in Table 5 for carboxyl and amino-ending prepolymers cured with four epoxides. Compared with the carboxyl-aziridine reaction (SPS 37-39, Vol. IV, pp. 103-106) the carboxyl-epoxide reaction is much slower. This conclusion is based on the assumption that gel time is a measure of the relative rates of such reactions. Telagen CT, for example, gelled in less than ½ hr at 100°C with two diaziridines, but it did not gel with Epon 828, a diepoxide, after 48 hrs at the same

Table 5. Reaction (curing) of carboxyl and amine terminated prepolymers with epoxides

Experiment No.	Prepolymer	Curing agent	Gel time hrs at 100°C	Shore A hardness		Gel time hrs at 150°C after 48 hrs at 100°C	Shore A hardness after 48 hrs at 100°C plus 18 hrs at 150°C
				After 24 hrs at 100°C	After 48 hrs at 100°C		
1	HC 434	DEN 438	>48	Fluid	Fluid	1 ½ to 2	48
2		Epon 828	>48	Fluid	Fluid	1 ½ to 2	34 (29) ^a
3		ERL 0510	>6 <21	8	16	—	—
4		Shell X801	>48	Fluid	Fluid	1 ½	37
5	Telagen CT	DEN 438	>48	Fluid	Fluid	1 ½ to 2	12
6		Epon 828	>48	Fluid	Fluid	1 ½ to 2	12
7		ERL 0510	>6 <21	2	6	—	—
8		Shell X801	>48	Fluid	Fluid	1 ½	23
9	Butarez CTL	DEN 438	>33 <48	Fluid	Soft ^b	—	68 (48) ^a
10		Epon 828	>33 <48	Fluid	Soft ^b	—	60 (37) ^a
11		ERL 0510	>6 <21	11	27	—	—
12		Shell X801	>6 <21	Soft ^a	3	—	—
13	PPO-COOH	DEN 438	—	Fluid	Fluid	18	Soft
14		Epon 828	—	Fluid	Fluid	—	Fluid (thick)
15		ERL 0510	—	Fluid	Fluid	5	20
16		Shell X801	—	Fluid	Fluid	15	Soft
17	Polyether-diamine L-3	DEN 483	Immediate	—	—	—	—
18		Epon 828	50 min	1 (very tacky)	4 (very tacky)	—	—
19		ERL 0510	60 min	20	21	—	—
20		Shell X801	75 min	9	16	—	—

^aValues in parentheses indicate hardnesses of the interior of the sample.
^bNot measurable on the Shore A scale.

temperature. With the exception of Butarez CTL, none of the other carboxyl-ending prepolymers gelled after 48 hrs exposure to heat at 100°C. Gelling occurred however at 150°C after 1 to 2 hrs. Butarez CTL has shown more reactivity with both aziridines and epoxides than the other two carboxyl-ending poly(butadienes) tested. The PPO-COOH reacted more slowly than the carboxyl-ending poly(butadienes) with the epoxides, and the products obtained were softer.

The triepoxide ERL 0510 was more reactive than the other epoxides tested. This probably is due to the presence of a tertiary nitrogen atom in the molecule. Tertiary amines catalyze the opening of the oxirane ring (Ref. 19). The order of the reactivity of the epoxides with any of the carboxyl-ending prepolymers was as follows: ERL 0510 > Shell X 801 > DEN 438 > Epon 828.

b. The amino-epoxide reaction. The amino-ending poly(propylene oxide), L-3, reacted much faster with the

four epoxides tested than it did with the aziridines (SPS 37-39, Vol. IV, pp. 103-106). Immediate gelation of the epoxy novolac DEN 438 occurred when L-3 came in contact with it. A softer and much more extensible product was formed with Epon 828 than with the triepoxides, Shell X 801 and ERL 0510.

c. Homopolymerization of the epoxides. Homopolymerization of epoxides is a possible side reaction in the carboxyl-epoxide reaction. The data in Table 6 show that both uncatalyzed and acid catalyzed (with HCl) homopolymerization rates are slower than the rate of the carboxyl-epoxide reaction (Table 5). However, tertiary amine (benzyltrimethylamine) catalyzed homopolymerizations are fast and can be competing reactions.

d. Catalysis of the carboxyl-epoxide reaction. Table 7 summarizes the test results for the catalysis of the carboxyl-epoxide reaction. Two epoxides were used for

Table 6. Homopolymerization of epoxides

Experiment No.	Epoxide	Catalyst ^a	Gel time, hrs at 100°C	Gel time, hrs at 150°C after 48 hrs at 100°C	Hardness short D, after 48 hrs at 100°C plus 16 hrs at 150°C
1	Epon 828	None	>48	Fluid	Fluid
2		HCl	>48	Fluid	Fluid
3		Benzyltrimethylamine	1	—	79
4	ERL 0510	None	>48	>2 <16	Soft ^b
5		HCl	>48	>2 <16	30
6		Benzyltrimethylamine	>24 <40	—	79
7	Shell X801	None	>48	Fluid	Fluid
8		HCl	>48	Fluid	Fluid
9		Benzyltrimethylamine	>32 <48	—	60
10	DEN 438	None	>48	>5 <18	Soft ^b
11		HCl	>48	>5 <18	Soft ^b
12		Benzyltrimethylamine	0.2	—	82

^aCatalyst concentration used: 1.8% by weight.
^bNot measurable on the Shore A scale.

Table 7. Catalyst tests for the carboxyl-epoxide reaction
(Telogen CT with Epon 828 and Shell X801)

Experiment No.	Catalyst ^c	Telogen CT and Epon 828			Telogen CT and Shell X801		
		Gel time, hrs at 100°C	Shore A hardness after 48 hrs at 100°C	Shore A hardness after 48 hrs at 100°C, plus 18 hrs at 150°C	Gel time, hrs at 100°C	Shore A hardness after 48 hrs at 100°C	Shore A hardness after 48 hrs at 100°C, plus 18 hrs at 150°C
1	Hydrochloric acid (38%)	>48	Fluid	40 (5) ^a	>48	Fluid	42 (3) ^a
2	Acetic acid, glacial	>48	Fluid	26 (3)	>48	Fluid	17
3	Benzyltrimethylamine	4	Soft ^b	Skinned	4	Soft ^b	2
4	Tetramethyl amm. hydroxide	3 1/2	Soft ^b	Skinned	3 1/2	Soft ^b	Soft ^b
5	Sodium thiosulfate	>33 <48	Soft ^b	13	>48	Fluid	23
6	Dibutyltin diacetate	>48	Fluid	18 (4)	>48	Fluid	25
7	Stannous octoate	>33 <48	5	11	>33 <48	1	13
8	Cobalt naphthenate	>33 <48	4	23 (12)	>33 <48	4	50 (25)
9	None	>48	Fluid	12	>48	Fluid	23

^aValues in parentheses indicate hardnesses of the interior of the sample.
^bNot measurable on the Shore A scale.
^cCatalyst concentration used: 1.8% by weight.

this study, Epon 828 and Shell X 801. The carboxyl-ending prepolymer selected was Telagen CT.

In the absence of catalyst (Expt. 9) gelation did not occur after 48 hrs at 100°C with both epoxides. The two acids (HCl and glacial acetic acid) seemed to show very little catalytic activity (Expts. 1 and 2). The two bases, benzyldimethylamine and tetramethylammonium hydroxide induced gelation in 4 hrs or less. Products obtained, however, were very soft. This fact leads one to consider that homopolymerization of the epoxides might have taken place and that the Telagen CT might have acted as a plasticizer to yield the soft products. The other catalysts, sodium thiosulfate, dibutyltin diacetate, stannous octoate and cobalt naphthenate showed catalytic activity.

e. Thermal sterilization of some of the products. All the prepolymers cured with the four epoxides of this study were exposed to thermal sterilization conditions of 3 cycles of 36 hrs each at 145°C in dry nitrogen. The thermal sterilization of products from PPO-COOH is in progress and therefore, data are not reported. Table 8 summarizes the results obtained. All samples had been cured 48 hrs at 100°C, prior to thermal exposure at 145°C, except Nos. 1, 2, 4, 5, 6 and 8, which had been exposed an additional 18 hrs at 150°C.

Thermal cycling increased the hardness of all samples.

The exposed surfaces of the samples were harder than the interior sections. Exceptions to this were samples of HC-434 and Telagen CT cured with ERL 0510 (Expts. 3 and 7), and all polyetherdiamine samples (Expts. 13-16).

Percent weight losses were low in most cases probably because of the thermal pretreatment that the samples underwent prior to thermal sterilization.

3. Future Work

Studies of the reactions of the carboxyl-terminated prepolymers with various curatives, and the properties of the products obtained, will be continued.

N67 12125 E. Studies on Sterilizable Elastomers

E. F. Cuddihy and J. Moacanin

Elastomeric flexible foams are being considered for use as liners in sterilizable solid propellant rocket motors

Table 8. Effect of thermal sterilization on carboxyl- and amino-terminated prepolymers cured with epoxides

Experiment No.	Prepolymer	Curing agent	% Weight loss after thermal exposure ^a	Shore A hardness, after thermal exposure ^a	
				Surface	Interior
1	HC 434	DEN 438	0.111	68	58
2		Epon 828	0.000	57	43
3		ERL 0510	0.510	55	55
4		Shell X801	0.233	52	45
5	Telagen CT	DEN 438	0.054	50	33
6		Epon 828	0.022	53	35
7		ERL 0510	0.174	33	33
8		Shell X801	0.169	56	37
9	Butarez CTL	DEN 438	0.020	77	52
10		Epon 828	0.017	71	49
11		ERL 0510	0.139	52	46
12		Shell X801	0.229	64	46
13	Polyetherdiamine L-3	DEN 438	—	—	—
14		Epon 828	0.260	6	6
15		ERL 0510	0.526	25	25
16		Shell X801	0.645	17	17

^a After 3 cycles of 36 hrs each at 145°C in dry nitrogen.

because of their potential capability to relieve thermal stresses during sterilization heat cycles. A study of techniques for preparing foams from elastomers was described previously (SPS 37-36, Vol. IV, pp. 153-154), along with efforts to develop sterilizable elastomers (SPS 37-36 and 37, Vol. IV, pp. 154-159, 150-153, respectively). The initial studies dealt with a polybutadiene-acrylic acid (PBAA) liquid prepolymer cured with a variety of imines. A number of excellent elastomers could be obtained, but none of the materials were sterilizable. Therefore, we turned our effort from PBAA to elastomers based on carboxyl-terminated polybutadiene.

1. Elastomers from Carboxyl-Terminated Polybutadiene (HC-434)

A carboxyl-terminated polybutadiene prepolymer HC-434, purchased from the Thiokol Corporation, was used for this study. A series of elastomers were prepared using a variety of diimine curatives. Most of the elastomers cured in a few hours at temperatures between 70 and 100°C; however, the imine designated HX-740 (Fig. 13) failed to yield a cured elastomer at these conditions. All the quick-curing imine materials failed when subjected to three consecutive heat sterilization cycles (40 hrs at 146°C for each cycle).

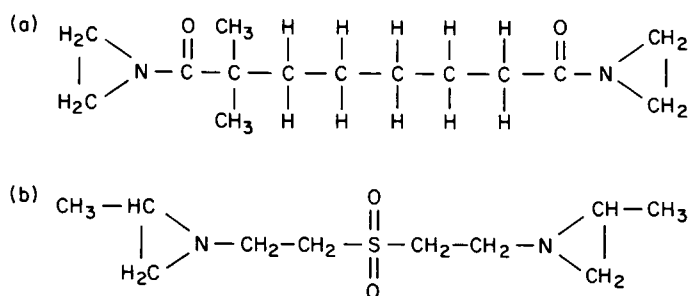


Fig. 13. Structures of imine curatives: (a) HX-740 (3M Company); ZC-466 (Thiokol Corp.)

With HX-740, no satisfactorily cured elastomers were obtained even after one week at temperatures between 70 and 100°C, but excellent elastomers were obtained when the cure temperature was increased to 146°C. Values of Shore A hardness versus cure time in hours at 146°C for two imine/carboxyl ratios (Fig. 14) show that good elastomers can be obtained within 16 to 24 hrs. Moreover, properties continue to improve over the total required sterilization time of 120 hrs, indicating continuing cure during this period. Some mechanical properties of HX-740 elastomer are shown in Table 9.

Table 9. Tensile strengths and elongations at break for elastomers^a prepared from HX-740 diimine curative and HC-434

Cure time, hrs	Tensile strength @ break, psi	Elongation @ break, %
16	22	> 540
24	30	> 540
72	42	> 540
96	46	> 540
258	53	520

^a 1.10 imine/carboxyl equivalents ratio
Samples cured @ 146°C
^b Exceeded instron travel
Crosshead speed = 0.2 in./min
Sample length = 1 in.

For comparison, the Shore A hardness versus cure time in hours at 146°C are shown in Fig. 15 for a quick-curing elastomer prepared with the imine curative ZC-466 (Fig. 13). Optimal Shore A values are obtained within 2 to 3 hrs after which the material begins to soften rapidly. Similar behavior is observed for the other quick-curing elastomers.

In general, no elastomer prepared from a single imine curative has been found to be sterilizable; and there seems to be a correlation between the rapid degradation during sterilization and the rate of achieving the initial cure. The only workable approach toward developing sterilizable elastomers has been demonstrated with the HX-740 system wherein sterilizability is achieved because of its slow cure under sterilization conditions. The disadvantage for this system is the inability to achieve structural integrity under the usual cure temperature range of 70-100°C.

2. An Approach to Quick-Cured Sterilizable Elastomers

During the sterilization of some of the quick-cured elastomers, deposits of materials which seemed to contain the imine curative were found in the ovens. This suggested that chemical reversion for the carboxyl-imine reaction took place yielding back the starting materials and, therefore, implied that the carboxyl groups on the prepolymer were again available for reaction.

It was reasoned, therefore, that elastomers prepared with a mixture of ZC-466 and HX-740 would achieve quick-cure at 146°C by the ZC-466 reaction, and then

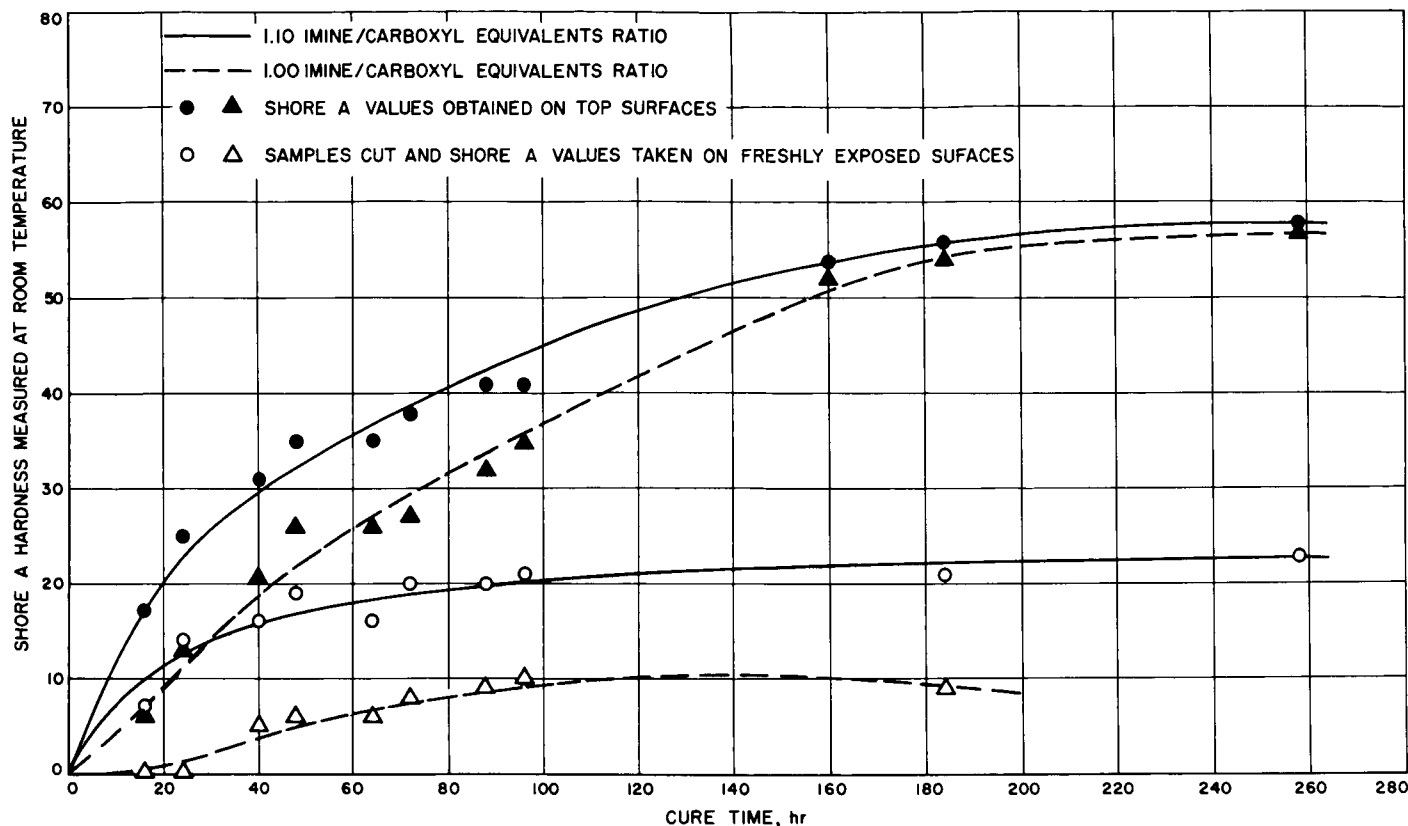


Fig. 14. Shore "A" hardness versus cure time in hours at 146°C for elastomers prepared from HX-740 diimine curative and HC-434 prepolymer

as the ZC-466 imine starts to revert, the slower curing HX-740 imine would react with the freed carboxyl groups thus preserving the elastomer.

Accordingly, elastomers were prepared having a fixed ZC-466 concentration and varying amounts of HX-740. In all cases, quick-cure was obtained in 1 hr at 146°C. The Shore A values for these elastomers agreed well with those obtained for exclusively ZC-466 cured elastomers. The effects of sterilization on the Shore A hardness of these mixed-imine elastomers are shown in Fig. 16. Elastomer A contained only ZC-466, and it was observed to soften and degrade rapidly with increasing sterilization, its Shore A dropping from an initial 33 to 0 after the second cycle. Elastomer F contained only HX-740 and as expected its properties improved with increasing sterilization. The curves for elastomers B, C, D and E are intermediate between A and F and the Shore A level increases with increasing HX-740 content. Note that the Shore A values for elastomer E approach and ultimately equal the values obtained for elastomer F. Elas-

tomer E contains the same level of HX-740 as elastomer F, and, after the ZC-466 has chemically reverted, elastomer E should then have the properties of an HX-740 elastomer. Note also that elastomer C retained essentially a constant Shore A value through sterilization, indicating the ability to prepare elastomers which will preserve a property during sterilization. Some mechanical properties of elastomer C are given in Table 10.

3. Summary and Future Direction

A sterilizable elastomer was prepared from HC-434 prepolymer and HX-740 diimine curative. This elastomer cures slowly at 146°C and achieves sterilizability because it continues to cure slowly during the high temperature sterilization. Initial cure period for this material is 1 to 2 days at 146°C.

The feasibility of preparing elastomers which cure quickly and preserve properties during sterilization was demonstrated for an elastomer prepared with a mixed imine curative composed of HX-740 and ZC-466.

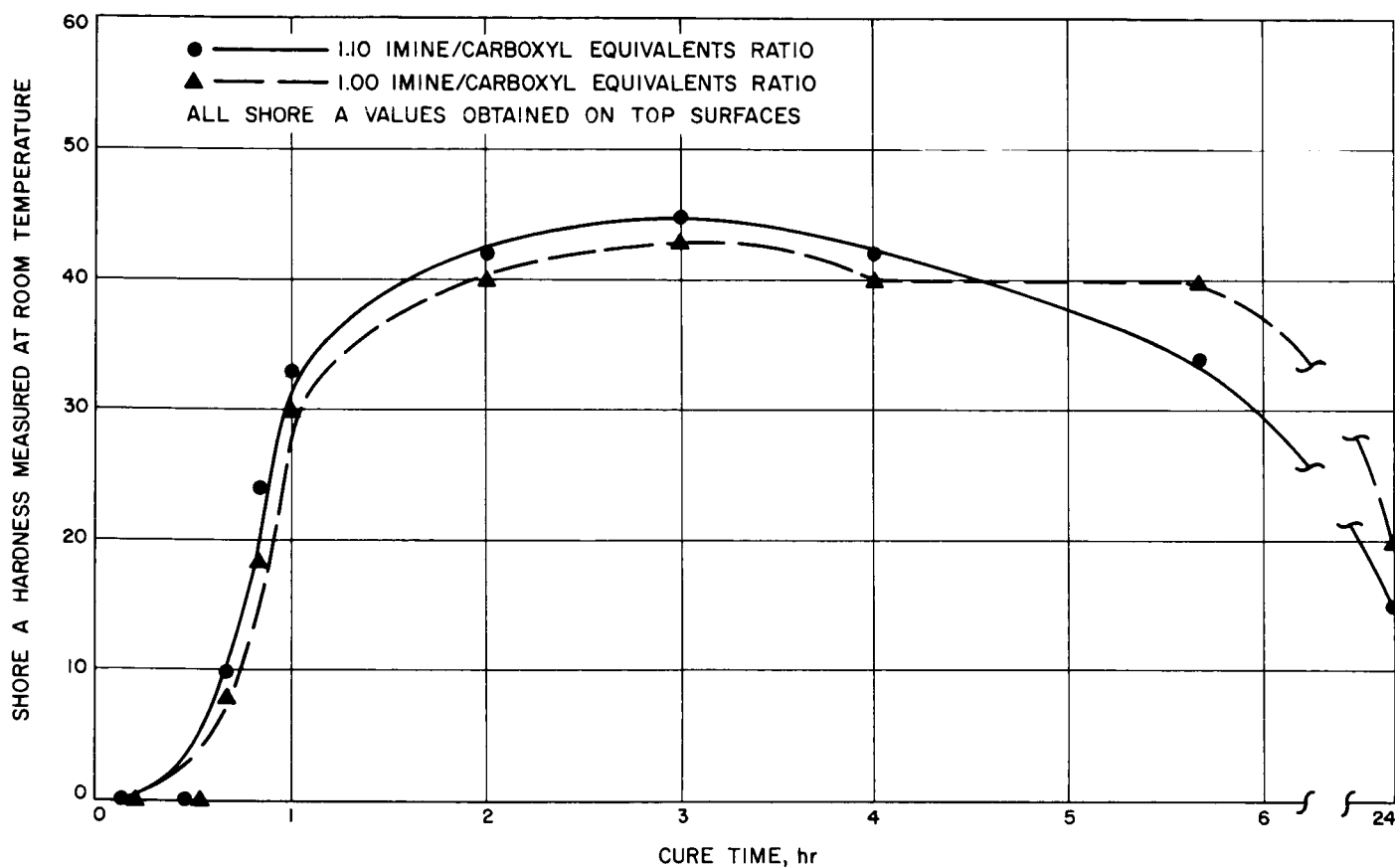


Fig. 15. Shore A hardness versus cure time in hours at 146°C for elastomers prepared from ZC-466 diimine curative and HC-434 prepolymer

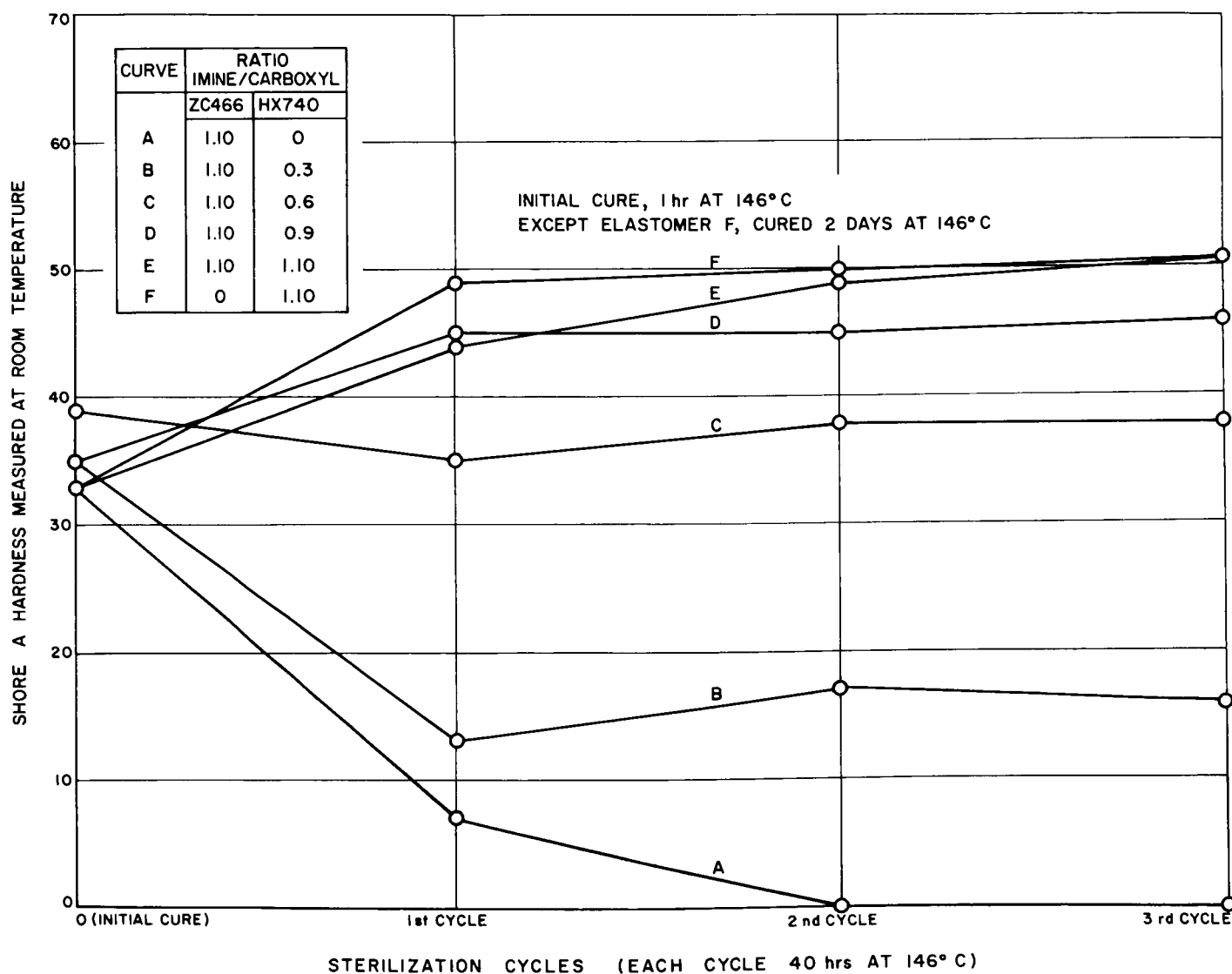


Fig. 16. Effect of sterilization on the Shore A hardness of elastomers prepared from HC-434 prepolymer and varying amounts of ZC-466 and HX-740 diimine curatives

Table 10. Tensile strengths and elongations at break for elastomers^a prepared from HC-434 pre-polymer and ZC-466 and HX-740

Sterilization ^b cycle	Tensile ^c strength @ break, psi	Elongation ^c @ break, %
0	62	25
1	39	24
2	31	16
3	23	13

^a 0.6 imine/carboxyl equivalent ratio of HX-740 and 1.10 imine/carboxyl equivalents ratio of ZC-466
Samples initially cured 1 hr at 146°C

^b Sterilization cycle consists of a 40 hr exposure to 146°C

^c Crosshead speed = 0.2 in./min
Sample length = 1 in.

Future work will investigate some of the dynamic mechanical properties of HX-740 elastomers with special emphasis on understanding the chemical structure of the elastomer during sterilization.

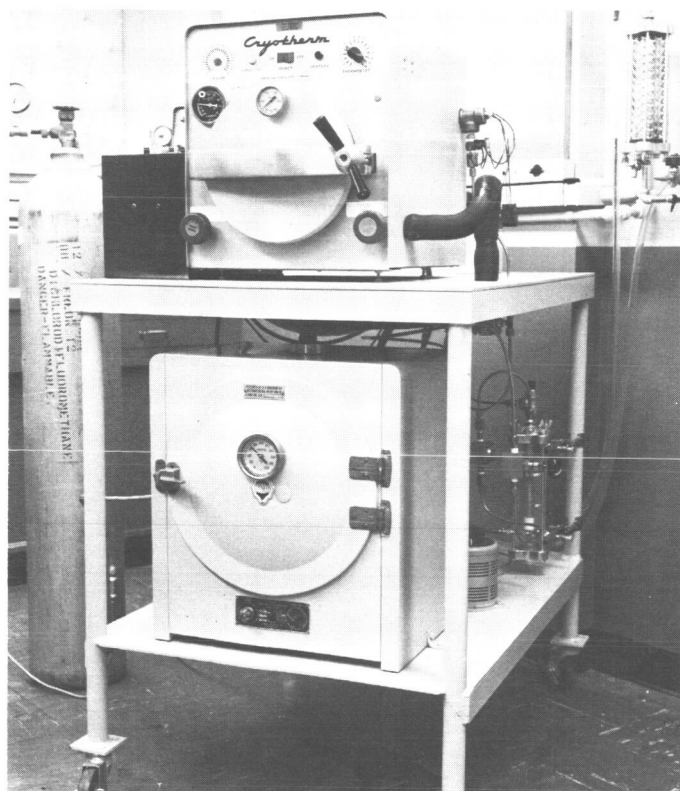


Fig. 17. Automatic ethylene oxide decontamination setup (front view)

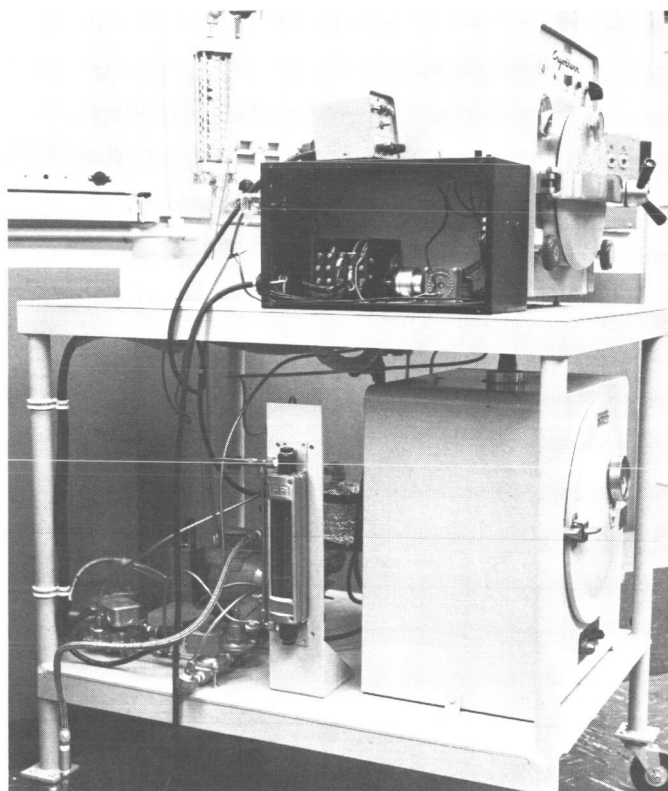


Fig. 18. Automatic ethylene oxide decontamination setup (side view)

F. An Automatic Ethylene Oxide Decontamination System

R. H. Silver and S. H. Kalfayan

1. Introduction

The design and construction of an automatic ethylene oxide (ETO) decontamination system described below was initiated several months ago in the Polymer Research Section at JPL. The apparatus is completely automated to sequence the decontamination of test samples of polymeric products through six or more identical, controlled cycles, each composed of four separate phases. The specified time, temperature and relative humidity are manually preset and are then automatically maintained for each phase of each cycle.

2. Description of Apparatus

a. The decontamination chamber. A commercially available gas sterilizer (AMSCO Can-O-Gas Portable Sterilizer) (Ref. 20) served as the basic decontamination chamber (Figs. 17 and 18). This unit lacked the facilities

to meet the applicable JPL ethylene oxide-dichlorodifluoromethane (ETO/ CCl_2F_2) decontamination specifications (Ref. 21). In order to meet the specified requirements, particularly those concerning continuous recirculation and preconditioning of the ETO/ CCl_2F_2 with respect to temperature, relative humidity and ETO concentration, the components and accessories described below had to be added. A schematic diagram of the system is given in Fig. 19.

b. Integral vacuum and recirculating pump. An integral vacuum-pressure pump (Lieman Model 201) was incorporated into the system to serve either as a vacuum pump to exhaust the system, or as a pressure pump to circulate the conditioning air and recirculate the ETO/ CCl_2F_2 mixture. The pump was adjusted to deliver approximately 0.2 ft³/min of gas through the system.

c. The preheating chamber. To ensure the complete gasification of the ETO/ CCl_2F_2 composition, the decontamination specifications (Ref. 20) require preheating of the sterilizing mixture before entering into the decontamination chamber. This was accomplished by passing the ETO/ CCl_2F_2 through coils of stainless steel tubing situated inside a modified vacuum oven (Cenco Model 95050), kept at a temperature 8-10°F higher than that of the decontamination chamber.

d. Humidity detection and control apparatus. The relative humidity of the gas flowing through the decontamination chamber could be preset and maintained at values within $\pm 3\%$, by means of a "bubbler" type humidifier and a commercially available humidity indicator/controller (Model 301, El-tronics, Inc., Warren,

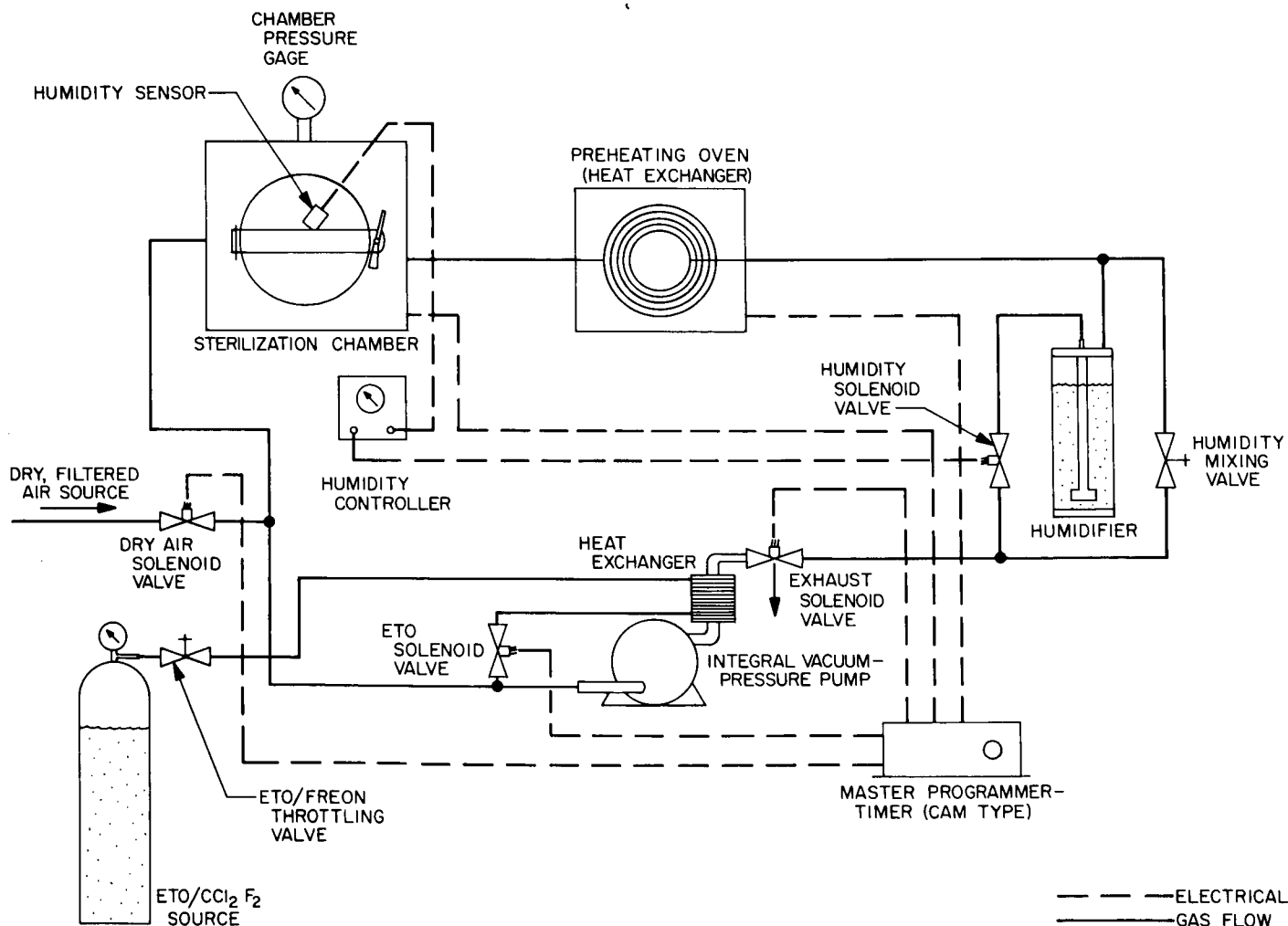


Fig. 19. Automatic ETO/ CCl_2F_2 decontamination apparatus schematic diagram

Pa.). As the sensor element, which is placed in the decontamination chamber, detects a change in relative humidity, a solenoid valve is actuated allowing a flow of moisture-saturated gas to mix with the main gas flow (dry air or dry $\text{ETO}/\text{CCl}_2\text{F}_2$). The humidifier is replenished with distilled water when the supply falls below a certain level.

e. Master cycle timer-programmer. The sequence of events necessary to complete a number of typical decontamination cycles is initiated and controlled by a master five-cam timer-controller (Model 5-ALR 60/9-36 HQR, Mirarik Electric, Los Angeles). Each of a series of four cams can be set to actuate each of the system components described above, in the proper time sequence. At the end of the last cycle, the fifth cam shuts down the entire system automatically. To start a multicycled decontamination sequence, the operator merely presses a button to set the time control into operation.

f. Other components. Components necessary to complete the system are shown in Figs. 18 and 19. These include appropriate pressure regulators, pressure gages, solenoid valves and a flow meter. A heat exchanger connected to the exhaust end of the pump was also added to the system as further assurance of the complete gasification of the sterilizing mixture. The partially liquid $\text{ETO}/\text{CCl}_2\text{F}_2$ coming from the supply cylinder passes through this heat exchanger, consisting essentially of coiled copper tubing wrapped around a brass spool. The heat to the exchanger is supplied by the compression of air from previous circulations.

3. Description of Operation

A complete six cycle decontamination sequence runs as follows: First, the operator loads the decontaminating chamber with the test specimens and closes the door. Next, the chamber pressure and chamber temperature settings are made, which determine the ETO concentration (Fig. 20), relative humidity, and temperature of the preheated gas. Then the master timer-programmer is readied by adjusting the cams controlling the: (a) humidification and air-wash; (b) initial vacuum; (c) $\text{ETO}/\text{CCl}_2\text{F}_2$ exposure; and (d) final vacuum. The humidification phase and the final air-wash phase are the same.

When the operator pushes the start button, the first cam switch closes, and energizes the dry air solenoid valve (Figs. 18 and 19), causing dry air to enter the humidifier; then, laden with enough moisture, the air passes through the preheating chamber, enters the de-

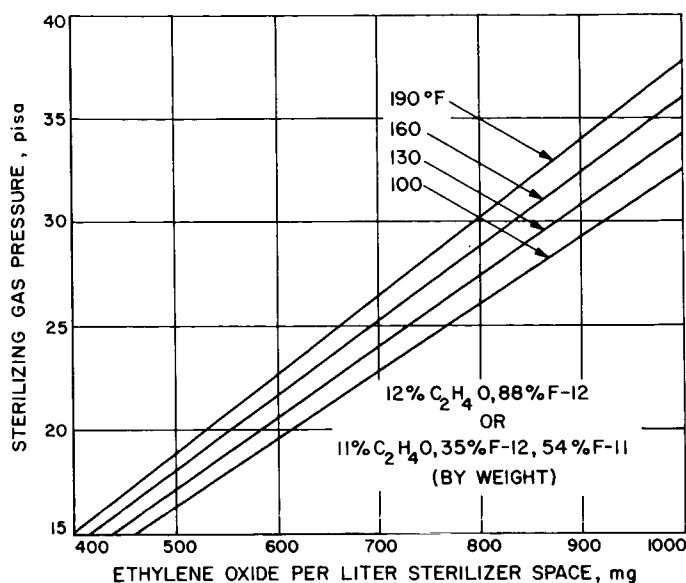


Fig. 20. Dependence of ethylene oxide concentration on temperature and pressure

contamination chamber and is finally exhausted to the atmosphere. The switch then opens, de-energizing the dry air solenoid valve. Now, the system is evacuated to 27 in. of Hg, within a period determined by the setting of the second cam.

After the second cam rotates through a preset angle, the switch of the third cam is closed, energizing the $\text{ETO}/\text{CCl}_2\text{F}_2$ solenoid valve, causing the decontaminating gas mixture to be introduced first into the preheating chamber and then into the decontaminating chamber, until the total vapor pressure of the mixture reaches the preset limit. The mixture is then recirculated, during which a portion of the flowing gas passes through the humidifier until the desired relative humidity level is reached. The third cam then rotates through its preset angle, opening its switch and stopping the flow of decontaminating gas. The fourth cam switch then closes, de-energizing the exhaust solenoid valve, again evacuating the entire system.

This sequence is repeated five more times, when a stepping relay cam arrangement shuts down the entire system and ends the decontamination procedure.

4. Conclusions

An automatic $\text{ETO}/\text{CCl}_2\text{F}_2$ decontamination system capable of meeting the existing JPL specification VOL-50503-ETS (Ref. 21) for piece parts and materials has been

constructed. The setup is readily adaptable to varying the decontamination parameters, such as, number of cycles, ETO concentration, temperature, relative humidity, flow rate and ETO exposure time.

Automation of the decontamination procedure, which up to the present has been a manually controlled operation, will result in saving labor and increasing accuracy in the control of the decontamination parameters.

References

1. Landel, R. F., and Fedors, R. F., Chapter IIIB, "Rupture of Amorphous, Unfilled Polymers," in *Fracture Processes in Polymeric Solids, Phenomena and Theory*, B. Rosen, Ed., Interscience Publishers, New York, 1964.
2. Flory, P. J., *J. Chem. Phys.*, **18**, 108, 1950.
3. Bills, K., and Salcedo, F. S., *J. Appl. Phys.*, **32**, 2364, 1961.
4. Kraus, G., *J. Appl. Poly. Sci.*, **7**, 861, 1963.
5. Cluff, E. F., Gladding, E. K., and Pariser, R., *J. Polymer Sci.*, **45**, 341, 1960.
6. Treloar, L. R. G., *The Physics of Rubber Elasticity*, 2nd Ed., Oxford Press, London, Chapter 7, 1958.
7. Demaree, N. C., and Taylor, D. F., *J. Dental Research*, Vol. 41, No. 4, 1962.
8. Hollenback, G. W., and Vallyani, A. A., *J. So. Calif. Dental Assoc.*, Vol. 33, No. 9, p. 422.
9. Landel, R. F., and Smith, T. L., *J. Am. Rocket Soc.*, Vol. 31, No. 5, p. 599, 1961.
10. Eilers, H., "Viscosity of Emulsions of a Highly Viscous Substance as a Function of Concentration," *Kolloid Z.*, Vol. 97, pp. 313-321, 1941.
11. Smallwood, H. M., "Limiting Law of the Reinforcement of Rubber," *J. Appl. Phys.*, Vol. 15, pp. 758-766, 1944.
12. Landel, R. F., Moser, B. G., and Bauman, A. J., *Proceedings of the 4th International Congress of Rheology*, Brown University, Providence, R. I., August 27, 1963, Interscience Publishers, Inc., New York, 1965.
13. Moser, B. G., Weich, Jr., R. E., and Landel, R. F., "A Theory of the Sedimentation Volume of a Randomly Packed Bed of Monodisperse Spheres," presented at the 40th National Colloid Symposium, University of Wisconsin, Madison, Wisconsin, June 14-16, 1966, to be published in the *Journal of Colloid Chemistry*.
14. Scott, G. D., *Nature*, Vol. 188, p. 908, 1960.
15. Brunauer, S., Emmett, P. H., and Teller, E., *J. Am. Chem. Soc.*, Vol. 60, p. 309, 1938.
16. Cannon, W. A., *Nature*, Vol. 197, p. 1000, 1963.
17. Ingham, J. D., Lawson, D. D., Manatt, S. L., Rapp, N. S., and Hardy, J. P., *J. Macro. Chem.*, **1**, pp. 75-91, 1965.
18. Irwin, R. S., and Kharasch, N., *J. Am. Chem. Soc.*, **82**, pp. 2502-2505, 1960.

References (Cont'd)

19. Narracott, E. S., "The Curing of Epoxide Resins," *British Plastics*, Vol. 26, pp. 120-123, 1953.
20. Specification sheet, "Can-O-Gas Sterilizer," IC 608, American Sterilizer Company, Erie, Pa.
21. JPL Specification VOL-50503-ETS, January 12, 1966.

SPACE SCIENCES DIVISION

N67 12127

XIII. Space Instruments

A. Pulse Height Analyzer
Memory

W. J. Schneider

A pulse height analyzer is an electronic instrument capable of measuring the amplitude spectral density of input pulses. A rudimentary implementation of the instrument consists of a pulse height quantizer, a memory, and control electronics (Fig. 1).

Pulse height quantizers, normally employed, operate on pulses of 1 to 10 μ sec duration and 0-3 to 10 v amplitude. The output is normally a binary number of 5 to 12 bits. The binary number representing pulse amplitude is used as the address for the memory. The memory cycle is *random access, read-modify-write*. During data accumulation, *modify* implies *add one*. A sequential *read-only* or *read-write* is used during data readout. The implementation of random access core memory consisting of 512 words, 18 bits in length, intended for application in a space-borne pulse height analyzer is described here.

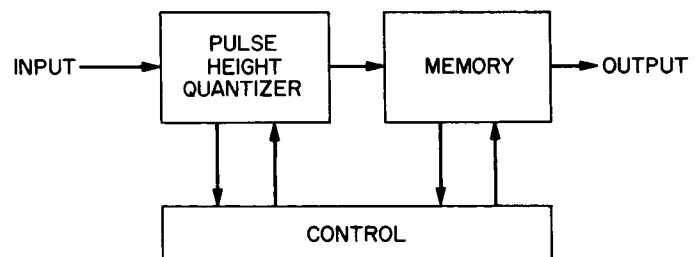


Fig. 1. Pulse height analyzer

1. Memory Description

a. Introduction. The essential part of a memory is the array of magnetic elements which stores or remembers the data. The individual magnetic elements are small (0.030-in. OD) ferrite toroids. The particular ferrite material employed exhibits a rectangular hysteresis loop, shown idealized in Fig. 2. As the magnetic field intensity in such a core is increased from zero, by increasing the current in its winding, the resultant flux density is dependent upon both the field intensity and the initial mag-

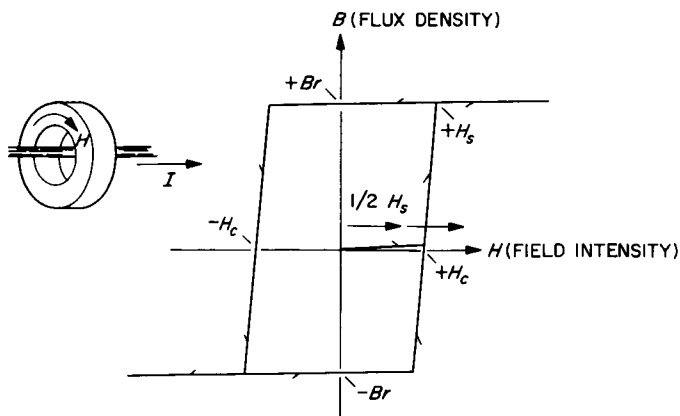
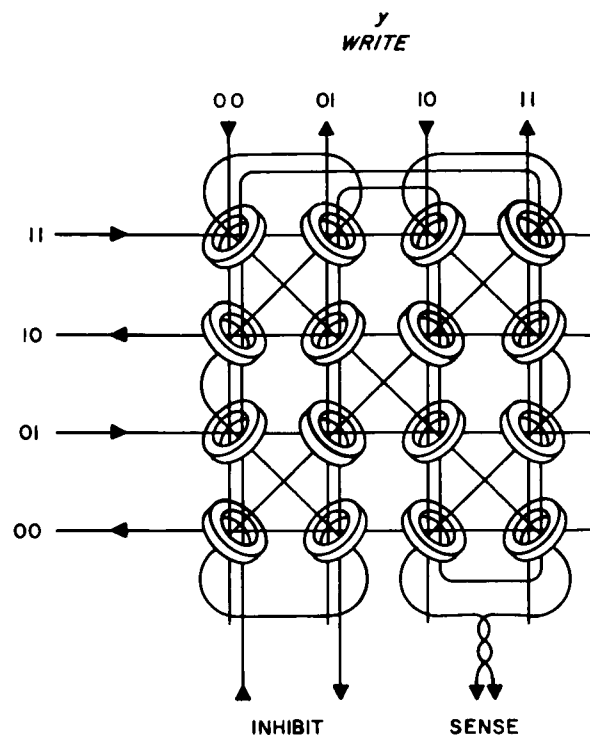


Fig. 2. Hysteresis loop

netic condition of the core. For the purpose of discussion, and because of its relevance to what follows, assume that the core was initially magnetized to a flux density of $-Br$, the remanence saturation flux density in the counter-clockwise direction. As the magnetic field intensity H is increased from zero, there is little or no increase in magnetic flux density B . When the magnetizing field intensity approaches the coercive force threshold H_c , further increases are accompanied by a rapid change in B . Once B reaches a saturation value, further increases in H again result in little or no flux change. If the magnetizing current is then decreased, the flux density follows the saturation contour. At zero field intensity, the material remains magnetized at the level of $+Br$, the remanent flux. If the current, and hence the magnetizing field, are reversed, brought to saturation, and then reduced to zero, similar events occur; and the core is left at the level of $-Br$. The remanence magnetization states $+Br$ to $-Br$ can thus be stored in the core indefinitely. $+Br$ may be arbitrarily designated as a logical *one* and $-Br$ as a logical *zero*.

A core may be switched from a *one* to a *zero* by the application of a current I_s through the winding sufficient to get the field to at least H_s . An essential requirement of a suitable core is that one-half of this current does not produce an H above the coercive force threshold, and that repeated application of $\pm \frac{1}{2}I_s$ (half-select) currents produce essentially no decrease in the stored remanence flux. Such traverses along the saturation contour are elastic, in that they achieve no permanent change in the flux level.

Such a core may then be used as an element in a coincident current memory system. In the 16-element array shown in Fig. 3, four x -select lines and four y -select lines are employed. A particular core may be selected and read by energizing one x and one y drive line. The drive cur-



ADDRESS - 1011
 $x = 10bb$
 $y = bb11$

	y			
	00	01	10	11
x	00			$\frac{1}{2} I_s$
	01			$\frac{1}{2} I_s$
	10	$\frac{1}{2} I_s$	$\frac{1}{2} I_s$	I_s
	11			$\frac{1}{2} I_s$

CORE CURRENT MATRIX,
ADDRESS 1011

Fig. 3 Core plane (4 × 4)

rents are limited to $\frac{1}{2}I_s$, and only one core receives the full select field intensity.

The 4×4 array may be thought of as a 16-word memory with one bit per word. The x and y drive line

have been partitioned from the address. For example, if word "eleven" is to be read, the address is 1011. The first two bits are assigned to x and the second two to y .

The sense winding passes through each core of the bit plane. If the selected core changes state, a voltage will be induced in the sense winding. Note that the relative direction in which the sense-winding and the drive-winding threads through the cores alternate from core to core of each row or column. This is done so as to minimize the voltage induced in the sense winding by elastic flux changes in half-selected cores. A secondary result is that the voltage polarity induced in the sense winding by switching of the selected core may be either positive or negative as a function of address.

The fourth wire in each core is called the inhibit winding. This wire is shown to enter each core in opposition to the *write* current direction of the x and y select drive wires. Operation of the inhibit winding in a *read-write* cycle is as follows:

Read. The addressed core receives $-x$ and $-y$ half-select currents and is driven toward the *zero* state. If it was previously in the *one* state, switching takes place and voltage is induced in the sense windings. Note that the *read* operation sets the cores of the selected word to the *zero* state.

Write. The addressed core receives $+x$ and $+y$ half-select currents; thus, the addressed core would be switched to the *one* state. The writing of a *one* may be inhibited by energizing the inhibit winding with a half-select current. The total current is thus reduced to $\frac{1}{2}I_s$ because of the cancelling effect of the inhibit current. The inhibit current is normally energized before either x or y drives are energized, thus avoiding a potential coincidence problem.

b. Drive mechanism. Each of the x and y drive lines must carry forward current for the *write* operation and reverse current for the *read* operation. This is accomplished by connecting the lines to a *write* current driver (CD) and *read* select driver (SD) at one termination and to a *read* current driver and a *write* select driver at the other (Fig. 4). The CD is seen in the figure to be a voltage source with a series limiting resistor, and the SD is a current sink. Energizing the x -*write* CD and the x -*write* SD produces the forward half-select current, while energizing the x -*read* SD and x -*read* CD produces the reverse half-select current.

c. Organization. As mentioned above, this memory uses two sets of select wires, x and y , and energizes them with half-select currents. The intersection of x and y is that set of 18 cores corresponding to the address. The address, itself, is a 9-bit binary word corresponding to 512 addresses (2^9). The memory could have been organized using 512 separate *read/write* drivers in $512, 1 \times 18$ core arrays. Use of a two-dimensional array makes it possible to factor 512 into 32 y and 16 x selection lines and to obtain a reduction from 512 to 48 *read/write* drivers. A further improvement is obtained by using a diode *and* gating on the sending and receiving ends of the selection lines. The current source is denoted as CD current driver, while the current sink is denoted as SC select driver. We then have $512 = (8SD, x) (4CD, x) (4SD, x) (4SD, x)$ corresponding to 20 *read/write* drivers. A simplified representation of the *read/write* drivers is shown in Fig. 4. The inputs to the driver gating structure are shown as binary numbers; the b 's correspond to ungated or *don't-care* terms of the address. Behind the *read* and *write* drivers is the 48-diode array which provides the numerical advantage of the *and* circuit, together with current reversal for *read* and *write* operations. Each of the selection wires feeds through 32 cores on each of the 18 mats (Fig. 5).

One sense amplifier and one inhibit driver are required for each of the 18 bits. Thus, the inhibit and sense windings pass through each of the 512 cores of one mat. When the *read* select currents are applied, the one selected core in each mat will be driven to a *zero* state. If a *one* was previously stored, the resulting voltage is amplified by the sense amplifier and used to set a corresponding data register flip-flop. The data register flip-flops are available as the memory output and are also available to the inhibit drivers through suitable gating (Figs. 4 and 5). A non-destructive *read* (or *read/restore*) cycle may be implemented by reading into the data register for temporary storage and then writing the same data into the selected address. Access to the data register flip-flops is provided for input data through *or* gates.

d. Core stack geometry. Core stack geometry and wiring are critical to memory speed, noise level, and drive impedance. A particularly compact stack has been achieved for this application. The core mats consist of 512 toroids each, in a 16×32 array. The cores have a diameter of 0.030 in. and are spaced 0.030 on centers as determined by the x and y select wires. Four mats, measuring less than $1 \times \frac{1}{2}$ -in. each, are assembled on each of five $2\frac{1}{8} \times 3\frac{1}{8}$ -in. printed circuit memory frames. The memory frames are then stacked, one above the other

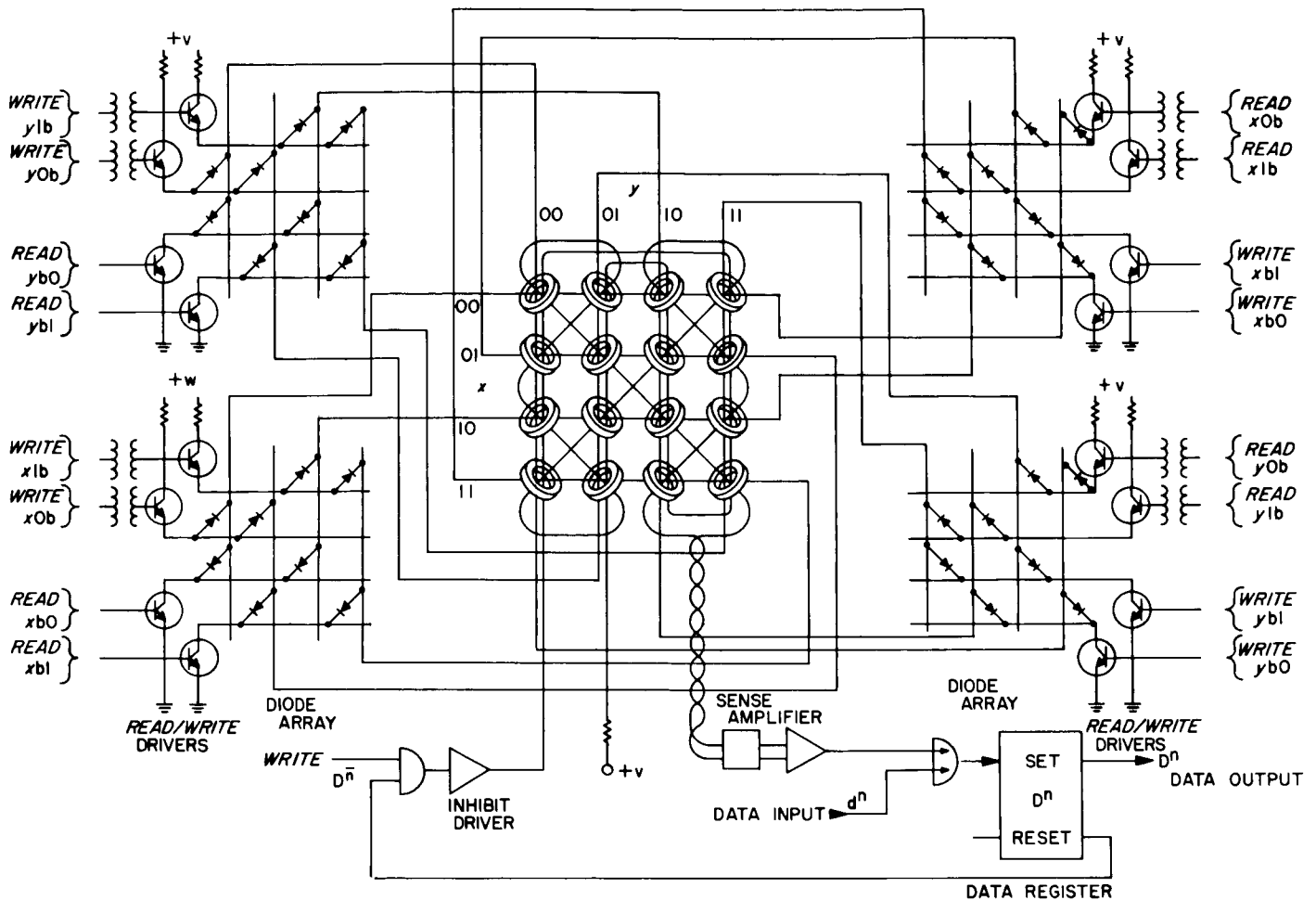


Fig. 4. Core plane (4 × 4) and drivers

(Fig. 6). The bottom position is occupied by an interconnection board, and the top position is occupied by the diode selection array. The particular x select wire is routed down through the 10 mats on the right side of the stack, wired to the left side by the interconnection board, and then up through the 10 mats on the left side of the stack to the diode array board. Both x and y select wires originate in, and return to, the diode array board. The four sets of inhibit and sense winding are taken directly from four memory frames, and two sets from the fifth frame. The interconnections between memory frames are made by welding or soldering extended tabs of printed circuit material.

2. Circuit Detail

a. Address register. The address register consists of nine Fairchild-type μ L926 j-k flip-flops connected for parallel

input or ripple counting. The register will accept the following inputs:

CLA, clear address:	a logic <i>zero</i> will unconditionally reset all address bits.
AAS, advance address scaler:	a transition from a logic <i>one</i> to logic <i>zero</i> will advance the address scaler by one.
SA ⁿ , set address Bit n :	a logic <i>one</i> on any of the 9 (0–8) SA lines will unconditionally set that bit.

The address register supplies assertion and negation outputs to the decoding gates.

b. Decoding; current drivers. The decoding gates are three input RTL integrated circuits, Fairchild-type

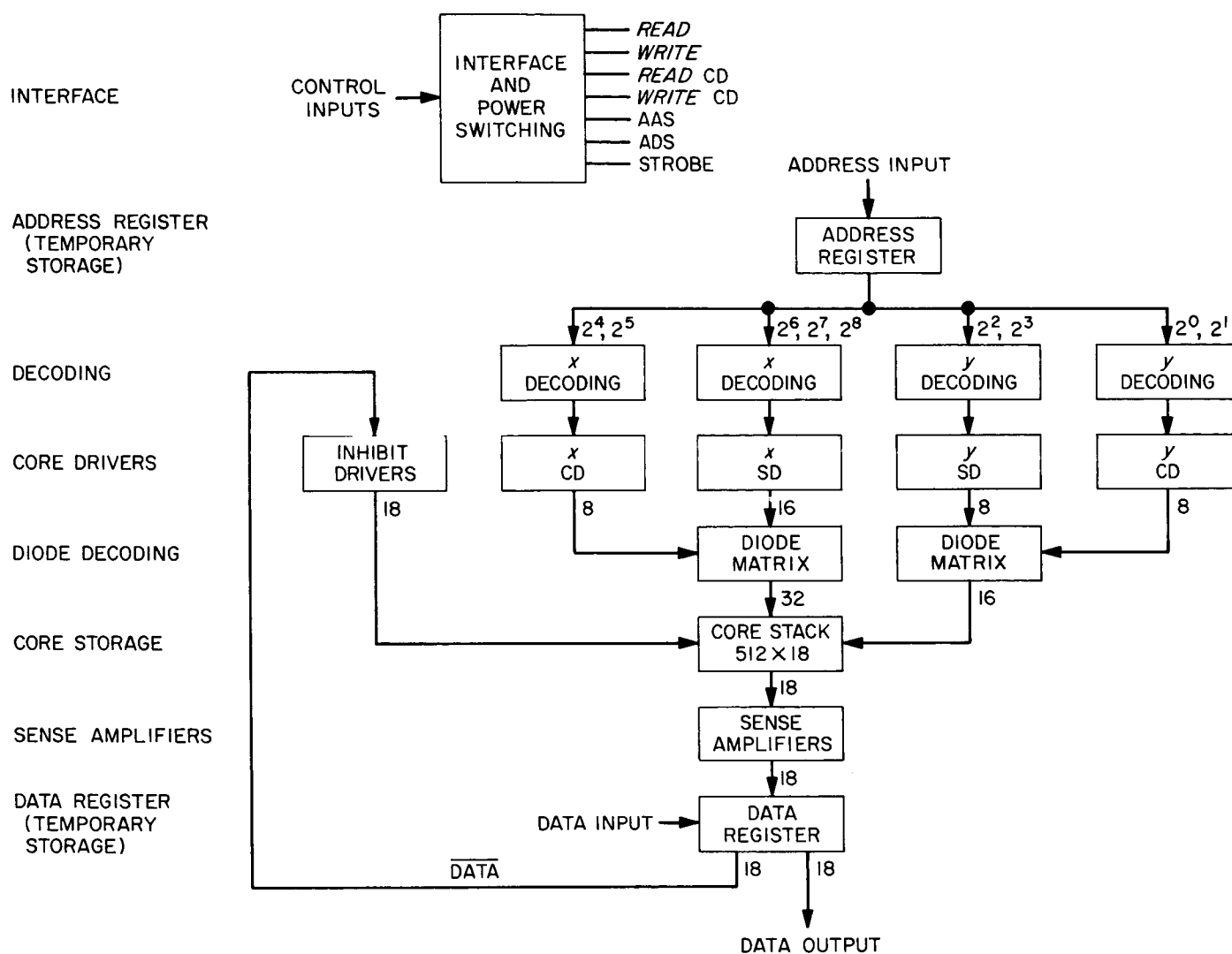


Fig. 5. Pulse height analyzer memory block diagram

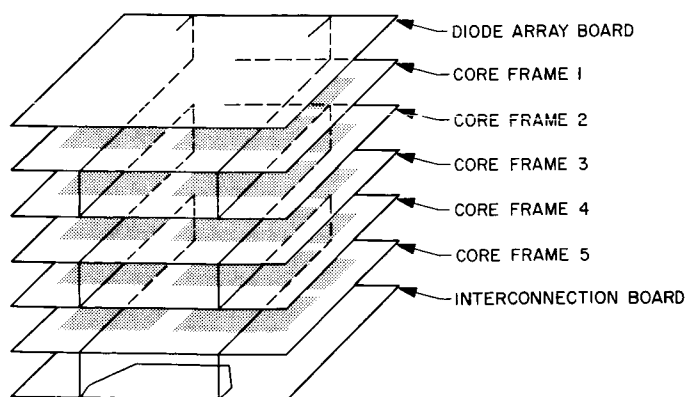


Fig. 6. Core stack

$\mu\text{L}915 (1/2)$. These three input gates act on two logic levels from the address register and a *read* or a *write* level. This is sufficient except in decoding the three high-order address bits (SA^6 , SA^7 , and SA^8) into the *x read/write* select drivers. Here an additional set of gates is provided for the SA^7 and SA^8 levels. Buffer amplifiers are provided on these outputs to meet the increased loading.

The select and current drive amplifiers employ discrete components to meet high current/high voltage requirements. The select drivers (Fig. 7) employ a $\mu\text{L}927$, a $\mu\text{L}900$, and an emitter follower to drive a grounded emitter switch. The current drivers (Fig. 8) use a grounded emitter

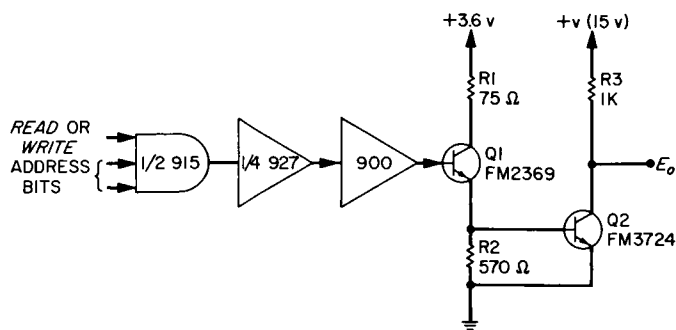


Fig. 7. Typical select driver

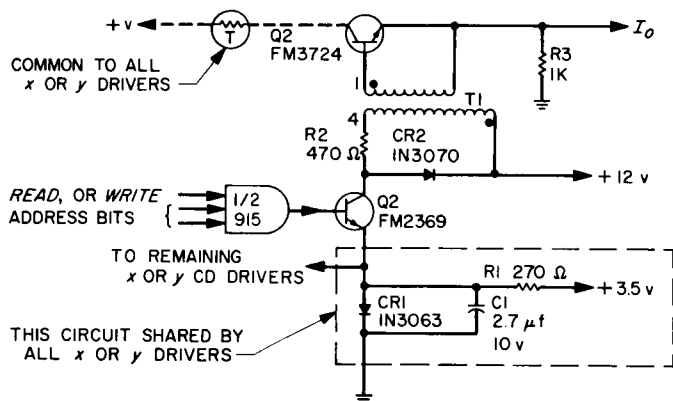


Fig. 8. Typical current driver

amplifier directly from the μ L915 gate and employ transformer coupling to provide current gain and isolation into a series switch.

The current and select drivers are biased off and hence require no standby current. The decoding gates and intermediate amplifiers receive power only during *read* or *write* commands. This command precedes the *read* or *write* current drive pulse by at least 250 nsec, which is adequate time to allow for stabilization of the circuits.

c. Sense amplifier. The Fairchild μ A711 dual comparator is used as the memory sense amplifier. This circuit consists of two differential comparator amplifiers with *or*'ed, strobed outputs. The signals received by the sense amplifier may contain common mode levels up to 500 mv, while the desired differential input is closer to 50 mv. Further, the leading and trailing edges of the select currents produce differential signals by direct induction and by elastic changes in the flux density of half-selected cores.

The Fairchild μ A711 sense amplifier employed produces full output for 5-mv signals. An input biasing network is

constructed of discrete components which both terminate the sense winding and provide 20-mv "zero" level bias for base clipping of the sense signal (Fig. 9). A strobing circuit is provided which enables the sense amplifier output for a 200-nsec interval, 300 nsec after the *read* current drivers are enabled. This is a common technique for signal-to-noise ratio improvement (Fig. 10).

The sense amplifier and bias network power are gated on with the *read* command signal 250 nsec prior to the *read* current drive pulse as a power conservation measure. Tests have shown that the sense amplifier stabilizes within 50 nsec after power turn-on.

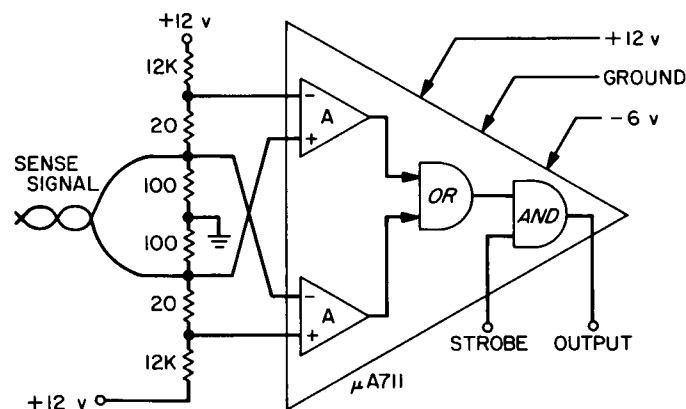


Fig. 9. Sense amplifier

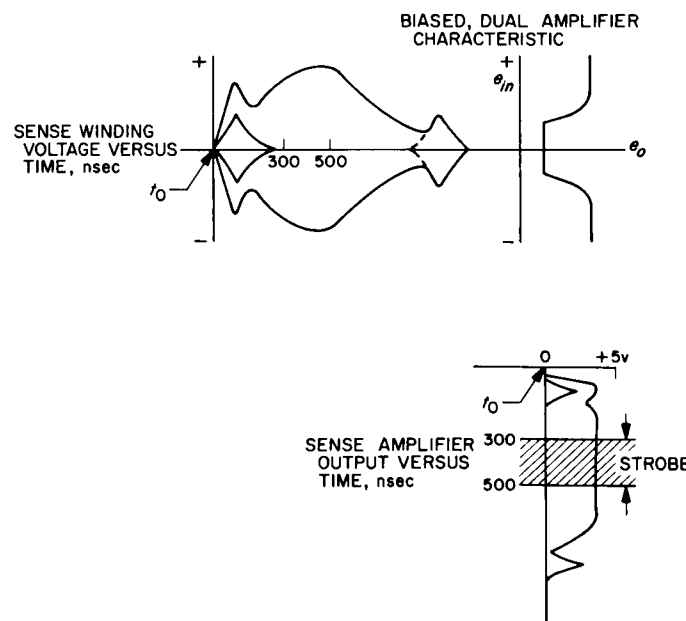


Fig. 10. Sense amplifier operation

d. Data register. The data, or output register, consists of 18 Fairchild μ L926 j-k flip-flops connected for parallel input or ripple counting. The register will accept the following inputs:

- CDS, clear data scaler:** a logic zero will unconditionally reset all data bits.
- ADS, advance data scaler:** a transition from a logic one to a logic zero will advance the data scaler by one.
- SDⁿ, set data register, Bit n:** a logic one from an external source will unconditionally set Bit n of the data register.
- SAⁿ, sense amplifier, Bit n:** an assertion output from sense amplifier n will unconditionally set Bit n of the data register.

The data register provides assertion outputs to the data register output lines Dⁿ and negation outputs to the inhibit drivers.

e. Inhibit driver. The inhibit drivers consist of a ($\frac{1}{2}$) μ L915 gate driving a discrete component emitter follower and the grounded emitter switch (Fig. 11). The inhibit drivers are biased off and require no standby current. The gates receive power when the *write* command is applied so that the inhibit current is established 250 nsec prior to the *write* current drive pulse.

The sense amplifier, data register flip-flop, and inhibit driver form a self-contained functional block and are packaged as a unit (Fig. 12).

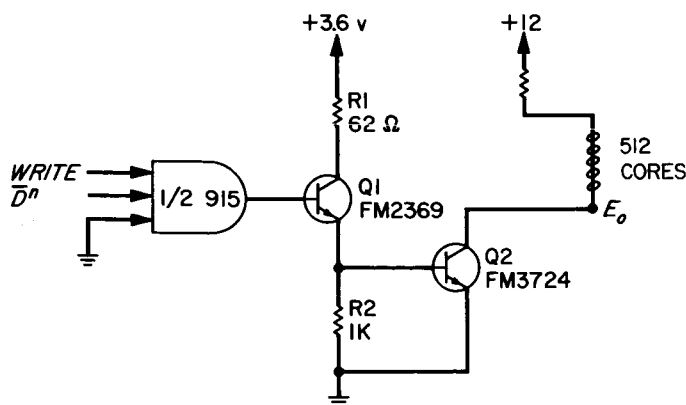


Fig. 11. Inhibit driver

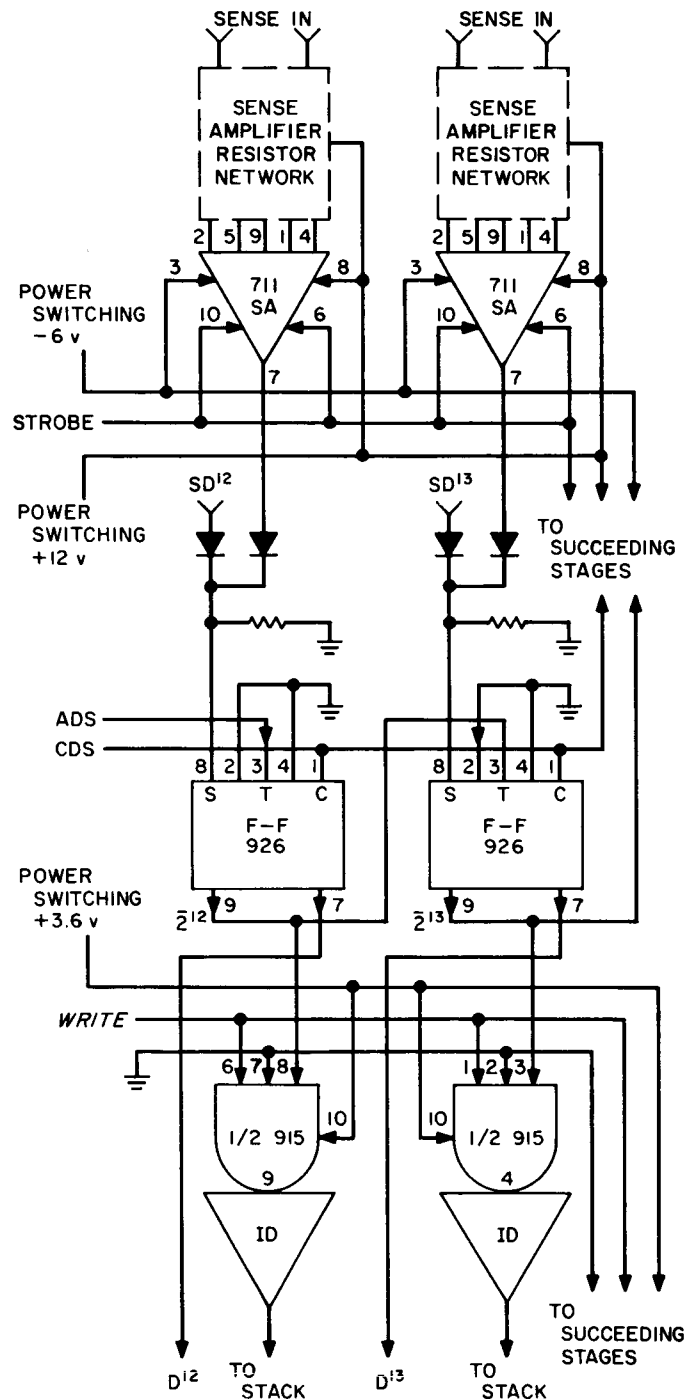


Fig. 12. Data register chain

f. Strobe generator. The strobe generator consists of two hybrid timing flip-flops, one for a 300-nsec delay, followed by one for the 200-nsec period. Timing is accomplished enabling a μ L915 gate, thereby initiating a capacitor discharge and using a discrete transistor amplifier as a threshold detector (Fig. 13). The two timing flip-flops are isolated by a μ L915 gate (Fig. 14). A μ L900

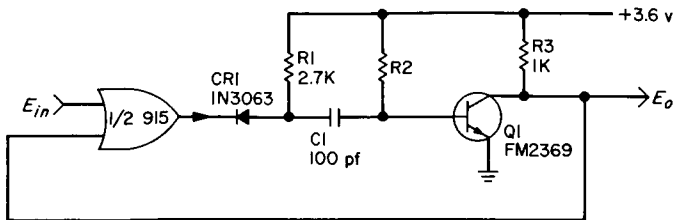


Fig. 13. Timing flip-flop

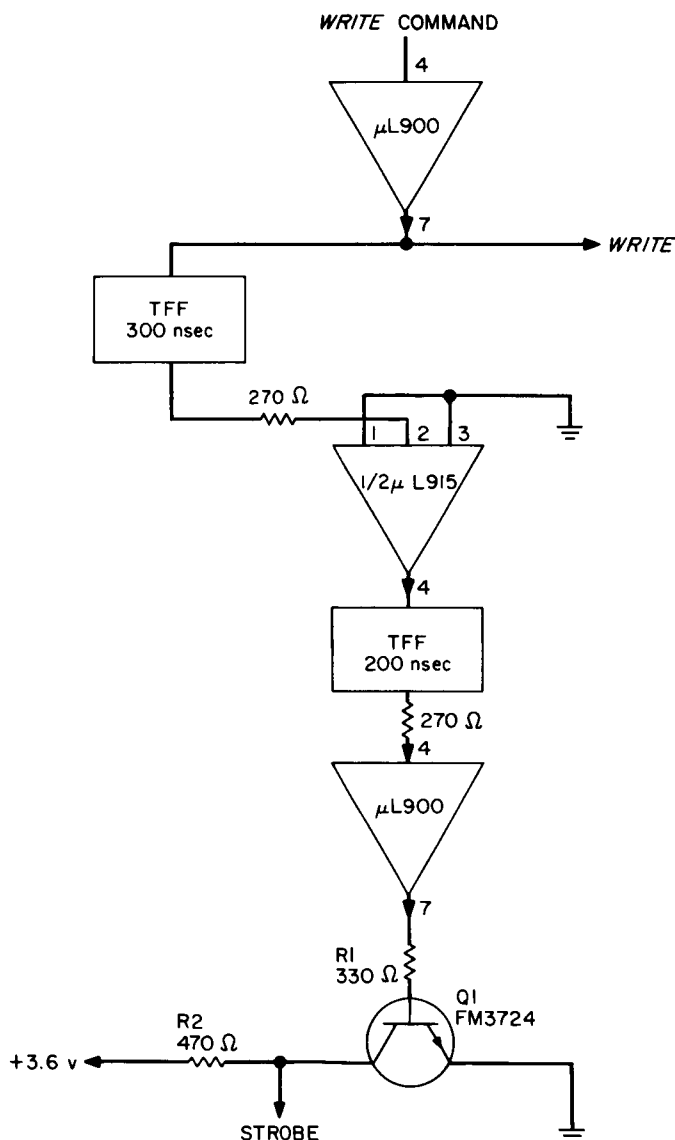


Fig. 14. Strobe generator

buffer amplifier drives a discrete switch to produce the strobe pulse.

g. Power switching. Power switching is by discrete component switches. μ L915's are used primarily as logic

level interfaces between signal circuits and the discrete amplifiers which drive the power switches (Fig. 15).

3. Performance

a. Timing. The memory does not contain internal programming. All required timing sequence signals must be provided by the pulse height analyzer or other equipment. The requirements are rather simple and are easily obtained from the analyzer; further, complete versatility is maintained. A *read-add one-write* cycle is described below:

- | | |
|---|-----------------------|
| 1. Clear data register (CDS) | 3.7 μ sec (min.) |
| Clear address register (CAS) | 1.85 μ sec (min.) |
| 2. Enter address (assertions SA^n) | 0.15 μ sec (min.) |
| 3. Read command | 1.5 μ sec (min.) |
| Precedes read CD command by | 0.5 μ sec (min.) |
| Energizes: decoding gates,
select drivers, and
sense amplifiers | |
| 4. Read current driver command | 1.0 μ sec (min.) |
| 5. Data ready within | 0.7 μ sec (max.) |
| 6. Add one propagation time (ADS) | 1.3 μ sec (max.) |
| 7. Write command | 1.7 μ sec (min.) |
| Precedes write CD command by | 0.5 μ sec (min.) |
| 8. Write current driver | 1.0 μ sec (min.) |

Timing of the memory cycle and interface signals is shown in Fig. 16.

b. Power consumption. The maximum power dissipated by the memory is tabulated below. These figures are obtained at a *read/write* cycle rate of 25/ μ sec. This corresponds to the maximum operational rate of the analyzer.

Mode	Power, w
Standby	3.63
Read restore	
All ones	5.95
All zeros	12.14
$\frac{1}{2}$ ones	9.04

c. Temperature. The circuits employ either Fairchild RTL integrated circuits or silicon transistors and are capable of operation from -55 to $+125^\circ\text{C}$. The cores

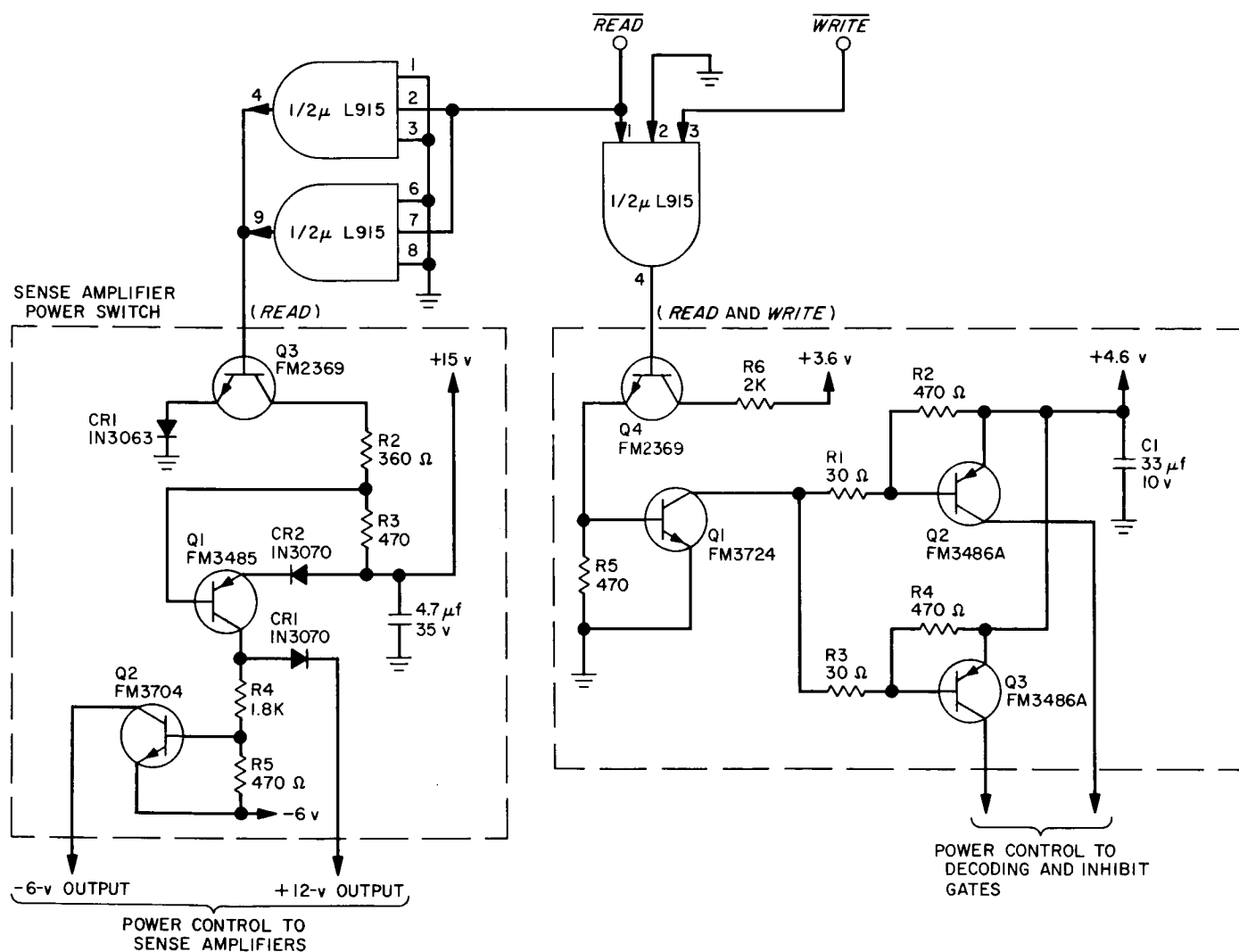


Fig. 15. Power switching

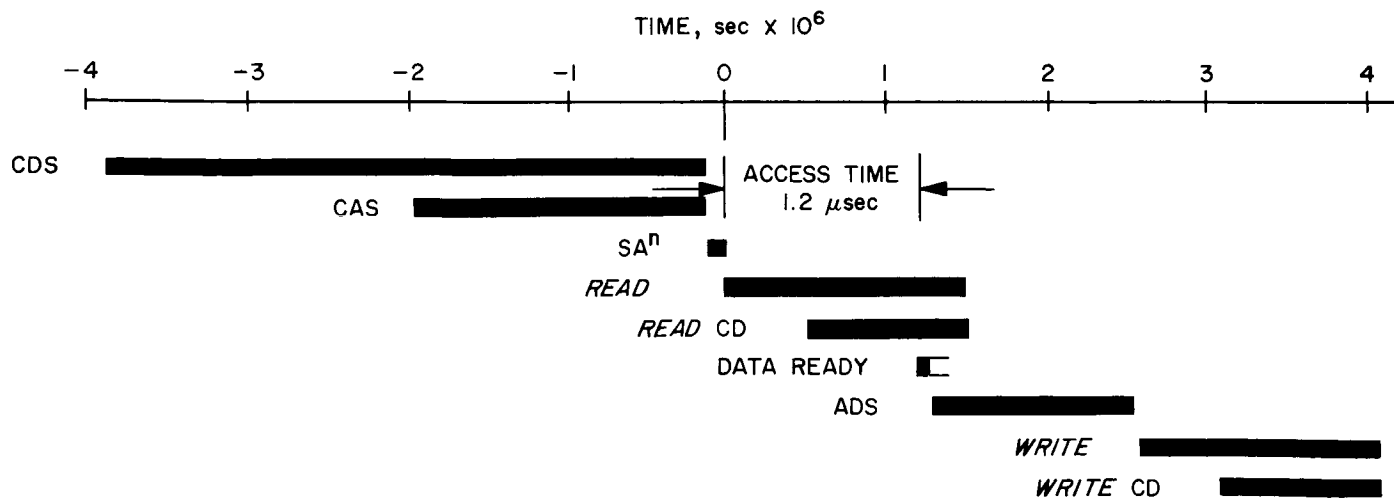


Fig. 16. Read-add one-write memory cycle

used are EMI-34-101, which are capable of operating from 0 to +71°C without drive current compensation. Temperature compensation of the select currents is employed and is expected to extend the operating temperature range from -55 to +125°C.

d. Packaging. Active components, flatpack integrated circuits, and TO-46 case discrete transistors, will be mounted in JPL stick modules. The core stack and stick modules will be housed in a 6- × 7- × 3-in. JPL module enclosure.

N67 12128

XIV. Bioscience

A. Gas Chromatography Column Development for Analysis of the Martian Atmosphere

W. F. Wilhite

This report presents one phase of a JPL project to develop a combination gas chromatograph-mass spectrometer (GC-MS) experiment for the *Voyager* program. After landing on the surface of Mars, the purpose of this experiment will be to analyze the atmosphere; analyze a sample of the Martian surface material for the presence of organic compounds; determine the state of equilibrium between individual constituents of the soil and the atmosphere; determine the state of oxidation or reduction of constituents of the soil; and to identify the thermally reactive constituents of the soil. The portion of the experiment covered by this report is the determination of atmospheric constituents.

The purpose of the development effort reported here was to provide a gas chromatographic column system capable of separating possible Martian atmosphere con-

stituents in which interest has been expressed. The separated constituents will then be identified by the mass spectrometer. Based on recommendations from the science staff at JPL and other sources, the following were chosen as the components that the GC-MS should be able to determine:

Hydrogen	Nitric oxide
Nitrogen	Nitrous oxide
Oxygen	Nitrogen dioxide
Argon	Ammonia
Carbon monoxide	Methyl fluoride
Carbon dioxide	Methyl chloride
Methane	Hydrogen sulfide
Water	Sulfur dioxide

The simplest way to separate these compounds, using gas chromatography, would be with the use of one column. Unfortunately, because of the wide variety of compounds represented by the list above, no one column packing material, prior to this development, was capable of performing such a separation. Water, because of its high polarity, was particularly difficult to determine by gas chromatography.

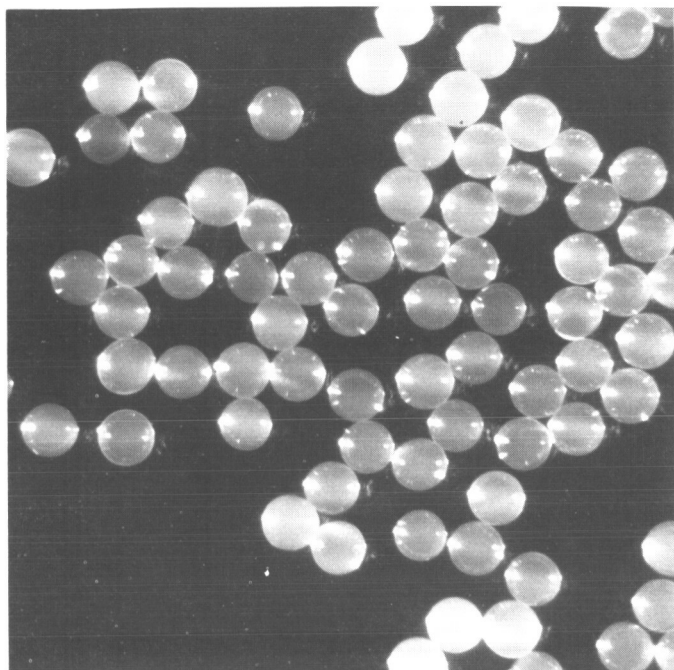


Fig. 1. Photomicrograph of porous polymer bead

At the start of this development, word was received of a new column packing material developed by Dow Chemical Company. The material was in the form of a porous polymer bead (Fig. 1) and was said to be capable of separating a variety of compounds, including water, very efficiently. On investigation, this material did indeed seem promising for our particular development. A subcontract was let to Dow to provide a column system to separate the required compounds.

The results of the contract were excellent in that many of these compounds were separated on one column (Fig. 2). Dow also demonstrated resolution of some additional compounds of possible interest. Two disadvantages still existed with the column provided by Dow, however. One was that nitrogen and carbon monoxide were not separated. These two components would be almost impossible to determine simultaneously by the flight mass spectrometer because of resolution limitations. The other difficulty was that the analysis was rather lengthy, taking approximately 55 min. Development was then started at JPL to improve this column so that the nitrogen-carbon

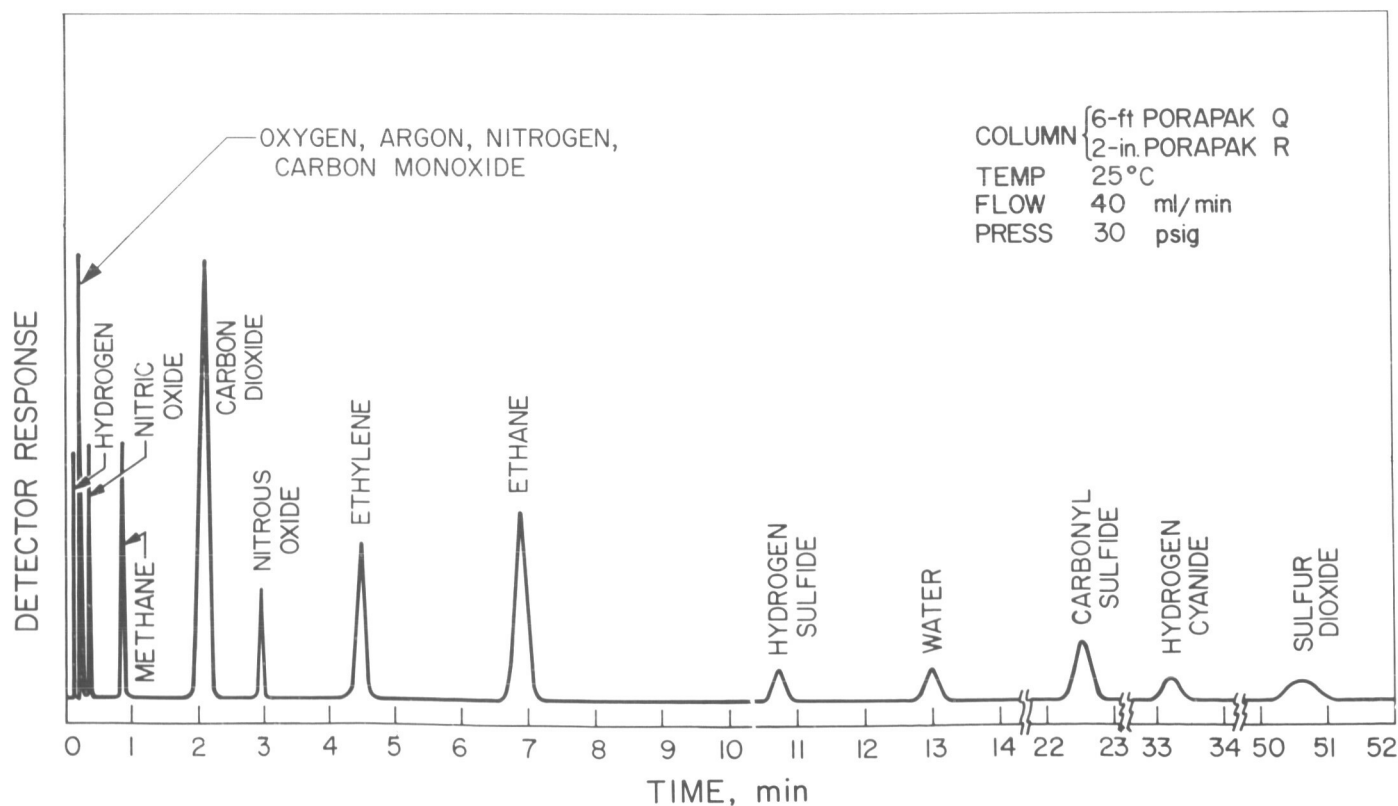


Fig. 2. Chromatogram showing separation on Dow-furnished column

monoxide separation could be made. The development also aimed at separation of several other compounds which Dow had not successfully resolved, and at a total analysis time of less than 15 min.

1. Experimental Procedure and Equipment

The development work was performed using the same diameter column tubing as the Dow-provided column; i.e., 1/8-in. OD, 0.100-in. ID. Porous polymer bead column packing used in the JPL phase of this development was purchased from Waters Associates who manufacture the material (under Dow license) under the trade name Porapak. For convenience of comparison, the flow rate of 40 ml/min used by Dow was also used in this work. All column development was performed using a Loenco Model 70 gas chromatograph. The standard commercial instrument was modified for a portion of the development by installing a JPL-designed sampling valve inside the column oven (Fig. 3) to provide slug injections of 100 μ l gas samples. This noticeably improved resolution of the nitrogen and oxygen-argon-carbon monoxide peaks.

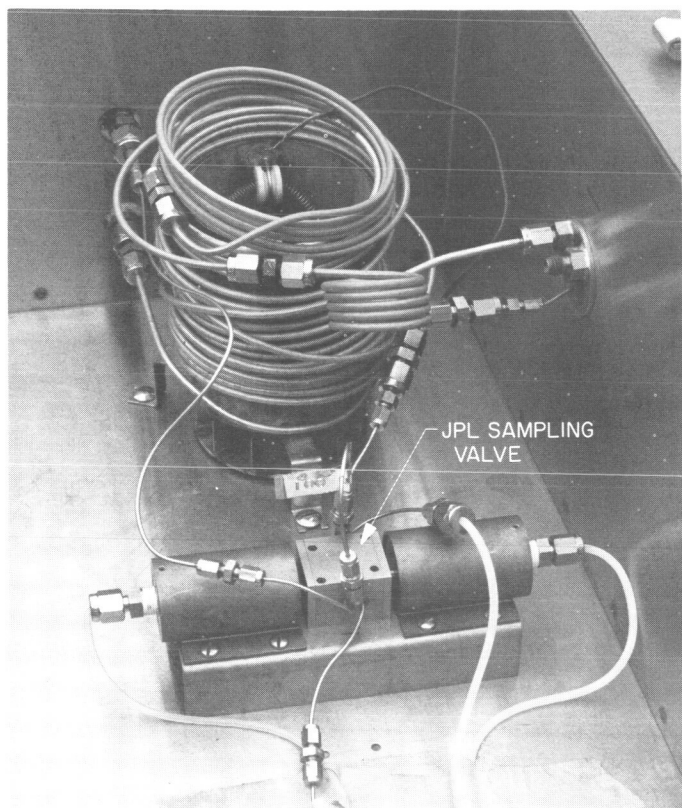


Fig 3. Installation of JPL sampling valve in Loenco column oven

Size of the detector internal volume also noticeably affected resolution. Work was started using the Loenco standard thermal conductivity (TC) detector. It was discovered, however, that the detector internal volume was too large, causing loss in resolution between peaks. A Carle micro thermal conductivity detector was substituted with a significant increase in resolution resulting. This detector was mounted in the detector oven of the Loenco gas chromatograph (Fig. 4). The detector readout was made on an Esterline Angus, 1/8-sec response, 1-mv potentiometric recorder. Identical columns were used on both sample and reference sides of the detector so that pressure drop would be the same on both sides of the system.

Carrier gas was routed through the syringe injection ports of the Loenco to the JPL gas sampling valve so that syringe injection of individual components could be made into the system. This was done in order to inject incompatible components singularly, and to identify components in gas mixtures by syringe-injecting them individually.

A Millaflow dual-flow controller was installed just ahead of the syringe injection ports to regulate flow of carrier gas to both the sample and reference sides of the system. The need for this flow control regulation is discussed in *Experimental Results*.

Mixtures of compatible gases were made, using a gas blending system, in 3-l, 304 stainless steel bombs, up to a

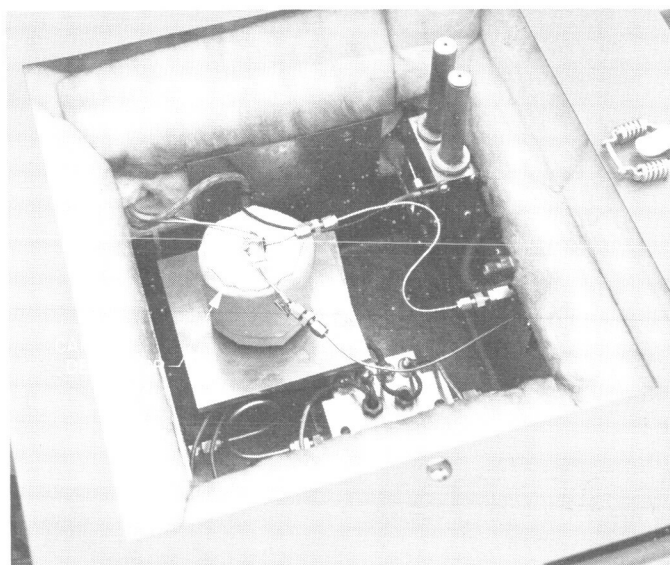


Fig. 4. Installation of Carle TC detector in Loenco detector oven

pressure of 100 psig. 100- μ l samples of these mixtures were then injected using the JPL sampling valve, which was actuated by bellows operated at 50 psi air pressure. This operation provided rapid (25-msec) valve actuation for improved sample injection.

2. Experimental Results

The first problem to be solved was separation of nitrogen and carbon monoxide. Since this would require a longer column than the one that Dow provided, a 16-ft column was made up, using 80–100 mesh Porapak Q. This approximated the particle size used in the Dow column. Because such a long column would retain and spread the sulfur dioxide peak, temperature programming was used to improve the peak shape and to shorten the analysis time.

The use of temperature programming resulted in poor baseline stability. The porous polymer bead is a plastic that expands greatly with temperature. This expansion in a packed column increases pressure drop across the column, decreasing the carrier gas flow rate. Since the extremely flow-sensitive Carle detector was being used, the decreasing flow resulted in a baseline drift as great as full scale in 2 min. The less flow-sensitive standard TC detector contained in the Loenco gas chromatograph was then tried. This improved baseline stability, but resolution between the carbon monoxide and nitrogen was lost because of the large internal volume of this detector. Flow control of the system was improved by installing a Millaflow dual back-reference flow controller ahead of the sampling valve. The flow controller regulated flow through both the reference and sample columns. Finally, through use of improved flow control and replacement of the 80–100 mesh Porapak Q with 50–80 mesh Porapak Q, excellent baseline stability was achieved. Using the larger particle size lessened, to a great extent, the change in pressure drop with temperature programming. Because of the high surface area of the porous polymer bead (100–600 m²/gm) there was no loss in separation efficiency in going to the larger particle size.

With 16 ft of Porapak Q good resolution of nitrogen and carbon monoxide was obtained, but many components of interest, including hydrogen sulfide, water, ammonia, and nitrogen dioxide were still unresolved. Development was then performed using the more polar Porapak materials to achieve the resolution of these desired components.

Various lengths of Porapak R, much more polar than Porapak Q, were added to the 16 ft of Porapak Q to

resolve these four components. Success was finally achieved by replacing 8 ft of the 16-ft Porapak Q column with Porapak R so that the final column consisted of 8 ft of 50–80 mesh Porapak Q in series with 8 ft of 50–80 mesh Porapak R. With these series columns, all components of interest were resolved except for oxygen, argon, and carbon monoxide which can be easily determined by the mass spectrometer. The peak shape for all components is excellent except for ammonia and nitrogen dioxide, which tail.

Some additional work was performed in the area of separating other interesting components on this column, such as formaldehyde, methyl alcohol, formic acid, and acetic acid. Under the operating conditions used to achieve resolution of the atmospheric components, these components were difficult to analyze. The acids in particular, especially acetic, tended to tail badly and had very broad peaks. A large improvement in peak shape of the acids was realized by operating isothermally at 200°C. However, in using temperature programming designed to separate the atmospheric constituents, formaldehyde and formic acid could be determined, although formic acid was not resolved from water under these conditions. Methyl alcohol, however, was easily resolved with excellent peak shape at between 13 and 14 min.

The resulting chromatogram is shown in Fig. 5 with the following operating parameters:

Column	8-ft, 0.100-in. ID, 50–80 mesh Porapak Q in series with 8-ft, 0.100-in. ID, 50–80 mesh Porapak R
Flow rate	40 ml/min
Pressure	31–48 psig
Temperature	Programmed from 25 to 150°C at 12 deg/min
Detector	Carle at 150°C with 35-ma current
Sample	100 μ l

3. Conclusion

It has been shown that, using a recently-developed porous polymer bead column packing material, resolution of nearly all components of interest in the Martian atmosphere can be achieved with one gas chromatographic column in less than 15 min.

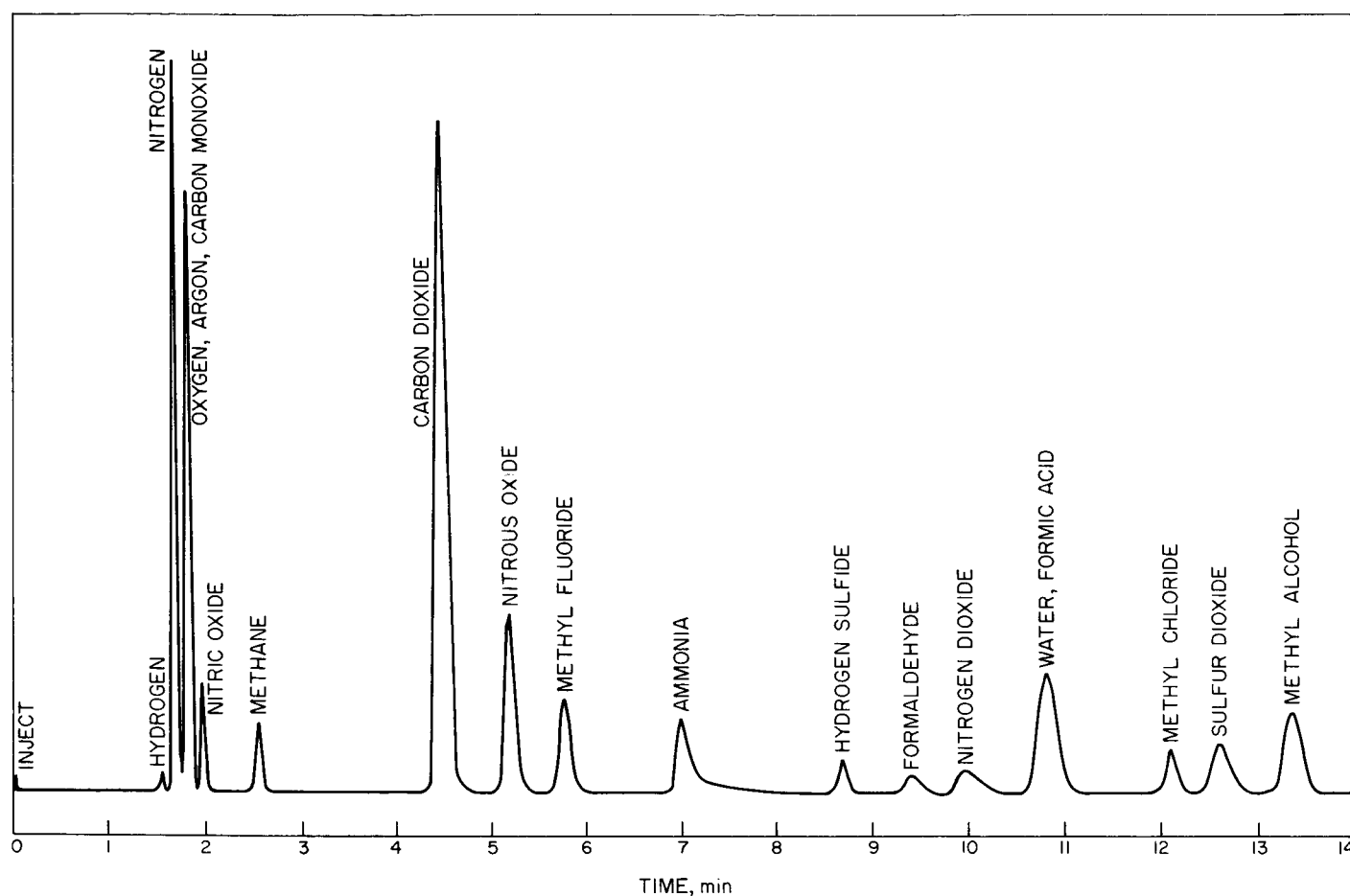


Fig. 5. Separation of components of Martian atmosphere

B. Soil Studies—Desert Microflora.

XIII. Identification of Some Algae from Antarctica

R. E. Cameron

1. Introduction

Antarctica is a cold, windy, arid, isolated continent located south of the Antarctic Convergence, generally between the 50th and 60th latitudes south. It is the world's fifth largest continent, with 5,000,000 square miles. Most of it is covered with glacier ice and snow, except for approximately 3000 square miles along the coasts and in some interior valleys. The Antarctic continent is also composed of the highest land mass, averaging 6500 ft above sea level.

Environment of the Antarctic is quite harsh. Constant winds, carrying ice and snow, sweep the continent, reaching more than 100 mph. Occasional gales blow down the "dry valley" areas, causing movement of sand and gravel, deflation of the surface, and sandblasting of rocks (Ref. 1).

Data on snow accumulation (including drifting snow) show an average equivalent precipitation of 4.5 in. at a site on the Ross Ice Shelf (Ref. 2). Precipitation and accumulation data for "dry valley" areas of Victoria Land, although not available, are probably much less (Ref. 1). Snowfalls are rare during the summer, and most of the winter snow disappears during the spring by sublimation to the dry atmosphere (Ref. 1).

Air temperatures may reach +42°F above zero on warm days, but are -50 to -100°F during the winter nights (Ref. 3). However, surface rock temperatures may reach 90°F (Ref. 4).

The Antarctic summer is short. In mid-April the Sun sets, and does not rise again until late August. Antarctica is the coldest region in the world.

Life forms in Antarctica are not abundant. No trees, shrubs nor other similar macrovegetation are present on the continent. The only conspicuous plants are mosses, lichens, and algae (Ref. 4). Native animal life consists primarily of sea birds, e.g., penguins and skuas, seals, and a few insects and arachnids, although some nematodes and potworms are found in soils of some areas (Ref. 5).

Despite the paucity of life on the continent, the waters surrounding Antarctica are known to be the richest in the world in nutrients. The rich supply of nutrients provides for a tremendous growth of phytoplankton, including diatoms and other algae. These organisms are the primary producers in the Antarctic food chain.

On the continent, vegetation consists primarily of cryptogams (mosses, lichens, algae, some fungi and three liverworts) (Ref. 5). Bacteria and yeasts are also present. Only three phanerogams have been found: two grasses and one pink. Lichen species are the most numerous (Ref. 4), but the fresh-water and terrestrial algae, whether free-living or as lichen components, are probably the most widespread (Ref. 3) and most abundant in terms of biomass (Ref. 5). Lichens and mosses thrive especially wherever guano has been deposited in bird rookeries. The algal habitats also include ice, snow, lakes, meltwater pools, soil, rock, and other cryptogams. In general, the algae are tolerant of a wide variation in environmental conditions, but there is no observable vegetation of any kind in the dry, ice-free land areas (Ref. 5).

It is expected that eventually a study of Antarctic plant life may provide information as to whether there were land masses connecting Antarctica with other continents of the southern hemisphere, and possibly the presence (or absence) of plants can give information as to the age of ice-free regions.

In regard to possible contamination, subsequent survival and reproduction of foreign life forms in the harsh Antarctic environment, it has been noted that, "man has not yet succeeded, by either accident or design, in introducing a new plant or animal species into Antarctica," (Ref. 5). However, later work has shown that of six introduced species of soil bacteria, one species did not show any decrease in numbers during the period of study of one austral summer in Antarctica (Ref. 6).

Knowledge of the plant life of Antarctica, the kinds of plants, their distribution, abundance, habitat, and physiology can also provide valuable background information prior to investigation of harsh, extraterrestrial environments, such as Mars, for possible life forms.

The purpose of this report is to present additional information on the algal flora of the Antarctic continent, especially with regard to examination and identification of previously unreported algal specimens. A comparison is given for species occurring in Antarctic and other desert areas investigated for the Desert Microflora Program.

2. Materials and Methods

Samples of visible algal vegetation were collected, primarily by Dr. Jacques S. Zaneveld,¹ from a variety of habitats in the Antarctic austral summer of January–February and November–December, 1964. Materials were collected principally in the eastern vicinity of the Ross Ice Shelf, Ross Island, McMurdo Sound, southern Scott Coast, Hillary Coast, and Shackleton Coast (Figs. 6 and 7).

More than 100 specimens were collected, dried, and taken to the United States. Parts of each specimen were deposited in the herbarium of Dr. Francis Drouet, Philadelphia Academy of Natural Sciences. Some of these latter specimens were subsequently examined microscopically at the Academy in October 29–31, 1965, and parts of 21 specimens were brought to JPL for additional study.

At the Laboratory, a direct microscopic examination was undertaken to identify all species within a sample, regardless of their abundance.

3. Results and Discussion

a. Antarctic algae. Typical populations and communities of algae in the 21 samples are shown in Table 1. In some specimens species of a single blue-green or green alga were observed, whereas in other specimens there was a mixture of blue-green algal species, or blue-green and green algal species. In one sample, No. 64-11-0010B, collected from the bottom of a frozen lake, there was an algal community composed of four filamentous blue-green algae and two filamentous green algae. Another sample, No. 64-02-0006, collected from a meltwater lake, contained five species of blue-green algae: three were filamentous and two were coccoid forms.

¹Institute of Oceanography, Old Dominion College, Norfolk, Virginia.



Map prepared by the American Geographical Society for the United States Antarctic Research Program under a grant from the National Science Foundation.

Fig. 6. Antarctica: southern algae sample collection area

Table 1. Location and habitat of Antarctic algal species

Specimen No.	Date	Collectors	Location and description of collection site	Specimen appearance and habitat	Species identified
64-01-0208	January 6, 1964	E. D. Schofield	Walcott Glacier Area, eastern shore of Lake Penny	Plentiful growth for about 2 m. On land and sandy gravel.	<i>Nostoc commune</i> ^a <i>Schizothrix calcicola</i> ^a <i>Anacystis montana</i>
64-12-0065	December, 1964	V. L. Yeats	Shackleton Glacier Altitude: 2000 ft	White on upper surface; dark brown on lower surface. On moss.	<i>Anacystis marina</i> ^a
64-01-0209	January 9, 1964	E. D. Schofield	Walcott Glacier Valley, 0.5 mi southeast of Lake Penny	Abundant over sand. Large clumps. On white salt deposit and hillside in depression.	<i>Schizothrix calcicola</i> ^a <i>Calothrix parietina</i> ^a <i>Nostoc sp. (young)</i> ^a
64-12-0066	December 3, 1964	J. L. Gressitt	Minna Bluff Victoria Land Altitude: 70 m	Fresh, greenish-orange. Along the edge of a frozen meltwater lake.	<i>Anacystis marina</i> ^a <i>Microcoleus vaginatus</i> ^a <i>Schizothrix calcicola</i> ^a <i>Protococcus grevillei</i>
64-12-0062	December 1, 1964	J. L. Gressitt	Swithbank Moraine in Shackleton Glacier. 85° 10' south, 66° 45' west Altitude: 1500 ft	Purple on upper surface. Grey on lower surface. Along border of frozen pond.	<i>Schizothrix calcicola</i> ^a
64-02-0090	February 25, 1964	J. S. Zaneveld and W. I. Simmonds	Granite Harbor, west coast of Ross Sea, Flat Iron Altitude: 40 ft	On rocks above sea.	<i>Schizogonium murale</i> ^a
64-01-0036	January, 1964	J. S. Zaneveld and W. I. Simmonds	Tent Island McMurdo Sound Altitude: 200 ft	On a sloping hillside, on bottom of basaltic lava, where meltwater had drained.	<i>Microcoleus vaginatus</i> ^a <i>Schizogonium murale</i>
64-01-0065	January 16, 1964	J. S. Zaneveld and W. I. Simmonds	Cape Evans Ross Island Lake D	Orangish-red patches of growth on bottom of meltwater. Some floating green growth.	<i>Oscillatoria chalybea</i> ^a <i>Microcoleus lyngbyaceus</i> ^a <i>Schizothrix calcicola</i> ^a <i>Protococcus grevillei</i>
64-02-0073	February 23, 1964	J. S. Zaneveld and W. I. Simmonds	Marble Point, west coast of Ross Sea Altitude: 25 ft	In a dry meltwater lake, approximately 500 ft offshore.	<i>Microcoleus paludosus</i> ^a <i>Microcoleus vaginatus</i> ^a <i>Schizothrix calcicola</i> ^a
64-02-0006	February 8, 1964	J. S. Zaneveld and W. I. Simmonds	Cape Hallett, Ross Sea, opposite Seabee Hook at Manhaul Glacier	In meltwater lake at foot of glacier.	<i>Microcoleus lyngbyaceus</i> ^a <i>Microcoleus vaginatus</i> ^a <i>Schizothrix calcicola</i> ^a <i>Anacystis montana</i> <i>Anacystis dimidiata</i>
64-01-0063	January 16, 1964	J. S. Zaneveld and W. I. Simmonds	Cape Evans Ross Island Lake B	Abundant greyish-green patches of growth on the bottom of meltwater.	<i>Calothrix parietina</i> ^a <i>Schizothrix calcicola</i> ^a <i>Nostoc sp. (old)</i> ^a
64-11-00148	November 13, 1964	J. S. Zaneveld, J. M. Curtis, and J. K. Fletcher	Cape Royds Clear Lake	Brownish, orange, and greenish growth. Along border of frozen lake.	<i>Microcoleus lyngbyaceus</i> <i>Schizothrix calcicola</i> ^a <i>Microcoleus vaginatus</i> ^a <i>Stichococcus flaccidus</i> <i>Schizogonium murale</i>
64-01-0207	January 17, 1964	T. E. Berg	Taylor Glacier Lake Chad, dry valley end. Snowbank Lake	Uppermost beach of Snowbank Lake.	<i>Nostoc commune</i> ^a <i>Microcoleus lyngbyaceus</i> ^a <i>Schizothrix calcicola</i> ^a

Table 1. (Cont'd)

Specimen No.	Date	Collectors	Location and description of collection site	Specimen appearance and habitat	Species identified
64-01-00328	January 9, 1964	J. S. Zaneveld and W. I. Simmonds	Marble Point	Brownish-green growth, up to 1.5-cm diameter. Along the border of meltwater pool.	<i>Microcoleus paludosus</i> ^a <i>Schizothrix calcicola</i> ^a <i>Nostoc</i> sp. (young) ^a <i>Protococcus grevillei</i>
64-01-0210	January 10, 1964	T. E. Berg	Walcott Glacier Valley	Greenish growth on salt.	<i>Schizothrix calcicola</i> ^a <i>Protococcus grevillei</i>
64-12-0092 (a-c)	December 28, 1964	J. S. Zaneveld, J. M. Curtis, and J. K. Fletcher	Cape Hodgson Black Island north by northwest of Cape	Dark purple growth. On mud along the border of meltwater pond.	<i>Microcoleus vaginatus</i> ^a
64-01-0031	January 14, 1964	J. S. Zaneveld and W. I. Simmonds	Cape Evans Ross Island	Dark green growth. On sloping bottom of basaltic lava in skua nesting place.	<i>Microcoleus vaginatus</i> ^a <i>Schizogonium murale</i> ^a
64-11-00108	November 11, 1964	J. S. Zaneveld, J. M. Curtis, and J. K. Fletcher	Cape Royds Ross Island Blue Lake	Orangish-green growth. On bottom of frozen lake.	<i>Microcoleus paludosus</i> ^a <i>Microcoleus lyngbyaceus</i> <i>Schizothrix calcicola</i> ^a <i>Nostoc commune</i> <i>Stichococcus bacillaris</i> <i>Microspora tumidula</i>
64-01-0112	January 26, 1964	J. S. Zaneveld and W. I. Simmonds	Cape Bird Ross Island	Bright green growth, when fresh. On rocks flooded by meltwater at the foot of the mountain.	<i>Prasiola crispa</i> ^a
64-02-0071	February 23, 1964	J. S. Zaneveld and W. I. Simmonds	Marble Point, west coast of Ross Sea Altitude: 25 ft	In a dry meltwater lake, approximately 500 ft offshore.	<i>Nostoc commune</i> ^a <i>Schizothrix calcicola</i>
64-12-0068	December 4, 1964	K. A. Wise	Shackleton Glacier area, east side of Barrett tributary glacier 84° 35' south, 173° 35' west Altitude: 1700-2300 ft	On moss. On top of hill.	<i>Anacystis marina</i> <i>Schizogonium murale</i>
^a Species identified by Dr. Francis Drouet.					



Map prepared by the American Geographical Society for the United States Antarctic Research Program under a grant from the National Science Foundation.

Fig. 7. Antarctica: northern algae sample collection area

A review of the phycological literature for freshwater algae of Antarctica (Ref. 7) shows that several of the algae identified in these samples may not have been reported previously. These would include *Schizogonium murale*, *Microspora tumidula*, *Stichococcus subtilis*, *S. flaccidus*, *Microcoleus paludosus*, *Oscillatoria chalybea*, and *Calothrix parietina*. However, because of unresolved differences in algal nomenclature, this cannot be stated with certainty and only a review of algal specimens collected and named by all previous investigators can resolve this problem. For example, 12 species of *Nostoc*, including 7 new taxa, have been described for Antarctica, but a microscopic examination of the specimens shows that morphologically they are all *Nostoc commune*! The numerous taxa and subtaxa of the Oscillatoriaceae described from Antarctica have been shown to be three common species (Ref. 8). Most of the coccoid blue-green algae can also be relegated to a few genera and species (Ref. 9).

Species of all algae identified in the Zaneveld collection are included in Table 2. Diagrams of the species, drawn from microscopic examination of the specimens, are given in Figs. 8 and 9. The observed algae included members of four families of blue-green algae and four families of green algae. Twelve species of blue-green algae and nine species of green algae were identified. Most of the algae were filamentous rather than coccoid forms.

The percent occurrence of each species is also indicated in Table 1. In general, the blue-green algae were observed more frequently than the green algae. The blue-green algae most frequently observed were *Schizothrix calcicola*, 60%; *Microcoleus vaginatus*, 39%; and *Microcoleus lyngbyaceus*, 27%. The most frequently observed green algae were *Protococcus grevillei*, 11%; and *Schizogonium murale*, 7%.

The greater percent of the species occurred in mesophilic or hydrophilic habitats, rather than xeric habitats (Table 2). There are evidently no algal species that are strictly xeric. However, certain morphological, and probably physiological, changes occur under xeric conditions. Filamentous green algae, e.g., *Stichococcus subtilis* and *Schizogonium murale*, become coccoid in arid soils. Until Antarctic algal material was examined it was not realized that *Schizogonium murale* was a component of desert soils and algal and lichen soil crusts, because it was observed only in the coccoid form in desert habitats. The Antarctic material showed the organism in various states of development, ranging from the coccoid through the filamentous state [Fig. 9 (g)].

b. Comparisons of Antarctic algae with other desert algae. Based upon the Zaneveld collection, the algae from Antarctica are similar to those found in other desert

Table 2. Occurrence of algal species in 100 samples collected from various Antarctic habitats

Blue-green algae	Occurrence, %	Habitat		Green algae	Occurrence, %	Habitat	
		Xeric	Mesophilic ^a			Xeric	Mesophilic ^a
Chroococcaceae				Volvocaceae			
<i>Anacystis dimidiata</i>	1		x	<i>Protococcus grevillei</i>	11	x	x
<i>Anacystis marina</i>	2		x	<i>Protococcus nivalis</i>	1		x
<i>Anacystis montana</i>	4		x	Ulotrichaceae			
<i>Coccochloris stagnina</i>	2		x	<i>Stichococcus bacillaris</i>	1		x
Nostocaceae				<i>Stichococcus flaccidus</i>	1		x
<i>Nostoc commune</i>	10		x	<i>Stichococcus subtilis</i>	3	x	x
<i>Nostoc sp.</i>	3	x	x	<i>Ulothrix flacca</i>	2		x
Rivulariaceae				<i>Ulothrix sp.</i>	8		x
<i>Calothrix parietina</i>	5		x	Microsporaceae			
Oscillatoriaceae				<i>Microspora tumidula</i>	1		x
<i>Microcoleus lyngbyaceus</i>	27		x	Schizogoniaceae			
<i>Microcoleus paludosus</i>	5	x	x	<i>Prasiola crispa</i>	5		x
<i>Microcoleus vaginatus</i>	39	x	x	<i>Prasiola sp.</i>	1		x
<i>Oscillatoria chalybea</i>	1		x	<i>Schizogonium murale</i>	7	x	x
<i>Oscillatoria irrigua</i>	1		x				
<i>Schizothrix calcicola</i>	60	x	x				

^aMay include hydrophilic habitats.

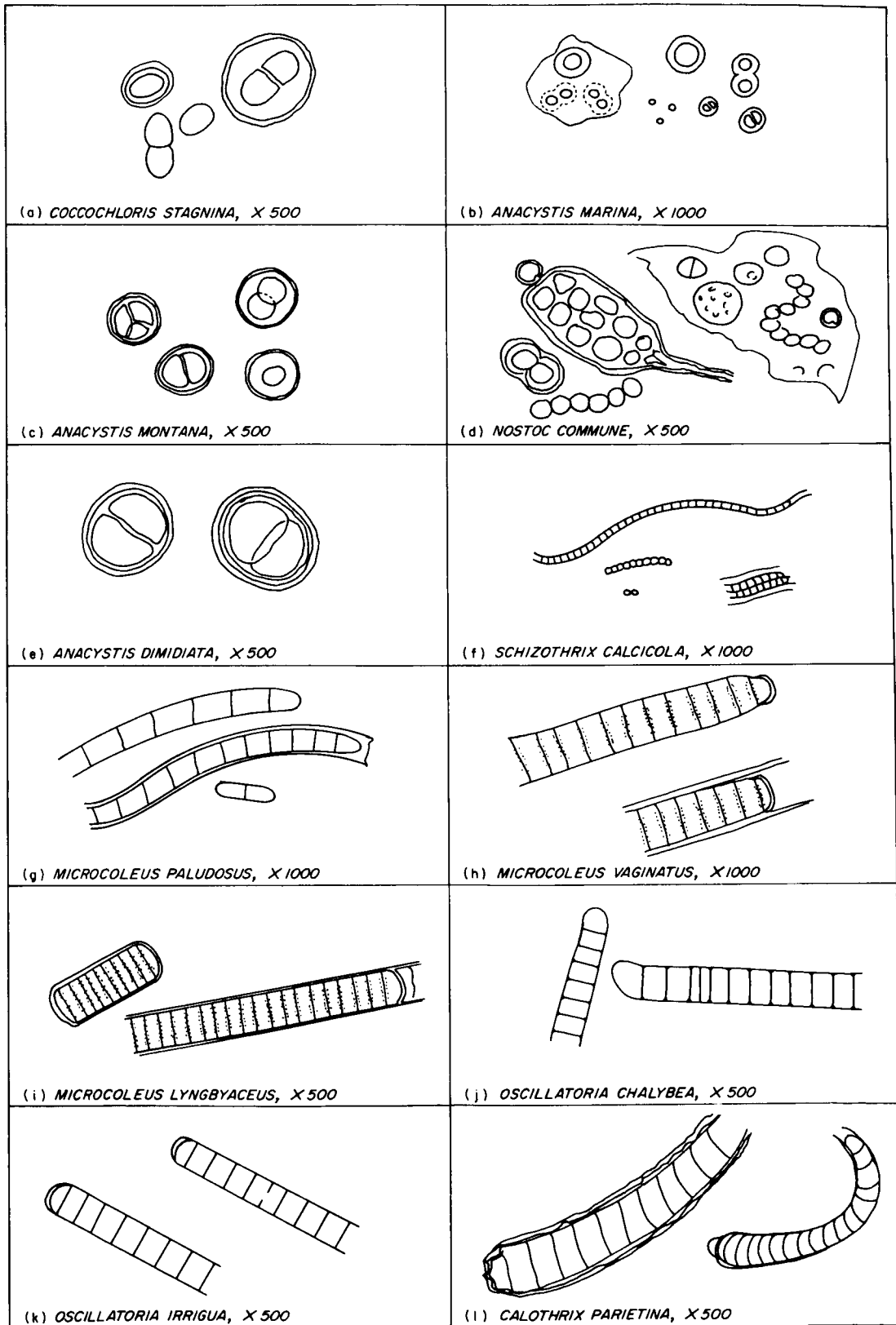


Fig. 8. Blue-green algae

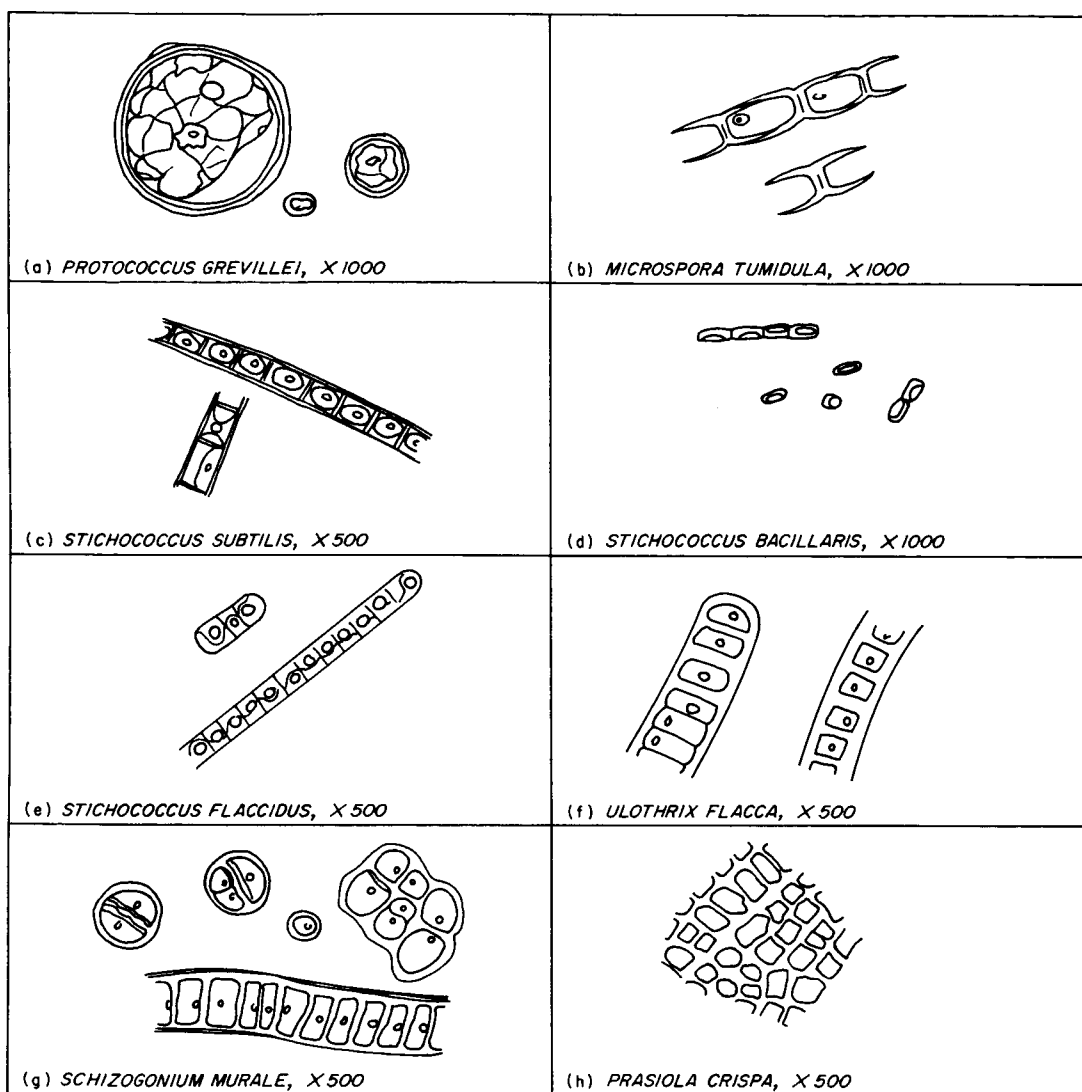


Fig. 9. Green algae

regions (Ref. 10). All of the blue-green algae (Table 2), have been found in temperate or tropical desert soils or more favorable environments having an adequate supply of available moisture. *Microcoleus paludosus*, *M. vaginatus*, and *Schizothrix calcicola* (Table 1) are typical components of desert soils. *Schizothrix calcicola* and *Microcoleus vaginatus* are the most abundant algae in Antarctica, as well as in desert regions. Although not observed in the Zaneveld collection, *Microcoleus chthonoplastes* is the third most abundant algal species in desert soils and it is also one of the three most common terrestrial oscillatorioid species in Antarctica (Ref. 8).

Protococcus grevillei, or similar coccoid algal forms, is the most abundant green alga in deserts. It is also appar-

ently one of the most abundant green algal species in Antarctica (Table 2.) *Schizogonium murale*, as indicated previously, may be more prevalent in desert soils than has been realized.

Some species of algae, which are relatively abundant in desert soils (Ref. 10) as well as other soils, were not observed in the Zaneveld collection and have not been reported for Antarctica (Ref. 7). Two of these species are *Scytonema hofmannii* and *Nostoc muscorum*. The reasons for their apparent absence in Antarctica are not known.

Moisture relationships and moisture availability have an obvious influence on the development of algae in Antarctica, as well as in typical desert regions. Members

of the *Chroococcaceae* (Tables 1 and 2) inhabit only mesophilic or hydrophilic environments whether in Antarctica or other regions. Typical *Nostoc commune* develops in desert regions, and apparently also in Antarctica, only when there is an adequate moisture supply for an extended time period. *Nostoc commune* is the only known alga from Antarctica that is capable of fixing atmospheric nitrogen (Ref. 11). *Calothrix parietina*, *Microcoleus lyngbyaceus*, and various *Oscillatoria* spp. also prefer mesophilic habitats and are not found in strictly xeric environments such as desiccated desert soils (Ref. 10).

Green algae observed in the Zaneveld collection also show the influence of moisture on their habitat (Tables 1 and 2). Filamentous green algae assume a coccoid form in xeric environments (Ref. 10). *Prasiola crispa* has not been found in deserts, but it forms a considerable and conspicuous development during the short summer season of melting ice in Antarctica (Ref. 9). Some species of *Prasiola* grow only in habitats rich in nitrogen compounds or in cold, swiftly flowing mountain streams (Ref. 12), and therefore would not be expected to occur in deserts. Although *Prasiola nevadensis* from a pool in a stream from Ruby, Arizona, has been described, an examination of the specimen shows that it is typical *Tetraspora gelatinosa*.

Lichenization or parasitization by fungi is a common feature shared by terrestrial Antarctic algae and the algae of warmer desert soils. The crustose lichen form is predominate in Antarctica (Ref. 13) and in other deserts (Ref. 10). Lichenization apparently permits a cooperative existence of fungi and algae in environments subjected to temperature extremes, periods of high solar radiation, wind and abrasion, rapid freeze-thaw cycles, desiccation, and prolonged drought.

Pigmentation of algal sheath material surrounding a trichome of cells, or in the matrix surrounding a group of cells, is a second conspicuous feature of desert algae and it is also apparent in Antarctic algae. In the Zaneveld collection, this phenomenon was observed for all members of the *Chroococcaceae*, *Nostoc commune*, *Calothrix parietina*, and filamentous masses of *Schizothrix calcicola*. Yellowish-brown to dark brown pigmentation evidently functions as a protective mechanism to solar radiation, temperature extremes, and drought. A hardening of the algal gelatinous material and formation of lamellations usually accompany the increase in pigmentation.

An increase in cell granules can also be observed. All of these factors may aid and protect Antarctic algae in their existence in an extremely harsh environment.

4. Concluding Remarks

Algal species were determined in all of the 100 specimens collected in Antarctica, primarily by Dr. J. S. Zaneveld. Twenty-one of the specimens were observed in detail by direct microscopic examination. Most of the algae were filamentous blue-greens. The most frequently observed blue-green algae were *Oscillatoriaceae*, including *Schizothrix calcicola*, *Microcoleus vaginatus*, and *Microcoleus lyngbyaceus*. The green algae were of lesser abundance. *Protococcus grevillei* was a typical coccoid green alga determined in 11 of the 100 specimens. A few diatoms were present in several of the specimens, including species of *Navicula* and *Fragillaria*.

Species which have not been previously reported for Antarctica were *Schizogonium murale*, *Microspora tumidula*, *Stichococcus subtilis*, *S. flaccidus*, *Microcoleus paludosus*, *Oscillatoria chalybea*, and *Calothrix parietina*. Several species of blue-green algae which are prominent in warmer desert regions are evidently absent in Antarctica. These included *Scytonema hofmannii* and *Nostoc muscorum*.

Except for *Prasiola crispa*, Antarctic algae in the Zaneveld collection have also been observed in temperate or tropical desert regions. Most of the Antarctic algae are mesophilic or hydrophilic species which grow and reproduce when water is available during the short Antarctic summer.

Protective mechanisms can be observed in some Antarctic algae which are also observed in other desert algae. These mechanisms included lichenization, brownish pigmentation, increased amount and consistency of sheath or matrix material, lamellation, and granule formation.

Physiological factors are undoubtedly important for Antarctic algae. The number of species which can be obtained in culture is far smaller than that originally present in samples (Ref. 11). By means of fluorescence microscopy, many of the algae examined in 21 of the specimens in the Zaneveld collection showed the red fluorescence of viable chlorophyll. Routine culture techniques did not promote the growth of these algae, although the cells remained viable throughout the incubation period. Preliminary cold or heat shock may promote the subsequent growth of Antarctic algae in culture. Reasons for failure in culturing Antarctic algae have been indicated by Holm-Hansen (Ref. 11).

References

1. Claridge, G. G. C., "The Clay Mineralogy and Chemistry of Some Soils from the Ross Dependency, Antarctica," *New Zealand Journal of Geology and Geophysics*, Vol. 8, pp. 186-220, 1965.
2. Stuart, A. W., and Bull, C., "Glaciological Observations on the Ross Ice Shelf near Scott Base, Antarctica," *Journal of Glaciology*, Vol. 4, pp. 399-414, 1963.
3. Eklund, C. R., and Beckman, J., "Antarctica," Holt, Rinehart and Winston, Inc., New York, 1963.
4. Llano, G. A., "The Flora of Antarctica," in "Antarctica," T. Hatherton, editor, Frederick A. Praeger, Publishers, New York, pp. 331-350, 1965.
5. Llano, G. A., "The Terrestrial Life of the Antarctic," *Scientific American*, Vol. 207, pp. 212-230, 1962.
6. Staley, J. T., and Boyd, W. L., "Soil Microorganisms of the Cape Hallett Area, Antarctica," *Ecological Society of America Bulletin*, Vol. 44, p. 38, 1963.
7. Hirano, M., "Freshwater Algae in the Antarctic Regions," in "Biogeography and Ecology in Antarctica," J. Van Mieghem and P. Van Oye, editors, Dr. W. Junk, Publishers, The Hague, pp. 127-193, 1965.
8. Drouet, F., "The Oscillatoriaceae and Their Distribution in Antarctica," *Polar Record*, Vol. 11, pp. 320-321, 1962.
9. Drouet, F., "A Brief Review of the Fresh-Water Algae of Antarctica," *Science in Antarctica. Part I: The Life Sciences in Antarctica. Publication 839. National Academy of Sciences, National Research Council, Washington, D.C.*, pp. 10-12, 1961.
10. Cameron, R. E. and Blank, G. B., "Desert Algae: Soil Crusts and Diaphanous Substrata as Algal Habitats," *Technical Report No. 32-971, Jet Propulsion Laboratory, Pasadena, California*, July 15, 1966.
11. Holm-Hansen, O., "Isolation and Culture of Terrestrial and Fresh-Water Algae of Antarctica," *Phycologia*, Vol. 4, pp. 43-51, 1964.
12. Smith, G. M., "The Fresh-Water Algae of the United States, Second Edition," McGraw-Hill Book Company, Inc., New York, 1950.
13. Dodge, C. W., "Lichens," in "Biogeography and Ecology in Antarctica," P. Van Oye and J. Van Mieghem, editors, Dr. W. Junk, Publishers, The Hague, pp. 194-200, 1965.

N67 12130

XV. Physics

A. On Rostoker's Test Particle Theorem

C.-S. Wu

Most analyses based on the BBGKY hierarchy involve rather complicated mathematical expressions, which greatly obscure the physical picture. Thus, attempts have been made to express results in terms of those obtained in the test particle problem. The works of Rostoker (Refs. 1 and 2) and Rosenbluth (Ref. 3) are particularly significant in this respect.

Here we attempt to show that within the framework of the Klimontovich formalism a theorem previously established by Rostoker (Ref. 2) can be recovered. For the sake of simplicity, we again consider a homogeneous plasma without external field. In this case, according to Rostoker, the time-asymptotic pair correlation function $G_{sr}(\mathbf{k}, \mathbf{v}, \mathbf{v}', t \rightarrow \infty)$ may be expressed as¹

$$n_s n_r G_{sr}(\mathbf{k}, \mathbf{v}, \mathbf{v}', t \rightarrow \infty) = P_{rs}^*(\mathbf{v}' | \mathbf{v}, \mathbf{k}, t \rightarrow \infty) n_s F_s(\mathbf{v}) + P_{sr}(\mathbf{v} | \mathbf{v}', \mathbf{k}, t \rightarrow \infty) n_r F_r(\mathbf{v}') \\ + \sum_q \int d^3 \underline{v} P_{sq}(\mathbf{v} | \underline{v}, \mathbf{k}, t \rightarrow \infty) P_{rq}^*(\mathbf{v}' | \underline{v}, \mathbf{k}, t \rightarrow \infty) n_q F_q(\underline{v}) \quad (1)$$

We shall call the time-asymptotic function $P_{sr}(\mathbf{v} | \mathbf{v}', \mathbf{k}, t \rightarrow \infty)$ the test particle function (in Fourier transform), which may be written as

$$P_{sr}(\mathbf{v} | \mathbf{v}', \mathbf{k}, t \rightarrow \infty) =$$

$$- \frac{4\pi e_s n_s \mathbf{k} \cdot \frac{\partial F_s}{\partial \mathbf{v}} e_r}{m_s k^2 \epsilon + (\mathbf{k}, \mathbf{k} \cdot \mathbf{v})(\mathbf{k} \cdot \mathbf{v} - \mathbf{k} \cdot \mathbf{v}' + i\lambda)} \quad (2)$$

P_{sr}^* represents the complex conjugate of P_{sr} . Here we remark that the reader should not confuse it with the operator $P_{sr}(\mathbf{v}, \mathbf{v}' | \mathbf{u}, \mathbf{u}', \mathbf{k}, -\mathbf{k})$ introduced in the preceding section.

To proceed with our discussion, we postulate that

$$\langle \delta N_s \delta N_r \rangle \sim \Delta \\ \langle \delta N_s \delta N_r \delta N_p \rangle \sim \Delta^2 \\ \langle \delta N_s \delta N_r \delta N_p \delta N_q \rangle \sim \Delta^2$$

¹We are considering a multispecies plasma.

where Δ is a small parameter.² Then it is easy to justify that if we only require our analysis to be accurate to first order in Δ , it is sufficient to replace the nonlinear equation (Ref. 5)

$$\frac{\partial N_s}{\partial t} + \mathbf{v} \cdot \nabla N_s - \frac{e_s}{m_s} \frac{\partial N_s}{\partial \mathbf{v}} \cdot \frac{\partial}{\partial \mathbf{v}} \sum_r e_r \int d^3 r' d^3 v' \frac{N_r(\mathbf{r}', \mathbf{v}', t)}{|\mathbf{r} - \mathbf{r}'|} = 0 \quad (3)$$

by the following approximate form, namely

$$\frac{\partial N_s}{\partial t} + \mathbf{v} \cdot \nabla N_s - \frac{n_s e_s}{m_s} \frac{\partial F_s}{\partial \mathbf{v}} \cdot \frac{\partial}{\partial \mathbf{v}} \sum_r e_r \int d^3 r' d^3 v' \frac{N_r(\mathbf{r}', \mathbf{v}', t)}{|\mathbf{r} - \mathbf{r}'|} = 0 \quad (4)$$

Since in this approximation the term we have neglected is proportional to $\delta N_s \delta N_r$, the error due to this approximation in the ultimate calculation of the function $\langle N_s(\mathbf{r}, \mathbf{v}, t) N_r(\mathbf{r}', \mathbf{v}', t) \rangle$ is of order Δ^2 .

Introducing the Fourier transform

$$N_s(\mathbf{k}, \mathbf{v}, t) = \int d^3 r e^{-i\mathbf{k} \cdot \mathbf{r}} N_s(\mathbf{r}, \mathbf{v}, t)$$

and solving Eq. (4) as an initial value problem, we can show that the time-asymptotic solution has the form³

$$N_s(\mathbf{k}, \mathbf{v}, t) = N_s(\mathbf{k}, \mathbf{v}, 0) e^{-i\mathbf{k} \cdot \mathbf{v} t} + \int d^3 \underline{v} \sum_q P_{sq}(\mathbf{v} | \underline{v}, \mathbf{k}) N_q(\mathbf{k}, \underline{v}, 0) e^{-i\mathbf{k} \cdot \underline{v} t} \quad (5)$$

The first term represents the solution without Coulomb interaction, and all particles move along straight lines. The second term represents the effect of polarization resulting from Coulomb interactions of the particles of s -species with particles of all species. Thus the test particle function P_{sq} can be viewed as a Green's function which characterizes the interaction between a particle of s -species with velocity \mathbf{v} and another particle of q -species with velocity \underline{v} . The resultant effect is therefore obtained by integrating over all values of \underline{v} and summing over all species. Now, since we can show that

$$\begin{aligned} \frac{1}{V} \langle N_s(\mathbf{k}, \mathbf{v}, t) N_r^*(\mathbf{k}, \mathbf{v}', t) \rangle &= \langle N_s(\mathbf{r}, \mathbf{v}, t) N_r(\mathbf{r}', \mathbf{v}', t) \rangle_{\mathbf{k}} \\ &= \int d(\mathbf{r} - \mathbf{r}') e^{-i\mathbf{k} \cdot (\mathbf{r} - \mathbf{r}')} \langle N_s(\mathbf{r}, \mathbf{v}, t) N_r(\mathbf{r}', \mathbf{v}', t) \rangle \end{aligned} \quad (6)$$

²A more formal and general statement can be made by introducing a cluster expansion as presented by Dupree (Ref. 4), but we will not make this effort.

³From now on, for simplicity, we will drop " $t \rightarrow \infty$ " in the argument of P_{sq} .

we find after substituting Eq. (5) into Eq. (6)

$$\begin{aligned}
 \langle N_s(\mathbf{r}, \mathbf{v}, t) N_r(\mathbf{r}', \mathbf{v}', t) \rangle_{\mathbf{k}} &= \langle N_s(\mathbf{r}, \mathbf{v}, 0) N_r(\mathbf{r}', \mathbf{v}', 0) \rangle_{\mathbf{k}} e^{-i\mathbf{k} \cdot (\mathbf{v} - \mathbf{v}') t} \\
 &+ \int d^3 \underline{\mathbf{v}}' \sum_q P_{rq}^*(\mathbf{v}' | \underline{\mathbf{v}}', \mathbf{k}) \langle N_s(\mathbf{r}, \mathbf{v}, 0) N_q(\mathbf{r}', \underline{\mathbf{v}}', 0) \rangle_{\mathbf{k}} e^{-i\mathbf{k} \cdot (\mathbf{v} - \underline{\mathbf{v}}') t} \\
 &+ \int d^3 \underline{\mathbf{v}} \sum_q P_{sq}(\mathbf{v} | \underline{\mathbf{v}}, \mathbf{k}) \langle N_q(\mathbf{r}, \underline{\mathbf{v}}, 0) N_r(\mathbf{r}', \mathbf{v}', 0) \rangle_{\mathbf{k}} e^{-i\mathbf{k} \cdot (\underline{\mathbf{v}} - \mathbf{v}') t} \\
 &+ \int d^3 \underline{\mathbf{v}} \int d^3 \underline{\mathbf{v}}' \sum_q P_{sq}(\mathbf{v} | \underline{\mathbf{v}}, \mathbf{k}) \sum_p P_{rp}^*(\mathbf{v}' | \underline{\mathbf{v}}', \mathbf{k}) \langle N_q(\mathbf{r}, \underline{\mathbf{v}}, 0) N_p(\mathbf{r}', \underline{\mathbf{v}}', 0) \rangle_{\mathbf{k}} e^{-i\mathbf{k} \cdot (\underline{\mathbf{v}} - \underline{\mathbf{v}}') t} \quad (7)
 \end{aligned}$$

However, we can write

$$\begin{aligned}
 \langle N_s(\mathbf{r}, \mathbf{v}, 0) N_r(\mathbf{r}', \mathbf{v}', 0) \rangle_{\mathbf{k}} &= (2\pi)^3 \delta(\mathbf{k}) n_s n_r F_s(\mathbf{v}, t) F_r(\mathbf{v}', t) \\
 &+ n_s n_r G_{sr}(\mathbf{k}, \mathbf{v}, \mathbf{v}', t) \\
 &+ n_s \delta_{sr} \delta(\mathbf{v} - \mathbf{v}') F_s(\mathbf{v}, t) \quad (8)
 \end{aligned}$$

and we observe that if we are only interested in the "long time" asymptotic behavior of the spectral function $\langle N_s N_r \rangle_{\mathbf{k}}$ we have

$$\begin{aligned}
 \langle N_s(\mathbf{r}, \mathbf{v}, 0) N_r(\mathbf{r}', \mathbf{v}', 0) \rangle_{\mathbf{k}} e^{-i\mathbf{k} \cdot (\mathbf{v} - \mathbf{v}') t} \\
 = (2\pi)^3 \delta(\mathbf{k}) n_s n_r F_s(\mathbf{v}, t) F_r(\mathbf{v}', t) \\
 + n_s \delta_{sr} \delta(\mathbf{v} - \mathbf{v}') F_s(\mathbf{v}, t) \quad (9)
 \end{aligned}$$

$$\begin{aligned}
 \sum_q \int d^3 \underline{\mathbf{v}}' P_{rq}^*(\mathbf{v}' | \underline{\mathbf{v}}', \mathbf{k}) \langle N_s(\mathbf{r}, \mathbf{v}, 0) N_q(\mathbf{r}', \underline{\mathbf{v}}', 0) \rangle_{\mathbf{k}} e^{-i\mathbf{k} \cdot (\mathbf{v} - \underline{\mathbf{v}}') t} \\
 = P_{rs}(\mathbf{v}' | \mathbf{v}, \mathbf{k}) n_s F_s(\mathbf{v}, t) \quad (10)
 \end{aligned}$$

$$\begin{aligned}
 \sum_q \int d^3 \underline{\mathbf{v}} P_{sq}(\mathbf{v} | \underline{\mathbf{v}}, \mathbf{k}) \langle N_q(\mathbf{r}, \underline{\mathbf{v}}, 0) N_r(\mathbf{r}', \mathbf{v}', 0) \rangle_{\mathbf{k}} e^{-i\mathbf{k} \cdot (\underline{\mathbf{v}} - \mathbf{v}') t} \\
 = P_{sr}(\mathbf{v} | \mathbf{v}', \mathbf{k}) n_r F_r(\mathbf{v}', t) \quad (11)
 \end{aligned}$$

$$\begin{aligned}
 \sum_q \sum_p \int d^3 \underline{\mathbf{v}} \int d^3 \underline{\mathbf{v}}' P_{sq}(\mathbf{v} | \underline{\mathbf{v}}, \mathbf{k}) P_{rp}^*(\mathbf{v}' | \underline{\mathbf{v}}', \mathbf{k}) \langle N_q(\mathbf{r}, \underline{\mathbf{v}}, 0) N_p(\mathbf{r}', \underline{\mathbf{v}}', 0) \rangle_{\mathbf{k}} e^{-i\mathbf{k} \cdot (\underline{\mathbf{v}} - \underline{\mathbf{v}}') t} \\
 = \sum_q \int d^3 \underline{\mathbf{v}} P_{sq}(\mathbf{v} | \underline{\mathbf{v}}, \mathbf{k}) P_{rq}(\mathbf{v}' | \underline{\mathbf{v}}', \mathbf{k}) n_q F_q(\underline{\mathbf{v}}, t) \quad (12)
 \end{aligned}$$

Making use of these expressions, we obtain

$$\begin{aligned}
 \langle N_s(\mathbf{r}, \mathbf{v}, t) N_r(\mathbf{r}', \mathbf{v}', t) \rangle_{\mathbf{k}} &= (2\pi)^3 \delta(\mathbf{k}) n_s n_r F_s(\mathbf{v}, t) F_r(\mathbf{v}', t) \\
 &- n_s \delta_{sr} \delta(\mathbf{v} - \mathbf{v}') F_s(\mathbf{v}, t) \\
 &= n_s n_r G_{sr}(\mathbf{k}, \mathbf{v}, \mathbf{v}', t) \\
 &= P_{rs}^*(\mathbf{v}' | \mathbf{v}, \mathbf{k}) n_s F_s(\mathbf{v}, t) + P_{sr}(\mathbf{v} | \mathbf{v}', \mathbf{k}) n_r F_r(\mathbf{v}', t) \\
 &+ \sum_q \int d^3 \underline{\mathbf{v}} P_{sq}(\mathbf{v} | \underline{\mathbf{v}}, \mathbf{k}) P_{rq}^*(\mathbf{v}' | \underline{\mathbf{v}}', \mathbf{k}) n_q F_q(\underline{\mathbf{v}}, t) \quad (13)
 \end{aligned}$$

This result represents Rostoker's formula for a multispecies plasma. It is apparent that Rostoker's theorem can be generalized to include a radiation field as well as an applied magnetic field very conveniently in the Klimontovich formalism.

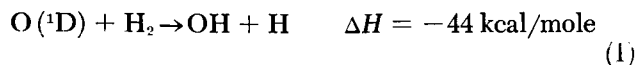
N67 12131

B. Reaction of O(¹D) With Hydrogen, Part II: The Unscavenged Case

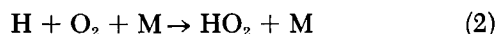
W. B. DeMore

1. Introduction

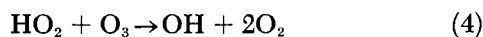
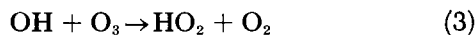
Part I of this report (SPS 37-39, Vol. IV, p. 157-161) described experiments on the photolysis of O₃-H₂-O₂ mixtures dissolved in liquid argon at 87°K. It was shown that O(¹D) reacts with H₂ with zero activation energy and that a major path is



Hydrogen atoms produced in Reaction (1) were found to be scavenged by O₂, as follows:



Therefore, the over-all scavenged reaction produces OH and HO₂ radicals. Product analysis showed that neither radical reacts with O₃ or H₂, and in particular that these radicals do not initiate a Norrish-type chain decomposition of O₃ (Refs. 6-8), in which the propagating steps are



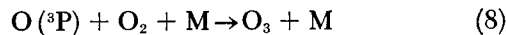
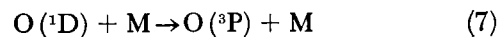
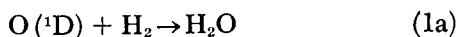
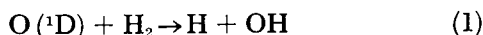
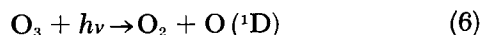
By contrast, H atoms not scavenged by O₂ react with O₃ and initiate a chain decomposition of O₃ which consumes at least 25 O₃ molecules per H atom. The present report describes experiments to determine the nature of the observed chain and the identity of the chain carriers.

2. Results

a. Chain length and chain termination. The total quantum yield (Φ_t) of O₃ disappearance consists of two parts: a contribution (Φ_s) from the initial photolysis process, and a contribution (Φ_c) from the chain process:

$$\Phi_t = \Phi_s + \Phi_c \quad (5)$$

The initial photolysis process is



As shown in Part I, Φ_s depends only on the H₂ concentration and is independent of O₂ in the concentration range used for scavenging. Therefore any observed dependence of Φ_t on O₂ concentration can be attributed to Φ_c .

The chain length L is defined by

$$L = \frac{\Phi_c}{\alpha\Phi_s} = \frac{1}{\alpha} \left(\frac{\Phi_t}{\Phi_s} - 1 \right) \quad (9)$$

where

$$\alpha = \frac{k_1}{k_1 + k_{1a}} \quad (10)$$

The number of chain cycles C is related to L by the expression

$$C = L/n \quad (11)$$

The quantity n is the number of O₃ molecules decomposed per chain cycle. It can be shown that

$$C = R_p / \Sigma R_t \quad (12)$$

where R_p is the rate of chain propagation, and ΣR_t is the sum of the rates of the termination steps.

Data on O₃ quantum yield behavior are plotted in Fig. 1 for two representative experiments. The different initial values of Φ_t/Φ_s are due to different initial concentrations of O₂ impurity. The ratio Φ_t/Φ_s declines rapidly as photolysis proceeds. Since a negligible quantity of H₂ is removed by the reaction, and since reaction products other than O₂ are not soluble in liquid Ar, the only significant changes occurring in the reaction mixture are disappearance of O₃ and appearance of O₂. It appears therefore that the decline of Φ_t/Φ_s is due to the inhibiting effect of O₂, and this idea is supported by the fact that Φ_t approaches Φ_s as photolysis nears completion.

No evidence can be found for any terminating process other than O₂ inhibition. Other terminating steps might become evident if it were possible to study the chain at lower O₂ concentrations, but it is impossible to do so because the system is self-inhibiting and also because some O₂ is present as an impurity. The extreme sensitivity of Φ_t to O₂ impurity can be illustrated by the fact that a 1-ppm O₂ impurity in the argon solvent provides as much

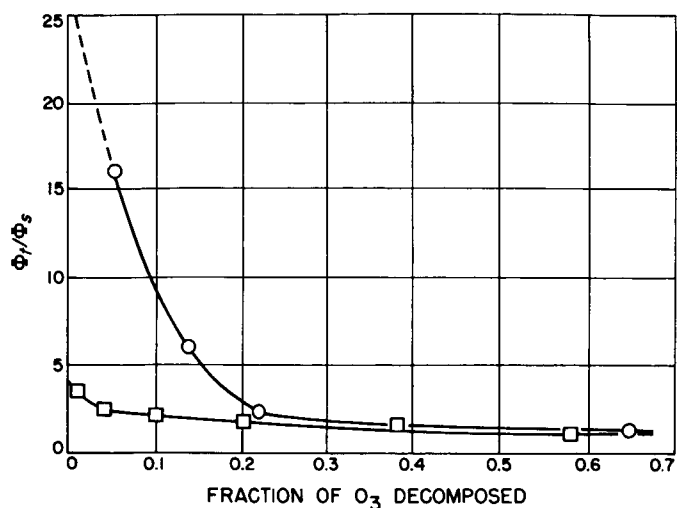


Fig. 1. Behavior of Φ_t/Φ_s for two representative experiments, showing decline of Φ_t/Φ_s as photolysis proceeds

O_2 as 10% decomposition of O_3 in a typical experiment. From Fig. 1, it can be seen that 10% decomposition of O_3 produces a drastic decrease in Φ_t/Φ_s .

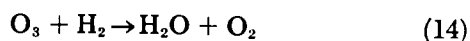
Since chain propagation involves a reaction with O_3 , the foregoing results combined with Eq. (12) show that the number of chain cycles C is proportional to the ratio O_3/O_2 in a particular mixture.

The data of Fig. 1, together with Eq. (9), show that chain lengths of at least 25 are obtained at high O_3/O_2 ratios. If α is less than unity, then the actual chain lengths will be proportionately greater.

b. Chain stoichiometry. Using methods described in Part I of this work, product analyses for water were carried out to determine if the chain stoichiometry is



or if both O_3 and H_2 are consumed concurrently, giving one H_2O per O_3 decomposed:



From Part I it is known that the initial photolytic reaction gives one H_2O per O_3 decomposed. The latter H_2O yield is independent of the chain process. Therefore the minimum expected H_2O yield, excluding any possible contribution from the chain, is given by

$$\frac{dH_2O}{dO_3} = -\frac{\Phi_s}{\Phi_t} \quad (15)$$

Eq. (15) can be integrated to give

$$\frac{\Delta H_2O}{-\Delta O_3} = \left(\frac{\Phi_s}{\Phi_t} \right)_{av}. \quad (16)$$

The quantity $(\Phi_s/\Phi_t)_{av}$ is the average value of the ratio (Φ_s/Φ_t) with respect to the fraction of O_3 decomposed, and may be obtained graphically from data plotted as in Fig. 1.

Eq. (16) thus gives the expected H_2O yield if the chain stoichiometry corresponds to Eq. (13). If the chain stoichiometry is that of Eq. (14), an H_2O yield of unity will be expected.

Table 1. Water analysis in the partly scavenged case ($D_2 = 0.14$ moles/liter)

O ₃ concentration, moles/liter × 10 ⁴		O ₃ decomposed, μ moles	D ₂ O produced, μ moles	D ₂ O yield, %	Φ _t /Φ _s		
Initial	Final				Initial	Final	Average ^a
6.2	1.34	1.90	1.63	86	1.2	1.1	1.15
4.7	0.22	1.75	1.39	79	1.95	1.0	1.47
4.8	0.22	1.79	1.18	66	3.5	1.2	1.8
8.0	2.6	2.11	0.60	28	16.0	1.3	4.5

^aAverage Φ_t/Φ_s was estimated graphically.

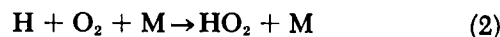
Table 1 shows water yields for experiments with varying average chain contributions to the over-all O_3 decomposition. For analytical reasons the experiments were carried out with D_2 instead of H_2 , and the subsequent discussion is based upon the assumption that there is no isotope effect in the water yield. The data are tabulated in order of increasing chain contribution. The results show clearly that the water yield decreases with increasing chain contribution. In each case the water yields can be accounted for, within experimental accuracy, by the non-chain process, i.e., by Eq. (16). The conclusion, therefore, is that the chain stoichiometry is $O_3 \rightarrow 3/2 O_2$.

3. Discussion

All of the results point to chain propagation by the reaction



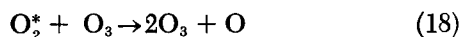
and chain termination by



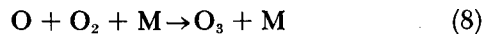
The asterisk in OH* is to distinguish OH produced by Reaction (17) from that formed by other processes. Evidence will be given that the reactivity of OH depends in some cases on the mode of formation, probably reflecting different degrees of vibrational excitation.

Questions then arise concerning two points: (1) the identity of the chain carrier produced by Reaction (17), and (2) the nature of the chain-propagating reaction which this carrier undergoes.

O₂ is a product of Reaction (17) but can be ruled out as a possible chain carrier. Although Reaction (17) could produce vibrationally or electronically (¹Δ_g or ¹Σ_g⁺) excited O₂, the only possible reaction with O₃ for any of these states would be



It is known that O atoms cannot propagate chain decomposition of O₃ in the present experiments, since their only fate is

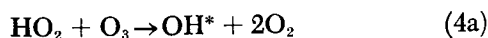
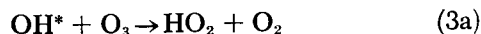


The foregoing argument is supported by the fact that photolysis of O₃ under similar conditions (Ref. 9), but with no H₂ present, does not result in chain decomposition, although both electronically and vibrationally excited O₂ are probably formed.

It may be concluded therefore that the chain carrier produced by Reaction (17) must be OH* and that OH* is more reactive than OH from Reaction (1). Electronic excitation of OH* is not a possibility since the first excited state of OH, ²Σ⁺, requires 92.5 kcal/mole and only 77 kcal/mole are available. On the other hand, the exothermicity of Reaction (17) is sufficient to excite OH* to the 9th vibrational level, and in fact infrared emission from levels up to the 9th has been observed (Ref. 10). It appears therefore that OH* can only be identified as vibrationally excited OH.

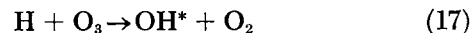
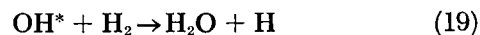
Turning now to question (2) previously mentioned, there are three possible sets of chain-propagating reactions which must be considered:

Set 1: Catalyzed chain decomposition of O₃ with OH* and HO₂ as carriers.



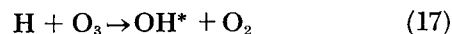
This mechanism, which is similar to the Norrish chain (Refs. 6-8), can be ruled out on grounds that HO₂ is known from previous results not to react with O₃ in the present reaction system. In addition, regeneration of OH* by Reaction (4a) could not reasonably be expected to occur with sufficient efficiency to explain the observed chain lengths.

Set 2: Chain oxidation of H₂ with OH* and H atoms as carriers:



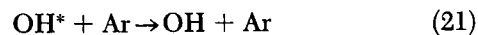
This mechanism is satisfactory in principle but can be ruled out as an important path because the chain does not produce water, as found by the product analysis results.

Set 3: Catalyzed chain decomposition of O₃ with OH* and H atoms as carriers:



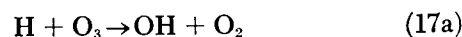
Reaction (20) was first proposed in a previous report from this Laboratory (SPS 37-38, Vol. IV, p. 152) to account for observations on the chain decomposition of O₃ in the gas phase. Arguments are given in SPS 37-38 to show that Reaction (20), although endothermic by 9 kcal/mole for OH, is not an improbable reaction of OH*.

Set 3 seems to be the only mechanism that is consistent with all the experimental observations. It does require however, that OH* have a lifetime of at least 10⁻⁶ sec in liquid argon, employing for this calculation the assumption that Reaction (20) has a rate constant not greater than 10¹⁰ liter/mole-sec, and taking a typical O₃ concentration of 10⁻⁴ mole/liter. For an estimated collision rate of 10¹² sec⁻¹ in liquid argon, the results therefore suggest that the reaction (at 87°K)



has a collision efficiency less than 10⁻⁶.

The results also provide information on the efficiency of OH* production by Reaction (17). If Reaction (17) occurred to some extent as follows:

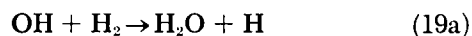


then the number of chain cycles C [Eq. (12)] would be given by

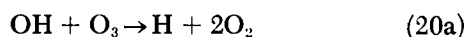
$$C = \frac{k_{17}}{k_{17a} + k_2 [O_2]/[O_3]} = L/n \quad (12a)$$

The experiments show that $L \geq 25$ and (from the proposed mechanism) $n = 2$, so that $C \geq 12$. It follows that $k_{17} \geq 12 k_{17a}$. In fact k_{17} is probably still greater compared to k_{17a} , because the dominant term in the denominator of Eq. (12a) arises from O_2 termination. It may be concluded that Reaction (17) produces OH^* with an efficiency of at least 92% and probably considerably greater. These results have an important bearing on the atmospheric Meinel bands, which are believed to arise from vibrationally excited OH produced by Reaction (17) (Ref. 11).

It is particularly noteworthy that OH^* reacts with O_3 but not H_2 , despite the fact that the H_2/O_3 ratio was approximately 200. The water yields in Table 1 require that k_{20}/k_{19} be at least 10^3 . The activation energy of the reaction



is not known with certainty but probably does not exceed 6 kcal/mole (Ref. 12). On the other hand, reaction of OH with O_3 according to

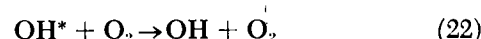


must have an activation energy of at least 9 kcal/mole, which is the endothermicity. Both Reactions (19) and (20) are exothermic even for the $v'' = 1$ vibrational state

of OH^* , which carries 10.2 kcal/mole. The results therefore show that vibrational energy of OH^* can be successfully used to overcome the activation energy of Reaction (20a) but not (19a). In general, very little is known about the effect of vibrational excitation in overcoming activation energy barriers. The present results suggest that the magnitude of the activation energy is not necessarily the determining factor.

A final point to be emphasized is the apparent failure of Reaction (1) to produce vibrationally excited OH capable of reacting according to Reaction (20). Reaction (1) is exothermic by 44 kcal/mole and could produce OH with up to four quanta of vibrational excitation. Gas phase studies of Reaction (1) have revealed emission from levels up to the second (Refs. 13 and 14). The present results indicate however that OH^* either is not formed with appreciable efficiency by Reaction (1) or else does not persist long enough to react with O_3 because of a lower initial state of excitation. A third possibility is that OH^* from Reaction (1) is unreactive compared to OH^* from Reaction (17) because of lower vibrational excitation.

The possibility exists, though somewhat remotely, that O_2 efficiently deactivates OH^* and thus serves as a chain terminator by the following reaction



This would account for the apparent unreactivity of OH^* produced in Reaction (1), since O_2 was present as a scavenger under conditions where Reaction (1) failed to initiate chain decomposition. Evidence against this hypothesis is that added CF_4 , in concentrations similar to O_2 , did not stop the chain.

References

1. Rostoker, N., *The Physics of Fluids*, Vol. 7, p. 479, 1964.
2. Rostoker, N., *The Physics of Fluids*, Vol. 7, p. 491, 1964.
3. Rostoker, N., and Rosenbluth, M. N., *The Physics of Fluids*, Vol. 3, p. 1, 1960.
4. Dupree, T. H., *The Physics of Fluids*, Vol. 6, p. 1714, 1963.
5. Klimontovich, Yu. L., *Zh. Eksperim. i. Teor. Fiz.*, Vol. 37, p. 735, 1959, (Translated from *Soviet Physics-JETP*, Vol. 10, p. 524, 1960).

References (Cont'd)

6. Norrish, R. G. W., and Wayne, R. P., *Proceedings of the Royal Society*, Vol. 288A, p. 361, 1965.
7. McGrath, W. D., and Norrish, R. G. W., *Nature*, Vol. 183, p. 235, 1958.
8. McGrath, W. D., and Norrish, R. G. W., *Proceedings of the Royal Society*, Vol. 254A, p. 317, 1960.
9. DeMore, W. B., and Raper, O. F., "Primary Processes in Ozone Photolysis," *The Journal of Chemical Physics*, Vol. 44, p. 1780, 1966.
10. Garvin, D., Broida, H. P., and Kostkowski, H. J., *Journal of Chemical Physics*, Vol. 32, p. 880, 1960.
11. Meinel, A. B., *Astrophysics Journal*, Vol. III, p. 555; Vol. 112, p. 120, 1950.
12. Kaufman, F., *Annales de Geophysique*, Vol. 20, p. 106, 1964.
13. Basco, N., and Norrish, R. G. W., *Canadian Journal of Chemistry*, Vol. 38, p. 1769, 1960.
14. Basco, N., and Norrish, R. G. W., *Proceedings of the Royal Society*, Vol. 260A, p. 293, 1961.

TELECOMMUNICATIONS DIVISION

N67 12132

XVI. Spacecraft Telemetry and Command

A. A System Reorganization of the Spacecraft Data Encoder

J. R. Kinkel

1. Introduction

The multiplexer, as a focal point for all spacecraft telemetry, must be capable of failing gracefully in the presence of catastrophic component failures. The probability that failures will corrupt sources of information increases sharply with the number of sensors to be multiplexed. To localize these failures, a new system organization and its implementation have been investigated simultaneously.

Two techniques were applied to achieve partial degradation on the *Mariner C* multiplexer. These may be called *double addressing* and *short counting*. *Double addressing* occurs when a switch on one multiplexer deck controls another deck of switches. Any one sensor on the subdeck must be addressed by two switches to be sampled. *Short counting* occurs because the analog

switches are sequenced by a shift register. When shifting fails in midregister, all analog switches beyond the failed stage cannot be addressed. Obviously, both techniques permit failure localization; however, in this paper an attempt will be made to reveal more graceful methods of degradation; i.e., less operational equipment will be sacrificed upon failure.

2. Integrated Circuits

a. Characteristics. Since the performance of a large switching array, such as the multiplexer, is heavily dependent on device technology, it is only natural that implementation with integrated circuits become a significant part of this investigation. The tight packing density and promise of reliability and power reduction have led to an exclusive consideration of metal-oxide-silicon field-effect transistors (MOS FET). Only those characteristics of the MOS FET crucial to this investigation will be discussed.

The MOS FET is a four-terminal device known for its isolation between the gate-substrate source-drain pair.

The electrical characteristics are like those of a pentode; a threshold voltage is defined by some value of conduction current. The sharp cutoff causes the apparent resistance of the source-drain path to vary abruptly from 10^3 to $10^{12} \Omega$. This behavior has led circuit designers to use the device as an approximation to an ideal switch. A slight digression to examine the physical characteristics of the MOS FET will reveal how misapplication can compromise the isolation between signals and thereby propagate failures.

Two channels of P-type material are diffused into an N-type substrate; these form the source and drain in Fig. 1. A path of P-type material in the substrate is created by a field between the source and drain. The field is caused by the presence of a dielectric—silicon dioxide—between the aluminum gate and the substrate. A negative gate potential, -5 to -20 v, causes current to flow from source to drain. The device is bilateral; source and drain are determined by their respective voltages.

b. Failure modes. Currently, the most common failure mode is caused by bonding external leads to the substrate, which results in both short and open circuits. As simple screening procedures usually eliminate these failures, they are of minor concern. Source-drain shorts caused by bulk semiconductor defects can also be detected in advance. However, short circuits between the gate and source-drain path, which are caused by puncturing the oxide layer and shorting the aluminum to the substrate, can occur after testing. A charge buildup or overvoltage applied to the gate will rupture the oxide, but good circuit design should prevent this phenomenon.

The presence of impurities or pinholes in the oxide layer permits a smaller voltage to rupture the dielectric. These cannot be detected by nondestructive testing or avoided by conservative circuit design. Although contamination of the oxide dielectric is very rare, it is impossible to predict when or where a short may occur. Therefore, redundancy techniques such as the quad switch (Fig. 2) *do not* increase reliability; rather they expose more gates to the possibility of rupture. *An objective of this investigation has been to prevent this type of failure from degrading the system.*

3. Transformation

a. Derivation. System reorganization was obviously necessary because (1) the multiplexer is the intersection of two switching trees, and (2) the opportunity for failure localization is extended by isolating these trees. To compare the new structure with the current system organization, a transformation will be discussed. This should show that the new organization is at least as reliable as the former and, in addition, possesses certain other desirable characteristics. Naturally, some problems of implementation arise; the solution of these will be covered in the remainder of the paper.

An abstraction of the *Mariner C* data encoder is shown in Fig. 3(a). Only one analog-to-digital converter (A/DC) is required because the analog switches of the multiplexer sample the sensors sequentially. Some failures in the multiplexer will mix signals from two or more sensors, with a resultant loss of information. When the A/DC fails to convert, all information is lost.

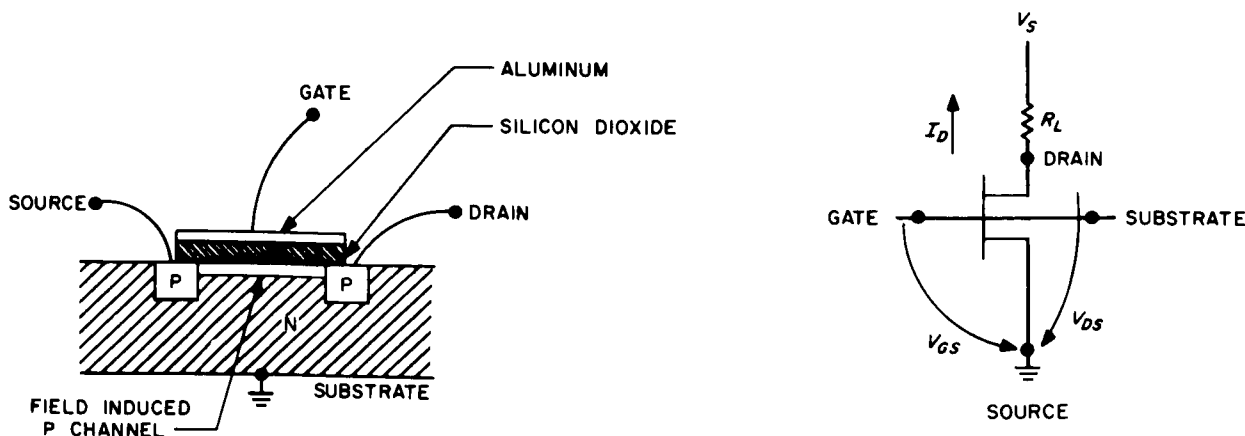


Fig. 1. Metal-oxide-silicon field-effect transistor

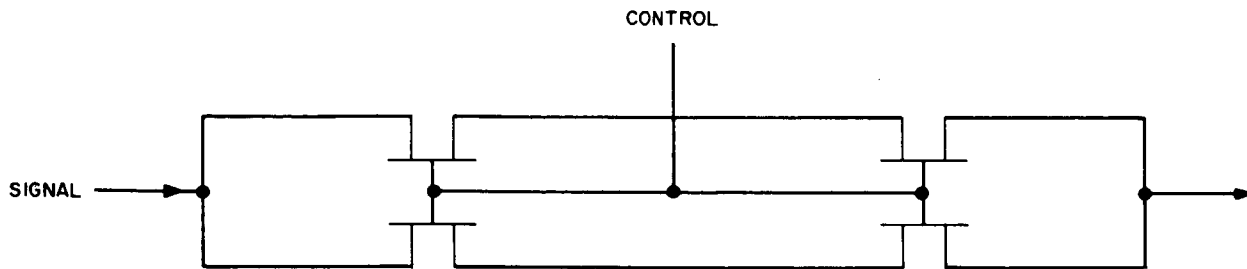


Fig. 2. MOS FET quad switch

In Fig. 3(b), several converters are shown; these prevent the loss of one A/DC from completely degrading the system. Each converter samples only one sensor, and the digitalized samples are interleaved by the multiplexer. *With independent signal processing before multiplexing, the system is not significantly degraded by the loss of an A/DC.* The functional characteristics of the multiplexer are essentially unchanged; less noise may be introduced by digital switching. The minimization of power consumption, weight, and volume will be outlined in detail.

Fig. 3(c) shows the shift registers implicit in each A/DC and the sequencer associated with the multiplexer. In Fig. 3(d), the sequencer is removed from the multiplexer and used for sequencing the A/DC shift registers. The multiplexer switching array is eliminated and the shift register becomes a switch functionally. With this organization the switching trees for addressing and gating are independent and contribute to the localization of failures. The introduction of individual converters has eliminated the total dependence on one A/DC and led to a dependable interface between sensors and the channel.

The shift register clearly isolates sensor or converter failures from the channel or other portions of the encoder. These failures may be propagated as data—all 1's, all 0's, or some truncated count—but only component failures in the last shift register stage can degrade the system.

b. Implications. Two implications of this system organization are worthy of mention. First, system complexity is a direct function of the number of sensors. Neither the dimension of the encoder or relationship of the sensors are constrained by signal processing: level adjustments, filtering, and conversion. *The consolidation of signal conditioning for each sensor will avoid the multiplicity of interfaces and noise problems which*

arise in a large system. Second, the sampling time and multiplexing rate become independent with parallel conversion. The sampling time is determined by the sensor response; multiplexing becomes a sequential interrogation of shift registers. This is a significant step toward obtaining mission independent equipment.

4. System Implementation

a. Pulse-width conversion. Analog-to-digital conversion for each sensor by the successive approximation method is impractical, as the power consumption, weight, and volume are excessive. The conversion is unnecessarily fast for the spacecraft sampling rates under consideration. To reduce the converter complexity—power, weight, and volume—slower conversion techniques were investigated. Of these, one of the simplest to implement with integrated circuits is a derivative of the ramp method.

The following circuit is not complete, but does convey the necessary information. Section 6 contains a discussion of experimental results and temperature compensation of the threshold voltage. In Fig. 4, the *negative voltage* E is applied to the capacitor when T1 is turned off. The resistance R_1 limits the current when T1 conducts. The voltage E exceeds the threshold voltage V_T of T2. With T2 conducting, the output voltage V_o remains at ground. As the gate voltage V_1 passes V_T , T2 turns off, and V_o returns to the supply voltage. By restricting E , the decay can be held to a linear portion of the exponential.

The time to reach the threshold voltage is obtained from

$$V_T = E \exp\left(\frac{-t}{RC}\right)$$

$$t = RC \ln \frac{E}{V_T}$$

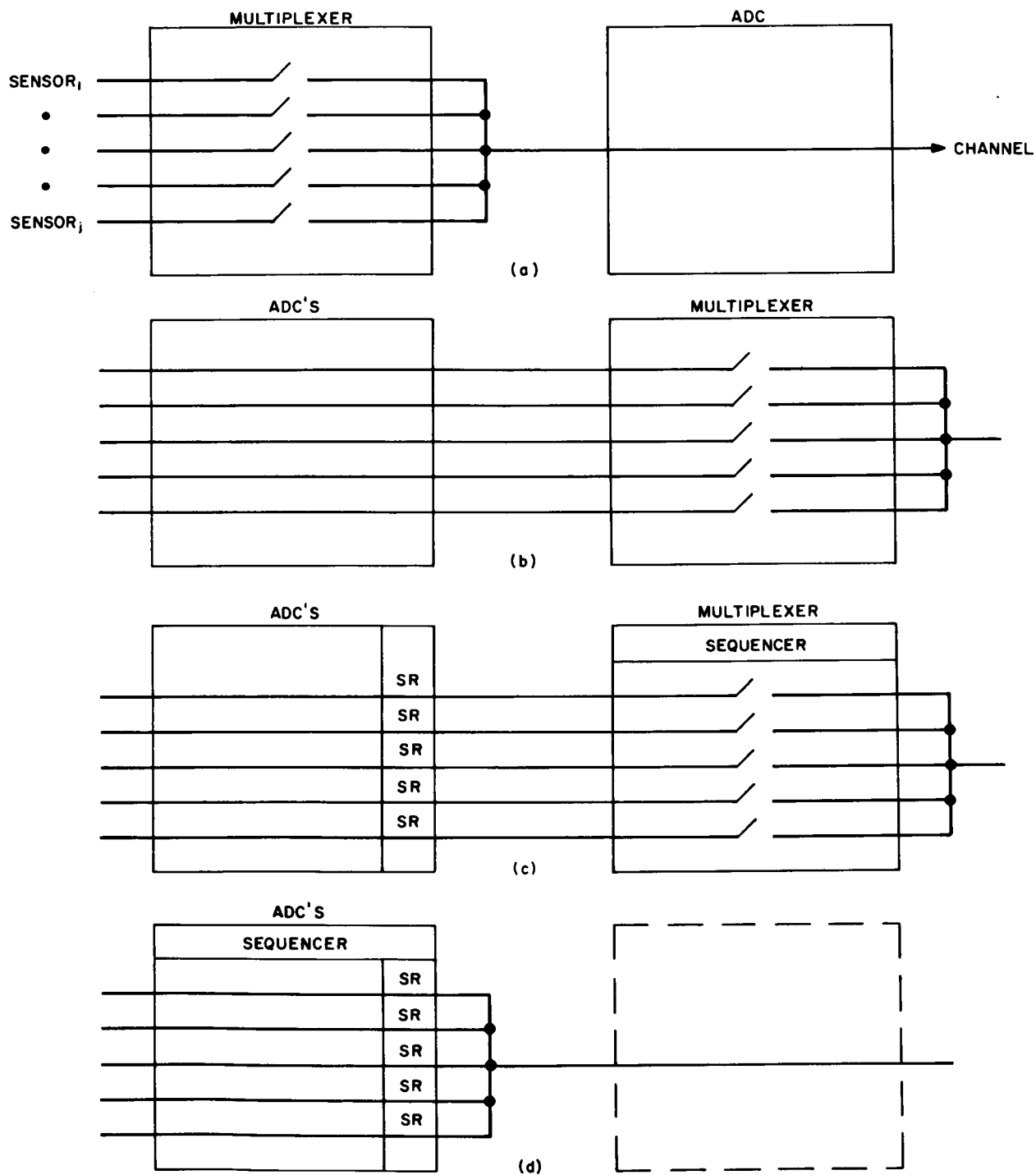


Fig. 3. System transformation

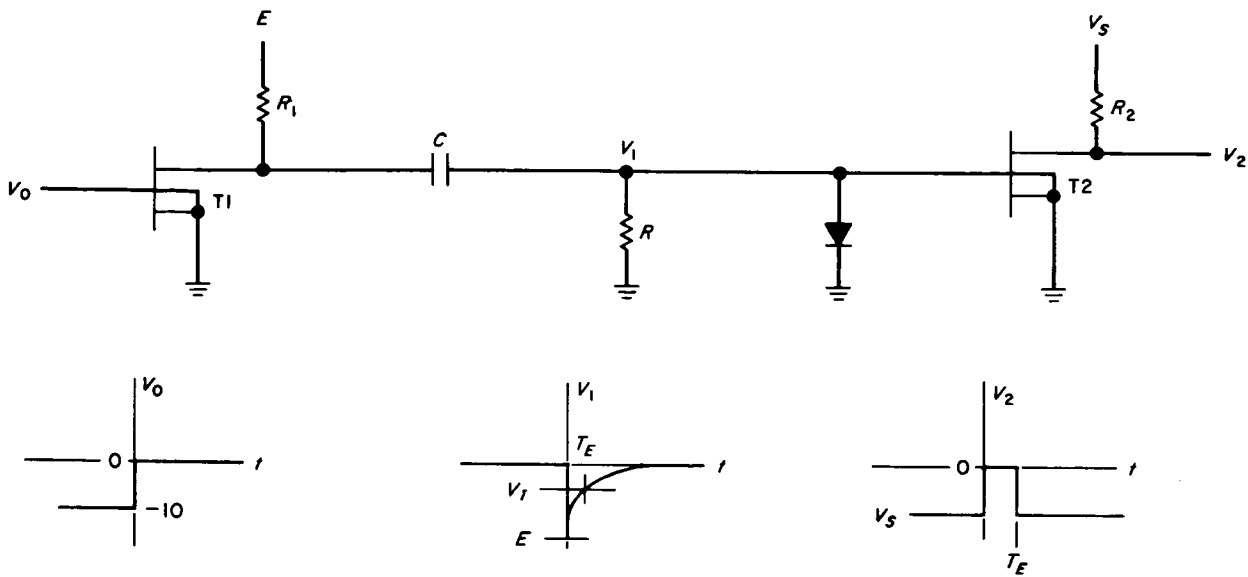


Fig. 4. Pulse-width conversion

where, for stability purposes,

$$V_T > E_1 \geq E \geq E_2.$$

Counting begins at

$$t_1 = RC \ln \frac{E_1}{V_T}$$

with a pulse width

$$\begin{aligned} t - t_1 &= RC \ln \left(\frac{E}{V_T} \right) - RC \ln \left(\frac{E_1}{V_T} \right) \\ &= RC \ln \frac{E}{E_1} \end{aligned}$$

To remain within a reasonably linear portion of the exponential curve

$$\frac{E_2}{E_1} = 1.11$$

so that

$$\ln \frac{E_2}{E_1} = 0.1044$$

The slope is

$$\frac{\partial t}{\partial E} = \frac{RC}{E}$$

and comparing the extremes

$$\frac{\frac{\partial t}{\partial E_{E=E_1}}}{\frac{\partial t}{\partial E_{E=E_2}}} = \frac{E_2}{E_1} = 1.11$$

Switching time of the MOS FET indirectly determines the minimum conversion time. State-of-the-art MOS FET counters consume very little power at 50 kHz. With two new developments—four-phase clocking and complementary logic—250-kHz counters will be available with no additional power consumption. Therefore a design goal has been to convert within 2 msec by counting during 1 msec with a 256-kHz clock. A maximum sampling rate of 250 samples/sec is permitted by allowing 2 msec for conversion and 2 msec during which the sample is multiplexed. This is the maximum sampling rate contemplated for a data compression system. Higher rates may be obtained by multiple converters properly phased.

To meet the design goal, the time constant is given by

$$\begin{aligned} t_2 - t_1 &= RC \ln \frac{E_2}{E_1} \\ &= RC(0.1044) = 10^{-3} \text{ sec} \\ RC &\approx 10^{-2} \end{aligned}$$

This product is not obtainable with the gate capacitance and back resistance of the MOS FET because of the

temperature instability of the resistance. Discrete components may be the only solution, since the product is beyond the range available with thin films. The remainder of the system, including regulation of the supply voltage, is realizable with the MOS FET technology.

b. Counter-shift register. As the counting rate determines the maximum sampling rate, the time to transfer information out of the counter determines the multiplexing rate. Since multiplexing requires a high-speed information transfer, it is not desirable to *count out* the digitalized sample. Sufficient speed is available with a shift register. A procedure for using the counter as a shift register will be outlined. This is motivated by two conditions: first, both counter and shift register must operate successfully to transfer information; second, parallel information transfer from the counter to the shift register can lead to undetectable failures which alter the information.

The derivation of a shift register from a counter is based on the realization that shifting is multiplication by 2 or adding a number to itself. With a ripple-through counter and with logic that simultaneously resets each 1 to 0, shifting is obtained. As an example, consider shifting (right) the following count, where σ is the time between shift pulses and ϵ is the flip-flop delay ($\sigma > 2\epsilon$).

Contents	Time
1 1 0 1 0 0 1	t_0
0 0 0 0	$t_0 + \epsilon$
0 1 1 0 1 0 0	$t_0 + 2\epsilon$
0 0 0	$t_0 + \sigma + \epsilon$
0 0 1 1 0 1 0	$t_0 + \sigma + 2\epsilon$
0 0 0	$t_0 + 2\sigma + \epsilon$
0 0 0 1 1 0 1	$t_0 + 2\sigma + 2\epsilon$
...	...
0 0 0 0 0 0 0	$t_0 + 6\sigma + \epsilon$

The counter-shift register is shown in Fig. 5. The shift pulses gated by the address tree and the output from the pulse-width converter are mutually exclusive inputs. When counting, the OR gates and flip-flops form a ripple-through counter. The state of the flip-flop is toggled by an input pulse; the Q output level indicates the *on* state, and the 1-0 output yields a pulse during the *on-off* transition. Shifting is performed by those flip-flops in the *on* state permitting themselves to be toggled. Before the next shift pulse, the flip-flops undergoing an *on-off* transition toggle the next successive flip-flops, thereby shifting

all 1's one stage. The OR gates delay the shifted pulses slightly to avoid hazards.

c. Addressing. In Fig. 3(d), the sequencer addresses the shift registers for multiplexing. Shift registers for gating analog switches have been used to minimize logic, with the penalty of *short counting* upon failure. To avoid logic dependencies in the addressing tree, a mechanism based on a counter and decoding logic is proposed. A comparison of the two schemes will reveal the reliability advantage of eliminating the serial dependence on a shift register.

Counter and shift register addressing trees are shown in Fig. 6. Pulses are used to shift a single 1 into, through, and out of the shift register, permitting at most one analog sensor to be gated at a time. The all *off* condition exists when the shift register contains all 0's. In comparison, the n -stage counter counts the input pulses modulo 2^n . N field-effect transistors decode the state of the counter to gate the shift pulses which clear one A/DC shift register. The all *off* condition exists when there are no shift pulses present; with the pulses, any state of the counter would clear some shift register.

Table 1 is a comparison of the number of sensors that become unaddressable when an *on/off* flip-flop failure occurs. The counter has only three stages; failures in the fourth through eighth stages are meaningless. *Short counting* occurs when a shift register flip-flop fails in the *off* state; all sensors associated with stages preceding the failed stages remain addressable. The failure of a shift register in the *on* state leaves only the failed-stage sensor addressable. A source-drain short circuit in an analog switch leads to exactly the same result.

Table 1. Sensor loss upon failure

Flip-flop stage	Counter		Shift register	
	Off	On	Off	On
1	7	7	8	7
2	6	6	7	7
3	4	4	6	7
4	0	0	5	7
5	0	0	4	7
6	0	0	3	7
7	0	0	2	7
8	0	0	1	7

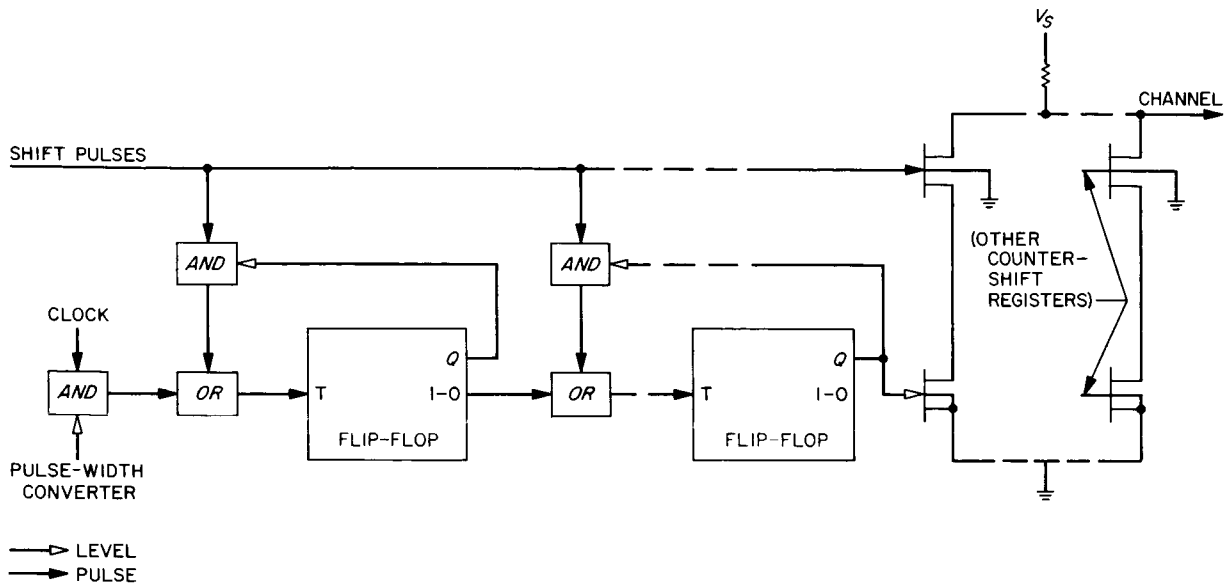


Fig. 5. Counter-shift register

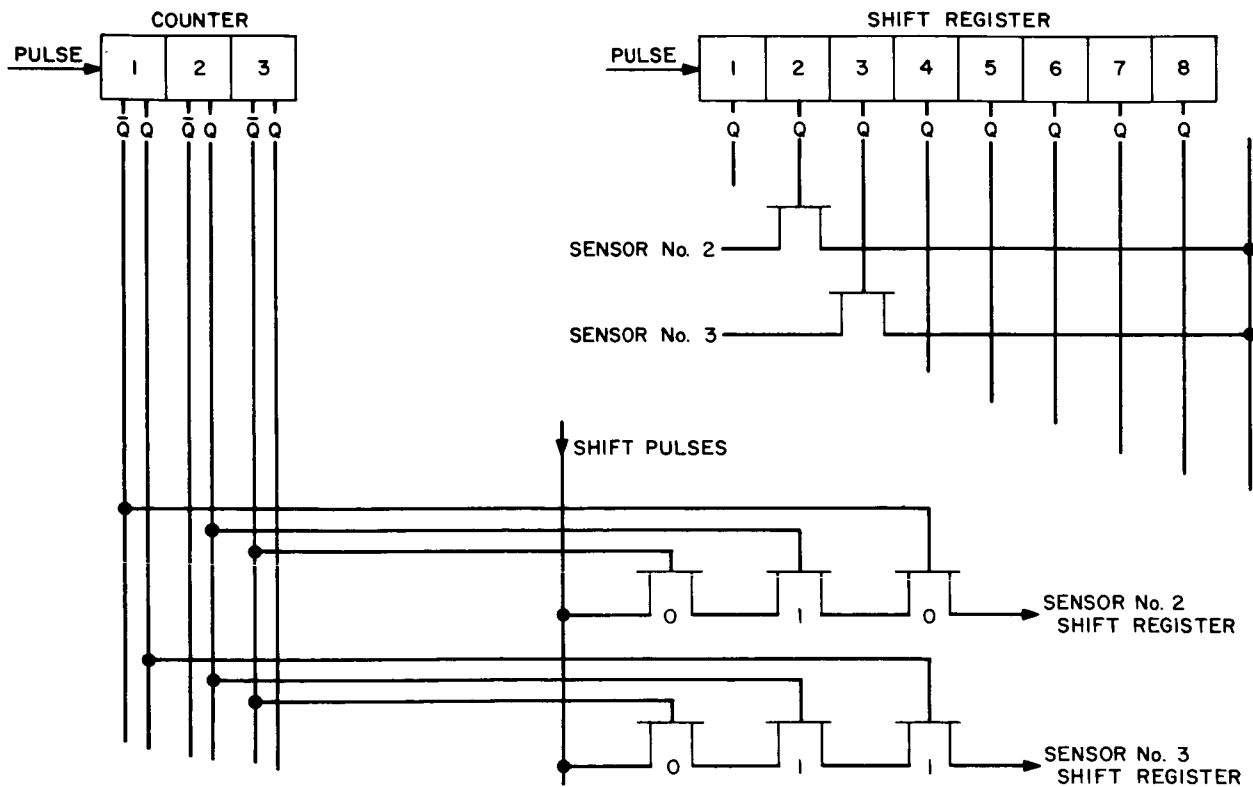


Fig. 6. Comparison of address trees

In the counter-decoding logic scheme, almost all single decoding transistor failures are localized. A source-drain short can compromise information from one other sensor. The address of this sensor is 0 for the position corresponding to the failed transistor and the same for all other transistors. The information is then compromised when the shift register is cleared prematurely by its faulty decoding logic. As an example, a source-drain short in the 2⁰ transistor of the sensor 3 gating logic can compromise information from sensor 2, but not vice versa.

One FET gate short circuit (oxide puncture) per sensor cannot compromise addressing any other sensors. Information from one other sensor may be compromised if the gate short causes an effective source-drain short and the above address relationship exists. The number of FET transistors required for address decoding would add the equivalent of one flip-flop stage to the three-stage counter. This is approximately half the logic required for addressing with an eight-stage shift register.

5. Functional Behavior

a. Interleaving. To minimize synchronizing logic and multiplexing time, the operations of A/D conversion and multiplexing should be interleaved. The most efficient procedure is to block convert and serial multiplex. Blocks of 32 sensors can be multiplexed in the sampling interval at the counter rates already discussed.

There are two basic building blocks that are compatible with interleaving. These are defined by the functional requirements of the encoder and the logic capabilities of the MOS technology. First is the pulse-width converter which includes signal conditioning and the second is a switching array. One converter per substrate is envisioned to permit conversion of the analog signal at the sensor. Field-effect transistors for switching analog signals require a larger area than those performing digital functions; this restricts the complexity of the substrate.

The switching array receives the response from several (eight) converters. It contains the counter and decoding gates for addressing and the counter-shift registers for conversion and multiplexing. The current MOS technology will permit processing inputs from eight sensors on the same substrate. The relationship of the converter and switching array substrates is shown in Fig. 7.

b. Subcommutation. Multiple sampling rates can be obtained by properly addressing the block address

counter (a block consists of four switching array substrates). Subcommutation with this system organization may also be achieved by distributing a sensor's output to several blocks. The sampling frequency is proportional to the number of blocks sampling the sensor. The sampling rates and number of sensors are flexible as there are no restrictions placed on the distribution of sensors. With multiple data paths for the sensor, there is less likelihood of losing critical information.

c. Failure response. From Fig. 7, it is possible to see which failure combinations will continuously degrade the channel. It was shown that MOS FET gate failures can occur in spite of the significant increase in reliability obtained with the technology. A design objective—to prevent this type of failure from degrading the system—has been achieved, since no single failure in the switching array or in a converter can degrade the channel. This is due to the fact that *the transfer of information is based on certain dynamic properties of the converter and switching array. Failures tend to lead to static behavior, with the resultant loss—not mixture—of information.*

Those combinations of failures critical to the channel must generally provide some semblance of clocking and shifting. For instance, if both FET's at the output of the counter-shift register short-circuit, the channel would be permanently degraded. Incidentally, a short circuit in the upper transistor and a 1 in the eighth stage of the counter-shift register will temporarily degrade the channel. The probability of this failure may be reduced by adding another FET in series, driven by the shift pulse train. It is quite unlikely that the counter-shift register will create count pulses from shift pulses or vice versa. For these failures to yield an output when the sensor is not being multiplexed, three or more transistors must short-circuit in special combinations. Failures in a converter or in its addressing logic (but not both) cannot degrade the channel.

6. Experimental Results: Pulse-Width Conversion

Analog-to-digital conversion with integrated circuits is complicated by the dependence of the gate threshold voltage on temperature. This voltage variation is shown in Fig. 8. The diagram reveals two temperature effects that cancel when the threshold voltage is defined by a current of 250 μ a. Note that the drain and gate voltages are the same. In the pulse-width converter, the transistors are biased to minimize the temperature dependence.

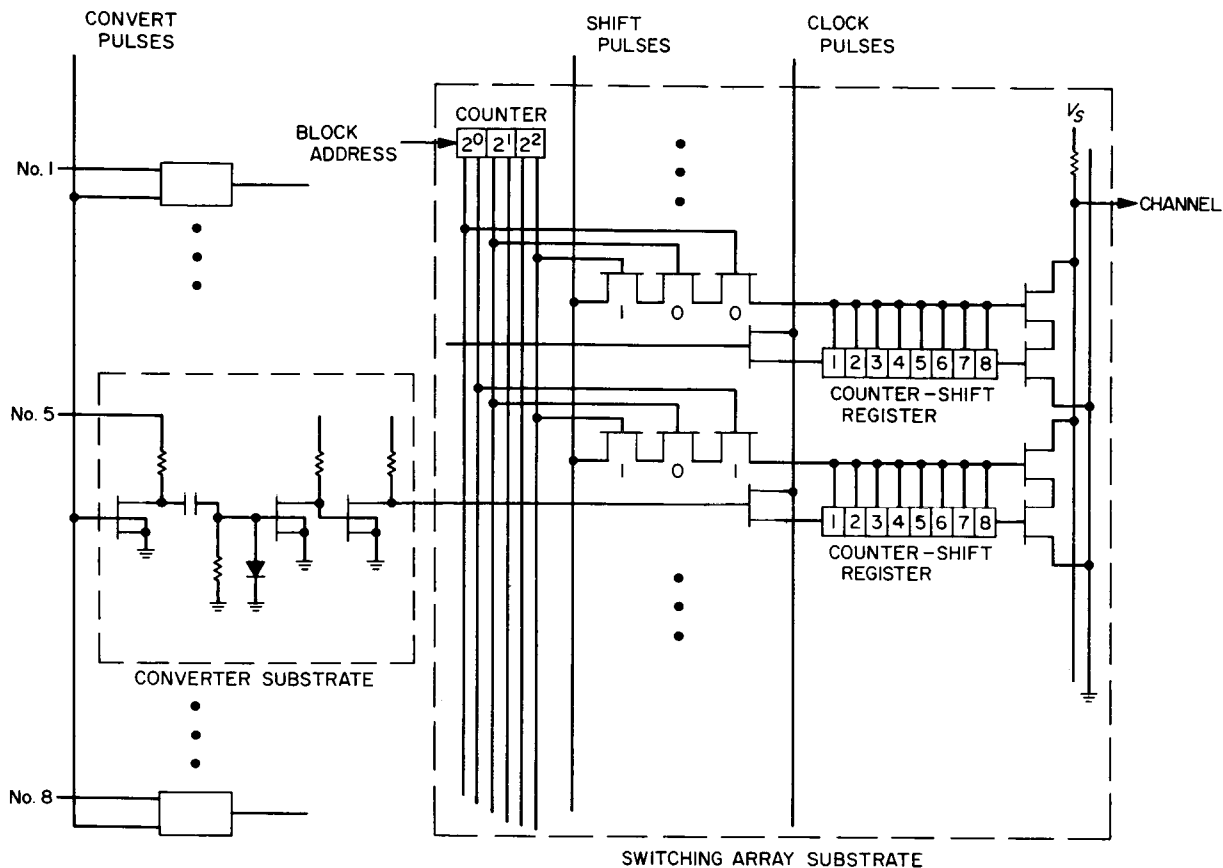
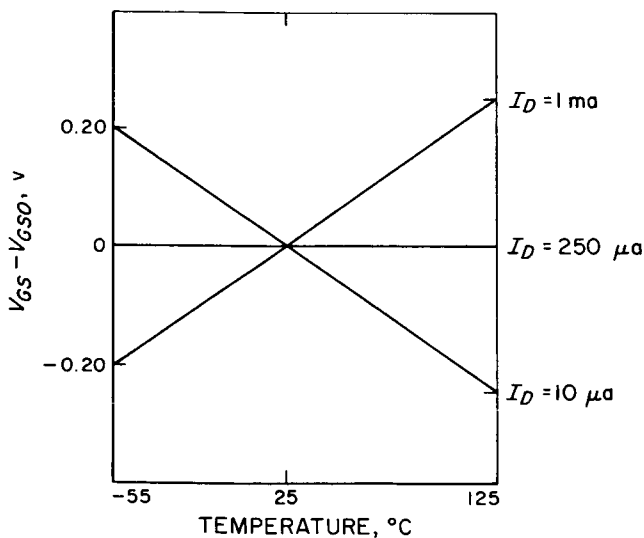


Fig. 7. Data encoder segment



NOTE: $V_{GSO} = V_{GS}$ AT 25°C
 $V_{DS} = V_{GS}$ IN ALL CASES

(SOURCE: GENERAL
 MICRO-ELECTRONICS)

Fig. 8. Temperature variation of gate-source voltage for a constant drain current

The converter in Fig. 9 is derived from a monostable multivibrator and contains the basic circuit of Fig. 4. The time in the unstable state is a function of the voltage E applied to the RC network controlling the gate voltage of T2. E is derived from the sensor voltage E_S and the voltage divider. The unstable state is reached when a triggering pulse is applied to T1. The amplitude and duration of the triggering pulse do not affect the duration of the output pulse if they are sufficient to switch T3 and T4. T4 ceases to conduct immediately, and the output drops to the negative supply voltage. Simultaneously, the voltage E is applied to the capacitor when T3 ceases to conduct. The isolation between T3 and T4 prevents spurious noise on the output line from contributing to the conversion. When the gate voltage of T2 (increasing from E to 0) reaches the threshold voltage V_{T2} , T2 ceases to conduct, T3 and T4 conduct, and the output voltage steps to ground.

Transistors T2 and T4 are crucial since their threshold voltages must be the same and constant with temperature. Regardless of temperature, a dual transistor permits

Experimentally,

$$t_1 = \tau \ln \frac{E_1}{V_T} = 659 \mu\text{sec}$$

$$t_2 = \tau \ln \frac{E_2}{V_T} = 1662 \mu\text{sec}$$

and, solving these equations, the effective time constant and threshold voltage are

$$\tau_{eff} = 0.961 \times 10^{-2} \text{ sec}$$

$$V_{T_{eff}} = -6.30 \text{ v}$$

These results are reasonably accurate in view of the fact that all resistances were $\pm 5\%$. The transfer function of the pulse-width converter is shown in Fig. 10. Average power consumption of the converter is less than 10 mw.

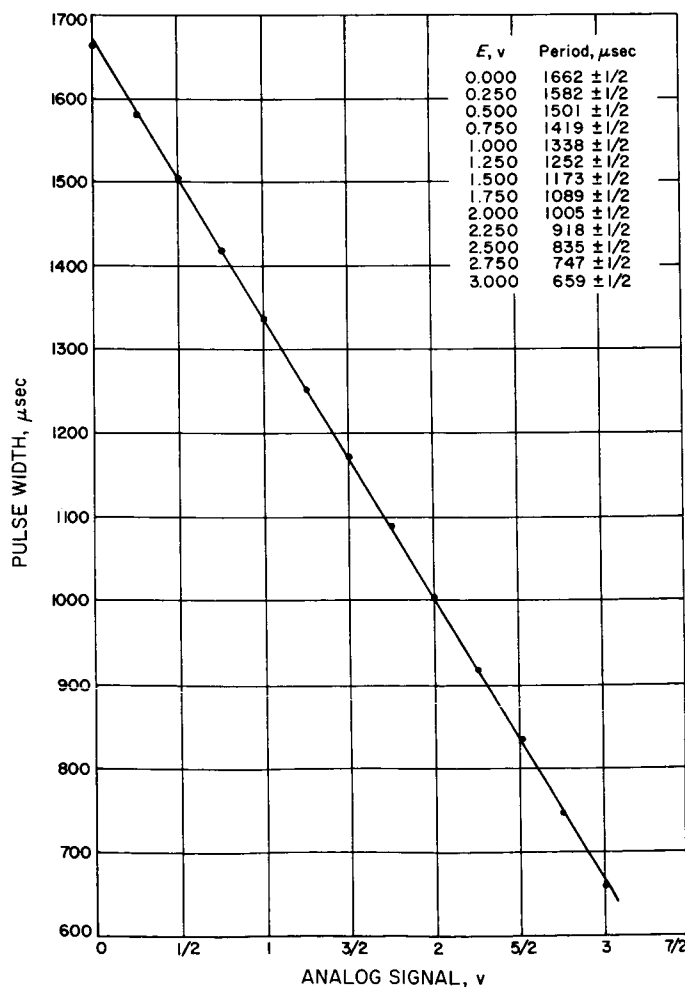


Fig. 10. Pulse-width converter transfer function

If fabrication techniques cannot match biasing resistances and threshold voltages, or if the temperature characteristic of Fig. 8 is only approximate, an additional means of temperature compensation may be necessary. No temperature measurements have been made at this time; consequently, the following remarks and circuit are unverified by experiment.

With gross temperature compensation by transistor biasing, matched pulse-width converters may permit masking fine temperature variations. The comparison method is shown in the schematic of Fig. 11. The pulse-width converters (PWC's) are turned on simultaneously by the triggering pulse. PWC 2, acting as the converter, turns off first, grounding the source of T9. T9 conducts while its gate voltage is at the negative supply. The conversion is complete when PWC 1, as the norm, turns off and T9 ceases to conduct. The output voltages are sketched in Fig. 11(b). The relationship between the analog signals and the output pulse are shown in Fig. 11(c).

The voltages V_1 and V_2 are given by

$$V_1 = E_2 \exp\left(\frac{-t}{R_1 C_1}\right)$$

$$V_2 = E \exp\left(\frac{-t}{R_2 C_2}\right), \quad V_T > E_1 \geq E \geq E_2$$

The times to reach the respective threshold voltages are

$$t_1 = R_1 C_1 \ln \frac{E_2}{V_{T_1}}$$

$$t_2 = R_2 C_2 \ln \frac{E}{V_{T_2}}$$

and the pulse width is

$$t_1 - t_2 = R_1 C_1 \ln \left(\frac{E_2}{V_{T_1}}\right) - R_2 C_2 \ln \left(\frac{E}{V_{T_2}}\right)$$

There are four possible sources of error:

- (1) a change of slope $R_1 C_1 = R_2 C_2 \neq RC$
- (2) differences in slope $R_1 C_1 \neq R_2 C_2$
- (3) variation of the threshold voltage $V_{T_1} = V_{T_2} \neq V_T$
- (4) substrate nonuniformities $V_{T_1} \neq V_{T_2}$

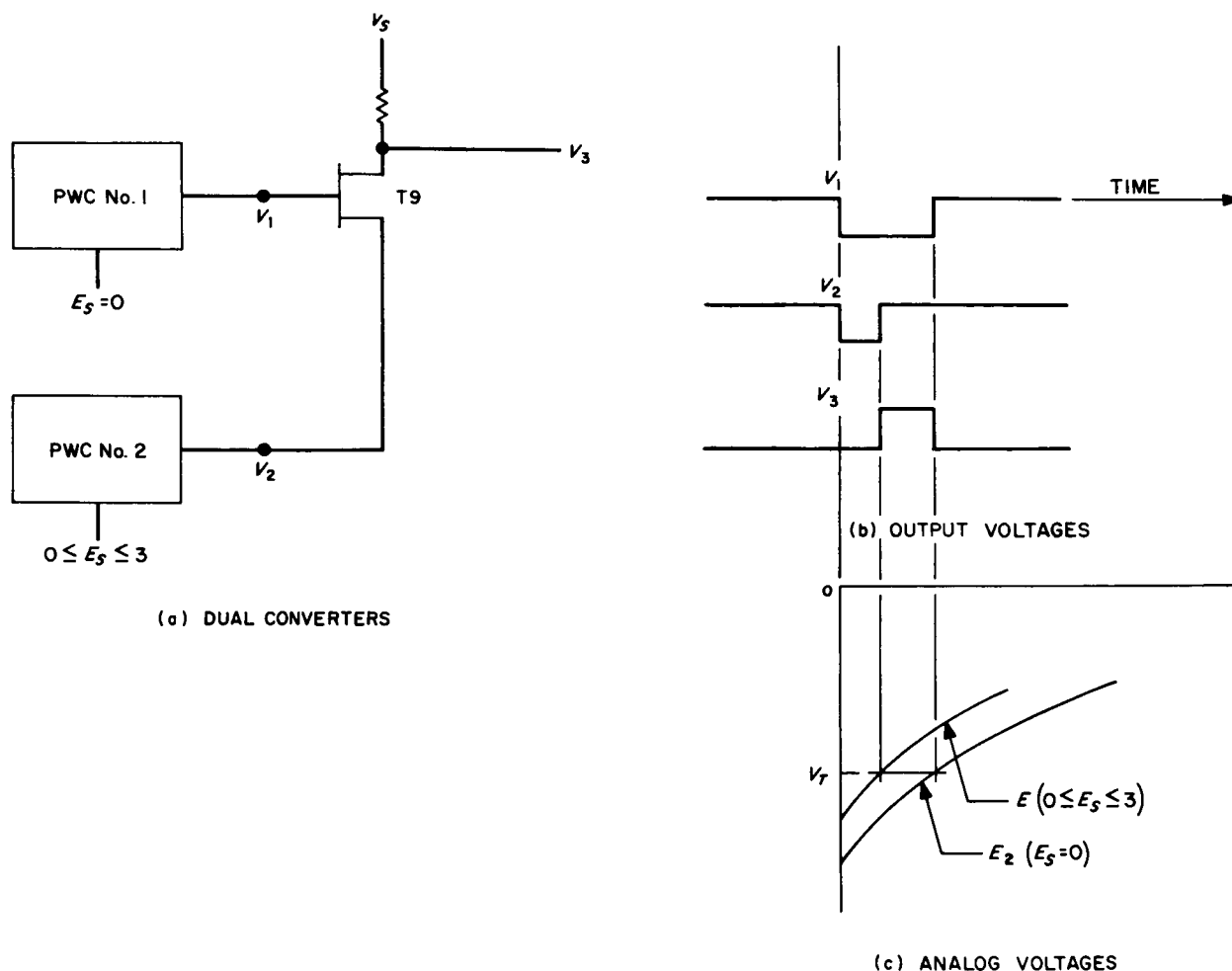


Fig. 11. Comparison method for fine temperature compensation

If (1) and (2) predominate, there is no point in exploiting this method for temperature compensation. In addition, the effect of (4) will be minimized by matching threshold voltages, so that, by assumption,

$$t_1 - t_2 = RC \ln \left(\frac{E_2}{V_{T1}} \frac{V_{T2}}{E} \right)$$

$$= RC \ln \frac{E_2}{E}$$

The remaining source of error—variation of the threshold voltage—is thereby eliminated from the expression for the pulse width.

Such *legerdemain* is not meant to be a substitute for experimental verification. Rather, a course for further development has been outlined to demonstrate that the problem is not as untractable as formerly believed.

N67 12133 B. A Definition of System Reliability

J. F. Meyer¹

1. Introduction

In the discussion that follows, we define a measure of system reliability that accounts not only for total success but also for the various degrees of partial success that a system might experience in realizing its specified behavior. To achieve this, we first define the system itself in terms of attributes that influence its reliability. The system then forms a base for developing such concepts as performance and utility; these, in turn, are used to define

¹This paper was written while the author was on leave of absence from the SR&AD Group, Section 334. He is currently completing requirements for the doctoral program in Communication Sciences at the University of Michigan, Ann Arbor.

system reliability. The latter half of the discussion is devoted to specializations that correspond to certain physically motivated constraints.

Most of the concepts needed for an understanding of the paper are developed as part of the discussion. It is assumed, however, that the reader has a basic familiarity with probability theory. Refs. 1 and 2 should serve as adequate references for the material presented here. One notational convenience that is used repeatedly and deserves explanation is the generalized identity function or "slot function" which we define as follows for an arbitrary set A and arbitrary integer n . If we let $A^{(n)}$ denote the n -fold Cartesian product of the set A , that is

$$A^{(n)} = \underbrace{A \times A \times \cdots \times A}_{n \text{ times}}$$

then the i^{th} slot function ($i = 1, 2, \dots, n$) is the function

$$\xi_i^n : A^{(n)} \rightarrow A$$

where

$$\xi_i^n(a_1, a_2, \dots, a_n) = a_i.$$

With the above exception, the notational conventions used are either self-explanatory or are developed as part of the discussion. Most of the arguments used are set-theoretic in nature and should not be difficult to follow.

2. The System

We wish to analyze the reliability of a physical system that realizes some specified input-output relation. In describing this system, we wish to distinguish the physical structure, the probabilistic nature of that structure, and the terminal behavior as related to that structure. Accordingly, we will represent such a system as follows:

DEFINITION 1. A system S is an ordered triple $S = (C, P, F)$

where

- (1a) C is the component set
- (1b) P is the probability space
- (1c) F is the behavior

This definition is obviously incomplete as the elements of S have only been named but not defined. Rather than complete the definition here, we will develop the notions

individually, thereby permitting us to discuss their motivation and interpretation along with their formalization.

3. The Component Set

In discussing the physical structure of a system, the terms "component" and "subsystem" are often used to refer to a part of the total physical system which in itself can be regarded as a system in the sense that it realizes some specified input-output relation. We will represent such substructures as follows:

DEFINITION 1a. The component set C is a finite set.

The elements $c \in C$ will be called *components* and under the intended interpretation represent the physical components of the system to be analyzed. At one extreme, a component could represent a single electronic device such as a resistor or transistor; at the other extreme, the components could be regarded as large, multi-device subsystems. The only requirements for a consistent interpretation are that distinct components represent distinct physical structures, that the component set represent the entire structure of the physical system, and that each physical structure represented realize an input-output relation.

4. The Probability Space

The probability space of a system S will represent a probabilistic description of component performance. As mentioned above, with each physical component represented in the component set C we associate an input-output relation. These component input-output relations will be referred to informally as operations. In addition, we assume that performance criteria can be established for each physical component such that one may determine whether a component successfully realizes its operation. By successful realization, we mean that for each physical input representing some element in the domain of the operation, the output satisfactorily (according to the criteria) represents the result of the operation.

Let S be a system with component set C . Throughout the remainder of the discussion we will denote components by natural numbers; that is,

$$C = \{1, 2, \dots, m\}$$

and will reserve the symbol m to represent the number of components. We are now prepared to formalize the probabilistic nature of the system.

DEFINITION 2. A failure state b is an m -tuple $b = (b_1, b_2, \dots, b_m)$

where

$$b_i \in \{0, 1\}, i = 1, 2, \dots, m.$$

If b is a failure state and $b_i = 1$, we say that component i is operational in state b . If $b_i = 0$, then i is not operational in state b .

DEFINITION 3. A failure-state function σ is a function $\sigma: T \rightarrow B$

where

- (1) T is time, the set of real numbers
- (2) B is the state space, the set $B = \{0, 1\}^{(m)}$ of all failure states.

The interpretations of failure state and failure-state function are quite natural. A failure-state function σ represents the result of a failure diagnosis performed on the physical system over the entirety of time. If component i is operational in state $\sigma(t)$, then the physical component represented by i successfully realizes its operation at a time represented by the real number t . In this case, we say that i is operational under σ at t . Similarly, if i is not operational in state $\sigma(t)$, we say that it is not operational under σ at t . As there should be little chance to confuse the notion of failure state with the more general concepts of state used in systems analysis, we will often refer to failure states and failure-state functions as simply states and state functions.

It is important to note that, under the intended interpretation, a component's being operational does not depend on the input it receives from other components of the system. In other words, if a component is operational, it will function properly given the proper input. Thus, a component can be operational even though the physical component it represents is not operating properly because of some faulty input signal or faulty power source.

A particular state function can be regarded as an outcome of an experiment conducted on the underlying physical system over an infinite period of time. The description space for the experiment then is a set of state functions representing all the possible elementary outcomes of the experiment. Thus, we are able to formalize the probabilistic nature of component performance as follows.

DEFINITION 1b. The probability space P is an ordered pair $P = (\Sigma, M)$

where

- (1) Σ is the description space, a set of state functions
- (2) M is the probability measure, a probability measure defined on a field F_Σ of subsets of Σ .

The interpretation to be given the space should be quite clear. If Σ' is a member of F_Σ , then $M(\Sigma')$ represents the probability that the outcome of the experiment is such that the state function describing it is in the set Σ' . Of course, one of the difficult practical problems of system reliability analysis is that of determining the measure M in a way that satisfactorily represents the physical interpretation and yet lends itself to practical methods of evaluation. This subject will be expanded later, but for the present the definition of system structure is complete. We now wish to consider the behavior of the system and how it relates to the reliability of the components.

5. The Behavior

We want to represent the behavior of a physical system in a way that will permit us to determine, as a function of component reliability, the reliability of realizing the functional requirements of the system. This is usually accomplished by specifying the system behavior in terms of a single input-output function and then determining the probability of successfully realizing this function; that is, the probability of total success. Experience has shown, however, that in many applications a range of partial success lies between the extremes of total success and total failure. Furthermore, the utility of the system varies with the degree of partial success. In such cases, an appraisal of system reliability in terms of total success is inadequate and, in certain instances, misleading.

Rather than consider the system as realizing a single system function, we can regard the system function as a set of functions whose simultaneous realization comprises the system behavior. Various degrees of partial success in realizing the system behavior can then be identified with various partitions of the function set determined by the success or failure in realizing the member functions. This point of view will be adopted in representing the behavior of the system, as it provides a rather simple means of capturing, at least to some extent, the elusive notion of partial success.

It would appear at first glance that the generalization to multifunction behavior could be analyzed by repeated application of conventional single-function techniques. This is indeed the case if one is interested only in the reliability with which the individual member functions are realized. However, in many applications, the various functions are related with respect to the information they convey to the system user. In these cases, one would like to consider compound events such as "both function A and function B are successfully realized" or "function A is successfully realized but function B is not." As we cannot, in general, compute the probability of such compound events knowing only the probability of successfully realizing the individual member functions, a more general form of analysis is required.

We begin by defining the functions which until now have been informally regarded as members or parts of the total system behavior.

DEFINITION 4. A system function f is an ordered pair $f = (A, I)$

where

- (1) A is the set of functional states for f , $A \subseteq B$ (the state space)
- (2) I is the time interval of f , a half-open real interval ($I = (s, t]$ where $s, t \in T$ and $s < t$).

Under the intended interpretation, a system function represents an input-output relation whose variables are a subset of the variables of the system input-output relation and range over time functions defined on the interval that we have called the time interval of f . The functional states are the failure states in which the system will successfully realize this input-output relation. The informal terminology "successfully realize" means the same as it did for the case of components and operations, and includes the need for success criteria. We are assuming that the set of states with this property is independent of time in the interval I ; i.e., for all $t \in I$ and for all state functions $\sigma \in \Sigma$, we can interpret $\sigma(t) \in A$ as meaning that the input-output relation is successfully realized at time t . To be precise, if $f = (A, I)$ is a system function, $\sigma \in \Sigma$, and $t \in I$, we then say that S is functional for f under σ at t if $\sigma(t) \in A$. If the case is such that $\sigma(t) \in A$ for all $t \in I$, then S realizes f under σ ; otherwise S fails to realize f under σ . (Note that the word "realizes" as used here differs in meaning from the way

we have used it informally and should be interpreted as "successfully realizes throughout the time interval of the function.")

It is the set of functional states, then, that relates component reliability and functional reliability. In practice, the problem of determining these states may be quite difficult, especially when the physical structure is highly redundant with respect to the function in question. This problem and the ease with which it may be solved will be discussed.

With the notion of system function now well established, the definition of system behavior can be quite simply stated.

DEFINITION 1c. The behavior F is a finite set of system functions $F = \{f_1, f_2, \dots, f_n\}$

where

$$f_j = (A_j, I_j), \quad j = 1, 2, \dots, n.$$

This, then, completes our definition of a system. Rather than summarize, we suggest that the reader carefully review the definitions and interpretations of the component set, the probability space, and the behavior, along with the associated definitions of failure state, failure-state function, description space, and system function. Thus far we have attempted to represent those properties of a system which appear to be significant in determining the reliability with which the system behaves. We now wish to consider the notion of reliability itself and make precise its meaning in terms of the elements of a system.

6. System Reliability

The reliability of a system is usually expressed as the probability that the system successfully realizes its specified behavior. However, we feel that such a measure does not account for the various degrees of partial success which the system might experience. Therefore, we will consider an alternative definition of system reliability which is intended to reflect the value of partial success.

Let $S = (C, P, F)$ be a system with component set C , probability space $P = (\Sigma, M)$, and behavior F , where $F = \{f_1, f_2, \dots, f_n\}$; i.e., there are n system functions. Letting ξ_i^n denote the i^{th} slot function (see Introduction), we can relate the state functions σ to the behavior as follows.

DEFINITION 5. The system performance X is a vector-valued random variable defined on the description space Σ as follows:

$$X: \Sigma \rightarrow \{0, 1\}^{(n)}$$

where

$$\xi_i^n(X(\sigma)) = \begin{cases} 1 & \text{if } S \text{ realizes } f_i \text{ under } \sigma \\ 0 & \text{if } S \text{ fails to realize } f_i \text{ under } \sigma \end{cases}$$

for $i = 1, 2, \dots, n$.

Assuming that the measure M is defined for sets of the form $X^{-1}(x)$ —i.e., $X^{-1}(x) \in F_\Sigma$ for all $x \in \{0, 1\}^{(n)}$ —the system performance may be probabilistically described by the function

$$p_X: \{0, 1\}^{(n)} \rightarrow [0, 1]$$

$$p_X(x) = M(X^{-1}(x)).$$

We interpret $p_X(x)$ as the probability that the system performance is x , and since the range of X is finite, the description is complete.

The reader should recall that S realizes $f_i = (A_i, I_i)$ under a state function σ if $\sigma(t) \in A_i$ for all $t \in I_i$. A particular value $x \in \{0, 1\}^{(n)}$ of the system performance then represents a rather refined picture of how the system realizes its specified behavior. If the performance is $(1, 1, \dots, 1)$, then all system functions are realized, and if the performance is $(0, 0, \dots, 0)$, no system function is realized. Between these extremes; that is,

$$(0, 0, \dots, 0) < x < (1, 1, \dots, 1)$$

we are representing the various degrees of partial success obtained by the system in physically realizing its specified behavior.

We now want to suggest the following means of measuring system performance. With each value $x \in \{0, 1\}^{(n)}$ we will associate a nonnegative real number which represents, in the opinion of the system user, the relative utility (gain, payoff) of the system when x is its performance. Denoting the nonnegative real numbers by R^+ we have:

DEFINITION 6. The utility function u for S is a function

$$u: \{0, 1\}^{(n)} \rightarrow R^+.$$

Under the interpretation, we identify the domain of u with the range of X and refer to a value of $u(x) \in R^+$ as the *utility of performance* x . By virtue of u being a real-valued function of a random variable, we may regard u itself as a random variable whose expectation represents how useful, on the average, the resulting system performance will be to the user. We feel this to be a meaningful measure of how reliably the system performs, since it accounts for the relative importance of achieving various levels of partial success. We formally identify expected utility with system reliability as follows:

DEFINITION 7. The reliability ρ_S of a system S is the mathematical expectation of the random variable $u(X)$; i.e.,

$$\rho_S = \sum_{x \in \{0, 1\}^{(n)}} p_X(x) u(x).$$

Using the definition of the probability function p_X , we can relate the system reliability directly to the component reliability; i.e.,

$$\rho_S = \sum_{x \in \{0, 1\}^{(n)}} M(X^{-1}(x)) u(x). \quad (1)$$

The above equation, which we will call the *reliability equation* for the system, is fundamental to the development since it relates utility of performance (the thing we are interested in) to component reliability (the thing we have some chance of determining experimentally).

From the reliability equation, we see that system reliability can be determined given the probability measure M , the system performance X , and the utility function u . Thus, if we wish to use the equation to compute the reliability of some physical system, we must be able to express the probability measure, the system performance, and the utility function that correspond to the particular physical system under consideration. In addition to requiring that these functions adequately represent the system in question, we should also require that they yield themselves to practical methods of computation. In general, very little can be said about how such requirements can be satisfied. We would, however, like to consider the question for a class of systems in which physical failures are permanent or catastrophic in nature and there is some restriction on the relation of component operations to system functions.

7. Permanent Failure of Components

Let us suppose that the physical system to be analyzed is such that component failures are permanent; i.e., once a physical component fails to realize its operation, this failure condition will persist. If $C = \{1, 2, \dots, m\}$ is the component set and σ is some state function, the permanent failure assumption can be precisely stated as follows.

DEFINITION 8. A component i fails permanently under σ if there exists a time $t \in T$ such that for all $x \in T$:

$$\xi_i^m(\sigma(x)) = \begin{cases} 1 & \text{if } x < t \\ 0 & \text{if } x \geq t. \end{cases}$$

If i fails permanently under σ , we call the time $t = \min\{x \mid \xi_i^m(\sigma(x)) = 0\}$ the *failure time of i under σ* . Under our assumption that all physical component failures are permanent, the state functions of the description space Σ are those under which all components $i \in C$ fail permanently. Let Σ_1 denote the set of all such state functions and consider the following correspondence between Σ_1 and $R^{(m)}$, the set of all m -tuples of real numbers.

$$\nu: \Sigma_1 \rightarrow R^{(m)} \quad (2)$$

where

$$\xi_i^m(\nu(\sigma)) = \text{the failure time of } i \text{ under } \sigma$$

for $i = 1, 2, \dots, m$.

One can easily verify that the function ν , as defined in Eq. (2), is both one-to-one and onto. Thus, in the case of permanent failures, (i.e., when $\Sigma = \Sigma_1$), we can write the description space Σ as $R^{(m)}$ where an element $r \in R^{(m)}$ denotes the state function $\nu^{-1}(r)$. In the discussion that follows, we will assume the description space to be so represented unless otherwise noted.

With a description space such as $R^{(m)}$, we are now able to say more about determining the probability measure. From probability theory, we know that a measure M , defined on a field of subsets² of $R^{(m)}$, can be determined by a probability distribution function Φ :

$$\Phi: T^{(m)} \rightarrow [0, 1]$$

where T is again the set of real numbers. For some fixed $t \in T^{(m)}$, Φ determines the value of M for the set

$$E_t = \{r \mid r \in R^{(m)} \text{ and } \xi_i^m(r) \leq \xi_i^m(t), \quad i = 1, 2, \dots, m\} \quad (3)$$

under the relation

$$M(E_t) = \Phi(t). \quad (4)$$

These values of M are then sufficient to determine the value of M for each element of the field. Thus, Φ completely describes M . We choose, therefore, to so represent the probability measure of a system S in the case where $\Sigma = R^{(m)}$, and will refer to Φ as the *distribution function of S* . Consequently, if S has distribution function Φ , its probability space P is $(R^{(m)}, M)$, where M is determined by Φ , as in Eq. (4).

By Eqs. (3) and (4), we can interpret the distribution function of a system as follows:

If $t \in T^{(m)}$, $t = (t_1, t_2, \dots, t_m)$, then $\Phi(t)$ is the probability that component i fails at or before time t_i , $i = 1, 2, \dots, m$.

We then have a reasonable chance of expressing the probability space for a particular physical system. In the case where the physical components fail independently, the task is simplified even further. Consider the events (subsets of $R^{(m)}$) defined as

$$E_s^i = \{r \mid \xi_i^m(r) \leq s\} \quad (5)$$

where s is some fixed element in T . If we let

$$M(E_s^i) = \Phi_i(s) \quad (6)$$

we can show that Φ_i is a probability distribution function (defined on T) where $\Phi_i(s)$ can be interpreted as the probability that component i fails at or before time s . The physical assumption that components fail independently corresponds to the requirement that the events

$$E_{t_1}^1, E_{t_2}^2, \dots, E_{t_m}^m$$

be mutually independent for each $t = (t_1, t_2, \dots, t_m) \in T^{(m)}$. If this is the case, we know that

$$M\left(\bigcap_{i=1}^m E_{t_i}^i\right) = \prod_{i=1}^m M(E_{t_i}^i). \quad (7)$$

If we let E_t be as in Eq. (3), then

$$\bigcap_{i=1}^m E_{t_i}^i = E_t \quad (8)$$

and, from Eqs. (4)–(8), it follows that

$$\Phi(t) = \prod_{i=1}^m \Phi_i(\xi_i^m(t)). \quad (9)$$

²In this case the field of Borel sets of the space $R^{(m)}$.

Therefore, in the case where failures are both permanent and independent, the component distribution functions Φ_i are enough to determine the system distribution function Φ , and hence the probability space P .

8. Permanent Failure of Functions

As the reader will recall, the reliability equation expresses system reliability in terms of the probability measure M , the system performance X , and the utility function u . In the previous section, we saw that the representation of M was simplified in the case where components fail permanently. We would now like to extend the notion of permanent failure to the system functions themselves, and relate this notion to the problems of determining the system performance X .

DEFINITION 9. A system function $f = (A, I)$ fails permanently under σ if, for all t , $u \in I$, whenever $\sigma(t) \notin A$ and $t \leq u$, then $\sigma(u) \notin A$.

In other words, f fails permanently under σ if, once S is not functional for f under σ , it remains so. We also say that f fails permanently when it does not fail at all; i.e., when S realizes f under σ . Before considering the conditions under which a function fails permanently, let us first examine the consequences of the definition.

Let $f = (A, I)$ be an arbitrary system function in the behavior of a system S with description space Σ . (We do not require here that component failures be permanent.) Let t_i denote the maximum element of the interval I ; i.e., $I = (s, t_i]$. Then we have

THEOREM 1. If $f = (A, I)$ fails permanently under σ , then S realizes f under σ if and only if $\sigma(t_i) \in A$.

Proof. (1) Suppose that S realizes f under σ . Then for all $t \in I$, $\sigma(t) \in A$ and, in particular, $\sigma(t_i) \in A$.

(2) Suppose that $\sigma(t_i) \in A$. Then we must show that S realizes f under σ . Assume that this conclusion is false; i.e., there exists a $t \in I$ such that $\sigma(t) \notin A$. Since, by hypothesis, f fails permanently and $t \leq t_i$, we see that $\sigma(t_i) \notin A$. This contradicts the assumption that $\sigma(t_i) \in A$, thereby proving the theorem.

Thus, in the case where f fails permanently under σ , we need only examine the value of σ at the end of the time interval I to determine whether the system successfully realizes f under that state function.

Suppose now that S is a system with behavior $F = \{f_1, f_2, \dots, f_n\}$, where each $f_i = (A_i, I_i)$ fails permanently under each $\sigma \in \Sigma$. Recalling the definition of system performance (Definition 5), we have

$$\xi_i^n(X(\sigma)) = \begin{cases} 1 & \text{if } \sigma(t_{I_i}) \in A_i \\ 0 & \text{otherwise} \end{cases} \quad (10)$$

for $i = 1, 2, \dots, n$.

In this case, system performance can be completely specified by a finite set of state functions. This we can see by considering the equivalence relation \equiv defined on Σ as follows:

$$\sigma_1 \equiv \sigma_2 \Leftrightarrow \sigma_1(t_{I_i}) = \sigma_2(t_{I_i}), \quad i = 1, 2, \dots, n \quad (11)$$

Since the range of any state function is finite and there are at most n distinct times t_{I_i} , we can conclude that \equiv has a finite number of equivalence classes. Furthermore, from Eq. (10),

$$\sigma_1 \equiv \sigma_2 \Rightarrow X(\sigma_1) = X(\sigma_2) \quad (12)$$

and therefore X is determined by a finite number of state functions.

At first glance, it appears that only a rather limited class of systems will have system functions such that each fails permanently under every state function. But, in fact, a rather weak restriction on the type of redundancy used in implementing the system functions ensures that functions fail permanently when components fail permanently. We prove this assertion in the section that follows.

9. Consistency

The reader will recall that a set of functional states A is a set of failure states representing component failure configurations in which the physical system successfully realizes a particular input-output relation. At present, there are no restrictions on the set A ; i.e., we require only that it be some subset of the state space B . In many physical situations, however, there are some constraints on how component operations relate to the input-output relations they realize. Therefore, we would like to consider one such constraint and examine its effect on system behavior.

In general, for any failure state $b \in B$, we can associate a set of components $C(b)$, where

$$C(b) = \{i | \xi_i^m(b) = 1\}. \quad (13)$$

Thus, $C(b)$ is simply the set of components which are operational when the system is in state b . Now suppose that $f = (A, I)$ is some system function, b is some fixed element in B , and the system S is functional for f under σ at t whenever $\sigma(t) = b$. Then we know that b is a functional state for f ; i.e., $b \in A$. Consider now some other failure state b' such that $C(b) \subseteq C(b')$; i.e., the operational components of the state b' include those of the functional state b . If the relation between the components C and the system function f is consistent in the sense that adding operational components does not destroy the property that S is functional for f , we should require that b' also be a functional state for f . Thus, we have

DEFINITION 10. A set of functional states A is consistent if, for all $a, b \in B$ such that $C(a) \subseteq C(b)$, $a \in A$ implies that $b \in A$.

A necessary and sufficient condition for consistency can be quite simply stated if we partially order the state space B in the natural way; that is,

$$a \leq b \Leftrightarrow \xi_i^m(a) \leq \xi_i^m(b), i = 1, 2, \dots, m \quad (14)$$

for all $a, b \in B$.

With respect to the partial order \leq , we can then show that

$$A \text{ is consistent} \Leftrightarrow \forall a, b \in B (a \leq b, \text{ and } a \in A \Rightarrow b \in A). \quad (15)$$

The physical interpretation of consistency is, in effect, a restriction on the kind of redundancy used in implementing a particular system function. The restriction is not that severe, however, as one can show that redundancy schemes such as "paralleling" and "majority voting" satisfy the consistency condition. We would also like to note that consistency, as defined here, is essentially equivalent to the notion of a "coherent system" (Ref. 3), if we restrict S to having a single system function (A, I) in its behavior, where A is consistent. On the other hand, if the behavior of S is represented by a set containing more than one system function, all of which have consistent functional state sets, it is not necessarily the case that S is coherent relative to some input-output function defined in terms of these system functions. This may be verified using a simple two-component, two-function example. Let S be a system where $C = \{1, 2\}$, $F = \{f_1, f_2\}$ and the functional states are given as

$$A_1 = \{(1, 1), (1, 0)\}$$

$$A_2 = \{(1, 1), (0, 1)\}.$$

Clearly, both A_1 and A_2 are consistent. Consider now an input-output function g whose realization corresponds to realizing f_1 or f_2 , but not both. The functional states of g are then

$$A_g = (A_1 \cap \bar{A}_2) \cup (\bar{A}_1 \cap A_2) = \{(1, 0), (0, 1)\}.$$

Since A_g is not consistent, the system S would not be coherent relative to the function g . On the other hand, functions such as g can be accounted for within the framework we have presented here. In this sense, the two notions differ.

We now wish to relate the notions of consistency, permanent component failures, and permanent function failures. In systems where components fail permanently we were able to write the state functions as m -tuples of real numbers where a particular $r \in R^{(m)}$ denotes the state function $v^{-1}(r)$ under the correspondence given in (2). Accordingly, we can let $r(t)$ denote the value of this function at time t ; that is,

$$r(t) = (b_1, b_2, \dots, b_m) \quad (16)$$

where

$$b_i = \begin{cases} 1 & \text{if } t < \xi_i^m(r) \\ 0 & \text{if } t \geq \xi_i^m(r) \end{cases}$$

for $i = 1, 2, \dots, m$.

We can then show that the state functions $r \in R^{(m)}$ have the following property.

THEOREM 2. $\forall t, u \in T (t \leq u \Rightarrow r(u) \leq r(t)).$

(The inequality on the right is the partial order defined in Eq. 14.)

Proof. Let $t, u \in T$ such that $t \leq u$. We must show then that

$$\xi_i^m(r(u)) \leq \xi_i^m(r(t)), \quad i = 1, 2, \dots, m.$$

Assume this is not the case; i.e., there exists an i such that

$$\xi_i^m(r(u)) > \xi_i^m(r(t)).$$

This is possible only if $\xi_i^m(r(u)) = 1$ and $\xi_i^m(r(t)) = 0$. We see from Eq. (16) that $u < \xi_i^m(r)$ and $t \geq \xi_i^m(r)$, and hence $u < t$. This contradicts the assumption that $t \leq u$ and the theorem is proved.

The fact that the state functions have this monotone nature enables us to show that a function will fail permanently under r if its functional states are consistent.

THEOREM 3. *If A is a consistent set of functional states then, for all $r \in R^{(m)}$, a system function $f = (A, I)$ fails permanently under r .*

Proof. Let r be some arbitrary state function in $R^{(m)}$. If f is successfully realized under r (i.e., for all $t \in I, r(t) \in A$), then Definition 9 is vacuously satisfied and f fails permanently under r . If not, let $t \in I$ such that $r(t) \notin A$ and let us consider the value of r at some later time $u \geq t$. Suppose that $r(u) \in A$. By Theorem 2, $r(u) \leq r(t)$, and since A is consistent, it follows from (15) that $r(t) \in A$. This cannot be the case, since $r(t) \notin A$. Therefore, we must conclude that $r(u) \notin A$, thereby proving that f fails permanently under r .

Thus, for systems whose components fail permanently and whose system functions have consistent functional states, once the components of S fail so that S is not functional for some system function f , no component failures occurring at a later time will compensate for earlier failures. A little more surprising is the fact that the converse of Theorem 3 is also true:

THEOREM 4. *If a system function $f = (A, I)$ fails permanently under r for all $r \in R^{(m)}$, then A is a consistent set of functional states.*

Proof. We find it convenient to prove an equivalent form of Theorem 4; that is:

If A is not consistent, then there exists an $r \in R^{(m)}$ such that $f = (A, I)$ does not fail permanently under r .

Suppose that A is not a consistent set of functional states. Then there exist states $a, b \in B = \{0, 1\}^{(m)}$ such that $a \leq b$, $a \in A$ and $b \notin A$. If we can exhibit a state function r such that at some time $t_0 \in I, r(t_0) = b$, and at some later time $t_1 \in I, r(t_1) = a$, then by Definition 9, f does not fail permanently under r .

First, let us choose three distinct times t_0, t_1 , and t_2 such that $t_0 < t_1 < t_2$ and $t_0, t_1 \in I$, where I is the time interval of f . Clearly, such a choice is possible. Let $a = (a_1, a_2, \dots, a_m)$ and $b = (b_1, b_2, \dots, b_m)$ be the failure states whose existence was guaranteed above, and consider the state func-

tion $r = (r_1, r_2, \dots, r_m)$ with failure times r_i determined as follows:

$$r_i = \begin{cases} t_0 & \text{if } a_i = b_i = 0 \\ t_1 & \text{if } a_i = 0, b_i = 1 \\ t_2 & \text{if } a_i = b_i = 1. \end{cases} \quad (17)$$

Since $a \leq b$, the conditions on the right are exhaustive and therefore the failure times of r are completely specified.

CLAIM. $r(t_0) = b$ and $r(t_1) = a$.

To prove the claim, we first show that $r(t_0) = b$; that is,

$$\xi_i^m(r(t_0)) = b_i, \quad i = 1, 2, \dots, m.$$

By Eq. (16) we have

$$\xi_i^m(r(t_0)) = \begin{cases} 1 & \text{if } t_0 < r_i \\ 0 & \text{if } t_0 \geq r_i. \end{cases} \quad (18)$$

Case (1): $\xi_i^m(r(t_0)) = 1$. By Eq. (18), we have $r_i > t_0$. Since, by Eq. (17), $r_i \in \{t_0, t_1, t_2\}$ and since $t_0 < t_1 < t_2$, we conclude that $r_i = t_1$ or $r_i = t_2$. In either case, b_i has to be 1, and so $\xi_i^m(r(t_0)) = b_i$.

Case (2): $\xi_i^m(r(t_0)) = 0$. Again, by Eq. (18), $r_i \leq t_0$. Since $t_0 < t_1 < t_2$, the only value of r_i satisfying this condition is $r_i = t_0$, and hence $b_i = 0$. Therefore, we again have shown that $\xi_i^m(r(t_0)) = b_i$.

Combining the two cases, we have proven that $r(t_0) = b$. In a similar fashion, we can prove that $r(t_1) = a$, thus proving the claim. Since we choose a and b such that $a \in A$, $b \notin A$, we have

$$r(t_0) \notin A, r(t_1) \in A.$$

Furthermore, t_0 and t_1 were such that $t_0, t_1 \in I, t_0 < t_1$, and therefore we have constructed a state function r under which f does not fail permanently. This concludes the proof of Theorem 4.

Combining Theorems 3 and 4, we have:

THEOREM 5. *A system function $f = (A, I)$ fails permanently under all $r \in R^{(m)}$ if and only if A is consistent.*

Therefore, for a function to fail permanently under all state functions, it is not only sufficient but also necessary that the functional states be consistent. In the case of permanent component failures, then, consistency is the weakest condition we can impose on the functional states

in order to satisfy the hypothesis of Theorem 1 for all state functions. This, in turn, allows us to partition the description space as in (11), and thereby simplify the reliability analysis.

N67 12134 C. On the Spectrum of Single-Sideband Phase Modulation by Normal Noise

J. C. Springett

1. Introduction

Single-sideband phase modulation (SSB/PM) may have possible application to capsule relay telemetry links in order to

- (1) relax some of the constraints imposed on double-sideband phase modulation (DSB/PM) approaches when a swept acquisition RF loop (APC receiver) is used, and
- (2) make maximum use of the available RF bandwidth which may be restricted by channel allocation and/or RF receiver design.

The baseband modulation used for a capsule relay link could be either continuous (analog) or discrete (binary and higher orders), or perhaps a combination of both. As in any nonlinear modulation system, the modulated carrier spectrum is dependent on the characteristic function of the modulating process, and will exhibit various degrees of spectral spreading (relative to baseband) as a function of the modulation intensity (or modulation index, etc.). In most analyses, the characteristic function is taken to be that of a sinusoidal or Gaussian signal since, in general, the characteristic function of other signals is difficult to obtain in a convenient form. For example, if a general Fourier series is used, we find that the expectation of an infinite product of exponentials must be evaluated. Thus, in this work, we choose a Gaussian modulating signal with the assumption that the proper choice of variance and spectral shape can approximate the actual modulating signal without significant error.

The object of this article is to derive the spectrum for SSB/PM and compare it with that of DSB/PM.

2. The Complex Analytic Modulation Function

A well-known result of complex analytic theory (Refs. 4 and 5) is, that given

$$z(t) = h(t) + j\hat{h}(t), \quad (1)$$

where h and \hat{h} are connected by the relation

$$\hat{h}(t) = \frac{1}{\pi} P \int_{-\infty}^{\infty} \frac{h(\lambda)}{t - \lambda} d\lambda, \quad (2)$$

and P denotes the Cauchy principal value, the power spectrum of $z(t)$ is

$$W_z(\omega) = \begin{cases} 4W_h(\omega), & \omega > 0 \\ 2W_h(\omega), & \omega = 0 \\ 0, & \omega < 0 \end{cases} \quad (3)$$

where $W_h(\omega)$ is the Fourier transform of the autocorrelation function $R_h(\tau)$ of $h(t)$. The function $\hat{h}(t)$ is referred to as the Hilbert transform of $h(t)$.

Middleton (Refs. 6 and 7) has shown for simultaneous carrier amplitude and angle modulation that skew or unsymmetrical spectra result when the amplitude and angle modulating signals have a nonzero cross correlation function.

For the case at hand, we wish to establish the relationship between the amplitude modulating signal $A(t)$ and the phase modulating signal $g(t)$ to yield complete suppression of the lower (or upper) sideband. We begin by writing

$$s(t) = A(t) \cos [\omega_c t + \beta g(t)], \quad A(t) > 0, \text{ all } t \quad (4)$$

$$s(t) = R_e \left[\exp \{ \alpha f(t) + j[\omega_c t + \beta g(t)] \} \right] \quad (5)$$

with $A(t) = \exp[\alpha f(t)]$, or we have a complex signal (denoted by the underbar) of the form

$$\underline{s}(t) = \exp \{ \alpha f(t) + j[\omega_c t + \beta g(t)] \}. \quad (6)$$

We now assume that the modulation signals $f(t)$ and $g(t)$ are low pass with effective cutoff frequency ω_0 , $\omega_0 \ll \omega_c$, and are independent of the carrier. Then, a necessary and sufficient condition for single sideband is that the low-pass function $\exp[\alpha f(t) + j\beta g(t)]$ be complex analytic, i.e., $\exp[\alpha f(t)] \cos[\beta g(t)]$ and $\exp[\alpha f(t)] \sin[\beta g(t)]$ be Hilbert transform pairs. As a result, we need to establish the relationship between α , β , $f(t)$ and $g(t)$ to satisfy this condition.

Assume

$$H \{ \exp [\alpha f(t)] \cos [\beta g(t)] \} = \exp [\alpha f(t)] \sin [\beta g(t)] \quad (7)$$

and

$$H \{ \exp [\alpha f(t)] \sin [\beta g(t)] \} = - \exp [\alpha f(t)] \cos [\beta g(t)] . \quad (8)$$

Writing the sine and cosine in their exponential forms and using the definition of the Hilbert transform (Eq. 2), we establish the following two relationships:

$$\int_{-\infty}^{\infty} \frac{\exp [\alpha f(\lambda) + j\beta g(\lambda)]}{\lambda - t} d\lambda = \pi j \{ \exp [\alpha f(t) + j\beta g(t)] \} , \quad (9)$$

$$\int_{-\infty}^{\infty} \frac{\exp [\alpha f(\lambda) - j\beta g(\lambda)]}{\lambda - t} d\lambda = -\pi j \{ \exp [\alpha f(t) - j\beta g(t)] \} . \quad (10)$$

The conditions for the convergence of the integrals to the right-hand side must now be established.

Titchmarsh (Ref. 8, p. 125) gives a theorem concerned with the existence of such integrals which satisfies the current assumption. The theorem states:

Let $\Phi(z)$, $z = x + jy$, be an analytic function, regular for $y > 0$, and let

$$\int_{-\infty}^{\infty} |\Phi(x + jy)|^2 dx$$

exist for every positive y , and be bounded. Then, as $y \rightarrow 0$, $\Phi(x + jy)$ converges in mean to a function $\Phi(x)$, and also $\Phi(x + jy) \rightarrow \Phi(x)$ for almost all x . For $y > 0$

$$\Phi(z) = \frac{1}{2\pi j} \int_{-\infty}^{\infty} \frac{\Phi(\xi)}{\xi - z} d\xi \quad (\xi \text{ real}).$$

If $\Phi(z) = U(x, y) + jV(x, y)$, $\phi(x) = u(x) - jv(x)$, the functions U , V , u , and v are connected by the following formulae and, in particular, f and g are conjugate.

$$U(x, y) = -\frac{1}{\pi} \int_{-\infty}^{\infty} \frac{\lambda - x}{(\lambda - x)^2 + y^2} v(\lambda) d\lambda,$$

$$V(x, y) = -\frac{y}{\pi} \int_{-\infty}^{\infty} \frac{v(\lambda)}{(\lambda - x)^2 + y^2} d\lambda,$$

$$v(x) = \frac{1}{\pi} P \int_{-\infty}^{\infty} \frac{u(\lambda)}{\lambda - x} d\lambda,$$

and

$$u(x) = -\frac{1}{\pi} P \int_{-\infty}^{\infty} \frac{v(\lambda)}{\lambda - x} d\lambda.$$

Also, $U(x, y) \rightarrow u(x)$ as $y \rightarrow 0$, and $V(x, y) \rightarrow -v(x)$ for almost all values of x .

We see then that the integrals 9 and 10 exist under the condition that

$$\begin{aligned} \Phi(z) &= \exp [\alpha f(x, y)] \cos [\beta g(x, y)] \\ &\quad + j \exp [\alpha f(x, y)] \sin [\beta g(x, y)] \end{aligned} \quad (11)$$

is analytic within the proper contour of integration. This establishes the fact that $\exp[\alpha f(x)] \cos[\beta g(x)]$ and $\exp[\alpha f(x)] \sin[\beta g(x)]$ are indeed Hilbert transform pairs. (Note that the factor of two is accounted for because the pole is on the real axis (cf., Whittaker and Watson, Ref. 9, p. 117)). By applying the Cauchy-Riemann conditions to $\Phi(z)$, Eq. 11, it is found that $\alpha = \beta$ and that the functions $f(x)$ and $g(x)$ also satisfy the Cauchy-Riemann conditions; i.e., $f(x, y) + jg(x, y)$ must be analytic. The remaining question to be answered is: What is the exact relationship between f and g ? There are innumerable $f(x, y)$ and $g(x, y)$ for which $f(x, y) + jg(x, y)$ is analytic; however, we must restrict ourselves to a class for which $f(x, y) \rightarrow f(x)$ and $g(x, y) \rightarrow g(x)$ as $y \rightarrow 0$, since in reality $f(x)$ and $g(x)$ are real-time functions. No conclusive proof is currently known which constrains f and g to be Hilbert transform pairs; however, in previous works (Refs. 10, 11, and 12), they have been taken solely as such, and all available evidence would tend to substantiate this choice in lieu of some more generalized relationship. As a result, for the remainder of this article we take $g(t) = \hat{f}(t)$, and the final forms of the complex analytic modulation function become

$$\underline{s}(t) = \exp \{ \alpha f(t) + j[\omega_c t + \alpha \hat{f}(t)] \} \quad (12)$$

$$\underline{s}(t) = \exp \{ \alpha \hat{f}(t) + j[\omega_c t - \alpha f(t)] \} \quad (13)$$

etc. The four possible forms give combinations of suppression of either the upper or lower sidebands and phase modulation by either f or \hat{f} .

An elementary example of the fact that $\underline{s}(t)$ has no frequencies below ω_c is obtained by letting $f(t) = \cos \omega_m t$, so that $\hat{f}(t) = \sin \omega_m t$ and

$$\underline{s}(t) = \exp \{ \alpha \cos \omega_m t + j[\omega_c t + \alpha \sin \omega_m t] \} \quad (14)$$

$$\underline{s}(t) = \exp(j\omega_c t) \exp[\alpha \exp(j\omega_m t)] \quad (15)$$

$$\underline{s}(t) = \exp(j\omega_c t) \sum_{n=0}^{\infty} \frac{\alpha^n}{n!} \exp(jn\omega_m t) \quad (16)$$

$$\underline{s}(t) = \sum_{n=0}^{\infty} \frac{\alpha^n}{n!} \exp[j(\omega_c + n\omega_m)t]. \quad (17)$$

The result is obvious.

3. The Second Moment Function of $\underline{s}(t)$

The second moment function of $\underline{s}(t)$ is defined by

$$M_s(t_1, t_2) = E \{ \underline{s}(t_1) \underline{s}^*(t_2) \}, \quad (18)$$

with the * denoting conjugation. As was stated earlier, the modulation and carrier are independent; now assume the ergodic hypothesis so that M_s depends strictly on the time difference $t_2 - t_1 = \tau$.

From Eq. 12,

$$M_s(\tau) = E \left[\exp \{ j[-j\alpha f(t) + \alpha \hat{f}(t) + \omega_c t] - j[j\alpha f(t + \tau) + \alpha \hat{f}(t + \tau) + \omega_c(t + \tau)] \} \right] \quad (19)$$

$$M_s(\tau) = \frac{1}{2} \exp(-j\omega_c \tau) E \left[\exp \{ j[-j\alpha f(t) + \alpha \hat{f}(t) - j\alpha f(t + \tau) - \alpha \hat{f}(t + \tau)] \} \right]. \quad (20)$$

We recognize the expectation in Eq. 20 to be nothing more than the fourth-order characteristic function

$$F[-j\alpha, \alpha, -j\alpha, -\alpha; \tau]$$

of the functions $f(t)$, $\hat{f}(t)$, $f(t + \tau)$, and $\hat{f}(t + \tau)$.

4. Normal Random Modulation

Consider a zero mean Gaussian modulating signal with variance σ^2 . As mentioned earlier, this choice has been made because of the convenient form of its fourth-order characteristic function. Now, if $f(t)$ is Gaussian, Dugundji (Ref. 4) has shown that $\hat{f}(t)$ is also Gaussian, as are the time shifts. Thus, we may write (Ref. 6)

$$F[\xi_1, \xi_2, \xi_3, \xi_4; \tau] = \exp \left(-\frac{1}{2} \sum_{j=1}^4 \sum_{k=1}^4 \xi_j, \xi_k, \mu_{jk} \right), \quad (21)$$

where $\xi_1 = -j\alpha$, $\xi_2 = \alpha$, $\xi_3 = -j\alpha$, $\xi_4 = -\alpha$, and $\mu_{jk} = E\{f_j f_k\}$. Calculating the moments, we obtain (see Refs. 4 and 5 for correlation properties):

$$\mu_{11} = E\{f^2(t)\} = \sigma^2$$

$$\mu_{22} = E\{\hat{f}^2(t)\} = \sigma^2$$

$$\mu_{33} = E\{f^2(t + \tau)\} = \sigma^2$$

$$\mu_{44} = E\{\hat{f}^2(t + \tau)\} = \sigma^2$$

$$\mu_{12} = \mu_{21} = E\{f(t) \hat{f}(t)\} = 0$$

$$\mu_{34} = \mu_{43} = E\{f(t + \tau) \hat{f}(t + \tau)\} = 0$$

$$\mu_{13} = \mu_{31} = E\{f(t) f(t + \tau)\} = R_f(\tau)$$

$$\mu_{24} = \mu_{42} = E\{\hat{f}(t) \hat{f}(t + \tau)\} = R_f(\tau)$$

$$\mu_{14} = \mu_{41} = E\{f(t) \hat{f}(t + \tau)\} = \hat{R}_f(\tau)$$

$$\mu_{23} = \mu_{32} = E\{f(t + \tau) \hat{f}(t)\} = -\hat{R}_f(\tau).$$

Thus,

$$F[\xi_1, \xi_2, \xi_3, \xi_4; \tau] = \exp \{ 2\alpha^2 [R_f(\tau) - j\hat{R}_f(\tau)] \}, \quad (22)$$

and

$$M_s(\tau) = \frac{1}{2} \exp(-j\omega_c \tau) \exp \{ 2\alpha^2 [R_f(\tau) - j\hat{R}_f(\tau)] \}. \quad (23)$$

It can be immediately seen that the form of $M_s(\tau)$ is identical to that of $\underline{s}(t)$, and therefore $M_s(\tau)$ is complex analytic. The second moment function of the actual modulating signal is obtained by taking the real part of Eq. 23.

Let us now compare the above result with that of DSB/PM. In this case, the amplitude modulation disappears, i.e., $f(t) \equiv 0$, and we can write, by collecting the appropriate μ_{jk} ,

$$M_{s(\tau)}_{DSB} = \frac{1}{2} \exp(-j\omega_c \tau) \exp \{ \alpha^2 [R_f(\tau) - \sigma^2] \}. \quad (24)$$

The total power in each case is given by $M_s(0)$ and for DSB is $\frac{1}{2}$ and for SSB $\frac{1}{2} \exp(2\alpha^2 \sigma^2)$. Note that for the case of DSB the power is constant and independent of the modulation, while for SSB it depends upon the intensity of amplitude modulation. Since it would be desirable to compare DSB and SSB on a total power basis, we let

P_{TOT} be the total power in each case, and as the carrier power P_c is given by $\lim_{\tau \rightarrow \infty} M_s(\tau)$, we have

$$\begin{aligned} \text{DSB} \\ P_c &= P_{TOT} \exp(-\alpha^2 \sigma^2) \\ P_{SB} &= P_{TOT} [1 - \exp(-\alpha^2 \sigma^2)] \end{aligned}$$

$$\begin{aligned} \text{SSB} \\ P_c &= P_{TOT} \exp(-2\alpha^2 \sigma^2) \\ P_{SB} &= P_{TOT} [1 - \exp(-2\alpha^2 \sigma^2)] \end{aligned}$$

It can be seen that the phase modulation index α must be a factor of $\sqrt{2}$ greater for DSB than for SSB to give the same powers. We also note that when all modulation is shut off the average power output of the SSB transmitter will be a factor of $\exp(2\alpha^2 \sigma^2)$ less than that for the DSB transmitter.

5. Calculated Results

In order to calculate the bandwidth advantage of SSB over DSB, it is necessary to consider some specific $R_f(\tau)$ and use a computer to obtain the Fourier transform of $M_s(\tau)$. The following baseband spectra have been assumed for this purpose:

$$W_1(\omega) = \begin{cases} 1, & |\omega| \leq 1 \\ 0, & |\omega| > 1 \end{cases} \quad (25)$$

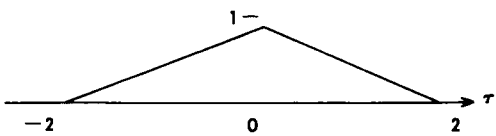
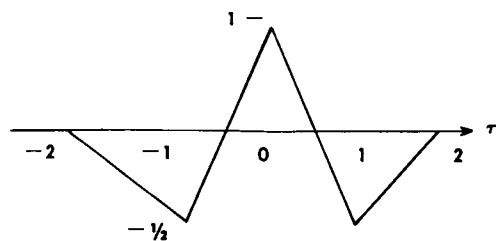
$$W_2(\omega) = \frac{\sin^2 \pi \omega}{(\pi \omega)^2} \quad (26)$$

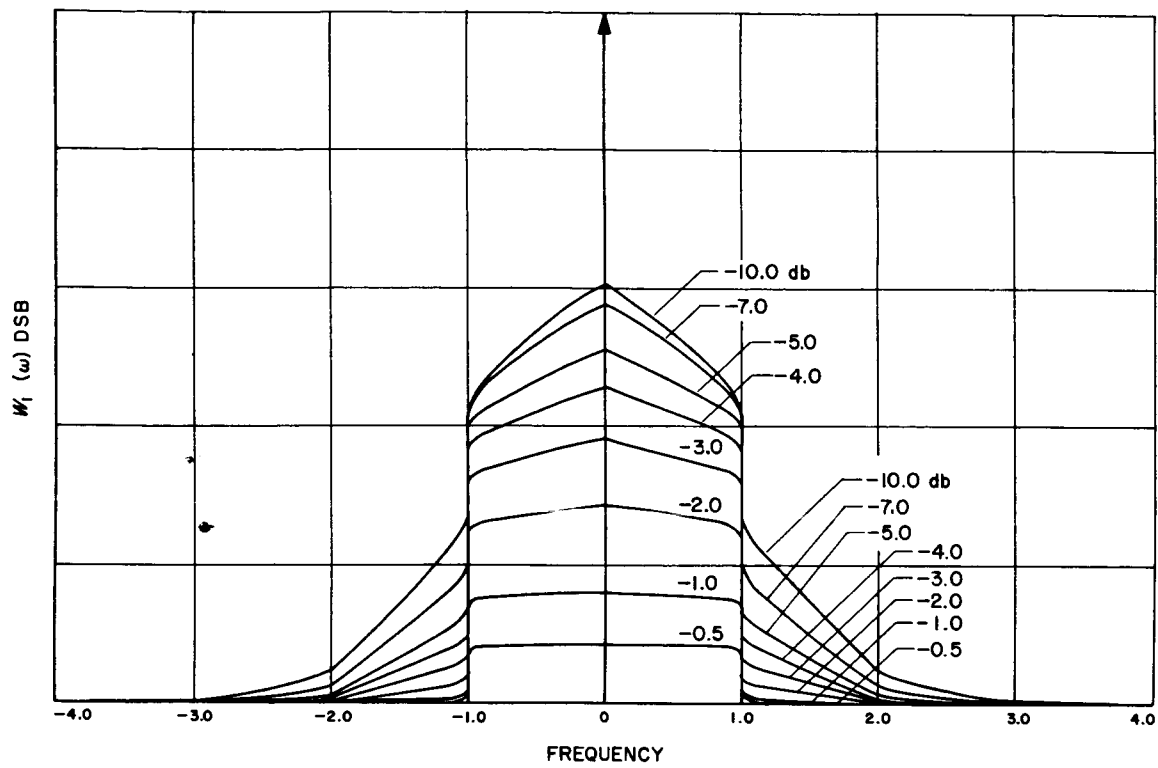
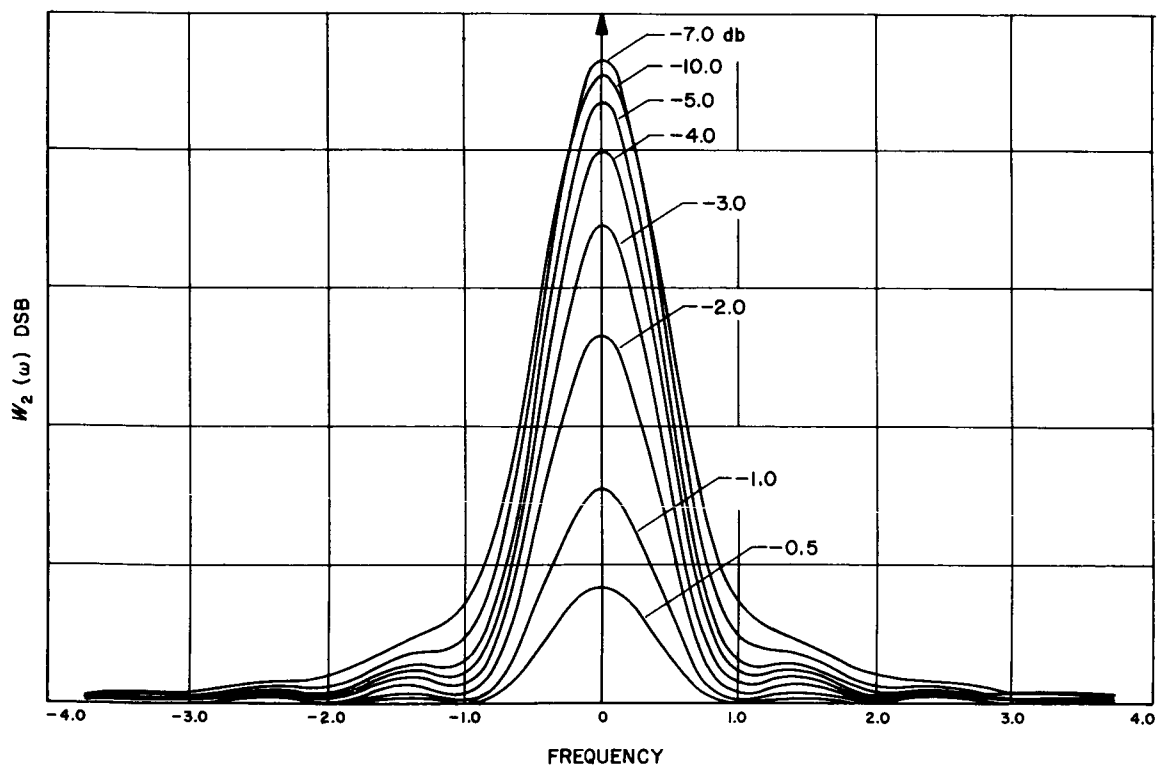
$$W_3(\omega) = \frac{\sin^4 (\pi \omega / 2)}{(\pi \omega / 2)^2} \quad (27)$$

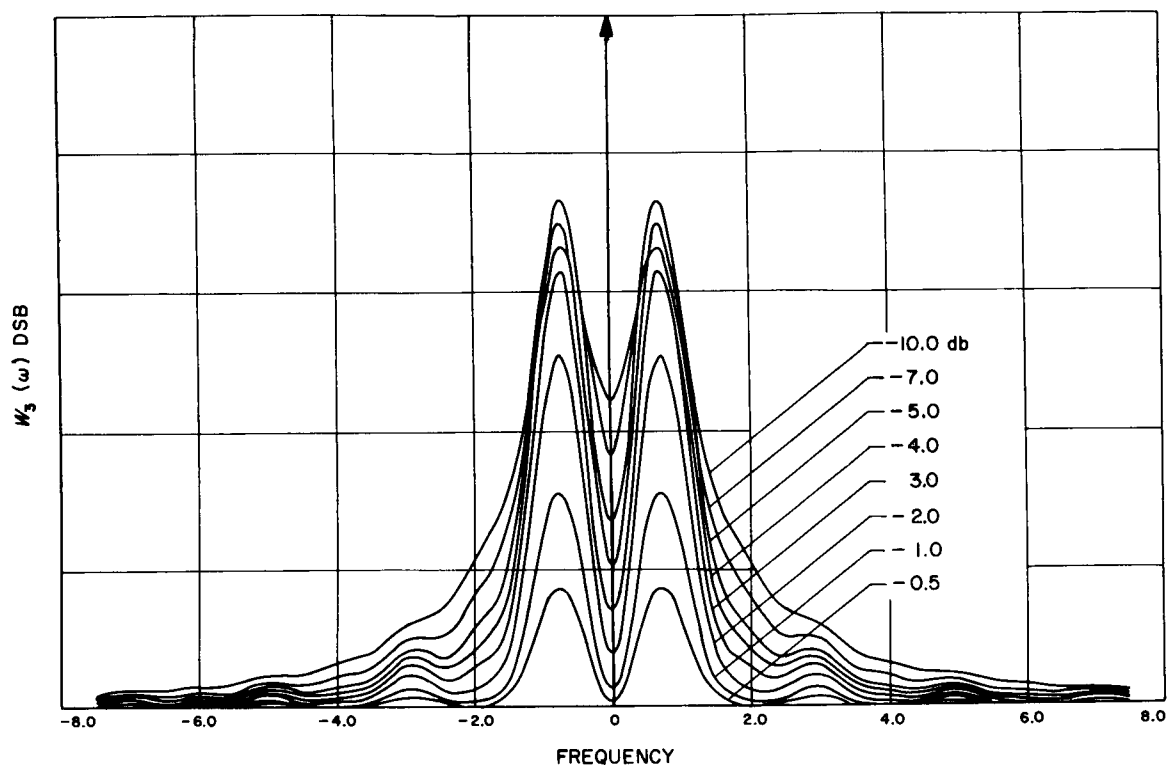
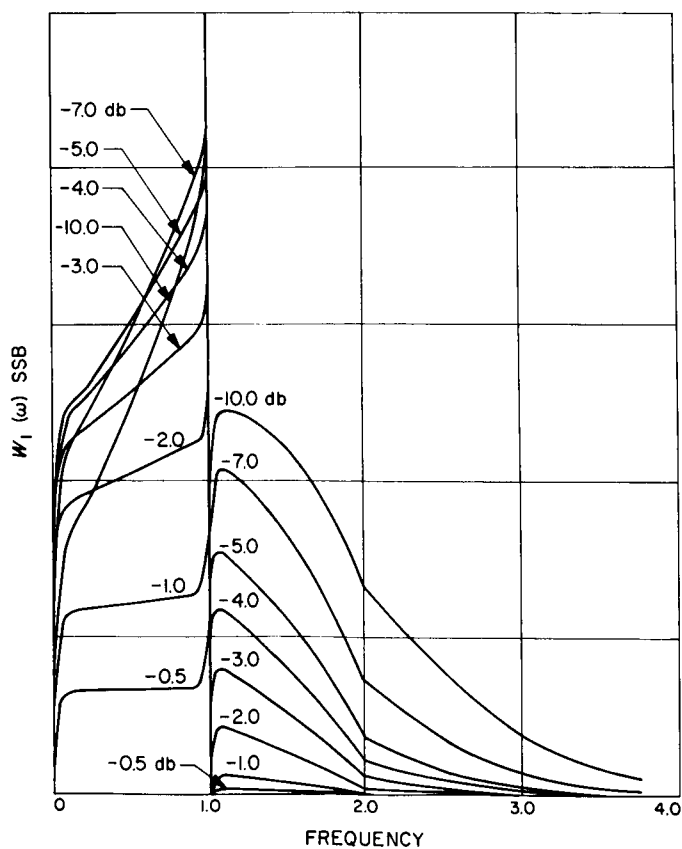
Eq. 25 is primarily of academic interest; Eq. 26 is that of the envelope of a random or pseudo-random binary sequence—e.g., a pseudo-noise (PN) code; and Eq. 27 of a sequence mod-2 the code clock (e.g., $\text{PN} \oplus 2f_s$). (See Ref. 13 for further details). The corresponding $R_f(\tau)$ and $\hat{R}_f(\tau)$ are given in Table 2.

The DSB and SSB plots of the three cases are given respectively in Figs. 12 through 17 for P_c/P_{TOT} ratios of $-0.5, -1, -2, -3, -4, -5, -7$, and -10 db. Of greatest interest is the bandwidth savings of SSB over DSB. For this purpose, the cumulative power with respect to frequency has been calculated, and results are shown in Tables 3, 4, and 5, with a certain percentage of total sideband power assumed recovered in each case. It is seen in each case that the bandwidth savings for low modulation index is very close to 50%. For higher modulation index, the savings for the rectangular spectrum is only 25%, while for the other two more practical situations there is a savings on the order of 40%. The percent bandwidth savings is a function of the roll-off rate of the spectrum of the modulating signal.

Table 2. Autocorrelation function

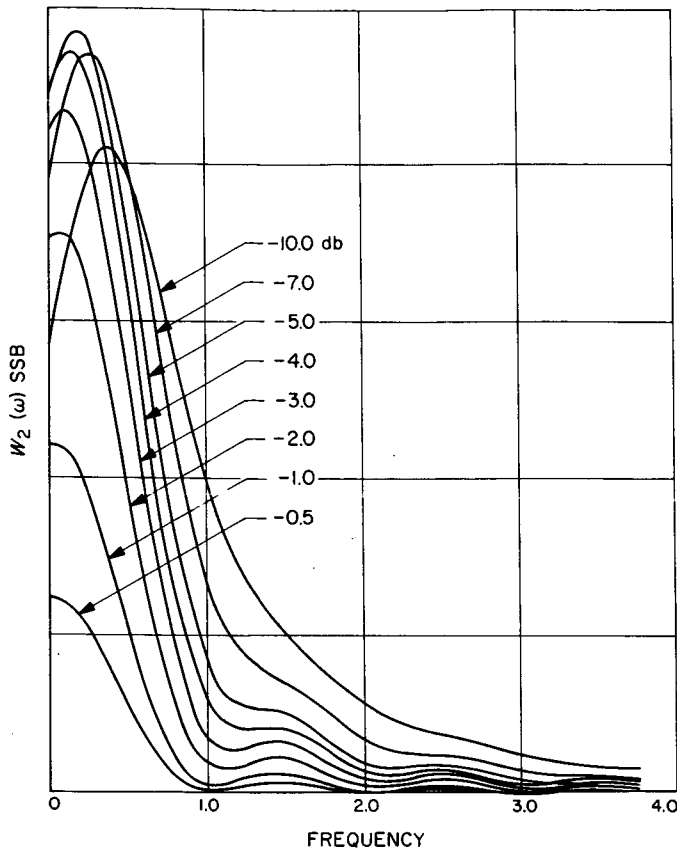
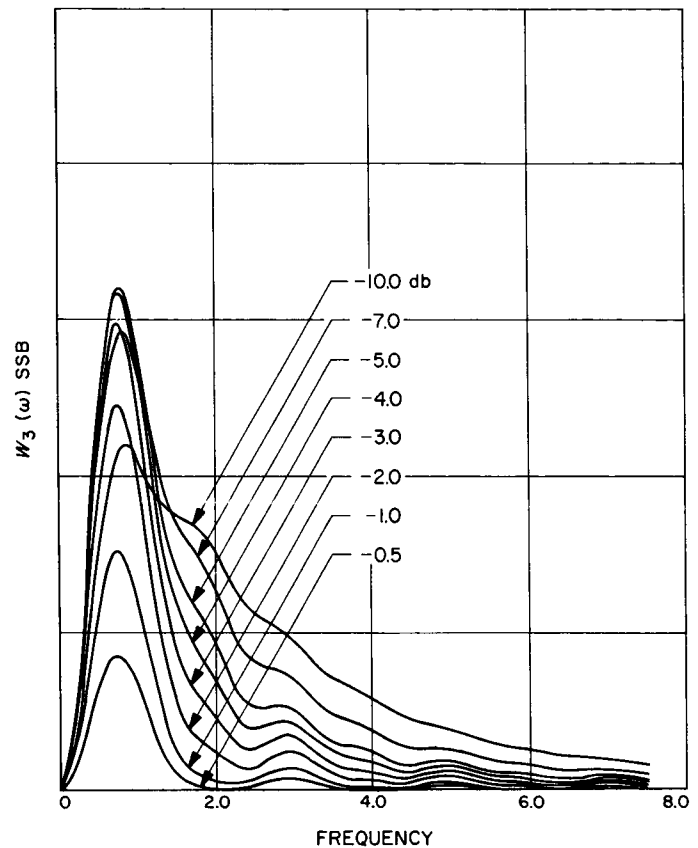
	$R_f(\tau)$	$\hat{R}_f(\tau)$
$W_1(\omega)$	$\frac{\sin \pi \tau}{\pi \tau}$	$\frac{\cos(\pi \tau) - 1}{\pi \tau}$
$W_2(\omega)$		$\frac{1}{\pi} \ln \left \frac{\tau+2}{\tau-2} \right + \frac{\tau}{2\pi} \ln \left \frac{(\tau+2)(\tau-2)}{\tau^3} \right $
$W_3(\omega)$		$\frac{\tau}{2\pi} \ln \left \frac{(\tau+1)(\tau-1)}{(\tau+2)(\tau-2)} \right + \frac{1}{\pi} \ln \left \frac{(\tau+1)^2(\tau-2)}{(\tau-1)^2(\tau+2)} \right $ $+ \frac{3\tau}{2\pi} \ln (\tau+1)(\tau-1) - 3\tau \ln \tau $

Fig. 12. Double-sideband spectrum for $W_1(\omega)$ Fig. 13. Double-sideband spectrum for $W_2(\omega)$

Fig. 14. Double-sideband spectrum for $W_3(\omega)$ Fig. 15. Single-sideband spectrum for $W_1(\omega)$ Table 3. Comparison of SSB and DSB for $W_1(\omega)$

P_c/P_{TOT} , db	Bandwidth to recover 90% SSB power ^a	Bandwidth to recover 90% DSB power ^a	Bandwidth saving of SSB over DSB
- 0.5	0.85	1.7	50%
- 1.0	0.88	1.7	48%
- 2.0	1.0	1.7	41%
- 3.0	1.2	1.8	33%
- 4.0	1.4	2.0	30%
- 5.0	1.6	2.2	27%
- 7.0	1.8	2.4	25%
-10.0	2.3	2.8	18%

^aBandwidth relative to $\omega = 1$, the cutoff frequency of the modulation.

Fig. 16. Single-sideband spectrum for $W_2(\omega)$ Fig. 17. Single-sideband spectrum for $W_3(\omega)$

6. Conclusion

In the foregoing presentation, the conditions necessary to achieve exact SSB/PM were explored and the second moment function for a Gaussian modulating signal was derived. Calculations for some specific modulating spec-

tral shapes showed that bandwidth savings of 40% can be achieved even for high modulation index. As a result, it may be concluded that the use of SSB might alleviate problems encountered when DSB modulation approaches the bandwidth constraint.

Table 4. Comparison of SSB and DSB for $W_2(\omega)$

P_c/P_{TOT} , db	Bandwidth to recover 90% SSB power ^a	Bandwidth to recover 90% DSB power ^a	Bandwidth saving of SSB over DSB
- 0.5	1.1	2.2	50%
- 1.0	1.2	2.4	50%
- 2.0	1.35	2.6	48%
- 3.0	1.5	2.8	46%
- 4.0	1.65	3.0	44%
- 5.0	1.85	3.2	42%
- 7.0	2.35	4.0	41%
-10.0	3.1	5.0	38%

^aBandwidth relative to $\omega = 1$, the first null in the modulation spectrum.

Table 5. Comparison of SSB and DSB for $W_3(\omega)$

P_c/P_{TOT} , db	Bandwidth to recover 85% SSB power ^a	Bandwidth to recover 85% DSB power ^a	Bandwidth saving of SSB over DSB
- 0.5	2.5	4.8	48%
- 1.0	2.7	5.2	48%
- 2.0	2.95	5.6	47%
- 3.0	3.25	6.0	46%
- 4.0	3.75	6.6	43%
- 5.0	4.3	7.2	41%
- 7.0	5.4	9.0	40%
-10.0	7.2	11.4	37%

^aBandwidth relative to $\omega = 1$. The first null in the modulating spectrum occurs at $\omega = 2$.

N67 12135

D. Tape Recorder With Incremental Playback Capabilities

E. Bahm

1. Introduction

Deep space missions impose the requirement of low playback rates on tape recorders because of the long communication distance between spacecraft and Earth, and variable playback rates will very often be required because of the changing distance. To operate at very low data rates, the speed of the magnetic tape must be very low. Maintaining a low, constant speed with very little speed ripple is difficult and requires a complex mechanism. The type of playback heads most generally used sense the rate of change of the flux induced by the magnetic tape; consequently, the output signal amplitude of the playback head is proportional to the tape speed. With this type of head, the lowest speed possible is 0.01 in./sec.

The following techniques are being studied to provide spacecraft recorders with the capability of playing back the recorded information at low and variable data rates.

a. Buffered tape recorder. A pair of solid-state or core memories of equal storage capacity is used between the tape recorder and the spacecraft transmitter. This technique makes use of the variable data rate capability of those memories. Transfer of data from the recorder into one of the memories takes place at a data rate suitable for the recorder; at the same time, the data from the second memory are transferred into the transmitter at the transmitting rate. As soon as the second memory is empty, the functions of the two memories are interchanged. Data are continuously clocked out of one of the memories, but data flow into the memories occurs in short bursts at higher data rates. Capacity of the memories may range from several hundred bits to several thousand bits.

The disadvantages of this approach are system complexity and the fact that the information must be recorded on tape in blocks equal to the capacity of each buffer memory. Gaps sufficiently long to prevent loss of information must be provided between these data blocks for stop and start of the recorder.

b. Tape recorders with flux sensitive playback heads. The magnetization pattern on the tape can be sensed with a head that detects magnetic flux magnitude rather than rate of change. One type of flux-sensing head uses the Hall effect; another type uses high-frequency biasing.

Neither technique has found widespread application. It is believed that a substantial development effort will be required to produce a flux-sensing head suitable for high-capacity spacecraft tape recorders.

c. Incremental playback. An incremental motion tape recorder plays data back one bit at a time by moving the tape in short uniform velocity steps. Upon outside command, the tape is rapidly accelerated to a prescribed speed suitable for the playback head. The speed is then held fairly constant by a velocity servo until one bit of the taped information is received. Immediately thereafter the tape is stopped, and the bit is fed into a flip-flop where it remains until called upon by the transmitter. The call of the transmitter also initiates the next increment of the recorder. The flip-flop may be replaced by an n -stage shift register. In this case, n bits will be reproduced at each increment of the recorder. Although this approach is relatively simple and well within the state of the art, it places severe requirements on the motor.

A careful study of these three techniques revealed that the first and third approaches had enough potential to justify immediate development efforts. This report describes the study of the incremental playback technique and the conclusions drawn from it.

2. Design of the Incremental Recorder

A study program was outlined during 1964 to determine the feasibility of accomplishing controlled incremental motion of magnetic tape at playback. A breadboard tape transport capable of handling several feet of $\frac{1}{4}$ -in. tape was to be constructed. The necessary electronic circuits for recording at constant speed and incremental playback were to be designed and built. No environmental requirements were placed on the recorder. The study was undertaken to determine the capabilities and limitations of such a recorder and to detect possible problems. A contract to perform this work was awarded to Ampex on August 23, 1965.

An initial design study resulted in the following decisions:

- (1) Direct capstan drive would be required to avoid the elasticity and backlash inherent in systems that employ speed reduction.
- (2) A printed motor was the best choice for the prime mover because of its uniform high torque and short response time. A modified unit—Model PC-368—

manufactured by Printed Motors, Inc., New York, was selected for this development.

A photograph of the breadboard tape recorder is presented in Fig. 18. Fig. 19 is an enlargement of the capstan assembly.

The perforated wheel in the photographs is the main capstan. It is mounted on the shaft of the printed motor. (The printed motor is mounted beneath the capstan assembly plate.) The capstan is rubber-coated to prevent slippage of the tape on the capstan. To the right of the

capstan is a low-inertia pivoted arm with an idler pulley on each end, which was provided to allow the short piece of tape around the capstan to perform short, rapid movements without requiring rapid acceleration of the complete tape loop.

A second motor was provided to drive the capstan/pinch wheel assembly, located in the center of the transport (see Fig. 18). This motor is servo-controlled to drive the tape in the storage loops such that the pivot arm is kept near the neutral position. (Recent experiments have shown that this motor is not necessary, because the elasticity of the tape is sufficient to decouple the main capstan from the inertial load of the tape storage loop assembly.)

The recording heads are pressed lightly against the coated side of the tape which is wrapped around the capstan. This technique is considered important for incremental operation as it prevents the tape elasticity from affecting the motor servo.

Fig. 20 is a block diagram of the recorder electronics. A prerecorded tachometer track on tape is used for measurement of the tape speed. A constant frequency was recorded in nonreturn-to-zero (NRZ) code at a density of 4000 flux reversals/in. The frequency derived from the tachometer track is used to servo-control the capstan motor for a constant tape speed of 1.2 in./sec. Two record/playback channels are provided for recording in NRZ(M) code: channel one for recording binary data, and channel two for recording the clock signal. (In this development model, these channels shared a single record amplifier, and the clock signal was recorded on both channels. This allowed measurement of interchannel time displacement errors. Recording of binary data was not considered necessary for the evaluation of this recorder.)

In the incrementing mode, used exclusively for playback, a start command is supplied to the "Start Input." The motor accelerates with full power until the tape speed reaches 1.2 in./sec. Then the speed servo reduces the motor current to maintain constant tape speed. As soon as a clock pulse is received from channel 2, a detector circuit shapes a stop pulse, which is fed into the "Stop Input" terminal. This causes a reverse current pulse to be supplied to the capstan motor for a short time, and this stops the motor rapidly. At low recording densities, normal friction forces are sufficient to stop the motor within the required angle without application of dynamic braking. By disconnecting the clock track output, the recorder can be operated at a continuous speed of 1.2 in./sec.

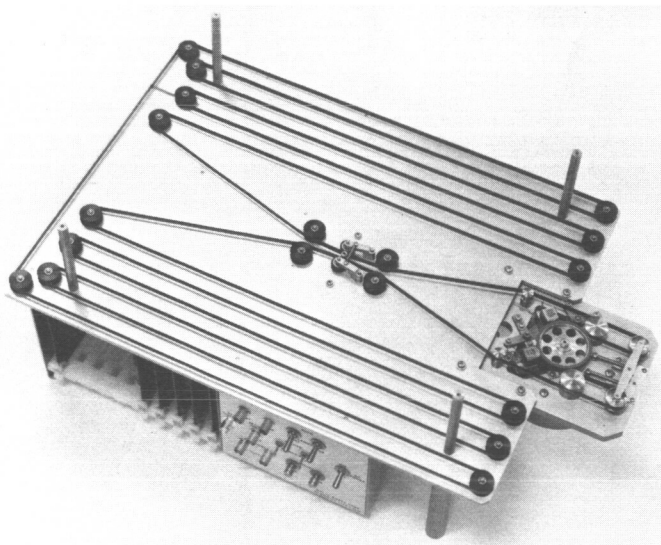


Fig. 18. Incremental tape recorder

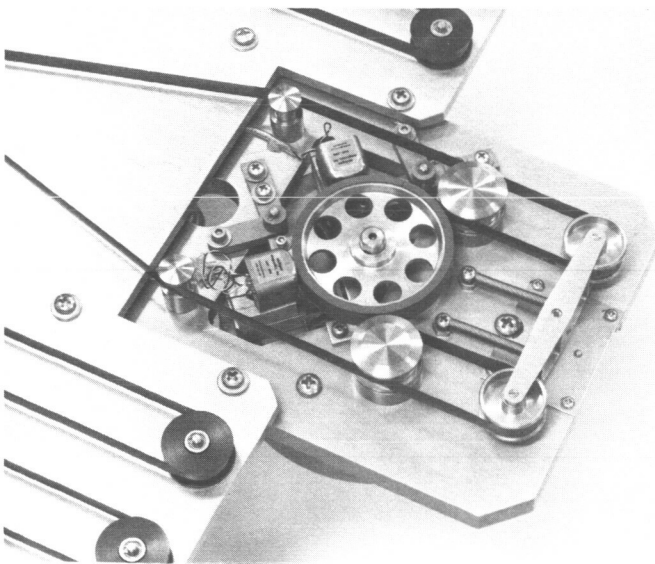


Fig. 19. Capstan assembly

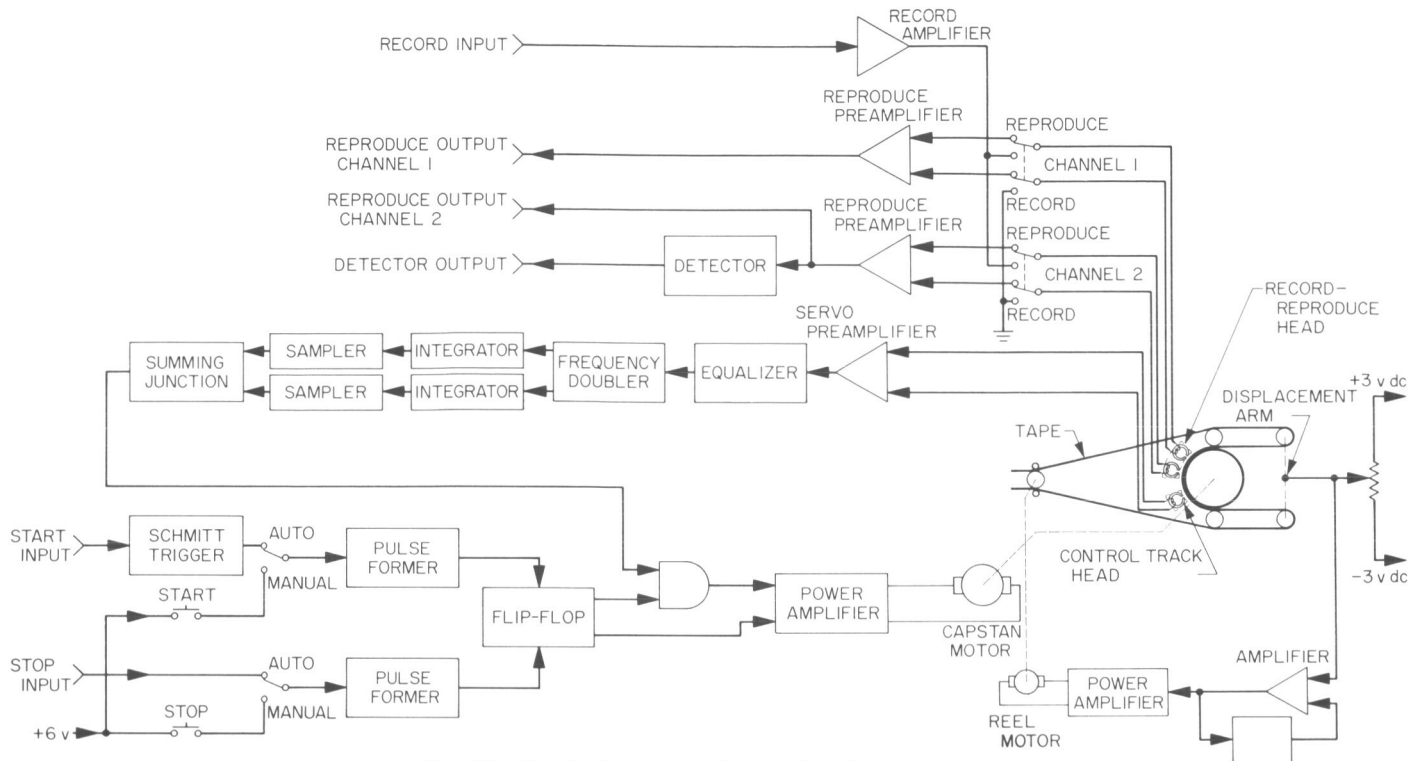


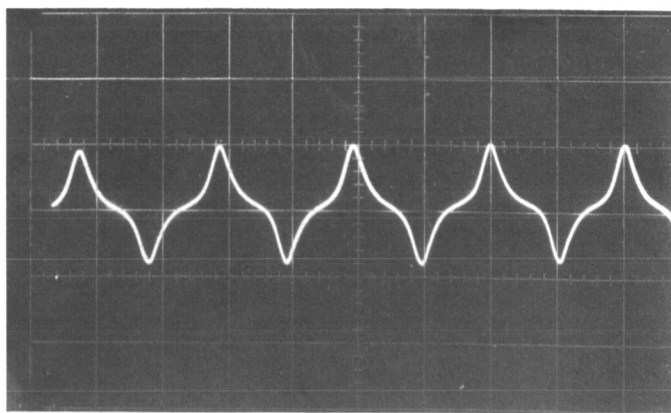
Fig. 20. Block diagram of recorder electronics

3. Performance of the Incremental Recorder

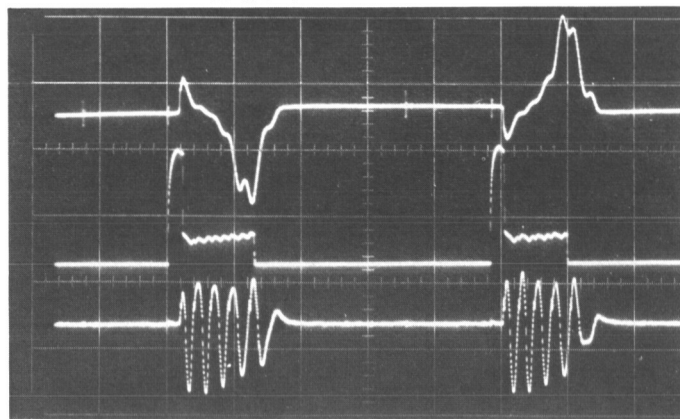
A series of binary one's was recorded in the NRZ(M) code on both channels at low recording density. Fig. 21a shows the output wave form when the tape is reproduced at constant speed. The top trace of Fig. 21b shows the output of the data channel when reproduced increment-

ally. It also shows the motor current (middle trace) and the signal from the tachometer track (bottom trace). In this case no reverse current was used for fast stop of the motor. The oscillogram of the motor current and

TOP TRACE: PLAYBACK SIGNAL (1 v/cm)
MIDDLE TRACE: MOTOR CURRENT (2 amp/cm)
LOWER TRACE: OUTPUT FROM TACHOMETER TRACK (2 v/cm)



(a) Reproduction at constant speed of 1.2 in./sec
(2 msec/cm, 2 v/cm)



(b) Incremental reproduction at 100 increments/sec
(2 msec/cm)

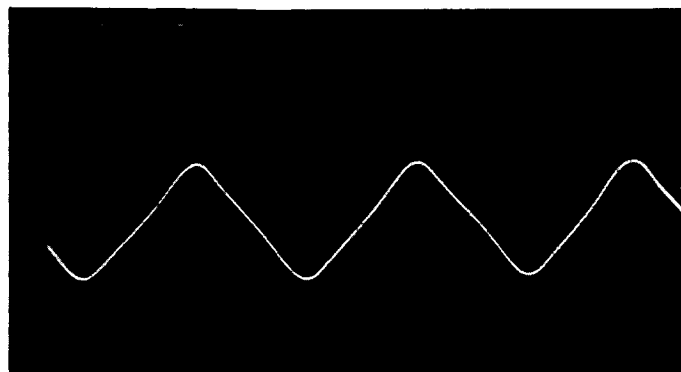
Fig. 21. NRZ(M) recording of 400 flux reversals/in.

tachometer signal shows that the tape is moving at the controlled speed for a considerable time and that it is starting and stopping very quickly. Start time can be adjusted within certain limits by changing the voltage applied to the motor, which determines the motor current during acceleration. Stop time is adjusted with the reverse voltage determining reverse motor current. There are two reasons for the short start and stop time:

- (1) The electrical time constant of the printed motor is less than 200 μ sec. As can be seen in Fig. 21b, the motor current is rising very rapidly and full motor torque is available almost instantaneously.
- (2) The motor must accelerate only to a very slow speed. The tape speed of 1.2 in./sec requires a motor speed of only 23 rpm.

From the tests at low recording densities, it was concluded that incremental operation should be possible at much higher recording densities. Fig. 22a shows the constant speed playback of the NRZ recording at higher recording density. The waveform is already close to a sine wave. In spite of this, reliable incremental playback was still possible. Fig. 22b shows playback signal, motor current, and tachometer signal at the higher recording density and at a higher repetition rate.

High recording density is desirable not only for obtaining good tape utilization, but the shorter step required during playback can be executed in a shorter time. Consequently, higher repetition rates are achievable with use of higher recording densities. Also, the energy per step of the incrementor is dependent upon the recording density.



(a) Reproduction at constant speed of 1.2 in./sec
(0.5 msec/cm, 2 v/cm)

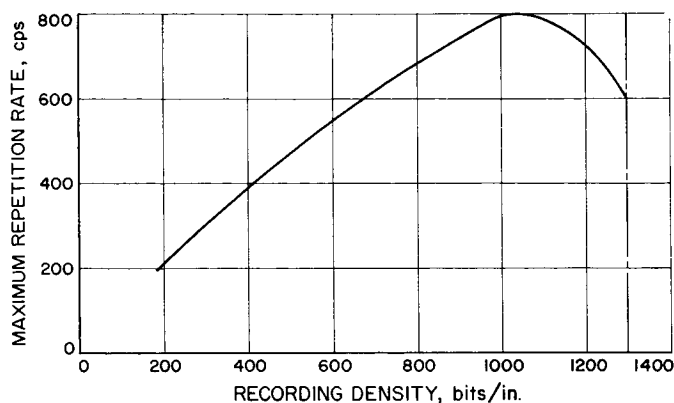
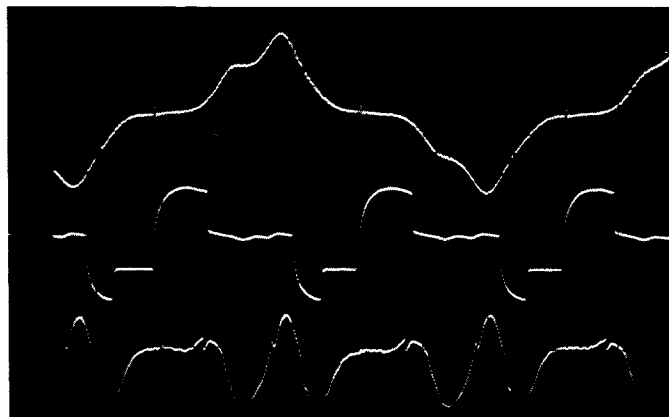


Fig. 23. Highest repetition rate possible while assuring stable operation (error rate less than 10^{-4})

Fig. 23 shows the highest repetition rates (which permitted stable and nearly error-free operation) as a function of recording density. The limit of reliable operation was 1300 flux reversals/in. The recorder was capable of degraded operation at even higher recording densities, but the error rate began to increase with the density at all repetition rates. Highest reliable repetition rate was 800 increments/sec, and was achieved at a density of 1000 flux reversals/in.

An important aspect of the study was the determination of the peak and average power required by the capstan motor and its control circuit. Both are functions of the recording density and the maximum repetition rate

TOP TRACE: PLAYBACK SIGNAL (1 v/cm)
MIDDLE TRACE: MOTOR CURRENT (2 amp/cm)
LOWER TRACE: OUTPUT FROM TACHOMETER TRACK
(2 v/cm)



(b) Incremental reproduction at 600 increments/sec
(0.5 msec/cm)

Fig. 22. NRZ(M) recording of 1000 flux reversals/in.

for which the incrementor is adjusted. If more power is available for acceleration and deceleration, start time and stop time can be reduced. This means that less time is required to perform one increment and, therefore, the repetition rate can be higher. The normal practice is to adjust peak motor power to a value just high enough to accomplish the required repetition rate at the specified recording density. Average power is then a direct function of the repetition rate. Fig. 24 shows average power versus repetition rate for various recording densities and different peak power adjustments. The maximum repetition rate at the particular adjustment and recording density is indicated by a small circle. It can be seen that the average power at any given stepping rate reaches a minimum at a recording density of 1000 bits/in.

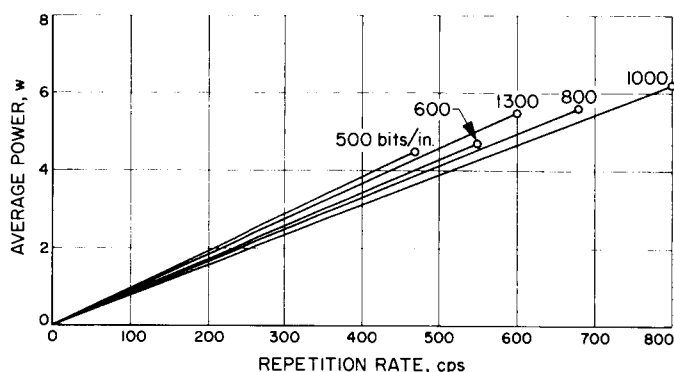


Fig. 24. Average power consumption of incrementor

The peak power required is a function of the maximum required repetition rate and is dependent to a lesser degree on recording density. It is independent of the repetition rate itself. The lowest value of peak power permitting reliable operation was 3.2 w. The maximum repetition rate obtained with the 3.2-w adjustment is plotted as a function of recording density in Fig. 25. In order to obtain higher repetition rates, peak power has to be higher. For the repetition rates of Fig. 23, the peak power was 12.3 w.

4. Conclusions

The study has shown that controlled incremental playback of a tape recorder is feasible. It also was demonstrated that the complexity of the control electronics is

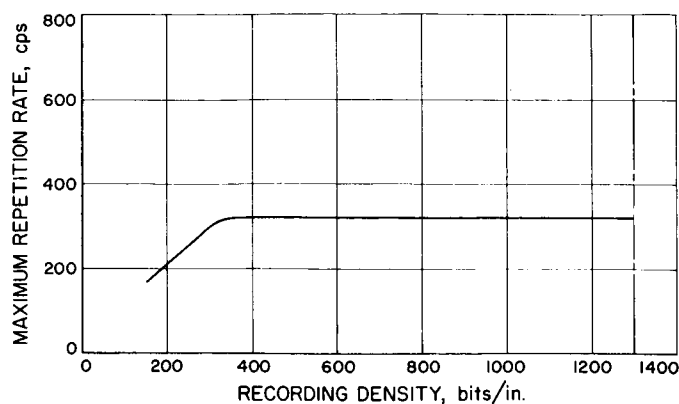


Fig. 25. Highest repetition rate with 3.2-w peak input power to incrementor

not prohibitive for spacecraft applications. The same is true for the power consumption. The error rate is higher than that of constant-speed tape recorders, and the control electronics must be carefully adjusted. However, this can be improved by using a slightly more sophisticated detection circuit. More than a thousand hours of incremental operation have been accumulated during the tests with no bearing or motor failure.

The only serious problem still unsolved concerns the capstan motor. The printed motor is not considered suitable for spacecraft applications as the brushes and a very thin, flexible armature disk make it sensitive to vibration, shock, and wear. The fact that repetition rates of 200 increments/sec are considered adequate shows that the printed motor performs much better than actually required. Data rates above 200 bits/sec can well be obtained by operating the recorder in the constant speed mode. Therefore, there may be other motors that are better suited for the space environment and are still capable of driving the incremental recorder at some reduced rate.

The next phase of this effort will be the study of different types of motors for spacecraft use. A very desirable feature of such a motor would be an iron-free armature winding to assure low electrical time constant and no magnetic retention. A brushless dc motor of this type, currently being fabricated by AiResearch Division of the Garrett Corporation, will be installed in the incremental recorder.

References

1. Kolmogorov, A. N., *Foundations of the Theory of Probability*, Chelsea Publishing Co., New York, 1956.
2. Parzen, E., *Modern Probability Theory and Its Applications*, John Wiley & Sons, Inc., New York, 1960.
3. Esary, J. D., and Prochan, F., "The Reliability of Coherent Systems," in *Redundancy Techniques in Computing Systems*, pp. 47-61. Edited by R. H. Wilcox and W. C. Mann, Spartan Books, Washington, D. C., 1962.
4. Dugundji, J., "Envelopes and Pre-Envelopes of Real Waveforms," *IRE Transactions on Information Theory*, Vol. IT-1, March 1953.
5. Deutsch, R., *Nonlinear Transformations of Random Processes*, Prentice-Hall, Inc., Englewood Cliffs, N.J., 1962.
6. Middleton, D., *On the Distribution of Energy in Noise and Signal Modulated Waves, II. Simultaneous Amplitude and Angle Modulation*, *Quarterly of Applied Mathematics*, Vol. 9, No. 4, January 7, 1952, pp. 337-354.
7. Middleton, D., *An Introduction to Statistical Communication Theory*, McGraw-Hill Book Co., Inc., New York, 1960.
8. Titchmarsh, E. C., *Introduction to the Theory of Fourier Integrals*, The Clarendon Press, Oxford, 1962.
9. Whittaker, E. T., and Watson, G. N., *A Course of Modern Analyses*, Cambridge University Press, London, 1963.
10. Barnard, R. D., "On the Spectral Properties of Single Sideband Angle Modulated Signals," *Bell System Technical Journal*, Vol. 43, November 1964, pp. 2811-2838.
11. Bedrosian, E., "The Analytic Signal Representation of Modulated Waveforms," *Proceedings of IRE*, Vol. 50, October 1962, pp. 2071-2076.
12. Dubois, J. I., and Aagaard, J. S., "An Experimental SSB-FM System," *IEEE Transactions on Communication Systems*, Vol. CS-12, June 1964, pp. 222-229.
13. Springett, J. C., *Telemetry and Command Techniques for Planetary Spacecraft*, Technical Report 32-495, Jet Propulsion Laboratory, Pasadena, Calif., January 15, 1965. (Also in *Advances in Communication Systems: Vol. I*, Academic Press, New York, 1965.)

N67 12136

XVII. DSIF Engineering

A. Antenna Structures: Evaluation Techniques of Reflector Distortions

M. S. Katow and L. W. Schmele¹

1. Introduction

Two techniques used to evaluate the distortion of the reflective surface of an antenna, the root-mean-square (RMS) and the radiation computer programs, have been discussed earlier (*SPS 37-23*, Vol. IV, p. 228; *SPS 37-21*, Vol. III, p. 28). Recent modifications to the RMS computer program have decreased the input data requirements and improved the accuracy and clarity of the answers. The modifications made were:

- (1) Upgraded coding in the program to add the focal length change as a variable included with all other parameters in the process of best fitting the paraboloid.

- (2) Added provisions to the program to selectively impose restraints or assignments of predetermined values to the position parameters of the best-fitting paraboloid. This allows partial input data for symmetrical load conditions and control on the individual degrees of freedom of the fitting paraboloid during the fitting process.
- (3) Added outputs of computer organized plots of contour levels of constant deviations of $\frac{1}{2}$ path length changes or errors from the fitting paraboloid. The contour charts are made by the Stromberg-Carlson 4020 plotter.
- (4) Added provisions to output the calculated average deviation of the $\frac{1}{2}$ path length errors after the best fit with the paraboloid. The calculation will serve as a check on the accuracy of the RMS figure.

As previously described (Ref. 1), the RMS figure may be used for RF performance evaluation of the deformed reflector. The individual normal error and path length change outputted at each joint in conjunction with the

¹Section 314.

Table 1. Definition of terms

A_i	= weighting function associated with the i^{th} point
b	= z component of the distortion vector = d_z
d	= distortion vector—this vector need not be in the plane shown
d	= projection of the normal component on the unit vector along the axis of the undeformed paraboloid
e	= increment path length change away from the focal point
f	= increment path length change toward the aperture plane
F	= focal length
K	= parabolic constant
S_1	= path length from paraboloid point i to the aperture plane
S_2	= path length from the focal point to the paraboloid point i
S_r	= cosine of angle between surface normal and radial direction
S_x, S_{x_i}	= direction cosine of the normal to antenna surface— x direction
S_y, S_{y_i}	= direction cosine of the normal to antenna surface— y direction
S_z, S_{z_i}	= direction cosine of the normal to antenna surface— z direction
u_i, v_i, w_i	= x, y, z components of the normal displacement δ_i
U_0, V_0, W_0	= rigid body displacements of paraboloid in $x, y,$ and z directions
x_i, y_i, z_i	= Cartesian coordinates of point i
α, β	= rigid body rotations of the paraboloid about x -axis and rotated y -axis, respectively
δ	= normal component of the distortion vector
δ_i	= normal displacement of point i
ΔPL_i	= path length change at point i

The above geometric definition of the path length change can also be derived as described in Footnote 2. In Fig. 2, the positive-sign normal distortion vector is shown.

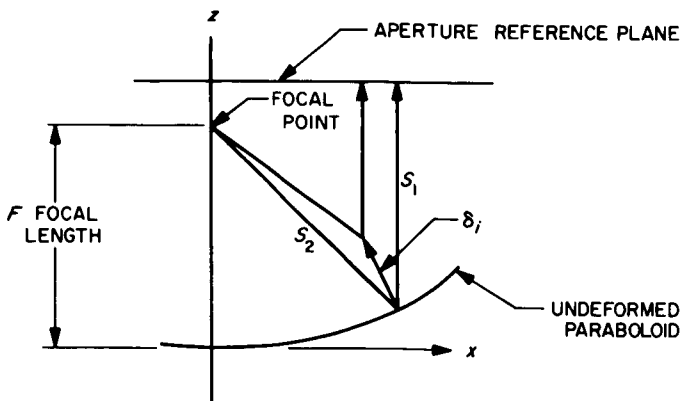


Fig. 2. RF path length change—analytical illustration

The original path length PL from the focal point to the aperture plane is given by

$$PL = S_1 + S_2$$

The distorted path length PL' is given by

$$PL' = S_1 - \delta_i \cdot S_z + [(S_z - \delta_i \cdot S_z)^2 + (\delta_i \cdot S_r)^2]^{1/2}$$

Thus, the path length change ΔPL is

$$\Delta PL = PL - PL'$$

$$\Delta PL = S_1 + S_2 - [(S_z - \delta_i \cdot S_z)^2 + (\delta_i \cdot S_r)^2]^{1/2} - (S_1 - \delta_i S_z)$$

which may be written as

$$\Delta PL = (S_z - \delta_i \cdot S_z)^2 \left\{ \left[1 + \frac{(S_i \cdot S_r)^2}{S_z - \delta_i S_z} \right]^{1/2} - 1 \right\} - 2 \delta_i \cdot S_z$$

The right-hand side may then be expanded into a Taylor series to obtain

$$\Delta PL = -2\delta_i S_z + \frac{1}{2} \frac{(\delta_i \cdot S_r)^2}{(S_z - \delta_i S_z)} - \frac{1}{4} \frac{(\delta_i S_r)^4}{(S_z - \delta_i S_z)^3} + \dots$$

which may be written as

$$\Delta PL = -2\delta_i S_z \left[1 + \frac{S_i S_z^2}{4(S_z - \delta_i S_z) S_z} - \frac{\delta_i^3 S_r^4}{8(S_z - \delta_i S_z)^3 S_z} + \dots \right]$$

It is seen that for $\delta_i \ll S_z$, terms involving higher powers of S_r may be neglected without appreciable loss of accuracy so that the path length change may be denoted by

$$\Delta PL = -2\delta_i \cdot S_z$$

The RMS of the $\frac{1}{2}$ path length change or error is computed after the least-squares fit or a constrained fit with selected restraints/assignments of the motion of the fitting paraboloid. It should be noted that the RMS will always be computed with respect to the position of the fitting paraboloid using the formula

$$RMS = \sqrt{\frac{\sum (\Delta PL_i)^2 A_i}{4 \sum A_i}}$$

From Ref. (2) and Footnote 2, the normal component of distortion from the best-fit paraboloid may be attributed to three components:

(1) surface distortions

$$\delta_{ia} = u_i S_{xi} + v_i S_{yi} + w_i S_{zi} \quad (5)$$

(2) change in focal length from the original paraboloid

$$\delta_{ib} = -K(x_i^2 + y_i^2) S_z \quad (6)$$

$$\text{where } K = \frac{1}{4} \left(\frac{1}{F} - \frac{1}{F'} \right)$$

(F being the focal length of the original paraboloid and F' the focal length of the best-fit paraboloid)

(3) rigid body motion of the paraboloid

$$\delta_{ic} = -U_0 S_{xi} - V_0 S_{yi} - W_0 S_{zi} + \alpha(z_i S_{yi} - y_i S_{zi}) + \beta(x_i S_{zi} - z_i S_{xi}) \quad (7)$$

Thus,

$$\delta_i = \delta_{ia} + \delta_{ib} + \delta_{ic}$$

and

$$\Delta PL = 2S_x u + S_y v + S_z w - S_z(x^2 + y^2)K - U_0 S_x - V_0 S_y - W_0 S_z + (z S_y - y S_z)\alpha + (x S_z - z S_x)\beta \quad (8)$$

The best-fit paraboloid is found by minimizing S , the sum of squares of residuals, i.e., path length changes, where

$$S = \sum_i (\Delta PL_i)^2 A_i \quad (9)$$

and where A_i is a weighting factor associated with the i^{th} point. Minimization is accomplished by setting the partials of S with respect to the six parameters $U_0, V_0, W_0, \alpha, \beta$, and K , equal to zero, and solving the resulting set of six linear normal equations:

$$\begin{aligned} \frac{\partial S}{\partial U_0} &= 2 \sum_i \frac{\partial \Delta PL_i}{\partial U_0} \Delta PL_i A_i = 0 \\ \frac{\partial S}{\partial V_0} &= 2 \sum_i \frac{\partial \Delta PL_i}{\partial V_0} \Delta PL_i A_i = 0 \\ \frac{\partial S}{\partial W_0} &= 2 \sum_i \frac{\partial \Delta PL_i}{\partial W_0} \Delta PL_i A_i = 0 \\ \frac{\partial S}{\partial \alpha} &= 2 \sum_i \frac{\partial \Delta PL_i}{\partial \alpha} \Delta PL_i A_i = 0 \\ \frac{\partial S}{\partial \beta} &= 2 \sum_i \frac{\partial \Delta PL_i}{\partial \beta} \Delta PL_i A_i = 0 \\ \frac{\partial S}{\partial K} &= 2 \sum_i \frac{\partial \Delta PL_i}{\partial K} \Delta PL_i A_i = 0 \end{aligned} \quad (10)$$

where

$$\begin{aligned} \frac{\partial \Delta PL_i}{\partial U_0} &= -S_{xi} \\ \frac{\partial \Delta PL_i}{\partial V_0} &= -S_{yi} \\ \frac{\partial \Delta PL_i}{\partial W_0} &= -S_{zi} \\ \frac{\partial \Delta PL_i}{\partial \alpha} &= z_i S_{yi} - y_i S_{zi} \\ \frac{\partial \Delta PL_i}{\partial \beta} &= x_i S_{zi} - z_i S_{xi} \\ \frac{\partial \Delta PL_i}{\partial K} &= -S_{zi} (x_i^2 + y_i^2) \end{aligned} \quad (11)$$

Substituting Eqs. (11) and (8) into Eq. (10) and defining

$$\begin{aligned} X_i &= S_{xi} U_0 + S_{yi} V_0 + S_{zi} W_0 + S_{zi} (x_i^2 + y_i^2) K \\ &\quad + (S_{zi} y_i - S_{yi} z_i) \alpha + (S_{xi} z_i - S_{zi} x_i) \beta \end{aligned} \quad (12)$$

$$Y_i = S_{xi} U_i + S_{yi} V_i + S_{zi} W_i$$

yields

$$\begin{aligned} \sum_i S_{xi} S_{zi}^2 X_i &= \sum_i S_{xi} S_{zi}^2 Y_i \\ \sum_i S_{yi} S_{zi}^2 X_i &= \sum_i S_{yi} S_{zi}^2 Y_i \\ \sum_i S_{zi}^3 &= \sum_i S_{zi}^3 Y_i \\ \sum_i S_{zi}^3 (x_i^2 + y_i^2) X_i &= \sum_i S_{zi}^3 (x_i^2 + y_i^2) Y_i \\ \sum_i S_{zi}^2 (S_{xi} y_i - S_{yi} z_i) X_i &= \sum_i S_{zi}^2 (S_{xi} y_i - S_{yi} z_i) Y_i \\ \sum_i S_{zi}^2 (S_{xi} z_i - S_{zi} x_i) X_i &= \sum_i S_{zi}^2 (S_{xi} z_i - S_{zi} x_i) Y_i \end{aligned} \quad (13)$$

Letting

$$\mathbf{d}_i = \begin{pmatrix} S_{xi} \\ S_{yi} \\ S_{zi} \\ S_{zi}(x_i^2 + y_i^2) \\ S_{xi} y_i - S_{yi} z_i \\ S_{xi} z_i - S_{zi} x_i \end{pmatrix} \quad (14a)$$

and

$$\mathbf{x} = \begin{Bmatrix} U_0 \\ V_0 \\ W_0 \\ K \\ \alpha \\ \beta \end{Bmatrix} \quad (14b)$$

Eq. (13) may be written in matrix notation as

$$\mathbf{Ax} = \mathbf{b} \quad (15)$$

where

$$\mathbf{A} = \sum_n A_i S_{zi}^2 \{ \mathbf{d}_i \} \{ \mathbf{d}_i \}^T$$

$$\mathbf{b} = \sum_n A_i S_{zi}^2 Y_i \{ \mathbf{d}_i \}$$

and Y_i is defined as in Eq. (12).

Solution of the set of six equations (Eq. 15) yields the six parameters of the vector \mathbf{x} which describes the rotational paraboloid best fitting the data.

For minimizing with restraints and/or assignments of selected parameters of the fitting paraboloid, Eq. (15) is modified; to assign the value of P_K to the K^{th} parameter, the matrix \mathbf{A} and the vector \mathbf{b}

$$\mathbf{A} = a_{ij}; i, j = 1, 2, \dots, 6$$

$$\mathbf{b} = b_j; j = 1, 2, \dots, 6$$

are modified such that

$$\bar{\mathbf{A}}\mathbf{x} = \bar{\mathbf{b}}$$

where

$$\bar{a}_{ij} = a_{ij} \text{ for } i \neq k$$

$$\bar{a}_{kj} = 0 \text{ for } j \neq k$$

$$\bar{a}_{kk} = 1.0$$

$$\bar{b}_j = b_j \text{ for } j \neq k$$

$$\bar{b}_k = P_k$$

4. Reduction of Field Data

Reduction of data can be obtained by either of two methods of field measurements. The first method uses an accurate angle-measuring theodolite rotatable around the axis of symmetry of the paraboloid, as shown in Fig. 3.

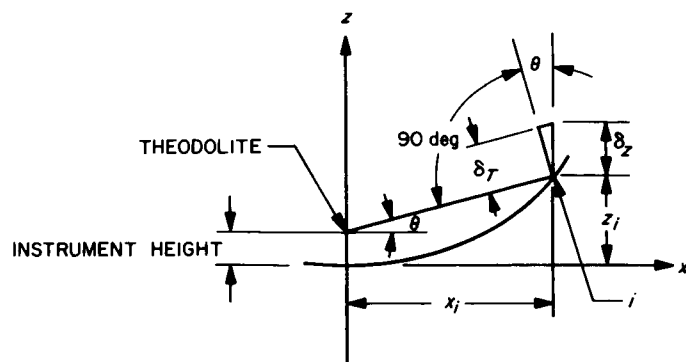


Fig. 3. Distortion measurements using theodolite

The apparent measured displacement δ_r of point i by the theodolite is indicated either by a small change in angle θ or by an optical micrometer as an offset δ_r . Although direction of the distortion vector does not necessarily lie in the direction of δ_r , it is assumed so. Within the program it is divided by $\cos \theta$, and the resulting δ_z is input as W data.

When an accurately contoured template is used to check the surface distortions, the error is measured normally at right angles to the surface, as shown in Fig. 4.

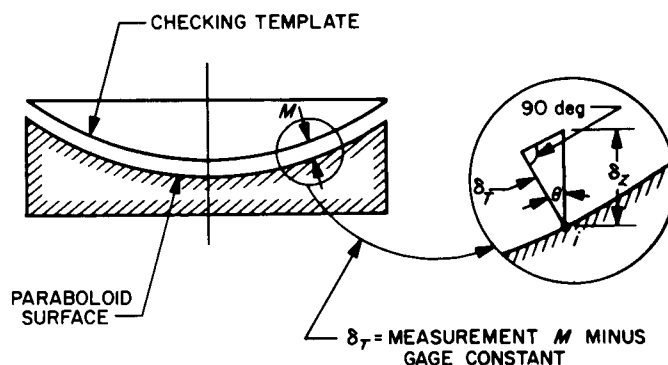


Fig. 4. Distortion measurements using template

In this method, δ_r is input as for the theodolite readings, and θ , the tangent angle of the curve at point i , is input as the theodolite angle. It is noted that the program uses the computed δ_z as the distortion vector which is compatible with the formulation that normalizes all input distortion vectors in the normal direction.

5. Analytical Data Inputs

The pre-computing and the quantity of the input data cards were minimized with the use of selective

restraints of degrees of freedom of the fitting paraboloid. It is axiomatic that a set of computer-generated deflections, from a symmetrical load on a symmetrical structure about the x - and y -axes planes, will also be symmetrical about the same axes. It follows that the best fitted paraboloid must have a symmetrical pattern of path length errors with no x nor y translations and no rotations about the x - and y -axes. In practice, when the deflection data is limited to a single quadrant with the same restrictions as to the types of loads and the structure as stated above, the RMS can be computed by the provisions for restraining the x , y translations and x , y rotations of the fitting paraboloid. For antisymmetric loads of a symmetric first-quadrant structure, the program generates the fourth quadrant before the best fit.

To compute an RMS for a reflector structure whose panels are adjusted to perfect parabolic shape at 45-deg elevation angle, two sets of deflections—one from a symmetric load and the other from an unsymmetric load—are needed. The program accepts the two sets of first-quadrant input data, generates the fourth quadrant, multiplies both sets of deflections by the input factors, and adds the resulting sets of deflections and computes the RMS.

If a peculiar requirement for a restraint is required, an option is available to select any combination of restraints.

6. Output Description

The output is illustrated in Fig. 5 for an assumed y and z translation and rotation about the x -axis.

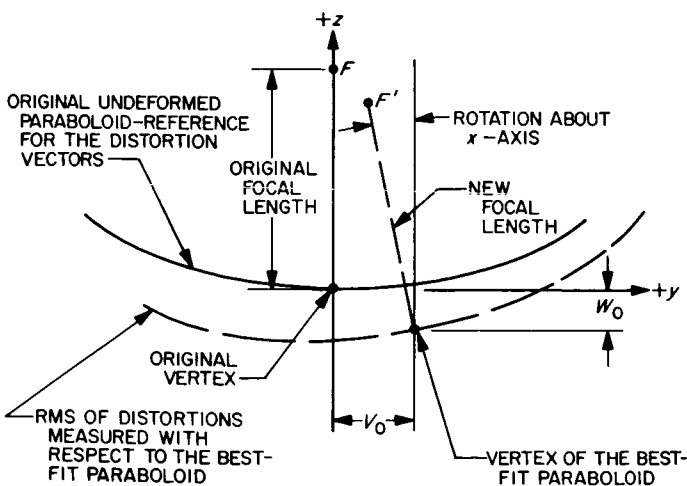


Fig. 5. Graphical illustration of the RMS output data

The minimization of RMS is first computed with respect to the original rigid body paraboloid (fixed focal length), followed by an added parameter to include the focal length change. Also, the normal error and the full path length error at each point are itemized.

To give an indication of the accuracy of the final numbers, the average deviations are computed. Inspection of normal calculations shows that the rigid body fit may not minimize at the minimum value, but with the added focal length variable, the minimum value is always obtained. A typical block of output is shown in Fig. 6.

7. RF Boresight Determination

The RF boresight may be computed from the output data. Fig. 7 indicates the result of ray tracing on Fig. 5, and shows the ray starting from the original focal point, rebounding off the vertex of the best-fit paraboloid at about 82% of the angle of incidence based on uniform illumination of the antenna.

It was assumed that the distortion vectors were symmetric about the y -axis and also that the RF feed point did not move from the original focal point. Since the sample best-fit location is typical of a normal antenna whose surface is set at a 45-deg elevation angle and measured at horizontal look, it is obvious that a small feed deflection caused by the quadripod can compensate for the reflector structure rotation.

8. Contour Levels Plots

Figs. 8 and 9 are sample RMS contour levels outputted by the Stromberg-Carlson plotter from the IBM 7094 computer produced tape. Both contour levels used the same input distortion data; however, in Fig. 8, the path length errors were plotted after a best fit, and in Fig. 9 the y and z vertex coordinates and the rotation about the x -axis of the fitting or, in this case, the measuring paraboloid were assigned.

The assignment numbers were determined by the distortions of the data targets used by the angle-measuring theodolite. When the parameters are correctly assigned, the zero-valued contour level must pass through the data points. The contour levels of Fig. 9 show that the distortion values actually read by the field theodolite are higher than the residuals after the best fit in Fig. 8. This is caused, of course, by the displacement of the nonrigid data plane.

BEST FIT PARABOLOID WITH MINIMUM PATH LENGTH IN LEAST SQUARES SENSE
AAS-210 SS*15-AS15 45 DEG SET ZENITH LOOK FULL DISH DATA 816 POINTS

ORIGINAL FOCAL LENGTH = 1067.290 NO. POINTS IN ANALYSIS = 816

INPUT DISTORTIONS OBTAINED ANALYTICALLY - OPTION -0

NORMAL ANALYSIS FOR INPUT DATA

MINIMIZATION OF RMS WITH RESPECT TO RIGID BODY MOTION

RMS OF 1/2 LAMBDA WEIGHTED BY AREAS = 0.083

DEVIATION OF THE MEAN - 1/2 LAMBDA S = -0.00231

SUM-UNIT AREA*1/2 LAMBDA = -3.770

SUM-UNIT AREAS = 816.000

X COORDINATE OF VERTEX = -0.000

Y COORDINATE OF VERTEX = -3.678

Z COORDINATE OF VERTEX = -0.079

ROTATION ABOUT X AXIS = -0.002364

ROTATION ABOUT Y AXIS = 0.000000

MINIMIZATION OF RMS WITH RESPECT TO FOCAL LENGTH CHANGE

RMS OF 1/2 LAMBDA WEIGHTED BY AREAS = 0.079

NEW FOCAL LENGTH = 1067.567

DEVIATION OF THE MEAN - 1/2 LAMBDA S = 0.00000

SUM-UNIT AREA*1/2 LAMBDA = 0.000

SUM-UNIT AREAS = 816.000

X COORDINATE OF VERTEX = -0.000

Y COORDINATE OF VERTEX = -3.678

Z COORDINATE OF VERTEX = -0.029

ROTATION ABOUT X AXIS = -0.002364

ROTATION ABOUT Y AXIS = 0.000000

ALL LENGTH UNITS ARE CONSISTENT WITH INPUT

ROTATION UNITS ARE RADIAN S

Fig. 6. Typical computer output

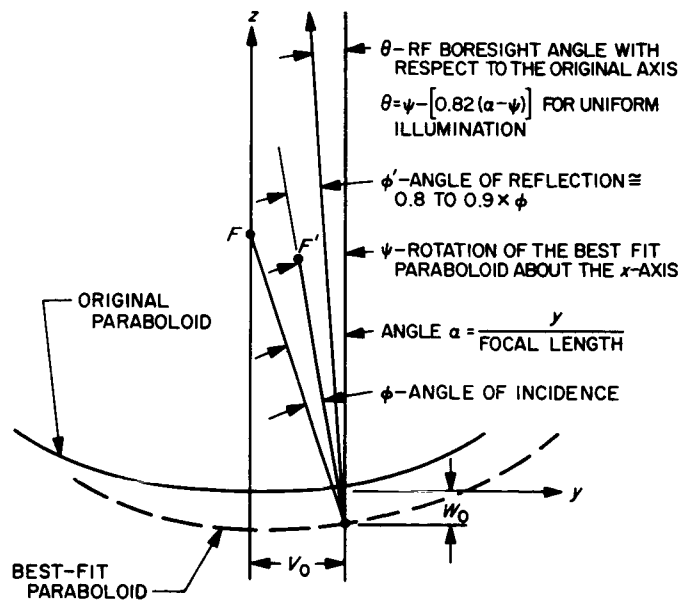
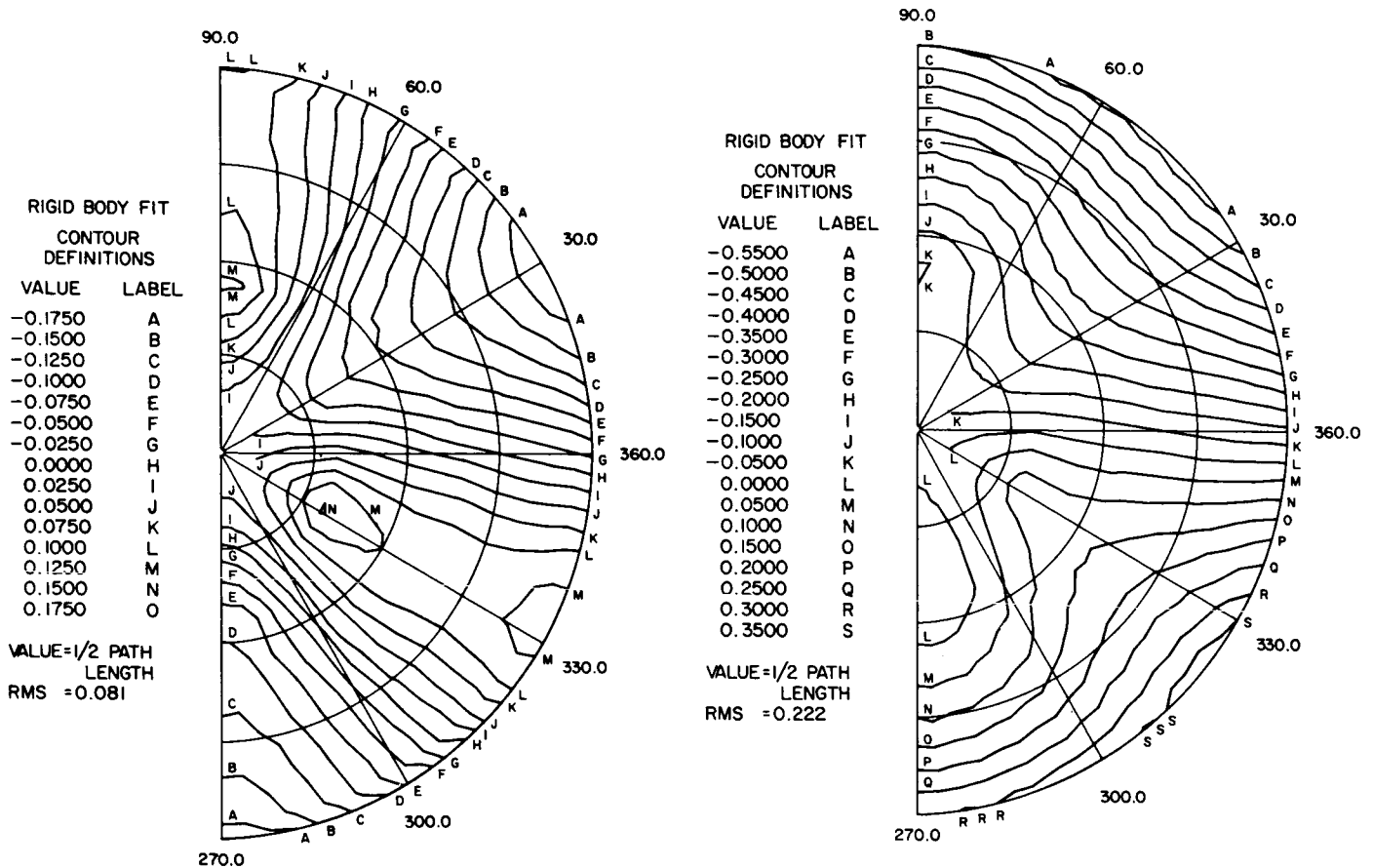


Fig. 7. RF boresight calculation from the RMS output data



References

1. Ruze, J., *Physical Limitations on Antenna*, Technical Report 248, Research Laboratory of Electronics, Massachusetts Institute of Technology, Cambridge, Mass., October 30, 1952 (ASTIA/AD-62351).
2. Utku, S., and Barondess, S. M., *Computation of Weighted Root-Mean-Square of Path Length Changes Caused by the Deformations and Imperfections of Rotational Paraboloidal Antennas*, Technical Memorandum 33-118, Jet Propulsion Laboratory, Pasadena, Calif., March 1963.

N67 12137

XVIII. Communications Elements Research

A. RF Techniques: 90-Gc Millimeter Wave Work

C. T. Stelzried and W. V. T. Rusch

The objective of the millimeter wave work is to investigate millimeter wave components and techniques to ascertain the future applicability to space communications and tracking. This involves the development of instrumentation for accurate measurements of insertion loss, VSWR, power, and equivalent noise temperatures. Millimeter wave circuit elements are being evaluated in a radio telescope system consisting of a 60-in. antenna and a superheterodyne radiometer (SPS 37-33, Vol. IV). The radio telescope was used to observe the temperature of the Moon at 90 Gc during the December 30, 1963 eclipse (SPS 37-26, Vol. IV, p. 181) and the most recent eclipse, December 18, 1964. These experiments were joint efforts by personnel from JPL and the Electrical Engineering Department of the University of Southern California.

A recent effort has been the determination of an estimate for the overall input signal attenuation due to the losses of the antenna surface, horn, and input waveguide. These losses are seen to be reasonably low (probably less than 1 db).

The Deep Space Network receiving antennas are painted with a special low-loss white plastic paint¹. This high-reflectance white paint has a long life and a low

spectral gloss which minimizes heating of the sub-reflector caused by the Sun. The 60-in. millimeter searchlight antenna was painted with a zinc chromate undercoat² and the special high-reflectance paint in order to perform solar observations. An attempt has been made to place an upper bound on the total radiometric input resistive losses as determined from radiometric observations.

A representation of the radiometric system used to evaluate resistive input losses is shown in Fig. 1. The total radiometer antenna, horn, and waveguide loss L_1 is assumed to be at an ambient temperature T_{01} . These losses are defined to the measurement reference flange at the output of the waveguide calibration switch. The effective noise temperature incident on the antenna (neglecting ground contributions and assuming $hf \ll kT$) due to the contribution of extraterrestrial radiation T'' and atmospheric losses $\alpha(x)$ at a temperature $T(x)$ is (Ref. 1)

$$T' = \frac{1}{L} T'' + \frac{1}{L} \int_0^l 2\alpha(x) T(x) L(x) dx \quad (1)$$

where

l = path length

$$L = \text{total loss, ratio} = e^{\int_0^l 2\alpha(x) dx}$$

$$L(x) = \text{partial loss, ratio} = e^{\int_0^x 2\alpha(x) dx}$$

¹According to JPL Specification DSIF STD 1006B, January 12, 1965.

²Fuller zinc chromate primer 3987 yellow.

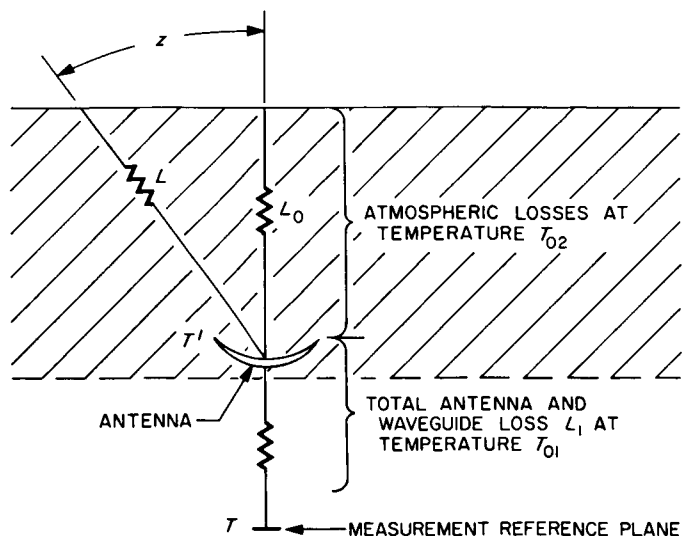


Fig. 1. Representation of atmospheric, antenna, and waveguide losses

Here the origin is taken at the source T'' . The exact attenuation temperature profile is difficult to obtain. A simplified model assumes $\alpha(x) = \alpha$ and $T(x) = T_{02}$ as constants for an effective atmosphere height over a flat Earth, so that with $L = e^{2\alpha l}$

$$T' = \frac{1}{L} T'' + \left(1 - \frac{1}{L}\right) T_{02} \quad (2)$$

The total atmospheric losses L_0 and L with zenith angles at vertical and z are related by

$$L = L_0^{\sec z} \quad (3)$$

The computed temperature at the radiometer waveguide reference flange with the antenna at a zenith angle z , neglecting extraterrestrial radiation, is

$$T_c = \left(1 - \frac{1}{L_1}\right) T_{01} + \frac{1}{L_1} (1 - L_0^{-\sec z}) T_{02} \quad (4)$$

The problem is to determine the best estimate of L_1 and T_{02} from a series of radiometric temperature measurements T as a function of the zenith angles

where

L_1 = overall RF input losses to the waveguide reference figure, ratio

T_{01} = temperature of the loss L_1 , °K

The variance (all summations in the following are from 1 to N , the number of observations)

$$\sigma^2 = \frac{1}{N} \sum (T - T_c)^2 \quad (5)$$

cannot be used for a least-squares treatment since T_c is nonlinear (Ref. 2, p. 255). Linearizing Eq. (1) with a Taylor series expansion, retaining only first order terms,

$$T_c \simeq T'_c + (L_1 - L'_1) \left. \frac{\partial T_c}{\partial L_1} \right|_{\substack{L'_1 \\ T'_{02}}} + (T_{02} - T'_{02}) \left. \frac{\partial T_c}{\partial T_{02}} \right|_{\substack{L'_1 \\ T'_{02}}} \quad (6)$$

where

$$\left. \frac{\partial T_c}{\partial L_1} \right|_{\substack{L'_1 \\ T'_{02}}} = \frac{T_{01} - T'_{02} (1 - L_0^{-\sec z})}{(L_1)^2}$$

$$\left. \frac{\partial T_c}{\partial T_{02}} \right|_{\substack{L'_1 \\ T'_{02}}} = \frac{1}{L'_1} (1 - L_0^{-\sec z})$$

and the primes refer to the previous calculated values in an iteration process. The variance can now be written

$$\sigma^2 \simeq \frac{1}{N} \sum \left[T - T'_c - (L_1 - L'_1) \frac{T_{01} - T'_{02} (1 - L_0^{-\sec z})}{(L'_1)^2} - (T_{02} - T'_{02}) \frac{(1 - L_0^{-\sec z})}{L'_1} \right]^2 \quad (7)$$

Differentiating with respect to L_1 and T_{02} and equating to zero

$$\left. \begin{aligned} \sum \left\{ T - T'_c + (T'_c - T_{01}) \frac{L_1 - L'_1}{L'_1} - \left[T'_c - \left(1 - \frac{1}{L'_1} \right) T_{01} \right] \left(\frac{T_{02} - T'_{02}}{T'_{02}} \right) \right\} \left(\frac{T'_c - T_{01}}{L'_1} \right) &= 0 \\ \sum \left\{ T - T'_c + (T'_c - T_{01}) \frac{L_1 - L'_1}{L'_1} - \left[T'_c - \left(1 - \frac{1}{L'_1} \right) T_{01} \right] \left(\frac{T_{02} - T'_{02}}{T'_{02}} \right) \right\} \frac{T'_c - \left(1 - \frac{1}{L'_1} \right) T_{01}}{T'_{02}} &= 0 \end{aligned} \right\} \quad (8)$$

Solving for L_1 ,

$$L_1 = L'_1 + L'_1 \frac{\left| \begin{array}{cc} \frac{1}{L'_1} \sum (T - T'_c) (T'_c - T_{01}) & \frac{1}{L'_1} \sum (T'_c - T_{01}) \left[T'_c - \left(1 - \frac{1}{L'_1} \right) T_{01} \right] \\ \frac{1}{T'_{02}} \sum (T - T'_c) \left[T'_c - \left(1 - \frac{1}{L'_1} \right) T_{01} \right] & \frac{1}{T'_{02}} \sum \left[T'_c - \left(1 - \frac{1}{L'_1} \right) T_{01} \right]^2 \end{array} \right|}{\Delta} \quad (9)$$

and T_{02} ,

$$T_{02} = T'_{02} + T'_{02} \frac{\left| \begin{array}{cc} -\frac{1}{L'_1} \sum (T'_c - T_{01})^2 & \frac{1}{L'_1} \sum (T - T'_c) (T'_c - T_{01}) \\ -\frac{1}{T'_{02}} \sum (T'_c - T_{01}) \left[T'_c - \left(1 - \frac{1}{L'_1} \right) T_{01} \right] & \frac{1}{T'_{02}} \sum (T - T'_c) \left[T'_c - \left(1 - \frac{1}{L'_1} \right) T_{01} \right] \end{array} \right|}{\Delta} \quad (10)$$

where

$$\Delta = \left| \begin{array}{cc} -\frac{1}{L'_1} \sum (T'_c - T_{01})^2 & \frac{1}{L'_1} \sum (T'_c - T_{01}) \left[T'_c - \left(1 - \frac{1}{L'_1} \right) T_{01} \right] \\ -\frac{1}{T'_{02}} \sum (T'_c - T_{01}) \left[T'_c - \left(1 - \frac{1}{L'_1} \right) T_{01} \right] & \frac{1}{T'_{02}} \sum \left[T'_c - \left(1 - \frac{1}{L'_1} \right) T_{01} \right]^2 \end{array} \right|$$

The computing iteration involves estimating the first value for L'_1 and T'_{02} (typically 1.0 and 100), computing L_1 and T_{02} from Eqs. (6) and (7), and repeating—always using the previously computed values until convergence. This technique is especially convenient with a digital computer. The probable error of the observation data points is

$$PE_T = 0.6745 \sqrt{\frac{\sum (T - T_c)^2}{N - 2}} \quad (11)$$

The probable errors of L_1 and T_{02} are found by expanding Eqs. (6) and (7) and summing the probable error terms (Ref. 2, p. 229)

$$PE_{L_1} = \frac{PE_T}{T'_{02} |\Delta|} \left[\sum \left\{ (T'_c - T_{01}) \sum \left[T'_c - \left(1 - \frac{1}{L'_1}\right) T_{01} \right]^2 - \left[T'_c - \left(1 - \frac{1}{L'_1}\right) T_{01} \right] \sum (T'_c - T_{01}) \left[T'_c - \left(1 - \frac{1}{L'_1}\right) T_{01} \right] \right\}^2 \right]^{1/2} \quad (12)$$

$$PE_{T_{02}} = \frac{PE_T}{L'_1 |\Delta|} \left[\sum \left\{ \left[T'_c - \left(1 - \frac{1}{L'_1}\right) T_{01} \right] \sum (T'_c - T_{01})^2 - (T'_c - T_{01}) \times \sum (T'_c - T_{01}) \left[T'_c - \left(1 - \frac{1}{L'_1}\right) T_{01} \right] \right\}^2 \right]^{1/2} \quad (13)$$

Only radiometric observational measurement errors are considered in this analysis. Bias errors can also occur from errors in L_0 , T_{01} , and z . Eqs. (6)–(10) have been programmed from the IBM 1620 computer and designated program CTS/21.

A series of sky temperature measurements have been

made with the 60-in. searchlight antenna located on the JPL Mesa antenna range.

A sample computer printout is shown in Fig. 2 for data taken on July 8, 1966. All observational data taken between February 9 and July 10, 1966, with the computed parameters are given in Table 1. The tabulated values

SKY TEMPERATURE MEASUREMENTS, DATA REDUCTION...CTS/21				JULY 8, 1966	
LO(ZENITH ATM. LOSS), DB= .78420 L1P= 1.00 TO2P= 100.00					
T, DEG. K	Z, DEG.	TO, DEG. C	TC	TC-T	
248.9000	84.50000	23.0000	257.2202	8.3202	
215.9000	80.00000	22.5000	206.5745	-9.3254	
172.0000	75.00000	22.5000	170.3774	-1.6225	
150.7000	70.00000	23.0000	147.3480	-3.3519	
133.2000	65.00000	22.5000	131.5940	-1.6059	
112.9000	55.00000	22.5000	112.1118	- .7881	
102.9000	49.50000	22.5000	105.2496	2.3496	
95.4000	45.50000	23.0000	101.4054	6.0054	
(WAVEGUIDE LOSS) L1, DB= .70559E+00			PEL1, DB= .58083E-02		
(ATM. TEMP.) TO2, DEG. K= .29522E+03			PETO2, DEG. K= .49201E+01		
			PET, DEG. K= .40361E+01		
NUMBER ITERATIONS= 3					

Fig. 2. Typical computer program printout (CTS/21) for July 8, 1966

Table 1. Tabulated 90-Gc sky temperature measurements

Number of observations	Input data					Computed data				
	Date, 1966	L_0 , db	T_{01} , °K	z , deg	T , °K	L_1 , db	PE_{L_1} , db	T_{02} , °K	$PE_{T_{02}}$, °K	PE_T , °K
7*	Feb. 9	0.50	288.8	66-50	89-113	0.67	0.022	336	57	4.7
9	May 29	0.41	285.5	45-84	88-213	0.93	0.004	350	6.7	3.1
8	June 14	0.80	302.7	45-83	72-190	0.47	0.005	239	6.3	3.7
9	June 23	0.62	306.7	45-85	80-261	0.48	0.003	321	3.8	3.1
8	June 25	0.78	303.7	40-75	82-162	0.23	0.007	297	10.1	3.7
6	June 26	0.49	297.8	43-78	100-179	0.95	0.005	366	9.3	2.2
6*	June 27	0.36	296.5	55-85	100-228	1.07	0.006	342	9.2	4.0
9*	July 5	0.76	294.7	45-85	84-234	0.45	0.004	266	3.8	3.0
8*	July 8	0.78	296.0	46-85	95-249	0.71	0.006	295	4.9	4.0
6*	July 10	0.71	295.5	45-75	101-138	1.18	0.012	192	22.6	4.5

*Indicated recomputed sequence where data points with $(T_0 - T)$ greater than 10°K were arbitrarily deleted.

for z and T indicate the range of the observational sequence. The ambient ground temperature T_{01} is that recorded halfway through a measurement sequence. Atmospheric loss L_0 is obtained from separate Moon observations (SPS 37-36, Vol. IV, p. 256). The average of the losses L_1 is 0.7 db with a probable error of 0.2 db per measurement. This is a much higher error than predicted by the error analysis (approximately 0.01 db), indicating comparatively large measurement bias errors. One source of error not considered is the change in antenna ground contribution with antenna zenith angle. Antenna back-lobe patterns are needed to correct this error. An indication of computational sensitivity in the atmospheric loss input data is obtained by recomputing with different assumed values for L_0 , as shown in Fig. 3 for the July 8 data. For this example the error in L_1 is approximately

$$\text{error } L_1 \simeq -\text{error } L_0 \quad (14)$$

Some of the bias errors are definitely due to the errors in the measured atmospheric zenith loss. Apparently the overall loss for the antenna, horn, and waveguide combination for this system are not excessive (probably less than 1 db). Additional information concerning the point could be obtained from direct reflective coefficient losses (Ref. 3) measured with a slotted line.

The 90-Gc radiometrically measured sky temperature T_{02} is shown in Fig. 4 plotted against thermal ground temperature T_{01} . A least-squares best-fit straight line is

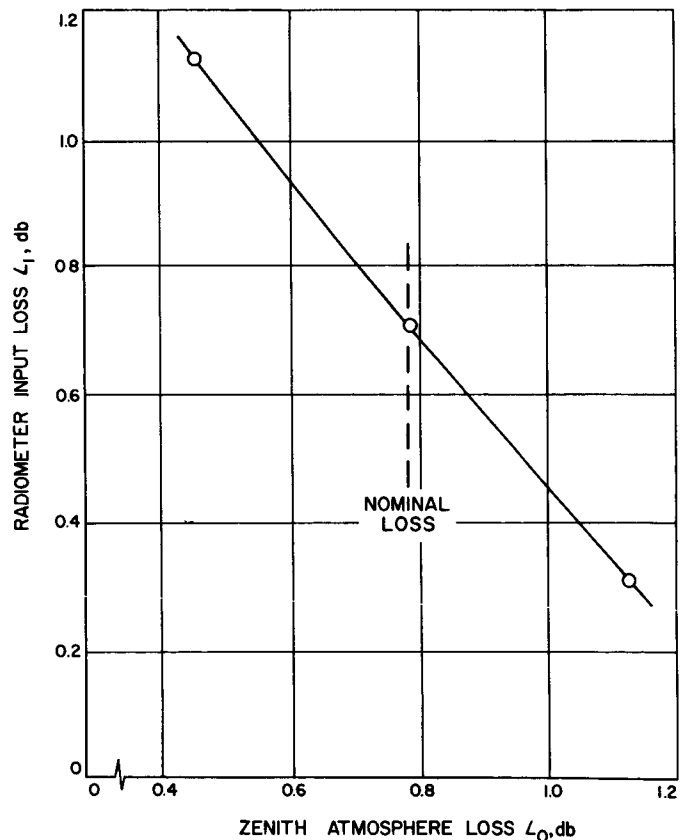


Fig. 3. Computed radiometer total input loss using various simulated values for the atmospheric loss

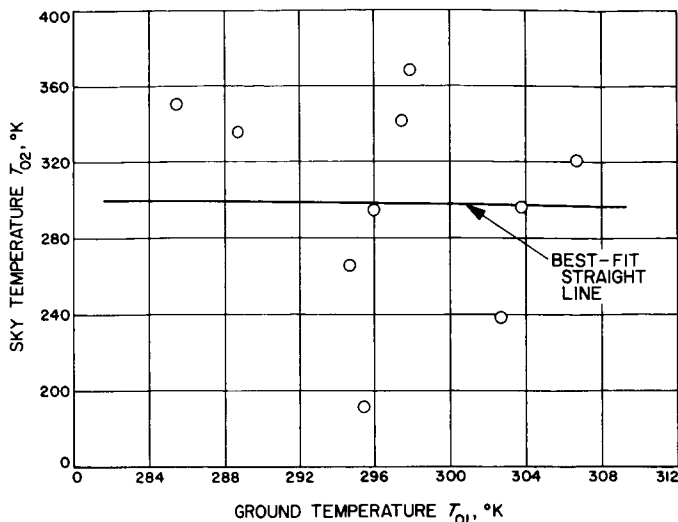


Fig. 4. Graph of sky temperature versus ground temperature

also shown. The probable error from the curve fit is 39°K for each data point; again, this is higher than that predicted from the individual observational sequence, further indicating measurement bias errors. Although some of the computed sky temperatures T_{02} are probably unrealistically high because of the bias errors, they are reported for completeness. Simultaneous sky temperature thermal profiles from balloon measurements would provide additional insight into these observations.

B. RF Techniques: Mismatch Errors on Noise Temperature Measurements

T. Y. Otoshi

1. Introduction

The analysis of mismatch errors on noise temperature measurements has recently been given more attention because of increasing interest in the development of very low noise antenna receiving systems and the absolute accuracies to which the noise temperatures of these systems can be calibrated.

Several recent technical news letters have appeared (Refs. 4, 5, and 6) concerning the effects of mismatch on the accuracy of the Y-factor method of measuring effective receiver noise temperature. The examples given in Ref. 4 point out the serious effects of mismatch errors on the calibration of receiver temperature, even when the

receiver and thermal reference standards have reasonable reflection coefficients. The mismatch error equations presented in these articles, however, do not include the case of the calibration of an unknown noise source, such as a gas tube, cryogenic load, or an antenna.

This report presents the general-case equations applicable to the mismatch errors in Y-factor measurements for calibration of a receiver and also any unknown noise source which is connected to the receiver through a two-port network. Several examples are also given which use reflection coefficients and typical Y-factors measured on the Mars Deep Space Station listening cone system.

2. Mismatch Error Analysis

a. General case. The following mismatch error analysis is based on the mismatch equations derived in a paper by the National Bureau of Standards (NBS) in March 1964 (Ref. 7). Although the equations were derived for the calibration of a noise source in a comparison-type measurement system, they can be extended to analysis of errors in a Y-factor measurement setup.

Fig. 5 shows a noise source T_G connected to the receiver through a two-port network, and also shows an equivalent noise source T_G'' connected directly to the receiver. The parameters shown in Fig. 5 are defined as follows:

$C_{11}, C_{12}, C_{21}, C_{22}$ = the scattering coefficients of any two-port network, such as a transmission line or an attenuator. (Definitions of these scattering coefficients may be found in Ref. 8.)

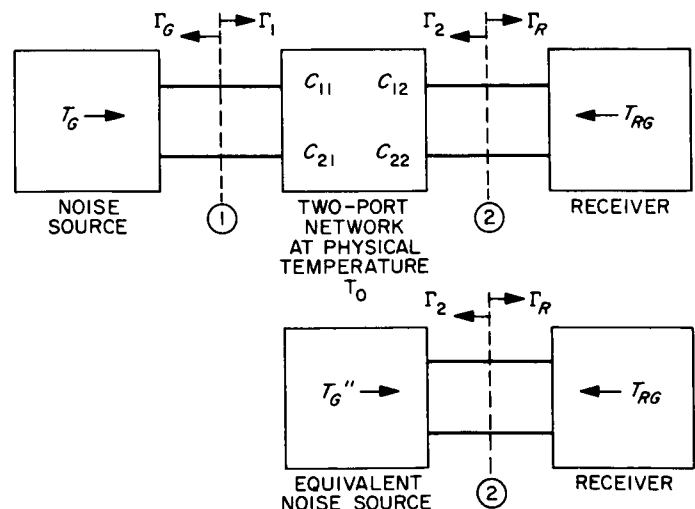


Fig. 5. Basic noise source and receiver system

Γ_G = voltage reflection coefficient of the noise source.

Γ_R = voltage reflection coefficient of the receiver.

Γ_1 = input voltage reflection coefficient as seen looking into the network at port 1, with a Γ_R load placed on port 2.

Γ_2 = input voltage reflection coefficient as seen looking into the network at port 2, with a Γ_G load placed on port 1.

The expressions for Γ_1 and Γ_2 , respectively, are

$$\Gamma_1 = C_{11} + \frac{C_{12} C_{21} \Gamma_R}{1 - C_{22} \Gamma_R} \quad (1)$$

$$\Gamma_2 = C_{22} + \frac{C_{21} C_{12} \Gamma_G}{1 - C_{11} \Gamma_G} \quad (2)$$

The temperatures shown in Fig. 5 are defined as follows:

T_G = the available noise source temperature, in °K, which can be delivered to the right of terminal surface 1. This temperature is delivered only when $\Gamma_G = \Gamma_1^*$ where * denotes the complex conjugate.

T_0 = the physical temperature of the two-port network, °K.

T_G'' = the equivalent available noise source temperature, in °K, which can be delivered to the right of terminal surface 2. This temperature is delivered only when $\Gamma_R = \Gamma_2^*$.

T_{RG} = the available receiver noise source temperature, in °K, which can be delivered to the left of terminal surface 2. This temperature is delivered only when $\Gamma_R = \Gamma_2^*$. It is important to note that T_{RG} is not the effective receiver noise temperature T_R'' which contributes directly to system noise temperature and will be defined later in this report.

The double-primed notations are used to denote equivalent noise source temperatures defined at the receiver reference plane (which is the same as terminal surface 2 in this case).

Using the NBS method, the total noise power absorbed by the receiver due to delivered noise power from noise

source T_G , the two-port network, and reflected receiver temperature would be given as

$$P_G =$$

$$kB \left[\underbrace{\alpha_1 \eta T_G}_{\text{delivered source temperature}} + \underbrace{(\alpha_2 - \alpha_1 \eta) T_0}_{\text{temperature generated by network}} + \underbrace{\alpha_2 \frac{|\Gamma_2|^2 T_{RG}}{1 - |\Gamma_2|^2}}_{\text{reflected receiver temperature}} \right] \quad (3)$$

where

k = Boltzmann constant, 1.380×10^{-23} joules/°K

B = bandwidth, cps

$$\alpha_1 = \frac{(1 - |\Gamma_G|^2)(1 - |\Gamma_1|^2)}{|1 - \Gamma_G \Gamma_1|^2} \quad (4)$$

$$\eta = \frac{|C_{21}|^2 (1 - |\Gamma_R|^2)}{|1 - C_{22} \Gamma_R|^2 (1 - |\Gamma_1|^2)} \quad (5)$$

$$\alpha_2 = \frac{(1 - |\Gamma_2|^2)(1 - |\Gamma_R|^2)}{|1 - \Gamma_2 \Gamma_R|^2} \quad (6)$$

The general case mismatch factor α is equal to the ratio of power delivered across a terminal surface to the available source power. The η term is the network efficiency equal to the ratio of source power delivered to the receiver to that delivered to the network.

When Eqs. (4), (5), and (6) and the following identity³

$$(1 - \Gamma_1 \Gamma_G)(1 - C_{22} \Gamma_R) = (1 - C_{11} \Gamma_G)(1 - \Gamma_2 \Gamma_R) \quad (7)$$

are substituted into Eq. (3), the following expression is obtained:

$$P_G = kB \left[\frac{(T_G - T_0)(1 - |\Gamma_G|^2)|C_{21}|^2(1 - |\Gamma_R|^2)}{|1 - C_{11} \Gamma_G|^2 |1 - \Gamma_R \Gamma_2|^2} + \frac{T_0(1 - |\Gamma_2|^2)(1 - |\Gamma_R|^2)}{|1 - \Gamma_2 \Gamma_R|^2} + \frac{T_{RG} |\Gamma_2|^2 (1 - |\Gamma_R|^2)}{|1 - \Gamma_2 \Gamma_R|^2} \right] \quad (8)$$

Rewriting Eq. (3) by substituting

$$\tau = \left(\frac{\alpha_1 \eta}{\alpha_2} \right) \quad (9)$$

³This identity is exact only for two-port networks. Substitutions of Eqs. (1) and (2) into Eq. (7) will prove this identity.

results in

$$P_g = kB \left\{ \alpha_2 [(T_g - T_0)\tau + T_0] + \frac{\alpha_2 |\Gamma_2|^2 T_{Rg}}{1 - |\Gamma_2|^2} \right\} \quad (10)$$

Substitution of Eqs. (4) through (7) into Eq. (9) gives

$$\tau = \frac{|C_{21}|^2 (1 - |\Gamma_g|^2)}{|1 - C_{11} \Gamma_g|^2 (1 - |\Gamma_2|^2)} \quad (11)$$

The total noise power absorbed by the receiver (see Fig. 5) due to noise power from an equivalent source T_g'' and reflected receiver temperature is

$$P_g = kB \left[\alpha_2 T_g'' + \frac{\alpha_2 |\Gamma_2|^2 T_{Rg}}{1 - |\Gamma_2|^2} \right] \quad (12)$$

Note that α_2 can be regarded as a mismatch factor between the source T_g'' and the receiver. Equating Eq. (10) to Eq. (12) gives

$$T_g'' = (T_g - T_0)\tau + T_0 \quad (13)$$

The term τ in Eq. (13) may be thought of as a power transmission coefficient for the mismatched case, and is analogous to the L^{-1} symbol commonly found in literature for the analysis of matched systems. It is interesting to note that the equivalent source temperature T_g'' at any reference plane can be calculated for the mismatched case from Eq. (13) and will be independent of the receiver used. For the special case of a lossless and matched two-port network, Eq. (11) becomes

$$\tau = 1$$

so that

$$T_g = T_g''$$

as would be expected.

b. Effective receiver noise temperature. Referring to Fig. 6, define the effective receiver noise temperature as the temperature T_R'' , which when placed at the input terminals of the receiver, if the receiver were noise free, will produce the same power output as that obtained when a 0°K noise source temperature is placed at the input terminals of the actual receiver. The power delivered to the receiver from this hypothetical noise source is then given as

$$P_R = kB [T_R'' (1 - |\Gamma_R|^2)] \quad (14)$$

c. Y-factor mismatch error on the calibration of a noise source. As shown in Fig. 7, consider an unknown noise

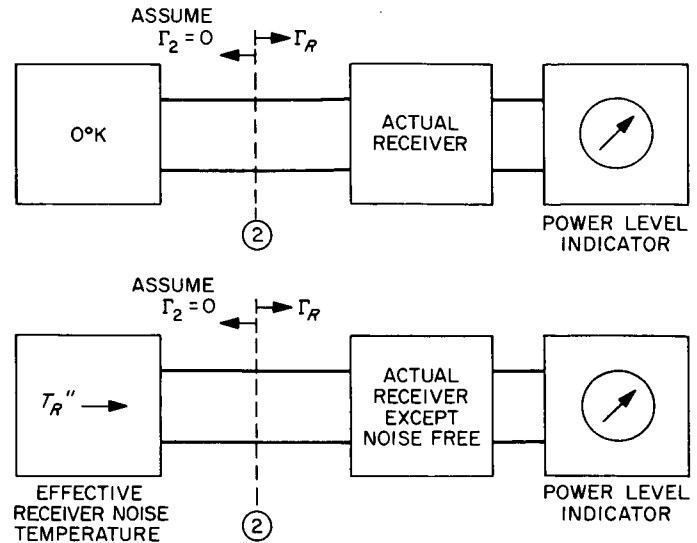


Fig. 6. Block diagram depicting concept of effective receiver noise temperature

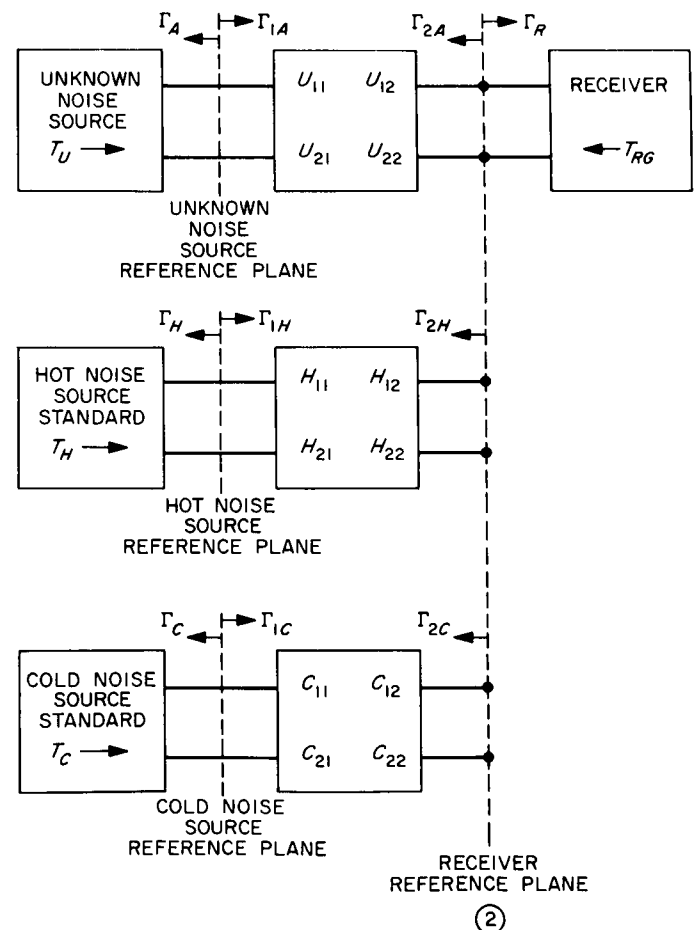


Fig. 7. Block diagram for Y-factor calibrations of an unknown noise source temperature

source T_U and known hot and cold noise source temperatures T_H and T_C , connected to the receiver by two-port networks represented by U , H , and C scattering matrices, respectively. These networks also include the scattering coefficients of a common switch assembly. Application of Eqs. (10) and (12) to this configuration gives the following powers absorbed by the receiver when connected sequentially to the three noise sources:

$$P_U = kB\alpha_{2U} \left\{ [(T_U - T_0) \tau_U + T_0] + \frac{|\Gamma_{2U}|^2 T_{RG}}{(1 - |\Gamma_{2U}|^2)} \right\} = kB\alpha_{2U} \left[T''_U + \frac{|\Gamma_{2U}|^2 T_{RG}}{(1 - |\Gamma_{2U}|^2)} \right] \quad (15)$$

$$P_H = kB\alpha_{2H} \left\{ [(T_H - T_0) \tau_H + T_0] + \frac{|\Gamma_{2H}|^2 T_{RG}}{(1 - |\Gamma_{2H}|^2)} \right\} = kB\alpha_{2H} \left[T''_H + \frac{|\Gamma_{2H}|^2 T_{RG}}{(1 - |\Gamma_{2H}|^2)} \right] \quad (16)$$

$$P_C = kB\alpha_{2C} \left\{ [(T_C - T_0) \tau_C + T_0] + \frac{|\Gamma_{2C}|^2 T_{RG}}{(1 - |\Gamma_{2C}|^2)} \right\} = kB\alpha_{2C} \left[T''_C + \frac{|\Gamma_{2C}|^2 T_{RG}}{(1 - |\Gamma_{2C}|^2)} \right] \quad (17)$$

The additional subscript letters, U , H , and C are used to describe the particular noise source cases.

If the receiver gain remains constant during the measurements, then two measured Y -factors would be

$$Y_{UC} = \frac{P_C + P_R}{P_U + P_R} \quad (18)$$

$$Y_{CH} = \frac{P_H + P_R}{P_C + P_R} \quad (19)$$

Solving for P_R and P_U by manipulation of Eqs. (18) and (19) gives

$$P_R = \frac{P_H - P_C Y_{CH}}{Y_{CH} - 1} \quad (20)$$

$$P_U = \frac{P_C (Y_{UC} Y_{CH} - 1) - P_H (Y_{UC} - 1)}{Y_{UC} (Y_{CH} - 1)} \quad (21)$$

and substituting from Eqs. (14) through (17) gives

$$T''_R = \frac{\alpha_{2H} \left[T''_H + \frac{|\Gamma_{2H}|^2 T_{RG}}{(1 - |\Gamma_{2H}|^2)} \right] - \alpha_{2C} \left[T''_C + \frac{|\Gamma_{2C}|^2 T_{RG}}{(1 - |\Gamma_{2C}|^2)} \right] Y_{CH}}{(1 - |\Gamma_R|^2) (Y_{CH} - 1)} \quad (22)$$

and

$$T''_U = \frac{\alpha_{2C}}{\alpha_{2U}} \left[T''_C + \frac{|\Gamma_{2C}|^2 T_{RG}}{(1 - |\Gamma_{2C}|^2)} \right] \frac{(Y_{UC} Y_{CH} - 1)}{Y_{UC} (Y_{CH} - 1)} - \frac{\alpha_{2H}}{\alpha_{2U}} \left[T''_H + \frac{|\Gamma_{2H}|^2 T_{RG}}{(1 - |\Gamma_{2H}|^2)} \right] \frac{(Y_{UC} - 1)}{Y_{UC} (Y_{CH} - 1)} - \frac{|\Gamma_{2U}|^2}{1 - |\Gamma_{2U}|^2} T_{RG} \quad (23)$$

It can be seen from the above that if the reflection coefficients of the equivalent noise sources as seen by the receiver are identical in their amplitudes and phases, then

$$\frac{\alpha_{2C}}{\alpha_{2U}} = 1$$

$$\frac{\alpha_{2H}}{\alpha_{2U}} = 1$$

and the mismatch errors of the calibration of T''_U can be reduced significantly. From the general definition given by Eq. (13),

$$T''_U = (T_U - T_0) \tau_U + T_0 \quad (24)$$

which gives

$$T_U = T_0 - (T_0 - T''_U) \frac{1}{\tau_U} \quad (25)$$

If the phases of the reflection coefficients are not known, then only the temperature limits can be calculated to give an indication of the mismatch errors. The following gives the expressions for computing the maximum and minimum effective receiver noise temperatures:

$$(T''_R)_{max} = \frac{(\alpha_{2H})_{max} \left[(T''_H)_{max} + \left(\frac{|\Gamma_{2H}|^2 T_{RG}}{1 - |\Gamma_{2H}|^2} \right) \right] - (\alpha_{2C})_{min} \left[(T''_C)_{min} + \left(\frac{|\Gamma_{2C}|^2 T_{RG}}{1 - |\Gamma_{2C}|^2} \right) \right] Y_{CH}}{(1 - |\Gamma_R|^2) (Y_{CH} - 1)} \quad (26)$$

$$(T''_R)_{min} = \frac{(\alpha_{2H})_{min} \left[(T''_H)_{min} + \left(\frac{|\Gamma_{2H}|^2 T_{RG}}{1 - |\Gamma_{2H}|^2} \right) \right] - (\alpha_{2C})_{max} \left[(T''_C)_{max} + \left(\frac{|\Gamma_{2C}|^2 T_{RG}}{1 - |\Gamma_{2C}|^2} \right) \right] Y_{CH}}{(1 - |\Gamma_R|^2) (Y_{CH} - 1)} \quad (27)$$

The expressions for $(\alpha_{2H})_{max}$, $(\alpha_{2H})_{min}$, $(\alpha_{2C})_{max}$, $(\alpha_{2C})_{min}$, $(T''_H)_{max}$, $(T''_H)_{min}$, $(T''_C)_{max}$, and $(T''_C)_{min}$ are tabulated in Table 2.

The following are the expressions used to find the maximum and minimum values of the unknown source temperature defined at the receiver reference plane.

$$(T''_U)_{max} = \frac{(\alpha_{2C})_{max} \left[(T''_C)_{max} + \frac{|\Gamma_{2C}|^2}{1 - |\Gamma_{2C}|^2} T_{RG} \right] (Y_{UC} Y_{CH} - 1)}{(\alpha_{2U})_{min} Y_{UC} (Y_{CH} - 1)} - \frac{(\alpha_{2H})_{min} \left[(T''_H)_{min} + \frac{|\Gamma_{2H}|^2}{1 - |\Gamma_{2H}|^2} T_{RG} \right] (Y_{UC} - 1)}{(\alpha_{2U})_{min} Y_{UC} (Y_{CH} - 1)} - \frac{|\Gamma_{2U}|^2 T_{RG}}{(1 - |\Gamma_{2U}|^2)} \quad (28)$$

Table 2. Mismatch error parameters for receiver and noise source temperature calculations

Parameter	Equation	Maximum and minimum values (for max. use top signs; for min. use bottom signs)
τ_U	$\frac{ U_{21} ^2 (1 - \Gamma_U ^2)}{ 1 - U_{11} \Gamma_U ^2 (1 - \Gamma_{2U} ^2)}$	$\frac{ U_{21} ^2 (1 - \Gamma_U ^2)}{(1 \mp U_{11} \Gamma_U)^2 (1 - \Gamma_{2U} ^2)}$
τ_H	$\frac{ H_{21} ^2 (1 - \Gamma_H ^2)}{ 1 - H_{11} \Gamma_H ^2 (1 - \Gamma_{2H} ^2)}$	$\frac{ H_{21} ^2 (1 - \Gamma_H ^2)}{(1 \mp H_{11} \Gamma_H)^2 (1 - \Gamma_{2H} ^2)}$
τ_C	$\frac{ C_{21} ^2 (1 - \Gamma_C ^2)}{ 1 - C_{11} \Gamma_C ^2 (1 - \Gamma_{2C} ^2)}$	$\frac{ C_{21} ^2 (1 - \Gamma_C ^2)}{(1 \mp C_{11} \Gamma_C)^2 (1 - \Gamma_{2C} ^2)}$
T''_H	$(T_H - T_0) \tau_H + T_0$	For $T_H \leq T_0$, $(T_H - T_0) \left[\frac{ H_{21} ^2 (1 - \Gamma_H ^2)}{(1 \pm H_{11} \Gamma_H)^2 (1 - \Gamma_{2H} ^2)} \right] + T_0$
T''_C	$(T_C - T_0) \tau_C + T_0$	For $T_C \leq T_0$, $(T_C - T_0) \left[\frac{ C_{21} ^2 (1 - \Gamma_C ^2)}{(1 \pm C_{11} \Gamma_C)^2 (1 - \Gamma_{2C} ^2)} \right] + T_0$
α_{2U}	$\frac{(1 - \Gamma_{2U} ^2)(1 - \Gamma_R ^2)}{ 1 - \Gamma_{2U} \Gamma_R ^2}$	$\frac{(1 - \Gamma_{2U} ^2)(1 - \Gamma_R ^2)}{(1 \mp \Gamma_{2U} \Gamma_R)^2}$
α_{2H}	$\frac{(1 - \Gamma_{2H} ^2)(1 - \Gamma_R ^2)}{ 1 - \Gamma_{2H} \Gamma_R ^2}$	$\frac{(1 - \Gamma_{2H} ^2)(1 - \Gamma_R ^2)}{(1 \mp \Gamma_{2H} \Gamma_R)^2}$
α_{2C}	$\frac{(1 - \Gamma_{2C} ^2)(1 - \Gamma_R ^2)}{ 1 - \Gamma_{2C} \Gamma_R ^2}$	$\frac{(1 - \Gamma_{2C} ^2)(1 - \Gamma_R ^2)}{(1 \mp \Gamma_{2C} \Gamma_R)^2}$

$$(T''_U)_{\min} = \frac{(\alpha_{2C})_{\min}}{(\alpha_{2U})_{\max}} \left[(T''_C)_{\min} + \frac{|\Gamma_{2C}|^2 T_{RG}}{1 - |\Gamma_{2C}|^2} \right] \frac{(Y_{UC} Y_{CH} - 1)}{Y_{UC} (Y_{CH} - 1)} \\ - \frac{(\alpha_{2H})_{\max}}{(\alpha_{2U})_{\max}} \left[(T''_H)_{\max} + \frac{|\Gamma_{2H}|^2 T_{RG}}{1 - |\Gamma_{2H}|^2} \right] \frac{(Y_{UC} - 1)}{Y_{UC} (Y_{CH} - 1)} - \frac{|\Gamma_{2U}|^2}{1 - |\Gamma_{2U}|^2} T_{RG} \quad (29)$$

For calculating the maximum and minimum values of the unknown noise source temperature at the noise source reference plane for the case $T''_U < T_0$,

$$(T_U)_{\max} = T_0 - [T_0 - (T''_U)_{\max}] \frac{1}{(\tau_U)_{\max}} \quad (30)$$

$$(T_U)_{\min} = T_0 - [T_0 - (T''_U)_{\min}] \frac{1}{(\tau_U)_{\min}} \quad (31)$$

where values of $(T''_U)_{\max}$ and $(T''_U)_{\min}$ are determined from Eqs. (28) and (29) and the expressions for $(\tau_U)_{\max}$ and $(\tau_U)_{\min}$ are tabulated in Table 2.

For the special case where the measurement system has a matched receiver, matched sources, identically mismatched symmetrical networks, and negligible reflected receiver temperature contributions, then Eqs. (22), (23), and (25) reduce to the basic equations

$$T''_{R0} = \frac{T''_{H0} - T''_{C0} Y_{CH}}{Y_{CH} - 1} \quad (32)$$

$$T''_{U0} = \frac{T''_{C0} (Y_{UC} Y_{CH} - 1) - T''_{U0} (Y_{UC} - 1)}{Y_{UC} (Y_{CH} - 1)} \quad (33)$$

$$T_{U0} = T_0 - (T_0 - T''_{U0}) L_{U0} \quad (34)$$

where the zero subscripts are used to refer to this basic case. In Table 3, the equations for the basic case parameters are tabulated for comparison with Table 2. The L symbols are used to denote the dissipative line loss factors (which are the reciprocals of the network efficiencies in the matched receiver case).

The basic equations given by Eqs. (32) through (34) are sometimes used directly for absolute temperature calculations without the realization that they are only exact for the special case conditions stated above or when the system is perfectly matched. In the general case, unless the system is reasonably well matched, it is important to calculate the uncertainties produced by mismatch errors and to consider all of the parameters which contribute to mismatch errors.

Table 3. Parameters for receiver and noise source temperature calculations using basic Y-factor equations

Parameter	Equation
L_{U0}^{-1}	$\frac{ U_{21} ^2}{1 - U_{11} ^2}$
L_{H0}^{-1}	$\frac{ H_{21} ^2}{1 - H_{11} ^2}$
L_{C0}^{-1}	$\frac{ C_{21} ^2}{1 - C_{11} ^2}$
T''_{H0}	$(T_H - T_0) L_{H0}^{-1} + T_0 = (T_H - T_0) \frac{ H_{21} ^2}{(1 - H_{11} ^2)} + T_0$
T''_{C0}	$(T_C - T_0) L_{C0}^{-1} + T_0 = (T_C - T_0) \frac{ C_{21} ^2}{(1 - C_{11} ^2)} + T_0$

3. Sample Cases

The mismatch error equations given by Eqs. (26) through (31) have been set up on an IBM 1620 computer program. The computer program computes effective receiver temperature T''_R and unknown antenna noise source temperatures T''_A and T'_A defined at the receiver and antenna reference flanges, respectively. The average temperatures as well as deviations from the averages are computed from the maximum and minimums. For purposes of comparison, basic temperatures calculated from Eqs. (32) through (34) are also computed by the program.

Typical parameters measured on the Mars DSS listening cone system (SPS 37-38, Vol. IV, pp. 180-186) were selected for sample-case computer program inputs. The T_H and T_C thermal noise standards used on this Mars cone are the waveguide ambient and liquid-nitrogen-cooled terminations, respectively. Although the antenna line of this system cannot be strictly treated as a two-port device (because of the presence of an orthomode transducer and phasing section), the examples help to illustrate the error order of magnitudes produced by various mismatches on the measurement of antenna temperature.

The following are the computer program input data used for the Mars cone case as it presently exists. These data were based on actual 2295-Mc measurements.

Measured Y-factors

$$Y_{UC} = 3.673681$$

$$Y_{CH} = 3.450651$$

Nitrogen-Cooled-Termination Noise Source

$$T_o \simeq 77.743^\circ\text{K}$$

$$|C_{11}| = 0.0104$$

$$|C_{21}| = 0.992807 \text{ (corresponding to 0.0627-db attenuation)}$$

$$|\Gamma_c| = 0.00398$$

$$|\Gamma_{2c}| = 0.0144$$

Ambient Load Noise Source

$$T_H = T_o = 290.472^\circ\text{K}$$

$$|H_{11}| = 0.010$$

$$|H_{21}| = 0.994260 \text{ (corresponding to 0.050-db attenuation)}$$

$$|\Gamma_H| = 0.010$$

$$|\Gamma_{2H}| = 0.01567$$

The ambient load network parameters $|\Gamma_H|$, $|H_{11}|$, and $|H_{21}|$ were not actually measured and are not generally needed when $T_H = T_o$ (see Eq. 16). The parameters were arbitrarily chosen for use on the subsequent cases.

Table 4. Sample cases for Mars listening cone assuming various matched conditions

Case number	Mars cone system match conditions	Average noise temperatures and mismatch error limits			Difference between average and noise temperatures from basic equations		
		$T''_R, ^\circ\text{K}$	$T''_A, ^\circ\text{K}$	$T'_A, ^\circ\text{K}$	$(T''_{K_{AVG}} - T''_{R0}), ^\circ\text{K}$	$(T''_{A_{AVG}} - T''_{A0}), ^\circ\text{K}$	$(T'_{A_{AVG}} - T'_{A0}), ^\circ\text{K}$
1 ^a	Mismatched sources Mismatched lines Mismatched receiver	7.9242 ± 0.8213	16.2441 ± 0.7233	5.5942 ± 1.6906	0.0175	-0.0184	-1.0511
2	Matched sources Mismatched lines Mismatched receiver	7.9057 ± 0.5390	16.2703 ± 0.5559	6.6535 ± 0.5748	-0.0010	0.0078	0.0082
3	Mismatched sources Matched lines Mismatched receiver	7.8969 ± 0.3704	16.2894 ± 0.4755	6.6208 ± 0.4918	-0.0098	0.0269	-0.0245
4	Mismatched sources Mismatched lines Matched receiver	7.9240 ± 0.0253	16.2420 ± 0.0233	5.5943 ± 0.9652	0.0174	-0.0205	-1.0510
5	Matched sources Matched lines Mismatched receiver	7.9067 ± 0.0000	16.2625 ± 0.0000	6.4653 ± 0.0000	0.0000	0.0000	0.0000
6	Matched sources Mismatched lines Matched receiver	7.9057 ± 0.0000	16.2670 ± 0.0000	6.6501 ± 0.0000	-0.0010	0.0045	0.0048
7	Mismatched sources Matched lines Matched receiver	7.8965 ± 0.0000	16.2858 ± 0.0000	6.6171 ± 0.0000	-0.0101	0.0233	-0.0282
8	Matched sources Matched lines Matched receiver	7.9067 ± 0.0000	16.2625 ± 0.0000	6.6453 ± 0.0000	0.0000	0.0000	0.0000

^a Mismatched condition of Mars listening cone as it actually exists at the present time.

Antenna Noise Source

$$\begin{aligned}
 |U_{11}| &= 0.0306 \\
 |U_{21}| &= 0.982924 \text{ (corresponding to 0.1496-db} \\
 &\quad \text{attenuation)} \\
 |\Gamma_U| &= 0.0525 \text{ (worst case tolerance added)} \\
 |\Gamma_{2U}| &= 0.0133
 \end{aligned}$$

Receiver

$$\begin{aligned}
 |\Gamma_R| &= 0.1122 \\
 T_{RG} &= 10^\circ\text{K (assumed)}
 \end{aligned}$$

Table 4 shows the results of calculation for the various sample cases. Case 1 applies to the mismatched conditions of the Mars listening cone as it presently exists, and gives an average effective receiver temperature of 7.92°K , with a $\pm 0.82^\circ\text{K}$ peak uncertainty, and an average antenna temperature of 5.59°K at the antenna reference flange, with a $\pm 1.69^\circ\text{K}$ peak uncertainty due to mismatch errors.

The difference between this average antenna temperature and that calculated from the basic Y-factor equation is -1.05°K . Assuming the same measured Y-factors, applicable reflection coefficients for the subsequent cases (2 through 8) were set equal to zero, and the expected changes in attenuations and the $|\Gamma_2|$ reflection coefficients were accounted for in the inputs to the computer program. The subsequent sample cases illustrate how mismatch error uncertainties can be reduced by improving various matches in the measurement system and the corresponding convergence of the average and basic calculated temperature values.

From the examples given, it can be concluded that in order to reduce uncertainties in the absolute calibrations of the noise temperatures of unknown noise sources (including antennas), it is very important that the noise sources, noise source transmission lines, and receiver be well matched.

References

1. Stelzried, C. T., "Temperature Calibration of Microwave Thermal Noise Sources," *IEEE Transactions on Microwave Theory and Techniques*, Vol. MTT-13, No. 1, January 1965, p. 128.
2. Worthing, A. G., and Geffner, J., *Treatment of Experimental Data*, John Wiley and Sons, New York, 9th Printing, 1943, p. 255.
3. Stacey, J., *Research and Experimentation on Space Applications of Millimeter Waves*, SSD-TDR-63-48, Report TDR-169(3250-41), TN-1, Aerospace Corporation, El Segundo, Calif., May 21, 1963, p. 48.
4. Merlo, D., Houghton, E. W., and Halford, G. J., "Effect of Some Component Tolerances and Measuring Errors on Noise Measurements," *Electronics Letters*, Vol. 1, No. 9, November 1965, pp. 250-251.
5. Woods, D., "Effect of Some Component Tolerances and Measuring Errors on Noise Measurements," *Electronics Letters*, Vol. 2, No. 2, February 1966, p. 47.
6. Merlo, D., Houghton, E. W., and Halford, G. J., "Effects of Some Component Tolerances and Measuring Errors on Noise Measurements," *Electronics Letters*, Vol. 2, No. 6, June 1966, p. 226.
7. Wells, J. S., Daywitt, W. C., Miller, C. K. S., "Measurement of Effective Temperatures of Microwave Noise Sources," *IEEE Transactions on Instrumentation and Measurement*, Vol. IM-13, March 1964, pp. 17-28.
8. Ginzton, E. L., *Microwave Measurements*, McGraw-Hill Book Company, New York, 1957, p. 321.

N67 12139

XIX. Spacecraft Radio

A. Low Data Rate Telemetry
RF System Development

R. B. Postal and C. M. Potts

1. Introduction

A solid-state 2295-MHz transmitter is being developed as a subassembly for a telecommunication system capable of surviving a high impact on a lunar or planetary surface. Major considerations in this development are resistance to high impact levels (10,000 g @ 1 msec) and sterilizability. The transmitter will generate a level of 3 w minimum at 2295 MHz with a DC to RF conversion efficiency of 10%. Design goals for this system are given in Table 1.

2. Circuit Description

Fig. 1 is a block diagram of the S-band high-impact solid-state transmitter. The transmitter circuitry will be housed in three separate modules to simplify electrical and environmental testing.

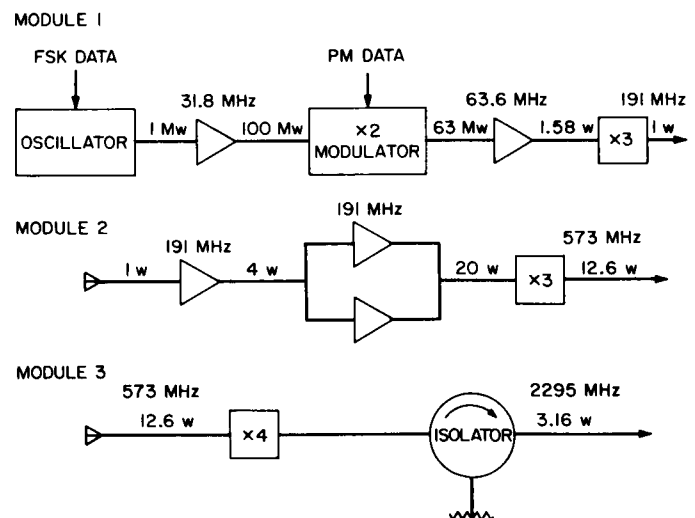


Fig. 1. Low data rate S-band high impact solid-state transmitter

a. Module 1

Fig. 2 is a photograph of a typical Module I. A description of the circuitry contained in this module follows.

Table 1. Design goals for the 3- to 5-w solid-state high impact transmitter

Electrical			
Input	Voltage DC power	28 ±2 v 30 w (max)	
Output (all environmental conditions)	Frequency	Unmodulated (selectable between 2290 and 2300 MHz)	
	Stability	Condition Shock (≤10,000 g) Temperature (0–55°C) Voltage (±2 v) Age (1 yr)	Δf/f max ±2 × 10 ^{−6} ±2 × 10 ^{−6} ±1 × 10 ^{−8} ±1 × 10 ^{−8}
	Phase jitter	Static Vibration	<6-deg peak at strong signal, APC receiver with 12-Hz bandwidth <4-deg peak/g rms with 100-Hz bandwidth
	Level	3 w (min)	
	Load impedance	50 Ω (nominal) VSWR ≤1.3:1	
	Sideband levels	>40 db below carrier (2290 to 2300 MHz) >60 db below carrier (all other frequencies)	
	Bandwidth	>10 MHz, p-p ripple, = 1 db (max)	
Modulation	Frequency shift keyed	Bandwidth Sensitivity Linearity	150 kHz 100 Hz/v (min); 15 kHz/v (max) <±2.5% deviation from linear char- acteristic
		Max. deviation	±5 times the above sensitivities
	Phase modulated	Bandwidth Sensitivity Linearity	±1.5 MHz (3 db) 1 rad/v ≤±2.5% deviation from linear char- acteristic
		Max. deviation	±2.5 rad/w above linearity
Environmental			
Impact resistance	≤10,000 g at 1 msec		
Temperature	Dynamic range, Mariner C TA thermal vacuum (−10°C to +75°F) Sterilization, six 60-hr cycles at 135°C		
Vibration	Per JPL Spec. 30250 C		
Physical			
PM system (three modules)	Weight Size Volume	2.2 lb 4.1 × 1.8 × 1.5 in. each 33.3 in. ³ (total)	
PM and FSK system (four modules)	Weight Size Volume	2.93 lb 4.1 × 1.8 × 1.5 in. each 44.4 in. ³ (total)	

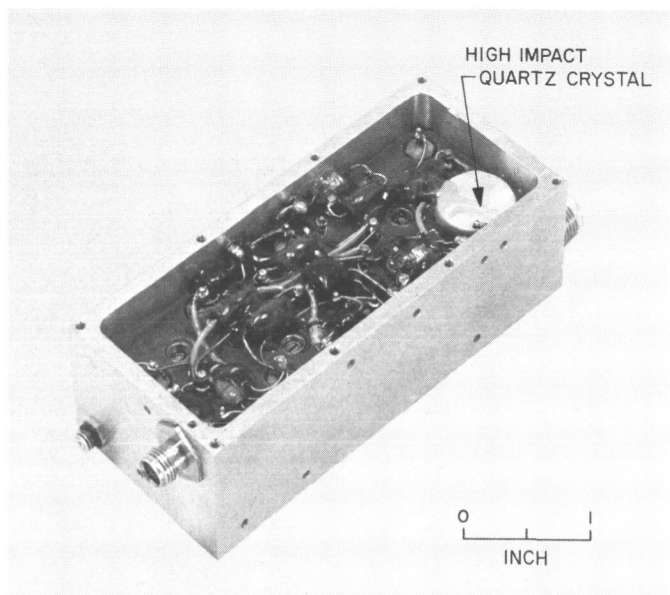


Fig. 2. Module I low data rate telemetry transmitter

31.875-MHz FSK modulator/oscillator. The frequency-shift keyed (FSK) modulator generates a 31.875-MHz crystal-controlled signal whose frequency is dependent upon data input level. Fig. 3 shows the basic oscillator configuration to be a modified Colpitts oscillator with collector-to-base regeneration. The transistor amplifier operates Class A in a common emitter configuration. Low-level feedback is provided by a capacitive divider (C1, C2) across the collector resonant circuit. The feedback loop is a low impedance circuit consisting of an inductor (L2), a voltage variable capacitor (CR1), and a series resonant quartz crystal (Y1). A time variant voltage (data) is applied across the varactor thereby changing the phase of its resonant circuit. The crystal

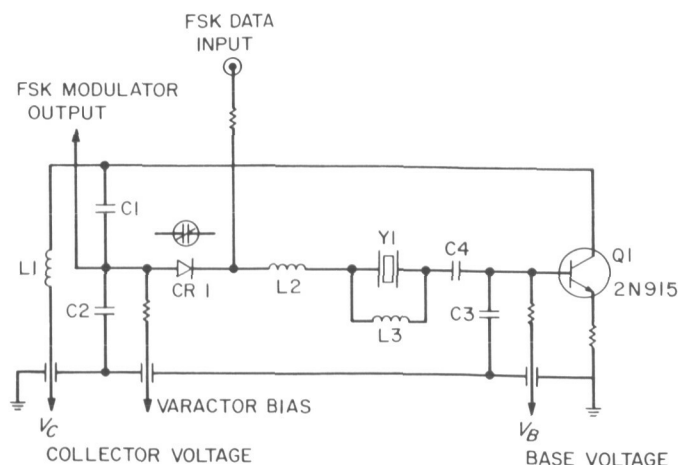


Fig. 3. 31.875-MHz FSK modulator/oscillator

corrects for this phase change, which results in an output frequency shift. Loading of the crystal by inductor L3 selects a phase characteristic of the crystal that cancels the nonlinearity of the varactor diode. Proper selection of L3 permits a linear response of oscillator frequency versus data voltage.

31.8-MHz amplifier. This stage, in which a 2N2369 transistor operates Class AB in a common emitter configuration, provides isolation and 20-db gain between the FSK modulator and the following varactor frequency doubler.

Varactor doubler-PM modulator. The doubler-modulator uses two PC137 varactor diodes in a balanced push-push configuration. This configuration was selected for its ability to reject the fundamental input frequency. A rejection of the fundamental input frequency of 30 db is attainable without selection of diodes. Nominal insertion loss of this doubler is 2 db. The doubler also serves as a phase modulator by translating a time variant varactor bias level into the required linear phase deviation.

The succeeding amplifier and varactor tripler provide the gain, isolation, and frequency multiplication necessary to obtain the required Module I output parameters.

b. Module II

Fig. 4 is a photograph of a typical Module II. Circuitry contained in this model consists of two 191-MHz power amplifiers and a varactor tripler.

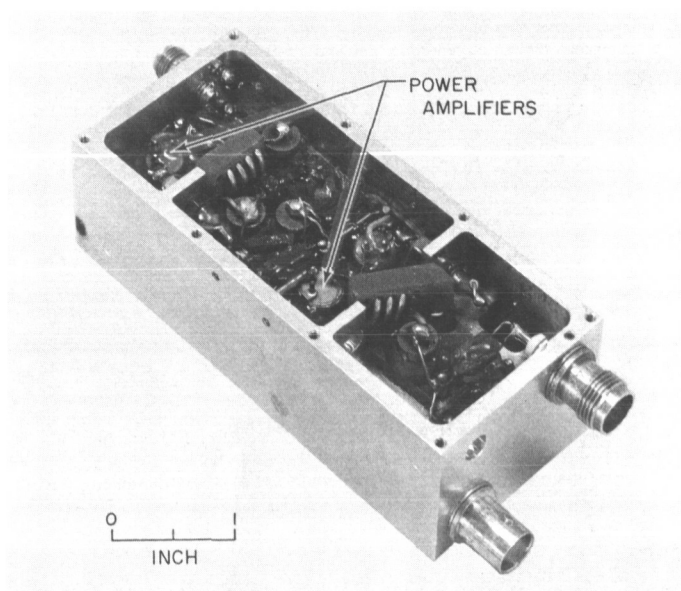


Fig. 4. Module II low data rate telemetry transmitter

191-MHz power amplifiers. The first power amplifier consists of a 2N3375 transistor operating Class C in a common emitter configuration. A power gain of 6 db in this amplifier develops a 191-MHz level of 4 w with a collector efficiency of 60%.

The second power amplifier utilizes two 2N3632 transistors connected in parallel, in a common emitter configuration, to provide the required 20-w drive level to the $\times 3$ varactor multiplier. Collector efficiency of this amplifier stage is 55%.

191- to 573-MHz tripler. This $\times 3$ varactor multiplier employs a 1N4387 varactor diode in a shunt configuration. A 573-MHz Module II output level of 12.6 w is developed with a tripler conversion efficiency of 60%.

c. Module III

As shown in Fig. 1, Module III consists of a $\times 4$ varactor multiplier and associated isolator. It is proposed that stripline techniques be applied in the development of the $\times 4$ multiplier. The ferromagnetic isolator will be developed to provide maximal isolation to the transmitter from any reflected output signals. This isolation prevents spectrum breakup and diode damage caused by reflected power.

3. Development Status

The transmitter circuitry and packaging for Modules I and II are being developed at JPL. The crystal assembly used in Module I is being developed by Valpey Fisher Corp., under JPL Contract 951080. The ferrite isolator used in Module III is being developed by Rantec Corp. under JPL Contract 951565. The stripline portion of Module III will be developed by a vendor still to be selected.

Engineering models of Modules I and II, with the exception of the 573-MHz tripler and FSK oscillator, have successfully passed 10,000-g impact tests. The 573-MHz tripler has been breadboarded and subjected to high impact tests. This tripler passed impact levels of 5,000 g, but failed at 10,000 g. The failure was caused by excessive stress on the varactor diode terminal. Due to inadequate mounting and bonding techniques of associated components, the varactor diode was broken. The unit is presently being reworked to correct the design deficiencies.

Work has begun on the development of the FSK oscillator. Module I, with a fixed frequency oscillator, and

Module II, with the exception of the 573-MHz tripler, have been tested over the *Mariner C* type approval (TA) temperature range (-10 to $+75^\circ\text{C}$). Except for minor variations in output characteristics at temperature extremes, no serious problems have been encountered. As yet, neither unit has been subjected to the sterilization cycle.

In support of this design effort, a component qualification program (sterilizability and high impact shock) has been carried on concurrently by the JPL Engineering Mechanics Division. This program is necessary to ensure the selection of components capable of surviving the extreme impact levels and temperature ranges.

N67 12140

B. High Impact Antenna Study: Coaxial Cavity Radiator

K. Woo

1. Introduction

Two families of S-band, low gain, circularly polarized, high impact antennas are being developed for future planetary landing missions. The first, the indirect family, consists of antennas that can survive when the impact loads are transmitted to them through their mounting structures. Such antennas would be useful if the capsule could protect the antenna from any direct impact loads. The second, the direct impact family, consists of antennas that can survive when the impact loads are applied directly to their radiating elements. Such antennas would be essential if the initial impact of a capsule on a planetary surface might be the antenna itself.

The projected impact load for indirect impact antennas is a shock of 10,000 g imparted into the antenna mounting structure. The projected impact load for direct impact antennas is yet to be defined, as all high impact work at JPL to date has been of the indirect type. Since the g-level description for the indirect type is no longer meaningful in this case, parameters that characterize a direct impact must still be established. The electrical design objectives for both families of antennas are presently set as:

$$\begin{aligned} \text{VSWR: } &< 1.2 \text{ at } 2295 \pm 5 \text{ MHz} \\ &< 1.3 \text{ at } 2115 \pm 5 \text{ MHz} \end{aligned}$$

Gain: 4 to 8 db

Coverage: Hemispheric, 3-db beamwidth ≤ 120 deg

Ellipticity: < 6 db within ± 60 deg from beam axis

Power handling capability: 100 to 500 w

One of the antennas currently under investigation (SPS 37-35, Vol. IV, pp. 278-281), a coaxial cavity radiator, has been found capable of meeting the electrical requirements as well as withstanding direct high impact applied to its radiating aperture. This article reports the preliminary test results of the antenna.

2. Antenna Design

As shown in Fig. 5, the antenna is composed of a section of coaxial aluminum waveguide, shorted at one end and open at the other. The dimensions of the cavity are such that only the TE_{11} wave mode will resonate at the frequency of interest. The cavity is excited from two orthogonally located input terminals near the shorted

end. The center conductor of each terminal extends completely across the cavity into the inner wall, as shown. When the terminals are fed with equal power in time quadrature, circularly polarized waves will be radiated at the open end of the cavity. In the experiments performed, the proper power and phase were obtained by utilizing a 3-db hybrid having a 90-deg phase difference between its two outputs. The feeding line was connected to the input arm of the hybrid, and the antenna terminals were connected by equal-length transmission lines to the output arms of the hybrid.

3. High Impact Test

High impact testing of the antenna was carried out with a special horizontal shock tester (Ref. 1). Referring to Fig. 6, the antenna was fastened to the back plate (a) of an aluminum mounting fixture with four screws (b), and the plate was then bolted to the mounting fixture proper (c), with the antenna face in. The front plate (d) of the assembly was attached to the specimen carriage

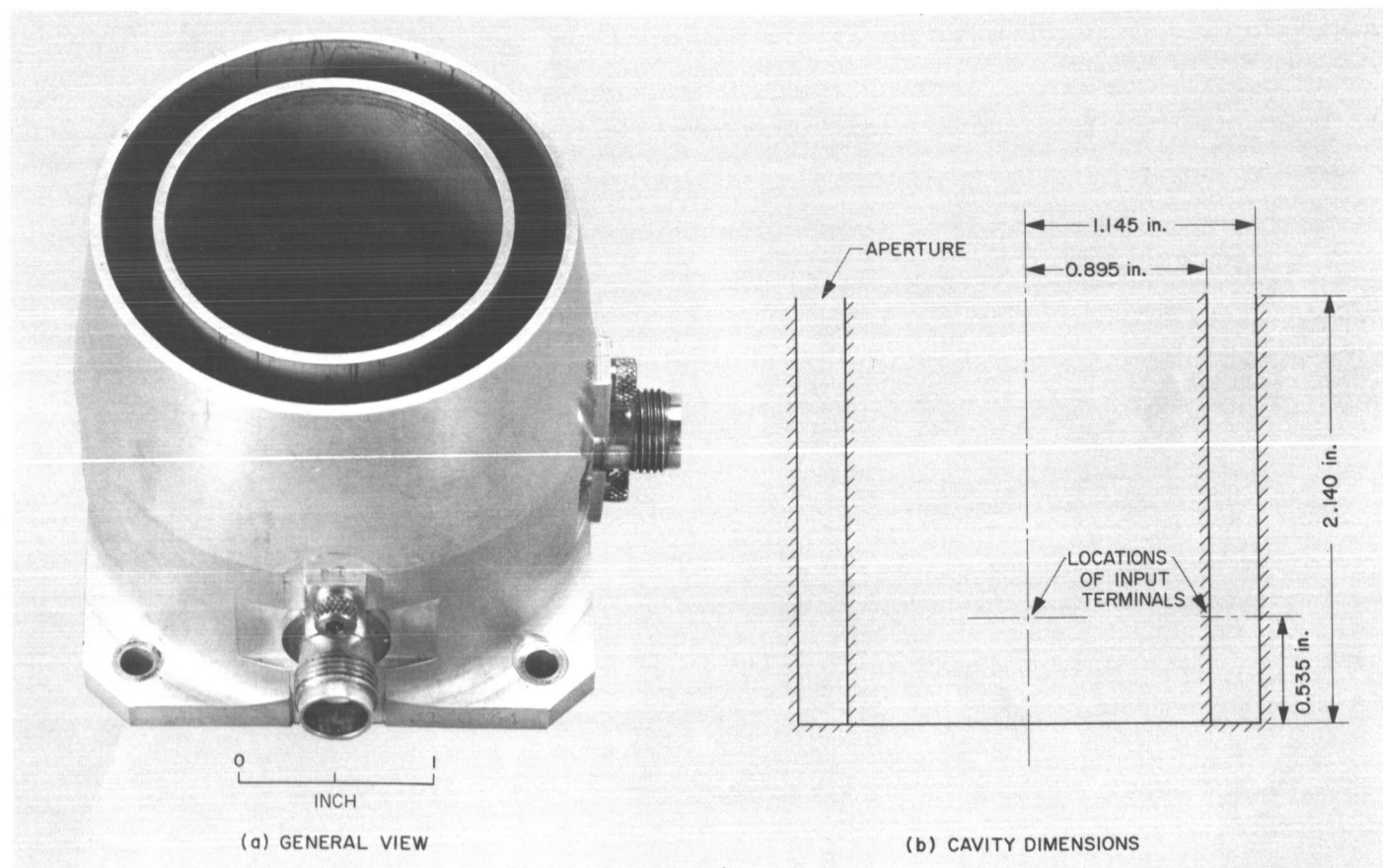


Fig. 5. Coaxial cavity radiator before impact

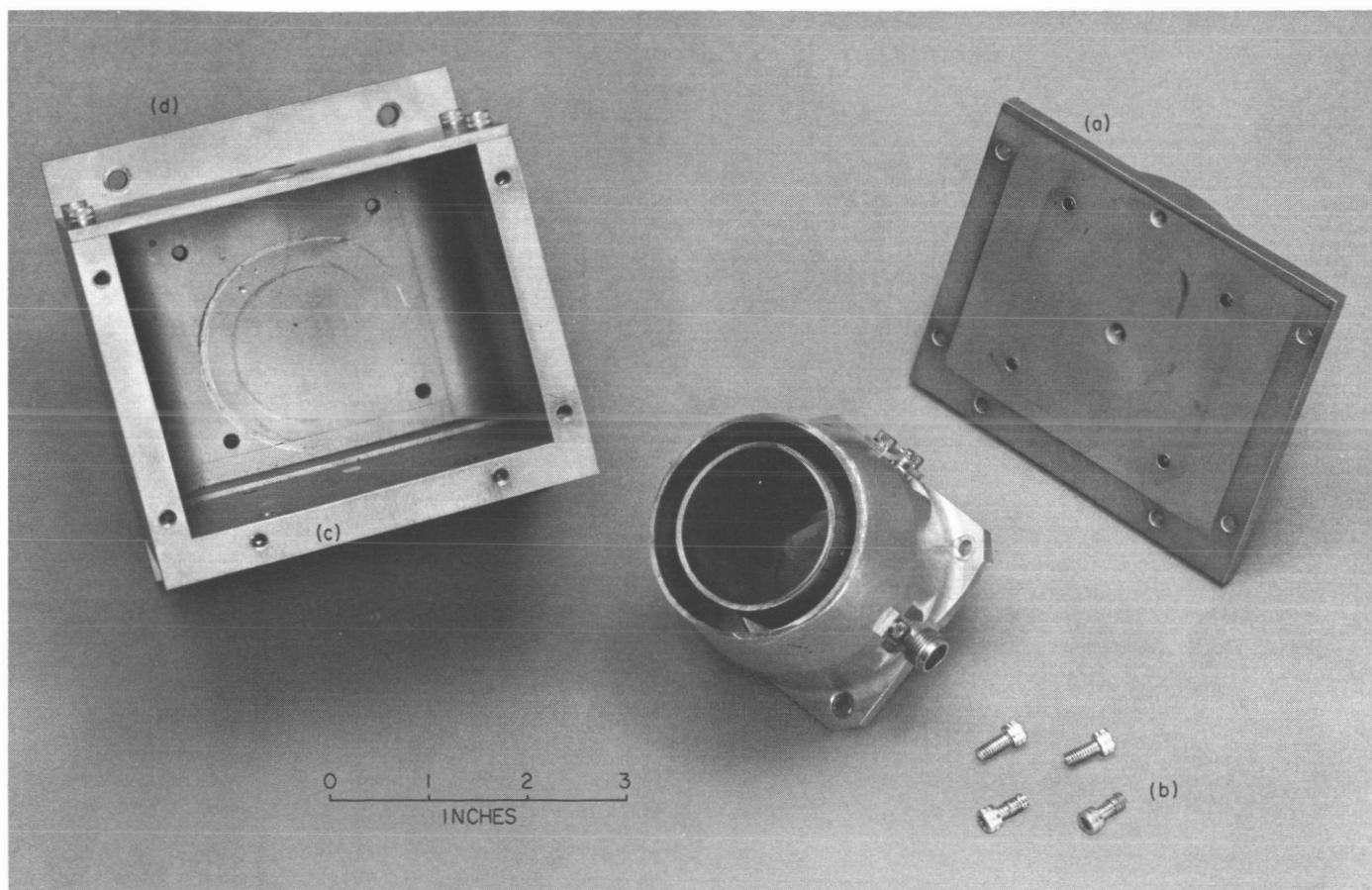


Fig. 6. Antenna mounting fixture after impact

of the tester, and the carriage was then impacted against an annealed copper target. As designed, upon impact the antenna would experience an indirect shock transmitted to it through the fixture structure. However, when the assembly was in the process of decelerating from an impact of about 10,000 g , the threads of the tapped holes for the four screws holding the antenna were stripped. As a result, the antenna separated from the back plate and made a direct high impact on the front plate. The cavity surface was bruised and the aperture was deformed. Depressions were also cut into the front plate, as shown in Fig. 6.

4. Results

Fig. 7 shows the damaged antenna and its aperture deformation drawn to scale. Since this was an unintentional direct impact and the criteria for direct impact have not been developed, the mechanical aspects of the impact are not fully understood. Whether the antenna would have suffered more severe physical damage in an

actual landing remains unanswered; however, it is important to note that the electrical performance of the antenna deteriorated very little as the result of this impact. Figs. 8 and 9 show, respectively, the radiation patterns of the right circularly polarized (RCP) component and the left circularly polarized (LCP) component, taken before and after the impact at 2298 MHz, along two mutually perpendicular cuts (clock angles 0 and 90 deg; see Fig. 7). As can be seen from either cut, the RCP pattern did not change appreciably. Therefore, the gain and beamwidth of the antenna were only slightly modified. The increase in power associated with the LCP component was not large enough to significantly degrade the performance of the antenna system. The VSWRs measured before and after the impact at 2298 MHz were 1.2 and 1.3, respectively, at the input to the hybrid.

On the basis of the results obtained, it was concluded that the antenna would have survived an actual landing if the same physical damage had been inflicted on it by the landing impact. Consequently, with proper design,

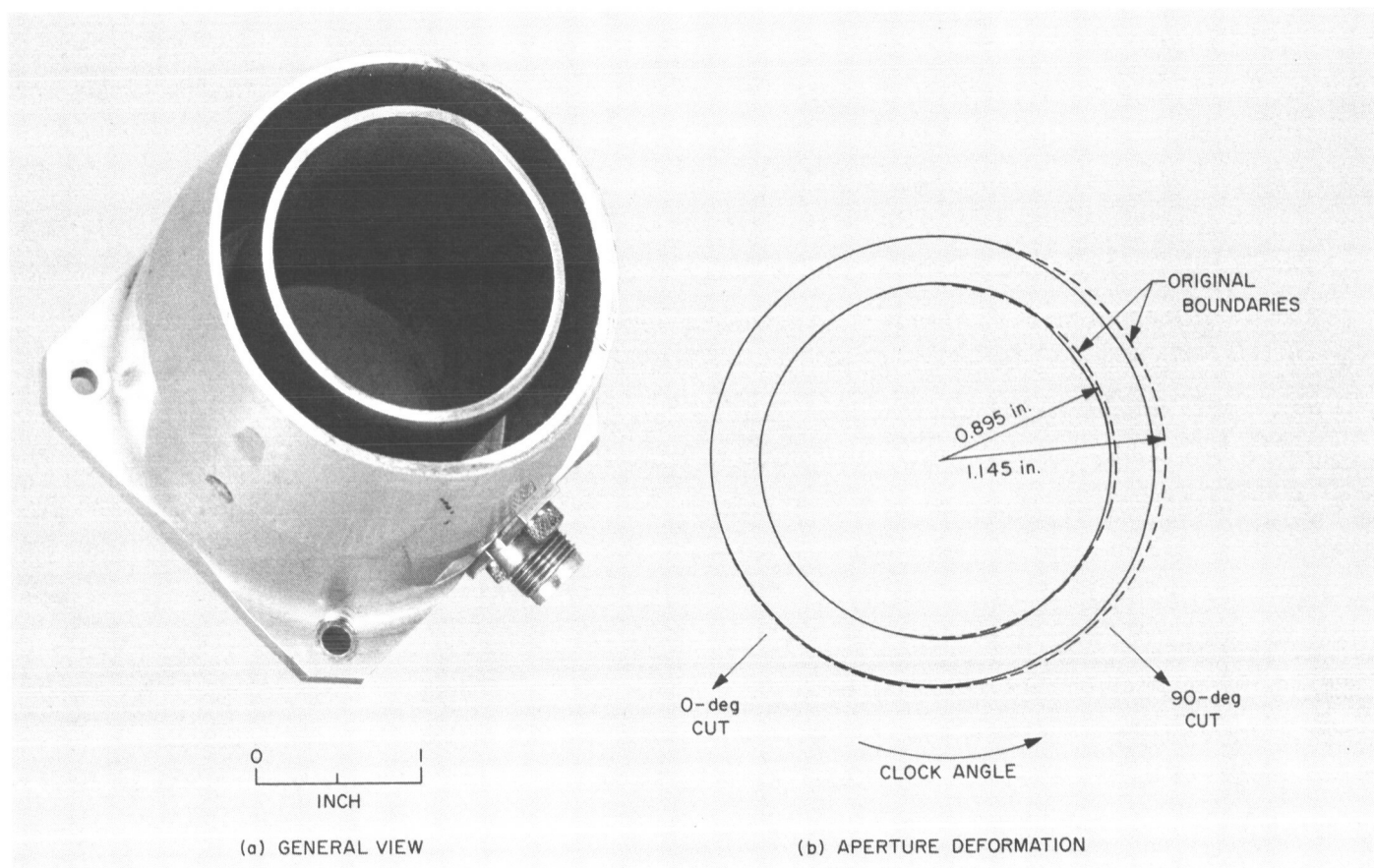


Fig. 7. Coaxial cavity radiator after impact

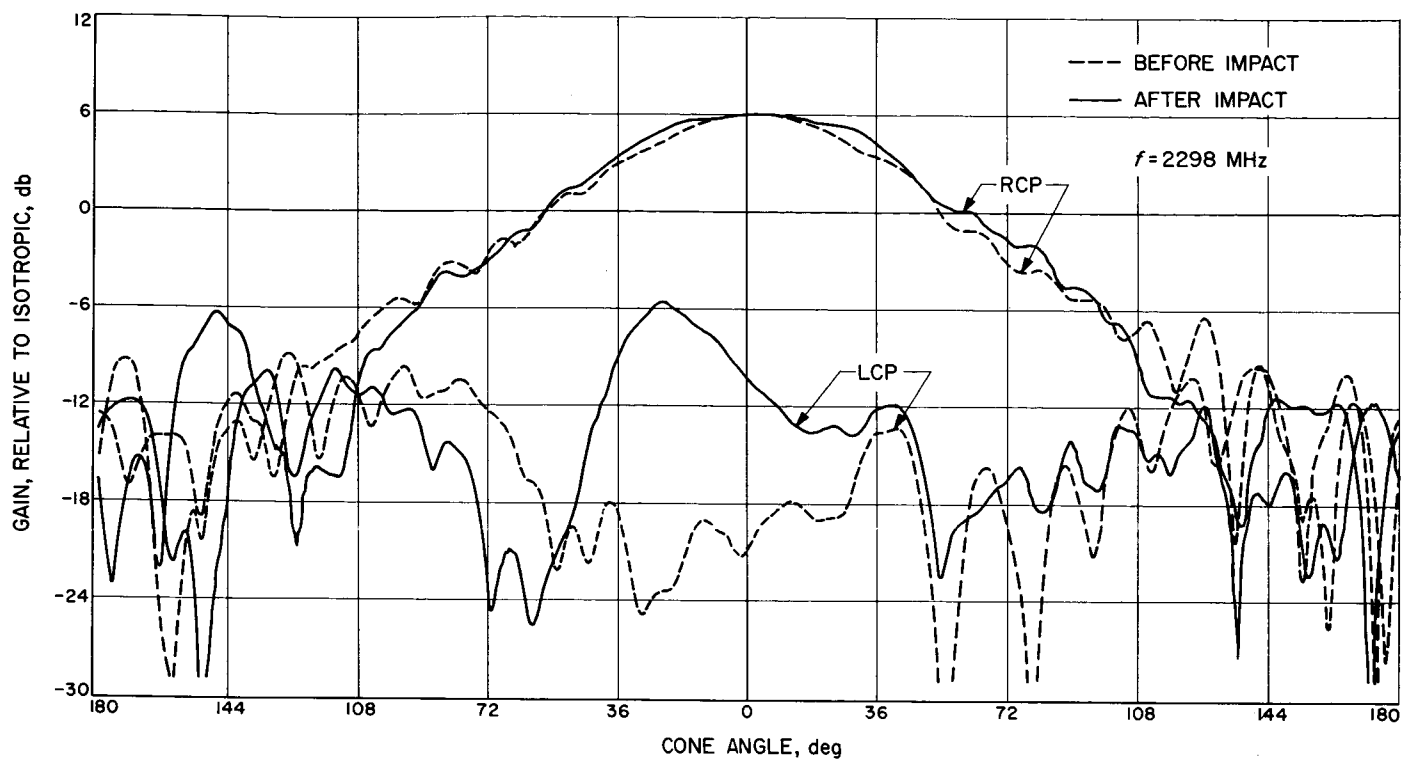


Fig. 8. Radiation patterns before and after impact, 0-deg cut

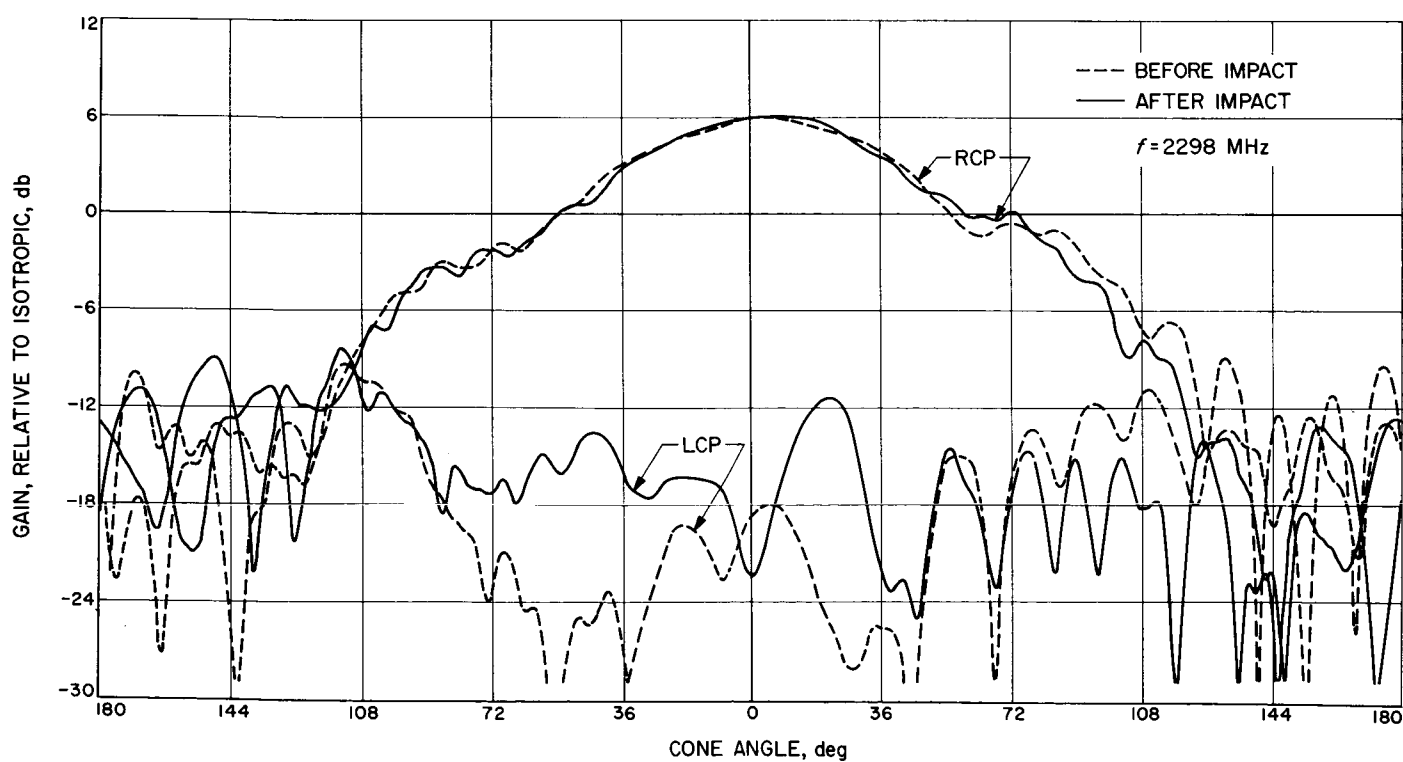


Fig. 9. Radiation patterns before and after impact, 90-deg cut

radiators of this type can be used as direct high impact survival antennas in future planetary landing missions.

In order to carry on the study, the High Impact and Advanced Technology Group¹ at JPL has initiated a program to (1) characterize a direct impact, (2) develop

¹Section 355.

a standard for direct impact testing, and (3) provide a facility for testing direct impact antennas.

The electrical properties of the coaxial-cavity-type antenna are being further investigated. The frequency bandwidth and power handling capability are among the characteristics of interest. Additional results will be reported in later issues of the SPS.

Reference

1. Lonborg, J. O., *High Impact Survival*, Technical Report 32-647, Jet Propulsion Laboratory, Pasadena, California, September 30, 1964.

N67 12141

XX. Communications Systems Research

A. Combinatorial Communications:
Search for Cyclic Hadamard
Matrices¹

R. Thoene and S. W. Golomb

1. Introduction

Cyclic Hadamard matrices of order N are known to exist for $N \equiv 0 \pmod{4}$, if at least one of the following conditions is also satisfied: $N = p + 1$, where p is prime; $N = p(p + 2) + 1$, where p and $(p + 2)$ are both prime; $N = 2^n$. As N grows in size, the frequency with which any of the above conditions is satisfied decreases. Therefore, relatively few of the values of $N \equiv 0 \pmod{4}$ are settled by this means. This is an article on the results of an effort to determine the existence of cyclic Hadamard matrices for values of N which were heretofore unsettled.

2. Approach

A *cyclic Hadamard matrix* possesses all of the properties of general Hadamard matrices. It can be thought of as a matrix in which all the entries in the first row and

first column are 1's. The second row is some sequence of 1's and -1's. Each succeeding row, exclusive of the first column, is a cyclic permutation of the second row. Since a necessary condition on Hadamard matrices is that the dot product of any two rows must be zero, it is sufficient that the second row of a cyclic Hadamard matrix, exclusive of the first column, be such that its autocorrelation is -1 everywhere out of phase (assuming that the sequence repeats and the autocorrelation is performed on a sequence of length $N - 1$). This implies that $N/2$ of the entries in the sequence of length $N - 1$ must be -1's and the remainder 1's in order that the dot product of the first two rows be zero. However, to use exhaustive techniques with as many degrees of freedom as yet exist, in order to determine the existence of cyclic Hadamard matrices, is prohibitive. Therefore, the problem was approached from the standpoint of difference sets.

A *difference set* with parameters $v = 4t - 1$, $k = 2t - 1$, and $\lambda = t - 1$ corresponds to a cyclic Hadamard matrix of order $4t$. If the difference set exists, it has a multiplier which is dependent on the divisors of $k - \lambda = t$. This multiplier divides the integers modulo v into cosets, thus reducing the degrees of freedom of assigning 1's and -1's by assigning these values to the cosets as a unit rather than to each individual member of the sequence. Hence, the problem of searching for $v = 4t - 1$, $k = 2t - 1$,

¹Prepared under JPL contract 951016 with the University of Southern California, Electrical Engineering Dept., Los Angeles.

$\lambda = t - 1$ difference sets, and equivalently cyclic Hadamard matrices, can, to a greater extent than would be possible without the multiplier theorem, be approached by performing an exhaustive search on a digital computer.

In employing the above technique, for each different assignment of 1's and -1's to the individual cosets, the first test is to determine if the number of -1's that were accordingly assigned to the individual members of the sequence of length $N - 1$ is equal to $N/2$. Only those sequences which satisfy this condition require further testing; the others are no longer candidates. Next, the autocorrelation is computed, beginning with a phase difference of one element and increasing this difference until either the autocorrelation for a particular phase shift is other than -1 or the phase difference becomes $(N - 1)/2$. In either case, the disposition of the test sequence is determined: failure to generate the proper Hadamard matrix

if the autocorrelation is anywhere other than -1 (except when in phase); success if the phase difference reaches $(N - 1)/2$ without the -1 condition being violated.

3. Results

Although many irregularities occur, the number of cosets which are generated for a particular value of N generally increases as N grows in size. This fact and the increased length of the generated sequences for larger values of N combine to increase, in the extreme, computer time required to settle the issue for larger matrices. The cases considered were confined to $N \leq 1000$ (Table 1). Even then, 54 of these 250 cases could not be tested, due to the time each would have required on the USC Honeywell 800 computer. Of the 196 remaining cases, 95 had already been settled by virtue of $N - 1$ being prime or a twin prime product, or N being a power of 2. The 101 cases which could be tested in what was deemed a reasonable length of computer time (the longest required on the order of four hours of machine time, the shortest only seconds, and the others, with few exceptions, less than 30 min) revealed that no cyclic Hadamard matrix derivable from a difference set exists for these values.

Table 1. Existence of cyclic Hadamard matrices^a

$\begin{smallmatrix} a \\ b \end{smallmatrix}$	0	100	200	300	400	500	600	700	800	900
4	E	E	U	S	S	E	U	U	U	U
8	E	E	S	E	S	S	E	S	S	E
12	E	S	E	E	S	E	S	U	E	E
16	E	S	S	U	S	S	U	U	S	U
20	E	S	S	S	E	S	E	E	U	E
24	E	S	E	E	S	E	U	U	E	S
28	S	E	E	S	S	S	U	E	E	S
32	E	E	U	E	E	U	E	S	U	U
36	E	U	S	S	U	S	S	U	S	U
40	S	E	E	S	E	S	U	E	E	S
44	E	E	S	S	E	S	E	E	U	U
48	E	S	U	E	S	E	E	S	S	E
52	S	E	E	S	U	S	U	E	S	S
56	S	S	E	S	S	U	S	S	U	S
60	E	S	S	E	S	U	E	U	E	S
64	E	E	E	S	E	E	U	U	E	S
68	E	E	U	E	E	U	S	S	S	E
72	E	U	E	S	S	E	U	U	S	E
76	S	U	U	S	U	S	S	S	S	U
80	E	E	S	E	E	S	S	U	S	S
84	E	S	E	E	S	S	E	U	E	E
88	S	S	U	U	E	E	U	E	E	S
92	S	E	S	S	E	S	E	S	U	E
96	S	S	S	S	U	U	S	U	S	S
100	S	E	U	U	E	E	S	S	E	S

^aKey: E ~ Cyclic Hadamard matrix known to exist from previously published results.

S ~ Cyclic Hadamard matrix derivable from difference set found not to exist by this study.

U ~ Unsettled.

$N = a + b$, order of the Hadamard matrix.

N67 12142

B. Combinatorial Communications: Enumeration of a Special Class of Permutations

R. Stanley

1. Summary

Let π be a permutation a_1, a_2, \dots, a_n of the symbols $1, 2, \dots, n$. We say that π contains a *run* of length t , if for some i and k , $1 \leq i \leq n$, $1 \leq k \leq n$, we have $a_i = k$, $a_{i+1} = k + 1, \dots, a_{i+t-1} = k + t - 1$. All numbers are regarded as taken mod n ; for instance, the permutation 235461 contains the run 6123 of length 4. Let $F(n, t)$ denote the number of permutations of $1, 2, \dots, n$ which contain no runs of length t (or greater). Our object is to estimate the function $F(n, t)$ for fixed t .

In Section 2, we consider the case $t = 2$. We obtain a recurrence relation for $F(n, 2)$, compute its generating function, give a closed expression for it, and derive its complete asymptotic expansion. In particular we show that the probability that a random permutation of $1, 2, \dots, n$ has no runs of length 2, approaches $1/e$ as $n \rightarrow \infty$.

The situation becomes more complicated when $t > 2$. We are unable to give as exact results as obtained for $t = 2$, but use of the principle of inclusion and exclusion enables us to develop a method which yields the asymptotic expansion of $F(n, t)$. Here we get the probability that a random permutation of $1, 2, \dots, n$ has no runs of length t , $t > 2$, approaches 1 as $n \rightarrow \infty$.

2. Permutations With No Runs of Length Two

It is convenient to work with the function $G(n, t) = (1/n) F(n, t)$. If we consider two permutations as equivalent, if they are cyclic shifts of each other, then $G(n, t)$ enumerates the number of equivalence classes of permutations containing no permutation with a run of length t .

We claim that the number of classes of cyclically equivalent permutations containing precisely k runs of length 2, $1 \leq k \leq n-2$, is $\binom{n}{k} G(n-k, 2)$. For there are $\binom{n}{k}$ ways of choosing which k runs occur, namely, the $\binom{n}{k}$ ways of choosing k elements from the set $\{12, 23, 34, \dots, n1\}$. Each choice partitions the set $\{1, 2, \dots, n\}$ into $n-k$ subsets, each subset representing symbols which must remain adjacent. For instance, the choice $12, 23, 56$ when $n = 7$ gives the partition $123, 4, 56, 7$. The number of cyclically inequivalent ways of rearranging the parts of the partition without introducing any new runs is clearly $G(n-k, 2)$, and the assertion follows.

When $k = n-1$ the argument breaks down, as the partition $123 \dots n$ introduces the extra run $n1$. If we define $G(0, t) = 1$, then the above result is also valid for $k = n$. Hence, we obtain the recurrence relation

$$G(n, 2) = (n-1)! - \left[\sum_{k=1}^n \binom{n}{k} G(n-k, 2) - n \right] \quad (1)$$

The $-n$ term appears to cancel the term $\binom{n}{1} G(1, 2) = n$. If we put $G_k = G(k, 2)$, then Eq. (1) can be written symbolically as

$$(n-1)! + n = (1 + G)^n, \quad (2)$$

where exponents are changed to subscripts after expanding the right side by the binomial theorem. Eq. (2) provides a rapid method for calculating $G(n, 2)$. Table 2 gives the values for $1 \leq n \leq 15$.

We now define the generating functions

$$G(x) = \sum_{n=0}^{\infty} \frac{G(n, 2)}{n!} x^n,$$

$$F(x) = \sum_{n=0}^{\infty} \frac{F(n, 2)}{n!} x^n,$$

Table 2. Values of $G(n, 2) = 1/n F(n, 2)$

n	$G(n, 2)$
1	1
2	0
3	1
4	1
5	8
6	36
7	229
8	1,625
9	13,208
10	120,288
11	1,214,673
12	13,496,897
13	162,744,944
14	2,128,047,988
15	29,943,053,061

Clearly $F(x) = 1 + xG'(x)$. We compute

$$\begin{aligned} G(x) e^x &= \left(\sum_{n=0}^{\infty} \frac{G(n, 2)}{n!} x^n \right) \left(\sum_{m=0}^{\infty} \frac{x^m}{m!} \right) \\ &= \sum_{n=0}^{\infty} \left(\sum_{k=0}^n \frac{G(k, 2)}{k! (n-k)!} \right) x^n \\ &= \sum_{n=0}^{\infty} \frac{1}{n!} \left(\sum_{k=0}^n \binom{n}{k} G(k, 2) \right) x^n \\ &= \sum_{n=0}^{\infty} \frac{1}{n!} \left[n + (n-1)! \right] x^n \\ &= \sum_{n=1}^{\infty} \frac{x^n}{n} + x \sum_{n=0}^{\infty} \frac{x^n}{n!} + 1 \\ &= -\log(1-x) + xe^x + 1. \end{aligned}$$

Hence

$$G(x) = e^{-x} [1 - \log(1-x)] + x, \quad (3)$$

and

$$F(x) = 1 + xG'(x) = xe^{-x} \left(\frac{x}{1-x} + \log(1-x) \right) + x + 1.$$

From Eq. (3) we get

$$\begin{aligned} \sum_{n=0}^{\infty} \frac{G(n, 2)}{n!} x^n &= \left(\sum_{i=0}^{\infty} \frac{(-1)^i x^i}{i!} \right) \left(1 + \sum_{j=1}^{\infty} \frac{x^j}{j} \right) + x \\ &= \sum_{n=0}^{\infty} \left(\sum_{k=0}^{n-1} \frac{(-1)^k}{k! (n-k)} \right) x^n + \sum_{n=0}^{\infty} \frac{(-1)^n x^n}{n!} + x \end{aligned}$$

Equating coefficients gives

$$G(n, 2) = n! \sum_{k=0}^n \frac{(-1)^k}{k! (n-k)} + (-1)^n, \quad n \neq 1 \quad (4)$$

and

$$F(n, 2) = nG(n, 2) = n! \sum_{k=0}^n \frac{(-1)^k}{k!} \frac{n}{n-k} + n(-1)^n, \quad n \neq 1. \quad (5)$$

Eqs. (4) and (5) can also be obtained from the principle of inclusion and exclusion (Ref. 3, Ch. 3 or Ref. 5, Ch. 2).

We now use Eq. (5) to obtain the asymptotic expansion of $F(n, 2)/n!$. We have

$$\begin{aligned} \frac{F(n, 2)}{n!} &= \sum_{k=0}^n \frac{(-1)^k}{k!} \frac{n}{n-k} + \frac{(-1)^n}{(n-1)!} \\ &= \sum_{k=0}^n \frac{(-1)^k}{k!} \left[1 + \frac{k}{n} + \left(\frac{k}{n}\right)^2 + \cdots + \left(\frac{k}{n}\right)^r + \frac{n}{n-k} \left(\frac{k}{n}\right)^{r+1} \right] + \frac{(-1)^n}{(n-1)!} \\ &= \sum_{k=0}^{\infty} \frac{(-1)^k}{k!} \left[1 + \frac{k}{n} + \left(\frac{k}{n}\right)^2 + \cdots + \left(\frac{k}{n}\right)^r \right] + \sum_{k=0}^n \frac{(-1)^k}{k!} \frac{n}{n-k} \left(\frac{k}{n}\right)^{r+1} - \sum_{k=n+1}^{\infty} \frac{(-1)^k}{k!} \left[1 + \frac{k}{n} \right. \\ &\quad \left. + \left(\frac{k}{n}\right)^2 + \cdots + \left(\frac{k}{n}\right)^r \right] + \frac{(-1)^n}{(n-1)!}. \end{aligned}$$

Hence

$$\begin{aligned} n^r \left| \frac{F(n, 2)}{n!} - \sum_{k=0}^{\infty} \frac{(-1)^k}{k!} \left[1 + \frac{k}{n} + \left(\frac{k}{n}\right)^2 + \cdots + \left(\frac{k}{n}\right)^r \right] \right| \\ &= \left| \sum_{k=0}^{n-1} \frac{(-1)^k k^{r+1}}{k! (n-k)} - n^r \sum_{k=n+1}^{\infty} \frac{(-1)^k}{k!} \left[\frac{1 - \left(\frac{k}{n}\right)^{r+1}}{1 - \frac{k}{n}} \right] + \frac{(-1)^n n^r}{(n-1)!} \right| \\ &\leq \sum_{k=0}^{\log n} \frac{k^{r+1}}{k! (n-k)} + \sum_{k=\log n}^{n-1} \frac{k^{r+1}}{k! (n-k)} + n^r \left| \sum_{k=n+1}^{\infty} \frac{(-1)^k}{k!} \frac{1 - \left(\frac{k}{n}\right)^{r+1}}{1 - \frac{k}{n}} \right| + \frac{n^r}{(n-1)!} \\ &< \frac{(\log n)(\log n)^{r+1}}{n - \log n} + \frac{n^{r+1} \cdot n}{(\log n)!} + n^r \frac{1}{(n+1)!} \left[\frac{1 - \left(\frac{n+1}{n}\right)^{r+1}}{1 - \left(\frac{n+1}{n}\right)} \right] + \frac{n^r}{(n-1)!} \end{aligned}$$

The next to last term is obtained by using the fact that the error in truncating an alternating series of decreasing terms tending to zero is less than the first term omitted.

Clearly

$$\lim_{n \rightarrow \infty} \frac{\log (\log n)^{r+2}}{n - \log n} = 0.$$

Moreover, using the estimate $x! > (x/e)^x$

$$\begin{aligned} \lim_{n \rightarrow \infty} \frac{n^{r+2}}{(\log n)!} &\leq \lim_{n \rightarrow \infty} \frac{n^{r+2}}{(\log n/e)^{\log n}} \\ &= \lim_{n \rightarrow \infty} e^{(r+3) \log n - (\log n)^2} \\ &= 0. \end{aligned}$$

Next

$$\begin{aligned} \lim_{n \rightarrow \infty} \frac{n^r}{(n+1)!} \left[\frac{1 - \left(\frac{n+1}{n}\right)^{r+1}}{1 - \left(\frac{n+1}{n}\right)} \right] \\ = \lim_{n \rightarrow \infty} \frac{(n+1)^{r+1} - n^{r+1}}{(n+1)!} \\ = 0. \end{aligned}$$

Finally

$$\lim_{n \rightarrow \infty} \frac{n^r}{(n-1)!} = 0$$

If we put

$$b_r = \sum_{k=0}^{\infty} \frac{k^r (-1)^k}{k!}$$

then we have just established the asymptotic expansion

$$\frac{F(n, 2)}{n!} = \sum_{r=0}^s \frac{b_r}{n^r} + o\left(\frac{1}{n^{s+1}}\right).$$

The numbers b_r can be computed as follows: First

$$b_0 = \sum_{k=0}^{\infty} \frac{(-1)^k}{k!} = \frac{1}{e}.$$

We now have

$$\begin{aligned} b_{r+1} &= \sum_{k=0}^{\infty} \frac{k^{r+1} (-1)^k}{k!} \\ &= \sum_{k=1}^{\infty} \frac{k^r (-1)^k}{(k-1)!} \end{aligned}$$

$$\begin{aligned} &= \sum_{k=0}^{\infty} \frac{(k+1)^r (-1)^{k+1}}{k!} \\ &= - \sum_{k=0}^{\infty} \frac{(-1)^k}{k!} \sum_{j=0}^r k^j \binom{k}{j} \\ &= - \sum_{j=0}^r \binom{k}{j} b_j, \end{aligned}$$

or symbolically

$$b^{r+1} = -(1+b)^r.$$

This recurrence relation shows that b_r is always an integer multiple of $1/e$, say $b_r = (1/e) a_r$.

If we write

$$b(x) = \sum_{r=0}^{\infty} \frac{b_r}{r!} x^r,$$

then similarly to the derivation of Eq. (3) we get

$$-b(x) e^x = \sum_{r=0}^{\infty} \frac{b_{r+1}}{r!} x^r = b'(x).$$

Hence

$$b(x) = e^{-e^x}.$$

If c_r denotes the number of partitions of a set of r elements, then it is well known (Ref. 4) that

$$\sum_{r=0}^{\infty} \frac{c_r}{r!} x^r = e^{e^x - 1}.$$

Hence the a_r are the so-called Blissard or umbral inverses of the set partition function c_r (Ref. 3, p. 27).

The above results are summarized by the following theorem, which also gives the values of a_r for $0 \leq r \leq 20$.

Theorem 1. Let $F(n, 2)$ be the number of permutations of $1, 2, \dots, n$ with no runs of length 2 and put $G(n, 2) = (1/n) F(n, 2)$. Then

$$(i) \quad n + (n-1)! = \sum_{k=0}^n \binom{n}{k} G(k, 2).$$

$$(ii) \quad \sum_{k=0}^{\infty} \frac{G(k, 2)}{k!} x^k = e^{-x} [1 - \log(1-x)] + x,$$

$$\sum_{k=0}^{\infty} \frac{F(k, 2)}{k!} x^k = x e^{-x} \left[\frac{x}{1-x} + \log(1-x) \right] + x + 1.$$

$$(iii) \quad F(n, 2) = n! \sum_{k=0}^{n-1} \frac{(-1)^k}{k!} \frac{n}{n-k} + n(-1)^n, n \neq 1.$$

$$\begin{aligned}
 \text{(iv)} \quad \frac{F(n, 2)}{n!} \sim \frac{1}{e} & \left(1 - \frac{1}{n^2} + \frac{1}{n^3} + \frac{1}{n^4} - \frac{2}{n^5} - \frac{9}{n^6} \right. \\
 & - \frac{9}{n^7} + \frac{50}{n^8} + \frac{267}{n^9} + \frac{413}{n^{10}} - \frac{2180}{n^{11}} - \frac{17731}{n^{12}} \\
 & - \frac{50533}{n^{13}} + \frac{110176}{n^{14}} + \frac{1966797}{n^{15}} + \frac{9938669}{n^{16}} \\
 & + \frac{8638718}{n^{17}} - \frac{278475061}{n^{18}} - \frac{2540956509}{n^{19}} \\
 & \left. - \frac{9816860358}{n^{20}} + \cdots + \frac{a_k}{n^k} + \cdots \right),
 \end{aligned}$$

where

$$\sum_{k=0}^{\infty} \frac{a_k}{k!} x^k = e^{-e^{x+1}}.$$

In particular, the probability that a random permutation of $1, 2, \dots, n$ has no runs of length 2 is

$$\frac{F(n, 2)}{n!} \rightarrow \frac{1}{e} = 0.36788 \cdots \text{ as } n \rightarrow \infty.$$

3. An Asymptotic Formula for Arbitrary t

The main result of this section is the following theorem:

Theorem 2. Let $F(n, t)$ be the number of permutations of $1, 2, \dots, n$ with no runs of length t . Then

$$\frac{F(n, 3)}{n!} = 1 - \frac{1}{n} - \frac{3}{2} \frac{1}{n^2} - \frac{14}{3} \frac{1}{n^3} + o\left(\frac{1}{n^4}\right),$$

$$\frac{F(n, 4)}{n!} = 1 - \frac{1}{n^2} - \frac{5}{n^3} - \frac{29}{2} \frac{1}{n^4} + o\left(\frac{1}{n^5}\right),$$

while for fixed $t > 4$

$$\begin{aligned}
 \frac{F(n, t)}{n!} = 1 - \frac{1}{n^{t-2}} - \frac{(t-2)(t+1)}{2} \frac{1}{n^{t-1}} \\
 - \frac{t(t+1)(3t^2-5t-10)}{24} \frac{1}{n^t} + o\left(\frac{1}{n^{t+1}}\right).
 \end{aligned}$$

Proof. The proof is based on the principle of inclusion and exclusion referred to earlier. Let $w(i_1, i_2, \dots, i_r)$ be

the number of permutations of $1, 2, \dots, n$ with runs of length t beginning on the symbols i_1, i_2, \dots, i_r . Let $W(r) = \sum w(i_1, i_2, \dots, i_r)$, where the sum is taken over all subsets $\{i_1, i_2, \dots, i_r\}$ of $\{1, 2, \dots, n\}$ with r elements. It follows from the principle of inclusion and exclusion that

$$n! - W(1) + W(2) - W(3) < F(n, t)$$

$$< n! - W(1) + W(2) - W(3) + W(4).$$

If we can show that

$$W(4)/n! = o\left(\frac{1}{n^{t+1}}\right),$$

then

$$\frac{F(n, t)}{n!} = 1 - \frac{W(1)}{n!} + \frac{W(2)}{n!} - \frac{W(3)}{n!} + o\left(\frac{1}{n^{t+1}}\right).$$

Then to complete the proof of Theorem 2 we need only calculate $W(1)$, $W(2)$, and $W(3)$.

We now show that for $t > 2$,

$$W(r)/n! = o\left(\frac{1}{n^{t+r-3}}\right).$$

This will be seen to be false for $t = 2$, which explains why this case was handled separately. For each subset $T = \{i_1, i_2, \dots, i_r\}$ of $S = \{1, 2, \dots, n\}$, we associate a partition of n as follows: the set T partitions S into subsets of symbols which must remain adjacent in order for a permutation to have runs of length t beginning on i_1, i_2, \dots, i_r . The number of elements in each subset is taken to be a term in the partition of n .

Example: Let $n = 15$, $t = 3$, $T = \{2, 5, 7, 8, 12\}$. Then S is partitioned into the subsets $\{1\}$, $\{2, 3, 4\}$, $\{5, 6, 7, 8, 9, 10\}$, $\{11\}$, $\{12, 13, 14\}$, $\{15\}$. This yields the partition $15 = 1 + 1 + 1 + 3 + 3 + 3 + 6$.

Let $n = b_1 + 2b_2 + \dots + nb_n$ be the partition of n induced by T . Observe that $b_1 \geq n - rt$, with equality holding when each element of T belongs to a distinct subset of the partition of S . Hence, there are at most $\binom{r}{t}$ distinct partitions of S induced by all subsets T with r elements, since we can assume that r elements of T are chosen from a specified set of size rt .

Given the partition $n = b_1 + 2b_2 + \cdots + nb_n$, there are

$$n \frac{\left(\sum_{i=1}^n b_i - 1\right)!}{b_1! b_2! \cdots b_n!}$$

ways of choosing subsets of S with this partition (with the property that each subset of order i must contain i consecutive elements of S). For each choice, there are

$$n \left(\sum_{i=1}^n b_i - 1\right)!$$

ways of rearranging these subsets to give different permutations of S . Hence

$$W(r) \leq \binom{rt}{r} \max \frac{n^2 \left(\sum_{i=1}^n b_i - 1\right)!}{b_1! b_2! \cdots b_n!}, \quad (6)$$

where the maximum is taken over all partitions of n which can arise from subsets T of order r .

Now if $b_2 + \cdots + b_n = b$, then

$$\sum_{i=1}^n b_i \leq n - bt - (r - b) + b,$$

since $b_2 - b_3 - \cdots - b_{t-1} = 0$ and there are r runs of length t . Hence, from Eq. (6) we get

$$\begin{aligned} \frac{W(r)}{n!} &\leq \binom{rt}{r} \frac{n^2 (n - bt + 2b - r - 1)!^2}{b_1! n!} \\ &= \binom{rt}{r} \frac{n^2 (n - bt + 2b - r - 1) (n - bt + 2b - r - 2) \cdots (n - bt + b - r)}{n(n-1)(n-2) \cdots (n - bt + 2b - r)} \\ &= 0 \left(\frac{1}{n^{bt - 3b + r}} \right). \end{aligned}$$

Since $b \geq 1$, we get

$$bt - 3b + r \geq t + r - 3 \text{ when } t > 2.$$

Note that this is false for $t = 2$, whenever $b > 1$. It follows that

$$\frac{W(r)}{n!} = 0 \left(\frac{1}{n^{t+r-3}} \right), t > 2,$$

as asserted.

We now complete the proof by calculating $W(1)$, $W(2)$, and $W(3)$ for n sufficiently large to "accommodate" all runs in question.

One run of length t can begin on any one of n symbols, leaving $(n-t)!$ ways of permuting the $n-t$ remaining symbols and n ways of shifting and permuting cyclically. Hence

$$W(1) = n^2 (n-t)!, \quad n \geq t+1.$$

Note that

$$\frac{F(n, t)}{n!} \geq 1 - \frac{W(1)}{n!} = 1 + 0 \left(\frac{1}{n^{t-2}} \right),$$

so that this simple estimate suffices to show that the probability that a random permutation has no runs of length $t > 2$ approaches 1 as $n \rightarrow \infty$.

Two runs of length t can occur in one of two ways: (i) one run of length $t+1$, $t+2$, \cdots , $2t-1$, or (ii) two disjoint runs of length t . In the first case, one run of length $t+i$ can begin on any one of n symbols, leaving $(n-t-i)!$ ways of permuting the $n-t$ remaining symbols and n ways of shifting each permutation cyclically. In the second case, there are $n(n-2t+1)/2$ ways of choosing two disjoint runs of length t , $(n-2t+1)!$ ways of permuting the $n-2t+1$ subsets that remain when one run is fixed in place, and n ways of shifting each permutation cyclically.

Hence

$$W(2) = \sum_{i=1}^{t-1} n^2 (n-t-i)! + \frac{n^2 (n-2t+1)}{2} (n-2t+1)!,$$

$$n \geq 2t+1.$$

Three runs of length t can occur in one of three ways: (i) one run of length $t+2, t+3, \dots, 3t-2$, (ii) one run of length t and one of length $t+1, t+2, \dots, 2t-1$, or (iii) three disjoint runs of length t . In the first case, as before, one run of length $t+i$ can begin on any one of n symbols, leaving $(n-t-i)!$ ways of permuting the $n-t$ remaining symbols and n ways of shifting each permutation cyclically. Now, however, we get an additional factor of $i-1$, as there are $i-1$ places on which the middle run can begin. In the second case, there are $n(n-2t+1-i)$ ways of choosing two disjoint runs of length t and $t+i$, $(n-2t+1-i)!$ ways of permuting the $n-2t+1-i$ subsets that remain when one run is fixed in place, and n ways of shifting each permutation cyclically. In the third case, there are $n(n-3t+2)(n-3t+1)/6$ ways of choosing three disjoint runs of length t , $(n-3t+2)!$ ways of permuting the $n-3t+2$ subsets that remain when one run is fixed in place, and n ways of shifting each permutation cyclically.

Hence

$$W(3) = \sum_{i=2}^{2t-2} (i-1) n^2 (n-t-i)! + \sum_{i=1}^{t-1} n^2 (n-2t+1-i) (n-2t+1-i)! + \frac{n^2 (n-3t+2)(n-3t+1)}{6} (n-3t+2)!,$$

$$n \geq 3t+1.$$

We leave it to the intrepid reader to expand $1 - W(1)/n! + W(2)/n! - W(3)/n!$ in a power series in $1/n$ and verify that the terms given in the statement of the theorem are correct. With this the proof of Theorem 2 is complete.

It is evident that the above procedure can be continued to give the asymptotic expansion of $F(n, t)/n!$ to any desired accuracy.

N67 12143 C. Coding Theory: Moments of Weight Distributions

R. Stanley

1. Introduction

In Section 2 of this report, a general combinatorial formula is developed which allows calculation of sums of the type

$$\sum_{v \in S} [\sigma(v)]^t, \quad 0 \leq t \leq r$$

where S is a set of vectors v , $\sigma(v)$ is the sum of the coordinates of v , and r is an integer depending on a special property of the set S . In Section 3, this formula is applied to (n, k) binary codes and yields explicit formulas for the sums

$$\sum_{i=0}^n i^t a_i, \quad 0 \leq t < d$$

where a_i words of the code have weight i , and d is the minimum weight of the dual code. When enough information about a code is known, these equations may suffice to determine its weight distribution. As an example, we calculate the weight distribution of the dual Golay $(23, 11)$ code without using J. MacWilliams' formula.

2. A Combinatorial Formula

Let $P = \{x_1, \dots, x_p\}$ be a subset of a commutative ring R , and let S be a subset of order s of the direct product $P^n = P^x P^x \dots P^x$ (n times). Assume that S has the following property for some integer $r \leq n$:

(1) The restriction of S to any r coordinates contains all $p^r r$ -tuples of elements of P the same number of times. (This necessitates $p^r | s$.)

Let $\sigma(v)$ denote the sum (in R) of the coordinates of the element v of S . We then have:

Theorem 1. For $0 \leq t \leq r$, the sum

$$\sum_{v \in S} [\sigma(v)]^t$$

depends only on P, n, s (not on S), and we have

$$\frac{p^n}{s} \sum_{v \in S} (\sigma(v))^t = \sum_{v \in P^n} (\sigma(v))^t. \quad (2)$$

Proof. Denote the vectors in S by

$$\begin{aligned} & (v_{11}, v_{12}, \dots, v_{1n}) \\ & (v_{21}, v_{22}, \dots, v_{2n}) \\ & \vdots \\ & (v_{s1}, v_{s2}, \dots, v_{sn}). \end{aligned} \quad (3)$$

Expanding by the multinomial theorem, we get

$$\begin{aligned} \sum_{v \in S} (\sigma(v))^t &= \sum_{i=1}^s (v_{i1} + v_{i2} + \dots + v_{in})^t \\ &= \sum_{i=1}^s \sum_{\substack{a_1 + a_2 + \dots + a_n = t \\ 0 \leq a_i \leq n}} \frac{n!}{a_1! a_2! \dots a_n!} v_{i1}^{a_1} v_{i2}^{a_2} \dots v_{in}^{a_n} \\ &= \sum_{\substack{a_1 + a_2 + \dots + a_n = t \\ 0 \leq a_i \leq n}} \frac{n!}{a_1! a_2! \dots a_n!} \left(\sum_{i=1}^s v_{i1}^{a_1} v_{i2}^{a_2} \dots v_{in}^{a_n} \right). \end{aligned}$$

In the sum in parenthesis, at most t of the exponents a_1, a_2, \dots, a_n are nonzero, say $a_{i_1}, a_{i_2}, \dots, a_{i_m}$. As i ranges from 1 to s , it follows by property (1) that the set $\{v_{i_1}, v_{i_2}, \dots, v_{i_m}\}$ ranges through a complete set of p^m -tuples, with each m -tuple occurring the same number (p^{s-m}) of times. Hence, the sum in parenthesis depends only on P, s , and a_1, a_2, \dots, a_n . Therefore, the entire sum depends only on P, s , and n , as asserted.

Consider the array obtained by repeating Eq. (3) $p^{n/s}$ times. This array contains p^n vectors and satisfies property (1). The set P^n also contains p^n vectors and satisfies property (1) for any $r \leq n$. Hence, by what we have just proved, we must have Eq. (2) holding, and the proof of Theorem 1 is complete.

The proofs of the following simple observations are left to the reader.

(A) If a set S satisfies property (1), then the set obtained by restricting the vectors of S to any $m < n$ coordinates also satisfies property (1). (This corresponds to *puncturing* a code.)

(B) Assume that the set P is closed under addition, so that it forms an additive group, and that a set $S \subseteq P^n$ satisfies property (1). If v is any vector in P^n , then the set $S + v = \{v_0 + v : v_0 \in S\}$ also satisfies property (1). In particular, if S is a subspace of P^n over R satisfying property (1), then all its cosets satisfy (1).

Example. Define two $n \times n$ matrices of 0's and 1's to be *equivalent* if one can be transformed into the other by complementing appropriate rows and columns. It is easily verified that this definition of equivalence indeed gives an equivalence relation. In fact, if we regard the 0's and 1's as belonging to the field $GF(2)$, then the equivalence class containing the 0 matrix forms an additive group of order 2^{2n-1} whose cosets are the other equivalence classes. These equivalence classes always satisfy property (1) for $r = 3$ (but never for $r = 4$). If we now regard the underlying ring R as the ordinary integers, and if C is any equivalence class, then Theorem 1 tells us that

$$\sum_{v \in C} \sigma(v) = \frac{2^{2n-1}}{2^{n^2}} \sum_{k=0}^{n^2} k \binom{n}{k} = n^2 2^{2n-2},$$

$$\sum_{v \in C} [\sigma(v)]^2 = \frac{2^{2n-1}}{2^{n^2}} \sum_{k=0}^{n^2} k^2 \binom{n}{k} = n^2 (n^2 + 1) 2^{2n-3},$$

$$\sum_{v \in C} [\sigma(v)]^3 = \frac{2^{2n-1}}{2^{n^2}} \sum_{k=0}^{n^2} k^3 \binom{n}{k} = n^4 (n^2 + 3) 2^{2n-4}.$$

3. Applications to Group Codes

Let V be an (n, k) group code over the field $GF(q)$, i.e., a k -dimensional subspace of the vector space of all n -tuples over $GF(q)$. The next theorem then gives the largest value of r for which property (1) is valid.

Theorem 2. The set V satisfies property (1) for $r = d - 1$ but not $r = d$, where d is the minimum weight of the dual code.

Proof. Let v be a word in the dual code with exactly d nonzero entries. Since v is orthogonal to every word of V , this specifies a linear relation which must hold among some d coordinates of the words in V . Hence, these d coordinates cannot be chosen arbitrarily, so $r \leq d - 1$.

Conversely, assume that property (1) fails for some $r \leq d - 1$. Thus, there are some r coordinates whose entries cannot be chosen arbitrarily. If we restrict the vectors in V to these r coordinates, we get a proper subspace of the space of all r -tuples over $GF(q)$. The orthogonal complement of this subspace contains more than one vector and hence a vector v_0 of positive weight $\leq r$. If we now extend v_0 to an n -tuple by putting 0's in the $n - r$ missing coordinates, we get a word of positive weight $\leq r$ orthogonal to V , a contradiction. Theorem 2 is proved.

Now assume that $q = 2$, so that V is a binary code. If we regard the 0's and 1's as ordinary integers for the purpose of applying Theorem 1, then $\sigma(v)$ is simply the

weight of the word v . Hence, from Theorem 1 and 2 there follows:

Theorem 3. If an (n, k) binary code has a_i words of weight i and if d is the minimum weight of the dual code, then

$$\sum_{i=0}^n i^t a_i = \frac{1}{2^{n-k}} \sum_{j=0}^n j^t \binom{n}{j}, \quad 0 \leq t \leq d-1.$$

Theorem 3 then gives d linear equations which the a_i satisfy. In Table 3, expressions for the function

$$f(t) = \sum_{j=0}^n j^t \binom{n}{j}$$

for $0 \leq t \leq 6$, are given for reference.

Table 3. Values of $f(t) = \sum_{j=0}^n j^t \binom{n}{j}$

t	$f(t)$
0	2^n
1	$n2^{n-1}$
2	$n(n+1)2^{n-2}$
3	$n^2(n+3)2^{n-3}$
4	$n(n+1)(n^2+5n-2)2^{n-4}$
5	$n^2(n^2+10n^2+15n-10)2^{n-5}$
6	$n(n+1)(n^4+14n^3+31n^2-46n+16)2^{n-6}$

For practical purposes, it can always be assumed that the minimum weight of the dual of a binary (n, k) code satisfies $d > 2$. For, if $d = 1$, then one coordinate of V is always 0, while if $d = 2$, then V has repeated columns. Since $d > 2$, we can calculate the variance μ of the weight distribution:

$$\begin{aligned} \mu &= \frac{1}{2^k} \sum_{i=0}^n i^2 a_i - \left(\frac{1}{2^k} \sum_{i=0}^n i a_i \right)^2 \\ &= \frac{1}{2^n} \sum_{j=0}^n j^2 \binom{n}{j} - \left[\frac{1}{2^n} \sum_{j=0}^n j \binom{n}{j} \right]^2 \\ &= \frac{n}{4}. \end{aligned}$$

This is necessarily the variance of the binomial distribution on n tries with success probability $\frac{1}{2}$.

Example. Using the methods of Solomon and McEliece (SPS 37-35, Vol. IV, pp. 340-348), it can be shown that the words of the dual Golay (23, 11) code have weight 0, 8,

12, or 16. And the dual of this code has minimum weight 7, so by Theorem 3,

$$a_8 + a_{12} + a_{16} = 2^{11} - 1$$

$$8a_8 + 12a_{12} + 16a_{16} = 23 \cdot 2^{10}$$

$$64a_8 + 144a_{12} + 256a_{16} = 23 \cdot 24 \cdot 2^9.$$

These equations are easily solved, giving

$$a_8 = 506 = 22 \cdot 23,$$

$$a_{12} = 1288 = 56 \cdot 23,$$

$$a_{16} = 253 = 11 \cdot 23.$$

N67 12144

D. Coding Theory: Efficient Solutions of Equations for Decoding

R. McEliece

1. Introduction

In SPS 37-39, Vol. IV, pp. 219-226, Berlekamp, Rumsey, and Solomon presented methods of solving certain algebraic equations over finite fields of characteristic 2; such equations turn up in decoding procedures for Bose-Chaudhuri codes. We give here a more general approach to the same problem, and succeed in giving explicit solutions to many equations. These solutions are easily mechanized. In section 3, we indicate how these solutions represent a considerable saving of effort over previous methods. References to the fundamentals of linear algebra and Galois theory can be found in Ref. 6.

2. Theoretical Results

Throughout this section, K and k represent fields.

Theorem 1. Suppose K is a normal extension of k , and let σ be an automorphism of K/k . View K as a vector space over k and consider the linear transformations $\rho = \sigma - 1$ and $\tau = 1 + \sigma + \sigma^2 + \cdots + \sigma^{r-1}$, where r is the order of σ . Then the range of ρ is precisely the null space of τ .

Proof. Let $|K:k| = n$, and denote by R_0, R_1 and T_0, T_1 the null space and range of ρ and τ , respectively. Now $\rho(x) = 0$, if and only if $\sigma(x) = x$, so that $R_0 = k_\sigma$, the

fixed field of σ . Also, $|K:k_\sigma| = r$ so that $\dim(R_1) = n - (n/r)$. Furthermore, $\tau[\rho(x)] = 0$ identically so that $R_1 \leq T_0$. If we view K as a vector space over k_σ , τ becomes a linear functional on K/k_σ (in fact it is the trace of K/k_σ), and is not identically zero since the powers of σ are distinct and so, linearly independent. Thus, τ has rank 1 as a linear transformation of K/k_σ and so has rank n/r as a linear transformation of K/k . Consequently, $\dim T_0 = n - (n/r)$ and so $R_1 = T_0$. Theorem 1 is proved.

Theorem 1 gives, in effect, necessary and sufficient conditions for this equation

$$\sigma(x) - x = a \quad (1)$$

Proof.

$$\begin{aligned} \sigma(a * b) - (a * b) &= \sum_{1 \leq i < j \leq r} \sigma^i(a) \sigma^j(b) - \sum_{0 \leq i < j \leq r-1} \sigma^i(a) \sigma^j(b) \\ &= b[\sigma(a) + \cdots + \sigma^{r-1}(a)] - a[\sigma(b) + \cdots + \sigma^{r-1}(b)] \\ &= b[\tau(a) - a] - a[\tau(b) - b] \\ &= b\tau(a) - a\tau(b). \end{aligned}$$

This proves Theorem 2.

Theorem 2 allows us to solve Eq. (1) immediately. For, suppose $\tau(a) = 0$. Choose b as any element with $\tau(b) = 1$; then Theorem 2 gives

$$\sigma(b * a) - (b * a) = a.$$

Other solutions are found by adding elements of k_σ to one solution.

We note that whenever $\text{char}(K) \neq r$, we can choose $b = 1/r$, and the solution takes a particularly neat form:

$$x = \left(\frac{1}{r} * a\right) = \sum_{i=1}^{r-1} \frac{i}{r} \sigma^i(a). \quad (2)$$

3. Applications

We now confine our attention to finite fields of characteristic 2. Thus, let $K = GF(2^k)$, $k = GF(2)$. The Galois group is cyclic of order k in this case, and the automorphisms are $\sigma_l : x \rightarrow x^{2^l}$, $l = 0, 1, \dots, k-1$. The fixed

to have a solution in K ; i.e., Eq. (1) has a solution, if and only if $\tau(a) = 0$. We remark that if Eq. (1) holds, and $y \in k_\sigma$, then $\sigma(x + y) - (x + y) = a$, so that the set of solutions to Eq. (1) is an additive coset of k_σ in K .

But Theorem 1 is in no way constructive; it gives no hint as to what the solutions to Eq. (1) are. We now present a constructive proof of the sufficiency of the condition $\tau(a) = 0$ for Eq. (1) to have a solution. Letting $a, b \in K$, define

$$a * b = \sum_{0 \leq i < j \leq r-1} \sigma^i(a) \sigma^j(b)$$

Then we have

$$\text{Theorem 2. } \sigma(a * b) - (a * b) = b\tau(a) - a\tau(b)$$

field k_l of σ_l is $GF(2^{(l,k)})$. Theorem 1 reduces to the following:

Theorem 3. The equation $x^{2^l} + x = a$, $a \in GF(2^k)$, $l < k$, has either no roots or $2^{(l,k)}$ roots in $GF(2^k)$. It has $2^{(l,k)}$ roots, if and only if $\tau_l(a) = 0$, where τ_l is the trace of $GF(2^k)/GF(2^{(l,k)})$.

If $l = 1$, then of course we have the simple quadratic equation $x^2 + x = a$. From the remark at the end of section 2, we see that if k is odd, that a solution to the quadratic is given by

$$x = \sum_{\substack{1 \leq i \leq k-2 \\ i \text{ odd}}} a^{2^i}$$

For example if $k = 7$, and $\text{trace}(a) = 0$, $x = a^2 + a^8 + a^{32}$ is the required solution.

And these solutions are easy to mechanize. For, if the elements of $GF(2^k)$ are represented as k -tuples of zeros and ones, the operation $x \rightarrow x^2$ can be represented by a nonsingular $k \times k$ matrix S over $GF(2)$. Then if

$$T = \sum_{i=1,3,\dots,k-2} S^i$$

then $x = a \times T$ represents a solution to Eq. (1).

When k is even the situation is not so simple; for in this case $\tau(1) = 0$. Perhaps the easiest solution in this case is to generate $GF(2^k)$ by an irreducible polynomial p of trace 1 and degree k . Then in this representation the matrix B of the transformation $x \rightarrow xb$, where b is a root of p , is simply the companion matrix for p . In this case $x = a \cdot Q$ is a solution, where Q is the matrix given by

$$Q = \sum_{i=0}^{k-2} S^i (1 + B + \cdots + B^{i+1})$$

Both of these methods, but especially that given for k odd, require less computation than the methods described in SPS 37-39, Vol. IV, pp. 219-226.

N67 12145 E. Coding Theory: The Index of Comma Freedom In Iterative Codes

J. Stiffler

1. Introduction

Iteration is one method of constructing large error-correcting code dictionaries by combining several smaller ones (Ref. 7). One of the chief advantages of these codes is in the relative simplicity of the associated decoding algorithm. Generally, it is no more difficult to decode the iterated code than to decode each of the codes which were combined to produce it. Another feature of iterated codes to be demonstrated in this article is the propagation of the comma-free properties of the component codes. In particular, it will be shown that the index of comma freedom grows essentially as rapidly as the length of the code words in the process of iteration.

2. Iterated Codes

Let G_1 and G_2 be the generator matrices of two linear error-correcting codes having q^{k_1} and q^{k_2} words of n_1 and n_2 symbols per word, respectively, both defined over the field of q elements, $GF(q)$. Then the iterated code is the code generated by the Kronecker product $G_1 \times G_2$ of the two generators, G_1 and G_2 . The properties of iterated codes are summarized in the following theorem.

Theorem 1. If G_i generates a linear (n_i, k_i) error-correcting code over $GF(q)$, and if the minimum Hamming distance separating any two words in the code

is d_i , then the code generated by the Kronecker product $G_1 \times G_2$ has the dimension $(n_1 n_2, k_1 k_2)$ and has minimum distance at least $d_1 d_2$.

Proof. Consider an arbitrary linear combination of the rows of $G_1 \times G_2$. Because any word in the code generated by G_1 contains at least d_1 nonzero elements, any word in the code generated by $G_1 \times G_2$ must contain d_1 or more occurrences of some nonzero multiple of some word in the dictionary generated by G_2 . But since any word in the code generated by G_2 must contain at least d_2 nonzero elements, any word in the Kronecker product code must contain at least $d_1 d_2$ nonzero elements. Because no linear combination of the $k_1 k_2$ rows of $G_1 \times G_2$ produces the all-zeros vector, the dimension of $G_1 \times G_2$ must be $k_1 k_2$. Finally, the length of any word in the dictionary generated by $G_1 \times G_2$ is obviously $n_1 n_2$ and the theorem is proved.

3. The Index of Comma Freedom

Let D_1 be the dictionary generated by any generator G_1 containing the all-ones vector $(1, 1, \dots, 1)$, and let $D'_1 = D_1 + c_1$ be the coset of D_1 obtained by adding term-by-term over $GF(q)$ the vector $c_1 = (\alpha_1, \alpha_2, \dots, \alpha_{n_1})$ to each of the words of D_1 . Let D_2 and $D'_2 = D_2 + c_2$ be similarly defined in terms of G_2 (also containing the all-ones vector) and $c_2 = (\beta_1, \beta_2, \dots, \beta_{n_2})$. Finally, let D be the dictionary generated by $G_1 \times G_2$ and $D' = D + c$ its coset, where

$$\begin{aligned} c &= (\alpha_1 + c_2, \alpha_2 + c_2, \dots, \alpha_{n_1} + c_2) \\ &= (\alpha_1 + \beta_1, \alpha_1 + \beta_2, \dots, \alpha_1 + \beta_{n_2}, \alpha_2 \\ &\quad + \beta_1, \alpha_2 + \beta_2, \dots, \alpha_{n_1} + \beta_{n_2}) \end{aligned}$$

Using these definitions, we can prove the following theorem.

Theorem 2. If D'_1 has an index of comma freedom s_1 and D'_2 an index of comma freedom s_2 , then D' has an index of comma freedom s bounded by

$$s \geq \min(n_1 s_2, n_2 s_1)$$

Proof. The theorem can be proved quite easily upon observing the following two properties of any word w in D :

(1) w is of the form

$$w = x_{i_1} x_{i_2} \cdots x_{i_n}$$

where the x_i are words in D_2 .

(2) The symbols w_{in+j} , $i = 0, 1, \dots, n_1 - 1$ of the word $w = (w_1, w_2, \dots, w_{n_1 n_2})$ constitute a code word in D_1 for every w and every $j = 1, 2, \dots, n_2$. (Both of these statements simply reflect the fact that if a_i is a word in a linear code dictionary A defined over $GF(q)$, then αa_i is also, where α is an element in $GF(q)$.) As an almost immediate consequence of these two statements, we have for any word w' in D' the statements

(1') w' is of the form

$$w' = x'_{i_1}, x'_{i_2}, \dots, x'_{i_{n_1}}$$

where the x'_i are words in D'_2 .

(2') The symbols w'_{in+j} , $i = 0, 1, \dots, n_1 - 1$ of the word $w' = (w'_1, w'_2, \dots, w'_{n_1 n_2})$ constitute a code word in D'_1 for every w' and every $j = 1, 2, \dots, n_2$. (These statements follow from statements (1) and (2) upon making the addition observation that if $a_0 = (1, 1, \dots, 1)$ is a word in the linear dictionary A , then $a_i + \alpha a_0$ is also, for any word a_i in A and any element α in $GF(q)$.)

Now let w and w' both be words in D' , and consider any overlap of ww' beginning with the $(i+1)$ st symbol of w and ending with the i th symbol of w' . If $i \neq 0$, modulo n_2 , this overlap is a sequence of $n_1 n_2$ -tuples, all of which could occur as overlaps of words of D'_2 . Accordingly, all of these overlap words must differ in at least s_2 component positions from any word in D'_2 , and the overlap ww' must differ from any word in the dictionary D' in at least $n_1 s_2$ component positions. Similarly, if $i = 0$, modulo n_2 , ($i = \nu n_2$, $\nu \neq 0$) the symbols

$$w_{\nu n_2+j}, w_{(\nu+1)n_2+j}, \dots, w_{(n_1-1)n_2+j} w'_j w'_{n_2+j}, \dots, w'_{(\nu-1)n_2+j}$$

constitute, for each $j = 1, 2, \dots, n_2$, an n_1 -tuple which could occur as an overlap of two words from D'_1 . Thus, each of these $n_2 n_1$ -tuples must differ in at least s_1 positions from any word in D'_1 , and the corresponding overlap of ww' must differ from any word in the dictionary D' in at least $n_2 s_1$ positions. Since all nontrivial overlaps of any two words in D' have been accounted for, we have shown that

$$s \geq \min n_1 s_2, n_2 s_1$$

and the theorem is proved.

Notice that this proof is equally valid when the union of the dictionaries $D' + \alpha_1 a$, $D' + \alpha_2 a$, \dots , $D' + \alpha_q a$ is used rather than D' above, where D' is as previously de-

fined, $a = (1, 1, \dots, 1)$ is the all-ones $n_1 n_2$ -tuple, and α_i is the i th element in $GF(q)$. Thus, the Kronecker product construction can be used repeatedly, with a corresponding increase in the index of comma freedom at each step. In short, the index of comma freedom can be made to grow as rapidly as the word length, via the Kronecker product construction outlined here.

N67 12146

F. Digital Communication and Tracking: Calculation of Range-Clock Jitter

R. C. Tausworthe

1. Introduction

There are two effects in a ranging-clock tracking loop which must be taken into account, before an accurate analysis of clock-jitter for a ranging subsystem can be made. First, the RF carrier reference loop has jitter in it, and this degrades the ranging sideband power. Second, jitter in the clock loop itself causes a certain amount of range-code decorrelation which alters the clock-loop S-curve. Both of these effects degrade performance of the loop and raise ranging threshold.

2. Cascade-Loop Model of a Ranging Receiver

The receiver we consider is shown in Fig. 1; there is an RF carrier reference loop whose job it is to track the relatively slowly-changing phase components of the input (due to doppler, etc.), and there is a subsystem for extracting the clock component of the ranging code.

At the receiver input, an equivalent waveform of the following form

$$x_0 = A(2)^{1/2} \sin [\omega_0 t + d(t) + \psi(t)] + n_0(t) \quad (1)$$

is assumed, in which A is the rms signal amplitude; ω_0 is the VCO no-signal frequency; $d(t)$ is the slowly varying phase offset due to doppler, VCO drift, etc.; $\psi(t)$ is the range-code angle modulation lying outside the loop pass-band; and $n_0(t)$ is a wideband noise with spectral density N_0 over the band of interest (N_0 is the double-sided density).

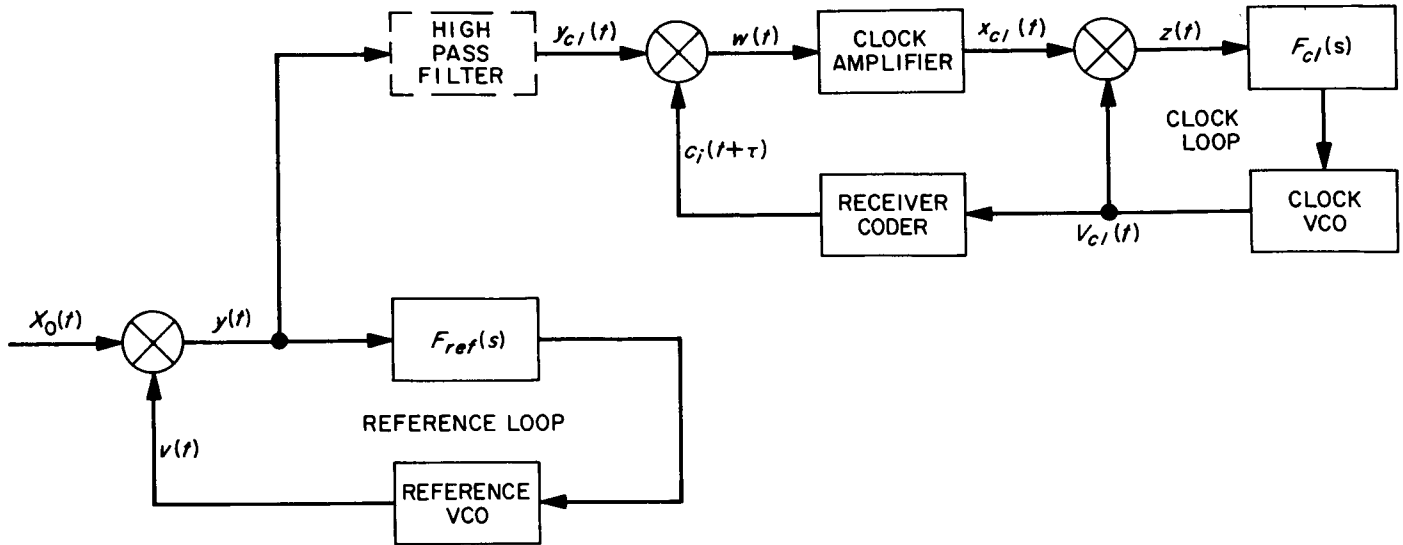


Fig. 1. Cascade loop model of the ranging receiver

The reference loop in the receiver is designed to track the doppler function $d(t)$, i.e., its voltage controlled oscillator (VCO) output is of the form

$$v(t) = (2)^{1/2} \cos [\omega_0 t + \hat{d}(t)] \quad (2)$$

and, thus, as a result, the phase detector output contains both the reference loop phase error $\phi_{ref} = d(t) - \hat{d}(t)$ as well as the information $\psi(t)$.

$$y(t) = A \cos \phi_{ref} \sin \psi + A \cos \psi_0 \sin \phi_{ref} + n(t) \quad (3)$$

The noise $n_0(t)$ is heterodyned to $n(t)$ at baseband by $v(t)$, so $n(t)$ has N_0 as its spectral density.

At this point, we suppose that ϕ_{ref} is a zero-mean Gaussian random process with variance a^2 , and that the code modulation angle is ψ_0 :

$$|\psi(t)| = \psi_0 \quad (4)$$

The reference loop filter $F_{ref}(s)$ is unable to respond to the high-frequency variations in $y(t)$, and thus, insofar as the reference loop is concerned, the receiver input could as well have been

$$x_{ref}(t) = (A \cos \psi_0) (2)^{1/2} \sin [\omega_0 t + d(t)] + n_0(t) \quad (5)$$

for then the phase detector output would have been

$$y_{ref}(t) = A \cos \psi_0 \sin \phi_{ref} + n(t) \quad (6)$$

which is the same as Eq. (3) with the high frequency term removed. The carrier reference loop can thus be considered separately, with an equivalent input power

$$A_{ref}^2 = A^2 \cos^2 \psi_0 \quad (7)$$

With this input, the reference loop phase error variance a^2 is given by

$$a^2 = \frac{N_0 \omega_{L(eq)} \Gamma_{ref}}{A^2 \cos^2 \psi_0 \gamma_{ref}^2} \quad (8)$$

in which Γ is the limiter performance factor; $\omega_{L(eq)}$ is the equivalent reference-loop bandwidth; and γ^2 is a function relating to the loop nonlinearity. Once a^2 is known, the variance of $\phi_{ref} \pmod{2\pi}$ can be computed directly. (See Ref. 8 for further details, especially pp. 58–59 for formulas.)

3. Range Clock Jitter

The input to the clock loop is a high-pass waveform; the high pass filter indicated in Fig. 1 is merely an algebraic convenience to avoid considering the low frequency terms of no consequence to the clock loop. That is, we need consider only

$$y_{cl}(t) = (A \cos \phi_{ref}) \sin \psi(t) + n(t) \quad (9)$$

The modulation, as we have indicated, is a binary waveform

$$\psi(t) = \psi_0 c(t) \quad (10)$$

where $c(t)$ is a binary unit-magnitude ranging code, $|c(t)| = 1$. Thus,

$$y_{cl}(t) = (A \sin \psi_0 \cos \phi_{ref}) c(t) + n(t) \quad (11)$$

The coder is generating one of the ranging receiver codes $c_i(t + \tau)$ in the standard fashion (Ref. 9) to be multiplied by $y_{cl}(t)$, which produces

$$w(t) = A_\psi \cos \phi_{ref} c(t) c_i(t + \tau) + n_1(t) \quad (12)$$

For convenience, we have put $A_\psi = A \sin \psi_0$. Further, $n_1(t)$ is $n(t) c_i(t + \tau)$, so because $n(t)$ is very wideband, the spectral density of $n_1(t)$ is essentially the same as that of $n(t)$ and $n_0(t)$, viz., N_0 .

The particular ranging codes we assume here are designed so that there is a clock-component in the multiplier output, i.e.,

$$c(t) c_i(t + \tau) = R_i(\tau) \text{sgn} [\sin(\omega_{cl} t)] + \text{wideband component} \quad (13)$$

The function $R_i(\tau)$ above is the envelope of the correlation between $c(t)$ and $c_i(t + \tau)$; it is depicted in Fig. 2 for a typical code. For convenience, we set $k_i = R_i(0)$ and $h_i = R_i(t_0)$.

The tuned clock amplifier essentially eliminates the wideband component and discards all but the first clock harmonic, so the input to the clock loop is

$$x_{cl}(t) = \left[\frac{4}{\pi} R_i(\tau) A_\psi \cos \phi_{ref} \right] \sin \omega_{cl} t + n_2(t) \quad (14)$$

The spectral density of $n_2(t)$ at ω_{cl} is still N_0 .

The clock VCO attempts to track the phase of the loop input

$$v_{cl}(t) = (2)^{1/2} \cos(\omega_{cl} t - \phi_{cl}) \quad (15)$$

which produces the following output at the clock-phase detector:

$$s(t) = \left(\frac{4}{\pi} k_i A_\psi \cos \phi_{ref} \right) \left[\frac{R_i(\tau)}{k_i} \sin \phi_{cl} \right] + n_3(t) \quad (16)$$

The code symbol period is derived from the clock frequency; and in fact, if t_0 denotes one symbol time,

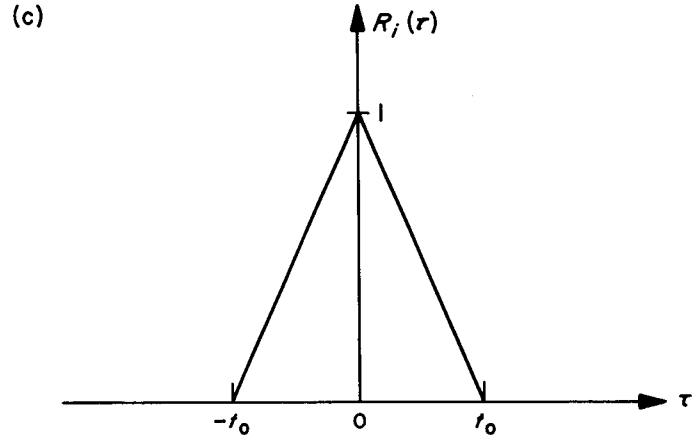
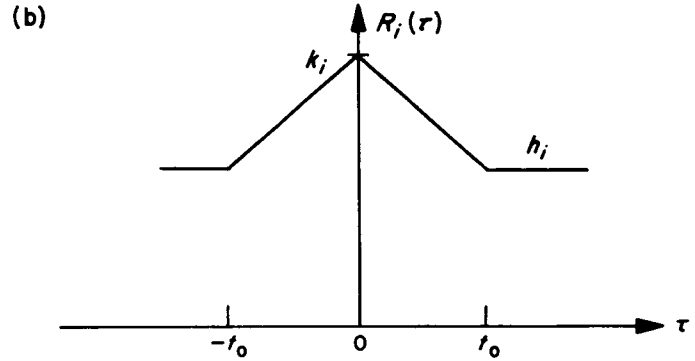
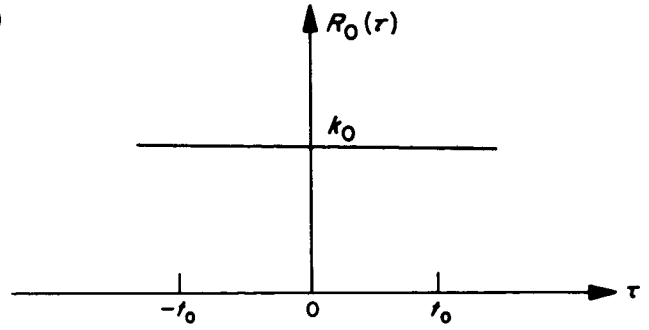


Fig. 2. Envelope of correlation between $c(t)$ and $c_i(t + \tau)$: (a) correlation envelope during initial clock acquisition; (b) correlation envelope during component acquisition; (c) full code correlation envelope

$$\omega_{cl} = \pi/t_0 \quad (17)$$

Thus the offset between the incoming code and the local one takes on some mean value τ_0 , but jitters about somewhat.

$$\tau = \tau_0 + \left(\frac{t_0}{\pi} \right) \phi_{cl} \quad (18)$$

As a result

$$z(t) = \left(\frac{4}{\pi} k_i A_\psi \cos \phi_{ref} \right) \left[\frac{R_i \left(\tau_0 + \frac{t_0}{\pi} \phi_{cl} \right) \sin \phi_{cl}}{k_i} \right] + n_3(t) \quad (19)$$

Eq. (19) now points out the effects to be analyzed quite clearly: the effective power in the ranging sideband is decreased by $\cos \phi_{ref}$ and the S-curve is altered from $\sin \phi_{cl}$ to the expression

$$\left[R_i \left(\tau_0 + \frac{t_0}{\pi} \phi_{cl} \right) \sin \phi_{cl} \right] / k_i.$$

4. Computing the Effects of Reference Jitter

The mean value of $\cos \phi$ when ϕ is a zero mean Gaussian variate with variance a^2 is

$$\begin{aligned} E[\cos \phi_{ref}] &= \int_{-\infty}^{+\infty} \cos \phi \frac{1}{a(2\pi)^{1/2}} e^{-\phi^2/2a^2} d\phi \\ &= e^{-a^2/2} \end{aligned} \quad (20)$$

and its variance is

$$\begin{aligned} E[\cos^2 \phi - \mu^2] &= \int_{-\infty}^{+\infty} \cos^2 \phi \frac{1}{a(2\pi)^{1/2}} e^{-\phi^2/2a^2} d\phi - \mu^2 \\ &= \frac{1}{2}(1 - e^{-a^2})^2 \end{aligned} \quad (21)$$

The autocorrelation function of $\cos \phi$, viz. $R_{\cos \phi}(\tau)$, is readily found by applying Price's theorem and the result is

$$\begin{aligned} R_{\cos \phi}(\tau) &= e^{-a^2} \cosh R_\phi(\tau) \\ &= e^{-a^2} \left[1 + 2 \sinh^2 \frac{R_\phi(\tau)}{2} \right] \end{aligned} \quad (22)$$

The spectral density of $\cos \phi$ is thus one with a spike at the origin, and a density about this spike produced by random variations in ϕ . For ω in a neighborhood of the origin, the spectrum of $\cos \phi$ is approximately

$$S_{\cos \phi}(j\omega) = e^{-a^2} \delta(f) + 2e^{-a^2} \int_{-\infty}^{+\infty} \sinh^2 \frac{R_\phi(\tau)}{2} d\tau \quad (23)$$

Although the integral can be numerically evaluated when ϕ comes from a second-order loop, the result is approximately the same if we assume $R_\phi(\tau)$ takes the relatively simpler form

$$R_\phi(\tau) = a^2 e^{-2\omega_L |\tau|} \quad (24)$$

The spectral density of $\cos \phi$ is thus approximately

$$\begin{aligned} S_{\cos \phi}(j\omega) &= e^{-a^2} \delta(f) + 4e^{-a^2} \int_0^\infty \sinh^2(a^2/2) e^{-2\omega_L \tau} d\tau \\ &= e^{-a^2} [\delta(f) + \text{Cinh}(a^2)/\omega_L] \end{aligned} \quad (25)$$

for ω in the immediate neighborhood of ω_{cl} ; $\text{Cinh}(x)$ is the hyperbolic cosine integral

$$\begin{aligned} \text{Cinh}(x) = \int_0^x \frac{\cosh t - 1}{t} dt \approx x^2 e^x (0.2327 - 0.1985x + 0.0774x^2 - 0.01678x^3 \\ + 0.002076x^4 - 0.0001366x^5 + 0.000003706x^6) \end{aligned} \quad (26)$$

To find the spectrum at the input to the clock loop, one merely convolves $S_{\cos \phi}(j\omega)$ with that of the pure clock signal [Eq. (14)]; the spike portion of Eq. (25) contributes to the clock signal, while the density portion adds to the noise.

As a result, the input to the clock loop has an equivalent power

$$A_{cl}^2 = \frac{8}{\pi^2} k_i^2 A^2 \sin^2 \psi_0 e^{-a^2} \quad (27)$$

and an equivalent noise density approximately equal to

$$\begin{aligned} N_{cl} &= N_0 + \frac{8}{\pi^2 w_{L(eq)}} A^2 \sin^2 \psi_0 k_i^2 e^{-a^2} \text{Cinh}(a^2) \\ &= N_0 \left\{ 1 + \frac{8\Gamma_{ref}}{\pi^2 \gamma_{ref}^2} \tan^2 \psi_0 k_i^2 a^{-2} e^{-a^2} \text{Cinh}(a^2) \right\} \end{aligned} \quad (28)$$

5. Computation of Clock-Loop Jitter

If the clock jitter ϕ_{cl} is assumed to be a zero mean Gaussian process with variance b^2 , then b^2 must satisfy (Ref. 8)

$$\begin{aligned} b^2 &= \frac{\pi^2 N_{cl} w_{cl(eq)} \Gamma_{cl}}{8 [A^2 k_i^2 \sin^2 \psi_0 e^{-a^2}] \gamma_{cl}^2} \\ &= \left(\frac{\pi^2}{8k_i^2} \right) \left(\frac{N_{cl}}{N_0} \right) \left(\frac{w_{cl(eq)}}{w_{L(eq)}} \right) \left(\frac{\Gamma_{cl}}{\Gamma_{ref}} \right) \left(\frac{\gamma_{ref}^2}{\gamma_{cl}^2} \right) (\cot^2 \psi_0) a^2 e^{a^2} \end{aligned} \quad (29)$$

the variance σ_{cl}^2 is related to b^2 through Eq. 9-12 of Ref. 8.

All the functions above are known at this point, except γ_{cl} and η_{cl} , which then determine $w_{cl(eq)}$, and allow solutions to Eq. (28) to be found.

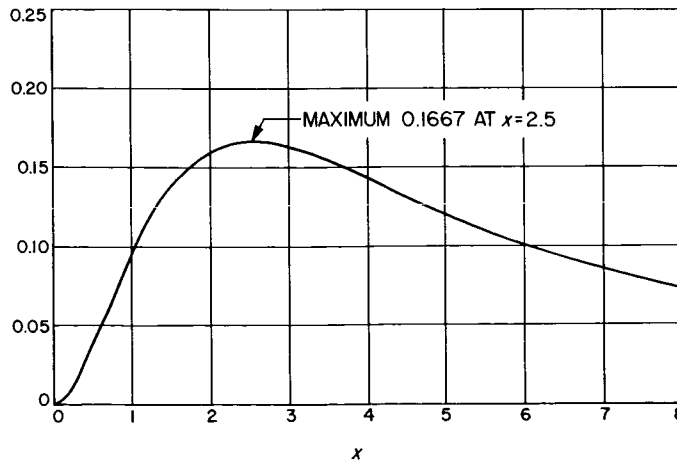


Fig. 3. Plot of $e^{-x} \text{Cinh}(x)$

In the acquisition process, there are three distinct types of loop behavior: the first is during clock acquisition, or later, when a component is not yet acquired, when $R_i(\tau)$ is constant (Fig. 2(a)); the clock loop tracks the same as loops previously treated (Ref. 8). However, when a component is found, there is increased correlation, and the S-curve is altered by the function shown in Fig. 2(b). Finally, when the code is completely acquired, the S-curve is altered by the function in Fig. 2(c). Mathematically, we can treat these the same by computing the performance as if the S-curve were

$$f(\phi_{cl}) = \begin{cases} [\lambda + (1 - \lambda)(1 - |\phi_{cl}/\pi|)] \sin \phi_{cl} & \text{for } |\phi_{cl}| \leq \pi \\ \lambda \sin \phi_{cl} & |\phi_{cl}| > \pi \end{cases} \quad (30)$$

The value of λ is k_i/h_i [Fig. 2(b)].

Given $f(\phi_{cl})$, then η_{cl} and γ_{cl}^2 are computed by the formulas (9-4) and (9-15) of Ref. 8:

$$\begin{aligned} \eta_{cl} &= \frac{1}{b^2} \int_{-\infty}^{+\infty} \phi_{cl} f(\phi_{cl}) p(\phi_{cl}) d\phi_{cl} \\ \gamma_{cl}^2 &+ \frac{1}{b^2} \int_{-\infty}^{+\infty} f^2(\phi_{cl}) p(\phi_{cl}) d\phi_{cl} \end{aligned} \quad (31)$$

The results are

$$\begin{aligned} \eta_{cl} &= \lambda e^{-b^2/2} + (1 - \lambda) I_{1,1,1}(b) \\ \gamma_{cl} &= \lambda^2 b^{-2} e^{-b^2} \sinh b^2 + 2\lambda(1 - \lambda) I_{0,1,2}(b) + (1 - \lambda)^2 I_{0,2,2}(b) \end{aligned} \quad (32)$$

in terms of an integral $I_{l,m,n}(x)$ given by

$$I_{l,m,n}(x) = \frac{1}{x^3} \left(\frac{2}{\pi} \right)^{1/2} \int_0^\pi t^l \left(1 - \frac{t}{\pi} \right)^m \sin^n t e^{-t^2/2x^2} dt \quad (33)$$

Plots of $I_{1,1,1}(x)$, $I_{0,1,2}(x)$, and $I_{0,2,2}(x)$ appear in Fig. 4. Excellent approximations over the range shown are

$$I_{1,1,1}(b) = \exp(-0.496b - 0.856b^2 + 0.329b^3 - 0.039b^4)$$

$$I_{0,1,2}(b) = \exp(-0.606b - 1.159b^2 + 0.517b^3 - 0.069b^4)$$

$$I_{0,2,2}(b) = \exp(-1.220b - 0.925b^2 + 0.492b^3 - 0.071b^4) \quad (34)$$

At this point all of the functions in Eq. (29) are evaluated; variances b^2 and the corresponding σ_{cl}^2 are readily found by computer solutions.

6. An Example

As an illustration to the foregoing analysis, we here compute the clock-loop performance of the Mark I rang-

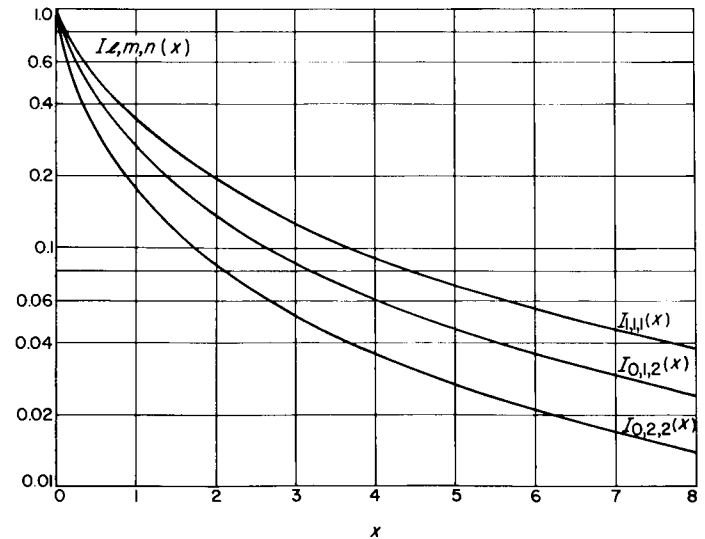


Fig. 4. Graphs of the functions $I_{1,1,1}(x)$, $I_{0,1,2}(x)$, and $I_{0,2,2}(x)$

ing system (SPS 37-29, Vol. III, p. 12-19). Specifically, we assume that both the carrier and clock loops have loop filters of the form

$$F(s) = \frac{1 + \tau_2 s}{1 + \tau_1 s} \quad (35)$$

with $\tau_2 \ll \tau_1$. At a design power level² $P_0 = kTw_{L_0}$, the damping factor of each loop is set $\zeta_0 = 0.707$. The modulation index is set so that

$$\frac{P_{\text{carr}}}{P_{\text{clock}}} = \frac{w_{L_0(\text{carr})}}{w_{K_0(\text{clock})}} = \frac{12}{0.8} = 15. \quad (36)$$

²This definition of design point is not the same as threshold as defined in Ref. 8; threshold there was defined to be $A_0^2 = N_0 w_L = kT/2 w_{L_0}$.

The remainder of the loop parameters is given in Table 4, and the acquisition profile is displayed in Fig. 5. The resulting theoretical performance is illustrated in Fig. 6 for each stage in the acquisition procedure. Notice particularly at very low signal levels that better tracking results with 77.5%-53% correlation than with the full code (100%-0%). However, this is not the case over the useful operating range. In the worst case, i.e., during first component acquisition, about 12-13 db separate the performance of the carrier loop from that of the clock loop in terms of input power.

Table 4. Ranging receiver parameters

Parameter	Carrier loop	Clock loop
W_{L_0}	12.0 Hz	0.8 Hz
ζ_0	0.707	0.707
b_H	2200 Hz	2200 Hz
P_0/kTw_{L_0}	0.0 db	0.0 db
P/P_{total}	-0.280 db	-12.040 db
Correlation profile		
Component	Correlation	
	k_i	h_i
Clock only	0.53	0.53
First component unacquired	0.28	0.28
First component acquired	0.53	0.28
Second component acquired	0.77	0.53
Total code acquired	1.00	0.00

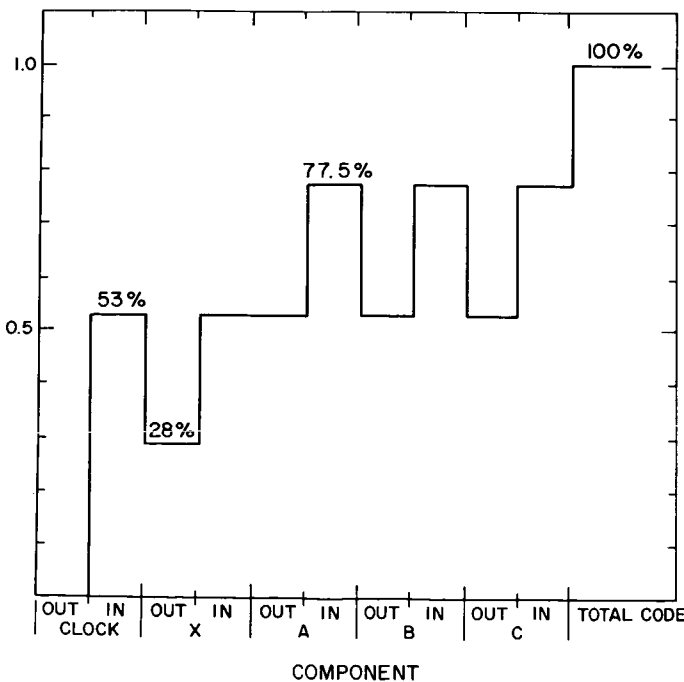


Fig. 5. Acquisition profile of the Mark I ranging system

N67 12147

G. Data Compression: A Lower Bound for Epsilon Entropy

E. Posner and H. Rumsey, Jr.

1. Summary

This article gives a lower bound for the asymptotic behavior of the epsilon entropy of a Gaussian stochastic process on the unit interval under square-error fidelity criterion. The lower bound is apparently weaker than the one previously obtained, but is easier to work with.

2. Introduction

The epsilon entropy of a probabilistic metric space has been discussed in recent issues of this Summary (SPS 37-34, -36, -38, Vol. IV, pp. 292-296, 313-323, 248-251, respectively). Essentially, the epsilon entropy is the minimum number of bits necessary to describe experimental outcomes within ϵ . In our case, the experiment consists in observing the sample function of a Gaussian process for one second. The fidelity or distance is the mean square distance. A lower bound previously obtained for the epsilon entropy of a Gaussian process X of mean 0 has been obtained previously. It is

$$H_\epsilon(X) \geq \log \left[\frac{1}{\mu S \left(0, \frac{\epsilon}{(2)^{1/2}} \right)} \right], \quad (1)$$

where μ denotes probability, and $S(0, \epsilon/2)$ denotes the sphere of radius $\epsilon/2$ about the origin in the space $L_2[0, 1]$ of square-integrable functions on the unit interval.

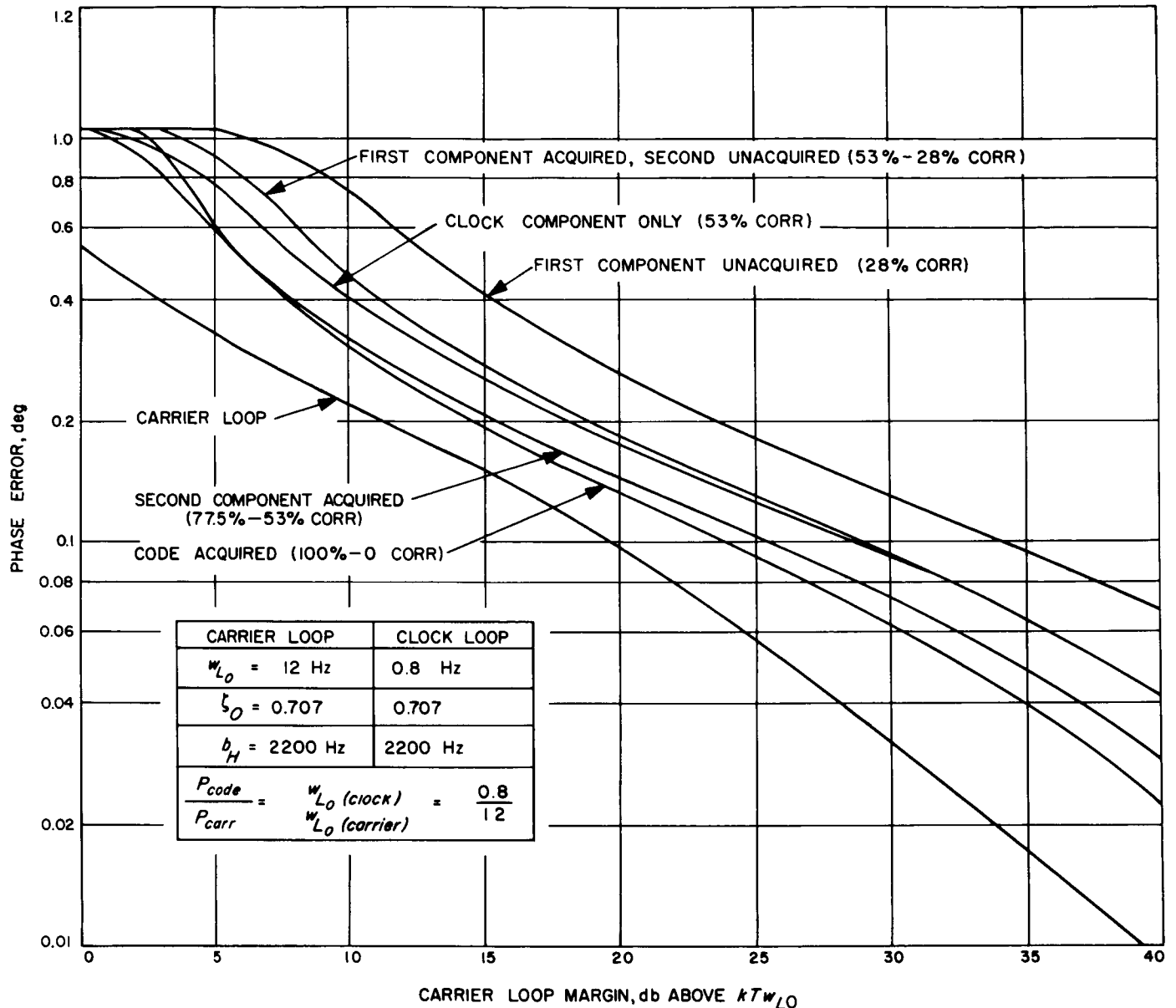


Fig. 6. Performance of carrier and clock loops during and after acquisition

In this note, another lower bound for $H_\epsilon(X)$ is given, valid as $\epsilon \rightarrow 0$. This lower bound is worse than Eq. (1) in many cases, but has the advantage of being easier to compute.

3. Yaglom's Bound

In Ref. 10, p. 108, a result of A. M. Yaglom is given. Define for the purposes of this article the "Russian ϵ -entropy" $H_\epsilon^R(X)$ of a Gaussian process X to be the infimum of the mutual information $I(X, Y)$ taken over the class of all L_2 -stochastic processes Y such that the

joint distribution of (X, Y) on $L_2[0, 1] \times L_2[0, 1]$ has the property that

$$E \left(\int_{t=0}^1 (X - Y)^2 dt \right) \leq \epsilon.$$

The Russian definition is motivated by the desire to prove channel capacity theorems of Shannon type, rather than by data compression. Nevertheless, it will be observed in the next section that $H_\epsilon^R(X) \leq H_\epsilon(X)$.

Let $\sigma_1^2 \geq \sigma_2^2 \geq \dots$ be the eigenvalues of the Gaussian process on $[0, 1]$. That is,

$$X(t) \sim \sum_{n=1}^{\infty} \sigma_n y_n \phi_n(t), \quad (2)$$

where $\{y_n\}$ are independent unit normal random variables, and the $\phi_n(t)$ are of unit norm and orthogonal on $[0, 1]$. Yaglom's result is that

$$H_\epsilon^R(X) = \frac{1}{2} \sum_{\sigma_n^2 > \epsilon^2} \log \left(\frac{\sigma_n^2}{\theta^2} \right), \quad (3)$$

where θ is chosen to satisfy

$$\sum_{n=1}^{\infty} \min(\theta^2, \sigma_n^2) = \epsilon^2. \quad (4)$$

4. Relation between H_ϵ and H_ϵ^R

Suppose we have an ϵ -partition of $X = L_2[0, 1]$, covering all of X except for a set of probability 0, by open sets of diameter $\leq \epsilon$ such that the entropy of the partition is close to $H_\epsilon(X)$, which is the infimum of the entropies of all ϵ -partitions. Let X denote the random variable given by choosing a fixed point y_i in each set U_i of the partition. That is, for points x in the i th set U_i of the partition, Y takes the value y_i . In other words, the joint distribution on $L_2 \times L_2$ is given by assigning probability 0 to sets of the form $(U_i, \{y_j\})$, $j \neq i$, and probability $\mu(A)$ to sets of the form $(A, \{y_i\})$, where $A \subset U_i$.

Since $\text{diam } U_i \leq \epsilon$,

$$\int_0^1 (X - Y)^2 dt \leq \epsilon,$$

and Y is one of the processes occurring in Yaglom's definition. Now it is readily verifiable that for this choice of Y ,

$$I(X, Y) = - \sum_{i=1}^{\infty} \mu(U_i) \log \mu(U_i). \quad (5)$$

Hence, the sum given by Eq. (5) is at least equal to $H_\epsilon^R(X)$. Consequently, $H_\epsilon(X) \geq H_\epsilon^R(X)$, as promised.

5. Calculation of the Lower Bound

We have now proved

$$H_\epsilon(X) \geq \frac{1}{2} \sum_{\sigma_n^2 > \theta^2} \log \left(\frac{\sigma_n^2}{\theta^2} \right), \quad (6)$$

where θ satisfies Eq. (4).

For the Wiener process, we have

$$\sigma_n^2 = \frac{1}{\pi^2 (n - 1/2)^2} \sim \frac{1}{\pi^2 n^2}.$$

The parameter θ is readily computed to satisfy

$$\theta \sim \frac{1}{N\pi}, \quad (7)$$

where N satisfies

$$N \sim \frac{2}{\pi^2 \epsilon^2}. \quad (8)$$

Hence,

$$H_\epsilon(X) \geq \frac{1}{2} \sum_{n=1}^{2/\pi^2 \epsilon^2} \log \frac{N^2}{n^2} = \log \frac{N^N}{N!} \sim N = \frac{2}{\pi^2 \epsilon^2}. \quad (9)$$

Since we already had

$$H_\epsilon(X) \geq \frac{1}{4\epsilon^2} \quad (10)$$

and $1/4 > 2/\pi^2$, Eq. (9) is not as good as Eq. (10) for the Wiener process. However, since we do not know $S(0, \epsilon)$ for other processes, Eq. (6) gives new information, even if it is not the best bound.

For example, if X is the band-limited Gaussian process with constant spectral density on $[-\gamma, \gamma]$, it is known (Ref. 11, p. 218) that

$$\sigma_n^2 \sim 2\pi \left(\frac{\gamma}{4} \right)^{2n+1} / (n!)^2 \quad (11)$$

Carrying through the calculations given by Eq. (6) yields

$$H_\epsilon(X) \gtrsim \frac{1}{2} \frac{\log^2 \left(\frac{1}{\epsilon} \right)}{\log \log \left(\frac{1}{\epsilon} \right)} \quad (12)$$

On the other hand, our previous results using product partitions (communicate by sending information only about the coefficients y_n in Eq. (2)) gave

$$H_\epsilon(X) \leq \frac{1}{2} \frac{\log^2\left(\frac{1}{\epsilon}\right)}{\log \log\left(\frac{1}{\epsilon}\right)}. \quad (13)$$

Combining Eqs. (12) and (13) yields

$$H_\epsilon(X) \sim \frac{1}{2} \frac{\log^2\left(\frac{1}{\epsilon}\right)}{\log \log\left(\frac{1}{\epsilon}\right)} \quad (14)$$

for a band limited process $X(t)$ with constant spectral density on any interval symmetric about 0. Eq. (14) is the first (nonfinite dimensional) Gaussian process X whose epsilon entropy has been determined asymptotically. This is also the first infinite-dimensional class of processes for which it is known that the data compression scheme which transmits only the coefficients in the Karhunen expansion is asymptotically optimum, i.e., gives an average number of bits which is asymptotically minimum.

N67 12148

H. Information Processing: A Bivariate Goodness-of-Fit Test

T. Pitcher³

1. Introduction

In a recent issue of this Summary (SPS 37-38, Vol. III, pp. 34-35), the problem of loss-of-lock estimation was considered when an extra "out-of-lock indicator" channel is available. Bivariate extreme-value theory was used in that reference to estimate error and erasure probabilities in these *Mariner*-type command detectors. Since one must fit a bivariate distribution with a bivariate extreme-value distribution, one would like a bivariate goodness-of-fit test.

This article derives a new test for this purpose. The test proposed here is similar to the Kolmogorov-Smirnov univariate test, which has been used at JPL in extreme-value

applications to single-channel command systems, such as on *Ranger*. The present test is not, however, distribution-free, since a transformation must first be performed which depends on the alleged distribution. The transformations are simple enough, however, to make the test useful in bivariate extreme-value theory.

2. The Transformation

We wish to test whether or not the joint density of the random variables X and Y is given by the known function f . Consider the new variables

$$\tilde{X} = \int_{-\infty}^{\infty} \int_{-\infty}^x f(u, v) du dv$$

$$\tilde{Y} = \int_{-\infty}^Y f(X, v) dv / \int_{-\infty}^{\infty} f(X, v) dv.$$

Here \tilde{X} is the marginal distribution of X , and Y is the conditional distribution of \tilde{Y} given X . It is known that \tilde{X} and \tilde{Y} are independent and uniformly distributed on $[0, 1]$. To see this, let $F^{-1}(x)$ and $H(x, y)$ be the functions defined by

$$\int_{-\infty}^{\infty} \int_{-\infty}^{F^{-1}(x)} f(u, v) du dv = x$$

$$\int_{-\infty}^{H(x, y)} f(x, v) dv / \int_{-\infty}^{\infty} f(x, v) dv = y;$$

then

$$\begin{aligned} P(\tilde{X} \leq a, \tilde{Y} \leq b) &= P[X \leq F^{-1}(a), Y \leq H(X, b)] \\ &= \int_{-\infty}^{F^{-1}(a)} \left[\int_{-\infty}^{H(x, b)} f(u, v) dv \right] du \\ &= \int_{-\infty}^{F^{-1}(a)} b \int_{-\infty}^{\infty} f(u, v) dv du = ab, \end{aligned}$$

as required.

3. Empirical Distributions

If we set

$$\phi(x, y) = \begin{cases} 1 & \text{if } x \leq y \\ 0 & \text{if } x > y \end{cases}$$

then the empirical joint distribution of \tilde{X} and \tilde{Y} based on n independent samples (x_i, y_i) , $i = 1, \dots, n$ is

$$F_n(x, y) = \frac{1}{n} \sum_{i=1}^n \phi(x_i, x) \phi(y_i, y)$$

³Consultant, University of Southern California, Mathematics Department, Los Angeles, California.

and the corresponding marginal distributions are

$$M_n^{(1)}(x) = \frac{1}{n} \sum_{i=1}^n \phi(x_i, x)$$

$$M_n^{(2)}(y) = \frac{1}{n} \sum_{i=1}^n \phi(y_i, y).$$

The empirical function

$$\begin{aligned} G_n(x, y) &= (n)^{1/2} F_n(x, y) - x M_n^{(2)}(y) - y M_n^{(1)}(x) + xy \\ &= \frac{1}{(n)^{1/2}} \sum_{i=1}^n [\phi(x_i, x) - x] [\phi(y_i, y) - y] \end{aligned}$$

converges in law to a Gaussian random variable $\xi(x, y)$ for each (x, y) , by the central limit theorem. We have

$$E[G_n(x, y)] = 0;$$

$$\begin{aligned} E[G_n(x, y) G_n(u, v)] &= \frac{1}{n} \sum_{i=1}^n \sum_{j=1}^n E\{[\phi(x_i, x) - x] [\phi(y_i, y) - y] [\phi(x_j, u) - u] [\phi(y_j, v) - v]\} \\ &= \frac{1}{n} \sum_{i=1}^n E\{[\phi(x_i, x) - x] [\phi(x_i, u) - u]\} E\{[\phi(y_i, y) - y] [\phi(y_i, v) - v]\} \\ &= [\min(x, u) - xu] [\min(y, v) - yv]. \end{aligned}$$

It can be shown, as in the one-dimensional case, that the asymptotic distribution of $G_n(x, y)$ is that of the two-dimensional Gaussian process having the mean and variance computed above (Ref. 12).

If we let $\psi_1(x)$ and $\psi_2(y)$ be independent versions of the "Brownian bridge," i.e. Gaussian processes with mean 0 and variance

$$E[\psi_i(s) \psi_i(t)] = \min(s, t) - st$$

then we can represent ξ as

$$\xi(x, y) = \psi_1(x) \psi_2(y).$$

4. Goodness-of-Fit Criterion

If we now take, as the criterion of goodness-of-fit,

$$I_n = \int_0^1 \int_0^1 G_n^p(x, y) w(x) w(y) dx dy$$

its asymptotic distribution, under the hypothesis that X and Y are independent and uniform, can be proved to be that of

$$\begin{aligned} &\int_0^1 \int_0^1 \xi^p(x, y) w(x) w(y) dx dy \\ &= \left(\int_0^1 \psi_1^p(x) w(x) dx \right) \left(\int_0^1 \psi_2^p(y) w(y) dy \right). \end{aligned}$$

Since the terms in the product on the right are independent, this distribution can be computed for any p and w

for which the corresponding one-dimensional distributions have been computed.

Similarly, if we take

$$S_n = \sup_{x, y} |G_n(x, y)|$$

as the criterion of goodness-of-fit, then its asymptotic distribution will be that of

$$\begin{aligned} \sup_{x, y} |\xi(x, y)| &= \sup_{x, y} [|\psi_1(x)| |\psi_2(y)|] \\ &= [\sup_x |\psi_1(x)|] [\sup_y |\psi_2(y)|] \end{aligned}$$

which can be computed from the (known) distribution of $\sup_x |\psi_1(x)|$.

5. Dependence on the Distribution

If we perform the inverse transformation

$$(\bar{x}, \bar{y}) = [F^{-1}(x), H(x, y)]$$

we get

$$\int_0^1 \int_0^1 |G_n(x, y)|^p dx dy = \int_{-\infty}^{\infty} \int_{-\infty}^{\infty} |\bar{G}_n(\bar{x}, \bar{y})| d\bar{x} d\bar{y}$$

where

$$\bar{G}_n(\bar{x}, \bar{y}) = \frac{1}{n} \sum_{i=1}^n [\phi(\bar{x}_i, \bar{x}) - F(\bar{x})] [\phi(\bar{y}_i, \bar{y}) - H^{-1}(\bar{x}, \bar{y})].$$

The new density function $A(\bar{x}, \bar{y})$ is given by

$$A(\bar{x}, \bar{y}) = \frac{f[\bar{F}(\bar{x}), \bar{y}] \int_{-\infty}^{\infty} f(\bar{x}, v) dv}{\int_{-\infty}^{\infty} f[F(\bar{x}), v] dv}$$

In other words, G_n transforms into the same function in terms of the new distribution, but the new density function $A(\bar{x}, \bar{y})$ is not equal to $f(\bar{x}, \bar{y})$ unless $F(\bar{x}) = \bar{x}$. The same comment holds for the sup criterion. This would seem to indicate that x should be chosen as the variable whose marginal distribution is the more nearly uniform of x and y .

N67 12149

1. Communication Systems Development: Probability Distributions and Error Rates in Spacecraft Receivers

W. Lindsey

1. Introduction

In present-day deep-space communications systems, bit rates used to communicate with the spacecraft, i.e., the command link, are normally around one bit/second. Further, the reliability with which the transmitted commands are detected must be high. Thus, the probability with which the data demodulator may err is usually set around one error in 10^5 . In practice, the mechanized version of the data demodulator must be tested prior to actual flight and its performance verified before it becomes a part of the overall system.

Due to the low error probability, the time required to establish experimentally whether or not the theoretically specified error rate is obtained at the specified signal-to-noise ratio (SNR) is on the order of several hours. If it is further desired to establish an actual experimental curve of error probability versus SNR, the amount of test time becomes prohibitive (not to mention the large amounts of equipment, manpower, etc., required). One approach which has been used in the past to reduce the amount of test time employs the application of Gumbel's

extreme value theory (Refs. 13, 14, and 15) to the problem of estimating low error probabilities.

Another approach (to be considered here) which would further reduce the testing time is that of developing analytical expressions which specify the required probability distributions in terms of the system parameters. The parameters of this distribution could, therefore, be measured in the laboratory and used to determine the error probability.

2. System Model

In a *Mariner* type of communication system, two channels are employed in the transmission of command data to the spacecraft. One channel is used for conveying the command data, and the second channel is used to convey timing information for operation of the cross-correlators, viz., bit sync and subcarrier phase sync. This timing information is derived in the spacecraft by means of a double loop-tracking device. The inner loop of this double loop is a phase-locked loop which tracks the subcarrier while the outer loop is forced to follow the sync code. Subcarrier phase sync is therefore obtained from the voltage-controlled oscillator (VCO) output of this device, and bit sync is obtained by placing a state detector on the output of the code generator in the outer loop. Since these two timing references are derived in the presence of noise, one expects the performance of the data detector to be degraded below that obtained if perfect synchronization were established.

Thus, the sample statistics in the presence of timing errors are no longer fitted by the standard Gaussian distribution but rather become a mixture of two probability distributions. For low error rates, the "tail" of this distribution becomes important, and it is here that the theory of extreme value statistics becomes of aid when this distribution is unknown. Of course, the amplitude distribution may be measured; however, conventional measurements of the amplitude distribution again present problems in test time, unless the shape of the distribution is known exclusive of the parameters which define it. Here, we present this probability distribution and show that it is characterized by two parameters which are easily measured in the laboratory, thus saving test time over that provided by the method of extreme-value statistics. We further use this result to specify the probability that the data detector will err.

In the implementation of a phase-coherent detector which uses cross-correlation techniques and the double

loop-tracking device, an accurate subcarrier phase reference is more important in ensuring reliable operation of the data detector than is the bit sync reference. From a detection theoretic point of view, this is obvious. Consequently, we shall neglect in the derivation any degradation in the performance of the data detector due to a noisy bit sync. In the region of interest, this may be considered to be a higher order effect and neglected, as is done in the case of double frequency terms.

3. Differenced Cross-Correlator Output Statistics⁴

Before we present the derivation of the differenced cross-correlator output statistics $p(q)$, we define several basic communication parameters which serve to characterize the distribution $p(q)$ and the performance of the receiver, i.e., the probability of error. First, there is the SNR $R = E/N_0 = ST/N_0$. This parameter represents the ratio of the received signal energy E to the one-sided spectral density of the noise. The parameter T denotes the duration of the data bits. The signal cross-correlation coefficient λ is a measure of the degree of sameness of the two transmitted signals $w_1(t)$ and $w_2(t)$, i.e.,

$$\lambda = \frac{1}{E} \int_0^T w_1(t) w_2(t) dt \quad (1)$$

where

$$E = \int_0^T w_k^2(t) dt = ST; k = 1, 2. \quad (2)$$

For the case of phase-shift keying, $w_1(t) = -w_2(t)$ and $\lambda = -1$. Another convenient parameter which arises in the analysis is given by $\rho = 2(1 - \lambda)R$.

In order to shorten the subsequent material, we shall draw heavily upon previous results (Refs. 16 and 17). The approach which we shall take is to make use of the method of conditional probabilities; i.e., we shall develop expressions for the particular parameter, distribution, or moment of interest, conditioned by the fact that the system phase error is fixed at ϕ rad. Thus, by averaging over the condition, which is random, we easily determine the behavior of interest as the system phase error takes on all possible values.

⁴By differenced-correlator outputs, we mean the value obtained by sampling (at the conclusion of the signaling interval) the output of the correlator which is matched to $w_1(t)$ and the correlator which is matched to $w_2(t)$ and differencing the result. If, however, $w_1(t) = -w_2(t)$, only one correlator is required.

We begin our analysis by specifying the differenced-statistics at the output of the cross-correlators given a fixed value of ϕ . Given the waveform $y(t)$, we are interested in determining the probability density of the difference

$$q = \int_0^T y(t) [w_1(t) - w_2(t)] dt \quad (3)$$

for it is this difference upon which a decision is made. If $q > 0$, we announce w_1 and if $q < 0$, we announce w_2 .

Since, for a fixed ϕ , the input to the cross-correlator is Gaussian, the output of the cross-correlator is also Gaussian. In fact, the normalized-conditional output statistics of the cross-correlator differences, contingent upon the phase error being ϕ rad and the signal $x_1(t)$ being transmitted, are characterized by

$$p(q_1|\phi) = \frac{1}{(2\pi)^{1/2}} \exp \left[-\frac{(q_1 - (\rho)^{1/2} \cos \phi)^2}{2} \right] \quad (4)$$

In the presence of noise only, the normalized-conditional output statistics are characterized by

$$p(q_2|\phi) = \frac{1}{(2\pi)^{1/2}} \exp(-q_2^2/2) = p(q_2) \quad (5)$$

and, naturally, the output statistics are independent of the system phase error.

The probability distribution of the phase error is important in specifying the differenced-correlator output statistics and the performance of the receiver. It is well known that the response distribution of a phase-locked loop is highly dependent on the filter which is placed in the loop (Refs. 18 and 19). In particular, the nonlinear response of a phase-locked loop tracking a sinusoid in the presence of white Gaussian noise is known only for a few special cases, viz., the so-called first-order loop (Refs. 18 and 19) and the loop which contains an RC-circuit loop filter (Ref. 18).

In practice, the loop filter of greatest interest for carrier tracking is the proportional-plus-integral-control type; however, the response distribution for the loop phase-error is known only in an approximate form (Ref. 20). Furthermore, experimental evidence shows that the phase-error distribution obtained using the proportional-plus-integral-control type of loop filter is closely related

(for SNR where phase-locked loops are generally expected to work) to the response distribution given in Ref. 21. The resemblance, of course, is because the region of operation is usually in the vicinity where linear phase-locked loop theory applies, viz., the region where the variance of the phase-error is approximately the reciprocal of the SNR existing in the bandwidth of the tracking loop. Consequently, in what follows, we base the receiver phase-error distribution on the results which are available in Refs. 14 and 15.

Thus, for the probability density of the phase-error ϕ , we postulate:

$$p(\phi) = \frac{\exp(\alpha \cos \phi)}{2\pi I_0(\alpha)}; \quad |\phi| \leq \pi \quad (6)$$

where $I_0(x)$ is the imaginary Bessel function of zero order and argument x . The parameter α , characterizing the performance of the subcarrier tracking loop, represents the SNR existing in the tracking loop, viz.,

$$\alpha = \frac{2P}{N_0 W_L} \quad (7)$$

where P is the power in the sync channel, N_0 is the single-sided noise spectral density, and W_L is the bandwidth of

the carrier tracking loop defined from the linear phase-locked loop theory, i.e.,

$$W_L = \frac{1}{2\pi j} \int_{-j\infty}^{j\infty} |H(s)|^2 ds \quad (8)$$

where $H(s)$ is the closed loop transfer function.

Further, α gives some indication of the degree of coherence between the observed carrier phase and the estimated carrier phase. If, for example, $\alpha = 0$, the probability distribution of the phase measurement is uniformly distributed. At the other extreme, i.e., $\alpha = \infty$, the measurement is perfect, and the probability distribution of the phase measurement is a delta function centered at the true value of observed carrier phase. This corresponds to the perfectly synchronized case. For sufficiently large signal strength, the tracking loop may be linearized, and the distribution $p(\phi)$ becomes Gaussian-distributed with zero mean and variance α^{-1} .

Thus, we have postulated a phase error distribution which checks with linear phase-locked loop theory at one extreme and which is intuitively satisfying at the other extreme of weak signal conditions.

The output statistics $p(q_1)$ may be obtained by averaging over the distribution of the phase error. Carrying out this averaging yields

$$\begin{aligned} p(q_1) &= \int_{-\pi}^{\pi} p(\phi) p(q_1, \phi) d\phi \\ &= \frac{\exp\left[-\frac{2q_1^2 + \rho}{4}\right]}{(2\pi)^{1/2} 2\pi I_0(\alpha)} \sum_{k=-\infty}^{\infty} I_k(\rho/4) I_{2k}(\alpha + (\rho)^{1/2} q_1) \exp(j\pi k) \end{aligned} \quad (9)$$

where $I_k(x)$ is the modified Bessel function of order k and of argument x .

Illustrated in Figs. 7 and 8 are the differenced-correlator output statistics for various values of the parameter α and for two values of ρ . The values of ρ were chosen such that the error rate is 10^{-3} (typical for telemetry systems) and 10^{-5} (typical for command systems) when the timing noise is zero, i.e., perfect phase synchronization. From either of these figures, we notice the following results:

- (1) The distribution $p(q)$ does not depend on the parameter α , if the input to the detector is only noise. In this case, $p(q)$ is always Gaussian.
- (2) Under the hypothesis that signal plus noise is present, we see that $p(q)$ is highly dependent on

the value of α , or equivalently, the reference signal timing error.

- (3) The distribution $p(q)$ is bimodal for small α , i.e., large timing errors. This property may be attributed to the mixing of two probability distributions.
- (4) The distribution $p(q)$ is asymmetric for large values of α , i.e., small timing errors. This asymmetry has been experimentally observed by J. C. Ashlock of JPL.
- (5) For $\alpha = \infty$, $p(q)$ is Gaussian with mean $(\rho)^{1/2}$. This corresponds to the condition of zero timing noise or perfect time synchronization.
- (6) For $0 < \alpha < \infty$, the mean of $p(q)$ is less than $(\rho)^{1/2}$.

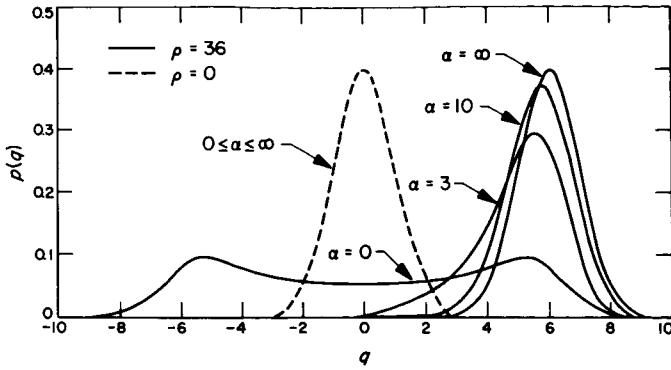


Fig. 7. Output statistics, $p(q)$ vs q for various values of, α ($P_E = 10^{-3}$)

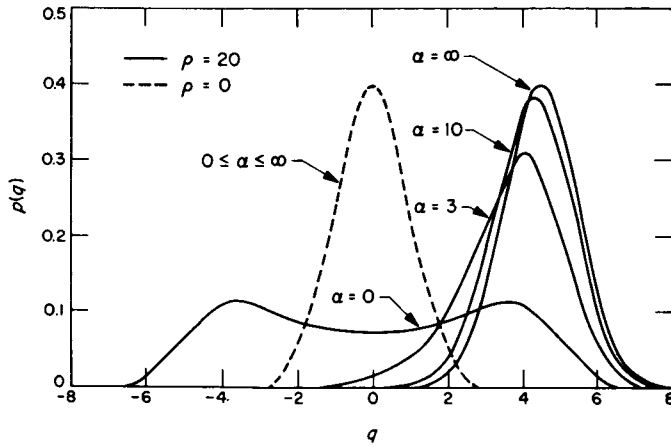


Fig. 8. Output statistics, $p(q)$ vs q for various values of, α ($P_E = 10^{-5}$)

In practice, the moments of this distribution are of interest. In particular, the mean of the differenced-cross-correlator output may be computed using Eqs. (4) and (6), and the fact that the mean is given by

$$\bar{q}_1 = \int_{-\infty}^{\infty} \int_{-\pi}^{\pi} q_1 p(q_1 | \phi) p(\phi) d\phi dq_1. \quad (10)$$

Substituting Eqs. (6) and (9) into Eq. (10) and carrying out the necessary integration gives

$$\bar{q}_1 = (\rho)^{1/2} \frac{I_1(\alpha)}{I_0(\alpha)}. \quad (11)$$

The mean-squared value of the differenced-cross-correlator output may be determined from

$$\bar{q}_1^2 = \int_{-\infty}^{\infty} \int_{-\pi}^{\pi} q_1^2 p(\phi) p(q_1 | \phi) d\phi dq_1. \quad (12)$$

Substituting Eqs. (4) and (6) into Eq. (12) and carrying out the necessary integration gives

$$\bar{q}_1^2 = 1 + \frac{\rho}{2} + \frac{\rho}{2} \left(\frac{I_2(\alpha)}{I_0(\alpha)} \right). \quad (13)$$

Thus, the variance of the distribution $p(q_1)$ may be obtained from Eqs. (11) and (13), i.e.,

$$\sigma_{q_1}^2 = 1 + \frac{\rho}{2} + \frac{\rho}{2} \left(\frac{I_2(\alpha)}{I_0(\alpha)} \right) - \rho \left(\frac{I_1(\alpha)}{I_0(\alpha)} \right)^2. \quad (14)$$

In practice, the expressions for the moments may be used in the laboratory to check a particular design.

Fig. 9 shows the effects on the normalized mean \bar{q}_1 and the variance $\sigma_{q_1}^2$ of the distribution $p(q_1)$ as a function of the tracking loop SNR α . The normalization is with respect to the values of the mean and variance of $p(q_1)$, when there is zero timing error. For SNR in the tracking loop greater than $\alpha = 10$ db, the mean and variance of $p(q_1)$ are relatively unaffected. This result may be used

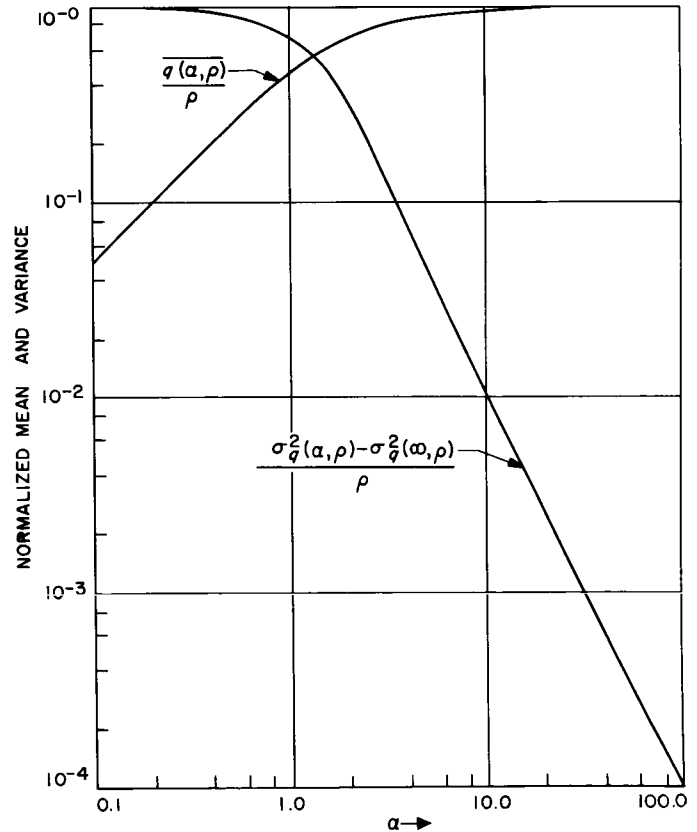


Fig. 9. Normalized mean and variance vs SNR and tracking loop

in setting power levels when designing phase-measuring tracking loops.

4. Performance of the Data Detector

We now turn to the problem of specifying the probability that a set of cross-correlators will err in making a decision. The method which we shall employ is that of computing the conditional error probability; the condition being that the system phase error is fixed to ϕ rad. Assuming, without loss of generality that $x_1(t)$ was transmitted, the probability of error is one minus the probability that the decision made is correct. The probability that the decision is correct is the probability that the output of that filter matched to signal $x_2(t)$ is less than the output of the filter matched to $x_1(t)$. This probability is given by

$$P_E(\phi) = 1 - \int_{-\infty}^{\infty} p(q_1|\phi) dq_1 \int_{-\infty}^{q_1} p(q_2|\phi) dq_2. \quad (15)$$

Substituting Eqs. (4) and (5) into Eq. (15) and simplifying the result yields

$$P_E(\phi) = \frac{1}{2\pi} \int_{(\beta)^{1/2} \cos \phi}^{\infty} \exp\left(-\frac{x^2}{2}\right) dx = E \operatorname{erfc}[\beta^{1/2} \cos \phi] \quad (16)$$

where $\beta = \rho/2 = R(1 - \lambda)$. The average error rate is easily obtained by averaging Eq. (16) over the phase error distribution $p(\phi)$ given in Eq. (6), i.e.,

$$P_E = \frac{1}{\pi} \int_0^{\pi} \frac{\exp(\alpha \cos \phi)}{I_0(\alpha)} E \operatorname{erfc}[\beta^{1/2} \cos \phi] d\phi. \quad (17)$$

The integrals in Eq. (17) may be evaluated (Refs. 16 and 17); however, a closed-form result, at this point, seems to be extremely difficult.

Plotted in Fig. 10 is the probability that the detector will err versus R for different values of α . Notice the "bottoming" of the error rate as R increases. This says

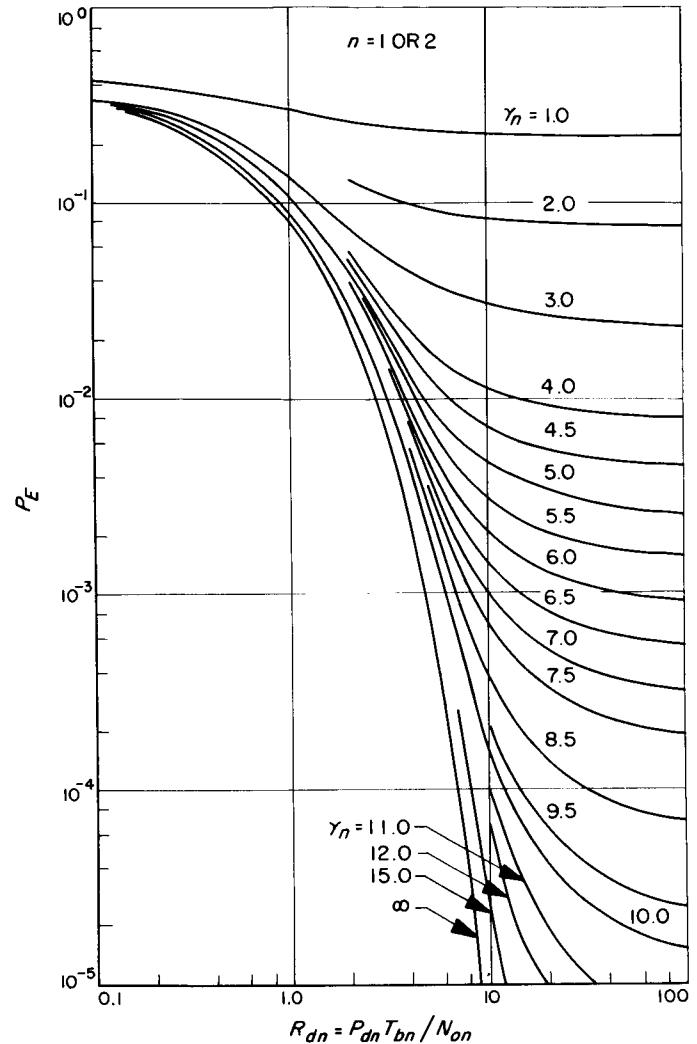


Fig. 10. P_E vs $R = ST/N_0$ for various values of SNR and carrier tracking loop

that, as more energy is placed into the information bearing signal, the ultimate performance of the system is governed by the SNR in the subcarrier tracking loop.

References

1. Ryser, H. J., *Combinatorial Mathematics*, John Wiley & Sons, Inc., 1963.
2. Hall, M., Jr., "A Survey of Difference Sets," *Proceedings American Mathematical Society*, Vol. 7, 1956.
3. Riordan, J., *An Introduction to Combinatorial Analysis*, John Wiley & Sons, Inc., New York, 1958.
4. Rota, G., "The Number of Partitions of a Set," *American Mathematical Monthly* 71, pp. 498-504, 1964.

References (Cont'd)

5. Ryser, H. J., *Combinatorial Mathematics*, The Mathematical Association of America, 1963.
6. Zariski, A., and Samuel, P., *Commutative Algebra*, Vol. 1, Van Nostrand Princeton, 1959.
7. Peterson, W. W., *Error Correcting Codes*, the M.I.T. Press and John Wiley & Sons, Inc., New York, pp. 81-85, 1961.
8. Tausworthe, Robert C., *Theory and Practical Design of Phase-Locked Receivers*, Technical Report 32-819, Vol. I, Jet Propulsion Laboratory, Pasadena, Calif., February 15, 1966.
9. Titsworth, Robert C., "Optimal Ranging Codes," *IEEE Transactions PTG-SET*, Vol. SET-10 No. 1, March 1964.
10. Kolmogorov, A. N., "Theorie der Nachrichtenübermittlung," *Arbeiten Zur Informationstheorie*, Vol. I, pp. 91-116, 1957.
11. Widom, Harold, "Asymptotic Behavior of the Eigenvalues of Certain Integral Equations, II," *Archive for Rational Mechanics and Analysis*, Vol. 17, pp. 215-229, 1964.
12. Prokhorov, Yu. V., "Convergence of Random Processes and Limit Theorems in Probability Theory," in translation, *Theory of Probability and its Applications*, Vol. 1, pp. 157-214; (esp. sect. 2.4), 1956.
13. Gumbel, E. J., "Statistical Theory of Extreme Values and Some Practical Applications," *National Bureau of Standard Applied Mathematics Series*, No. 33, 1954.
14. Posner, E. C., "The Application of Extreme-Value Theory to Error-Free Communication," *Technometrics*, Vol. 7, No. 4, November 1965.
15. Ashlock, J. C., and Posner, E. C., "The Application of the Statistical Theory of Extreme Values to Spacecraft Receivers," *Proceedings of the National Telemetry Conference*, Prudential Center, Boston, Mass., May 10-12, 1966.
16. Lindsey, W. C., "Optimal Design of One-Way and Two-Way Coherent Communication Links," *IEEE Transactions on Communication Technology*, August 1966.
17. Lindsey, W. C., "Phase-Shift-Keyed Signal Detection With Noisy Reference Signals," *IEEE Transactions on Aerospace and Electronics Systems*, Vol. AES-2, No. 4, pp. 393-402, July 1966.
18. Tikhonov, V. I., "Influence of Noise on Phase-Locked Oscillator Operation," *Avtomatika i Telemekhanika*, Akademya Nauk SSSR, Vol. 20, September 1959; "Phase-Lock Automatic Frequency Control Operation in the Presence of Noise," *Avtomatika i Telemekhanika*, Akademya Nauk, SSSR, Vol. 21, p. 301, March 1960.
19. Viterbi, A. J., "Phase-Locked Loop Dynamics in the Presence of Noise by Fokker-Planck Techniques," *Proceedings of the IEEE*, pp. 1737-1753, December 1963.
20. Charles, F. J., and Lindsey, W. C., "Some Analytical and Experimental Phase-Locked Loop Results For Low Signal-to-Noise Ratios," *Proceedings of the IEEE*, September 1966.
21. Lindsey, W. C., and Charles, F. J., "A Model Distribution for the Phase Error in Second Order Phase-Locked Loops," *IEEE Transactions on Communication Technology*, October 1966.